



Ph.D.
**“APPLIED SCIENCES TO WELLNESS
AND SUSTAINABILITY”**

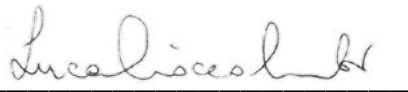
Cycle XXXVI
2020-2023

**Improvement of Environmental and
Energetic Performance of Waste Treatment
Facilities**

Disciplinary Scientific Sector: ING-IND/09

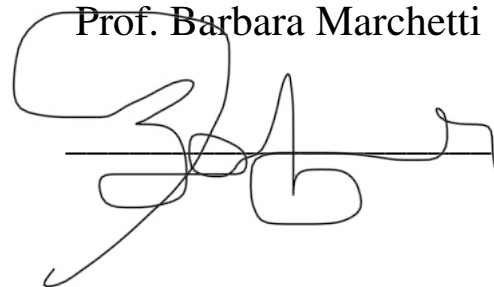
Tutor

Prof. Luca Cioccolanti



Co-Tutor

Prof. Barbara Marchetti



Ph.D. Candidate

Giovanni Biancini



ABSTRACT

The objective of this thesis is to contribute to the existing literature on waste processing by examining innovative approaches that can be implemented in both small-scale facilities and larger waste-to-energy power plants. The enhancement of the environmental and energetic efficiency of treatment facilities is associated with two significant challenges in the field. These challenges include minimising the amount of non-recyclable materials that are sent to landfills at the end of their useful life, as well as implementing sustainable methods for treating the wastewaters and leachates generated during the waste treatment process. It is expected that the volume of residual municipal solid waste streams would escalate in the coming years, posing a significant challenge to the lifespan of landfills. The economic viability of centralised waste treatment is frequently impeded by the substantial expenses linked to the transportation of waste to dedicated facilities, which can concurrently lead to the emission of extra pollutants. Consequently, there is an increasing interest on the notion of decentralised waste treatments. In addition, there is a considerable amount of residual municipal solid waste that is produced in mechanical and biological treatment plant that is sent to nearby landfills, generating different criticalities. First, both the landfill lifetime and the soil usage are negatively affected by the continuum waste disposal until there is no more space. Secondly, the unrecovered material mixture is not valorised for energy production, either electrical or thermal, representing a real energy loss. Similar considerations can be made regarding wastewater treatment plants, where liquid waste is channelled for the purpose of undergoing purification treatment before being ultimately released into the surrounding ecology. The implementation of bioremediation technologies offers a viable and promising sustainable alternative to wastewater treatment plants, as it has the potential to mitigate the effects of liquid waste. Consequently, the ideas put forward in this work are intended for implementation in the context of local waste treatment, and are the following ones:

- The gasification of municipal solid wastes and its integration with various energy systems is being explored to optimise the utilisation of residual waste and reduce the reliance on landfills for waste disposal. Their gasification can be used to solve this issue. The amount of waste sent to landfill would be considered lower the energy recovered might be used directly to cover the consumption of the mechanical-biological treatment unit or sell to the grid and lastly, the thermal power could be distributed with a district heating network system. From the economic perspective, the gasification system can provide additional revenues, like avoided cost for treating externally the RDF, like sending it to energy intensive industries

(steel, clinker), treat further waste but having the same exploit pace of the landfill, and generate electricity and heat that is remunerated according to market prices.

- The paradigms of a green circular economy foster the reutilization of the waste into new resources like biofuels. Biofuels can be obtained in other ways in the field of waste treatment. Biomass pyrolysis may increase the performance of the process especially if integrated to large scale thermal waste treatments.
- Wastewaters represents another critical aspect to consider in the design of novel and sustainable treatment solutions. The application of microalgae in the bioremediation of wastewater and leachates produced in these facilities, with the subsequent utilisation of the biomass for the production biofuel production, is being investigated.

The detailed discussion of the literature concerning waste gasification is reported in Chapter 3. Then, in Chapter 4, the investigation of the potential energy that can be recovered by such system is done by realising a thermodynamic model in Aspen Plus of the gasification unit and syngas combustion. Different codes have been written to simulate the design and off-design performance of three power system units, involving traditional Rankine cycle and high temperature organic Rankine cycles (ORC), as well as supercritical CO₂ (sCO₂) Brayton cycles in Matlab environment. The codes written are reported in the Appendix I at the end of the thesis. For each power unit, an additional study is defined for assessing the size of a potential district heating network (DHN), that can be reverted also for centralised cooling by means of adsorption chillers.

In the Chapter 5 and Chapter 6, the focus is pointed to liquid biofuel generation. First, in Chapter 5, a transient 0D model of the fast biomass pyrolysis is modelled in Matlab and validated according to literature models. The model addresses the composition of the pyrolysis gas containing condensable (tars) and incondensable elements, by considering variations of the mass flow rates and the heat supplied. The code, available in Appendix II, is suitable for successive improvements when the experimental data obtained in a dedicated pilot plant will be available. The pyrolysis model is done in collaboration with the Mälardalens University (MDU) of Sweden.

Similarly, Chapter 6 is focused on the application of the microalga *Scenedesmus obliquus* for biofuel production from a synthetic growing medium obtained from the wastewater composition collected in the waste treatment facility of the case studio. The investigation is carried out by a set of different laboratory analyses conducted in collaboration with the Marche Polytechnic University (UNIVPM). The growth behaviour of *Scenedesmus obliquus* has been characterized in terms of concentration, dry mass, optical density, and lipid composition. Appendix III reports the images collected during one of three consecutive experimental analyses.

In Chapter 7 the life cycle assessment methodology is applied to a real treatment facility operating in Italy, described in Chapter 2, used as a case studio. The environmental analysis points out different aspects of the benefits brought by the integration of renewable energy and residual municipal solid waste gasification. The studies are supported by the data of the utilities usage, energy production and liquid/residual waste composition.

To Eleonora

SUMMARY

ABSTRACT	II
LIST OF FIGURES	XI
LIST OF FIGURES (appendix)	XV
LIST OF TABLES	XVIII
CHAPTER 1 General Introduction	1
1.1 The Issue of Waste Treatment Systems	1
1.2 Objective of the research and research questions	6
1.3 Pyrolysis and gasification for waste valorisation	7
1.4 Biofuel production from biomass pyrolysis	13
1.5 Microalgae implementation.....	17
1.6 Environmental footprint assessment by means of Life Cycle Assessment methodology ...	20
1.7 Conclusions	23
Abbreviations	23
CHAPTER 2 DESCRIPTION OF THE WASTE TREATMENT FACILITY	25
2.1 Waste treatment system.....	25
2.2 Environmental emissions of the facility	28
2.2.1 Gas Emissions	28
2.2.2 Liquid Emissions.....	29
2.2.3 Soil Emissions.....	31
2.3 CHP unit and biogas generation	32
2.4 Mechanical-biological treatment unit.....	32
2.5 Preliminary power plant assessment with gasification.....	36
2.6 Conclusions	37
Abbreviations	37

CHAPTER 3 STATE OF ART OF GASIFICATION AND THERMODINAMIC MODELLING 38

3.1 Gasification of MSW..... 38

3.1.1 Introduction..... 38

3.2 Gasification Models 51

3.3 Materials and methods..... 53

3.3.1 Model description 53

3.4 Results and discussions 60

3.4.1 Model Validation 60

3.4.2 Syngas production from the composting facility 67

3.4.3 Sensitivity Analysis..... 69

3.5 Conclusions 77

Nomenclature 77

CHAPTER 4 COMBINED COOLING, HEATING AND POWER GENERATION FROM RMSW GASIFICATION 81

4.1 Introduction 81

4.2 Modelling of the systems and their components 84

4.2.1 The Integrated Treatment system..... 85

4.2.2 Gasification and Combustion section 85

4.2.3 Power systems..... 87

4.2.4 The district heating and cooling network (DHCN)..... 98

4.3 Results 101

4.3.1 Power cycle comparison 101

4.3.2 Sensitivity Analysis with DHN..... 107

4.3.3 Sensitivity analysis with users' demand 110

4.4 Conclusions 114

Nomenclature 115

CHAPTER 5 INTEGRATION OF BIOMASS PYROLYSIS..... 119

5.1	Introduction	119
5.2	Pilot Plant Configuration.....	120
5.3	Problem Statement	122
5.4	Methodology	123
5.4.1	Pyrolysis kinetics	123
5.4.2	Matlab Model.....	127
5.5	Result and Discussions.....	130
5.5.1	Model Validation	130
5.5.2	Time Extension	136
5.5.3	Mass rate sensitivity.....	138
5.5.4	Upscaling and integration into the gasification system	140
5.6	Conclusions	140
	Nomenclature	143
	Abbreviations	144
	Subscripts.....	145
	Greek letters	145
CHAPTER 6	MICROALGAE HARVESTING FOR BIOFUEL PRODUCTION	146
6.1	Introduction	146
6.2	Materials and Methods	147
6.2.1	Leachate and Wastewaters	147
6.2.2	Medium Preparation.....	147
6.2.3	Laboratory Equipment	148
6.2.4	Gas Chromatography	153
6.2.5	Numerical Model	155
6.3	Results and Discussion.....	160
6.3.1	Experimental campaign April-May 2022	160
6.3.2	Experimental campaign November 2022- February 2023	161

6.3.3	Lipid Analysis R1-R2-R3	167
6.3.4	Estimation of biofuel production	169
6.3.5	Numerical analysis	169
6.4	Discussion	171
6.5	Conclusions	172
	Nomenclature	172
	Abbreviations	173
	Subscripts	174
	Greek letters	174
CHAPTER 7	Life Cycle Assessment of the municipal solid waste treatment facility	175
7.1	Introduction	175
7.2	Materials and Methods	176
7.2.1	System Description	176
7.2.2	Goal and scope	176
7.2.3	System Boundaries.....	177
7.2.4	Inventory analysis	178
7.2.5	Impact categories and Life Cycle Impact Assessment.....	181
7.3	Results and discussions	182
7.3.1	Base case Scenario	183
7.3.2	Sensitivity Analysis.....	187
7.3.3	Photovoltaic implementation	189
7.3.4	Gasification process implementation	191
7.4	Conclusions	196
	Nomenclature	196
	CONCLUSIONS AND FUTURE WORKS	199
	ACKNOWLEDGEMENTS.....	202
	APPENDIX I: MATLAB CODES FOR POWER CYCLES	203

APPENDIX II: MATLAB CODES FOR WOOD PYROLYSIS.....	234
APPENDIX III: MICROALGAE GROWTH IN LABORATORY	248
APPENDIX IV: LIST OF PAPERS	321
APPENDIX V: LIST OF SOFTWARE	323
REFERENCES	324

LIST OF FIGURES

Fig. 1-1. Waste composition from composting facilities in Italy [11]. The colours represent different European waste codes (EWC). Image taken from [39].	5
Fig. 1-2. Microalgae products chain value in the market [95].	18
Fig. 2-1. Overview of the waste treatment facility under analysis, with detailed infographics of the relevant sections.	27
Fig. 2-2. Pictures of the different sections in the facility. a) MBT unit, b) anaerobic digesters, c) volumetric dome, d) aerobic stabilisation shed, e) scrubbers and f) sanitary landfill.	28
Fig. 2-3. Material and energy flows in a standard composting facility (a), and with MBT implementation (b) [138].	32
Fig. 3-1. Scheme of the gasification process developed in Aspen Plus.	53
Fig. 3-2. Flowsheet of the Gasifier. In grey colour are reported the main sections: pyrolysis (for material decomposition), air inlet, ethylene, tar and other compounds formation, combustor, and gasification reactors. Two additional utility parts are present: one for the assessment of syngas dry composition through measurement and another for verifying the overall heat balance.	55
Fig. 3-3. Flowsheet for the assessment of the Heat of Reaction for reactions R8, R9, R10.	56
Fig. 3-4. Modelling approach of the gasifier.	58
Fig. 3-5. Validation results of the model for Plastics and Biomass feedstock, including average error at the bottom. The intensity of its greyscale expresses the normalised error.	63
Fig. 3-6. Deviation of the model compared to the experimental results for waste plastics (above) and biomass (below). In the latter case, tars and Ethylene exceed the range of the histogram plot.	64
Fig. 3-7. Influence of the ER and F on the optimized variables of the model.	66
Fig. 3-8. Influence of the ER and F on the calculator blocks variables of the model.	67
Fig. 3-9. Results of the model for the waste material produced in the MBT system.	68
Fig. 3-10. F vs. HHV logarithmic trend. The points are taken from Table 3-7.	70
Fig. 3-11. Interpolating Surface for C_{uncomb} [176].	71
Fig. 3-12. Interpolating Surface for C_{gasif} . [176].	71
Fig. 3-13. Interpolating Surface for T_{R6app} . [176].	72
Fig. 3-14. Interpolating Surface for T_{R6app} . [176].	72
Fig. 3-15. Interpolating Surface for $C-C_2H_4$.	72
Fig. 3-16. Interpolating Surface for $H-C_2H_4$.	73

Fig. 3-17. Interpolating Surface for C-Tar.....	73
Fig. 3-18. Interpolating Surface for H-Tar.....	73
Fig. 3-19. Model results for the gasification of the different residual wastes produced in the three MBT facilities [32]	76
Fig. 4-1. Scheme of the modelling framework with the relevant sections.....	84
Fig. 4-2. Overview of the general process layout including gasification and power generation.....	85
Fig. 4-3. Flowsheet used for the syngas combustion.	86
Fig. 4-4. The considered types and layouts of the three types of power systems are associated to seven units.	88
Fig. 4-5. The main parameters of the solvers used for the power plants in MATLAB.	89
Fig. 4-6. Scheme of the ST power plant solver.....	91
Fig. 4-7. T-s diagram of: a) Toluene; b) MM; and c) MDM [xxx].....	92
Fig. 4-8. Solver schematics for ORC.	94
Fig. 4-9. Solver schematics for sCO ₂ Brayton Cycle.....	97
Fig. 4-10. T-s diagram of the ST power plant for the CS1 feedstock.	101
Fig. 4-11. T-s Diagrams of the different power units.	103
Fig. 4-12. Overall conversion efficiencies referred to the feedstock's chemical energy, for CS1 and CS2.	106
Fig. 4-13. Overall conversion efficiencies referred to the feedstock's chemical energy, for CS1 and CS2, for the sensitivity scenario.	109
Fig. 5-1. Circulating fluidized bed boiler (CFB). Image taken from Google Earth of one the Mälarenergi boilers [227], [228].	121
Fig. 5-2. Picture of the Pilot Plant (a) and its axonometric view (b).	121
Fig. 5-3. Side view of the Pilot Plant and list of the various components.	122
Fig. 5-4. Sketch of the pyrolysis model coded in Matlab.	128
Fig. 5-5. RMSE minimization with SQP algorithm, down to 17.25%.	132
Fig. 5-6. The concentration of the various solid wood constituents at 4.05 s, 8.10 s, and 12.15 s. .	134
Fig. 5-7. Concentrations of the CO, CH ₄ , LVG, xylan, and temperature profile at 4.05 s, 8.10 s, and 12.15 s.....	135
Fig. 5-8. Temperature (magenta) and concentration profile of cellulose (red), CO, CH ₄ , xylan, and LVG (blue) in the extended simulation.	136
Fig. 5-9. Mass flow rate (green), concentrations (red and blue), and temperature (magenta) profiles were obtained with the model.....	139

Fig. 5-10. Conceptual layout of the integrated gasification system including the pyrolysis section.	140
Fig. 5-11. Detailed process layout of the system including the pyrolysis section.	141
Fig. 5-12. Output of the simulation with reference to the ORC cycle in a) design condition and at b) 75% load, and for the biomass pyrolysis. The c) temperature of the reactor and d) overall liquid yield are reported.	142
Fig. 6-1. On the left, <i>S. obliquus</i> strains. On the right: solution A flask status after 3% v/v dilution (Solution “A”).....	148
Fig. 6-2. Biobench PBR. Dimensions reported in mm.	149
Fig. 6-3. Incubator a) and laboratory refrigerator b).....	150
Fig. 6-4. Laboratory equipment used for measuring the microalga growth: a) optical microscope, b) Burker cell counter chamber, c) filter ramp, d) ARGO TCN 50 oven, e) spectrophotometer UV-30.	151
Fig. 6-5. Other equipment used for lipid extraction. Rotavapor BUCHI R-210 on the left, centrifuge UNIVERSAL 320R on the right.	153
Fig. 6-6. Example of calibration for C18:1 and C18:2.	155
Fig. 6-7. Process comparison between <i>S. obliquus</i> oil and SFO.	156
Fig. 6-8. Aspen Plus flowsheet of the biodiesel from microalgae production process.	157
Fig. 6-9. Examples of lipids, TG form of C17:1 on top, and di-galactosyl-diacylglyceride C14:1 glycolipid, on the bottom.....	159
Fig. 6-10. Trends of temperature, O ₂ , pH and pressure inside the PBR after one week from solution A injection.	160
Fig. 6-11. Experiment conditions registered in the PBR during R1. The vertical purple lines represent some of the dry mass samplings.	161
Fig. 6-12. Experiment conditions registered in the PBR during R2. The vertical purple lines represent some of the dry mass samplings.	162
Fig. 6-13. Experiment conditions registered in the PBR during R3. The vertical purple lines represent some of the dry mass samplings.	162
Fig. 6-14. Outcome of the experimental analyses for R1, R2 and R3 in terms of Cells counted, Dry mass concentration and OD.	166
Fig. 6-15. R3 chromatograph chart obtained with GC solutions, with details of the peaks detected in the analysis.	168

Fig. 7-1. Detailed diagram of the material and energy flows in the analysed domain (blue lines for energy and waste inputs, red for material outputs, violet for energy output, and orange for internal flows).....	178
Fig. 7-2. Results of the LCA for the facility under investigation (colors represent the different subprocesses).....	184
Fig. 7-3. Impact factors vary according to the results of the uncertainty analysis. There is a non-negligible deviation of the data.	186
Fig. 7-4. Comparison of the impact categories in the facility under investigation with those of a standard sanitary landfilling treatment process.	186
Fig. 7-5. Sensitivity analysis between the base case system (blue color) and that with Ecoinvent data (orange).....	187
Fig. 7-6. Comparison analysis of the system with and without the CHP functioning.....	188
Fig. 7-7. Top view of the proposed PV plant above the facility rooftop.	190
Fig. 7-8. Uncertainty analysis related to PV implementation.	191
Fig. 7-9. Process diagram of the gasifier combined with the steam power plant unit.	193
Fig. 7-10. LCIA of the facility integrated with the gasifier compared to incineration (orange) and landfilling (yellow).	194
Fig. 7-11. Endpoint indicator (EF 3.0 method) for the different treatment systems.....	195

LIST OF FIGURES (APPENDIX)

Fig. X3-1. Bürker haemocytometer R1 , 22-11-21 (DAY 4) 9:00, 1,833 cells μl^{-1}	249
Fig. X3-2. Bürker haemocytometer R1 , 22-11-21 (PR DAY 4.4) 19:00, 2,500 cells μl^{-1}	250
Fig. X3-3. Bürker haemocytometer R1 , 22-11-21 (PR DAY 6) 9:00, 2,250 cells μl^{-1}	251
Fig. X3-4. Bürker haemocytometer R1 , 22-11-21 (PR DAY 6) 9:00, 2,750 cells μl^{-1}	252
Fig. X3-5. Bürker haemocytometer R1 , 22-11-23 (PR DAY 6.4) 19:00, 5,250 cells μl^{-1} (1).....	253
Fig. X3-6. Bürker haemocytometer R1 , 22-11-23 (PR DAY 6.4) 19:00, 5,250 cells μl^{-1} (2).....	254
Fig. X3-7. Bürker haemocytometer R1 , 22-11-24 (PR DAY 7) 9:00, 3,667 cells μl^{-1} (1).....	255
Fig. X3-8. Bürker haemocytometer R1 , 22-11-24 (PR DAY 7) 9:00, 3,667 cells μl^{-1} (2).....	256
Fig. X3-9. Bürker haemocytometer R1 , 22-11-24 (PR DAY 7.4) 19:00, 3250 cells μl^{-1}	257
Fig. X3-10. Bürker haemocytometer R1 , 22-11-25 (PR DAY 8) 9:00, 2,167 cells μl^{-1}	258
Fig. X3-11. Bürker haemocytometer R1 , 22-11-25 (PR DAY 8.4) 19:00, 333 cells μl^{-1}	259
Fig. X3-12. Bürker haemocytometer R1 , 22-11-28 (PR DAY 11) 9:00, 6,750 cells μl^{-1} (1).....	260
Fig. X3-13. Bürker haemocytometer R1 , 22-11-28 (PR DAY 11) 9:00, 6,750 cells μl^{-1} (2).....	261
Fig. X3-14. Bürker haemocytometer R1 , 22-11-28 (PR DAY 11.4) 19:00, 3,667 cells μl^{-1}	262
Fig. X3-15. Bürker haemocytometer R1 , 22-11-29 (PR DAY 12) 9:00, 9,833 cells μl^{-1} (1).....	263
Fig. X3-16. Bürker haemocytometer R1 , 22-11-29 (PR DAY 12) 9:00, 9,833 cells μl^{-1} (2).....	264
Fig. X3-17. Bürker haemocytometer R1 , 22-11-29 (PR DAY 12.4) 19:00, 5,750 cells μl^{-1} (1).....	265
Fig. X3-18. Bürker haemocytometer R1 , 22-11-29 (PR DAY 12.4) 19:00, 5,750 cells μl^{-1} (2).....	266
Fig. X3-19. Bürker haemocytometer R1 , 22-11-30 (PR DAY 13.1) 13:00, 6,333 cells μl^{-1} (1).....	267
Fig. X3-20. Bürker haemocytometer R1 , 22-11-30 (PR DAY 13.1) 13:00, 6,333 cells μl^{-1} (2).....	268
Fig. X3-21. Bürker haemocytometer R1 , 22-12-01 (PR DAY 14) 9:00, 12,500 cells μl^{-1} (1).....	269
Fig. X3-22. Bürker haemocytometer R1 , 22-12-01 (PR DAY 14) 9:00, 12,500 cells μl^{-1} (2).....	270
Fig. X3-23. Bürker haemocytometer R1 , 22-12-02 (PR DAY 15.4) 19:00, 15,167 cells μl^{-1} (1).....	271
Fig. X3-24. Bürker haemocytometer R1 , 22-12-02 (PR DAY 15.4) 19:00, 15,167 cells μl^{-1} (2).....	272
Fig. X3-25. Bürker haemocytometer R1 , 22-12-05 (PR DAY 18) 9:00, 31,750 cells μl^{-1} (1).....	273
Fig. X3-26. Bürker haemocytometer R1 , 22-12-05 (PR DAY 18) 9:00, 31,750 cells μl^{-1} (2).....	274
Fig. X3-27. Bürker haemocytometer R1 , 22-12-05 (PR DAY 18) 9:00, 31,750 cells μl^{-1} (3).....	275
Fig. X3-28. Bürker haemocytometer R1 , 22-12-05 (PR DAY 18.4) 19:00, 36,833 cells μl^{-1} (1).....	276
Fig. X3-29. Bürker haemocytometer R1 , 22-12-05 (PR DAY 18.4) 19:00, 36,833 cells μl^{-1} (2).....	277
Fig. X3-30. Bürker haemocytometer R1 , 22-12-05 (PR DAY 18.4) 19:00, 36,833 cells μl^{-1} (3).....	278
Fig. X3-31. Bürker haemocytometer R1 , 22-12-06 (PR DAY 19) 9:00, 26,333 cells μl^{-1} (1).....	279
Fig. X3-32. Bürker haemocytometer R1 , 22-12-06 (PR DAY 19) 9:00, 26,333 cells μl^{-1} (2).....	280

Fig. X3-33. Bürker haemocytometer R1 , 22-12-06 (PR DAY 19.4) 19:00, 36,413 cells μl^{-1} (1)....	281
Fig. X3-34. Bürker haemocytometer R1 , 22-12-06 (PR DAY 19.4) 19:00, 36,413 cells μl^{-1} (2)....	282
Fig. X3-35. Bürker haemocytometer R1 , 22-12-07 (PR DAY 20.1) 13:00, 42,083 cells μl^{-1} (1)....	283
Fig. X3-36. Bürker haemocytometer R1 , 22-12-07 (PR DAY 20.1) 13:00, 42,083 cells μl^{-1} (2)....	284
Fig. X3-37. Bürker haemocytometer R2 , 22-12-15 (PR DAY 1) 9:00, 1,833 cells μl^{-1}	285
Fig. X3-38. Bürker haemocytometer R2 , 22-12-15 (PR DAY 1.2) 13:00, 3,167 cells μl^{-1}	286
Fig. X3-39. Bürker haemocytometer R2 , 22-12-15 (PR DAY 1.4) 19:00, 2,333 cells μl^{-1} (1).....	287
Fig. X3-40. Bürker haemocytometer R2 , 22-12-15 (PR DAY 1.4) 19:00, 2,333 cells μl^{-1} (2).....	288
Fig. X3-41. Bürker haemocytometer R2 , 22-12-16 (PR DAY 2) 9:00, 2,667 cells μl^{-1} (1).....	289
Fig. X3-42. Bürker haemocytometer R2 , 22-12-16 (PR DAY 2) 9:00, 2,667 cells μl^{-1} (2).....	290
Fig. X3-43. Bürker haemocytometer R2 , 22-12-16 (PR DAY 2.2) 13:00, 3,583 cells μl^{-1}	291
Fig. X3-44. Bürker haemocytometer R2 , 22-12-16 (PR DAY 2.4) 19:00, 1,333 cells μl^{-1}	292
Fig. X3-45. Bürker haemocytometer R2 , 22-12-19 (PR DAY 5) 9:00, 2,083 cells μl^{-1} (1).....	293
Fig. X3-46. Bürker haemocytometer R2 , 22-12-19 (PR DAY 5) 9:00, 2,083 cells μl^{-1} (2).....	294
Fig. X3-47. Bürker haemocytometer R2 , 22-12-19 (PR DAY 5.2) 13:00, 2,833 cells μl^{-1} (1).....	295
Fig. X3-48. Bürker haemocytometer R2 , 22-12-19 (PR DAY 5.2) 13:00, 2,833 cells μl^{-1} (2).....	296
Fig. X3-49. Bürker haemocytometer R2 , 22-12-19 (PR DAY 5.4) 19:00, 7,667 cells μl^{-1} (1).....	297
Fig. X3-50. Bürker haemocytometer R2 , 22-12-19 (PR DAY 5.4) 19:00, 7,667 cells μl^{-1} (2).....	298
Fig. X3-51. Bürker haemocytometer R2 , 22-12-19 (PR DAY 5.4) 19:00, 7,667 cells μl^{-1} (3).....	299
Fig. X3-52. Bürker haemocytometer R2 , 22-12-20 (PR DAY 6) 9:00, 4,083 cells μl^{-1} (1).....	300
Fig. X3-53. Bürker haemocytometer R2 , 22-12-20 (PR DAY 6) 9:00, 4,083 cells μl^{-1} (2).....	301
Fig. X3-54. Bürker haemocytometer R2 , 22-12-20 (PR DAY 6.2) 13:00, 2,083 cells μl^{-1} (1).....	302
Fig. X3-55. Bürker haemocytometer R2 , 22-12-20 (PR DAY 6.2) 13:00, 2,083 cells μl^{-1} (2).....	303
Fig. X3-56. Bürker haemocytometer R2 , 22-12-20 (PR DAY 6.4) 19:00, 6,083 cells μl^{-1} (1).....	304
Fig. X3-57. Bürker haemocytometer R2 , 22-12-20 (PR DAY 6.4) 19:00, 6,083 cells μl^{-1} (2).....	305
Fig. X3-58. Bürker haemocytometer R2 , 22-12-20 (PR DAY 6.4) 19:00, 6,083 cells μl^{-1} (3).....	306
Fig. X3-59. Bürker haemocytometer R2 , 22-12-21 (PR DAY 7) 9:00, 4,417 cells μl^{-1} (1).....	307
Fig. X3-60. Bürker haemocytometer R2 , 22-12-21 (PR DAY 7) 9:00, 4,417 cells μl^{-1} (2).....	308
Fig. X3-61. Bürker haemocytometer R2 , 22-12-21 (PR DAY 7.2) 13:00, 4,583 cells μl^{-1} (1).....	309
Fig. X3-62. Bürker haemocytometer R2 , 22-12-21 (PR DAY 7.2) 13:00, 4,583 cells μl^{-1} (2).....	310
Fig. X3-63. Bürker haemocytometer R2 , 22-12-21 (PR DAY 7.4) 19:00, 4,333 cells μl^{-1} (1).....	311
Fig. X3-64. Bürker haemocytometer R2 , 22-12-21 (PR DAY 7.4) 19:00, 4,333 cells μl^{-1} (2).....	312
Fig. X3-65. Bürker haemocytometer R2 , 22-12-22 (PR DAY 8) 9:00, 1,000 cells μl^{-1}	313
Fig. X3-66. Bürker haemocytometer R2 , 22-12-22 (PR DAY 8.2) 13:00, 3,583 cells μl^{-1}	314

Fig. X3-67. Bürker haemocytometer R2 , 22-12-22 (PR DAY 8.4) 19:00, 3,883 cells μl^{-1} (1).....	315
Fig. X3-68. Bürker haemocytometer R2 , 22-12-22 (PR DAY 8.4) 19:00, 3,883 cells μl^{-1} (2).....	316
Fig. X3-69. Bürker haemocytometer R2 , 22-12-23 (PR DAY 9) 9:00, 3,167 cells μl^{-1} (1).....	317
Fig. X3-70. Bürker haemocytometer R2 , 22-12-23 (PR DAY 9) 9:00, 3,167 cells μl^{-1} (2).....	318
Fig. X3-71. Bürker haemocytometer R2 , 22-12-23 (PR DAY 9.2) 13:00, 2500 cells μl^{-1}	318
Fig. X3-72. Bürker haemocytometer R2 , 22-12-23 (PR DAY 9.4) 19:00, 12,333 cells μl^{-1} (1).....	319
Fig. X3-73. Bürker haemocytometer R2 , 22-12-23 (PR DAY 9.4) 19:00, 12,333 cells μl^{-1} (2).....	320

LIST OF TABLES

Table 1-1. Chemical reactions occurring in gasification.	8
Table 2-1. Parameters to be measured annually with the relevant limits for flue gas monitoring points.	29
Table 2-2. Gaseous emissions from the system.	29
Table 2-3. Average composition of landfill leachate.	30
Table 2-4. Average composition of wastewater collected in the system.	30
Table 2-5. Parameters are to be measured annually with the relevant limits for compost quality. ...	31
Table 2-6. High-quality compost composition	31
Table 2-7. Performance data of the CHP unit.	32
Table 2-8. RMSW sample composition of 2019, 2020 and 2021.	35
Table 2-9. Chemical composition of RMSW in 2019-2020.	36
Table 3-1. Summary of different gasifiers in literature.	40
Table 3-2. Chemical reactions used in the model [22], [169].	56
Table 3-3. Summary of the feedstock properties	60
Table 3-4. Experimental data reported by Arena [145] and Parrillo [61] regarding waste/biomass gasification.	61
Table 3-5. Set of the correlations and averaged variables used in the model ($x = ER$)	65
Table 3-6. Composition of the residual waste produced at the MBT unit.	68
Table 3-7. Value of F and HHV for different feedstock materials	69
Table 3-8. Reconstructed ultimate analysis of the RDF for the six MBT scenarios [175].	70
Table 3-9. Coefficients of the interpolating surface for each variable of the model.	74
Table 3-10. Summary of the air gasification of the different RDF materials with ER sensitivity. ...	76
Table 4-1. Produced and exchanged power in the gasification plant considering different feedstocks.	87
Table 4-2. Toluene and Cyclopentane characteristics [210]–[212]	93
Table 4-3. EEC distribution assumed for the study.	100
Table 4-4. Performance of the power systems for CS1 and CS2.	105
Table 4-5. Complementary results of Table 4-4 with sensitivity analysis on T_{DHN}	107
Table 4-6. Score of every power system.	113
Table 5-1. List of the reactions used in the pyrolysis model [47], [233].	126
Table 5-2. Mass flow rates obtained in [233] and used in the RMSE formula.	129
Table 5-3. Validation of the model with sensitivity and optimization.	130

Table 5-4. Temperature approaches of the chemical reactions used in the model.	132
Table 5-5. Molar concentration and relative increment for the various components during pyrolysis.	137
Table 6-1. Summary of the differences between the various experiments in terms of dry mass and cell counting.	152
Table 6-2. Correlations obtained after the calibration with FAME mix.	155
Table 6-3. Elements counted in each experimental run, based on a daily average.	164
Table 6-4. Summary table for growth rate and division time of the three runs.	165
Table 6-5. Biodiesel specifications as per UNI EN 14214.	170
Table 6-6. Utilities usage in biodiesel production from SO and SFO.	170
Table 7-1. Energy distribution in the system boundary.	180
Table 7-2. Outcome of the Monte-Carlo simulation.	185
Table 7-3. Characterization of the impact factors related to the scenarios compared to RDF gasification implementation.	194

CHAPTER 1

GENERAL INTRODUCTION

1.1 The Issue of Waste Treatment Systems

The intensity of climatic abnormalities (with the associated human and economic losses) records an upward trend and correlates with the intensification of human activities [1] as demonstrated by the multiannual reports of the International Panel on Climate Change (IPCC) [2]. National and international institutions have defined guidelines for implementing corrective actions to contain global warming. For instance, the signatory countries of the Paris Agreement aim to reduce the global average temperature rise below the maximum limit of 2 °C, even though the threshold is likely to be overcome. Policies of circular and green economy models [3]–[5] are used to design a more sustainable society that can reduce emissions and the pace of resource depletion. In addition, the recent energy crisis is putting further pressure on Europe for a secure, reliable, and competitive energy supply. Efficient energy solutions focused on circular economy measures could provide a significant contribution towards a sustainable transition of the energy sector. The circular economy paradigm is often quoted in the recent guidelines promoted by international organizations, and it embraces a wide variety of areas where environmental-focused actions are enacted. Moreover, during the last years of the 20th century, attention to the environment and its relative fragility have been progressively consolidated in many contexts. The energy system has undergone substantial transformations due to the increasing use of renewable energy technology across all industries. Europe had a notable growth of approximately 50% in the generation of renewable electrical energy between the years 2010 and 2019 [6]. Municipal solid waste (MSW) management is one of these areas: if the best practices about recycling and waste-to-energy (W2E) generation are followed, consistent environmental benefits can be achieved.

In this framework, the planning of proper waste management represents a critical asset for supporting the circular economy models. Many topics concerning the handling of waste are often not properly perceived by the population that considers it as a problem and not as an opportunity. Classical examples are the “NIMBY” (Not In My BackYard) protests, where the realization of centralized treating systems are blocked by the local community (causing the penalization of the entire waste

logistics) or the improperly sorting of diverse waste categories, reducing de facto the efficiency of door-to-door waste collection. The investigation of optimal solutions aimed at enhancing the recycling process and minimising environmental emissions is a crucial element in achieving a fully circular economy. The unique features of the waste treatment sector are given by the embedment of diverse engineering fields, which raises the possibility of establishing a polyhedric research framework that pursues parallel, intercommunicating, optimization pathways. Institutions encourage the development of solutions that can reduce these threats and improve the whole logistics by embracing circular economy paradigms. For instance, the European Commission aims at 55% emissions reduction by 2030 and at carbon neutrality by 2050 through a framework of different packages. The European Directives have been recently implemented in Italy and a national recovery plan [7] has been issued to invest in structural and advanced projects that implement renewable and sustainable technologies that can mitigate the human footprint in the environment. Hence, the valorisation and impact minimization of MSW is a paradigm that plays a crucial role in the framework set by circular economy policies [8] especially because in 2020, Europe produced approximately 500 kg of municipal solid waste per capita [9]. Moreover, the load exerted on the landfills is quantified in 763 Mtons for the same year. This amount is most likely expected to increase in the next decades, since there is an increasing trend of landfilled material between 2010 and 2020, from 2.1 Mtons in 2010 to 7.3 Mtons in 2020 in Italy.

In the literature, there are many studies related to the techniques adopted in the waste management sector, focusing on the potential benefits achievable using renewable energy integration. Recycling stands out as the most eco-friendly end-of-life solution, which emits fewer greenhouse gases than the conventional W2E treatment methods. Despite its widespread adoption in Europe [10], the complete recovery of the materials is still not feasible. In the simple disposal scenario, the lifetime of the landfills will be shorter (while more soil will be reserved for new landfills) if no policies are developed for reversing the projections of waste generation [11]–[13]. Valorising the unrecovered material mixture for energy recovery is strategically more advantageous than landfilling, especially when combined heat and power production is sought. Nonetheless, it is usually obtained from thermal treatments that are not emissions-free, especially if referred to the airborne ecosphere where tons of carbon dioxide molecules are released.

Only in the last decades, the attention has been moving from landfilling [14] to other treatment paradigms that imply the thermal conversion of waste. A notorious and consolidated example is the incineration technology [15], where the chemical energy of the residues is converted to electricity and heat to be sold in the grid and district heating networks. The incineration consists of the

combustion of MSW which is a heterogenous mixture of waste materials variable in terms of size, lower heating value (LHV), moisture, and ash content. Such variety represents an issue. The use of traditional fuels like natural gas [16] to stabilise the conversion is a practical solution adopted anywhere. The energy of the flue gases is used to produce steam in a heat recovery steam generator (HRSG) connected to traditional Rankine cycles. Subsequently, electrical power is produced in the turbines while thermal power may be recovered at the condensers if the configuration of the facility allows energy production in cogeneration mode [17], i.e. with district heating networks. The other issue of incineration is the significant production of exhaust gases [11]–[13] that must be carefully treated before atmospheric release [18]. Dedicated systems are used for pollutant removal like DeNO_x reactors, scrubbers, electrostatic filters, activated carbons [16], [19], [20]. The flue gas flow rate is strictly dependent upon the amount of air used for the total waste combustion, almost always in excess compared to the stoichiometric amount. Besides incineration, there are two alternative solutions for the thermal conversion of waste: pyrolysis and gasification. Pyrolysis is an endothermic process where the feedstock is thermally decomposed to elemental compounds in gaseous, liquid, and solid-state, without any air supply in the reactor [21]. Gasification is still an endothermic process but the lower amount of air compared to incineration (below stoichiometric amount) [22] provides heat that sustains the conversion of the solid fuel into a synthetic gas or “syngas” that can be used for hydrogen/energy production [23]. Despite the intrinsic penalty of the conversion, gasification provides less emissions compared to incineration [24]–[26] but it has operational disadvantages and complex process handling, especially due to the aforementioned composition variability.

The organic fraction of MSW can be considered as a biomass that releases biogenic emissions. The exploitation of this material may have a substantial impact in the future within the field of renewable energy sources, owing to its widespread adoption globally and its potential to provide support for intermittent energy sources. According to Terna [27], the installation of generation units fed with biomass-related resources in Italy, has exceeded 4 GW, corresponding to almost 7% of the total renewable energy capacity (58 GW) of the country. Biomass can be derived from a diverse range of sources, including not only MSW but also wood and agricultural and industrial leftovers. Composting facilities, i.e. locations where the organic fraction of municipal solid waste (OFMSW) is collected and stored, turn part of the disposed material into an organic nitrogen-rich soil fertilizer to be used instead of chemical fertilizers thus obtaining a net environmental benefit [28]. Anaerobic digestion is seldom used to treat biomass residues into raw biogas with a biological conversion. In particular, the parameters governing the extent of the reactions occurring in the process of digestion necessitate the application of heat at low temperatures. This heat facilitates the transformation of organic waste into

biogas of superior quality, distinguished by the prevalence of methane [29]. The biogas is burnt in Internal Combustion Engines (ICEs) for electricity generation only or in combined heat and power (CHP) generator. Therefore, a portion of the thermal power generated by the CHP unit can be utilised for regulating the temperature within the anaerobic digestion reactors. This temperature control is typically maintained within the range of 35°-45° C to establish a mesophilic regime inside the reactor [30].

As regards the main MSW waste stream, it is composed of a heterogeneous mixture of unrecycled materials, which cannot be recovered by a door-to-door collecting mechanism. However, it can be valorised by cold processes, i.e. the mechanical-biological treatment units (MBT). The residues of “cold treatments” such as MBT are heterogeneous materials mainly composed of plastics, paper, and textiles that cannot be further recovered. With the introduction of MBT, it is possible to sort, shred, and recover materials without recurring to hot waste treatments [31], [32]. In this way, the typical combustion emissions are avoided. On the contrary, these systems require a significant amount of electricity to properly operate. The ultimate waste stream, alias residual municipal solid waste (RMSW) can either be landfilled or valorised through the final thermal conversion. The high content of unrecyclable waste plastics (15-30%) provides a high LHV content compared to the initial MSW. Under particular conditions, the RMSW can either be defined as refuse-derived fuel (RDF) or solid recovered fuel (SRF). The Italian regulations initially referred to Legislative Decree No. 133/2005 [33] which established strict rules for waste facilities (emissions, control devices, permits) and suggested energy recovery methods (electricity generation, thermal flows, industrial steam) using waste materials allowed by the regulations. Next, Legislative Decree No. 152/2006 [34] defines RDF and high-quality RDF as fuel derived from waste according to the UNI 9903-1 [35] standard, and the former is considered as a renewable source with the Legislative Decree No. 205/2010 [36], therefore suitable for thermal treatment.

After having introduced this different treatment system, it is possible to characterise the Italian scenario as follows: 30% - 33% of the yearly municipal waste undergoes recycling processes, approximately 22% - 23% of the waste is directed into composting facilities, while another 20% is allocated W2E incineration systems [37] and the residual fraction to final disposal at sanitary landfills. Hence, the amount of RMSW produced in composting facilities and mechanical/biological treatment can be significant. Fig. 1-1 shows the average composition of the final wastes produced in such facilities with the indication of the corresponding European waste codes (EWC) [38]. Most of the organic matter of MSW (OFMSW) is converted to compost and biogas, while minor fractions (EWC 190501-03-99) are a waste of this conversion process. The other main waste streams are represented

by the EWC 191212, i.e. the RMSW suitable RDF production for 39.30%, followed by the aggregated production of wastewaters (WW) and leachates (LC) for 27.50% of the total amount. Therefore, reducing their intrinsic burden with appropriate treatment and remediation operations is a mandatory action in the field of waste treatment.

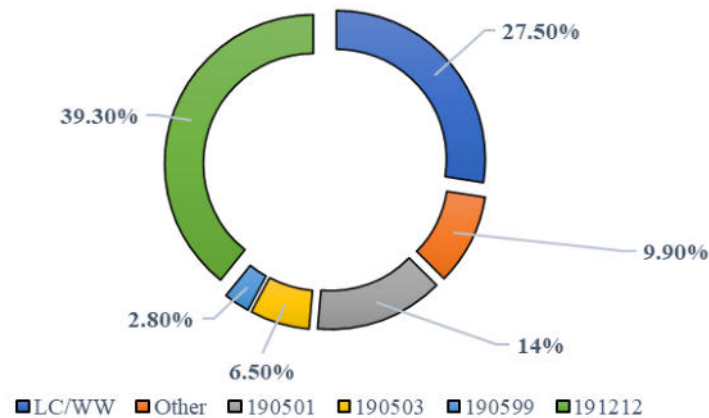


Fig. 1-1. Waste composition from composting facilities in Italy [11]. The colours represent different European waste codes (EWC). Image taken from [39].

The liquid waste stream produced in the dislocated facilities is collected and sent to centralized wastewater treatment plants (WWTP), which perform the final purification before releasing the clean water into the environment and sanitization of the residual sludge [40]. Advanced solutions are proposed either for valorise the sludge for energy applications [41], [42], or to treat wastewater directly in the original place. In this case, emissions from transport can be avoided, as well as the costs for the external treatment.

This overview of the actual solutions used in the field of waste management has remarked on the importance of exploiting the potential of the materials at their end-of-life. When recycling is not possible anymore, final residues can be valorised for energy applications instead of landfilling, which impacts the most in terms of land usage and the water ecosphere, as mentioned in the previous paragraph. However, the atmospheric emissions resulting from the combustion of waste materials, or the ones related to its transportation to centralised and distant treatment facilities, represent another burden for the environment. For this reason, it is mandatory to seek novel solutions that can reduce the impacts of waste treatment at a capillary level while reducing the loads exerted on centralised systems. An analogy is made concerning the diffusion of small-scale renewable energy production systems (photovoltaic, wind, anaerobic digestion, and so forth), considering RMSW air gasification and in-situ wastewater treatment with microalgae as strong candidates for future implementations.

1.2 Objective of the research and research questions

The objective of the research is to find novel solutions that can be implemented to optimize existing waste treatment processes from energetic and environmental points of view. The first goal is to maximize the conversion of the wastes' chemical energy into electricity and thermal energy supply for winter while cooling energy for the summer by using waste gasification integrated with different power systems. The second goal is to expand the state of art about biofuel production promoting the usage of waste heat and wastewater streams, and hence adopting a circular economy paradigm that reduces the impacts of waste management to the ecosphere.

Four main research questions are used to support this extensive research based either on practical issues limiting the operability of the treatment systems, or the knowledge gaps present in the literature. The questions are listed as follows:

RQ1: What are the strengths and weaknesses of adopting RMSW gasification? How can it be a valuable solution for increasing the value of wastes, yet reducing the environmental footprint of W2E systems? This particularly refers to Chapter 3 and Chapter 4. The study of the relevant literature depicted a lack of thermodynamical models for fluidised bed gasification that use a heterogeneous and variable feedstock composition, typical for RMSW – RDF. Moreover, additional models have been developed for different power systems, namely the Hirn cycle, Organic Rankine cycles, and supercritical carbon dioxide Brayton cycles, with the goal of identifying the best system for the temperature and powers involved in the process. This study is extended also to the design of a district heating and cooling network under different process conditions.

RQ2: Similarly, to RQ1, what is a possible way of integrating biomass pyrolysis as well as similar W2E systems, as an efficient solution for increasing the overall energy recovery performance and plant flexibility? The study is discussed in Chapter 5, where a dynamic model of a fast pyrolysis reactor is integrated into the gasifier for producing liquid biofuel when there is a limited thermal demand in the district heating network. The main contribution expressed in the chapter is the combination of the pyrolysis model with the gasifier and a specific power cycle, according to the results of Chapter 4.

RQ3: The literature on microalgae cultivation and wastewater remediation is supported by different experimental studies, and this biomass is promoted as a possible strategic asset for biofuel production. A set of different experimental studies, conducted in a laboratory-scale photobioreactor are discussed in Chapter 6. The aim is to validate the results already reported in the literature while providing

additional considerations when dealing with high-pollutant wastewater. However, the inclusion of a thermodynamic model of a biodiesel production facility is included to address the possible issues that may arise when microalgae-based oils are used to obtain a biofuel suitable for internal combustion engines. The combination of the experiments and the model offers a comprehensive investigation that arose from the following research question: “What is the outcome of microalgae cultivation for biodiesel production, both at the laboratory level and commercial level, with a real wastewater composition?”.

RQ4: A solution that is fully environmentally sustainable is unreal. Therefore, there are inevitable consequences when choosing a specific way of waste treatment due to the implicit emissions that the latter produces. Therefore, it is necessary to use other tools that can provide a correct methodology for assessing the environmental burdens of any solution. A final research question is identified for the scope using the typical methods of the Life Cycle Assessment (LCA) analyses. In particular, the question aims to characterize the emissions associated with the integrated waste treatment facility including compost generation, biogas production, and mechanical-biological of MSW. The discussion is given in Chapter 7, and it includes the outcome of the analyses reported in the previous chapters. To the best of the author’s knowledge, there is a lack of comparative LCA studies that evaluate the performance of the integrated system derived from Chapter 4.

The four questions underscore the vital role of a multidisciplinary approach in supporting research within the waste treatment domain. This approach brings together diverse fields, synergizing their strengths to tackle the complex challenges of waste treatment. By breaking down traditional barriers, this method fosters innovative solutions and a more comprehensive understanding, ultimately driving the advancement of sustainable waste management practices.

1.3 Pyrolysis and gasification for waste valorisation

The traditional solution used for valorise the RMSW in W2E facilities is with “hot treatments”, mostly like incineration [43]. Integrating incinerators with district heating networks has the potential to raise the overall energy recovery efficiency to 60% [44]. However, alternative W2E solutions beyond incineration have been assessed based on their energy efficiency, pollution emissions, and economic viability. Biomasses, OMSW and RMSW can be valorised also by pyrolysis and gasification [45]–[47]. Pyrolysis is the cheapest thermal decomposition process that breaks down the feed material into three main components: oil, gas, and solid residues. This process occurs in the absence of oxygen, as there is no air supply, and it relies on an external heat source to initiate the

chemical reactions. An aspect of pyrolysis is how the yields of oil, gas, and solid residues can vary depending on factors such as temperature and the type of plastics used as feedstock. In many cases, the oil phase tends to be the predominant product of interest. This oil, often referred to as pyrolysis oil or bio-oil, holds promise for energy production and transportation applications due to its potential as a renewable and sustainable source of liquid fuel [48]. Pyrolysis has the lowest temperature among the three solutions, 500-700 °C in the absence of oxygen and without an oxidizing agent. Pyrolysis converts the input element into 50-60% liquid (pyrolysis oils), 20-30% solid char, and the remainder into pyrolysis gas. Gasification, however, is considered an interesting option because of its: i) higher efficiency, ii) lower environmental impact, and iii) possibility to produce syngas and/or biofuel and biochemical compared to incineration which is however the most widespread technology for the MSW energy valorisation.

Gasification occurs with higher temperatures than pyrolysis and is used to produce new gaseous fuels from a solid feedstock, in this case, MSW. The gasification is a thermochemical process, in which any carbonaceous substance in the feedstock is converted into syngas mainly consisting of H₂ and CO at intermediate temperatures (> 700 °C) using a lean oxidation process [49]. The composition of the produced syngas and its LHV vary significantly based on the oxidation agent used in the process. Air is the most common oxidant, but it dilutes the produced gas with N₂ resulting in a syngas with less energy content. Chemical gasification reactions can progress to different degrees depending on the process conditions such as temperature and pressure and the raw material used. For combustion reactions, gasification typically uses one-fifth to one-third of the oxidant compared to conventional combustion, which means an equivalence ratio (ER) of less than 0.5. Through a process known as partial oxidation, this only oxidizes a fraction of the carbon contained in the feedstock material. The primary byproducts of gasification fuels are CO and H₂, with just one part of the carbon completely oxidized to CO₂. The resulting syngas is a mixture of these gases with the presence of variable quantities of CH₄. The main chemical reactions that take place in gasification are reported in Table 1-1 [50].

Table 1-1. Chemical reactions occurring in gasification.

Reaction	Enthalpy	Name
$C + CO_2 \leftrightarrow 2CO$	$\Delta H = +172 \text{ kJ mol}^{-1}$	Boudourd
$C + H_2O \leftrightarrow CO + H_2$	$\Delta H = +131 \text{ kJ mol}^{-1}$	Water-gas
$C + 2H_2 \leftrightarrow CH_4$	$\Delta H = -74.8 \text{ kJ mol}^{-1}$	Hydrogassification
$CO + H_2O \leftrightarrow CO_2 + H_2$	$\Delta H = -41.2 \text{ kJ mol}^{-1}$	Water-gas shift
$2CO + 2H_2 \leftrightarrow CH_4 + CO_2$	$\Delta H = -247 \text{ kJ mol}^{-1}$	Metanation
$CO + 3H_2 \leftrightarrow CH_4 + H_2O$	$\Delta H = -206 \text{ kJ mol}^{-1}$	Metanation 2

The most important reactions that affect the quality of the syngas are those of methanation and the conversion of water into gas. The operating temperatures are lower than combustion, i.e. around 800-850 °C on average [50]–[52] with the addition of oxidizing agents, such as pure oxygen (the most virtuous), air (presence of nitrogen which penalizes the yield) or steam (its production is necessary more energy-intensive than the others). The chemistry of gasification is quite complex and is realized through a series of transformations occurring in the gasifier reactor. In a gasifier, the carbonaceous raw material undergoes several processes and/or reactions:

- Dehydration - Any free water content of the raw material evaporates, leaving the material dried, and the evolving water vapor can enter subsequent chemical reactions.
- Pyrolysis - This occurs when the raw material is exposed to the temperature in the gasifier. Devolatilization and rupture of weaker chemical bonds occur, releasing volatile gaseous substances such as methane, and hydrogen vapours, as well as producing a high molecular weight char which will then undergo gasification reactions.
- Combustion - Volatile products and part of carbon react with oxygen to form anhydride CO_2 , and CO and, in doing so, provide the necessary heat for the subsequent gasification reactions.
- Gasification - The remaining char reacts with CO_2 and steam to produce CO and H_2 .
- Water-gas shift and methanation - these are separate reversible gas phase reactions that occur simultaneously according to the condition of the gasifier.

From a thermodynamic point of view, the reactions are reversible and impose a strong influence on the thermal efficiency and composition of the syngas produced by a process of gasification. Among the fundamental parameters that characterize a gasifier, are the temperature, the pressure, the type of gasifying agent, and the residence time (or permanence) of the material to be gasified. Temperature is a crucial parameter as it can affect the composition of the syngas produced and its calorific value; the latter is inversely proportional to the temperature of the gasifier bed which, if sufficiently high, promotes steam cracking and conversion of carbon resulting in less tar formation, increased syngas yields and with more hydrogen content. Regarding the operating pressure, a gasifier can be designed both to work at atmospheric pressure or under pressure. The latter, more effective but also more expensive, not only allows lower tar yield and more syngas but also allows to reduce the CO_2 content. Furthermore, in gasification, the heat necessary for the process is supplied, totally or partially, by partial combustion reactions which reduce the need for heat inputs from the outside. The solutions

tested are generally tailored to the production of fuel in the gaseous phase, not excluding the combination of a pyrolyzer [53], [54] in a way that increases the flexibility of the treatment process.

The following gasifier types can be found:

- Fixed bed gasifiers (updraft and downdraft), are moderately susceptible to process conditions;
- Entrained flow gasifiers, operating according to the particle size of the solid fuel;
- Fluidized bed gasifiers [55] which can be boiling, circulating, or dual bed. They are currently the most common ones, as they are cheap, although their efficiency can vary significantly;
- Plasma gasifiers [56], [57]. They allow maximum flexibility in terms of rejection but are expensive and in the pilot stage.

Fixed bed or mobile gasifiers commonly operate at high pressures (25-30 bar). Raw materials in the form of large particles are charged at the top of the refractory coated gasification vessel and move slowly downwards through the bed, reacting with the high oxygen content gas introduced at the bottom of the gasifier that flows in counter current upwards in the gasifier. The basic configuration is the same as present in common blast furnaces. Reactions within the gasifier occur in different "zones". In the "zone of drying" at the top of the gasifier, the incoming material is heated and dried, cooling the gas produced before it leaves the reactor. Subsequently, it is further heated and devolatilized by gas at a higher temperature as it descends through the "zone of carbonization". In the next zone, the "gasification zone", the devolatilized material is gasified by a reaction with steam and carbon dioxide. Near the bottom of the gasifier, in the "combustion zone" operating at maximum temperature, oxygen reacts with the residue charred.

In drag-flow gasifiers, the feed of raw material and oxidizer (air or oxygen) and/or vapour occur in equicurrent to the gasifier. This results in the oxidant and the vapour dragging the surrounding particles of raw material through the gasifier in a dense cloud. Drag flow gasifiers operate at temperature and high pressure and with extremely turbulent flows, which causes a rapid gasification conversion and thus high productivity. Gasification reactions occur at a very high velocity (the typical residence time is of the order of a few seconds), with high carbon conversion efficiencies (98-99.5%). Tar, oil, phenols, and other liquids produced by the devolatilization of coal within the gasifier are decomposed into hydrogen, carbon monoxide, and small quantities of light hydrocarbon gases. Flow gasifiers entrained may handle virtually any raw material and produce clean and tar-free syngas. Given the high operating temperatures, this type of gasifier dissolves coal ash in inert glass slag. On the other hand, the high temperatures involved in this gasification tend to shorten the life of the system components, including the refractory ones. In addition, it may be necessary to add additional flows

or the variation of some mixing parameters of the raw material to obtain good characteristics of slagging.

Fluidised bed gasifiers suspend raw material particles in an oxygen-rich gas so that the resulting bed inside the gasifier acts as a fluid. These gasifiers employ mixing and efficiently mix carbon particles with carbon particles already in the gasification phase. To support the fluidification or suspension of carbon particles inside the gasifier is normally used small raw material (<6 mm). The material enters from the side of the reactor, while the steam and the oxidant enter near the bottom with a sufficient speed to completely suspend or thin the reactor bed. Thanks to the accurate mixing inside the gasifier, a constant temperature is maintained in the bed. Gasifiers normally operate at moderately high temperatures to obtain an acceptable carbon conversion rate (e.g., 90-95%) and to decompose the most tar, oils, phenols, and other liquid by-products. However, the operating temperatures are usually lower than the ash melting temperature to avoid clinker formation and the possibility of draining the bed. This, to its time, means that fluidized bed gasifiers are more suitable for relatively reactive, low-ranking, and other fuels such as biomass. The attention of research in recent years has been greatly attracted by one type of gasification which involves the use of heterogeneous fuels such as municipal waste and biomass which is then called co-gasification. For example, Fremaux et al. [58] investigated the conversion of wooden feedstocks in a steam gasifier producing an H₂-rich gas by varying relevant operating parameters such as the steam/biomass ratio, the reactor temperature, and the biomass particle size. In particular, the higher temperature increases the hydrogen content in the syngas due to the thermal cracking of tars and the water gas shift reaction. The variation of the reactor temperature from 700 °C to 900 °C, in a run of 30 min with medium biomass particles (1-2.5 mm) and a steam/biomass (S/B) ratio of one, produced an increase of hydrogen content around 25%.

Initially, the studies on gasification were related to integrated coal-based systems (IGCC) [59] and only later on referred to different biomass-based waste materials [60]. The performance of gasification processes is influenced by various factors and parameters. These include the chemical composition of the feedstock, the type and size of the gasifier, the choice of gasifying agent, and the operating temperature and pressure. Additionally, factors like residence time, feedstock preparation, the use of catalysts, and post-gasification syngas cleanup processes are also essential considerations. The interactions among these parameters are complex, and extensive research and optimization efforts are undertaken to enhance gasification efficiency, reduce emissions, and tailor syngas production for specific applications. For example, Parrillo et al. [61] conducted an experimental sensitivity analysis of Eucalyptus chips in a pilot-scale bubbling gasifier, varying the equivalence ratio (ER). Another example of biomass gasification, coupled with an organic Rankine cycle (ORC)

system for energy production, was reported by Marcantonio et al. [62], where olive tree pruning was gasified with cold gas efficiency (CGE) of 89% and generated more than 200 kWe at the regime. Other studies explored the co-gasification of a mixture of plastics and biomasses. Pinto et al. [63] used a fluidized bed steam gasifier fed with pine biomass and waste polyethylene plastic obtaining a higher heating value (HHV) of the syngas of 18.3 MJ kg⁻¹. The authors of the study achieved noteworthy results concerning the hydrogen content, reaching 50% in volume with 20% w/w of polyethylene (PE) content in the feedstock. They also observed that the steam-to-waste ratio had a limited impact on the syngas yield. The study suggested that a steam-to-waste ratio above 0.6 is required for efficient gasification. Mastellone et al. [23] examined a diverse mixture composed of various combinations of coal, waste plastic, and wood within a bubbling fluidized bed reactor. The aim was to assess the viability of gasifying heterogeneous materials. The findings revealed that the inclusion of wood in the mixture resulted in cleaner syngas production, primarily due to the absence of heavy hydrocarbons and tar. However, it was noted that the syngas derived from this mixture had a moderate heating content, ranging from 2 to 4 kW per kilogram of fuel.

There has been a growing interest in the gasification of plastics derived from RMSW due to their substantial energy content, which can reach up to 40 MJ kg⁻¹. Among the various sources of plastics, RDF obtained from the MBT process has garnered significant research attention. Numerous pilot plants, operating at various scales, have been constructed for the specific purpose of investigating the gasification of RDF plastics. In particular, Arena et al. [61] developed a pilot-scale bubbling bed gasifier with a thermal power of 500 kWt and 30-100 kg h⁻¹ of inlet feeding rate, Win et al. presented [64] a smaller gasifier having a feeding rate of 20-25 kg h⁻¹ and Kim et al. [65] performed different test conditions in a laboratory-scale gasifier at 0.1-0.5 kg h⁻¹ feeding rate. In a gasification process, the presence of tars, which encompass a diverse range of heavy hydrocarbons including phenols, furans, naphthalene, and other polycyclic aromatic hydrocarbons (PAHs), poses a greater undesired challenge compared to mere combustion. As a result, numerous studies in the literature have focused on evaluating not only the composition of the syngas and process efficiency but also the specific tar yield and solutions for its cracking or removal. Cho et al. [66] investigated a similar reactor, with comparable feed rates, obtaining a tar yield above 1,000 mg Nm⁻³. Jeong et al. [67] gasified polyethylene plastic with active carbon. Data on tar production vary in a wide range because of the influence of many process parameters that rule the phenomena occurring inside a gasifier. According to Yang et al. [68], from a global perspective it is forecasted a total RDF generation of 2.6 billion metric tons by 2030. Noteworthy, USA, China, and India are the major waste producers in the world (2018 Statista data [69]) respectively with 258, 220.4, and 168.4 million metric tons of waste.

However, the United States only recovers 12% of its waste energy, indicating a poor performance overall. Therefore, there is a strong potential for the diffusion of gasification to produce fuels like syngas and hydrogen from such waste. However, from the first experimental investigations, the formation of tar compounds that look like black-brown viscous liquid caused problems. This is mainly due to its adhesion on the surface of the downstream machinery used, which would lead to the malfunction of the complex system with the consequent compromise of the whole process. In addition, other problems such as the production of other undesirable dark residues and the discharge of NO_x , H_2S , and SO_x . In conclusion, biomass gasification may generate clean syngas that can be used in equipment having moving parts, but the syngas obtained from MSW gasification should be used in other ways to produce energy.

Other studies have explored the co-gasification of biomass and plastics mixtures finding promising energy conversion performance. For instance, Pinto et al. [70] investigated the addition of polyethylene plastic to the pine biomass wastes in a fluidized bed steam gasifier. Mastellone et al. [71] used a bubbling fluidized bed reactor to demonstrate the feasibility of gasification of a more diverse feedstock composition consisting of coal, waste plastic, and wood. The presence of wood and coal in the mixture with plastics brought lower tar production but also lower syngas-specific energy. Recently, Parrillo et al. [72] conducted experimental tests in a pilot-scale bubbling fluidized bed gasifier able to treat up to 100 kg h^{-1} of feedstock by varying the plastics/biomass ratio. They found that the plastics/biomass ratio and ER considerably influence the gasifier performances like the CGE being between 0.64 and 0.81 encountered during different experiments of several blending ratios. In their experiments, plastics provided more concentration compared to biomass gasification, from 9 g Nm^{-3} (pure plastic) down to 1.8 g Nm^{-3} . The co-gasification process of waste-derived fuels and biomasses is considered more advantageous thanks to one reduced formation of tar slag, and the actual yield of the process. Different co-gasification studies [73]–[75] concluded that the addition of biomass may increase the yield of H_2 and CO in proportion to the increase in the share of biomass. Moreover, the addition of biochar produces higher yields of H_2 than using biomass in co-gasification while effectively reducing more tar than biomass at low gasification temperatures.

1.4 Biofuel production from biomass pyrolysis

The utilisation of biofuel obtained from waste treatment serves as a crucial intersection between waste management and the production of renewable energy. The process involves the transformation of diverse organic substances, such as agricultural residues, municipal solid waste, and industrial by-products, into viable sources of energy. This approach provides environmental advantages through

the reduction of landfill waste and the mitigation of greenhouse gas emissions, while also increasing resource efficiency and adhering to the ideals of a circular economy. Not only is liquid biofuel production from microalgae discussed in this thesis, but also the implementation of pyrolysis in large-scale incineration systems.

The “hot” waste treatment facilities like gasification and incineration provide both electrical and thermal power after the conversion of MSW. These systems are designed for a maximum treatment capacity and hence provide a maximum amount of energy to be delivered to the grid or district heating. The district heating demand varies during the year, therefore off-design conditions are likely to be expected throughout the year, which penalises the overall conversion efficiency and inevitably brings more variations of the waste stream mass flow rate. The direct consequence of this is a lower combined efficiency, principally related to the off-design characteristics of the power units (steam turbines and cooling condenser) response and then from a lower combustion efficiency of the boiler. The discussion provided in Chapter 4 demonstrates that district cooling can mitigate this bottleneck by producing cooling power. However, this is not the only feasible solution that can be adopted to keep the boiler fully operational. One of the solutions proposed is to use the fast pyrolysis of biomass to produce liquid biocrude that can be qualitatively improved with downstream refinery processes. The heat that is not required in the heat recovery steam generator can be used for sustaining the endothermic reactions occurring in pyrolysis.

During the hot season, this demand can be significantly lower than in the cold season, or seldom almost absent [76]. This condition causes the W2E systems to a forced off-design partialization, where the efficiency of the system is lower [77], [78] as well as the amount of waste treated. The use of a district cooling network can be justified in places where high temperatures are expected during the summer, especially for the Mediterranean countries. However, for the northern European countries, this solution may not provide additional benefits than the use of a simple district heating network, but most likely further costs for the piping and absorption chillers. The relatively low values of the Cooling Degree Days [79] demonstrate that other technologies should be chosen in the short and long term [80] for space cooling.

In this context, one possible solution is the add a parallel biofuel production line that could be activated when the district heating demand is low. The logic behind this approach is to exploit the wastes’ energy by defining an operating range between the combined energy generation (cold season) and biofuel generation (hot season) that i) minimizes the time in off-design operation, ii) tackles the inevitably related global efficiency reduction of the W2E facility, iii) keep fixed as much as possible the amount of waste treated hourly. Moreover, the production of the new co-product offers more

chances of profitability and an expansion to biofuel markets besides waste treatment. There are different ways to achieve this solution, but one of the most promising and sustainable is the integration of biomass conversion in existing incinerators' boilers [81], [82]. By a rearrangement of the reactor, is in theory possible to use the heat released by the combustion of RDF or RMSW to do a primary conversion of biomass-based feedstock into row biofuels, either liquid or gaseous. As discussed in the various Chapters of the thesis, biomass-based feedstocks have great adaptability for pyrolysis and gasification conversion processes. For the former, the resulting syngas is rich in hydrogen/methane and has fewer undesired elements like tars, making it suitable for direct combustion in gas turbines, ICE, or used, together with biogas for upgraded biomethane production [83]. The comprehensive literature on biomass pyrolysis investigates many aspects of the process, from the thermos-chemical aspect [84] to the economic feasibility of industrial-scale facilities [85]. The main products of pyrolysis, i.e. biochar (solid), crude oil (liquid), and pyrolysis gas can offer a wide range of applications. As an example, biochar can be used as a pollutant removal in wastewater treatment [86]. The liquid biocrude oil can be upgraded to form more stable transportation fuels with high energy content, predominantly with the hydrodeoxygenation process [87]. The gas phase is considered less important than biochar and biooil, however, the use of this pyrolysis product as a gas fuel for energy generation can bring interesting benefits in terms of material exploitation [88]. Different parameters affect pyrolysis [45]. As pointed out by Zhang et al. [88], several factors influence pyrolysis and the yields of each phase. First, the particle size and type of biomass. Higher particle size brings low tar formation but increases gas and solid phase yields. Feedstock composition significantly affects pyrolysis outcomes. The type of biomass or organic material used, the presence of moisture, as well as lignin, cellulose, and hemicellulose contents, influence the outcome of pyrolysis and the yields of the various phases. Moreover, proper catalysts can favour one phase more than the others. Regarding the process parameters, residence time, temperature, and heating rate are considered to be the most important variables in pyrolysis. The residence time, together with temperature, distinguishes slow from fast pyrolysis. The latter takes place at temperatures around 500 °C and residence times in the order of seconds and maximizes the liquid yield up to 80% [89]. Slow pyrolysis occurs at similar temperatures but the gas phase residence time is up to 30 min [86], and it is particularly well-suited for the production of high-quality biochar. The heating rate is another governing factor in pyrolysis. In general, higher heating rates lead to major volatile releases. Further, steeper heating rates encourage gas yield more than tar formation [90]. The combinations of these factors give pyrolysis a versatility advantage compared to gasification and incineration. However, several technical challenges permeate the control of the process, like feedstock variability, intensive energy demand, and scaling-up issues. For this reason, there are a few stand-alone full-scale production facilities in

Europe [91]. In conclusion, the combination of pyrolysis, gasification, and incineration brings strong interests both in academia and in the industrial sector.

Different studies analytically address this interoperability. Kohl et al [82] investigated the integration of biomass fast pyrolysis in a municipal CHP 30 MW_t plant in design and off-design mode, i.e. from 90% to 50% of the nominal capacity. In particular, the heat required for the fast pyrolysis is released by the hot flue gas from the CHP plant in a counter-current sand/flue gas heat exchanger with the following reasonable temperatures: sand 550 °C – 450 °C, flue gases 850 °C – 480 °C. After, pyrolysis gases are usually quenched in a spray cooler with cooled pyrolysis oil to maximise the liquid yield and be co-fired in the boiler as well. As the authors claim, this mode of integration should be common for all types of boilers and can increase the yearly operation hours by 57%. Noteworthy, the integration can slightly penalize the overall efficiency of the plant due to the consumption of the auxiliary service units, however, this aspect is balanced by the increased operational time. The coupling is hence thermodynamically possible and offers energetic and environmental advantages. Björnsson et al. [92] extensively evaluated these advantages in a similar CHP plant operating on average 5,300 hours year⁻¹. A dual fluidized bed is created by connecting the pyrolysis unit to the existing circulating fluidized bed (CFB) boiler. The pyrolysis unit would be supplied by either sawdust or logging residues and deliver char and pyrolysis gas to the CFB boiler, for heat and power production. The heat and power for the pyrolysis system would be supplied internally and would thus decrease the net heat and power output from the CHP plant. The authors suggest that the lower efficiency of the pyrolysis unit should be considered when the continued operation is foreseen since the wood material would be not used strategically. However, from an emission perspective, the inclusion of pyrolysis would not tackle the sustainability of the process. The carbon footprint of the crude bio-oil is between 1.7 and 4.0 g CO_{2eq}/MJ, which is under the threshold of the EU RED II for sustainable power (37 g CO_{2eq}/MJ). Salman et al. [81] studied instead the profitability of the gasification integration in existing CHP plants for the polygeneration of dimethyl ether (DME) or methanol. Similarly to the previous study, the interchangeability between the “boiler” mode and the “gasification” mode is driven by the district heating (DH) demand curve. When the DH demand is satisfied, the excess heat is used in the gasification line. The resulting syngas can be converted into methanol or DME with slightly diverse process layouts. The economic assessment, which delves into the uncertainties of the biofuel production costs, manufacturing costs, and discount rate, favours DME production more than methanol. With DME, the payback period (PBP) is 7 years while PBP for methanol is up to 10 years. Moreover, sensitivity analysis and Monte Carlo simulations show that DME production is more economically viable than methanol production. As reported by Kohl et al,

the overall efficiency is lower than pure CHP operation, but the fact that additional products are obtained from the waste's treatment gives a consistent improvement. One of the most important studies in the sector is the one of Dutta et al. [93] from the National Renewable Energy Laboratory (NREL). The group investigated the feasibility of bio-oil production (with upgraded techniques) from biomass with real vendor quotes and high-fidelity flowsheet simulations run in Aspen Plus, showing its conceptual feasibility even in a stand-alone configuration. In conclusion, the integration of biofuel production into waste treatment facilities is promising and can solve the challenges brought by partial load operation, at a conceptualization level. However, there are very limited experimental investigations that can validate the assumptions or demonstrate the practical implementation of these solutions. The next section discussed the pilot plant under construction that has the role of addressing those research questions.

This practical problem has been noted in the waste boiler of Mälarenargi in Västerås, which uses the CFB boiler technology for RDF complete combustion. A pilot plant is being built to demonstrate the feasibility of biomass pyrolysis by retrofitting the G-valve of a scaled CFB reactor, which however will operate in gasification mode and with biomass feedstock.

The intrinsic nature of the problem requires the establishment of a dynamic modelling framework. A dynamic model of the pyrolysis must be realised to better characterise a load-following behaviour of this W2E configuration.

1.5 Microalgae implementation

Wastewater and leachates represent significant environmental hotspots for this system, that contribute negatively to climate change and pollutant release. While treatment in dedicated facilities represents the base case solution, liquid waste can be treated with other peculiar phytoremediation processes involving microalgae. Microalgae are a particular and niche biomass that have different applications, from low-grade biofuels to highly valuable pharmaceuticals production. Their great potential is only comparable to their difficulty in scaling up and full-scale production, but it has been widely proven that microalgae are an important source of high-value molecules such as pigments, proteins, and fatty acids, which are increasingly appreciated in the market, especially compared with other synthetic and traditional alternative molecules. Interests in biodiesel production from microalgae are expected to continue to rise in the future, however, the economic sustainability of microalgae cultivation still raises some concerns due to the high realization costs, limited productivity, consistent energy

demand, cost for sterilization and chemicals [94]. Studies at the laboratory level are still needed despite the comprehensive supporting literature on microalgae.

One interesting and foremost technology that may be used for local wastewater treatment is the integration with microalgae harvesting. Biomass production from microalgae has created strong interests in academia and the industrial sector. Many studies proved that microalgae are an important source of high-value molecules such as pigments, proteins, fatty acids, and vitamins which are increasingly appreciated in the market, especially compared with other synthetic and traditional alternative molecules. The microalgae market can be simply represented in Fig. 1-2.

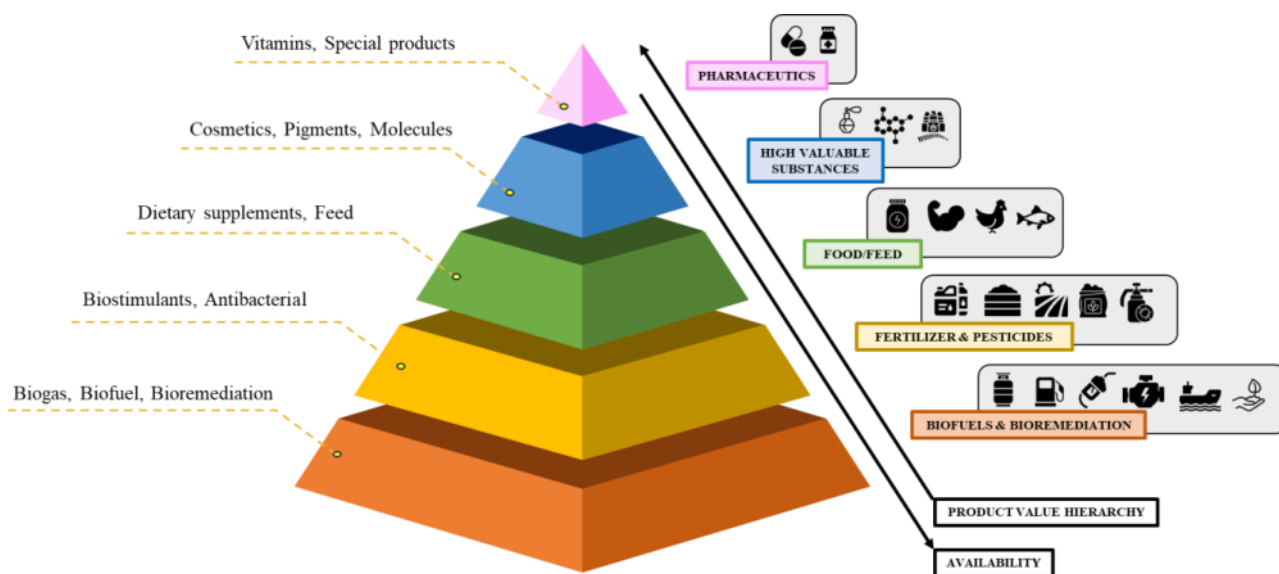


Fig. 1-2. Microalgae products chain value in the market [95].

The numerous microalgae application [95] ranges from cheap biomass production, suitable for biofuel generation and bioremediation, pesticides, fertilizers, biostimulants, and valuable products for the food sector like dietary supplements and vitamins, to special molecules, cosmetic products, and pharmaceutical applications. The economic sustainability of microalgae cultivation has been deeply studied for years. Typical values for microalgae derivatives range from 3 \$ gallon⁻¹ for biofuels, 80-160 \$ kg⁻¹ for fatty acids, and up to 2500 \$ kg⁻¹ for specific applications [96], [97]. Despite these niche derivatives, the products at the bottom of the pyramid of Fig. 1-2 have production and economic bottlenecks that limit industrial-scale demonstrations. The economic performance for similar scenarios can be enhanced if there are cheap energy and material waste streams (wastewaters, flue gases, low-grade heat) that can be integrated into the microalgae production as a source of nutrient and energy supply that can minimize the utilization of raw materials (i.e., nitrogen, carbon dioxide, and so forth). Therefore, the strength of cheap microalgae products relies upon the integration with other systems, like wastewater treatment [98], [99]. Studies show that microalgae can remove a

significant fraction of elements like nitrogen, phosphates, and sulphates, down to 10% of the original content, bringing then a reduction of the total chemical oxygen demand (COD) of the WW. For instance, Massa et al. [100] used the microalgae *Tetradismus (Scenedesmus) obliquus*, *Botryococcus braunii*, *Arthospira Maxima* for treat different diluted anaerobic liquid digestate in repeated batch photobioreactors (PBR), showing the performance of the microalgae in removing nitrates and phosphates contained in the liquid waste, and its adaptability to grow in the medium. Moreover, the authors reported also the lipid content and the lipidic profiles. The maximum lipid content was detected for *S. obliquus* in a range between 12-14% of the total dry weight and mostly composed of the free fatty acids (FFA) between C16 and C18. According to the review of Hoekman et al. [101], the lipid content widely varies according to the type of microalgae, process conditions, and growing medium. *S. obliquus* may arrive slightly above 20% of lipids, while *Botryococcus braunii* to 75% at maximum and *Chlorella vulgaris - emersonii* around 60%. The benefit of treating wastewater while producing biomass with an exploitable lipid content brought the focus of the research on investigating the feasibility of biofuel and biogas production. As an example, Thorin et al. [102] used different mixtures of microalgae strains and sewage sludge samples to address the quality and yield of the biogas their the anaerobic co-digestion. The analyses showed synergy between the two biomasses in terms of yield and exploitable energy, justifying the microalgae integration in the main sewage sludge treatment process. Slightly different is exploiting the lipid content in a microalga oil for biofuel production. The oil can be used in the catalytic transesterification/esterification reactions [103]–[105] for biodiesel production. The fuel can either be used internally to reduce the utilities involved in the treating process or, if the minimum regulatory requirements are respected, sold to the market. In this way, the usage of microalgae fully characterizes the typical framework inherent to circular economy models. Nonetheless, the current state of the art for these technologies is slowly progressing to consolidated industrial practices [106], [107], but still addressing the technical and economic feasibility at the laboratory level or pilot plant demonstrations. For instance, Ho et al. [108] studied the growth of the *S. obliquus* strain in a PBR for 12 days, its lipid content, and the attitude of the microalga to absorb CO₂ dissolved in the growing medium at different concentrations. Trivedi et al. [109] monitored and enhanced lipid production by a two-stage cultivation process in nitrogen starvation. These studies have validated the capacity of the microalga to endure within municipal wastewaters, to amass substantial levels of fatty acids triggered by environmental stress (such as nitrogen starvation), its adaptability, and its rapid growth rate in conducive environments.

1.6 Environmental footprint assessment by means of Life Cycle Assessment methodology

These treatment systems can be successfully investigated using a Life Cycle Assessment (LCA) approach. In general, LCA is a well-known comprehensive methodology used to evaluate the environmental impact of a product throughout its entire life cycle, encompassing manufacturing, disposal, and all stages in between. LCA is particularly effective in quantifying the environmental burden associated with a process, product, or system over its anticipated lifespan, spanning from initial assembly to final waste generation and management. The characterization of a system is achieved through the collection of a substantial quantity of data, mostly consisting of primary data obtained from real field measurements, as well as secondary data used to describe the background system. One notable advantage of this methodology lies in its ability to mitigate the burden-shifting paradigm, which refers to a scenario where a system has high performance in certain impact categories but experiences a decline in others. The objective of a comprehensive environmental characterization is accomplished by utilising a series of midpoint/endpoint indicators that measure the associated burden. As discussed in the introduction, the LCA has 4 major steps: goal and scope, Life Cycle Inventory (LCI), Life Cycle Impact Assessment (LCIA), and an interpretation phase on the results obtained. These steps present an iterative framework, where many assumptions are revised, especially for background data in the LCI. The outcome of an LCA study has multiple benefits. LCIA can identify the major burdens on the system, like sources of intensive material and energy usage or process inefficiencies. Secondly, once the target is defined, appropriate actions may be evaluated as alternative scenarios of the base case. Indeed, LCA can support policymakers in planning optimal measures. Appropriate analyses need to focus on the consistency of the data, the uncertainty quantification, and sensitivity scenarios [110]. Indeed, when a comparison between different treatment systems is performed, critical aspects may arise, and sensitivity studies are recommended. A heterogeneous coexistence of papers supports the literature relevant to LCA analyses of waste treatment facilities. For instance, Khandelwal et al. [111] analysed a series of LCA investigations on the multiple solutions for W2E management solutions, mostly limited to Europe and Asia. The review included LCA studies for landfills, mechanical and biological (MBT) units, thermal treatment including incineration, pyrolysis, and gasification, and biological treatment, i.e. anaerobic digestion and composting. In literature, many life cycle assessment (LCA) studies inspected the performance of these systems. In the review paper on LCA investigations for 250 W2E case studies by Astrup et al. [112], it was reported an average net electrical efficiency of 19% for 87 typical W2E incinerators. Relating to thermal treatments, Fruergard et al. [113] expressed the performance of different solutions

for W2E recovery systems with comparative studies. They concluded that in Denmark, the utilisation of incineration with energy recovery is a viable option for managing both residual waste and organic waste, provided that suitable measures are taken to ensure effective flue gas cleaning. Still referring to incineration, the work of Morselli et al. [114] demonstrated the beneficial impact of energy generation, notwithstanding the possible adverse effects on human health resulting from the discharge of dangerous pollutants into the environment. Moving to the Italian scenario, Buttol et al. [115] examined the district of Bologna and employed LCA as a decision-support tool for local authorities. Their findings underscored the significance of the methodology in establishing a sustainable approach to waste valorisation. Grosso et al. [116], emphasised the significance of incorporating anaerobic digestion with the current W2E systems. They quantified this integration as having the potential to yield a maximum environmental benefit of +37%. Landfills represent the worst efficient way to treat waste from the environmental point of view but have large margins of enhancement. Sauve et al. [117] reported a footprint perspective about MSW landfills in Europe is given. A proper energy recovery may result in a reduction of the impact categories up to 20-40%. In [118], Lee et al. conducted a quantitative analysis of the greenhouse gas (GHG) emissions originating from a representative sanitary landfill. The researchers emphasised the significant role of methane as the primary issue in terms of gas emissions generated by these waste management processes. Damgaard et al. [119], instead, focused also on the impact of the leaches produced in a landfill on groundwaters in a long-term timeframe. The geography location is an important parameter when describing a landfill, especially when a forecast of the leachate production to the annual waste flow rate is the goal of the study. Caprile and Ripa [120] expressed the influence of waste composition with high organic content on the environmental burden of landfilled waste in Argentina. The incorporation of biogenic emissions results in an almost 50% increase in the global warming effects caused by carbon dioxide in all the examined scenarios, in contrast to estimations that just consider the environmental burden of fossil carbon. Therefore, also biogenic CO₂ emissions must be accounted for. Regarding biowaste treatment, Cusenza et al. [121] examined the effects of residual waste generated by the agro-food industry in Sicily, specifically focusing on the implementation of energy recovery using biomass-based waste management practices. Based on their research, the implementation of a CHP unit has the potential to achieve a substantial 66% decrease in emissions related to climate change.

The environmental impact of an anaerobic digestion plant, which incorporates energy recovery from biogas conversion, was documented by Fantin et al. [122] by ISO standard 14040 [123]. The study stated favourable results indicating a decrease in emissions that contribute to global warming and acidification during the whole lifespan of the plant. Other studies focused on technology-specific

performance assessments like in the one of Starr et al [124]. They examined the mitigated effects of various advanced biogas upgrading methods, including chemical/amine cleaning and bottom ash recovery. Their findings indicated that bottom ash recovery demonstrates the highest level of environmental efficiency. Blengini et al. [125] and Cadena et al. [126] subsequently employed a similar methodology in their respective studies on aerobic composting plants situated in Italy and Spain. Both individuals emphasised the significance of the collection process, the exclusion of certain items such as recovered materials and fertilisers, and the assessment of the waste input. Indeed, the analysis of the impact of landfills has been effectively examined [117]–[119] with the same adaptable methods that LCA can offer. Moreover, several works have implemented the LCA methodology to assess the environmental impact of microalga production systems with wastewater remediation [127]–[129] even integrated with microalgae production. For example, Pérez-López et al. [130] compared different outdoor PBRs for the prediction of the best configuration from the environmental perspective considering the seasonality. Sun et al. [131] clearly expressed the importance of the methodology in the quantification of the benefits achieved when the recovery and recycling paradigms are applied in large-scale microalgae production systems from wastewater. Ferreira et al. [132] compared different methods for microalgae harvesting (gravimetric sedimentation, coagulation, biofilm reactor). In the study of Tua et al. [133], the application of microalgae harvesting to energy purposes could bring consistent energy savings and thus environmental benefits. Despite a large amount of studies in the field, several intrinsic issues arise for the development of a clear green framework such as data uncertainties [134], emission quantification related to specific time frames [135], [136] and background system modelling [137], geography influence [111]. LCA is a method used to evaluate the environmental impacts of a product, process, or activity throughout its entire life cycle. LCA is a widely known holistic methodology that assesses the environmental footprint through the entire life of the product investigated, from its manufacturing to disposal [110]. This includes stages from raw material extraction and production to use, disposal, and potential recycling or reuse. LCA aims to provide a comprehensive view of the environmental burdens associated with different choices and guide decision-making toward more sustainable options. Indeed, LCA can support policymakers in planning optimal measures. The burden-shifting issue, always discussed in a LCA analysis, is a statement about the side implications of plausible solutions in an environmental concern. This is the reason why appropriate analyses need to focus on the consistency of the data, the uncertainty quantification, and sensitivity scenarios for obtaining a consistent LCA study.

1.7 Conclusions

In this Chapter, the main issues concerning the field of waste treatment are presented. Recycling is considered to be the most virtuous approach for embracing a sustainable circular economy paradigm. Anyway, it is not possible to achieve complete material recovery from wastes, therefore landfilling and centralised incineration are the standard treatments used for the scope. Their impact affects various ecosystems, especially due to the release of pollutants into the soil, the water, and the atmosphere. The scope of this thesis is to investigate other valuable alternatives that can be implemented at smaller scales and can reduce the load exerted on centralised systems. Gasification is considered as the main technology discussed in this thesis and it is linked to various power systems for combined energy generation. Then, the attention is moved to biofuel production from fast pyrolysis of wooden biomass and microalgae cultivation in closed PBR, using diluted wastewater as a growing medium. Different thermodynamical models are developed for the gasifier, the power systems, the pyrolysis, and the biodiesel production facility, while experimental investigations are conducted in the laboratory to address biomass productivity. The modeling approach used for each component/system takes into account the gaps present in the relevant literature. Finally, the Life Cycle Assessment methodology is used to characterise the impact of a real treatment system that accounts for several processing units like compost production, mechanical and biological treatment units, sanitary landfill, and power generators. The data from this system is used to support the studies expressed in the following chapters.

Abbreviations

CFB	Circulating fluidized bed
CGE	Cold Gas Efficiency
CHP	Combined Heat and Power
COD	Chemical Oxygen Demand
DME	Dimethyl Ether
ER	Equivalence Ratio
EWC	European Waste Code
HRSG	Heat Recovery Steam Generator
ICE	Internal Combustion Engine
IGCC	Integrated Gasification Combined Cycle
IPCC	International Panel of Climate Change

LC	Leachate
LCA	Life Cycle Assessment
LCI	Life Cycle Inventory
LCIA	Life Cycle Impact Assessment
LHV	Lower Heating Value
MBT	Mechanical Biological Treatment
MSW	Municipal Solid Waste
NIMBY	Not in My Backyard
NREL	National Renewable Energy Laboratory
ORC	Organic Rankine Cycle
PBP	Payback period
PBR	Photobioreactor
RDF	Refuse-Derived Fuel
RMSW	Residual Municipal Solid Waste
sCO ₂	Supercritical CO ₂
SRF	Solid Recovered Fuels
W2E	Waste-To-Energy
WW	Wastewater
WWTP	Wastewater treatment plant

CHAPTER 2

DESCRIPTION OF THE WASTE TREATMENT FACILITY

2.1 Waste treatment system

The case study waste treatment is a municipal company that deals with the treatment of waste from different areas near the upper Tevere Umbro, located in the town of Città di Castello. In the locality of Belladanza, the company has a controlled landfill with methane collection to be used for energy recovery and a mechanical-biological treatment plant (MBT) that allows the production of soil improver and bio-methane.

The system has been designed to handle an annual treatment capacity of 100,000 metric tons of municipal solid waste (MSW), including both organic fraction of municipal solid waste (OFMSW) and residual municipal solid waste (RMSW). The construction of the composting section was successfully concluded in 2018. After a thorough preliminary assessment phase for its startup procedures, full operations commenced in 2019. In the initial stages of the pandemic, the facility faced saturation of its capacity due to a substantial increase in waste generation. This rise was primarily attributed to the temporary closure of nearby waste treatment facilities. Consequently, the quality and yield of the produced biogas were negatively affected. Different functional areas characterize the site:

- the MBT unit, where materials from unrecyclable MSW, such as fermentable organic matter, scrap metals, glass, and bulk debris, are recovered with magnetic attractors and a series of rotary sieves. The main advantages brought by the MBT process are the reduction of the landfilled material and the avoided green-house gas (GHG) emissions that inevitably arise in a typical incinerator system. The machineries used in the separation not only compel an increase of the commodities consumption (water, energy, fuel), but also enhance the compost and biogas production.
- several anaerobic digesters aided with ventilation and temperature control systems, where organic matter is fermented by mesophilic bacteria, release biogas. The former has a variable composition of CO₂ and CH₄ respectively around 40% and 55%;

- a volumetric dome for biogas storage, suited with a safety combustion flare for quality and process control.
- a combined heat and power (CHP) production unit for 700 kW_e/400 kW_t design load, fed with the biogas produced in the digesters and collected in the dome. The efficiency at 100% load, is 83.6% (42.1% electric efficiency, 41.5% thermal efficiency) and slightly higher at partial loads, i.e. 84.4% and 84.8% respectively at 75% and 50%. Flue gas temperature is around 460 °C and suitable for additional thermal recovery, but no heat exchangers were installed. The heat is conveyed to the digesters by a cooling water piping network and sustains the chemical reactions required for putrescine the OFMSW;
- the aerobic stabilization section for compost production, obtained as the refinement of the digestate produced and stationed under an open shed; The production of the compost consists of an anaerobic digestion at a regime temperature of 45 °C. Reactor temperatures are kept constant thanks to integrated boilers and a co-generator installed for the energy enhancement of the biogas produced by digestion. The digestate is then aerobically stabilized and refined; from this phase, high-quality compost (HQC) is obtained, intended for sale, and low-quality compost (LQC) is used for the landfill coverage.
- an air treatment section, represented by six scrubbers and a biofiltration unit for air treatment which have the role to capture the atmospheric pollutants released in the air and maintain negative gauge pressure across the various sections. The biofilter is composed by organic porous material that traps the pollutants and odours sucked by the scrubbers, and its total size is 2,530 m²;
- the sanitary landfill for the disposal of the RMSW, either from MBT or external supply. An expansion of the actual capacity is foreseen in the next years in order to have 410,000 m³ available in total;
- An Internal Combustion Engine (ICE) system fuelled by the biogas generated within the sanitary landfill, with a nominal power capacity of 250 kW_e. Notably, the CHP unit's electrical output is predominantly utilized for self-consumption in the air treatment procedure, recognized as the most energy-demanding operation on-site. Conversely, all the energy generated by the landfill ICE system is fed into the grid.

Before treatment, MSW are pre-treated in the unloading section. The system is designed to accommodate around 100 ktons of waste per year. The incoming annual waste are treated as follows: more than 50 ktons year⁻¹ of residual MSW, produced by external treatment facilities, are directly

sent to the sanitary landfill, while almost 50 ktons year⁻¹ are sent to the composting facility and the MBT composting section. The heterogenous residual waste produced in these units are sent to the landfill as well, for an annual volume of 30 ktons, of which 11 ktons are LQC Hence, the overall amount of residual waste landfilled is 80 ktons year⁻¹, while the amount of HQC sold in the market is about 2 ktons year⁻¹. The overview of the system is presented in Fig. 2-1, while in Fig. 2-2 are shown the pictures of the relevant subsections of the treatment facility.



Fig. 2-1. Overview of the waste treatment facility under analysis, with detailed infographics of the relevant sections.



Fig. 2-2. Pictures of the different sections in the facility. a) MBT unit, b) anaerobic digesters, c) volumetric dome, d) aerobic stabilisation shed, e) scrubbers and f) sanitary landfill.

Additional data is reported in Chapter 7 dedicated to the life cycle assessment study, where data is described in the section related to the inventory analysis.

2.2 Environmental emissions of the facility

2.2.1 Gas Emissions

There are different gaseous emissions points monitored in the facility, but mainly related to the biofilter and the flue gases of the CHP and ICE units. At the emissions monitoring point following the biofilter, the compounds NH_3 (max 5 mg Nm^{-3}), H_2S (max 5 mg Nm^{-3}) and odour (max 60 UOE m^{-3}) are measured every 24 hours. Regarding the CHP and ICE units, the flue gas sensor is active for 295 days with 24h sampling time. The flow rate is $3,000 \text{ m}^3 \text{ h}^{-1}$ and the temperature of $550 \text{ }^\circ\text{C}$, whereas the flue gas meter of the landfill generator group has the same sampling frequency but provides a

single flow rate of 1,500 m³ h⁻¹ and a temperature of 470 °C. Table 2-1 reports the other parameters recorded annually and their associated maximum limit.

Table 2-1. Parameters to be measured annually with the relevant limits for flue gas monitoring points.

Parameter	Limit
Dust	10 mg Nm ⁻³
HCl	10 mg Nm ⁻³
Total Organic Carbon (TOC)	150 mg Nm ⁻³
HF	2 mg Nm ⁻³
NO _x	450 mg Nm ⁻³
SO ₂	50 mg Nm ⁻³
CO	500 mg Nm ⁻³

The hourly gaseous emissions produced in the biofilter, CHP, and ICE units as reported in Table 2-2. The total emissions are obtained by multiplying the tabled values with the expected air/biogas volume flow rates. For instance, the annual volumetric flow rate of the air treated in the biofilter is around 14,200,000 Nm³ year⁻¹, which gives the following emissions: 669 kg year⁻¹ of ammonia, 5 kg year⁻¹ of HCl, 680 kg year⁻¹ of volatile organic substances (SOV) and 9,300 kg year⁻¹ of total organic carbon (TOC).

Table 2-2. Gaseous emissions from the system.

Element	Amount [mg Nm ⁻³]		
	Biofilter	CHP	ICE
Particulates	-	1.24	3
TOC	64.5	116	93
CO	-	89	373
NO _x	-	147	272
SO ₂	-	-	1
HCL	-	-	3
H ₂ S	0.035	-	-
NH ₃	4.64	-	-
VOS	4.71	-	-

2.2.2 Liquid Emissions

Leachate and wastewater compositions represent the predominant aqueous emissions within the system under consideration. The facility comprises a network of seventeen distributed collection points, used to monitor whether the pollutant concentration thresholds meet legal standards. In

particular, four collection points are in the perimeter of the sanitary landfill, while eleven are spread in the composting facility and two are associated with the air treatment section (scrubber and biofilter). Samples are collected and controlled to check the pollutant concentrations. The measurements must be done every trimester for the leachates and every year for wastewaters. For leachates, threshold limits are defined for substances like dioxins and furans (polychlorinated biphenyls, perfluoro-octane-sulfonic acid, poly-chlorinate naphthalene, and so forth). The annual production of leachates is 12 ktons year⁻¹, whereas wastewater is only 4 ktons year⁻¹. Table 2-3 and Table 2-4 define the average composition of these fluids. The amount of nitrogen (as ammonia), chlorine, and metal content has a non-negligible environmental impact.

Table 2-3. Average composition of landfill leachate.

Leachate (12 kton year⁻¹)	U.M.	Mean	S.D.
pH	-	7.74	0.55
COD	mg l ⁻¹	16,110	12,679
Nitrogen (as Ammonia)	mg l ⁻¹	3,528	953
Chlorine	mg l ⁻¹	2,809	731
Metals*	mg l ⁻¹	37	20
Phenols	mg l ⁻¹	4.41	2.69
Toluene	mg l ⁻¹	0.02	0
(m,p)-Xilene	mg l ⁻¹	0.01	0

* Contains Arsenic, Cadmium, Chromium, Iron, Manganese, Nickel, Lead, Copper, Zinc.

Table 2-4. Average composition of wastewater collected in the system.

Wastewaters (4 kton year⁻¹)	U.M.	Mean	S.D.
pH	-	9.38	1.08
Dry Matter (105 °C)	%	1.93	0.76
Ash	%	0.87	0.31
COD	mg l ⁻¹	13,678	6,128
BOD5	mg l ⁻¹	8929	4415
Nitrogen (as Ammonia)	mg l ⁻¹	20,791	4,004
Chlorine	mg l ⁻¹	21,109	4,231
Metals*	mg l ⁻¹	559	145
Phenols	mg l ⁻¹	35	16

* Contains Arsenic, Selenium, Cadmium, Mercury, Chromium, Iron, Manganese, Nickel, Lead, Copper, Zinc.

2.2.3 Soil Emissions

The most relevant soil emissions are represented by the metals inside the HQC sold to the market. If the limits, as expressed in Table 2-5, are overcome the residual compost becomes LQC and is used to cover the landfill. The control of the compost must be done every month according to the limits reported in the legislative decree 75/2010.

Table 2-5. Parameters are to be measured annually with the relevant limits for compost quality.

Parameter	Limit
Moisture (105 °C)	50
pH	6-8.8
Pb	140 mg kg ⁻¹
Ni	100 mg kg ⁻¹
Cd	1.5 mg kg ⁻¹
Hg	1.5 mg kg ⁻¹
Cu	230 mg kg ⁻¹
Cr VI	0.5 mg kg ⁻¹
TOC	34.1% dry matter
Total Organic Nitrogen (TON)	80% dry matter
C/N ratio	25%
Plastic and Glass	0.5% dry matter

Table 2-6 reports the actual composition of the HQC produced in the composing section. The quality is expressed by the high content of the nitrogen, which is suitable for soil fertilizing and hence substitutes eventual chemical fertilizers available in the agricultural market.

Table 2-6. High-quality compost composition

Element	High-Quality compost (HQC)	
	Amount	U.M.
Metals ⁽¹⁾	224.46	Mg kg ⁻¹
Potassium	1.53	
Sodium	1.26	
Calcium	3.92	
Magnesium	0.77	% d.b.
TOC	45.48	
TON	95.83	
C/N ratio	19.41	

(1) Contains lead, nickel, cadmium, mercury, copper, chromium, selenium, arsenic, and zinc.

2.3 CHP unit and biogas generation

Table 2-7 reports the main performance data of the CHP unit with load variation. As concerns the ICE unit, only the nominal power (250 kW) is known, no further data are available besides the energy production.

Table 2-7. Performance data of the CHP unit.

Parameter	CHP		
	100% Load	75% Load	50% Load
Electrical Power [kW]	700	525	350
Thermal Power [kW]	379	309	242
Fuel Consumption [kW]	1,664	1,290	920
El. Efficiency	42.1	40.7	38
Th. Efficiency	41.5	43.7	46.8
Total Efficiency	83.6	84.4	84.8

The monthly-averaged annual production of biogas from the anaerobic digestion is 612,400 m³ (around 64 tons) plus 218,100 m³ (15 tons) sent to flare. The related electricity production is about 961,900 kWh mainly used for self-consumption. The biogas produced at the landfill, instead, is equal to 970,200 m³ (98.5 tons) which is converted to 1,265,000 kWh of electric energy.

2.4 Mechanical-biological treatment unit

The main advantages of the MBT process are a reduction in the amount of waste that ends up in landfills and an avoidance of the GHG that usually arises from burning MSW. Fig. 2-3 illustrates the overall impact of such a unit on the composting process. The machinery employed for separation necessitates higher consumption of resources such as water, energy, and fuel. However, it also results in an improvement in both compost and biogas production.

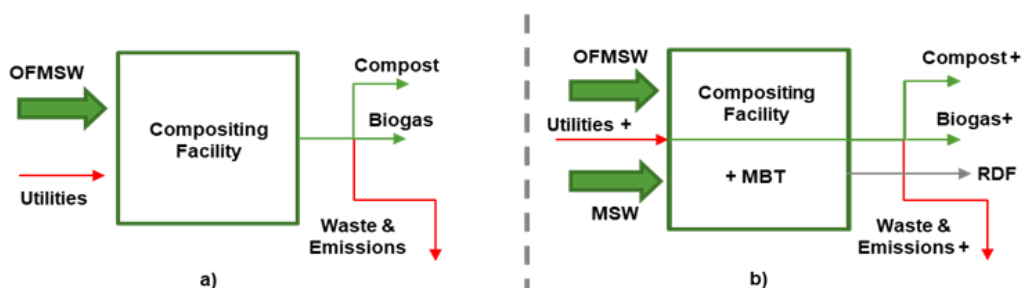


Fig. 2-3. Material and energy flows in a standard composting facility (a), and with MBT implementation (b) [138].

It is worth noting that the residual solid waste material can be effectively reused for the production of refuse-derived fuels (RDF), which are solid pellet-like substances specifically designed for energy-

intensive applications like blast furnaces, clinker production, and steel manufacturing. The process of RDF production not only represents an environmentally responsible approach to waste management but also contributes to reduce the volume of materials ultimately sent to landfills.

This potential integration of RDF production into the waste management system is justified by the substantial volume of 20,000 tons per year of RMSW currently generated within the MBT unit. This circumstance underscores the pressing need for an efficient use of the available sanitary landfill capacity, thus ensuring a more sustainable and eco-friendly approach to waste disposal. Furthermore, if the RMSW is processed locally rather than shipped to outside facilities, or even outside of Italy, fewer emissions associated with transportation are anticipated, and gasification has less of an impact than incineration. [26], [139]. Additional revenues may be obtained if RMSW-based RDF is used for energy production, especially if cogeneration is adopted. They can also cover the utilities required for the cold treatment of MSW, especially related to the MBT unit. Therefore, in the next sections, a simplified estimation of the energy that can be recovered by RDF gasification is presented. The technology assumed is the combustion of the syngas in an external combustion chamber [139]. The heat from the flue gases is transferred to a heat recovery steam generator for combined energy production. The RMSW composition of the company in 2019 concerns 4 samples collected on the dates 14/03, 13/06, 19/09, and 11/12. The abbreviations are respectively 206/2019-C3, 537/2019-C3, 861/2019-C5, 1212/2019-C2. The quantity analysed is 150 kg, except for sample 206/2019-C3, which has a total effective of 144.4 kg. Three analyses were provided for 2020: 387/2020 of 20/05/20, 638/2020-c5 of 23/07/20, and 1119/2020 which summarizes the period from 28/10/20 to 10/11/20. Three further analyses were subsequently provided for 2021, namely 56/2021, 356/2021 and 773/2021. The fractions of material shown in Table 2-8 have been identified for each. The main elements of the undifferentiated are packaging plastic (32% in 2019, 46% in 2020, and 50% in 2021), paper/cardboard (about 27% in three years), and fabric rags (13% and 14% and 11%); in 2019 there is also a large percentage of diapers (10%). In addition, 4 analyses were provided on the chemical nature of the RMSW: samples 1903780-001 and 1913456-003 of 2019, analysed in a time frame of about 15 days (from 15/03 to 01/04, from 16/09 to 30/09) and the samples of 2020 2000610-003 and 686/2020-C2; for the first the measurement campaign was from 17/01 to 24/01, while for the second from 23/07 to 21/08. The most abundant waste materials are plastic (40%), paper (30%) and textile (10%). The chemical characterisation of the waste is given in Table 2-9. The analyses on the samples 1913456-003 and 2000610-003 express the RMSW lower heating value (LHV) [kJ/kg] varies significantly between the two measurements: 21,800 kJ kg⁻¹ (uncertainty of 95% equal to 760 kJ/kg) and 10,040 kJ kg⁻¹ (uncertainty 210 kJ kg⁻¹). It is not possible to know the precise composition of the

RMSW in such data, since the dates of performance of the analyses are different; however, the difference can be reasonably associated with a lower plastic content combined with a higher moisture content (the dry residue at 105 °C of the sample 2000610-003 is 66% against 75% of 1913456-003); the effects imposed by temperature and seasonal humidity are not excluded. This strong deviation is one of the main problems of the feasibility study because the energy content of the waste allows us to evaluate the thermal potential of the plant. The carbon and hydrogen fractions are also lower in the latter case. All emission values are below the legal limit.

Table 2-8. RMSW sample composition of 2019, 2020 and 2021.

RMSW	2019					2020				2021			
	206/2019-C3	537/2019-C3	861/2019-C5	1212/2019-C2	Mean	387/2020	638/2020-C5	1119/2020	Mean	56/2021	356/2021	773/2021	Mean
	Date of Analysis	14/03/2019	13/06/2019	19/09/2019		11/12/2019	20/05/2020	23/07/2020		28/10/2020-->10/11/20	20/01/2021	20/04/2021	
Organic content	2.1	0	0	0	0%	0	0	0	0.00%	0	0	0	0%
Coverage plastics	36.3	53.7	40.8	59.4	32%	71.1	86.3	47.4	46%	74.9	83	65.2	50%
Other plastics	0	0	10.2	6.3	3%	8	9	0	4%	5.4	1.6	2.5	2%
Yard trimmings	0	0	0	0	0%	0	0	0	0.00%	0	0	0	0%
Glass	6.3	8.4	0.8	0.6	3%	0.5	0	18	4%	2.3	1.4	0.9	1%
Aluminium	5.9	6.4	0.3	0.2	2%	0.1	0	0	0%	1	2.8	1	1%
Iron	1.2	0	0	0	0%	0	0	0	0%	0	0	0	0%
Wood	0	0	0.1	0	0%	0	0	1.5	0%	0	0	0	0%
Paper and cardboard	35.6	35.6	54	38.1	27%	44.3	16.5	60.3	27%	41.5	30	43.3	26%
Electronic wastes	0	0	0	0	0%	0	0	0	0%	0	0	0	0%
Leather	5.1	10.6	11.4	9.2	6%	7.5	0	0	2%	0	8.2	15.6	5%
Textile	26.6	12.6	14	24.3	13%	8.3	35.6	20.4	14%	22.5	15.3	11	11%
Diaper	23.1	15	14.4	9	10%	5	0	0	1%	2.4	6.5	8	4%
Tetrapack	2.2	3	0.5	0	1%	0.1	0	2.4	1%	0	0	0.2	0%
Hazardous	0	0.6	0	0	0%	0	0	0	0.00%	0	0	0	0%
Inert	0	0	0	0	0%	0	0	0	0.00%	0	0	0	0%
Other RMSW (under 20 mm)	0	0	0	0	0%	5.1	0	0	1%	0	0	0	0%
Bulk materials	0	0	0	0	0%	0	0	0	0.00%	0	0	0	0%
Bioplastics	0	4.1	3.5	2.9	2%	0	2.6	0	1%	0	0	0	0%
Other	0	0	0	0	0%	0	0	0	0.00%	0	1	2.3	1%
Total mass sample	144.4	150	150	150		150	150	150		150	150	150	

Table 2-9. Chemical composition of RMSW in 2019-2020.

DATA	15/03/2019--->01/04/2019		16/09/2019--->30/09/2019		17/01/2020--->24/01/2020		23/07/2020--->21/08/2020	
	Sample 1903780-001		Sample 1913456-003		Sample 2000610-003		Sample 686/2020-C2	
	Mean	Deviation (2 σ)	Mean	Deviation (2 σ)	Mean	Deviation (2 σ)	Mean	Deviation (2 σ)
Dry Matter	78.50%	$\pm 3.9\%$	75%	$\pm 5.3\%$	66%	$\pm 4.6\%$	97.70%	-
Ashes	15.40%	$\pm 0.77\%$	1.20%	$\pm 0.084\%$	14.00%	$\pm 0.98\%$	4.6%	-
H ₂ (Dry basis)	-	-	8.43%	-	5.65%	-	-	-
pH	7.68	± 0.38	5.92	± 0.3	6.63	± 0.33	8.2	-
TOC [mg kg ⁻¹]	384,000	$\pm 58,000$	418,000	$\pm 63,000$	268,000	$\pm 40,000$	28,333	-
Density [g cm ⁻³]	-	-	0.61	± 0.043	0.67	± 0.047	-	-
LHV [kJ kg ⁻¹]	-	-	21,800	± 760	10,040	± 210	-	-

2.5 Preliminary power plant assessment with gasification

The average LHV obtained for the year 2019 is 15,400 kJ kg⁻¹ with a sample standard deviation of 2,180 kJ kg⁻¹, while for 2020 the value is 18,450 kJ kg⁻¹ (higher due to the greater presence of plastics) and uncertainty of 3,040 kJ kg⁻¹; the average of the two annual values leads to characterise the RDF with a LHV of 17,000 kJ kg⁻¹ with deviation 2,860 kJ kg⁻¹. The dispersion data is amplified by the fact that the number of tests received is small. The size of the plant is calculated by multiplying the calorific value by the mass flow rate of incoming waste, equal to about 2.3-ton h⁻¹. Potentially, it is expected 13.8 MW, 6.4 MW, and 10.6 MW respectively.

The main product of gasification, syngas, must be assessed in terms of calorific value and specific heat, density, and yield from the fuel. The process parameters that most affect its enthalpy are the temperature, the chemical composition of the fuel, the pressure inside the gasifier and the amount of oxidant. For this purpose, the following assumptions were considered:

- Syngas temperature of 800 °C;
- Syngas density of 1,1 kg Nm⁻³;
- Syngas composition as reported in [140] at 800 °C (13.5% CO, 12% CO₂ and 19% H₂);
- Specific heat of each gas taken from Perry's handbook [141];
- Gasification efficiency, i.e. Cold Gas Efficiency (CGE) as 0.65.
- Syngas yield from referred to unitary kg of feedstock of 3,5 Nm³ kg⁻¹.

As expected, the LHV of the syngas varies in the range of 7.2-15.6 MJ Nm⁻³. From 20,000 ton year⁻¹ of RDF, it is possible to have 8,000 Nm³ h⁻¹ of syngas. Syngas energy can be directly employed for steam generation in a Rankine cycle that can generate electricity from the expansion section and

thermal energy from that for condensation. In conclusion, the expected power is between 1-2,2 MW_e while thermal output is between 2.3-5 MW_t. The wide range reflects the drawback of using gasification for this particular waste, i.e. the high influence of its composition. A proper gasifier must be chosen to handle this bottleneck.

2.6 Conclusions

In this Chapter, it has been described the system used as a case study. Landfill, anaerobic digestion, and mechanical and biological treatment unit are the most interesting sections. A preliminary quantification of the energy that can be recovered with residual municipal solid waste gasification is given, at will be the solution discussed in the next two chapters. Then, the focus of the thesis will be focused upon biofuel generation from microalgae harvesting and fast pyrolysis.

Abbreviations

CGE	Cold Gas Efficiency
CHP	Combined Heat and Power
ER	Equivalence Ratio [-]
GHG	Green House Gas
HQC	High-Quality Compost
ICE	Internal Combustion Engine
LCA	Life Cycle Assessment
LHV	Lower Heating Value [kJ kg ⁻¹]
LQC	Low-Quality Compost
MBT	Mechanical Biological Treatment
MSW	Municipal Solid Waste
OFMSW	Organic Fraction of Municipal Solid Waste
RMSW	Residual Municipal Solid Waste
TON	Total Organic Nitrogen

CHAPTER 3

STATE OF ART OF GASIFICATION AND THERMODYNAMIC MODELLING

3.1 Gasification of MSW

3.1.1 Introduction

Combustion, gasification, and pyrolysis are the main methods to convert energy from waste. The combustion process is carried out in incinerators, which valorise the waste by producing combined thermal and electrical power. Temperatures can reach up to 1,200 °C.

The search for the optimal gasifier design, accounting for size and composition, is a crucial endeavor in the field of energy conversion and sustainability. Gasification is a thermochemical process that converts solid or liquid carbonaceous materials into valuable gases like hydrogen, carbon monoxide, and methane. Finding the best gasifier involves a meticulous exploration of both its physical dimensions and the composition of the feedstock used. Size considerations are pivotal as they impact efficiency and scalability. Smaller gasifiers are suitable for decentralized applications, while larger ones may be more suitable for industrial settings. Optimizing size entails striking a balance between throughput and operational efficiency. The composition of the gasifier is equally vital. The choice of feedstock, such as biomass, coal, or waste materials, significantly influences gasification performance. Variables like moisture content, ash content, and elemental composition affect gas quality and environmental impact. A comprehensive review of the literature is indispensable to identify the most efficient gasifier configuration for a given application, as it can vary depending on factors like feedstock availability and regional energy needs. The purpose behind the quest for the ideal gasifier design, considering size and composition, is driven by the aspiration to replicate experimental results through the development of a robust thermodynamic model. This goal is driven by the desire to better understand and predict the gasification processes of refuse-derived fuels (RDF). Such a thermodynamic model would encompass various parameters, including temperature, pressure, feedstock composition, and gasifier size. It would need to consider complex chemical reactions, heat transfer mechanisms, and mass transport phenomena within the gasifier. The model's success lies in its ability to simulate these intricate processes and predict gas composition, energy output, and

environmental impacts under different operating conditions. The following references (Table 3-1) were taken from literature about experimental analyses of air gasification of plastic wastes.

- *Air gasification of mixed plastic wastes using a two-stage gasifier for the production of producer gas with low tar and a high caloric value* [65], ID1;
- *Study of hydrodynamic characteristics in a circulating fluidized bed gasifier for plastic waste by computational fluid dynamics modeling and simulation* [142], ID2;
- *Air gasification of PVC (polyvinyl chloride)-containing plastic waste in a two-stage gasifier using Ca-based additives and Ni-loaded activated carbon for the production of clean and hydrogen-rich producer gas* [143], ID3;
- *Air gasification of polypropylene plastic waste in fluidized bed gasifier* [144], ID4;
- *Fluidized bed gasification of waste-derived fuels* [145], ID5;
- *H₂-rich syngas production by fluidized bed gasification of biomass and plastic fuel* [140], ID6;
- *Co-gasification of Plastics and Biomass in a Dual Fluidized-Bed Steam Gasifier: Possible Interactions of Fuels* [146], ID7;
- *A techno-economic comparison of fluidized bed gasification of two mixed plastic wastes* [147], ID8;
- *Co-gasification of coal, plastic waste, and wood in a bubbling fluidized bed reactor* [71], ID9;
- *Conversion of mixed plastic wastes in a dual fluidized bed steam gasifier* [148], ID10;
- *Hydrogen production from steam gasification of polyethylene using a two-stage gasifier and active carbon* [67], ID11;
- *Characteristics of gas from the fluidized bed gasification of refuse paper and plastic fuel (RPF) and wood biomass* [64], ID12;

Refuse Derived Fuel (RDF) production and gasification in a pilot plant integrated with an Otto cycle ICE through Aspen plus modelling: Thermodynamic and economic viability [149], ID13.

Table 3-1. Summary of different gasifiers in literature.

Paper		Gasifier type				Operating Conditions							Feedstock		Syngas output (volumetric fraction)													CGE	
ID	Year	Gasifier type	Size [m]	Power [kW]	Agent	air flow rate [kg h ⁻¹]	ER	steam flow rate [kg h ⁻¹]	S/F	feed flow rate [kg h ⁻¹]	T [°C]	retention time [min]	feed type	Density [kg m ⁻³]	LHV [MJ Nm ⁻³]	N ₂	CO ₂	H ₂	CO	CH ₄	C ₂ H ₆	C ₂ H ₄	C ₂ H ₂	C ₃ +C ₄ +C ₅	Benzene	Toluene	Tar [mg Nm ⁻³]	CGE [%]	
ID1	2011	double stage fluidized bed	Lower: 0.11*0.39 Upper: phi0.16*0.34	-	air	-	0.21	-	-	-	0.43	802	42	Mixed plastic waste	-	13.44	50.99	3.96	14.18	6.56	15.7	0.5	6.06	-	0.48	1.48	0.07	3.22	-
							0.26				0.35	812	52			10.87	56.91	5.02	13.34	5.61	12.63	0.35	4.41		0.33	1.34	0.05	2.49	
							0.31				0.29	814	62			7.79	64.02	5.17	12.67	5.37	8.71	0.2	2.59		0.21	0.99	0.05	2.15	
							0.62				0.14	815.5	90			3.54	71.54	6.74	12.56	5.01	3.64	0.02	0.27		0.02	0.21	0	0.2	
							0.21				0.44	767.5	41			12.88	53.67	4.52	13.52	5.49	14.07	0.84	5.64		0.63	1.46	0.13	5.75	
							0.20				0.45	832.5	40			12.27	49.8	3.69	18.15	7.18	15.03	0.18	3.95		0.5	1.46	0.03	1.76	
							0.21				0.44	796	41			13.12	48.54	4.28	17.47	6.87	15.1	0.5	5.26		0.41	1.49	0.07	3.36	
							0.20				0.45	803	40			12.63	46.75	4.22	21.33	5.97	15.49	0.48	4.1		0.29	1.31	0.06	2.43	
							0.21				0.44	808.5	41			13.83	51.91	5.48	10.98	5.04	17.09	0.5	6.7		0.65	1.56	0.07	3.51	
							0.21				0.44	809.5	41			14.31	46.14	7.03	13.21	7.72	16.61	0.52	6.44		0.6	1.61	0.09	4.36	
							0.21				0.44	805.5	41			14.13	46.16	7.24	13.16	8.29	16.01	0.53	6.34		0.56	1.59	0.08	4.21	
					0.19				0.47	803.5	38			13.23	50.68	4.46	15.26	6.67	14.76	0.48	5.49	0.47	1.6	0.11	4.86				
ID2	2014	circulating fluidized bed gasifier	phi 0.15x6.2	-	air	-	-	-	-	7200	-	-	-	-	-	-	-	-	-	-	-	-	-	-	-	-	-	-	-

Paper		Gasifier type			Operating Conditions						Feedstock		Syngas output (volumetric fraction)													CGE				
ID	Year	Gasifier type	Size [m]	Power [kW]	Agent	air flow rate [kg h ⁻¹]	ER	steam flow rate [kg h ⁻¹]	S/F	feed flow rate [kg h ⁻¹]	T [°C]	retention time [min]	feed type	Density [kg m ⁻³]	LHV [MJ Nm ⁻³]	N ₂	CO ₂	H ₂	CO	CH ₄	C ₂ H ₆	C ₂ H ₄	C ₂ H ₂	C ₃ +C ₄ +C ₅	Benzene	Toluene	Tar [mg Nm ⁻³]	CGE [%]		
ID3	2015	double stage bubbling fluidized bed reactor	Lower: 0.11*0.39 Upper: phi0.16*0.34	-	air	-	0.32	-	-	-	0.29	804.5	61	LDPE	-	9.8	58.9	9.3	11.2	3.1	11.3	0.32	4.7	0.22	0.15	0.9	0.03	1,416	-	
							0.32	-	-	-	0.29	802	61	PP	-	10.5	53.6	7.1	13.4	8.5	11.4	0.33	4.5	0.18	0.13	0.92	0.03	1,145	-	
							0.33	-	-	-	0.29	808	62	PVC	-	10.4	55.3	7.4	11.6	8.6	10.5	0.31	5	0.12	0.15	0.88	0.03	1,331	-	
							0.32	-	-	-	0.29	799	61	complete mixture	-	9.3	54.2	6.2	14.2	11.7	9.1	0.27	3.3	0.13	0.08	0.86	0.03	1,184	-	
							0.32	-	-	-	0.30	803	60		-	6.4	50.5	6.3	29.8	6	7.3	0.01	0.03	0.003	0	0.03	0	-		
							0.32	-	-	-	0.29	796.5	61	-	6.9	48	3.7	29.7	11.7	6.8	0.01	0.06	0.004	0	0.06	0	-			
							0.32	-	-	-	0.28	800.5	64	-	7.8	46	0.7	29.8	15.5	7.7	0.02	0.08	0.004	0	0.12	0	-			
							0.29	-	-	-	0.33	800	163	-	9.6	53.2	7	17.9	6.3	10.7	0.27	3.5	0.14	0.11	0.81	0.04	1,687	-		
ID4	2006	fluidized bed gasifier	phi 0.1*4.2	-	air	7.76-15.51	0.2	-	-	-	703	constant	polypropylene plastic (dry basis)	-	-	51.51	9.17	4.53	20.34	6.11	8.34		-	-	-	-	-	-	-	-
							0.25	-	-	-	773			51.29	10.92	4.81	22.71	5.17	5.1		-	-	-	-	-	-	-			
							0.3	-	-	-	821			53.28	12.07	5.25	20.41	5.25	3.74		-	-	-	-	-	-	-			
							0.35	-	-	-	852			54.66	13.58	5.75	18.18	5.03	2.8		-	-	-	-	-	-	-			
							0.4	-	-	-	887			57.6	14.52	4.81	16.31	4.53	2.23		-	-	-	-	-	-	-			
							0.45	-	-	-	915			59.26	15.59	4.67	14.8	4.17	1.51		-	-	-	-	-	-	-			
							0.22	-	-	-	30-100			867	60	PE	570	7.5	64.70	9.60	9.50	2.40	9.10	-	4.70	-	-	-	-	-
0.31	-	-	-	-	898	-	-	570	6.3	68.00	10.40	8.10	2.20	7.10	-	4.20	-	-	-	-	-	-	81,000	63						

Paper		Gasifier type				Operating Conditions						Feedstock		Syngas output (volumetric fraction)											CGE				
ID	Year	Gasifier type	Size [m]	Power [kW]	Agent	air flow rate [kg h ⁻¹]	ER	steam flow rate [kg h ⁻¹]	S/F	feed flow rate [kg h ⁻¹]	T [°C]	retention time [min]	feed type	Density [kg m ⁻³]	LHV [MJ Nm ⁻³]	N ₂	CO ₂	H ₂	CO	CH ₄	C ₂ H ₆	C ₂ H ₄	C ₂ H ₂	C ₃ +C ₄ +C ₅	Benzene	Toluene	Tar [mg Nm ⁻³]	CGE [%]	
						0.2					845			570	7.9	64.10	9.10	9.10	2.80	10.40		4.50						160,000	55
						0.27					807			570	6.5	49.00	1.40	26.90	20.00	2.20		0.50						0	82
						0.2					819			570	7.6	45.10	1.60	30.10	18.40	3.40		1.40						0	74
						0.28					816			570	6.5	48.50	1.70	27.10	20.10	2.10		0.50						0	85
						0.31					825			570	6.3	50.30	3.30	24.00	19.50	2.00		0.90						0	88
						0.21					825			570	7.5	44.40	1.60	30.80	19.00	3.20		1.00						0	84
						0.29					850			570	6.4	47.20	1.20	29.10	20.90	1.50		0.10						0	92
						0.3					856			570	7.1	56.20	3.10	14.70	18.30	5.70		2.00						0	94
						0.23					818			460	6.9	46.20	2.30	30.60	17.50	2.80		0.60						0	79
						0.27					831			460	6.8	46.40	1.50	28.20	21.10	2.30		0.50						0	93
						0.24					829			460	7	45.70	1.70	29.50	19.90	2.50		0.70						0	84
						0.29					879			460	7.7	54.80	5.10	13.70	16.70	7.30		2.40						0	93
						0.31					914			340	5.2	68.50	11.40	6.60	4.80	6.30		2.40						56,000	58
						0.25					884			340	6.4	64.20	11.60	8.00	4.60	7.90		3.70						55,000	54
						0.22					869			340	6.8	66.30	11.10	6.80	3.70	7.30		4.80						99,000	54
						0.27					894			310	6.4	65.50	9.80	8.60	5.30	7.30		3.50						59,000	60
						0.24					890			310	7.9	61.00	10.90	9.60	4.50	8.60		5.40						32,000	69
						0.26					879			380	6.2	55.80	14.30	9.90	11.60	6.30		2.10						19,000	60
						0.31					915			380	5	60.70	14.10	7.90	10.90	4.90		1.50						14,000	54

Paper		Gasifier type				Operating Conditions						Feedstock		Syngas output (volumetric fraction)												CGE								
ID	Year	Gasifier type	Size [m]	Power [kW]	Agent	air flow rate [kg h ⁻¹]	ER	steam flow rate [kg h ⁻¹]	S/F	feed flow rate [kg h ⁻¹]	T [°C]	retention time [min]	feed type	Density [kg m ⁻³]	LHV [MJ Nm ⁻³]	N ₂	CO ₂	H ₂	CO	CH ₄	C ₂ H ₆	C ₂ H ₄	C ₂ H ₂	C ₃ +C ₄ +C ₅	Benzene	Toluene	Tar [mg Nm ⁻³]	CGE [%]						
ID6	2012	catalytic fluidized bed gasifier	phi 0,14*2,8	-	steam+air	2,9-5,6	0.34				899			d-RDF	260	5.2	64.70	13.40	5.90	7.60	6.60		1.80						15,000	48				
							0.28				896			d-RDF	260	5.7	62.30	12.30	7.90	8.70	7.00		1.80									43,000	46	
							0.23				869			d-RDF	260	6.9	57.90	12.80	9.20	9.10	8.30		2.70										54,000	49
														biomass + plastic pellets		6.54 [MJ/kg]	36.68	15.74	29.82	13.7	3.33	0.12	0.61					-	79					
														biomass + plastic pellets		3.83 [MJ/kg]	45.93	19.62	21.85	10.19	2.22	0.04	0.15					-	52					
														biomass + plastic pellets		7.72 [MJ/kg]	32.65	16.11	32.04	13.89	3.89	0.28	1.14	-	-	-	-	-	0	73				
														biomass + plastic pellets		7.30 [MJ/kg]	47.22	10	16.3	15.37	11.11							-	94					
														biomass + plastic pellets		6.12 [MJ/kg]	50.74	10.74	15.56	14.63	8.33							0	59					
	ID7	2013	dual fluidized bed	-	100	steam	-	-	-	-	-	-			Wood pellets	-	-	-	-	-	-	-	-	-	-	-	-	-	-	-	-			
									15	0.50	29.86	856			SLF- plastics	14.27	1.55	17.63	37.83	27.48	12.19		3.32											
14.3									0.50	28.56	855			SLF- plastics	16.01	1.92	16.63	36.06	24.96	15.31		5.11												

Paper		Gasifier type				Operating Conditions						Feedstock		Syngas output (volumetric fraction)											CGE					
ID	Year	Gasifier type	Size [m]	Power [kW]	Agent	air flow rate [kg h ⁻¹]	ER	steam flow rate [kg h ⁻¹]	S/F	feed flow rate [kg h ⁻¹]	T [°C]	retention time [min]	feed type	Density [kg m ⁻³]	LHV [MJ Nm ⁻³]	N ₂	CO ₂	H ₂	CO	CH ₄	C ₂ H ₆	C ₂ H ₄	C ₂ H ₂	C ₃ +C ₄ +C ₅	Benzene	Toluene	Tar [mg Nm ⁻³]	CGE [%]		
								13.7	0.73	18.70	852		SLF- plastics	17.63	2.14	16.85	37.39	18.45	18.43											
								13	1.30	10.03	850		SLF- plastics	17.49	2.40	16.85	45.58	8.23	22.19											
								15	0.44	34.31	851		MSW- plastics 50%	16.41	0.87	19.09	34.73	24.43	15.31											
								17	0.80	21.30	852		PE 50%	16.55	0.98	15.51	41.37	22.43	14.05											
								15	2.01	7.47	854		PE 100%	25.83	1.21	8.15	38.05	7.3	30.31											
								18.1	0.70	25.87	852		PE regrind 25%	14.00	0.63	16.18	43.58	25.09	10.93											
								16.7	0.81	20.63	850		PE regrind 50%	16.28	1.05	14.84	42.48	21.9	13.90											
								16.1	1.26	12.74	850		PE regrind 75%	16.14	0.72	8.37	49.34	24.16	12.65											

Paper		Gasifier type				Operating Conditions						Feedstock		Syngas output (volumetric fraction)												CGE				
ID	Year	Gasifier type	Size [m]	Power [kW]	Agent	air flow rate [kg h ⁻¹]	ER	steam flow rate [kg h ⁻¹]	S/F	feed flow rate [kg h ⁻¹]	T [°C]	retention time [min]	feed type	Density [kg m ⁻³]	LHV [MJ Nm ⁻³]	N ₂	CO ₂	H ₂	CO	CH ₄	C ₂ H ₆	C ₂ H ₄	C ₂ H ₂	C ₃ +C ₄ +C ₅	Benzene	Toluene	Tar [mg Nm ⁻³]	CGE [%]		
								14.8	1.98	7.49	848		PE regrind 100%		22.88	1.00	5.8	44.69	9.96	28.58	9.96									
ID8	2011	bubbling fluidized bed gasifier 100 kg/h maximum capacity	phi 0,38 l *5,9	500	air	-	0.21	-	-	-	890	-	SRA 1	-	9.58	64.23	9.74	8.56	3.97	7.63	0.14	3.24	0	-	2.39	-	2,600	71		
						80.41	0.24	25.1	SRA 2	9.4		63.74	9.57	8.38	5.21	7.13	0.04	3.24	0.38	2.19	1,100	79								
ID9	2010	bubbling fluidized bed gasifier 100 kg/h maximum capacity	phi 0,38 l *5,9	500	air	-	0.2	-	-	-	850	-	P1 (50% LS Lignite - 50% mixed	-	6.23	63.35	9.66	9.22	5.76	7.17	0	4.47	0.37	-	-	-	47,983	54		
						0.25	-	-	P1 (50% LS Lignite - 50% mixed	4.74		67.4	9.58	7.7	5.51	5.7	0.06	3.74	0.31	-	-	-	35,032	57						
						0.3	-	-	P1 (50% LS Lignite - 50% mixed	3.47		69.42	9.36	7.62	5.73	5.28	0	2.28	0.31	-	-	-	26,115	58						

Paper		Gasifier type				Operating Conditions					Feedstock	Syngas output (volumetric fraction)											CGE							
ID	Year	Gasifier type	Size [m]	Power [kW]	Agent	air flow rate [kg h ⁻¹]	ER	steam flow rate [kg h ⁻¹]	S/F	feed flow rate [kg h ⁻¹]	T [°C]	retention time [min]	feed type	Density [kg m ⁻³]	LHV [MJ Nm ⁻³]	N ₂	CO ₂	H ₂	CO	CH ₄	C ₂ H ₆	C ₂ H ₄	C ₂ H ₂	C ₃ +C ₄ +C ₅	Benzene	Toluene	Tar [mg Nm ⁻³]	CGE [%]		
													P2 (50% LS Lignite - 30% Mixed)		6.49															
													P3 (50% HS Lignite - 50% mixed)		5.94															
													P4 (50% HS Lignite - 30% Mixed)		6.02															
													P5 (60% LS Lignite - 40% wood)		4.65															
													P6 (60% HS Lignite - 40% wood)		4.65															
													P7 (100% Wood)		7.6															

Paper		Gasifier type				Operating Conditions						Feedstock		Syngas output (volumetric fraction)											CGE											
ID	Year	Gasifier type	Size [m]	Power [kW]	Agent	air flow rate [kg h ⁻¹]	ER	steam flow rate [kg h ⁻¹]	S/F	feed flow rate [kg h ⁻¹]	T [°C]	retention time [min]	feed type	Density [kg m ⁻³]	LHV [MJ Nm ⁻³]	N ₂	CO ₂	H ₂	CO	CH ₄	C ₂ H ₆	C ₂ H ₄	C ₂ H ₂	C ₃ +C ₄ +C ₅	Benzene	Toluene	Tar [mg Nm ⁻³]	CGE [%]								
ID10	2013	dual fluidized bed gasifier	-	100	steam	-	-	15	2	7.5	852	-	PE (dry basys)	-	25.8	0.44	8.12	37.9	7.22	30.23	1.2	14.89							19,536							
								15	2	7.5	855		PP (dry basys)		27.2	0	7.97	33.99	4.06	40.3	1.95	11.73										18,293				
								16.3	1.20	13.6	852		20PE+80PET (dry basys)		16.4	0.75	28.57	26.92	19.85	15.04	0.75	8.12													16,063	
								14.2	1.80	7.9	855		40PE+60PS (dry basys)		17	0.3	7.07	51.13	23.46	11.73	0.6	5.71														10,480
								15	2	7.5	835		50PE+50PP (dry basys)	19.4	0.59	5.11	46.92	21.96	16.7	1.05	7.67							3227								
ID11	2020	two stage fluidized bed gasifier	phi 0,16*0,38	-	steam	-	-	-	-	0.50	774	60	PE	-	28.36	6.94	1.78	34.99	9.13	23.38	1.20	17.62		1.15	3.2			8400	58							
											796	64	PE	-	12.4	3.47	7.35	64.71	11.59	12.72	0.03	0.05			0.08			0	70							
											803	66	PE	-	12.23	4.96	6.59	66.02	9.78	12.51	0.02	0.04			0.07			0	76							

Paper		Gasifier type				Operating Conditions						Feedstock		Syngas output (volumetric fraction)													CGE			
ID	Year	Gasifier type	Size [m]	Power [kW]	Agent	air flow rate [kg h ⁻¹]	ER	steam flow rate [kg h ⁻¹]	S/F	feed flow rate [kg h ⁻¹]	T [°C]	retention time [min]	feed type	Density [kg m ⁻³]	LHV [MJ Nm ⁻³]	N ₂	CO ₂	H ₂	CO	CH ₄	C ₂ H ₆	C ₂ H ₄	C ₂ H ₂	C ₃ +C ₄ +C ₅	Benzene	Toluene	Tar [mg Nm ⁻³]	CGE [%]		
											792	64	PE		12.22	6.12	5.71	64.77	10.83	12.39	0.03	0.08			0.08			6	83	
											789	65	PE		12.4	3.73	7.53	65.91	9.6	13.08	0.02	0.05			0.07			25	84	
											793	65	PE		12.46	4.14	10.68	62.01	8.22	14.74	0.03	0.07			0.01	0.11			10	78
											795	60	PE		12.22	4.72	12.18	60.6	7.74	14.48	0.04	0.1			0.01	0.13			0	71
											797	240	PE		15.33	5.21	10.65	55.47	8.82	14.8	0.62	3.31			0.07	0.98			2,500	80
ID12	2019	fluidized bed gasifier	phi 0,2*1,7	-	air	-	0.48	-	-	23	939	60	wood pellet + water dry basis	3.4	63	15.8	7.3	10.8	2.3	0.8								2500	46	
							0.39			23	790		wood pellet + water dry basis	4.3	60.8	15.7	6.4	12.4	3.3	1.4						3800	48			
							0.32			23	690		wood pellet + water dry basis	4.7	59.2	15.5	7.4	12.8	3.4	1.7							12,100	49		
							0.54			20	900		RPF + water dry basis	4.1	65.8	13.1	4.8	11.6	2.9	1.8							3,400	68		

Paper		Gasifier type				Operating Conditions						Feedstock		Syngas output (volumetric fraction)											CGE													
ID	Year	Gasifier type	Size [m]	Power [kW]	Agent	air flow rate [kg h ⁻¹]	ER	steam flow rate [kg h ⁻¹]	S/F	feed flow rate [kg h ⁻¹]	T [°C]	retention time [min]	feed type	Density [kg m ⁻³]	LHV [MJ Nm ⁻³]	N ₂	CO ₂	H ₂	CO	CH ₄	C ₂ H ₆	C ₂ H ₄	C ₂ H ₂	C ₃ +C ₄ +C ₅	Benzene	Toluene	Tar [mg Nm ⁻³]	CGE [%]										
							0.44			20	728		RPF + water dry basis		5.1	66.1	14.5	3.8	8.6	3		4						4,500	70									
							0.33			20	677		RPF + water dry basis		5.9	63.6	16.3	4.3	7.6	3.1		5.1						14,000	65									
ID13	2017	aspen model downdraft fixed bed gasifier	-	250	air	300	0.14					652		RDF	400	5.04	45.96	0.91	20.43	28.27	4.38										53							
							0.18				-		5.61			45.59	2.01	21.89	27.8	2.71															56			
							0.23					657							5.78	45.23	3.28	22.8	26.99	1.28												58		
							0.27					-							5.78	45.23	4.92	23.16	23.53	0.92													58	
							0.31	-	-			107	682						-																		57	
							0.36						-																									55
							0.41						703																									52
							0.45						-																									50
							0.5									723																						47

As shown in Table 3-1, there are different studies in the literature involving waste gasification. The type of the gasifier, as well as the feedstock characterization and syngas composition, have been reported, too. Most references have similar operating conditions: air as a gasifying agent, one or more gasification stages, the presence of boiling or circulating fluid bed composed of siliceous material such as sands and olivines, operating temperatures between 800 and 900 °C, and the amount of air varying between 0.2 and 0.6 of the ER. In the literature, this parameter is considered the most influencing the gasification process. The main problem of the reported publications concerns the flows of fuel and air, sometimes very small. For this reason, the best gasifier for size and process has been identified in ID5-8-9. In this gasifier, several tests [150] are performed for the conversion of plastic material and RDF. The P&ID diagram and additional process data may be found in [151]. It can handle between 30 and 100 kg h⁻¹ of fuel, up to a thermal input of 500 kW. The airflow rate remains about constant at 100 Nm³ h⁻¹ and is preheated by a series of electric resistances up to 600 °C. The gasification temperature is maintained around 850 °C; the syngas produced are sent in a cyclone and a scrubber to remove solid particles and the water vapour contained in it. The composition of the syngas, namely hydrogen, carbon monoxide, carbon dioxide, methane, and other light hydrocarbons (C₂H₂, C₂H₄, C₂H₆) are measured to determine the calorific value and known this, the efficiency of the process. The fuels tested range from a completely plastic material such as polyethylene "PE", "GS3" and "PLASMIX", characterized by a high calorific value, up to mixtures of plastics such as "NEOLITE", the "PDF" (plastic derived fuels) and "RDF"; the latter has lower chemical energy than the others, and therefore similar to those that would occur from the residues of the MBT of Belladanza. Specifically, the RDF material has the following mass composition (wet basis): carbon 56.8%, hydrogen 8.3%, nitrogen 0.5%, sulphur 0.6%, oxygen 15.7%, humidity 1.9% and ash 16.2%; the lower calorific value is 27,300 kJ kg⁻¹. Neolite instead has higher chemical energy (33,400 kJ kg⁻¹) due to the higher carbon content (68.1%) and hydrogen (13.1%). The PDF, similar in some ways to the RDF, is the least energetic of the three, with just 25,400 kJ kg⁻¹ of energy available. Three tests are reported with the RDF, two with the PDF and three with the Neolite. All were carried out on the same bed of Olivina by varying the amount of air at the entrance of the gasifier. The temperature of the fluid bed settles around 900 °C due to the combustion and conversion reactions of solid carbon, strongly exothermic, while the output syngas is not reported, however reasonably around 850 °C. The tests are characterized by the following equivalence ratios: 0.34, 0.28, 0.23 for RDF, 0.26 and 0.31 for PDF, 0.31, 0.25 and 0.22 for Neolite. Generally, the energy of the obtained syngas increases as the air ratio decreases, this is because less nitrogen is introduced into the system thus favouring gasification reactions, but penalizing combustion reactions. A side effect is the increase of the produced tar, that is condensable elements that are formed in the instantaneous

pyrolysis that the material undergoes at the entrance of the gasifier; the formation is more favoured by the lower temperature of the system. Olivine is however a good material because it promotes the decomposition of these elements in its constituents (carbon and hydrogen) the recorded values denote a low amount in syngas. It is possible to note that the conversion efficiency or cold gas efficiency (CGE) is always low: the maximum value corresponds to 0.6 for PDF-1 (ER equal to 0.26), while the minimum is 0.46 for RDF-2 (ER 0.28). The reason for this can be double: failure to convert all the carbon present in the fuel and formation of CO₂ instead of CO to the thermal equilibrium.

The tests in ID5 provided a dataset of 8 points having three compositions and different ERs. This limited number of data may not support a thermodynamic model. Therefore, additional data points with a similar fluidized bed gasifier were sought. Parrillo et al. [61] conducted similar tests with a fluidized bed gasifier involving biomass. A set of additional data points was obtained by varying the ER between 0.2 and 0.35. Air was used and preheated to 200 °C, lower than the 600 °C of the waste plastics. When biomass is used, gasification can give higher CGE than RDF. The maximum CGE was 0.74 at an ER of 0.31. Moreover, tars are lower: the maximum concentration registered was 5.1 g Nm⁻³, compared to the 130 g Nm⁻³ of ID5. The fluidized bed configuration is considered for the gasification of municipal solid waste blends as also suggested by Hameed et al. [57]. Indeed, compared to the fixed bed configuration, the former offers easier process handling, better scalability, and lower tar production.

3.2 Gasification Models

Despite the listed experimental works at the laboratory scale, only a few MSW/RDF gasifiers have been already installed and are in operation in waste management facilities in Europe [152] regardless of the lower environmental emissions if compared to incinerators. Furthermore, there is a lack of flexible but comprehensive gasification models in literature able to provide estimation of syngas production from heterogeneous material thus supporting preliminary feasibility energy plant analyses. However, there are several models in the literature about gasification in Aspen Plus. Andrés et al. [41] modelled the gasification of sewage sludge in a fluidized bed gasifier based on the nonstoichiometric equilibrium model and minimization of the Gibbs' free energy of the system. The 0D model (no geometry inclusion) was validated with good agreement compared to the experimental results. Fernandez-Lopez et al. modelled organic waste steam gasification with a dual gasifier [153] with a similar methodology approach based on Gibbs' energy. Similarly, Gagliano et al. [154], Lan et al. [155], Paviet et al. [156] and Vaijanath and Sapali [157] presented models for biomass-based

feedstocks based on the same approach, each one validating a single composition. Timsina et al. [158] instead tested his model on different feedstocks, successfully validating it but not including tar formation. Han et al. [159] modelled a downdraft biomass gasification process. The restricted chemical equilibrium approach was used to have a better validation of the model. In this way, only specified compounds are selected by the user to form at the equilibrium or different temperature approaches can be defined to account for the deviation from the chemical equilibrium. Nikoo and Mahinpey [160], as well as Kaushal and Tyagi [161] modelled a fluidized bed gasifier of biomass with several chemical reactions accounting for the kinetics of devolatilization, char formation, cracking and gas reforming. Advanced equations describing the bed hydrodynamics were used, too. Compared to the previous models, which use the RGIBBS block in Aspen Plus, here the RCSTR block is chosen for describing the dense bed and free-board regions. The continuous-flow stirred-tank reactor (CSTR) assumes perfect mixing in the geometry, a simple cave cylinder, in this case, 40x1400 mm. Even if such an extensive mathematical description of the gasifier is given, some inaccuracies still arise in the prediction of the syngas composition.

Puig-Gamero et al. [162] provided an auto thermal air gasifier of biomass involving different feedstocks: pine pellets, eucalyptus (two types) and pine from forest residues. Oxidation and reduction zones of the gasifier were modelled with the RPLUG block, i.e. suitable for characterize chemical reactions in plug-flow mode. Similarly to [160], [161] the model can predict well the syngas composition but high deviations of some components (CO, CO₂, H₂ and so forth) are present.

Moving to waste gasification, Lozano et al. [149] modelled the gasification of RDF including the necessary steps for its preparation (drying, shredding, briquetting) and the consequential syngas combustion in an internal combustion engine (ICE). The model was based on chemical equilibrium calculation with the notorious RGIBBS block linked with Matlab code to assess the equilibrium temperature. CO₂ and CH₄ contents prediction in the syngas was particularly accurate, but H₂ was slightly overestimated (+30%). In the end, the model estimated an energy recovery of around 11% of the total energy of the RDF waste. Rahma et al. [163] reverted to MSW gasification and CO₂ capture. Validated with experimental data on biomass gasification, the model provided a good estimation of the syngas properties via the classical energy minimization approach.

A simplified but comprehensive model of fluidized bed gasifier model that is known involving different plastic wastes is still missing. The model described in this Chapter is developed in the Aspen Plus V10 software environment [164]. The model has been taken from the biomass gasification model of Marcantonio et al. [62], used by Moradi et al. [165] for investigating the integration of a steam-injected micro gas turbine, and finally opportunely readapted for waste plastic gasification. Since

Aspen Plus is a steady-state solver, the inclusion of tars should be done with appropriate modelling blocks that characterize the kinetics of the reactor. The problem is that the latter strongly depends on the geometry of the system itself, at this phase unknown. To avoid unnecessary and complicated assumptions, a simplified approach has been used for the model. In fact. The flowsheet emulates different zones of the gasifiers operating with a “pseudo-equilibrium” approach. There are specified sections that allow the formation of elements that are not expected to form at the chemical equilibrium of the system, i.e. tars and ethylene. Furthermore, the model uses tuned coefficients for validation and sensitivity analysis. After many trials, a total of nine variables and thirteen parameters have been identified. Their discussion is reported in the next section.

3.3 Materials and methods

3.3.1 Model description

The gasification process consists of thermochemical reactions that transform the solid materials into gaseous fuel. The entire process is modelled into four main steps described in Chapter 2: drying, pyrolysis, combustion (oxidation) and reduction. An illustration of the logic of the gasification process modelled in Aspen Plus is reported in Fig. 3-1, concretized in the flowsheet reported in Fig. 3-2.

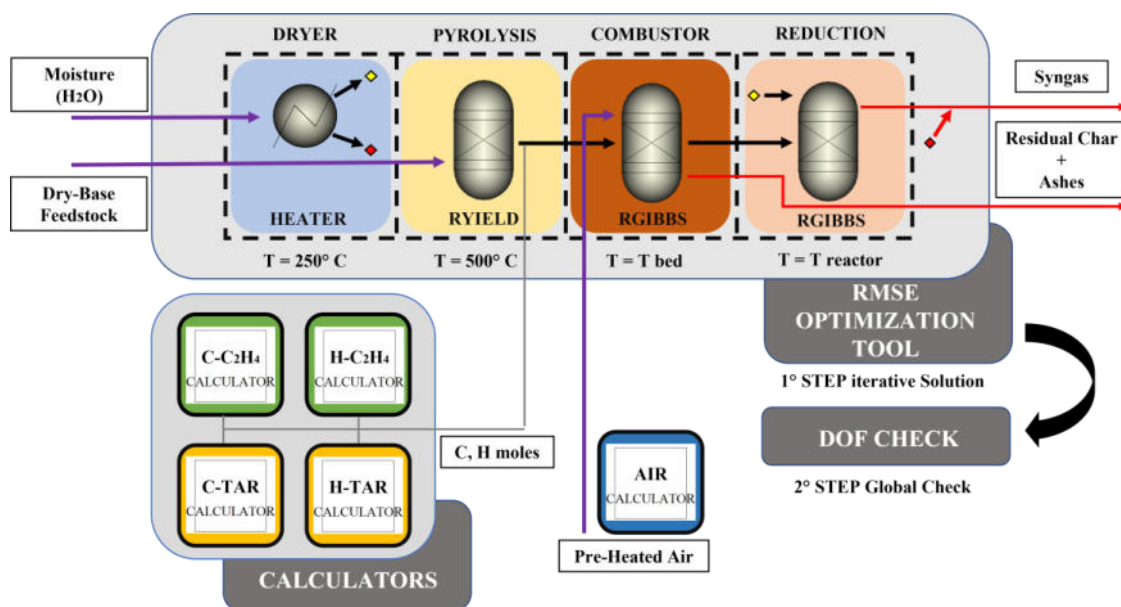


Fig. 3-1. Scheme of the gasification process developed in Aspen Plus.

The input material undergoes an initial drying process, which is depicted in the model using a heater block. Following the primary removal of moisture content, the material proceeds to a subsequent breakdown and volatilization process, simulated by a RYIELD block, where the mass fractions of the

various components defined in the ultimate analyses are set by a simple Fortran code. This block emulates the fast pyrolysis process and assesses the amount of thermal energy required for the decomposition of the solid feedstock. While small fractions of solid carbon and hydrogen are used for tars and ethylene production, most of the products from pyrolysis are sent to the combustor block which is modelled through a restricted chemical equilibrium RGIBBS block. Eventually, the products from the combustor are sent to a second equilibrium-restricted RGIBBS block for their reduction. The Peng-Robinson equation of state (EoS) combined with the Boston-Mathias modification [166], often adopted for energy systems modelling is used to determine the thermodynamic properties of the fluids and their mixtures [167]. The feedstock enthalpy of combustion h_{com} [kJ/kg] is defined as a non-conventional property and it is assumed equal to its high heating value (HHV). The Gibbs' free energy of a gaseous mixture, G_{mix} [kJ/kg], is calculated as:

$$G_{mix} = \sum_i^N n_i [\Delta G_{F(i)}^0 + RT \ln \left(\frac{n_i}{\sum_i^N n_i} \right)] \quad (3.1)$$

where $i = 1 \dots N$ is the number of the chemical species, each one having its own formation energy $\Delta G_{F(i)}^0$ [kJ/kg] at standard temperature and pressure conditions (1 atm, 273.15 K) and n_i [mol] is the molar content of component i . Hence, the equation is minimized in the variable space (n_1, \dots, n_N) using a Lagrangian function that uses the atom balance matrix as an imposed constraint [141]. In the study conducted by Moradi et al., a specific proportion of carbon and hydrogen moles was established to generate toluene and benzene as by-products during the process of tar generation following solid volatilization. Hence, in this study, the aforementioned methodology has been enhanced to incorporate the creation of specific compounds, namely benzene, toluene, and naphthalene. These chemicals are commonly observed in the gasification of municipal solid waste, as reported by Basu [45]. Furthermore, a similar approach is used for the formation of ethylene (C_2H_4) since this component does not take part in the chemical equilibrium. This component has been accounted for because it gives a relative contribution in the syngas LHV [kJ/kg], according to the following formula:

$$LHV_{syn,v} = 10,807 \times x_{H_2} + 12,696 \times x_{CO} + 35,768 \times x_{CH_4} + 60,136 \times x_{C_2H_4} \quad (3.2)$$

where x_j is the measured mole fraction of the i -th component in the produced syngas (CO , H_2 , C_2H_4 , CH_4). The numbers express the LHV of each component [168], and indeed ethylene has the highest one. Therefore, even if its presence is relatively low in the syngas, its inclusion in the calculation of the LHV can improve the validation of the model. Preliminary temperatures in each reactor have been set as follows: 250 °C for drying, 500 °C for the fast pyrolysis, 800 °C for the combustor which corresponds to the bed temperature, and 850 °C for the reduction, assumed from [145], [151].

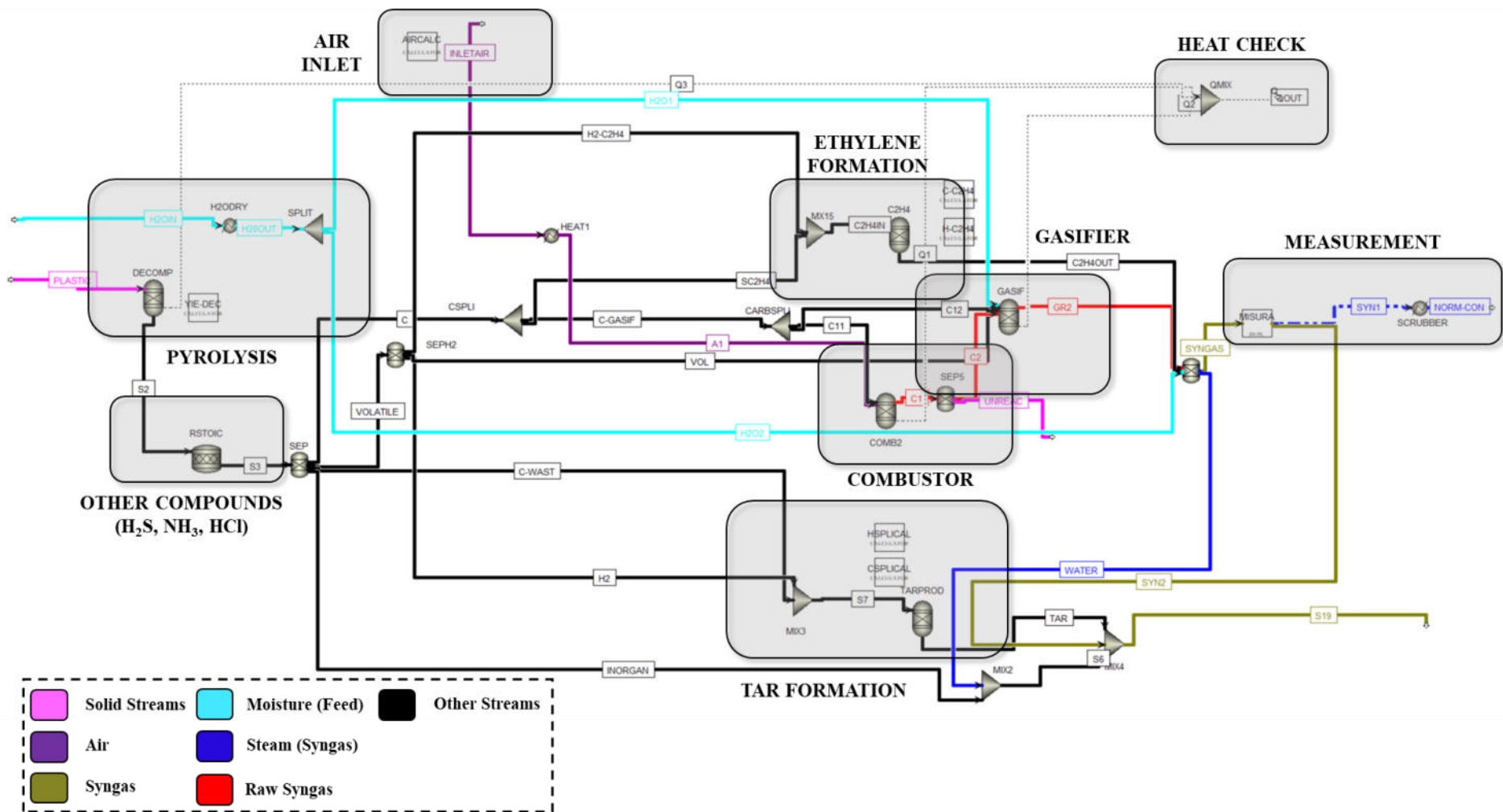


Fig. 3-2. Flowsheet of the Gasifier. In grey colour are reported the main sections: pyrolysis (for material decomposition), air inlet, ethylene, tar and other compounds formation, combustor, and gasification reactors. Two additional utility parts are present: one for the assessment of syngas dry composition through measurement and another for verifying the overall heat balance.

The operational performance and effectiveness of a gasifier are often dependent on a variety of chemical reactions, which can take place in a sequential or simultaneous manner. This study incorporates a specific subset of chemically relevant reactions into the model, as outlined in Table 3-2, where also the heat of formation of each reaction is reported [22].

Table 3-2. Chemical reactions used in the model [22], [169].

Reaction	Reaction name	Heat of reaction	Reaction number
$C_{(s)} + 0.5O_{2(g)} \rightarrow CO_{(g)}$	Char partial combustion	$(-111 \text{ MJ kmol}^{-1})$	(R1) COMB + GASIF
$C_{(s)} + O_{2(g)} \rightarrow CO_{2(g)}$	Char combustion	$(-394 \text{ MJ kmol}^{-1})$	(R2) COMB
$C_{(s)} + CO_{2(g)} \leftrightarrow 2CO_{(g)}$	Boudouard	$(+172 \text{ MJ kmol}^{-1})$	(R3) GASIF
$C_{(s)} + H_2O_{(g)} \leftrightarrow CO_{(g)} + H_2_{(g)}$	Water-gas	$(+131 \text{ MJ kmol}^{-1})$	(R4) GASIF
$H_{2(g)} + 0.5 O_{2(g)} \rightarrow H_2O_{(g)}$	H ₂ combustion	$(-283 \text{ MJ kmol}^{-1})$	(R5) COMB + GASIF
$CO_{(g)} + H_2O_{(g)} \leftrightarrow CO_{2(g)} + H_2_{(g)}$	Water-gas shift	$(-41 \text{ MJ kmol}^{-1})$	(R6) GASIF
$CH_{4(g)} + H_2O_{(s)} \rightarrow CO_{(g)} + 3H_{2(g)}$	Steam-Methane reforming	$(+206 \text{ MJ kmol}^{-1})$	(R7) GASIF
$S_{(s)} + H_{2(g)} \rightarrow H_2S_{(g)}$	[169]	$(-21 \text{ MJ kmol}^{-1})$	(R8)
$N_{(s)} + 1.5H_{2(g)} \rightarrow NH_{3(g)}$	[169]	$(-46 \text{ MJ kmol}^{-1})$	(R9)
$Cl_{2(g)} + H_{2(g)} \rightarrow 2HCl_{(g)}$	[169]	$(-185 \text{ MJ kmol}^{-1})$	(R10)

The reactions occurring from R1 to R4 are classified as heterogeneous reactions due to the involvement of solid carbon derived from the ultimate analysis of the feedstock. Reactions R5 to R7 are classified as homogeneous reactions instead. Reactions R8, R9, and R10 have been designated to encompass the generation of acid and base compounds, including H₂S, HCl, and NH₃, arising from the sulphur, chlorine, and nitrogen constituents within the feedstock material. The determination of the enthalpy change for these reactions has been conducted in Aspen Plus software through the utilisation of the RSTOIC reactor, depicted in Fig. 3-3. The reactor expresses the duty (-21 MW) for R8. The heat of reaction is obtained by dividing the reactor duty with the molar flow rate of the product, i.e. 1 kmol s⁻¹. Similar considerations can be made to assess the heat of the reaction for R9 and R10.

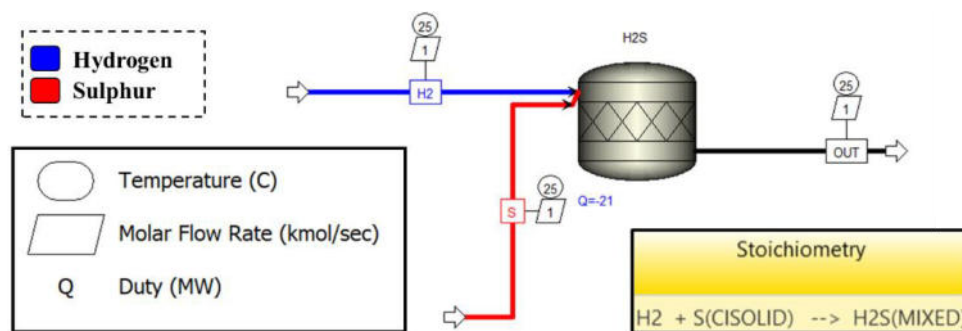


Fig. 3-3. Flowsheet for the assessment of the Heat of Reaction for reactions R8, R9, R10.

Autothermal conditions are attained during the gasification process when the heat produced by the exothermic reactions, specifically those related to the combustion of carbon and hydrogen (referred to as R1, R2, and R5), is equal to or greater than the heat required by the endothermic reactions. This includes the thermal energy necessary for the extraction of moisture from the feedstock, as well as the thermal energy required for its subsequent chemical decomposition. The condition described is commonly observed when air is employed as the gasifying agent. However, when steam is utilised, more energy is required due to its consumption in the highly endothermic steam-methane reforming reaction (R7). The observed outcome is significant increase in the *LHV* of the syngas. However, it is important to note that more heat input is required to facilitate the endothermic reactions and maintain the gasification process. The primary distinguishing feature of the combustor block is its involvement in combustion processes, including R1, R2, and R5, which result in the consumption of a significant portion of the oxygen present. These reactions involve the oxidation of carbon and hydrogen, which release heat and produce CO₂ and steam as products.

On the other hand, the reduction block incorporates many reactions, namely R1, R3-R4, and R6-R7. The endothermic reactions under consideration encompass reduction mechanisms wherein carbon dioxide, water vapour, and various other compounds undergo reduction to yield alternative molecules inside the syngas. In order to facilitate the reduction process and transform the feedstock into syngas, it is necessary to provide a certain amount of heat. The interconnection of distinct energy sources facilitates the integration between different blocks for the intended objective. The reactions R1 and R5 take place in both reactors. Some char particles may be carried along by the raw syngas and, as a result, interact with other products within the reduction reactor. In fact, after different simulations, some residues of solid carbon after the combustor were present in the raw syngas. Little traces of air were noted as well. However, the high rate of combustion [170] in reaction R5 promotes a strong interaction with the remaining air to hydrogen molecules and steam formation.

With reference to the model, the following parameters have been considered as inputs: (i) the temperature of the gasifier reactor, $T_{gasifier}$ [°C]; (ii) the temperature of the fluidized bed T_{bed} [°C]; (iii-iv) the temperature and pressure of the air, respectively T_{air} [°C] and P_{air} [bar]; (v) the feedstock composition; (vi) its internal energy; (vii-viii) the flow rates of the inlet streams (air and feed material); and (ix) the *ER* [-]. The outputs of the model, instead, are: (i) the syngas composition; (ii) its *LHV*; (iii) the tar and (iv) C₂H₄ yields.

In order to establish a relationship between the input data and the outputs generated by the model, a collection of tuning parameters has been identified. These tuning parameters are specifically selected to align with the key variables that have significance in the gasification process. The *ER* has been

found to correlate with four specific tuning parameters, while an additional five parameters have been assigned an average value derived from the composition of the feedstock. They are:

- R6-R7 temperatures approach (used in equation 3.1), respectively T_{R6app} [°C] and T_{R7app} [°C];
- the mass content of solid carbon, C_{uncomb} [-], that does not take part in the combustion reactions (R1-R2) and is considered as an inert fraction;
- the mass content of solid carbon, C_{gasif} [-], that participates in the heterogeneous gasification reactions R3-R4.

With reference to other parameters, they are:

- the temperature of the steam produced by the preliminary drying of the feedstock material, T_{dryer} [°C];
- the temperature of the fast pyrolysis process, T_{pyrol} [°C];
- the temperatures approach of reactions R3-R4, respectively T_{R3app} [°C] and T_{R4app} [°C];
- the steam fraction that does not take part in the gasification process, ST_{split} [-];

A scheme of the modelling concept is reported in Fig. 3-4.

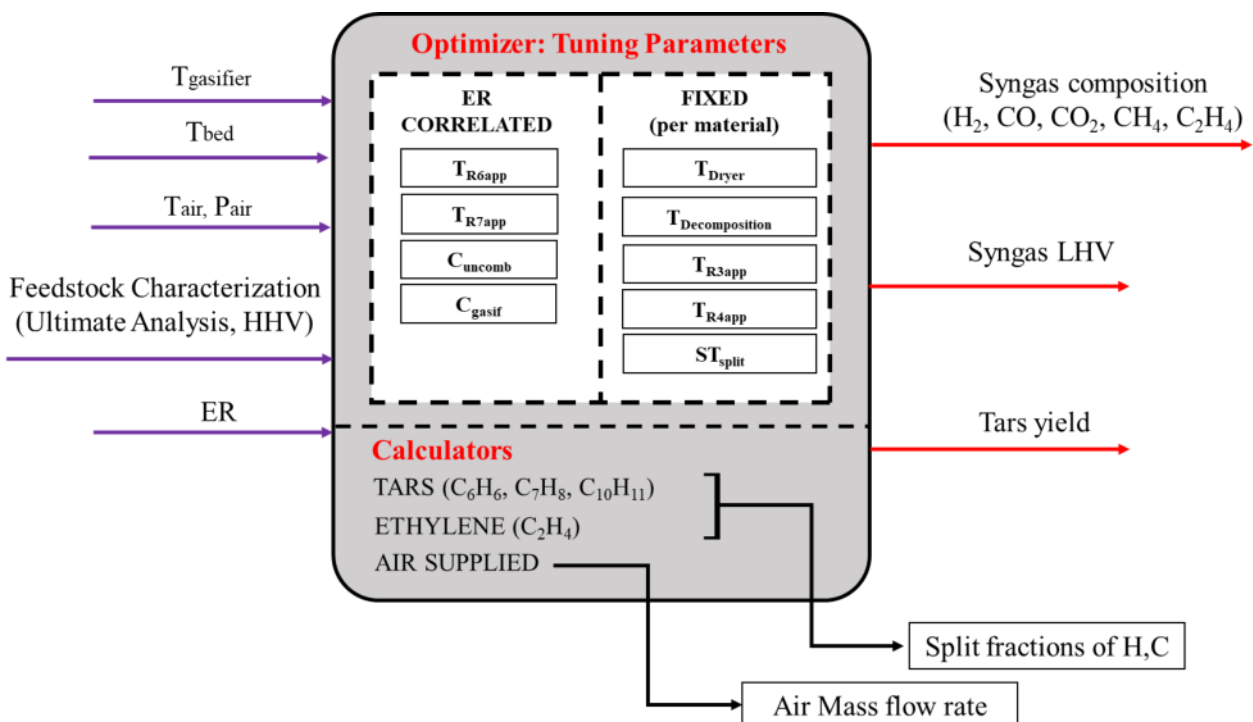


Fig. 3-4. Modelling approach of the gasifier.

Furthermore, the model incorporates five calculator blocks in addition to the tuning parameters. The inclusion of four calculator blocks enables the assessment of C_2H_4 and tar productions by employing

the molar balance of each chemical component. The composition of the tars assumed in the model is benzene (1 ring tar) C_6H_6 , toluene (1 ring tar) C_7H_8 and naphthalene (2 rings tar) $C_{10}H_8$. Their mass fractions are respectively 0.61, 0.23 and 0.15.

One calculator block is utilised for the determination of the air mass flow rate in the gasification process. The quantity in question is contingent upon the chemical composition of the feedstock, namely the mass fraction of carbon (C [-]), hydrogen (H [-]), oxygen (O [-]), and sulphur (S [-]) on a dry basis, as well as the moisture content (W [-]) on a wet basis. Furthermore, according to Basu [45] the air mass flow rate \dot{m}_{air} can be correlated to the ER according to the equation (3.3):

$$\dot{m}_{air} = \left[0.1153 \times C + 0.3434 \times \left(H - \frac{O}{8} \right) + 0.0434 \times S \right] \times \dot{m}_{feed} \times ER \times \frac{(100-W)}{100} \quad (3.3)$$

where \dot{m}_{feed} is the mass flow rate in $kg\ h^{-1}$. If the inlet mass flow rate of the feedstock is not specified, it can be calculated from the cold gas efficiency (CGE [-]) using the following equation (3.4):

$$\dot{m}_{feed} = \frac{Q_{syn} \times LHV_{syn,v}}{CGE \times LHV_{feed,m}} \quad (3.4)$$

where Q_{syn} [$Nm^3\ h^{-1}$] is the syngas flow rate, $LHV_{syn,v}$ is the lower heating value of the resulting syngas per cubic meter, while $LHV_{feed,m}$ is the lower heating value of the feedstock per kg on dry basis. The LHV ranges from 16 MJ kg^{-1} for the biomass (best estimate) to 43 MJ kg^{-1} for pure plastic such polyethylene. The typical values of the $LHV_{feed,m}$ of MSW-RDF range between 15-30 MJ kg^{-1} , and only rarely they exceed 35 MJ kg^{-1} . The $LHV_{wet,m}$ on wet mass basis, instead, can be obtained either by direct measurements, empirical correlations [171] or simply by means of equation 3.5 [172]:

$$HHV_{wet,m} = LHV_{feed,m} + \lambda \times W \quad (3.5)$$

where λ is the latent heat of vaporization of water which corresponds to 2,257 kJ kg^{-1} at ambient pressure. Considering the dry biomass, it is possible to express the $HHV_{dry,m}$ as follows:

$$HHV_{dry,m} = \frac{LHV_{feed,m} + W \times \lambda}{1 - W} \quad (3.6)$$

The syngas composition is determined by the model through the utilisation of an optimisation algorithm known as BOBYQA. This approach employs an iterative quadratic approximation technique to optimise an objective function while adhering to different constraints. The objective function to be minimised is the root mean squared error (RMSE):

$$RMSE_i = \sqrt{\frac{\Delta LHV_{syn,v}}{LHV_{syn,v}} + \frac{\Delta TAR_i}{TAR_i} + \sum_{j=1}^5 \frac{\Delta x_j}{x_j}} \quad (3.7)$$

where i is the i -th test, x_j is the measured mole fraction of the j -th component in the produced syngas (CO, CO₂, H₂, C₂H₄, CH₄), Δx_j is the squared difference between the predicted and the experimental values (the same notation is applied for ΔTAR_i and $\Delta LHV_{syn,v}$), TAR_i is the tar content entrained in the syngas and $LHV_{syn,v}$ the lower heating values of the syngas on volumetric basis. It is important to remark that the inclusion of the LHV term in the objective function is justified due to the possibility of obtaining the same LHV for different syngas compositions. The optimisation process concludes when the RMSE of less than 0.30 is attained. Subsequently, to ascertain the precision of the optimisation technique, the model conducts a subsequent iteration using the acquired values of the tuning parameters.

3.4 Results and discussions

In this section the validation of the model against experimental data available in the literature is initially presented. Later on, the performances of the air gasifier for a given feedstock composition from a real composting facility are assessed and eventually in subsection 3.4.3 a parametric analysis is carried out by varying the feedstock composition and some relevant tuning parameters of the fluidized bed gasifier.

3.4.1 Model Validation

As mentioned at the beginning of the Chapter, the developed model is validated against the experimental results obtained by Arena et al. [145] and Parrillo et al. [61] for different feedstock materials. Both pilot plants are fluidized bed air gasifiers. However, in the one studied by Arena et al. [145], [150], [151] plastic-based materials were used as input and air pre-heated up to 600 °C while in the one by Parrillo et al. [61] eucalyptus chips were the input material and air pre-heated up to 200 °C. Table 3-3 reports the properties of the considered feedstock materials, namely Neolite (NEO), packaging derived fuel (PDF), densified RDF (d-RDF), and Eucalyptus woodchips (EU), while Table 3-4 summarises the experimental results obtained by the authors in their works.

Table 3-3. Summary of the feedstock properties

Feedstock	N° of tests	Moisture (% w.b.)	Ultimate Analysis (d.b. – BE)							LHV [MJ kg ⁻¹]	HHV [MJ kg ⁻¹]
			C	H	O	Cl	S	N	ASH		

Neolite	3	0.6	68.51	10.26	14.39	0	0.1	0	6.74	33.4	35.8
PDF	2	5.6	57.1	8.157	27.86	0	0.11	0.53	6.25	25.4	28.8
RDF	3	1.9	57.9	8.46	16	0	0.61	0.51	16.51	27.3	29.7
Eucalyptus	10	10.8	48.67	5.21	41.71	0	0	0.39	4.02	15.7	17.6 ²

Table 3-4. Experimental data reported by Arena [145] and Parrillo [61] regarding waste/biomass gasification.

Experimental data	ER																		
	PDF		RDF			NE			EU										
	0.26	0.31	0.23	0.28	0.34	0.22	0.25	0.31	0.21	0.24	0.25	0.27	0.28	0.29	0.3	0.31	0.34	0.35	
CO	11.6	10.9	9.1	8.7	7.6	3.7	4.6	4.8	12.5	14.3	15	13.1	14.7	14.2	13.9	15.2	14.1	14.1	
CO ₂	14.3	14.1	12.8	12.3	13.4	11.1	11.6	11.4	18.3	16.8	17	17.3	16.3	15.9	15.8	15.5	16.1	15.1	
H ₂	9.9	7.9	9.2	7.9	5.9	6.8	8	6.6	14.7	12.3	13.7	11.4	12.2	13.3	10.9	10.9	11.1	10.1	
CH ₄	6.3	4.9	8.3	7	6.6	7.3	7.9	6.3	3.9	4.03	4.2	3.84	3.54	3.4	3.54	3.6	3.16	3	
C ₂ H ₄	2.1	1.5	2.7	1.8	1.8	4.8	3.7	2.4	1.36	1.71	1.22	1.7	1.26	1.15	1.43	0.94	1.07	0.92	
LHV	MJ Nm ⁻³	6.2	5	6.9	5.7	5.2	6.8	6.4	5.2	5.6	5.9	5.8	5.7	5.5	5.3	5.3	5.2	5.0	4.7
Tar	g Nm ⁻³	0.02	0.01	0.05	0.04	0.02	0.1	0.06	0.06	0	0	0	0.01	0	0	0	0	0	0

The primary factors influencing the chemical composition of each substance are the quantities of hydrogen, oxygen, and carbon. These components play a significant role in the overall analysis of the material on a dry basis. The inclusion of these three factors provides an adequate basis for a distinct characterisation of the overall feedstock material, thereby enabling the establishment of a representative function within the given scope. In particular, the following F function (equation 3.8) is defined to provide a representative value for the four tested feedstock materials:

$$F(H, O, C) = \left(\frac{H/C}{C}\right) \times \left(\frac{H+C}{100}\right) - \left(\frac{O/C}{C}\right) \times \left(\frac{O}{100}\right) \quad (3.8)$$

The function is contingent upon the ratios of hydrogen to carbon (H/C) and oxygen to carbon (O/C), which are multiplied by their corresponding mass fractions. Moreover, there is a potential correlation between the HHV and the presence of hydrogen and carbon in a material, since these elements lead to an elevation in the chemical energy. Conversely, an increase in oxygen content tends to have the opposite effect. The same trend can be clearly seen in the unified HHV correlation expressed by Channiwala et al. [171]. Therefore, the values of the F function for the feedstock materials reported in Table 3-4 are 0.2390, 0.6098, 0.7163 and 0.8755 for EU, PDF, d-RDF and NEO respectively. The model's objective function, specifically the RMSE of equation 3.6, attains maximum values of 0.169, 0.109, and 0.247 for PDF, RDF, and NEO, respectively. However, when tar generation is taken into

account, the maximum values for EU are significantly higher. The maximum value for the EU is 0.701, however it decreases to 0.289 when the production of tar and C₂H₄ is not taken into account. Given the limited relevance of the latter to the EU, it may be disregarded, hence demonstrating the appropriateness of the model in replicating the gasification process of the four studied materials under varying conditions. Fig. 3-5 and Fig. 3-6 report the results of the model validation in terms of average deviation from the experimental data of the considered parameters for all the input materials.

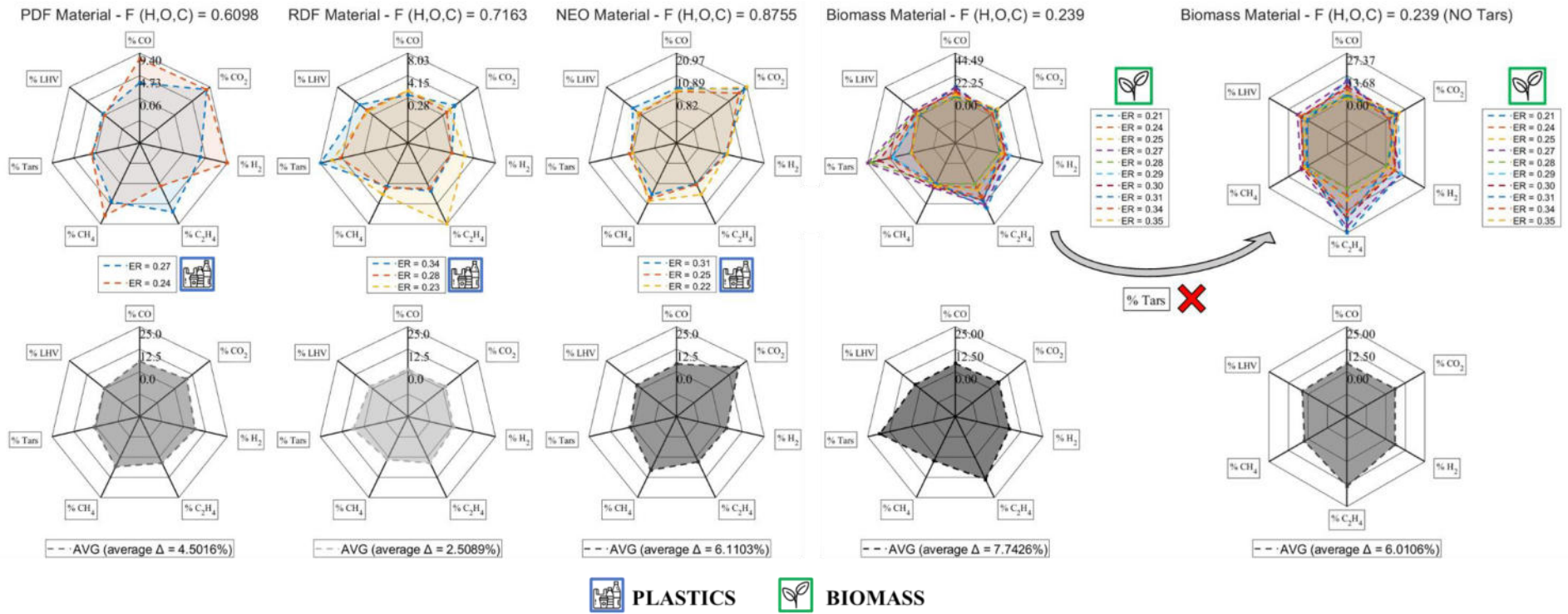


Fig. 3-5. Validation results of the model for Plastics and Biomass feedstock, including average error at the bottom. The intensity of its greyscale expresses the normalised error.

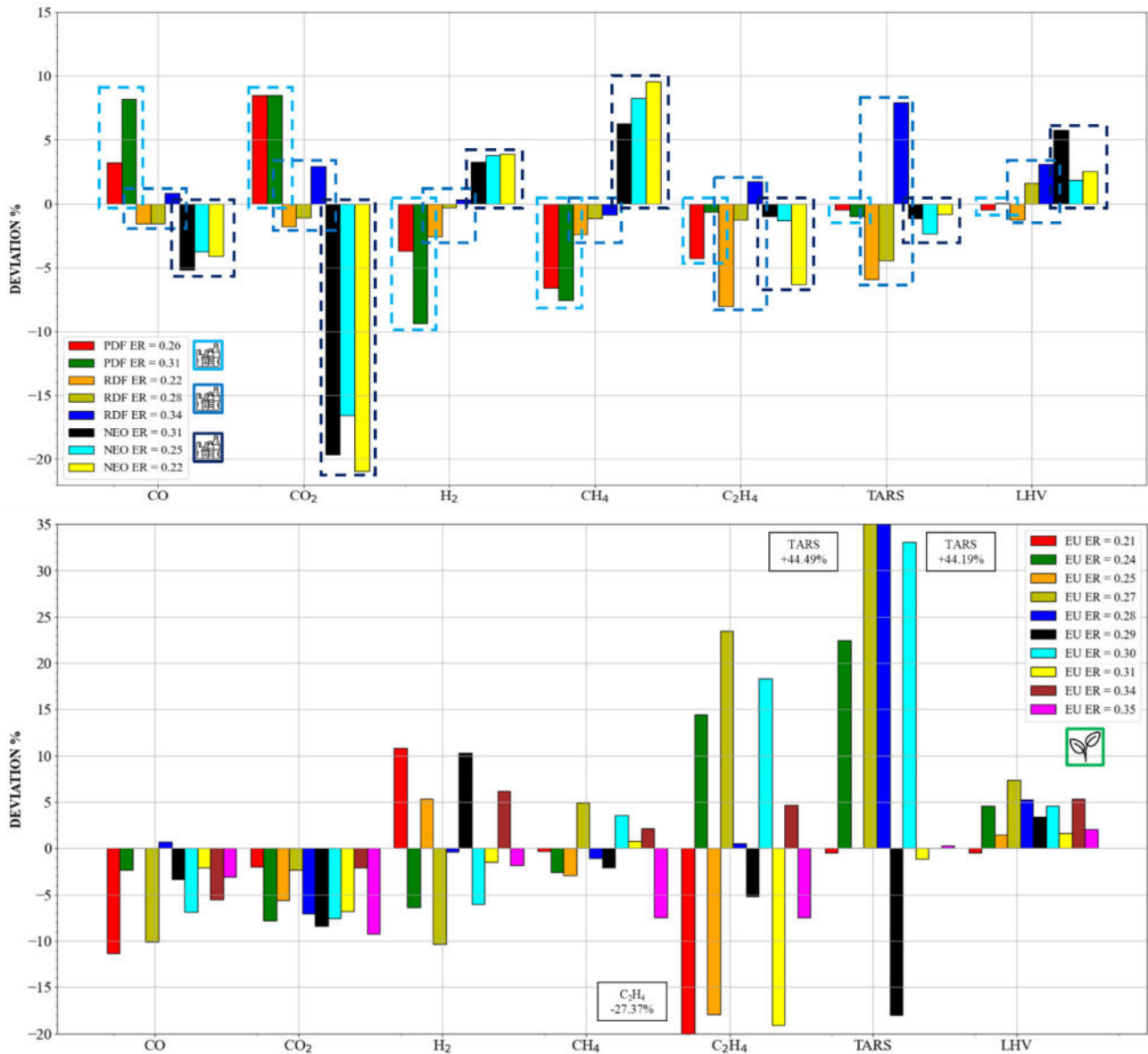


Fig. 3-6. Deviation of the model compared to the experimental results for waste plastics (above) and biomass (below). In the latter case, tars and Ethylene exceed the range of the histogram plot.

Based on the examination of these findings, it can be deduced that the model's estimation of syngas composition, when considering different feedstock materials and ER , exhibits variations ranging from -10.8% to 10.4% for H_2 , -7.5% to 9.5% for CH_4 , and -11.3% to 8.2% for CO , respectively. In terms of the molar proportion of CO_2 , it aligns with the experimental data, with the exception of NEO, which exhibits a difference ranging from -20.9% to $+8.5\%$. Anyhow, the $LHV_{syn,v}$ variation is limited to -1.3% and $+7.4\%$ since CO_2 fraction does not contribute to the thermal energy of the syngas while the absolute molar fractions of H_2 and CH_4 are low for PDF, RFD and NE respectively. In particular, the maximum variation of the $LHV_{syn,v}$ is obtained for EU at ER of 0.27 (7.4%) since the H_2 molar fraction is higher than for the other feedstocks. With reference to the tar significant discrepancies are

obtained for the EU biomass (from -20.7% to +44.5%). However, since the amount of tar is low the absolute error is still limited.

In contrast, when considering PDF, RFD, and NEO, the tar exhibits a rather narrow variation ranging from -2.3% to +7.9%, despite the significantly higher tar production in comparison to the EU. In the case of C_2H_4 , the criterion of 10% is generally adhered to by most feedstocks, with the exception of EU. The *ER* values for EU, specifically 0.21, 0.24, 0.25, 0.27, 0.3, and 0.31, deviate significantly from the threshold, with deviations of -23.4%, +14.4%, and -17.9% respectively.

As stated before, there exists a correlation between the *ER* and with the tuning parameters and tar production for each feedstock material. However, it is worth noting that there is a limited amount of experimental data available in the literature for plastic materials. As a result, it is not meaningful to establish correlations between tars to the *ER* only, since other physical variable should be included. Hence, detailed analysis of tar production is not discussed in sub-sections 3.4.2 and 3.4.3. Furthermore, besides *ER* also other operating parameters such as the temperature of the fluidized bed may affect the values of the tuning parameters thus increasing the approximation of these correlations. Therefore, a linear trend is assumed for such compounds and with reference to tars a decreasing trend with *ER* is considered in accordance with the studies of Cho and Xiao et al. [143], [144].

The relevant details are given in Table 3-5, which reports both the averaged values and the equations used for these correlations. As regards the plastic waste materials, linear and quadratic interpolating relations are assumed for PDF and RDF and NEO respectively.

Table 3-5. Set of the correlations and averaged variables used in the model ($x = ER$)

Variable		EU	PDF	RDF	NEO
Averaged	T_{dryer}	252.93	249.91	267.48	270.02
	T_{pyrol}	502.84	485.74	490.09	467.51
	T_{R3app}	-50.38	-120.03	-182.40	-185.18
	T_{R4app}	-68.73	-38.94	-101.59	-212.09
	ST_{split}	0.048	0.073	0.187	0.242
Correlated	T_{R6app}	$-208955x^3 + 188106x^2 - 55446x + 5294.3$	$1864.9x - 578.13$	$-18962x^2 + 12471x - 2122.2$	$16815x^2 - 9582.5x + 1131.1$
	T_{R7app}	$25693x^3 - 23735x^2 + 7169.2x - 911.29$	$-332.58x - 251.18$	$531.03x^2 - 712.41x - 200.26$	$-4642x^2 + 2755.4x - 783.34$
	C_{uncomb}	$454.23x^3 - 367.67x^2 + 95.001x - 7.4261$	$3.4177x - 0.6525$	$46.822x^2 - 23.495x + 3.0718$	$-19.383x^2 + 10.209x - 1.1108$
	C_{gasif}	$114114x^3 - 154992x^2 + 82465x^3 - 21441x^2 + 2717.9x - 133.41$	$-4.9175x + 2.0851$	$-109.51x^2 + 61.177x - 7.854$	$-26.929x^2 + 13.708x - 0.9485$
Calculateds	$C-C_2H_4$	$-0.06699x + 0.0718$	$-0.573x + 0.254$	$8.5573x^2 - 5.3388x + 0.9263$	$6.4277x^2 - 4.6489x + 0.9922$
	$H-C_2H_4$	$-0.098x + 0.1107$	$-0.6081x + 0.2743$	$9.4643x^2 - 5.6718x + 0.9441$	$-0.9493x^2 - 0.1107x + 0.2791$
	$C-Tar$	$-0.0623x + 0.0269$	$-0.2799x + 0.1456$	$-13.105x^2 + 6.1823x - 0.523$	$24.989x^2 - 14.88x + 2.4105$

	<i>H-Tar</i>	$-0.0511x + 0.0217$	$-0.1596x + 0.083$	$-7.3272x^2 + 3.4567x - 0.2924$	$13.4x^2 - 7.9792x + 1.2926$
--	--------------	---------------------	--------------------	---------------------------------	------------------------------

The trends of these correlations are reported in Fig. 3-7 and Fig. 3-8 for all the different materials with *ER* varying from 0.2 to 0.35. More precisely, Fig. 3-7 refer to the tuning parameters while Fig. 3-8 to the calculator blocks for the C_2H_4 and tar productions. The examination of the observed trend allows for an understanding of the impact of the chemical composition, expressed in terms of the *F* value for each material, on the various parameters. As later discussed in sub-section 3.3.3, a 3D surface is constructed to consider the exact composition of the RMSW for sensitivity analysis.

OPTIMIZED VARIABLES

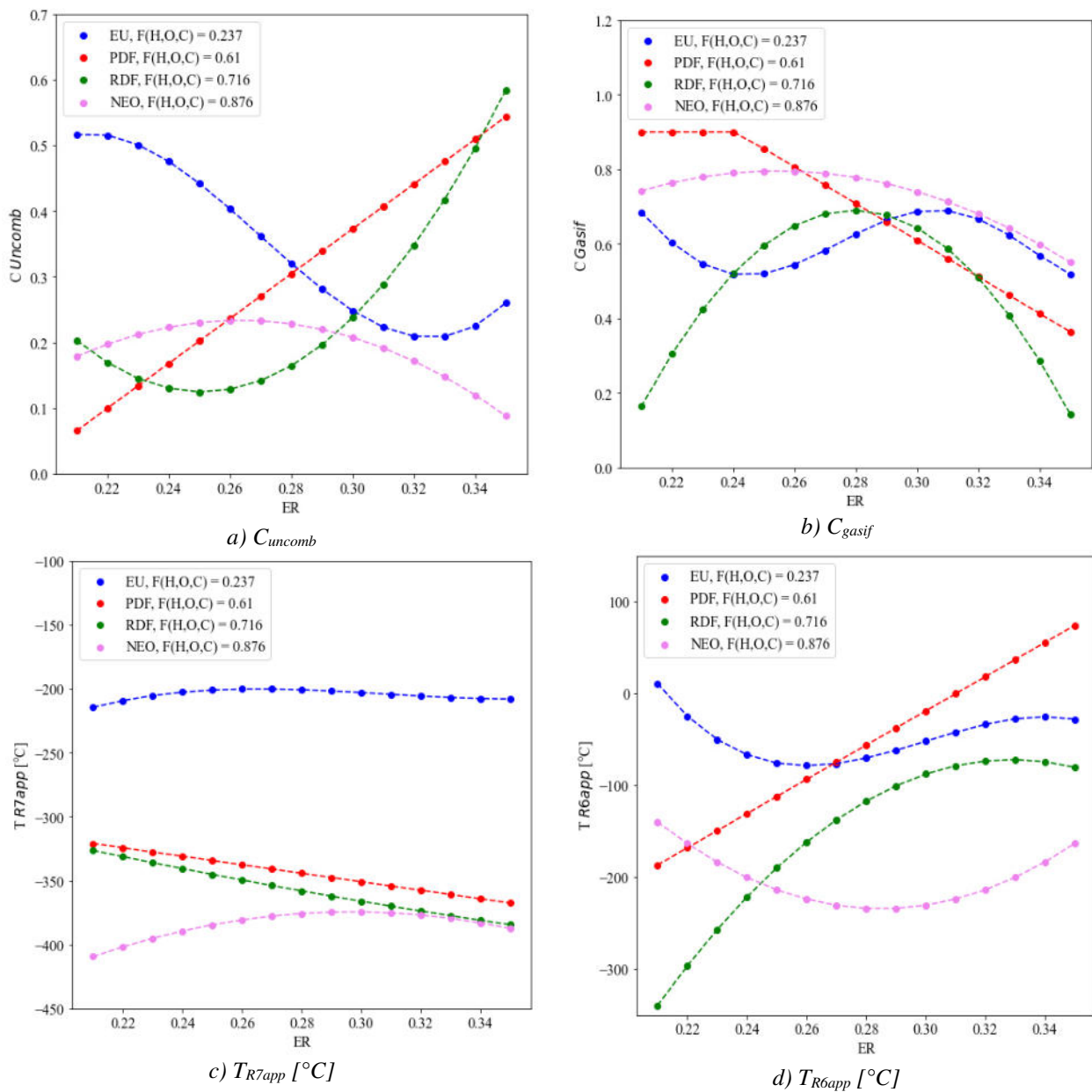


Fig. 3-7. Influence of the ER and *F* on the optimized variables of the model.

CALCULATORS BLOCKS

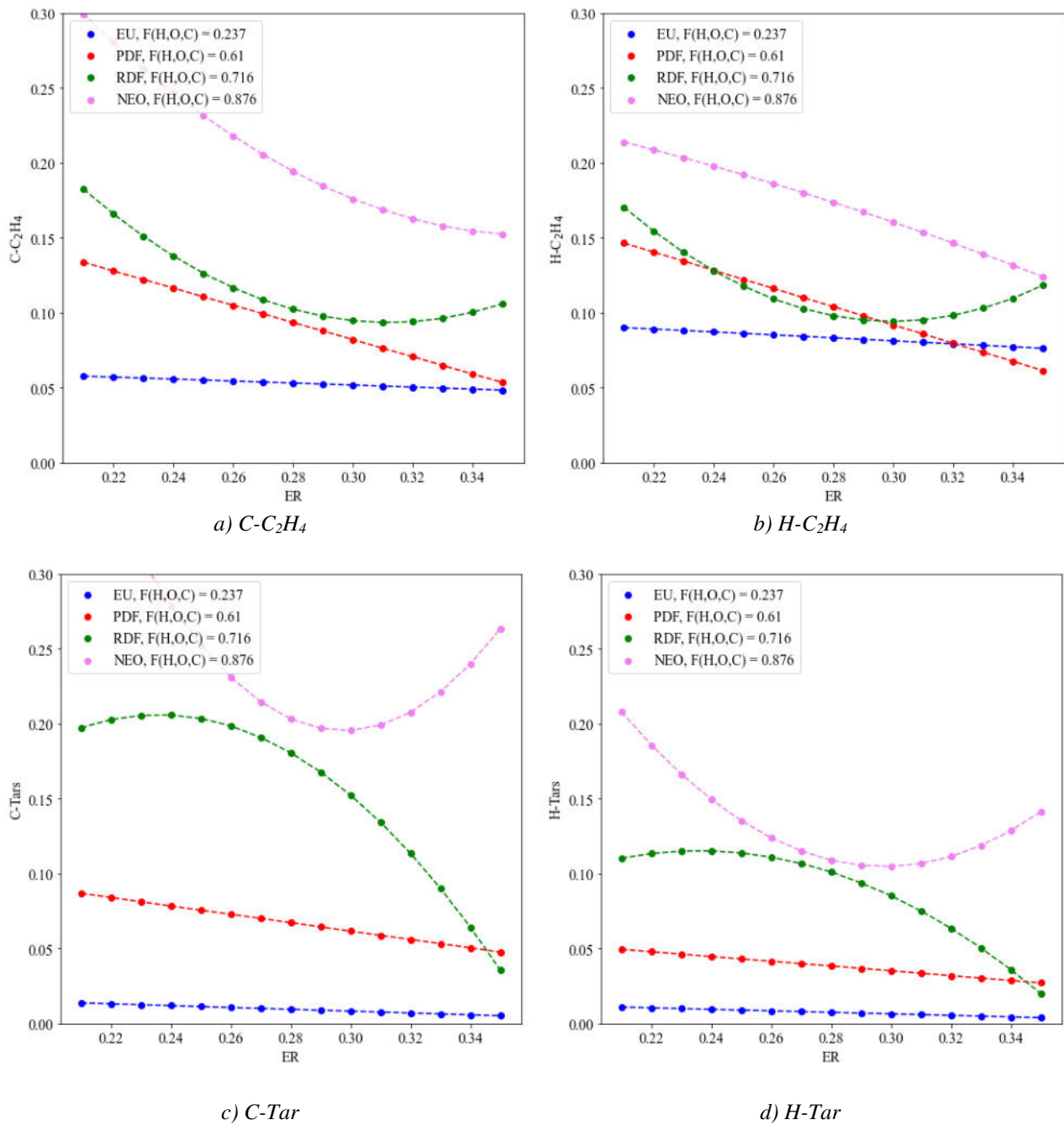


Fig. 3-8. Influence of the ER and F on the calculator blocks variables of the model.

3.4.2 Syngas production from the composting facility

Once validated against the experimental data point, the model is used to evaluate the performance of the air gasifier having as input the residual waste from the RMSW produced in the composting facility described in the Chapter 2. The most relevant information about the composition and the thermal

properties of the MBT residues are reported in Table 3-6, which summarizes the data reported in Table 2-9.

Table 3-6. Composition of the residual waste produced at the MBT unit.

Material	Mass content	Moisture (% w.b.)	Ultimate Analysis (% w.b.)							LHV [MJ kg ⁻¹]	HHV [MJ kg ⁻¹]
			C	H	O	CL	S	N	ASH		
Waste Plastic	32%										
Paper/Cardboard	27%										
Textile residues	13%	25	41.8	6.32	25.262	0.092	0.136	0.19	1.2	21.8	29.2
Leather, Rubber	10%										
Other	18%										

Hence, the material composition provided in Table 3-6 with an annual flow rate of 20 ktons year⁻¹ is considered as input to the model while the same correlations and average values previously defined for RDF are used. The *ER* is varied from 0.21 to 0.36 with 0.03 step, which corresponds to typical values adopted in fluidized bed air gasifiers. Fig. 3-9 reports the main results of the model in terms of dry syngas composition at normal conditions, $LHV_{syn,v}$, *CGE* and syngas flow rate. The tar production, which the model has quantified between a reasonable range of 10-200 kg h⁻¹, has been excluded from the results.

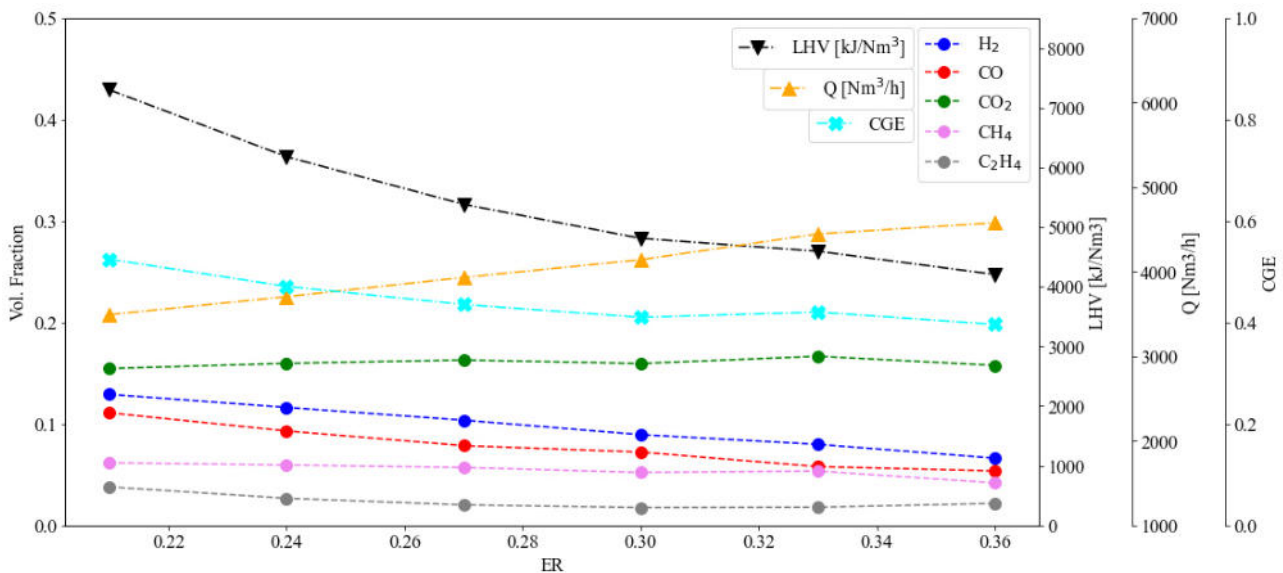


Fig. 3-9. Results of the model for the waste material produced in the MBT system.

In general, the volume fraction of H₂, CO and CH₄ tend to decrease with *ER* in accordance with the results reported by Arena while CO₂ trend is slightly shifted to the left (lower values of *ER*) compared to what reported in the reference. As expected, the $LHV_{syn,v}$ decreases with *ER* accordingly to the

syngas composition trend: the maximum value of 7,298 kJ Nm⁻³ is obtained at the minimum *ER* (0.21) while the lowest value of 4,205 kJ Nm⁻³ at the maximum *ER* (0.36). The *CGE* trend is in line with the *LHV_{syn,v}* except for *ER* = 0.33 since the increase in the syngas flow rate has a greater impact than the *LHV_{syn,v}* reduction.

3.4.3 Sensitivity Analysis

This section presents an evaluation of the performance of the fluidized bed air gasifier. The evaluation is conducted by modifying the composition of residual waste from MBT units, while also considering different *ER*. Bourtsalas and Themelis reported in their work [32] the compositions and the recovery efficiencies of six European MBT facilities for different waste materials. In particular, the following were included in their work: organic fraction, normal and corrugated cardboard (OCC), plastic materials as polyethylene (PET), low/high density polyethylene (L/H-DPE), polypropylene (PP), polystyrene (PS), polyvinylchlorides (PVC), metals, glass and other inert materials. Six RDF compositions (S1-S6) were determined based on the following assumptions: i) RDF was composed only of plastic and paper; ii) the amount of each kind of material was evaluated as simple difference between the input and the recycled fraction; iii) the composition was reported in terms of proximate and ultimate analysis. Furthermore, in the present work also the values of *F* and *HHV_{dry,m}* are calculated for each different feedstock material based on the data available in the following references: Han et al. [173] for Paper and PS, Burra et al. [75] for PET and PP, Cho et al. [66] for PVC and LDPE Garcia-Bacaicoa et al. [174] for and HDPE.

Table 3-7. Value of *F* and *HHV* for different feedstock materials

Param.	PAPER	EU	PVC	PET	PDF	RDF	NEO	PS	LDPE	PLMIX	PE	GS3	PP	HDPE
<i>F</i> (<i>H,O,C</i>)	-0.01	0.239	0.51	0.546	0.61	0.716	0.876	1.06	1.08	1.08	1.11	1.15	1.16	1.17
<i>HHV</i> ¹ [MJ kg ⁻¹]	13.3	17.6	19.6	22.8	26.9	27.8	33.6	38.4	40.3	40.5	40.9	43	43.4	44

1 – Evaluated by means of equation 3.5.

Therefore, a correlation between *F* and *HHV_{dry,m}* reported in Table 3-7 is defined based on the *HHV_{dry,m}* values of the various feedstocks. The logarithmic trend was the best one in terms of RMSE, as shown in the Fig. 3-10.

$$F = 0.9668 \times \ln(HHV) - 9.1697 \quad (3.9)$$

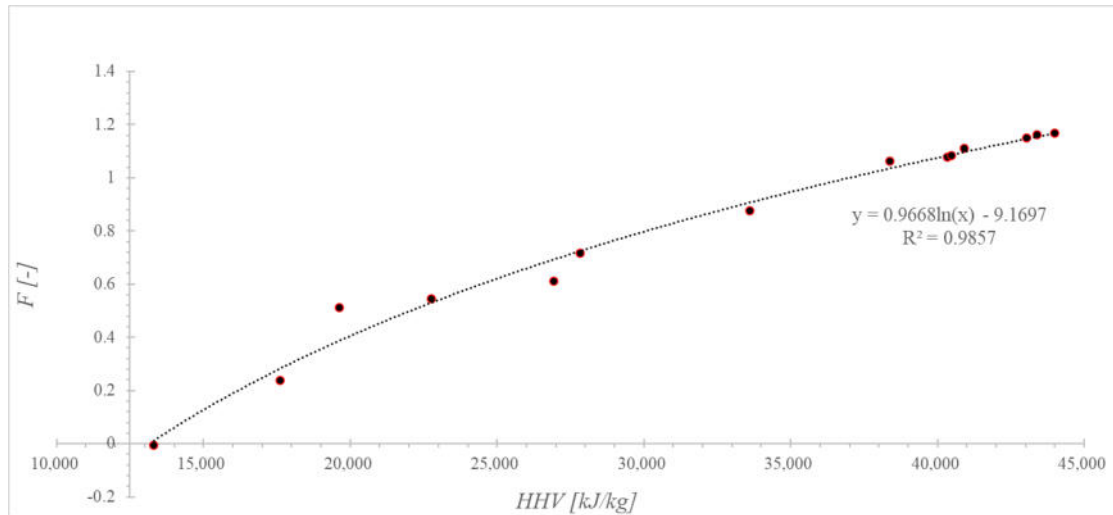


Fig. 3-10. F vs. HHV logarithmic trend. The points are taken from Table 3-7.

Then, from a given composition of the RDF mixture (S1-S6) as reported in Table 3-8 the $HHV_{dry,m}$ is calculated by means of equation 3.5.

Table 3-8. Reconstructed ultimate analysis of the RDF for the six MBT scenarios [175].

Material	Moisture (% w.b.)	F	Ultimate Analysis (% w.b.)							HHV [MJ kg ⁻¹]
			C	H	O	CL	S	N	ASH	
S1 (PL 77%, PA 23%)	6.03	0.9248	72.02	7.72	9.99	0.64	0.1	0.13	3.36	34.2
S2 (PL 68%, PA 32%)	8.31	0.8653	66.25	7.26	12.18	1	0.13	0.2	4.66	32.2
S3 (PL 51%, PA 49%)	13.05	0.7102	55.55	5.56	17.48	0.73	0.15	0.29	7.14	27.4
S4 (PL 63%, PA 37%)	16.37	0.5802	47.6	4.92	21.2	0.51	0.19	0.36	8.84	24.0
S5 (PL 65%, PA 35%)	17.06	0.5575	46.08	4.91	21.67	0.50	0.2	0.37	9.21	23.4
S6 (PL 54%, PA 46%)	14.32	0.6504	60.67	6.03	22.42	1.14	0.20	0.37	7.85	25.8

Eventually, using the correlations previously defined in sub-section 3.4.1 a 3D surface as a polynomial function of ER and F is defined for the tuning parameters T_{R6app} , T_{R7app} , C_{uncomb} , C_{gasif} and tar and C_2H_4 productions. The interpolating surface z has the following analytic formulation:

$$z = C_0 + C_1 x + C_2 y + C_3 x^2 + C_4 xy + C_5 y^2 + C_6 x^3 + C_7 x^2y + C_8 xy^2 + C_9 y^3 + C_{10} x^4 + C_{11} x^3y + C_{12} x^2y^2 + C_{13} xy^3 \quad (3.10)$$

where x is ER and y is F . The curve fitting Matlab toolbox where used for the purpose and the form “4-3” (polynomial order for x and y respectively) where defined. Higher degrees would not improve the fitting since a value of R^2 of 1 was obtained in every case. The coefficients of z are reported in the Table 3-9. It is worth to noting that in order to get a good accuracy of the surface F is varied only in the range 0.61-0.88 (which corresponds to the values for PDF, RDF and NEO) plus a 10% boundary

extension (± 0.027), and ER from 0.20 to 0.35. Fig. 3-11 to Fig. 3-18 show the surfaces obtained for the most impacting tuning parameters of the model.

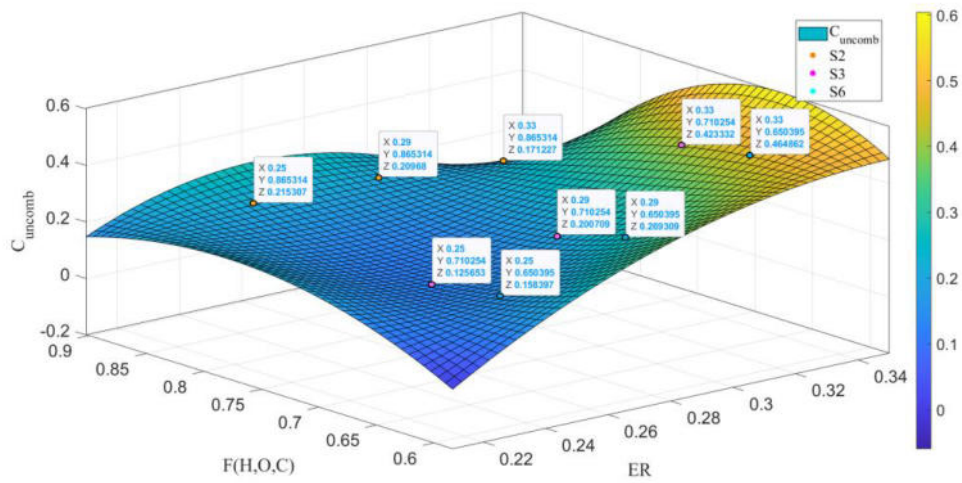


Fig. 3-11. Interpolating Surface for C_{uncomb} [176].

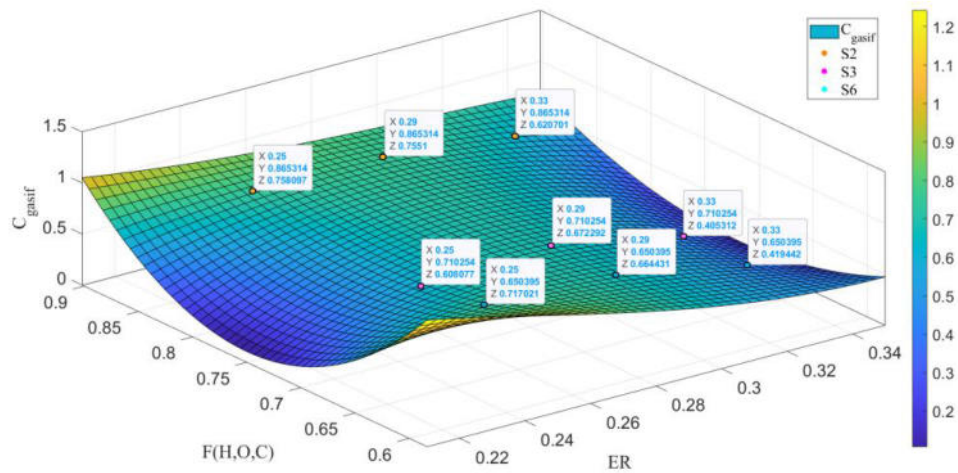


Fig. 3-12. Interpolating Surface for C_{gasif} . [176].

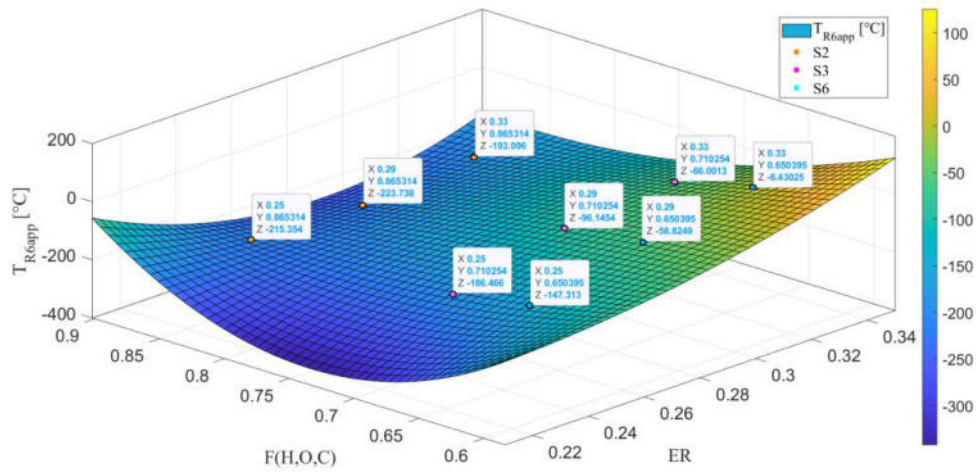


Fig. 3-13. Interpolating Surface for T_{R6app} . [176].

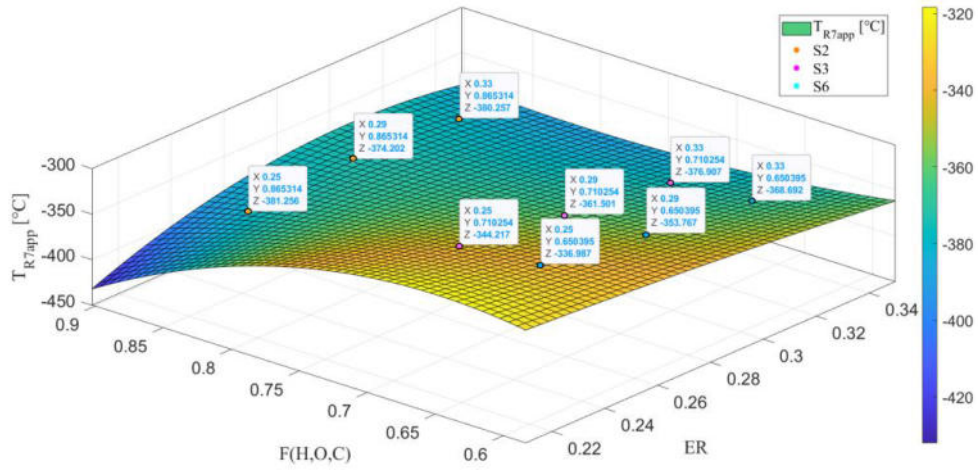


Fig. 3-14. Interpolating Surface for T_{R6app} . [176].

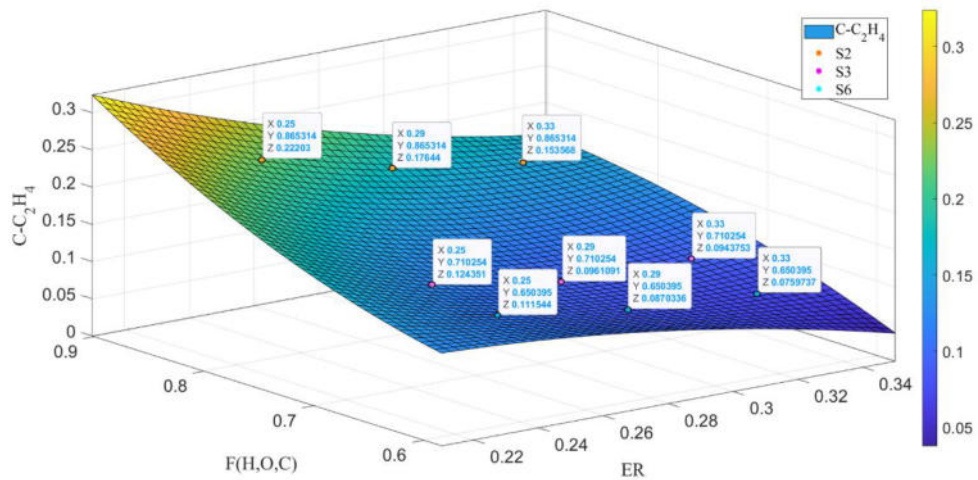


Fig. 3-15. Interpolating Surface for $C-C_2H_4$.

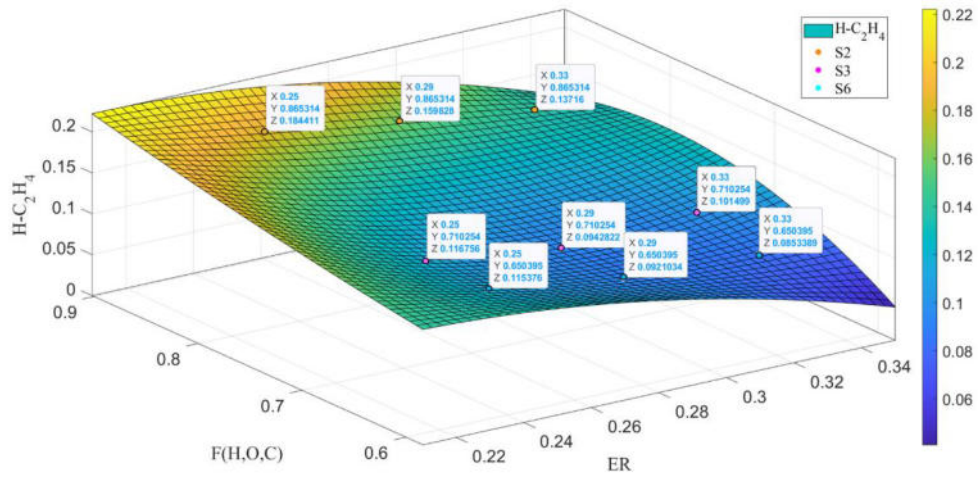


Fig. 3-16. Interpolating Surface for H-C₂H₄

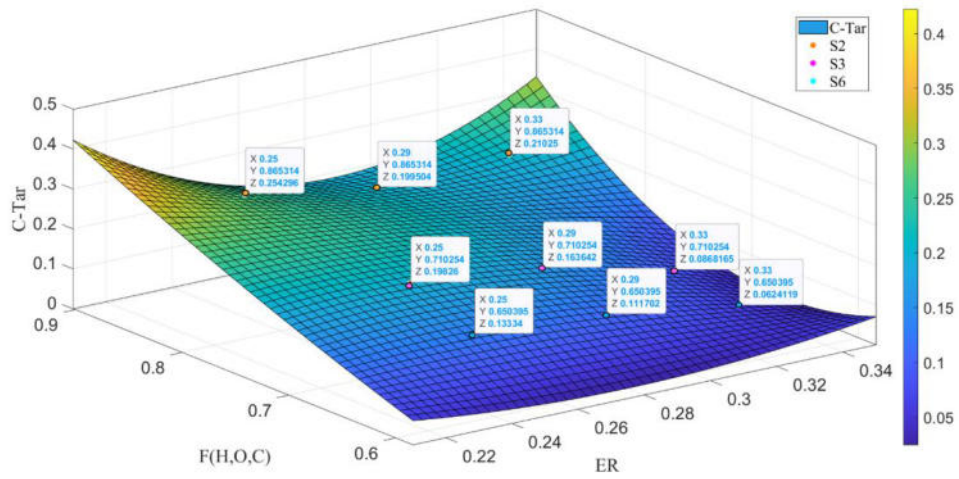


Fig. 3-17. Interpolating Surface for C-Tar.

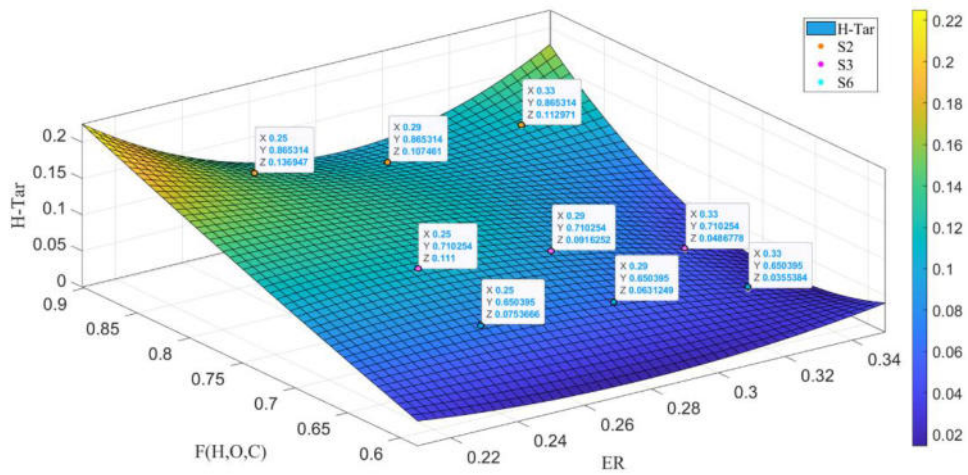


Fig. 3-18. Interpolating Surface for H-Tar.

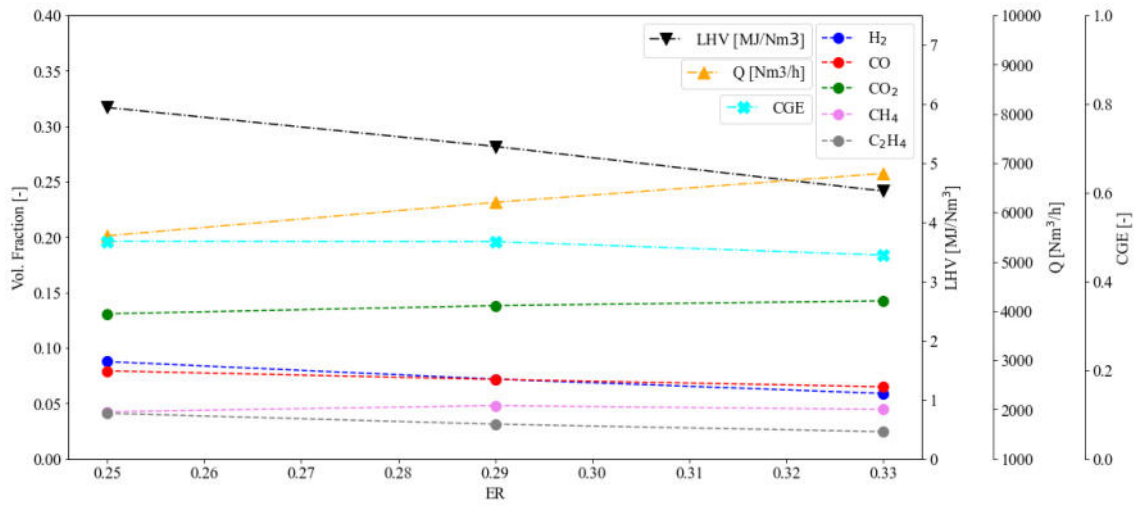
Table 3-9. Coefficients of the interpolating surface for each variable of the model.

Variable	C ₀	C ₁	C ₂	C ₃	C ₄	C ₅	C ₆	C ₇	C ₈	C ₉	C ₁₀	C ₁₁	C ₁₂	C ₁₃
C _{uncomb}	-122.67	921.09	340.66	-1674.73	-2570.80	-230.51	-1.45e-08	4709.95	1748.001	-4.38e-10	9.217e-09	5.25e-09	-3220.11	1.43e-09
C _{gasif}	231.06	-1442.56	-671.36	1884.32	4413.52	462.58	1388.69	-6966.83	-3109.66	6.66e-10	-510.60	-1027.88	5244.92	-2.18e-09
T _{R6app}	65704.20	-450394.77	-188880.20	770848.98	1288209.39	131495.59	6.88e-06	-2188605.02	-896300.17	2.05e-07	-4.373e-06	-2.45e-06	1516096.68	-6.73e-07
T _{R7app}	-7352.31	43529.78	21150.679	-64677.97	-130121.96	-15588.30	-6.20e-07	192105.69	95430.23	-1.85e-08	3.97e-07	2.16e-07	-141099	6.07e-08
C-C ₂ H ₄	-13.293	107.40	35.75	-203.08	-289.70	-22.20	-1.76	548.12	184.71	-5.25	1.11	6.36e-10	-352.73	1.72e-10
H-C ₂ H ₄	-20.77	163.99	58.53	-307.85	-459.23	-39.39	-2.63e-09	858.94	310.44	-7.91e-11	1.66e-09	9.49e-10	-580.69	2.59e-10
C-TAR	44.60	-354.61	-129.61	670.85	1024.04	93	5.60e-09	-1931.83	-726.44	1.71e-10	-3.54e-09	-2.04e-09	1363.93	-5.61e-10
H-TAR	24.40	-194.82	-70.82	369.17	562.06	50.75	3.06e-09	-1062.18	-398.22	9.42e-11	-1.92e-09	-1.12e-09	749.08	-3.08e-10

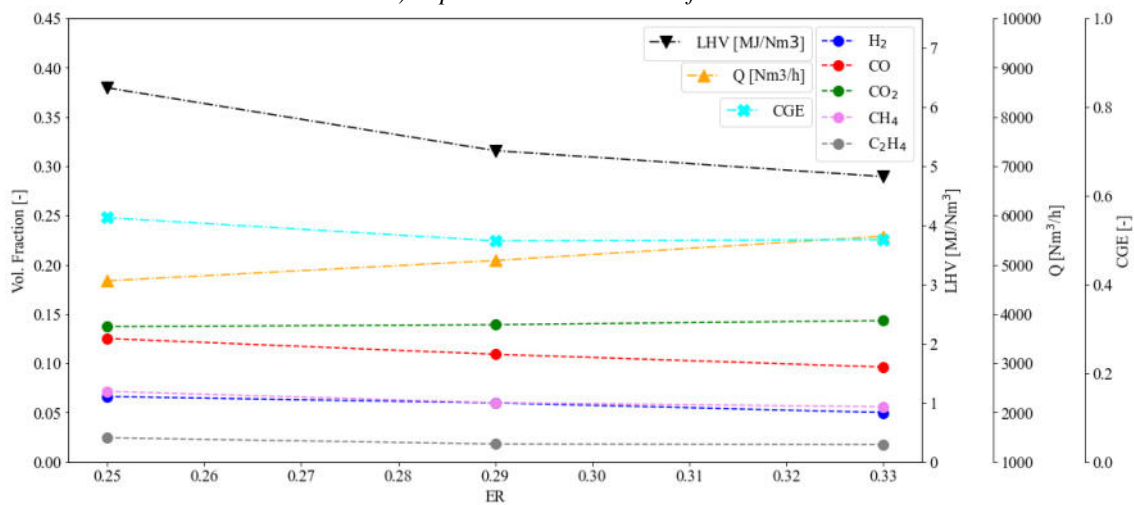
Among the six scenarios reported in Table 3-10, only S2, S3 and S6 fall inside the F range being F equal to 0.865 for S2, 0.71 for S3 and 0.65 for S6. For each case, ER is varied from 0.25 to 0.33 with a step of 0.04. The corresponding values of each parameter for the cases (i.e. the labels of Fig. 3-11 to Fig. 3-18), are defined in Aspen Plus.

Fig. 3-19 reports the main performance results of the model for the different residue waste composition S2, S3 and S6. Also in this case, it is evident that the $LHV_{syn,v}$ from each feedstock reduces with ER in accordance with the results reported in literature [66], [144]. The maximum values are obtained for an ER of 0.25 (6,585 kJ Nm⁻³ for S6, 6,322 kJ Nm⁻³ for S3 and 5,939 kJ Nm⁻³ for S2). The main reason of this result is related to the fact that by increasing the ER the oxidation reaction is promoted more than the reforming and cracking reactions thus bringing to the formation of CO₂,

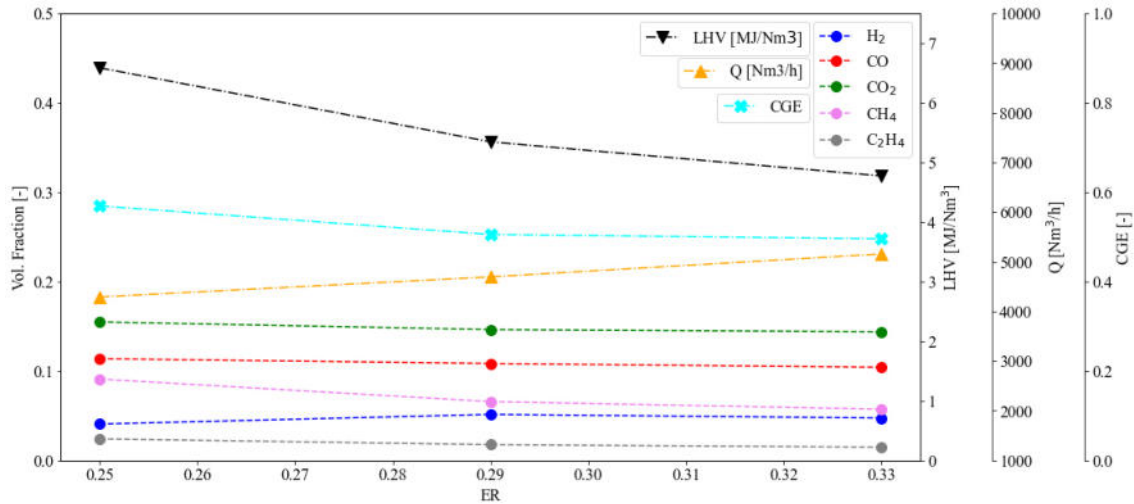
H₂O, and N₂, and the reduction of CO, CH₄ and H₂ concentration. Among the six scenarios reported in Table 3-10, only S2, S3 and S6 fall inside the *F* range being *F* equal to 0.865 for S2, 0.71 for S3 and 0.65 for S6. For each case, *ER* is varied from 0.25 to 0.33 with a step of 0.04. The corresponding values of each parameter for the cases (i.e. the labels of Fig. 3-11 to Fig. 3-18), are defined in Aspen. Fig. 3-19 reports the main performance results of the model for the different residue waste composition S2, S3 and S6. Also in this case, it is evident that the *LHV_{syn,v}* from each feedstock reduces with *ER* in accordance with the results reported in literature [66], [144]. The maximum values are obtained for an *ER* of 0.25 (6,585 kJ Nm⁻³ for S6, 6,322 kJ Nm⁻³ for S3 and 5,939 kJ Nm⁻³ for S2). The main reason of this result is related to the fact that by increasing the *ER* the oxidation reaction is promoted more than the reforming and cracking reactions thus bringing to the formation of CO₂, H₂O, and N₂, and the reduction of CO, CH₄ and H₂ concentration.



a) Aspen Plus model results for S2.



b) Aspen Plus model results for S3.



c) Aspen Plus model results for S6.

Fig. 3-19. Model results for the gasification of the different residual wastes produced in the three MBT facilities [32].

These changes in the reactions are also confirmed in the trend of the syngas components as reported in Table 3-10. The model has a high level of accuracy in predicting the patterns and fluctuations in hydrogen and light hydrocarbon production. In the case of S2, it is notable for having a greater proportion of plastic material in comparison to S3 and S6. This increased presence of volatile matter leads to higher concentrations of H₂ and C₂H₄. As regards the tar production is notable its reduction with *ER*. This trend can be explained by the fact that elevating the *ER* leads to a rise in the bed temperature, consequently enhancing tar cracking. In terms of overall efficiency, the scenario that exhibits the most advantageous outcomes is S6. This is due to its higher H₂ content and lower CO levels, which contribute to an improved gas yield when compared to scenarios S3 and S6. Additionally, the *CGE* of S6 surpasses 0.5 for all *ER* values. However, the values reported in Table 3-10 also remark the difficulties related to a successful gasification of a heterogenous waste material. Indeed, the *CGE* decreases with *ER* and in the case of high plastic content in the residue waste the equivalence ratio should be limited to avoid syngas production with low H₂ and CO concentrations.

Table 3-10. Summary of the air gasification of the different RDF materials with *ER* sensitivity.

Simulation	CGE	Q [Nm ³ h ⁻¹]	TAR [g Nm ⁻³]	Syngas Composition (% d.b.)						LHV [kJ Nm ⁻³]
				H ₂	CO	CO ₂	CH ₄	C ₂ H ₄	N ₂	
S2 ER = 0.25	0.490	5,524	38	8.77%	7.93%	13.07%	4.24%	4.10%	61.88%	5,939
S2 ER = 0.29	0.490	6,203	30	7.18%	7.16%	13.81%	4.80%	3.12%	63.92%	5,281
S2 ER = 0.33	0.459	6,788	15	5.89%	6.50%	14.24%	4.45%	2.45%	66.47%	4,526
S3 ER = 0.25	0.550	4,673	74	6.62%	12.51%	13.71%	7.14%	2.44%	57.59%	6,322
S3 ER = 0.29	0.498	5,084	51	5.98%	10.91%	13.91%	5.99%	1.81%	61.41%	5,260
S3 ER = 0.33	0.501	5,576	49	5.00%	9.61%	14.32%	5.59%	1.77%	63.71%	4,823

S6 ER = 0.25	0.569	4,290	56	4.06%	11.38%	15.48%	9.09%	2.41%	57.58%	6,585
S6 ER = 0.29	0.505	4,694	43	5.15%	10.84%	14.63%	6.58%	1.76%	61.05%	5,343
S6 ER = 0.33	0.496	5,156	21	4.74%	10.41%	14.38%	5.73%	1.48%	63.26%	4,772

3.5 Conclusions

The present Chapter focuses on the modelling aspect of municipal solid waste gasification using the Aspen Plus software. The study focuses on examining the usage of refuse-derived fuel obtained from the mechanical-biological treatment process as the main input for the air gasifier. The validation of the model is performed by a comparative analysis of experimental data obtained from previous studies on fluidized bed gasifiers, as documented in the existing literature. Overall, the model demonstrates a commendable level of precision in monitoring the key variables essential for gasification, namely the composition of the syngas, its *LHV* and the quantity of tar generated and carried along with the syngas. Nevertheless, the poor availability of the experimental data suitable for accurate prediction represents a limit. The model faces challenges related to variables such as bed temperature, interactions with bed particles, and more intricate processes like tar cracking. The dependence of the bed temperature, the interaction with the bed particles, and more complex phenomena such as the tars cracking represent the limits of the model. For this reason, outside the *F* function defined for the tested materials, the tar will not be taken into consideration. Then, the model is used to assess the syngas production from the residue of the MBT facility described in Chapter 2. The *LHV* of the produced syngas ranges from 7,300 kJ Nm⁻³ down to 4,200 kJ Nm⁻³ with increasing the *ER* in accordance with the results reported in the literature due to the molar fraction decrease of the most relevant compounds such as H₂, CH₄ and CO with *ER*. Eventually, a sensitivity analysis of different residual waste compositions produced in MBT facilities is performed. Three cases are modelled by changing the *ER* in the range of 0.25-0.33. It is found that the *LHV* and the *CGE* decrease with the *ER*, and the maximum conversion efficiency of 0.569 is obtained from the model for the S6 case and *ER* of 0.25, while the lowest one (0.459) is obtained for S2 and *ER* of 0.33. In summary, the verified model demonstrates its efficacy in forecasting the overall energy efficiency of a fluidized bed air gasifier that utilises diverse input materials. Consequently, it has the potential to facilitate initial assessments of the energy recovery potential from residual waste in composting plants. In the next Chapter, the syngas will be used to produce energy in different power systems.

Nomenclature

ASH Ash mass Fraction [-]

C	Carbon mass fraction [-]
C_{gasif}	Gasified carbon [-]
C_{uncomb}	Uncombusted carbon [-]
Cl	Chlorine mass Fraction [-]
F	Composition function [-]
G	Gibbs free energy [kJ kg ⁻¹]
G_{mix}	Gibbs free energy of a mixture [kJ kg ⁻¹]
H	Hydrogen mass fraction [-]
h_{com}	Enthalpy of combustion [kJ kg ⁻¹]
HHV	Higher Heating Value [kJ kg ⁻¹]
$\text{HHV}_{\text{dry, m}}$	HHV of the feedstock, dry mass based [kJ kg ⁻¹]
$\text{HHV}_{\text{wet, m}}$	HHV of the feedstock, wet mass based [kJ kg ⁻¹]
λ	Latent heat of vaporization [kJ kg ⁻¹]
LHV	Lower Heating Value [kJ kg ⁻¹]
$\text{LHV}_{\text{feed, m}}$	LHV of the feedstock, mass based [kJ kg ⁻¹]
$\text{LHV}_{\text{syn, v}}$	LHV of the syngas, volume based [kJ kg ⁻¹]
\dot{m}_{air}	Air mass flow rate [kg h ⁻¹]
\dot{m}_{feed}	Feed mass flow rate [kg h ⁻¹]
n	Molar content [mol]
N	Nitrogen mass Fraction [-]
O	Oxygen mass Fraction [-]
P	Pressure [bar]
Q	Syngas volumetric flow rate [Nm ³ h ⁻¹]
R	Universal gas constant, 8.314 [J mol ⁻¹ K ⁻¹]
S	Sulphur mass fraction [-]
ST_{split}	Steam Split Fraction
T	Temperature [°C]
T_{bed}	T of the gasifier bed [°C]
T_{dryer}	T of steam [°C]
T_{gasfier}	T of gasification [°C]
T_{pyrol}	T of fast pyrolysis [°C]
T_{R3app}	T approach of reaction R3 [°C]
T_{R4app}	T approach of reaction R4 [°C]

T_{R6app}	T approach of reaction R6 [°C]
T_{R7app}	T approach of reaction R7 [°C]
W	Moisture content, wet based [-]
x	Molar fraction

Acronyms

CGE	Cold Gas Efficiency
CHP	Combined Heat and Power (Unit)
CSTR	Continuous-flow stirred tank reactor
ER	Equivalence Ratio
d-RDF	Densified Residue Derived Fuel
EoS	Equation of State
EU	Eucalyptus
HDPE	High Density Polyethylene
IGCC	Integrated Coal Based System
LCA	Life Cycle Assessment
LDPE	Low Density Polyethylene
MBT	Mechanical-Biological Treatment
MFA	Material Flow Analysis
MSW	Municipal Solid Waste
NEO	Neolite material
OCC	Corrugated Cardboard
OMSW	Organic Municipal Solid Waste
ORC	Organic Rankine Cycle
PA	Paper
PAHs	Polycyclic Aromatic Hydrocarbons
PDF	Packaging Derived Fuels
PE	Polyethylene
PET	Polyethylene Terephthalate
PL	Plastic
PP	Polypropylene
PS	Polystyrene
PVC	Polyvinylchloride

RDF	Residue Derived Fuels
RMSE	Root Mean Squared Error [-]
RMSW	Residual Municipal Solid Waste
W2E	Waste to Energy

CHAPTER 4

COMBINED COOLING, HEATING AND POWER GENERATION FROM RMSW GASIFICATION

4.1 Introduction

The sustainable management of municipal solid waste (MSW) is a fundamental aspect of the circular economy framework and plays a crucial role in advancing a more resilient and competitive energy system in Europe [177]. The residual municipal solid waste (RMSW) is comprised of a diverse combination of non-recycled components that are derived from mechanical and biological processes in composting facilities. Throughout history, incineration has been widely recognized as the predominant waste-to-energy (W2E) method [112]. Besides, pyrolysis and gasification are alternative W2E processes for sustainable disposal of biomass, having lower environmental impacts and residual ash compared to incineration [178]. The pyrolysis uses external heat for a thermal decomposition of the feedstock into oil, gas, and solid residues with limited or absent air usage. Compared to pyrolysis, gasification better exploits the chemical energy of the feedstock and can be autothermal, i.e. sustained by the energy provided by different chemical reactions occurring simultaneously in the reactor. However, its complexity and inflexibility provided a lack of complete process control and a relatively low diffusion worldwide. Using RMSW is an interesting and challenging feedstock due to its high energy content of up to 40 MJ kg⁻¹ [64]. Nevertheless, the presence of condensing tars, which are a wide variety of heavy hydrocarbons like phenols, furans, naphthalene, and other polycyclic aromatic hydrocarbons is more problematic in the gasification process than in the combustion [150]. In addition, while the syngas produced from wood biomass can be used in gas turbines/micro-gas turbines and internal combustion engines (ICEs) [179], [180] after proper cleaning treatments [181], [182], the exploitation of syngas from plastic gasification is more challenging. The higher tar content and the lower ash melting point demand its use in external combustion cycles for a reliable operation and power supply [139]. Moreover, the composition of RMSW is versatile, which is a challenge for a gasifier system compared to agro-industrial feedstocks.

Among the different external combustion power cycles, steam turbine (ST) power plants are usually adopted in combination with MSW incinerators [183], [184]. Trinidad et al. [184] a comprehensive

exergy and environmental analysis on a steam turbine (ST) power plant combined with MSW incineration. Liu et al. [185] compared the potential of integrating MSW incineration and gasification with combined power plants in two Chinese cities. Their results showed that the exergy efficiency of MSW gasification is higher than MSW incineration with better environmental and economic performances despite the capital cost being 1.5-2 times more.

Organic Rankine cycle (ORC) systems serve as a viable alternative to ST power plants in the context of combined heat and power (CHP) applications, particularly for the distributed conversion of waste-to-energy (W2E) derived from residential municipal solid waste (RMSW). ORC systems function similarly to ST power plants based on the Rankine cycle principle. However, they utilise organic working fluids that are well-suited for low-temperature heat sources. Additionally, these systems operate at lower evaporation pressures and maintain pressures above atmospheric levels at the condenser. Moreover, it can be observed that the complexity of an ORC system is comparatively lesser when compared to a ST system designed for smaller capacities [186].

Many studies have focused on the use of ORC to valorise municipal waste in the literature. For example, Yatsunthea and Chaiyat [187] performed an energy, exergy, and economic analysis of a 25 kWe ORC unit integrated with a 100 kg h⁻¹ incinerator using refuse-derived fuel based on medical wastes, having a LHV of 26.92 MJ kg⁻¹, operating in Thailand. Although the absence of complete cost covering, the system remains more cost-effective compared to the alternative method of landfill disposal for hazardous wastes. Özahi et al. [188] performed a thermoeconomic optimization analysis of an ORC system adapted to an existing solid waste power plant finding toluene as the best working fluid. Ustaoglu et al. [189] conducted an exergy analysis of a CHP-ORC system fed by MSW incineration. They found that R141b was the best working fluid and the system was capable of achieving a combined efficiency of 80.25%.

Supercritical carbon dioxide (sCO₂) Brayton cycle power plants have garnered significant attention in recent times due to their notable gas density, which enables the construction of compact systems that are crucial for waste heat recovery purposes. Additionally, these power plants exhibit improved heat transfer in the heat exchangers, employ turbomachinery with lower pressure ratios, and possess a lower power-to-heat ratio, making them well-suited for combined heat and power (CHP) applications [178]. Indeed, the gas density at the outlet of the turbine in a sCO₂ can be about 10,000 times higher than the one in a steam turbine [190]. On the other hand, the low pressure of sCO₂ systems is usually above 75 bar due to the critical pressure of CO₂ of 73.8 bar. The system functions at elevated pressures, resulting in increased costs relative to other power systems of equivalent power output. Recently many researchers have focused their attention on the applications of sCO₂ [191],

[192], the system layout, optimization, and the components' designs and testing [193], [194]. For example, Cao et al. [195] conducted a 4E analysis and a multi-objective optimization of an innovative biomass gasifier integrated with a gas turbine and sCO₂ power cycle for CHP applications. In the study of Moradi et al. [178], the performances of micro-scale sCO₂ and gas turbine systems with bottoming ORC units combined with the gasification of the hazelnut shell were compared for decentralised trigeneration. Their study revealed that despite the lower electric efficiency of the sCO₂ system, it performs better for the provision of combined cooling heating, and power in residential buildings because of its lower power-to-heat ratio closer to that of the buildings compared to the gas turbine [196]. For instance, Tozlu et al. [197] analysed three different W2E scenarios using biogas from MSW landfilling in Turkey integrated with a sCO₂ power plant, an ORC system, and an ICE connected to a DHN. They found the sCO₂ power plant could increase the power generation by about 20% despite having a longer payback period, and the ORC system by about 10% compared to the ICE system.

The application of RMSW-driven CHP plants in district heating networks (DHN) is of interest in many countries since it can provide several benefits such as i) coverage of electricity and heating of districts; ii) high overall combined efficiency of power plants; iii) sustainable handling of MSW in urban areas; and iv) long lifetime of the investment up to 50 years. Currently, both the 4th and 5th generations of DHNs are based on inlet water temperatures lower than 70 °C [196], [198] enabling the direct use of low-temperature heat and reducing the energy losses of the networks. As a consequence, DHNs have great potential in reducing the energy consumption of the building sector in urban areas [199].

The literature review has highlighted the high potential of RMSW gasification as W2E technology and the scarcity of comparison of different power cycles for the provision of CHP in DHNs powered by the gasification of heterogeneous materials. This Chapter focuses on the numerical investigation of the possibility of air gasification of refuse-derived municipal solid waste described in Chapter 3 in conjunction with various power cycles for applications in district cooling and heating. The model of the fluidized bed air gasifier, which is discussed in Chapter 3, is linked with the models of steam turbine, ORC, and sCO₂ Brayton cycle power plants. This integration facilitates the concurrent generation of cooling, heating, and electricity inside district networks. The second, third, and fourth generations of distributed hash tables (DHNs) are under consideration. In addition, to meet the cooling requirements of the users and enhance the overall combined efficiency of the systems, the demand is fulfilled by employing an absorption chiller during the period of elevated temperatures. Therefore, the DHN being discussed in this context refers to a district heating and cooling network

(DHCN), which might potentially serve as a vital resource in the upcoming transition toward sustainable energy.

4.2 Modelling of the systems and their components

The comprehensive scheme adopted for modelling the framework is reported in Fig. 4-1. It remarks the gasification model, the energy conversion from the syngas to the power unit, their different configurations, and the linking to the DHCN.

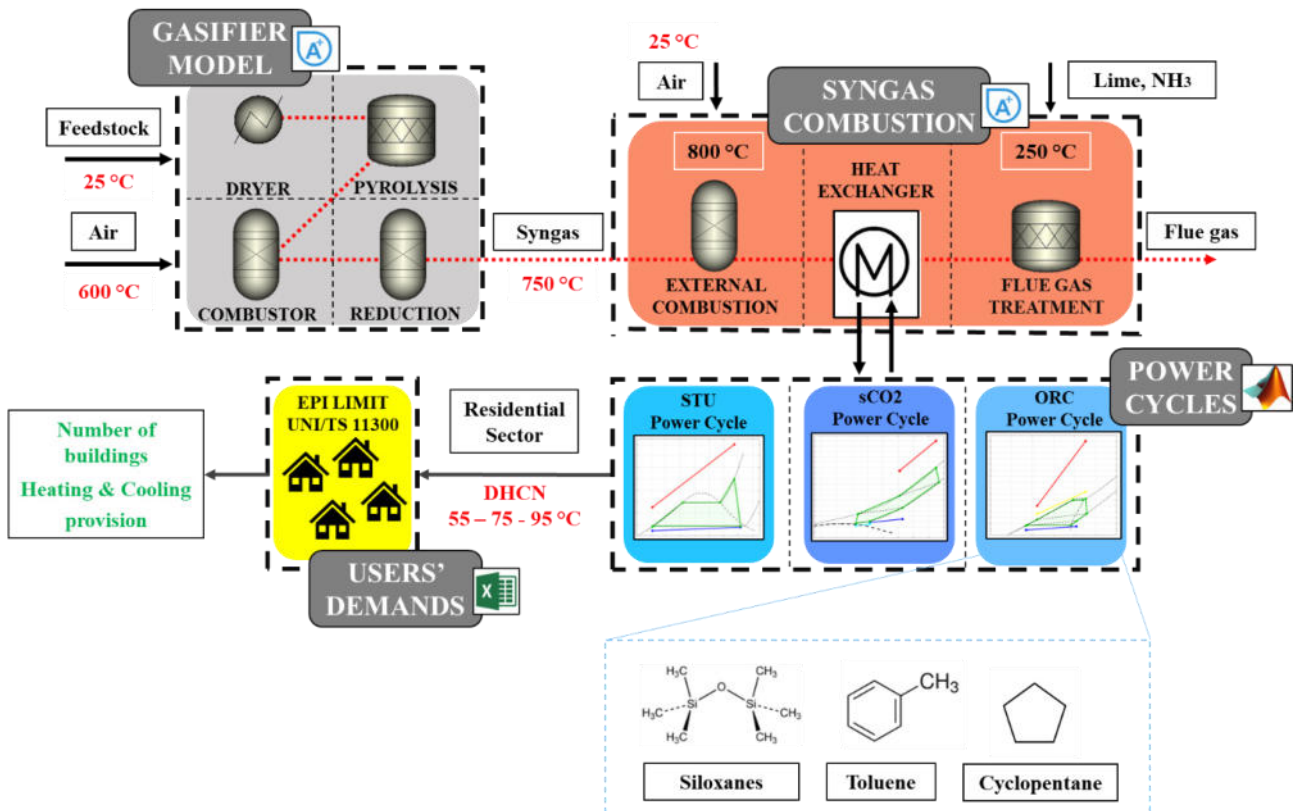


Fig. 4-1. Scheme of the modelling framework with the relevant sections.

After a brief description of the integrated system reported subsection 4.2.1, the model of the fluidized bed plastic-waste air gasifier coupled with external-fired combustion chamber recalled and presented in subsection 4.2.2. Subsection 4.2.3 describes the models of the different considered power plants. Both the ORC and the sCO₂ power systems are considered with and without recuperative heat exchangers. Finally, subsection 4.2.4 presents the methodology used for quantifying the number of residential buildings that can be supplied by the DHCN.

4.2.1 The Integrated Treatment system

The study is based on the most recent data collected by a mechanical-biological treatment unit (MBT) of OFMSW and RMSW of the facility under the case studio. The new layout of the system, including gasification, power generation, and district heating/cooling network is reported in Fig. 4-2. The various colors refer to the sections reported in the Fig. 2-1.

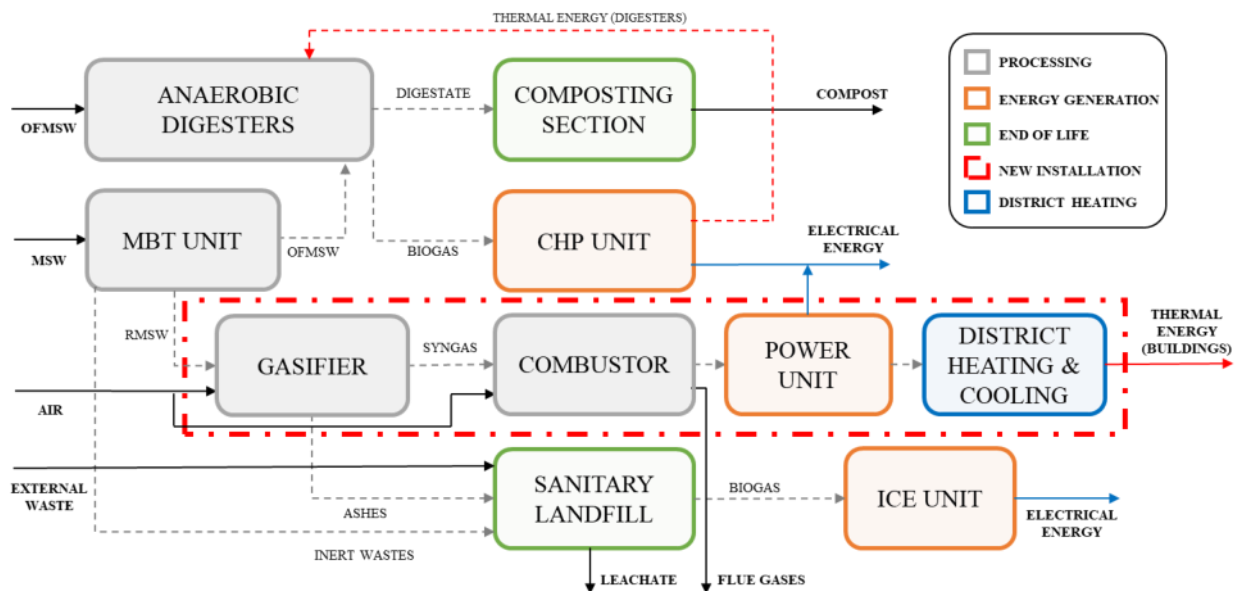
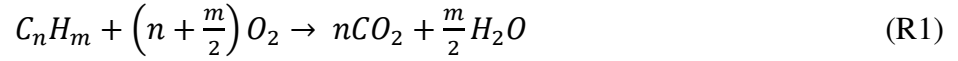


Fig. 4-2. Overview of the general process layout including gasification and power generation.

The RMSW is sent to the gasifier, then the resulting syngas is combusted in an external combustion chamber and the thermal energy of the flue gas is transferred to the power unit. The latter is connected to the DHCN for recover the waste heat of the power unit. With respect to the current situation, the proposed configuration would reduce the load on the landfill by limiting the disposal to inert materials and ashes only while increasing the energy valorisation of the MSW.

4.2.2 Gasification and Combustion section

The thermochemical model described in Chapter 3 can be summarized as shown in the Fig. 4-1. The RMSW undergoes an initial drying phase in the first block, followed by a further breakdown and volatilization process in the RYIELD block. The majority of the products derived from the pyrolysis process are directed towards the combustor block, also known as the RGIBBS block. Only minor portions of solid carbon and H₂ are allocated for the synthesis of tars and C₂H₄. The gasification process is ultimately represented by a second RGIBBS block in the model, which effectively mimics the reactions by reducing the Gibbs free energy of the reactants. Then, the syngas is externally fired according to the reactions R1-R2:



The air mass flow rate, \dot{m}_{air} [kg h⁻¹], for the syngas combustion, is evaluated from the stoichiometric combustion of the compounds and considering a certain excess of air, e , to assure its complete combustion. Hence, the air mass flow rate is calculated according to equations (4.1 to 4.4):

$$\dot{m}_{C_nH_m, st} = \dot{m}_{C_nH_m} \times 32 \frac{(n + m/4)}{(12n + m)} \quad (4.1)$$

$$\dot{m}_{CO, st} = \dot{m}_{CO} \times \frac{16}{12 + 26} = 0.571 \times \dot{m}_{CO} \quad (4.2)$$

$$\dot{m}_{CO, st} = \dot{m}_{CO, st} + \sum \dot{m}_{C_nH_m, st} \quad (4.3)$$

$$\dot{m}_{air, st} = \dot{m}_{CO, st} \times (1 + e) \quad (4.4)$$

where $\dot{m}_{air, st}$ is the stoichiometric air mass flow rate [kg h⁻¹], $\dot{m}_{C_nH_m, st}$ and $\dot{m}_{CO, st}$ are the stoichiometric air mass flow rates [kg h⁻¹] for full combustion of the hydrocarbon gases C_nH_m and of CO. The reactions R1-R2, as well as the equations 4.1-4.4 are implemented in the flowsheet reported in the Fig. 4-3. The red stream “Syngas” should be considered connected to the stream S19 of the Fig. 3-2.

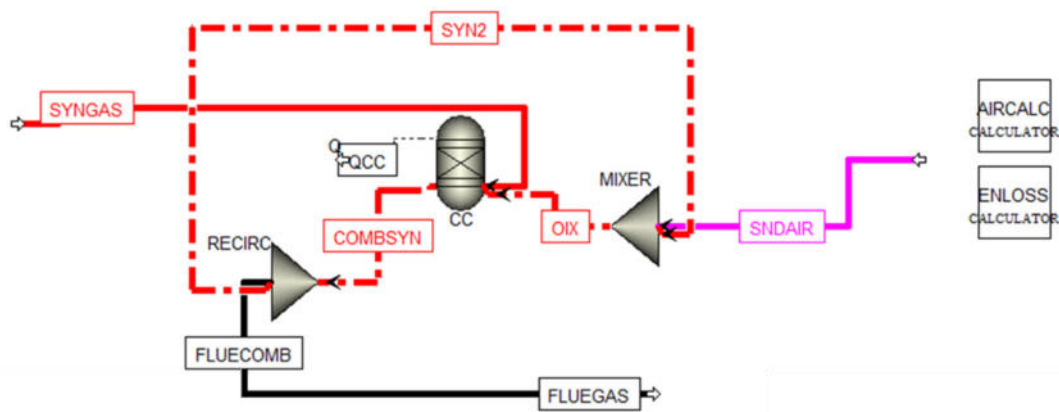


Fig. 4-3. Flowsheet used for the syngas combustion.

The combustor “CC” (RGIBBS block) works with a fixed flue gas recirculation ratio of 20% and excess air defined by a dedicated calculator block that fixes the flue gases temperature at 800 °C. The combustion efficiency is considered 95%. Then, the sensible heat of the gases is transferred to the power units. The final temperature of the gases before treatment is 250 °C since lower temperatures

may lead to the formation of corrosive substances on the chimney wall, while higher ones may result in failures of the gas cleaning equipment and lower energy recovery rates. The temperature is in accordance with the Italian incinerator regulations [200], [201] and having considered active carbons (lime) for the removal of acid compound (HCl, H₂S) and NO_x in the subsequent gas treatment section. The RMSW gasification potential is assessed using the real data from the case study as well as the literature data of other RDF compositions to consider its versatile composition. The composition of the case study (CS1) and that of S6 (CS2) scenario obtained in the previous Chapter, reported in Table 4-1, are used for the assessment of power generation potential. The latter has been chosen since it has the highest syngas *LHV* (6,600 kJ Nm⁻³), and a volumetric flow rate of 4,300 Nm³. Therefore, CS2 provides 28.25 MJ in total. Table 4-1 summarises the feedstocks properties and the corresponding thermal power input to the gasifier and the bottoming power cycle. The energy required for heating the air from ambient temperature to 600 °C is not accounted.

Table 4-1. Produced and exchanged power in the gasification plant considering different feedstocks.

Variable	CS1	CS2
Carbon	41.80	60.67
Hydrogen	6.32	6.03
Oxygen	25.26	22.42
Chlorine	0.09	1.14
Sulphur	0.14	0.2
Nitrogen	0.19	0.37
Ash	1.20	7.85
Moisture [%]	25.00	14.32
LHV [MJ kg ⁻¹]	21.30	21.80
\dot{Q}_{feed} [MW]	13.50	13.80
\dot{Q}_{in} [MW]	6.18	8.03
<i>CGE</i> [-]	44	52

4.2.3 Power systems

The schematic layout of ST, recuperative ORC, and recuperative sCO₂ power plants are depicted in Fig. 4-4, whereas the logic of each model is reported in Fig. 4-5. The ORC and sCO₂ systems are considered with and without a recuperator. Hence, in total of five different configurations of the power cycles are investigated, and their performance is assessed at design conditions. Heat exchangers are modelled using the ϵ -*NTU* method [202], [203] while the isentropic efficiency of the ST and ORC turbine considers the influence of the operating pressure based on a simplified off-design

equation reported in [78] and a semi-empirical model proposed by Macchi and Astolfi [204] respectively.

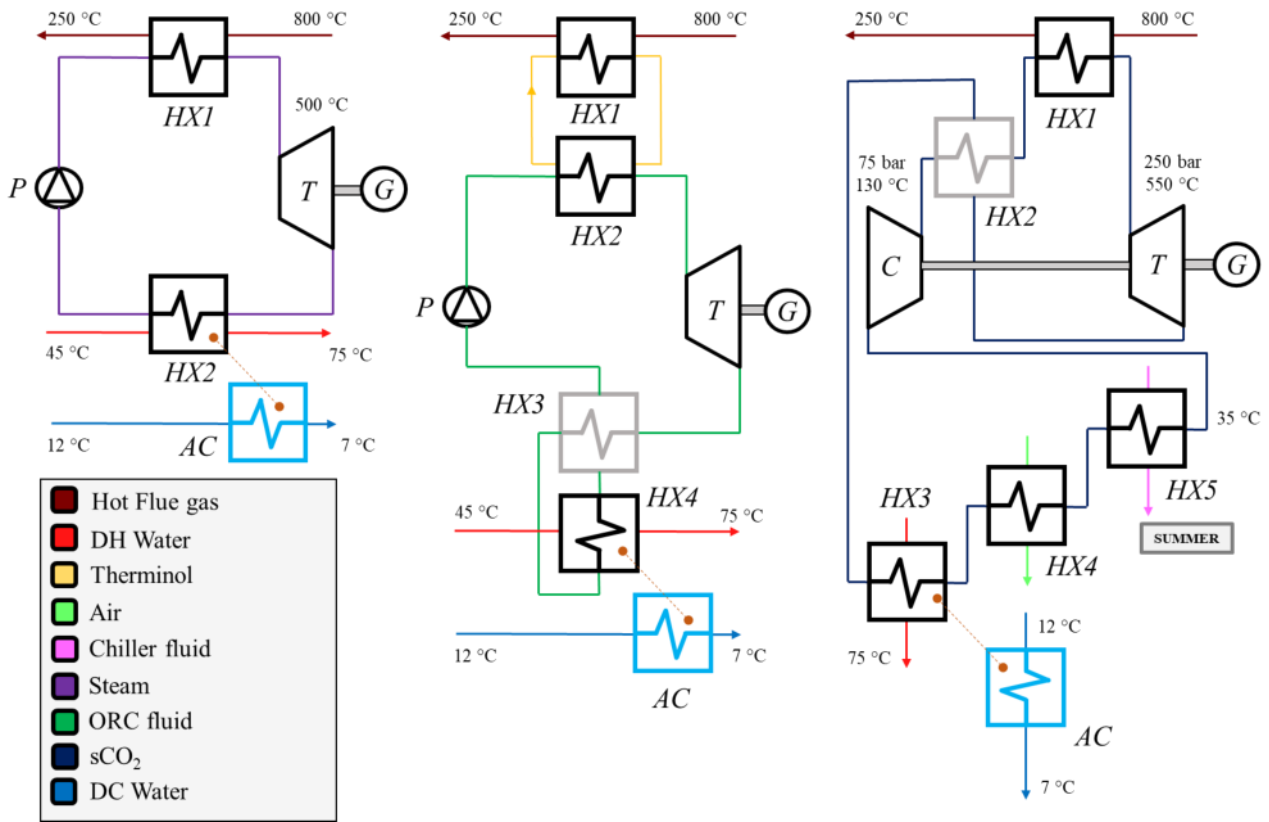


Fig. 4-4. The considered types and layouts of the three types of power systems are associated to seven units.

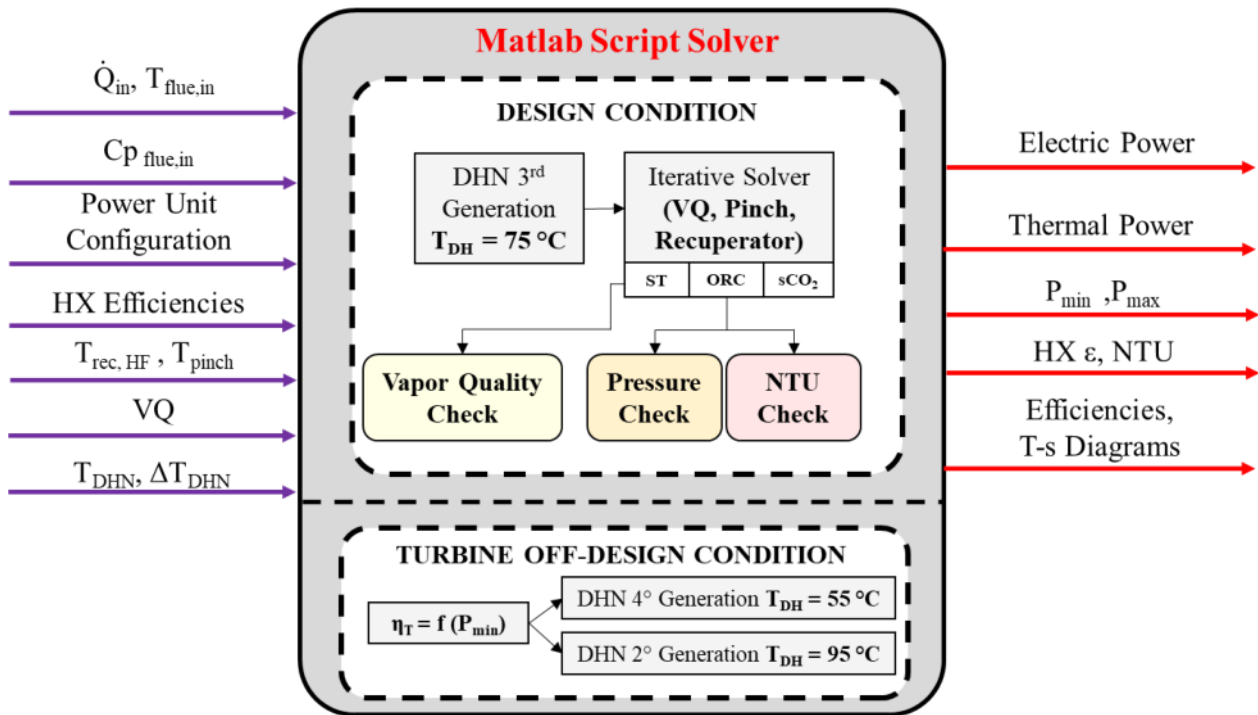


Fig. 4-5. The main parameters of the solvers used for the power plants in MATLAB.

The solver evaluates the net electric and thermal powers, cycle performance, pressure limitations, and characteristic points in the T-s diagrams based on the given flue gas specifications (\dot{Q}_{in} , T_{fg} , Cp_{fg}). Additional inputs are the heat exchanger (HX) efficiencies, temperature of the hot fluid after the recuperator ($T_{rec,HF}$), the water temperature in the DHN (T_{DHN}), and the water temperature difference of DHN ($\Delta T_{DHN} = 30 \text{ }^\circ\text{C}$).

The heat exchange efficiencies for recuperators and oil loops are 0.95, whereas for the remaining heat exchangers, the efficiency is 0.9. In the context of the ST system, it is essential to consider the vapour quality (VQ) in the design of the turbine. The appropriate discharge pressure is determined using an iterative process that takes into account the minimal pinch temperature ($T_{pinch} = 10 \text{ }^\circ\text{C}$) occurring in the condenser. In relation to the heat exchangers, it is considered that the maximum NTU assumed is 5. For compressors, pumps, and turbines, the electrical and mechanical efficiencies of 0.95 and 0.97 are assumed [178]. For district cooling, an absorption chiller is considered to be directly connected to the condensers. The datasheet pertaining to the selected model (WC2H series, LG [205]) reports a coefficient of prestaton (COP) of 0.74 and inlet hot water of 95°C , which is the temperature considered for the operation in the hot season. In the subsequent part, the power system models are examined with regards to the configurations depicted in Fig. 4-5. The outcomes of the models written in Matlab are afterward juxtaposed with analogous ones in Aspen Plus.

4.2.3.1 The steam turbine cycle

The adoption of a single-pressure level arrangement for the ST plant is being examined, taking into account the quantity of input biomass in the gasifier. In the evaluation of the performance, it is expected that the pump would function under design settings, as its power consumption is insignificant in comparison to the power generated by the turbine in steam turbine plants. In contrast, the off-design operating of the turbine is evaluated in relation to its isentropic efficiency [78]:

$$\eta_{t,OD} = \eta_{t,D} \times \left(\frac{\pi}{2} \times \sqrt[10]{\frac{\dot{m}_{OD}}{\dot{m}_D}} \right) \quad (4.5)$$

Hence, it can be inferred that the isentropic efficiency of the system is mostly influenced by partial load situations, as opposed to the alterations in discharge pressure resulting from fluctuations in the water temperature within the district heating network (ranging from 55 to 95 °C). In relation to heat exchangers, the effectiveness of the evaporator is determined based on temperature values, whereas an assumed value of 0.75 is assigned to the condenser's effectiveness. The structure of the solver is described as follows.

The solution method for the steam turbine incorporates three distinct iterative loops in order to adhere to the design constraints of vapour quality and district heating network temperature. The system is initially addressed with respect to the minimal surge pressure of the turbine. Subsequently, the maximum pressure is systematically adjusted through iterative processes until the appropriate vapour quality is attained. Then, the net efficiency of the system is determined, as well as the NTU. The off-design behaviour of the turbine is accounted for by equation 4.5, used for the 4th and 2nd district heating networks. A fixed electrical pump efficiency of 0.75 is defined for design and off-design configurations since the work of this component is negligible compared with the turbine power output.

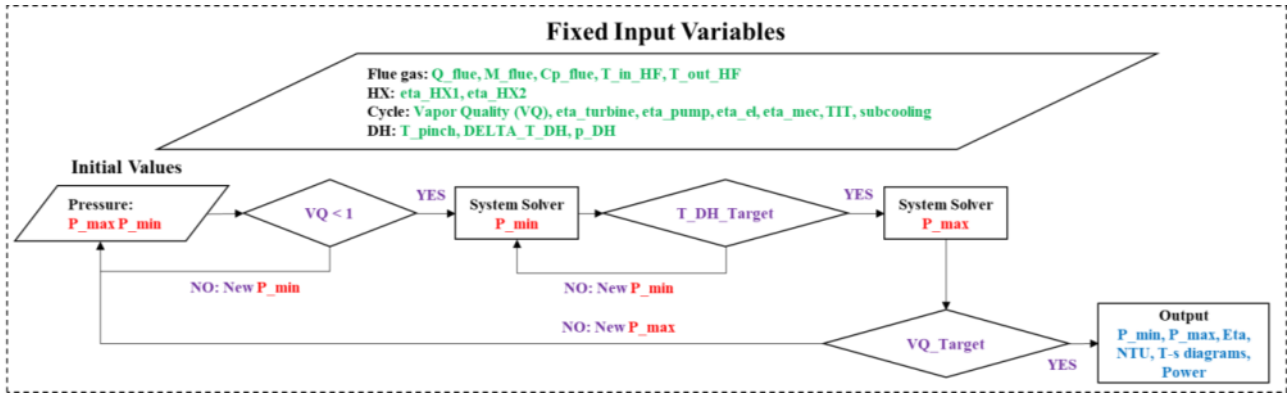


Fig. 4-6. Scheme of the ST power plant solver.

For the two HX present in the system, the following equations have been used for addressing the ε and NTU:

$$\varepsilon_{HX1} = \frac{\dot{Q}}{\dot{Q}_{max}} = \frac{C_{min} \times \Delta T_{min}}{C_{min} \times \Delta T_{max}} = \frac{T_{IT} - T_{w,in}}{T_{fg,in} - T_{w,in}} \quad (4.6)$$

$$NTU_{HX1} = -\frac{1}{r} \times \ln [(1 + r \times (1 - \varepsilon_{HX1}))] \quad (4.7)$$

$$NTU_{HX2} = -\ln (1 - \varepsilon_{HX2}) \quad (4.8)$$

$$r = \frac{C_{min}}{C_{max}} = \frac{\dot{m}_{min} \times c_{p,min}}{\dot{m}_{max} \times c_{p,max}} \quad (4.9)$$

where HX1 is evaporator and HX2 condenser, whereas $T_{w,in}$ [°C] is the water temperature at the inlet of the evaporator and $T_{fg,in}$ [°C] the inlet flue gas temperature (800 °C). the subscript “min” refers to the fluid having the minimum capacity rate C_{min} [W K⁻¹], while ΔT_{max} [°C] is the maximum temperature difference in any HX. For the first one, the cross-flow with unmixed cold water pipes [203] has been assumed. In theory, the evaporator should be divided into three more heat exchangers, corresponding to the economizer, vaporiser, and superheater. Equation 4.6 applies to economiser and superheater, while the vaporiser effectiveness should be defined likewise as did for the condenser. For the sake of simplicity, this aspect has been neglected. The purpose of the ε -NTU method is to derive the right UA [W K⁻¹] value of the heat exchanger, from which design its geometry. Here, the method is used only to avoid unfeasible thermodynamic design, i.e. when NTU exceed the range given.

4.2.3.2 The ORC system

Compared to ST plants, ORC systems have a lower encumbrance, faster response, and the capability to use a wide range of fluids depending on the temperature range [206]. In this case, a secondary loop using Therminol VP-1 [207] as diathermic oil transfers the heat of the flue gas to the working fluid at the evaporator. The proposed scheme of the power cycle is similar to those commercially provided by Turboden and Ormat [208]. The preliminary study on the potential ORC solutions [209] led to the choice of a single-pressure level subcritical cycle configuration both with and without the recuperator. The turbine efficiency is evaluated through the empirical correlation presented by Macchi and Astolfi in [204] for design and off-design conditions as follows:

$$\eta_{t,OD} = \sum_{i=1}^{15} A_i F_i \quad (4.10)$$

where A_i and F_i are semi-empirical coefficients depending on the dimensionless size parameter (SP) and volume ratio (V_r) of the turbine, evaluated at the isentropic condition. The maximum allowable values for SP and V_r are 1 and 400 respectively.

4.2.3.2.1 Fluid selection

Regarding the working fluids, a preliminary comparison between the super-dry fluids was done between toluene and the siloxanes Hexamethyldisiloxane (MM) and octamethyltrisiloxane (MDM) [210] in a dedicated Aspen Plus model that emulates the ORC configuration of Fig. 4-4. The study concluded that MM and MDM are a suitable choice for high-temperature ORC systems but generate less electrical power than toluene, as depicted in the T-s diagrams of Fig. 4-7.

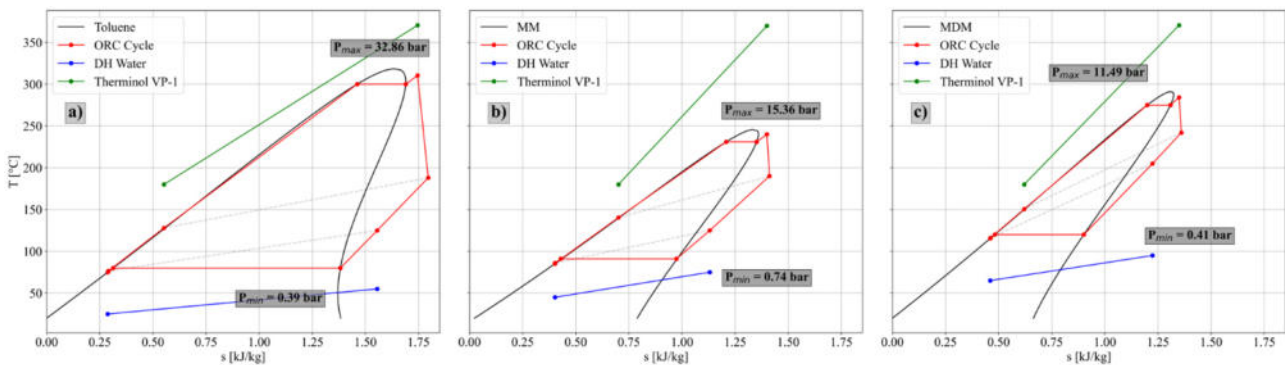


Fig. 4-7. T-s diagram of: a) Toluene; b) MM; and c) MDM [xxx].

Much of the siloxanes potential relies on the combined generation, in fact they offers more thermal power to be recovered at the condenser than cycloalkanes, but technological aspects limit their

operability, especially for MDM. Therefore, the power production was prioritized in the choice of the ORC working fluid.

Then, the final comparison between toluene and cyclopentane [211] was done. These working fluids are considered to have high critical temperatures and relatively high condensing pressures. Table 4-2 reports the main characteristics of these working fluids. The maximum operating pressure of the ORC is limited to 80% of the working fluid critical pressure. Further details on the algorithm of the ORC solver are presented after.

Table 4-2. Toluene and Cyclopentane characteristics [210]–[212]

Working Fluid	Chemical Formula	Molecular Weight [g mol ⁻¹]	GWP [kg CO ₂ eq.]	ODP [kg CFC-11 eq.]	T _{crit} [°C]	P _{crit} [bar]	T _{min} [°C]	T _{max} [°C]
Toluene	C ₇ H ₈	92.14	Low	0	318.6	41.1	85	350
Cyclopentane	C ₅ H ₁₀	70.08	Low	0	238.6	45.2	>0	300
MM (excluded)	C ₆ H ₁₈ OSi ₂	162.38	Low	0	245.9	19.2	30	290
MDM (excluded)	C ₈ H ₂₄ O ₂ Si ₃	236.53	Low	0	291.3	14.6	80	290

The structure of the solver for the recuperated ORC system is reported in Fig. 4-8. Compared to the ST, additional sections and iterations must be implemented. Four subsections are used for solving the i) ideal system ($\eta_t = 1$) without recuperator, ii) ideal system with recuperator, iii) real system without recuperator, and finally iv) real system with recuperator. Each section is described in the next paragraphs.

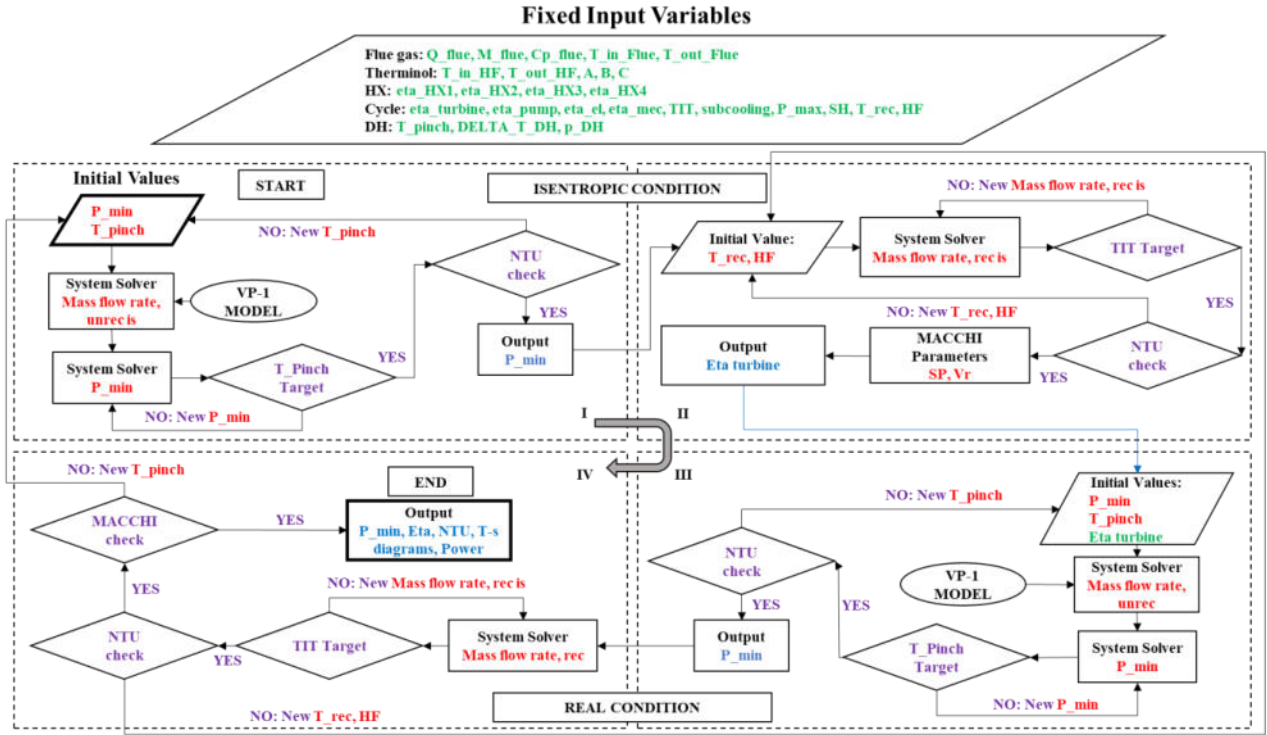


Fig. 4-8. Solver schematics for ORC.

For the four HX present in the system, the following equations have been used for addressing the HX effectiveness ϵ :

$$\epsilon_{HX1} = \frac{T_{fg,in} - T_{fg,out}}{T_{fg,in} - T_{oil,in}} \quad (4.11)$$

$$\epsilon_{HX2} = \frac{TIT - T_{ORC,in}}{T_{oil,out} - T_{ORC,in}} \quad (4.12)$$

$$\epsilon_{HX3} = \frac{T_{HF,in} - T_{HF,out}}{T_{HF,in} - T_{CF,in}} \quad (4.13)$$

$$\epsilon_{HX4} = \frac{T_{HF,out} - T_{cond,out}}{T_{HF,out} - (T_{DH} - \Delta T_{DH})} \quad (4.14)$$

where $T_{fg,out}$ [°C] is the flue gas outlet temperature (250 °C), $T_{ORC,in}$ [°C] the inlet temperature of the working fluid at the evaporator, $T_{oil,in}$ [°C] the inlet temperature of the diathermic oil (180 °C), $T_{oil,out}$ [°C] the outlet temperature (370 °C), $T_{HF,in-out}$ [°C] the temperatures of the “hot fluid” of the recuperator, $T_{CF,in}$ [°C] the relevant temperature for the “cold fluid”, $T_{cond,out}$ [°C] the temperature of the working fluid after the condenser. For the NTU , the following equations were used [202], [213]:

$$NTU_{HX1} = -\frac{1}{r} \times \ln [(1 + r \times (1 - \varepsilon_{HX1}))] \quad (4.15)$$

$$NTU_{HX2,1P} = \frac{1}{\sqrt{1+r^2}} \times \ln \frac{2 - \varepsilon_{HX2} \times [1 + r - \sqrt{(1+r^2)}]}{2 - \varepsilon_{HX2} \times [1 + r + \sqrt{(1+r^2)}]} \quad (4.16)$$

$$NTU_{HX2,nP} = \frac{1}{\sqrt{(1+r^2)}} \times \ln \frac{2 - \varepsilon_{HX2,P} \times [1 + r - \sqrt{(1+r^2)}]}{2 - \varepsilon_{HX2,P} \times [1 + r + \sqrt{(1+r^2)}]} \quad (4.17)$$

$$\varepsilon_{HX2,P} = \frac{1 - \left[\frac{(r \times \varepsilon_{HX2} - 1)}{\varepsilon_{HX2} - 1} \right]^{\frac{1}{P}}}{r - \left[\frac{(r \times \varepsilon_{HX2} - 1)}{\varepsilon_{HX2} - 1} \right]^{\frac{1}{P}}} \quad (4.18)$$

$$NTU_{HX3} = -\frac{1}{r} \times \ln [(1 + r \times (1 - \varepsilon_{HX3}))] \quad (4.19)$$

$$NTU_{HX4,1P} = \frac{1}{\sqrt{1+r^2}} \times \ln \frac{2 - \varepsilon_{HX4} \times [1 + r - \sqrt{(1+r^2)}]}{2 - \varepsilon_{HX4} \times [1 + r + \sqrt{(1+r^2)}]} \quad (4.20)$$

where P is the number of passages in the shell & tube heat exchanger configuration used for HX2 and HX4. The first one requires two passages while HX4 only one. HX1 and HX3 are assumed to have the cross-flow configuration. Inlet and outlet refer to the specific HX.

4.2.3.2.2 Section I: Ideal cycle not recuperated

The code assesses the minimum pressure of the system. To ensure the extended chemical stability of the organic working fluid, it is necessary to set the maximum permissible pressure at 80% of the fluid's critical pressure. In this iteration, the diathermal oil is (Therminol VP-1) mass flow rate is initially assessed, and then the working fluid mass flow rate. Properties of these fluids have been taken from Coolprop for the hydrocarbons and Aspen Plus 11 for Therminol VP-1. In particular, the specific heat capacity $C_{p,oil}$ [kJ kg⁻¹ K⁻¹] is expressed using a polynomial equation as follows:

$$C_{p,oil}(T) = c_1 + c_2 \times T + c_3 \times T^2 \quad (4.21)$$

where $c_1 = 1,462.4740$ [kJ kg⁻¹ K⁻¹], $c_2 = -0.7739$ [kJ kg⁻¹ K⁻²] and $c_3 = 0.0037$ [kJ kg⁻¹ K⁻³]. The implementation of an iterative approach continues until the minimal temperature differential at the pinch point is met, along with satisfying the maximum permissible NTU for the three heat exchangers.

4.2.3.2.3 *Section II: Ideal cycle recuperated*

The goal of the section is to model the recuperator and assess the turbine efficiency according to the equation proposed by Macchi and Astolfi [204] for multistage axial turbines. The calculation of the new mass flow rate is based on an initial estimate regarding the temperature of the hot gas at the outflow of the recuperator. The convergence criterion is imposed on the TIT temperature.

4.2.3.2.4 *Section III: Real cycle not recuperated*

The system is re-iterated from the beginning with the new turbine efficiency.

4.2.3.2.5 *Section IV: Real cycle recuperated*

In a manner related to Section II, an evaluation is conducted on the characteristics of the recuperated cycle, taking into account the isentropic efficiency of the actual turbine. In the event that the NTU criterion of the recuperator is not adhered to, the programme will go back to section 2 and proceed to revise the hot stream output temperature accordingly. If the new TIT and V_r are beyond the allowable limits, the code returns to loop I by updating the minimum pinch temperature difference.

4.2.3.3 *The sCO₂ system*

A sCO₂ power plant operates according to the closed Brayton cycle and compared to a ST plant, has the advantage of higher compactness which results in a high power-to-weight ratio and higher flexibility for district heating applications, due to its lower power-to-heat ratio [178]. Nevertheless, it is important to note that this particular system has a lower level of technology readiness when compared to both ST and ORC plants, de facto limiting its commercial diffusion. Additionally, the utilisation of high pressure in the supercritical fluid introduces a number of practical issues that are not still fully solved.

In the literature, different configurations have been investigated so far [214]. Despite the simple recuperative configuration is not the most efficient one, it is considered here to limit the overall complexity and have a fair comparison with the ST and the ORC systems.

The system is not expected to fall into the off-design situation by just changing the DHN requirement. However, some measures must be accounted for the complete sCO₂ cooling before the compression stage. A dry cooler and a chiller are considered in series to guarantee the temperature setpoint of 35 °C at the suction of the compressor. The latter operates in the hot season when the dry cooler cannot

maintain the design suction temperature of the compressor. The architecture of the simple recuperated sCO₂ Brayton cycle is reported in Fig. 4-9.

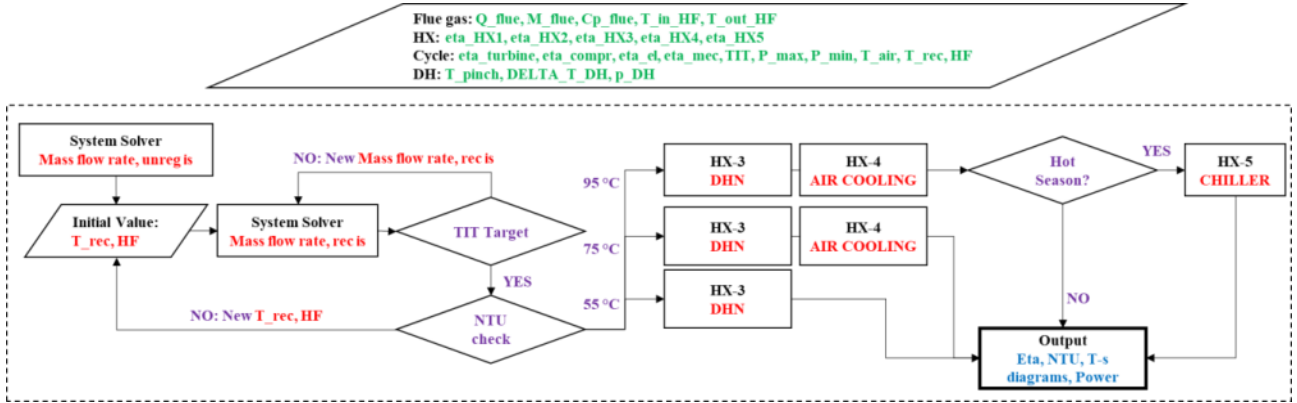


Fig. 4-9. Solver schematics for sCO₂ Brayton Cycle.

Since the pressure limits are fixed according to fluid properties and technological progress at present, the structure of the solver is easier than the former. However, the following considerations are of interest for the cooling process. When the DHN temperature is higher than 55 °C, an air cooler is switched on to cool the CO₂ down to 35 °C at HX4 and limits the power requested by the compressor. In the summer, the temperature of the cooling water in HX3 is set at 95 °C, as required by the absorption chiller unit. Hence, an additional chiller unit is used to cool the sCO₂ temperature down to the desired inlet temperature at the compressor. Therefore, another HX (HX5) is added to the cycle. The following relationships were used to assess ϵ and NTU for the four HX in the cycle. The seasonal heat exchanger HX5 has not been taken into account.

$$\epsilon_{HX1} = \frac{T_{fg,in} - T_{fg,out}}{T_{fg,in} - T_{sCO_2,in}} \quad (4.22)$$

$$\epsilon_{HX2} = \frac{T_{HF,in} - T_{HF,out}}{T_{HF,in} - T_{CF,in}} \quad (4.23)$$

$$\epsilon_{HX3} = \frac{T_{HF,out} - T_{HX4,in}}{T_{HF,out} - (T_{DH} - \Delta T_{DH})} \quad (4.24)$$

$$\epsilon_{HX4} = \frac{T_{HX4,in} - T_{HX5,in}}{T_{HX4,in} - T_{air,in}} \quad (4.25)$$

$$NTU_{HX1,1P} = \frac{1}{\sqrt{1+r^2}} \times \ln \frac{2 - \epsilon_{HX1} \times [1+r - \sqrt{(1+r^2)}]}{2 - \epsilon_{HX1} \times [1+r + \sqrt{(1+r^2)}]} \quad (4.26)$$

$$NTU_{HX1,nP} = \frac{1}{\sqrt{(1+r^2)}} \times \ln \frac{2 - \varepsilon_{HX1,P} \times [1+r - \sqrt{(1+r^2)}]}{2 - \varepsilon_{HX1,P} \times [1+r + \sqrt{(1+r^2)}]} \quad (4.27)$$

$$\varepsilon_{HX1,P} = \frac{1 - \left[\frac{(r \times \varepsilon_{HX1} - 1)}{\varepsilon_{HX1} - 1} \right]^{\frac{1}{P}}}{r - \left[\frac{(r \times \varepsilon_{HX1} - 1)}{\varepsilon_{HX1} - 1} \right]^{\frac{1}{P}}} \quad (4.28)$$

$$NTU_{HX2} = -\frac{1}{r} \times \ln [(1+r \times (1 - \varepsilon_{HX2}))] \quad (4.29)$$

$$NTU_{HX3,1P} = \frac{1}{\sqrt{1+r^2}} \times \ln \frac{2 - \varepsilon_{HX3} \times [1+r - \sqrt{(1+r^2)}]}{2 - \varepsilon_{HX3} \times [1+r + \sqrt{(1+r^2)}]} \quad (4.30)$$

$$NTU_{HX3,nP} = \frac{1}{\sqrt{(1+r^2)}} \times \ln \frac{2 - \varepsilon_{HX3,P} \times [1+r - \sqrt{(1+r^2)}]}{2 - \varepsilon_{HX3,P} \times [1+r + \sqrt{(1+r^2)}]} \quad (4.31)$$

$$\varepsilon_{HX3,P} = \frac{1 - \left[\frac{(r \times \varepsilon_{HX3} - 1)}{\varepsilon_{HX3} - 1} \right]^{\frac{1}{P}}}{r - \left[\frac{(r \times \varepsilon_{HX3} - 1)}{\varepsilon_{HX3} - 1} \right]^{\frac{1}{P}}} \quad (4.32)$$

$$NTU_{HX4,1P} = \frac{1}{\sqrt{1+r^2}} \times \ln \frac{2 - \varepsilon_{HX4} \times [1+r - \sqrt{(1+r^2)}]}{2 - \varepsilon_{HX4} \times [1+r + \sqrt{(1+r^2)}]} \quad (4.33)$$

$$NTU_{HX4,nP} = \frac{1}{\sqrt{(1+r^2)}} \times \ln \frac{2 - \varepsilon_{HX4,P} \times [1+r - \sqrt{(1+r^2)}]}{2 - \varepsilon_{HX4,P} \times [1+r + \sqrt{(1+r^2)}]} \quad (4.34)$$

$$\varepsilon_{HX4,P} = \frac{1 - \left[\frac{(r \times \varepsilon_{HX4} - 1)}{\varepsilon_{HX4} - 1} \right]^{\frac{1}{P}}}{r - \left[\frac{(r \times \varepsilon_{HX4} - 1)}{\varepsilon_{HX4} - 1} \right]^{\frac{1}{P}}} \quad (4.35)$$

The shell & tube configuration has been assumed for HX1-3-4, while the cross-flow for the recuperator only. The number of P passages is 3, 2 and 2 respectively for the three heat exchangers.

4.2.4 The district heating and cooling network (DHCN)

DHCNs have emerged as a dependable and environmentally sound approach for delivering heating and cooling services to buildings, leading to reduced expenses for end users [215]. The size of the

network is primarily determined by the nominal capacity of the energy production system and the geographical proximity of the users to the production site.

For each gasification scenario (CS1, CS2), a sensitivity of the DHN temperatures is conducted. The water temperature of 75 °C corresponding to the 3rd generation of DHN is considered as the design condition. Then, the off-design behaviour of the power units is investigated considering the 2nd generation ($T_{DHN} = 95$ °C), and the 4th generation DHN ($T_{DHN} = 55$ °C) [216], [217].

The heated floor area (A_{floor}) and the number of residential buildings (N_B) is estimated in accordance with the methodology proposed by Cioccolanti et al. [199]. More precisely, it is based on the calculation of the “Energy Performance Index” (*EPI*) defined by the Italian legislation to evaluate the thermal energy consumption of a building for space heating. The index is determined by various parameters, including the building's location, surface area, and shape. Since 2015, the global EPI has been implemented as a comprehensive indicator for assessing the energy consumption of buildings. The EPI takes into account many elements including illumination, ventilation, sanitary water usage, and internal loads. From a design perspective, using the EPI_{lim} is a simplifying methodology that reduces the input to just the building shape factor SF , the climate zone (zone “E” characterises the location of the W2E system) and the number of heating degree days (HDD). Then, the minimum number of residential buildings is calculated as in the equation 4.36 below:

$$N_B = \frac{(1 - L) \times \dot{Q}_{cond}}{\dot{Q}_B \times CF} \quad (4.36)$$

where \dot{Q}_{cond} [kW] is the thermal power at the condenser/bottom heat exchanger of the power plant, L the heat losses assumed equal to 10% of \dot{Q}_{cond} , and \dot{Q}_B is the maximum thermal power demand per building as in equation 4.37:

$$\dot{Q}_B = X_s \times (K_D + K_V) \times V_G \times (T_i - T_e) \quad (4.37)$$

where K_D [$W\ m^{-3}\ K^{-1}$] is the building dispersion coefficient and a function of the climate zone and building geometry, K_V [$W\ m^{-3}\ K^{-1}$] is the ventilation coefficient, V_G [m^3] is the gross volume of a building, T_i [°C] is the design indoor temperature (20 °C in winter), T_e [°C] is the minimum ambient temperature, and X_s is a design safety coefficient assumed 1.2. The present analysis focuses on the city of Perugia as the reference site. The CF, or simultaneity factor, is determined by dividing the minimal number of buildings by the number obtained from the computation of the EPI mentioned above. Table 4-3 reports the energy efficiency class EEC for the buildings assumed in the study,

according to the distribution expressed in [218] for the new certificates released in 2022 for the residential sector.

Table 4-3. EEC distribution assumed for the study.

Parameter	A4	A2	A2	A1	B	C	D	E	F	G
Distribution [218]	2.80%	1.20%	1.50%	1.90%	2.40%	4.40%	9.80%	16.30%	25.40%	34.30%
EPI _{lim} [kWh m ⁻² year ⁻¹]		34.02			57.93	80.46	103.45	137.93	195.40	229.89

The *EPI* can be calculated as:

$$EPI = \frac{\dot{Q}_{cond} \times H \times D}{A_{floor}} \quad (4.38)$$

where H [h day⁻¹] is the number of hours where heating occurs in winter, and D [day year⁻¹] are the expected days of heating throughout the year according to the DPR 412/93 [219]. Assuming $H = 14$ h day⁻¹, $D = 183$ day year⁻¹, and the values for A_{floor} obtained for each scenario, a value of 122.6 kWh m⁻² year⁻¹ is obtained in equation 4.38. The *EPI* lowers since there are more buildings classified with the class “A” and fewer labelled as “F” and “G”.

The procedure to calculate A_{floor} consists in different passages. First, the total surface A_{tot} [m²] of a residential building can be obtained according to equation 4.39:

$$A_{tot} = 2 \times \left(\frac{A_{net}}{10} \times h_B + 10 \times h_B + A_{net} \right) \quad (4.39)$$

where A_{net} [m²] is the net walkable building floor area and h_B [m] the height of the building. Values assumed for the former are respectively 110.2 m² [199] and 2.7 m. The net volume V_N [m³] is calculated with the product of A_{tot} and h_B , the gross volume V_G is 130% of V_N and is used to obtain the shape factor SF of the building as:

$$SF = \frac{V_G}{A_{tot}} \quad (4.40)$$

It is possible to obtain the available thermal energy Q_{DHN} [kWh] transferred with the DHN, as:

$$Q_{DHN} = \dot{Q}_{cond} \times H \times D \quad (4.41)$$

Then, the characterization of the residential building agglomerate is given by defining the seven energy classes “A” to “G” and obtaining the relevant $EPI_{lim,i}$. Finally, the A_{floor} can be obtained by taking the occurrence (d_i) of each EEC defined in Table 4-3:

$$A_{floor} = Q_{DHN} \times \sum_{i=1}^7 \frac{d_i}{EPI_{lim,i}} \quad (4.42)$$

4.3 Results

The results section is subdivided into three distinct subsections. Initially, a comparative study is conducted to assess the potential of various power cycles. Subsequently, a sensitivity analysis is performed by altering the composition of RMSW. Subsequently, a sensitivity analysis is conducted, wherein the DHN temperature is systematically varied, and the corresponding count of buildings connected to the DHN is determined for each individual scenario. In subsection 4.3.3, a methodology is introduced to determine the optimal power cycle design based on the specific requirements of the customers. There are 14 cases of fluctuation in the composition of syngas, and 21 scenarios of variation in the DHN temperature. Furthermore, this study examines an additional four specific scenarios for sCO₂ operation throughout the summer season, resulting in a comprehensive analysis of a total of 46 cases, which will be detailed in the subsequent sections.

4.3.1 Power cycle comparison

Fig. 4-10 reports the T-s diagram of the different power unit cycles for the CS1 reference case. The red line represents the syngas temperature variation, the blue one the cooling water temperature at the condenser, and the characteristic state points of the power cycle are reported in green.

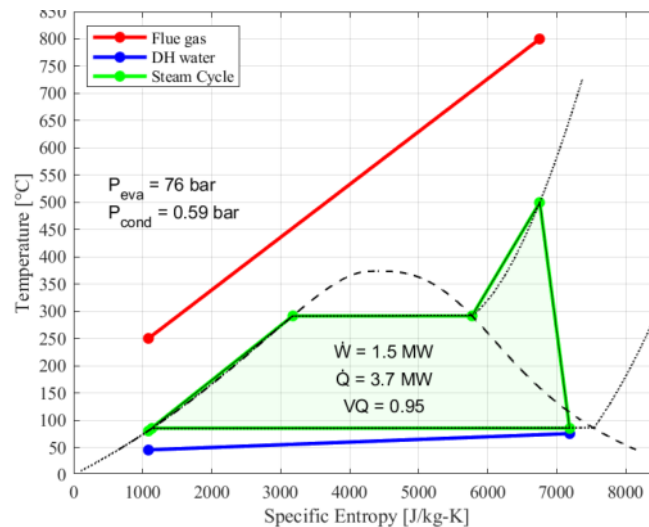


Fig. 4-10. T-s diagram of the ST power plant for the CS1 feedstock.

The net electric and thermal power outputs are around 1.5 MW and 3.7 MW. The CS2 scenarios exhibits net electric power output of 1.8 MW, and thermal power output ranging of 4.66 MW, respectively. The aggregate efficiency is approximately 81.5%. Referring to the feedstock, the overall efficiency is 38.5% (CS1) and 47.5% (CS2).

Fig. 4-11 presents the T-s graphs illustrating the thermodynamic processes of sCO₂ and ORC power plants. Figures (5a) and (5b) pertain to the sCO₂ power plant, illustrating its configurations with and without the recuperator, respectively. Meanwhile, Figures (5c-d) and (e-f) correspond to the ORC cycle, showcasing the utilisation of toluene and cyclopentane as working fluids, respectively. The blue hue depicted in the sCO₂ graphs signifies the temperature trajectory of the cooling air specifically at heat exchanger HX4, which is utilised to lower the temperature of the CO₂ to 35 °C. The yellow color in the ORC plots indicates the temperature trend of the diathermic oil at HX1.

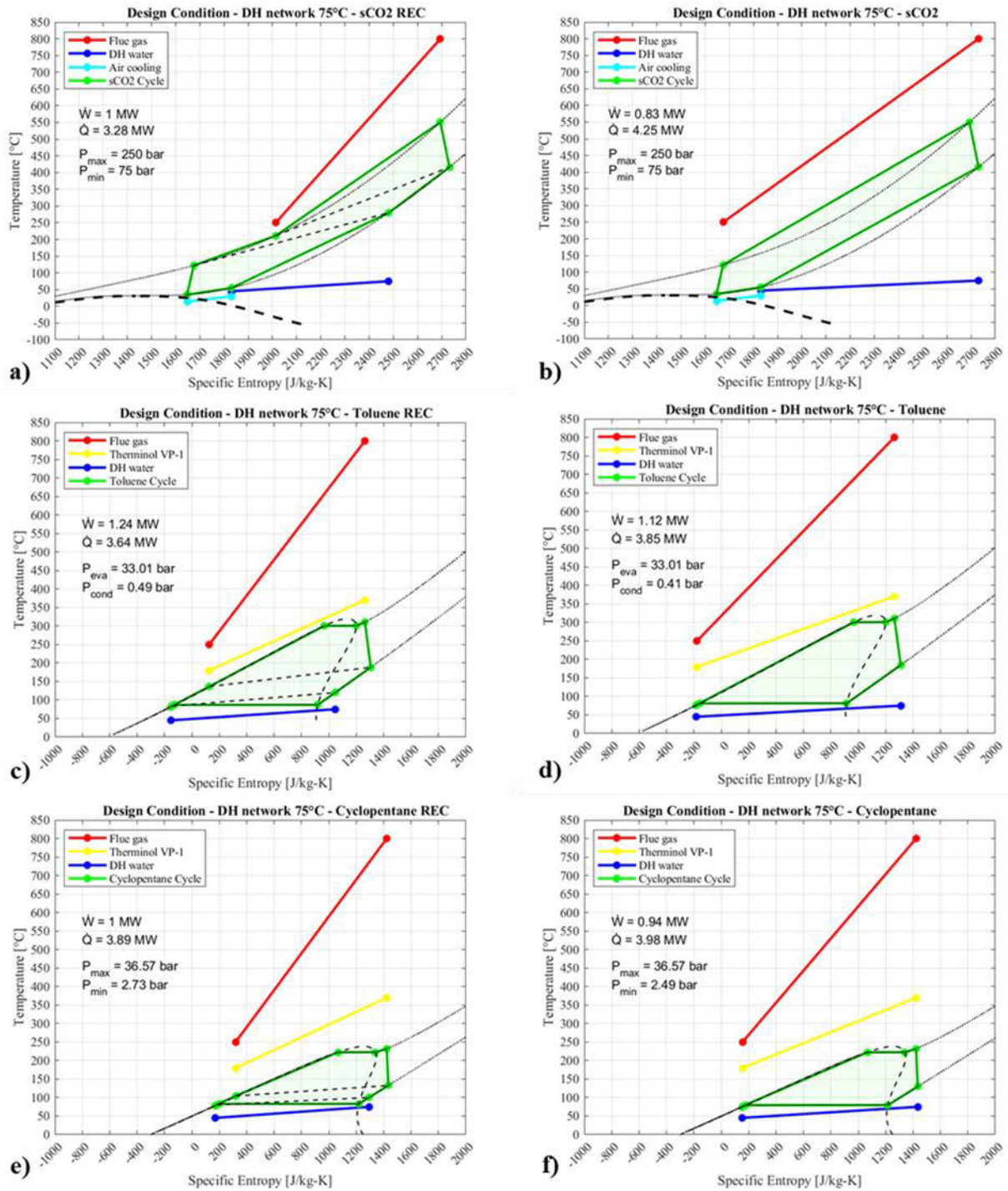


Fig. 4-11. T-s Diagrams of the different power units.

The condensing pressure of the ORC systems strongly depends on the type of fluid chosen. The toluene has a sub-atmospheric condensing pressure (0.41-0.49 bar), whereas the one of the cyclopentane is significantly higher (2.49-2.73 bar). Since the maximum pressure is fixed to 80% of the critical pressure of the fluid the pinch point at HX2 is lower in the case of toluene thus resulting in a higher heat exchanger effectiveness. As anticipated, the inclusion of a recuperator in the cycle results in an enhanced power-to-heat ratio. Specifically, in the case of sCO₂, the power generation

experiences an increase from 830 kW to 1,000 kW for CS1 and from 1,050 kW to 1,240 kW for CS2. Regarding the ORC, comparable patterns are observed for toluene. Specifically, the net power output exhibits an increase from 1,120 kW, and 1,370 kW to 1,240 kW (+10.7%), and 1,560 kW (+13.9%) for CS1 and CS2. Eventually, in the case of cyclopentane, the following power outputs are obtained: 940 kW and 810 kW without recuperator and 1,000 kW (+6.4%) and 860 kW (+6.2%) in the cooperative cycle. It is noteworthy that the utilisation of toluene enables the attainment of superior electrical efficiencies in comparison to cyclopentane, with average values of 19.4% and 15.6% respectively. Conversely, the recuperator has a detrimental impact on the thermal power production. In the case of sCO₂, the thermal output decreases from 4,250 kW and 5,360 kW to 3,280 kW (-22.8% and 4,200 kW (-21.6%). In ORC power plants, the use of the recuperator influences less the thermal power output reduction; it accounts for 3,640 kW (-5.8%) and 4,590 kW (-5.4%) for toluene and 3890 kW (-2.3%) and 4,910 kW (-2.2%) for cyclopentane in case of CS1, CS2 scenarios respectively. Consequently, the thermal efficiency for sCO₂ ranges from 52% to 66.7% without recuperator while it is in the range from 57% to 60.4% for ORC using toluene and 61.1% and 62.5% in the case of cyclopentane. In summary, the overall efficiency of the ORC power plants is around 77-78%, whereas the sCO₂ overall efficiency ranges from 67.1% to 79.7%. Table 4-4 and Fig. 4-12 summarize the obtained results and point out the maximum number of residential buildings that can be linked to the DHN. Each thermal power plant offered a varying number of residential buildings that may potentially be supplied by the DHN and, consequentially, the overall A_{floor} served. The value of CF obtained for the DHN is 0.57 for the location of the W2E.

Table 4-4. Performance of the power systems for CS1 and CS2.

POWER SYSTEM	\dot{Q}_{COND} [kW]	\dot{W} [kW]	FLUE GAS			FEED			N_B	A_{floor} [m ²]	
			η_{th} [%]	η_{el} [%]	η_{tot} [%]	η_{th} [%]	η_{el} [%]	η_{tot} [%]			
CS1	STU	3,700	1,500	58.0%	23.5%	81.6%	27.4%	11.1%	38.5%	652	71,882
	ORC TOL Rec	3,640	1,240	57.1%	19.5%	76.5%	27.0%	9.2%	36.1%	642	70,717
	ORC TOL	3,850	1,120	60.4%	17.6%	78.0%	28.5%	8.3%	36.8%	679	74,797
	ORC CYC Rec	3,890	1,000	61.0%	15.7%	76.7%	28.8%	7.4%	36.2%	686	75,574
	ORC CYC	3,980	940	62.4%	14.7%	77.2%	29.5%	7.0%	36.4%	702	77,322
	sCO ₂ Rec	3,280	1,000	51.5%	15.7%	67.1%	24.3%	7.4%	31.7%	578	63,723
	sCO ₂	4,250	830	66.7%	13.0%	79.7%	31.5%	6.1%	37.6%	749	82,568
CS2	STU	4,660	1,890	58.0%	23.5%	81.6%	33.8%	13.7%	47.5%	822	90,533
	ORC TOL Rec	4,590	1,560	57.2%	19.4%	76.6%	33.3%	11.3%	44.6%	809	89,173
	ORC TOL	4,840	1,370	60.3%	17.1%	77.3%	35.1%	9.9%	45.0%	853	94,030
	ORC CYC Rec	4,910	1,260	61.1%	15.7%	76.8%	35.6%	9.1%	44.7%	866	95,390
	ORC CYC	5,020	1,170	62.5%	14.6%	77.1%	36.4%	8.5%	44.9%	885	97,527
	sCO ₂ Rec	4,200	1,240	52.3%	15.4%	67.7%	30.4%	9.0%	39.4%	740	81,596
	sCO ₂	5,360	1,050	66.7%	13.1%	79.8%	38.8%	7.6%	46.4%	945	104,132

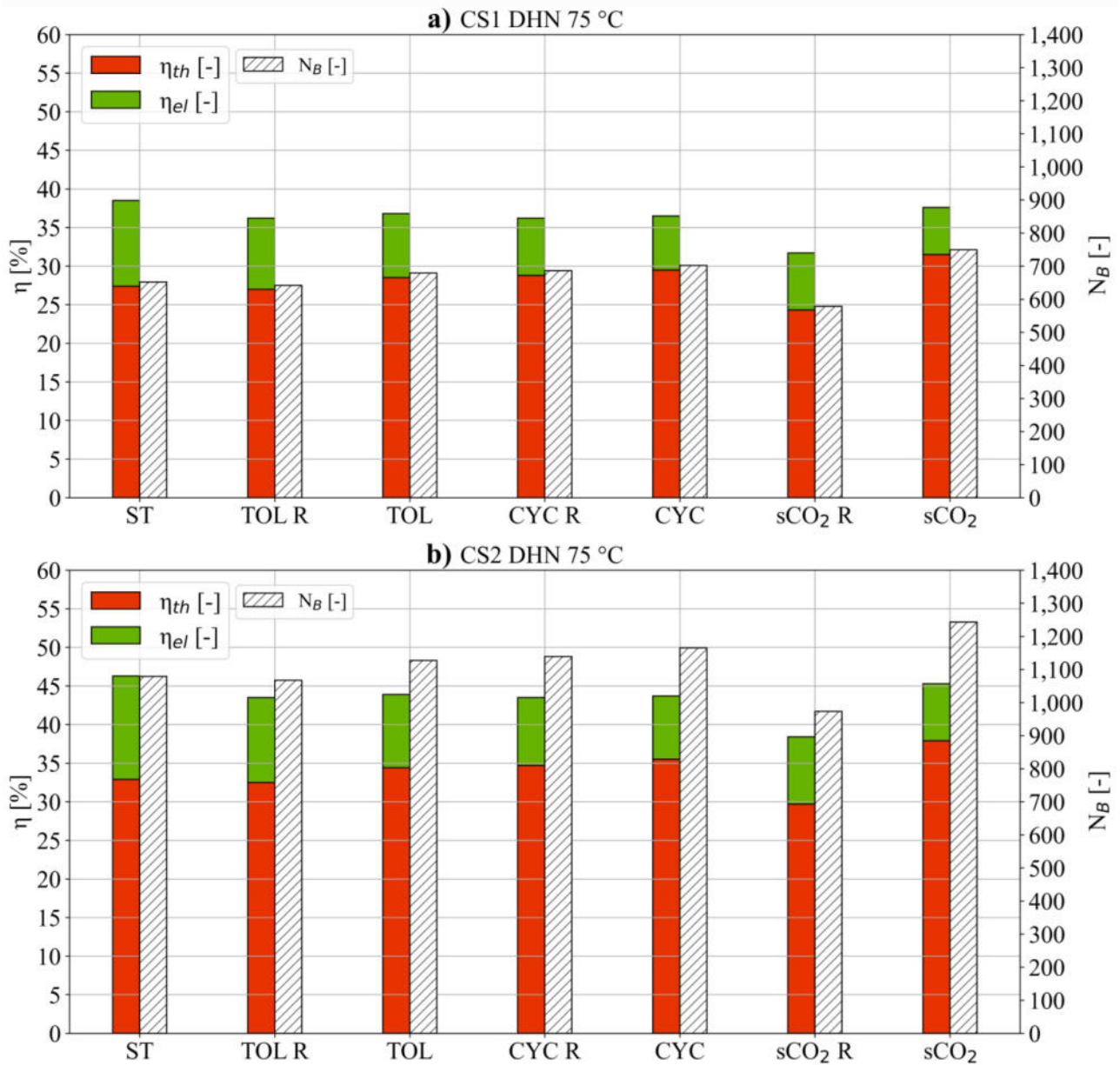


Fig. 4-12. Overall conversion efficiencies referred to the feedstock's chemical energy, for CS1 and CS2.

The average number of residences in the baseline CS1 scenario is 726, whereas for CS2 it is 814. From a thermal standpoint, the most optimal power unit is the sCO₂ for any given composition. The unit has the capacity to provide energy to 749-945 residential units. The implementation of the recuperator results in a notable enhancement in power efficiency, with a gain of 2.4% (specifically in relation to flue gas). However, it also imposes a significant drawback on thermal power, leading to an average reduction of 12.3%. The dimensions of the DHN decrease to 578 and 740, respectively. The changes exhibit greater prominence as compared to ORC systems, as the rise in power output is offset by a decline in thermal output. In terms of the overall total efficiency, the most significant

variance is observed in the case of toluene in CS1, with a decrease from 36.1% when utilising a recuperator to 36.8% when not utilising one.

4.3.2 Sensitivity Analysis with DHN

To evaluate the viability of RMSW gasification for decentralised power generation in various scenarios, the temperature of the water in the DHN is manipulated within the range of 55 °C to 95 °C, which aligns with the previous generation of DHNs. The deviation of the temperature by ± 20 °C from the intended value does not have a substantial impact on the operational characteristics of the power plants under consideration. A marginal deviation in the power-to-heat ratio is observed, yet the total efficiency remains highly similar. Additionally, the elevated temperature of 95 °C is also indicative of the operational state during the summer season when the absorption chiller is utilised to supply district cooling. The efficiency is reported by considering the coefficient of performance (*COP*) of the chiller during operation. Particular attention should be given to the sCO₂ cycle. The higher air temperature in summertime (30 °C) requires the operation of the additional chiller unit with a reduction of the net power production. A *COP* of 3.5 is assumed for the chiller. **Errore. L'autoriferimento non è valido per un segnalibro.** reports the complementary results of Table 4-4 with the variation of the water temperature in the DHCN. Similar concerns regarding electrical and thermal efficiency, as discussed before, can also be applied to this sensitivity analysis. In the interest of brevity, the overall combined efficiency is exclusively presented for both the cold and hot seasons when the absorption chiller is in operation. The assignment of cooling efficiency is not feasible at the lowest T_{DHN} due to the unsuitability of the temperature for the absorption chiller. **Errore. L'autoriferimento non è valido per un segnalibro.** and Fig. 4-13 report also the energy transferred by the DHCN addressed according to the operational time.

Table 4-5. Complementary results of Table 4-4 with sensitivity analysis on T_{DHN} .

POWER SYSTEM		\dot{Q}_{cond} [kW]	\dot{Q}_{cool} [kW]	\dot{W} [kW]	FLUE GAS		FEED		ENERGY [MWh/year]			N_B	A_{floor} [m ²]
					$\eta_{tot,W}$ [%]	$\eta_{tot,S}$ [%]	$\eta_{tot,W}$ [%]	$\eta_{tot,S}$ [%]	Heat	Cool	Electric		
CS1 55°C	ST	3,580	-	1,620	81.57%	-	38.52%	-	8,529	-	11,664	631	69,551
	ORC TOL Rec	3,640	-	1,260	76.86%	-	36.30%	-	8,672	-	9,072	642	70,717
	ORC TOL	3,820	-	1,150	77.96%	-	36.81%	-	9,101	-	8,280	673	74,214
	ORC CYC Rec	3,760	-	1,130	76.71%	-	36.22%	-	8,958	-	8,136	663	73,048
	ORC CYC	3,870	-	1,050	77.18%	-	36.44%	-	9,220	-	7,560	682	75,185
	sCO ₂ Rec	3,980	-	1,000	78.12%	-	36.89%	-	9,482	-	7,200	702	77,322
	sCO ₂	4,830	-	830	88.78%	-	41.93%	-	11,507	-	5,976	852	93,836
CS1 95°C	ST	3,810	2,820	1,380	81.41%	65.88%	38.44%	31.11%	9,076	1,862	9,936	672	74,019
	ORC TOL Rec	3,720	2,750	1,230	77.65%	62.43%	36.67%	29.48%	8,862	1,818	8,856	656	72,271
	ORC TOL	3,900	2,890	1,020	77.18%	61.33%	36.44%	28.96%	9,291	1,906	7,344	688	75,768
	ORC CYC Rec	4,030	2,980	860	76.71%	60.24%	36.22%	28.44%	9,601	1,969	6,192	710	78,294
	ORC CYC	4,100	3,030	810	77.02%	60.24%	36.37%	28.44%	9,768	2,003	5,832	723	79,653

	sCO ₂ Rec (W)	2,890	-	1,000	61.02%	-	28.81%	-	6,885	-	7,200	509	56,146
	sCO ₂ (W)	3,920	-	830	74.51%	-	35.19%	-	9,339	-	5,976	691	76,156
	sCO ₂ Rec (S)	-	2,200	740	-	46.12%	-	21.78%	-	1404	5,328	509	-
	sCO ₂ (S)	-	2,830	670	-	54.90%	-	25.93%	-	1904	4,824	691	-
CS2 55°C	ST	4,510	-	2,040	81.56%	-	47.46%	-	10,745	-	14,688	795	87,619
	ORC TOL Rec	4,590	-	1,570	76.70%	-	44.64%	-	10,935	-	11,304	809	89,173
	ORC TOL	4,820	-	1,380	77.20%	-	44.93%	-	11,483	-	9,936	850	93,641
	ORC CYC Rec	4,740	-	1,420	76.70%	-	44.64%	-	11,292	-	10,224	836	92,087
	ORC CYC	4,880	-	1,320	77.20%	-	44.93%	-	11,626	-	9,504	860	94,807
	sCO ₂ Rec	5,050	-	1,240	78.32%	-	45.58%	-	12,031	-	8,928	890	98,110
	sCO ₂	6,080	-	1,050	88.78%	-	51.67%	-	14,485	-	7,560	1,072	118,120
CS2 95°C	ST	4,800	3,550	1,740	81.43%	65.87%	47.39%	38.33%	11,435	2,345	12,528	846	93,253
	ORC TOL Rec	4,710	3,490	1,450	76.70%	61.51%	44.64%	35.80%	11,221	2,302	10,440	830	91,504
	ORC TOL	4,920	3,640	1,280	77.20%	61.26%	44.93%	35.65%	11,721	2,404	9,216	867	95,584
	ORC CYC Rec	5,080	3,760	1,080	76.70%	60.27%	44.64%	35.07%	12,102	2,482	7,776	896	98,693
	ORC CYC	5,170	3,830	1,020	77.08%	60.39%	44.86%	35.14%	12,317	2,526	7,344	911	100,441
	sCO ₂ Rec (W)	3710	-	1,240	61.64%	-	35.87%	-	8,839	-	8,928	654	72,077
	sCO ₂ (W)	4940	-	1,050	74.59%	-	43.41%	-	11,769	-	7,560	871	95,973
	sCO ₂ Rec (S)	-	2,830	1,000	-	47.69%	-	27.75%	-	1,802	7,200	654	-
	sCO ₂ (S)	-	3,560	840	-	54.79%	-	31.88%	-	2,400	6,048	871	-

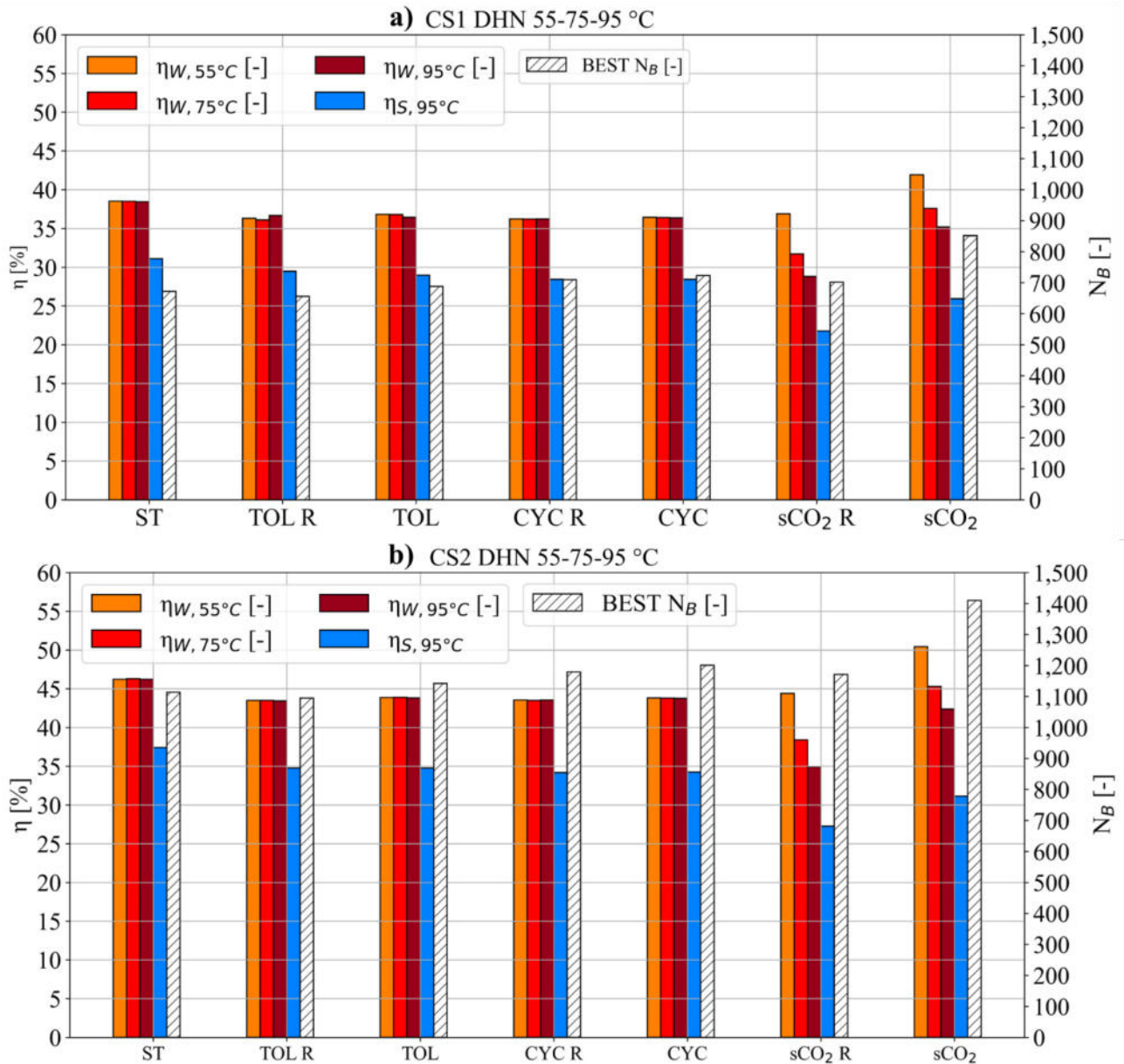


Fig. 4-13. Overall conversion efficiencies referred to the feedstock's chemical energy, for CS1 and CS2, for the sensitivity scenario.

In relation to the overall quantity of buildings to be provided for, there is a lack of consistent discrepancies observed between Table 4-4 and To evaluate the viability of RMSW gasification for decentralised power generation in various scenarios, the temperature of the water in the DHN is manipulated within the range of 55 °C to 95 °C, which aligns with the previous generation of DHNs. The deviation of the temperature by ± 20 °C from the intended value does not have a substantial impact on the operational characteristics of the power plants under consideration. A marginal deviation in the power-to-heat ratio is observed, yet the total efficiency remains highly similar. Additionally, the elevated temperature of 95 °C is also indicative of the operational state during the summer season when the absorption chiller is utilised to supply district cooling. The efficiency is

reported by considering the coefficient of performance (*COP*) of the chiller during operation. Particular attention should be given to the sCO₂ cycle. The higher air temperature in summertime (30 °C) requires the operation of the additional chiller unit with a reduction of the net power production. A *COP* of 3.5 is assumed for the chiller. **Errore. L'autoriferimento non è valido per un segnalibro.** reports the complementary results of Table 4-4 with the variation of the water temperature in the DHCN. Similar concerns regarding electrical and thermal efficiency, as discussed before, can also be applied to this sensitivity analysis. In the interest of brevity, the overall combined efficiency is exclusively presented for both the cold and hot seasons when the absorption chiller is in operation. The assignment of cooling efficiency is not feasible at the lowest TDHN due to the unsuitability of the temperature for the absorption chiller. **Errore. L'autoriferimento non è valido per un segnalibro.** and Fig. 4-13 report also the energy transferred by the DHCN addressed according to the operational time.

Table 4-5. Nevertheless, it is important to acknowledge that the most optimal power cycle configuration during the winter season is the simplified sCO₂, has the capability to provide heating to about 1,072 buildings with the lowest temperature district heating network (with the lowest T_{DHN}) with an overall efficiency of 50.4% (referred to feedstock energy). During the summer season, the most optimal power plant option is ST, which boasts a flue gas efficiency of 38.3%.

4.3.3 Sensitivity analysis with users' demand

The findings shown in Table 4-4 and To evaluate the viability of RMSW gasification for decentralised power generation in various scenarios, the temperature of the water in the DHN is manipulated within the range of 55 °C to 95 °C, which aligns with the previous generation of DHNs. The deviation of the temperature by ± 20 °C from the intended value does not have a substantial impact on the operational characteristics of the power plants under consideration. A marginal deviation in the power-to-heat ratio is observed, yet the total efficiency remains highly similar. Additionally, the elevated temperature of 95 °C is also indicative of the operational state during the summer season when the absorption chiller is utilised to supply district cooling. The efficiency is reported by considering the coefficient of performance (*COP*) of the chiller during operation. Particular attention should be given to the sCO₂ cycle. The higher air temperature in summertime (30 °C) requires the operation of the additional chiller unit with a reduction of the net power production. A *COP* of 3.5 is assumed for the chiller. **Errore. L'autoriferimento non è valido per un segnalibro.** reports the complementary results of Table 4-4 with the variation of the water temperature in the DHCN. Similar concerns regarding electrical and thermal efficiency, as discussed before, can also be applied to this sensitivity

analysis. In the interest of brevity, the overall combined efficiency is exclusively presented for both the cold and hot seasons when the absorption chiller is in operation. The assignment of cooling efficiency is not feasible at the lowest TDHN due to the unsuitability of the temperature for the absorption chiller. **Errore. L'autoriferimento non è valido per un segnalibro.** and Fig. 4-13 report also the energy transferred by the DHCN addressed according to the operational time.

Table 4-5 provide clear evidence of variations in power system performances within the DHCN, as influenced by the compositions of RMSW and the levels of water temperature. Determining the optimal solution for the valorisation of RMSW poses a challenge due to its inherent dependence on the specific requirements of consumers. Hence, the next part presents an efficient method that allocates a "score" to the various configurations, taking into account many priorities like energy need (power only, combined heat and power, combined trigeneration of cooling, heating and power), RMSW feedstock composition, DHN generation type, Users' energy demand. The energy demand in the residential sector is influenced by various factors, including as the geographical location of consumers, prevailing weather conditions, specific characteristics of buildings, the number of individuals in a household, and their consumption patterns. These factors contribute to constant and predictable changes in energy demand over time. The dynamic behaviour of the energy market, both electrical and thermal, was not taken into consideration. The inclusion of this supplementary level of detail has the potential to shift the focus away from the core objective of the article, which is centred on a qualitative exploration of waste valorisation. The users' energy demands element pertains specifically to the yearly heating and cooling requirements during the warm and cold seasons. For electricity, the average value of 2,700 kWh year⁻¹ [220] per building is assumed. Thermal requirements are taken from the corresponding methodologies. Hence, a score attributed to each power cycle configuration is given as:

$$SCORE = Score_{el,W} + Score_{he,W} + Score_{el,S} + Score_{co,S} + Score_{el,W+} + Score_{el,S+} \quad (4.43)$$

where $Score_{el,W}$ is the score for the electricity production in winter, $Score_{he,W}$ for the heat production in winter, $Score_{el,S}$ for the electricity production in summer and, $Score_{co,S}$ for the cooling production in summer, and $Score_{el,W+}$ is the score attributed to the electrical energy surplus compared to the buildings consumption in winter, and $Score_{el,S+}$ in summer.

The $Score_{el,W}$ (and similarly the other ones) can be calculated as:

$$Score_{el,W} = \frac{1}{i \times j} a_{el,W} \times (\bar{w}_{comp})^t \times \bar{M}_{ij} \times \bar{w}_{DH} \quad (4.44)$$

where $a_{el,W}$ is the weight for electricity production, $\bar{w}_{comp} = [w_{CS1} w_{CS2}]^t$ is the composition weight vector, $\bar{w}_{DH} = [w_{75^\circ C} w_{55^\circ C} w_{95^\circ C}]^t$ the district heating weight vector, and \bar{M}_{ij} is $i \times j$ matrix that collects the expected power (thermal) efficiency of the unit in each of the 6 scenarios. Each weight ranges from 0 to 1. The other production weights, $a_{he,W}$, $a_{el,S}$, and $a_{co,S}$ must be related to the heating, electricity and cooling consumption ratio Z in winter (Z_W) and summer (Z_S) and:

$$a_{he,W} = 1 - a_{el,W} \quad (4.45)$$

$$a_{co,S} = 1 - a_{el,S} \quad (4.46)$$

The ratio Z can be obtained from the annual energy building consumption. A simple linear correlation between Z and a_{el} can be defined:

$$a_{el} = \frac{1}{2}Z \quad (4.47)$$

Therefore, in the case where Z equals to 1, indicating an equal need for electricity and heat, the weights are the same. The weights $a_{el,S+}$ and $a_{el,W+}$ have a significant influence on the surplus electricity that is sold to the grid and is not utilised by the buildings connected to the DHCN. It is advisable to do an analysis based on hourly rates, as energy prices exhibit fluctuations over time, and there may arise circumstances in which such production is subject to penalties. In consideration of this particular study, the aforementioned issue has been rectified. The \bar{M}_{ij} matrix for $Score_{el,S+}$ becomes:

$$\bar{M} = \begin{bmatrix} 0 & 0 & \eta'_{13} \\ 0 & 0 & \eta'_{23} \end{bmatrix} \quad (4.48)$$

Where η'_{i3} [kW] is the corrected energy production:

$$\eta'_{i3} = \frac{\dot{W}_{i3} - \frac{C_B}{24 \times OP} \times N_B}{\dot{Q}_{in}} \quad (4.49)$$

In equation 4.49, \dot{W}_{i3} is the nominal power production, C_B [kWh] is the yearly electrical energy consumption of the buildings, assumed as 2,700 kWh year⁻¹, OP the operating days of the system and N_B the number of buildings in the DHCN. It is estimated that the system operates for a total of 300 days annually, aligning with the operational schedule of the composting facility being analysed. The

$Score_{el,W+}$ can be addressed using a similar methodology. Finally, the following weights are assumed: $\bar{w}_{comp} = [0.75 \ 0.25]^t$, $\bar{w}_{DH} = [1 \ 1 \ 1]^t$, $a_{el,W} = 0.0185$, $a_{he,W} = 0.9815$, $a_{el,S} = 0.1985$, $a_{co,S} = 0.8015$, $a_{el,W+} = 1$ and $a_{el,S+} = 1$. The values chosen for \bar{w}_{comp} consider the amount of waste that has a similar composition of CS1 and CS2.

A normal operating scenario (*NOP*) and two more cases are defined where only electricity (*ELY*) and thermal (*TH*) production are pursued. The final score results are reported in the Table 4-6 where in bold it is highlighted the highest score for each scenario.

Table 4-6. Score of every power system

POWER SYSTEM	SCENARIO SCORE		
	NOP	ELY	TH
STU	0.3171	0.2013	0.2303
ORC TOL Rec	0.2974	0.1666	0.2279
ORC TOL	0.2962	0.1434	0.2394
ORC CYC Rec	0.2909	0.1276	0.2428
ORC CYC	0.2910	0.1191	0.2478
sCO ₂ Rec	0.2556	0.1265	0.2051
sCO ₂	0.2969	0.1028	0.2621

According to Table 4-6, the ST represents the best choice for *NOP* (0.3171) and *ELY* (0.2013) scenarios, better than ORC and sCO₂ solutions. With respect to the ORC, it is seen that the inclusion of a recuperator leads to an enhancement in electrical efficiency, namely by 16.2% for toluene and 7.1% for cyclopentane. However, it is important to note that the recuperator has a negative impact on thermal recovery. Indeed, the scores in the TH scenario exhibit a decline from 0.2394 to 0.2279, and from 0.2478 to 0.2428, for the two respective working fluids. On the other hand, ORC exhibit somewhat lower energy efficiencies compared to ST and sCO₂ cycles. However, ORCs demonstrate minimal sensitivity to variations in T_{DHN} and RMSW composition. This characteristic highlights the remarkable adaptability and flexibility of ORC under diverse operational circumstances. In terms of power production, the toluene working fluid exhibits a minor advantage over cyclopentane. However, when considering thermal-only recovery, the latter should be prioritised.

Low-temperature DHN brings consistent benefits to the sCO₂ power cycle, especially in the case of CS2 composition. The number of supplied buildings may reach up to 1,072. Some considerations can be formulated by comparing these results with those in literature. In that paper, Moradi et al. [178]

stated a combined efficiency of a recuperative sCO₂ system of about 50% at full load operation, which is very similar to that obtained here. In contrast, Fan et al. [221], achieved a thermal efficiency of approximately 42% for a basic sCO₂ facility with a significantly higher thermal power input of approximately 27 MW under full load conditions. The outcomes achieved by the ORC systems in this study exhibit a resemblance to the findings reported by Vescovo and Spagnoli Specifically, the ORC systems demonstrate an overall efficiency ranging from 77% to 79% when operating with low-temperature cooling media. On the other hand, a notable disparity exists in the electrical efficiencies shown by Lai et al. [212] for an ORC system using toluene as a working fluid, which accounted for 20.4% for a simple configuration and 28.9% in the case of the recuperative cycle. In the current study, an electrical efficiency of 19.1% is achieved for the basic setup, while a higher efficiency of 21.2% is attained when utilising the recuperator. There are two primary factors contributing to the observed disparity in outcomes. Firstly, the present study utilises a *TIT* of 310 °C, which is higher than the one assumed by Lai et al in their study (350 °C) considering superheating. Secondly, variations in off-design turbine efficiency further contribute to the divergence in results. Another aspect that warrants attention is the off-design behaviour of power systems. In this analysis, focus was given to minor variations in condensing pressure, with particular emphasis on ORC and ST. The off-design behaviour resulting from the constant change of the mass flow rate during partialization was not taken into consideration, unlike other research documented in the literature [78], [222], [223]. This aspect will be the subject of future work dealing with the optimisation analysis of the integrated system for a given power plant and cycle configuration.

4.4 Conclusions

This Chapter examines several power cycles for harnessing the energy potential of RMSW gasification in composting facilities. The objective is to explore their suitability for supplying cooling, heating, and power in district-level applications. The heterogeneity of the RMSW composition and the different generation of the district heating network (i.e. different temperature levels) results to almost 70 possible scenarios. Therefore, a simplified methodology is proposed to rank the different configurations according to users' needs, RMSW composition, and DHCN temperature level. From the conducted analysis, the following main conclusions can be drawn:

- The ST power plant exhibits superior power generation capabilities compared to other power plants. However, its electrical efficiency is negatively impacted by elevated temperatures of the cooling medium, which can be attributed to outdated district networks or increased cooling

requirements during the summer season. However, when the emphasis is placed on power generation. Nevertheless, when power production is prioritised ST represents the best option;

- the recuperator increases the electrical efficiency of the sCO₂ and ORC power plants. However, it brings to a significant decrease of the related thermal efficiency in particular for the sCO₂;
- when thermal demand is prioritised, the best configuration is represented by the sCO₂ power plant without recuperator;
- ORC systems are not very sensitive with varying operating conditions and their overall efficiency is in the range of 77-78% for all the cases;
- more than 1,000 buildings can be connected by the DHCN for the considered scenarios;
- From an operational perspective, the utilisation of toluene as a working fluid result in condensing pressures that are below atmospheric pressure, while the opposite is noted for cyclopentane. This choice also offers the advantage of decreased complications when compared to other steam turbine setups;

In summary, the gasification of RMSW in combination with appropriate power cycles can satisfy the cooling, heating and power of a large number of residential users thus reducing the environmental burden of composting facilities and promoting the circular economy paradigm. This approach offers the advantage of mitigating the environmental impact associated with traditional composting facilities, while also fostering the principles of a circular economy. Taking into account the possible variations in energy usage as well as the features of the solid waste produced by residential users, it can be concluded that ORC systems are more suitable for this purpose.

Nomenclature

a	weight parameter [-]
A	Area [m ²]
A _i	Correlation parameter for ORC axial turbine efficiency [-]
c ₁	polynomial coefficient [kJ kg ⁻¹ K ⁻¹]
c ₂	polynomial coefficient [kJ kg ⁻¹ K ⁻²].
c ₃	polynomial coefficient [kJ kg ⁻¹ K ⁻³].
C _B	Yearly electricity consumption for a residential building [kWh year ⁻¹]
CF	Contemporaneity factor [-]
CGE	Cold Gas Efficiency
C _p	Specific heat [kJ kg ⁻¹ K ⁻¹]
D	Number of days for heating during winter [days]

d_i	occurrence of the EEC class [%]
ΔT_{DHN}	Temperature difference of the water in the DHN [°C]
EPI	Energy Performance Index [kWh m ⁻² year ⁻¹]
ER	Equivalence Ratio [-]
F_i	Correlation parameter for ORC axial turbine efficiency [-]
GWP	Global Warming Potential [kg CO ₂ eq.]
h	Cooling hours in summer [hours day ⁻¹]
H	Heating hours in winter [hours day ⁻¹]
h_B	Height of a building [m]
HDD	Heating Degree Days [days]
HHV	High Heating Value [MJ kg ⁻¹]
K_D	Dispersion Coefficient of the building [W m ⁻³ K ⁻¹]
K_V	Ventilation Coefficient of the building [W m ⁻³ K ⁻¹]
L	Energy loss of the DHN
LHV	Lower Heating Value [MJ kg ⁻¹]
\dot{m}	Mass flow rate [kg s ⁻¹]
\overline{M}_{ij}	Thermal power matrix [kW]
N_B	Number of buildings [-]
NTU	Number of Transfer Units [-]
OP	Operating days of the system [days]
ODP	Ozone Layer Depletion [kg CFC-11 eq.]
p	Pressure [bar]
\dot{Q}	Thermal Power [kW]
SF	Size factor of a building [-]
SH	Superheating degree [°C]
SP	Size Parameter [-]
T	Temperature [°C]
T_{pinch}	Temperature difference at the Pinch Point [°C]
T_{DHN}	Temperature of the hot water in the DHN [°C]
T_e	Minimum Ambient Temperature [°C]
T_i	Indoor Design Temperature [°C]
$T_{\text{REC, HF}}$	Temperature of the hot fluid after the recuperator [°C]
\overline{w}	vector of weights [-]

TIT	Turbine Inlet Temperature [$^{\circ}\text{C}$]
V_g	Gross Volume of a building [m^3]
V_g	Net Volume of a building [m^3]
VQ	Vapor Quality [-]
V_r	Volume Ratio [-]
\dot{W}	Power [kW]
X_s	Safety Factor [-]
Z	Electricity/heat ratio [-]

Acronyms

CHP	Combined heat and power
COP	Coefficient of performance
CYC	Cyclopentane
DHN	District Heating Network
DHCN	District Heating and Cooling Network
EEC	Energy Efficiency Class
ELY	Electricity scenario Only
HX	Heat Exchanger
ICE	Internal Combustion Engine
IS	Isentropic Condition
MBT	Mechanical-Biological Treatment
MSW	Municipal Solid Waste
NOP	Normal Operating scenario
OFMSW	Organic Fraction of MSW
ORC	Organic Rankine Cycle
R	Recuperator
RDF	Refuse-Derived Fuels
REC	Recuperator
RMSW	Residual Municipal Solid Waste
sCO ₂	Supercritical CO ₂ power cycle
ST	Steam Turbine power cycle
TH	Thermal scenario Only
TOL	Toluene
W2E	Waste-to-Energy

Subscripts

B	Building
comp	composition
compr	compressor
cond	condenser
crit	critical
D	Design
DH	District Heating
el	electrical
fg	flue gas
he	heating
HF	Hot Fluid
in	inlet
lim	limit
OD	Off-Design
oil	diathermic oil
rec	recuperator
S	Summer
t	turbine
th	thermal
tot	total
W	Winter

CHAPTER 5

INTEGRATION OF BIOMASS PYROLYSIS

5.1 Introduction

In Chapter 4, the use of district heating and cooling networks (DHCN) for energy distribution was discussed. However, the assumptions and conclusions obtained were referred to an operation near the design conditions. The provision of thermal energy must follow the demand of the residential-industrial sectors on an hourly schedule and may differ from the designed value. In order to avoid the partialization of thermal waste treatments, which reflect also in a reduction of the amount of the waste to be valorised, the heat can be supplied in a biofuel co-production line as an alternative to the DHCN. In this way, the treatment process may be stabilized through the year. The fast biomass pyrolysis can be integrated into existing boilers when liquid biofuels are of interest. The system described after is different from the fluidized bed configuration adopted in Chapters 3 and 4, being a circulating fluidized bed boiler (CFB) that can operate in gasification and incineration mode. CFB can be retrofitted with biomass thanks to a special component present in the main structure of the reactor, which is not present in the simpler fluidized bed configuration. The heat provided for pyrolysis is directly generated in the system, in particular, carried by the flow of the inert solids moving in the boiler. This is the operating way of the pilot plant described in the pilot plant of section 5.2. However, the power plant configuration of Chapter 4 can be integrated with pyrolysis if the steam generated in the heat-recovered steam generator (HRSG) is directed to the pyrolysis reactor instead of the steam turbine. Supercritical CO₂ Brayton cycles may be used as well since the temperatures involved are higher than in organic Rankine cycles, but additional piping is required to deliver the heat from the power cycle to the pyrolysis reactor. Therefore, the steam power plant is the best choice for fast pyrolysis integration.

The scope of this chapter is to investigate the process configuration focusing on the composition of the pyrolysis products and sketch a simple model that can be used when variations of the process conditions are expected. The satisfaction of the DHCN demand leads to a problem of load following which is difficult to fully characterise.

5.2 Pilot Plant Configuration

The pilot plant emulates the working principles of a CFB boiler. In those boilers, a bed of inert material (usually sand or limestone) is used as the base for combustion. Air or other fluidizing agent is blown from below, creating a turbulent and circulating motion within the bed. Solid fuels are fed into the combustion chamber from the side of the boiler and the particles mix with the circulating bed material, promoting an efficient combustion. Combustion of the fuel occurs within the fluidized bed, where fuel particles are suspended in the turbulent airflow and come into contact with oxygen. The continuous recirculation of bed material helps maintain a stable and uniform temperature within the combustion chamber, offering high versatility and adaptability to a wide range of solid fuels, including low-quality coals, biomass, and various waste materials and switch between (co)gasification having temperatures around 800-1000 °C [224] and (co)incineration, with temperatures up to 1400 °C [225]. The typical design of a CFB reactor comprehends four main sections (Fig. 5-1). On the bottom, there is the fluidized bed zone, where air, sand, and fuel particles are mixed, and combustion reactions occur. This is considered the lower zone of the riser, a tall pipe that allows a long residence time for the gas and the fine particles entrained within. The hot gas from the gasifier passes through a cyclone, which separates most of the solid particles. The syngas from gasification or flue gases from incineration are conveyed out from the cyclone and then sent to the heat exchangers of the downstream power generator unit, in a similar way as described in Chapter 4. Then, the solid particles are recovered in a return loop and re-directed to the fluidized bed zone. In this loop, it is installed a solid recovery device, named J-Valve or G-Valve [45], [226]. As depicted in Fig. 5-1, the retrofitting with biomass takes place in this component when the production of liquid biofuels is to be prioritized. For the mechanisms described in the introduction, the heat released from RDF incineration is partially used here for the fast pyrolysis of the biomass. The gas is sent to a quench line to condense the tars and then to hydrotreatment processes for bio-oil stabilization. The configuration described in Fig. 5-1 summarizes the real configuration of one of the boilers of Mälarenergi [227], [228], which can co-incinerate plastic wastes and biomass residues. Fig. 5-2 and Fig. 5-3 depict the pilot plant scaled version of the CFB boiler under construction.

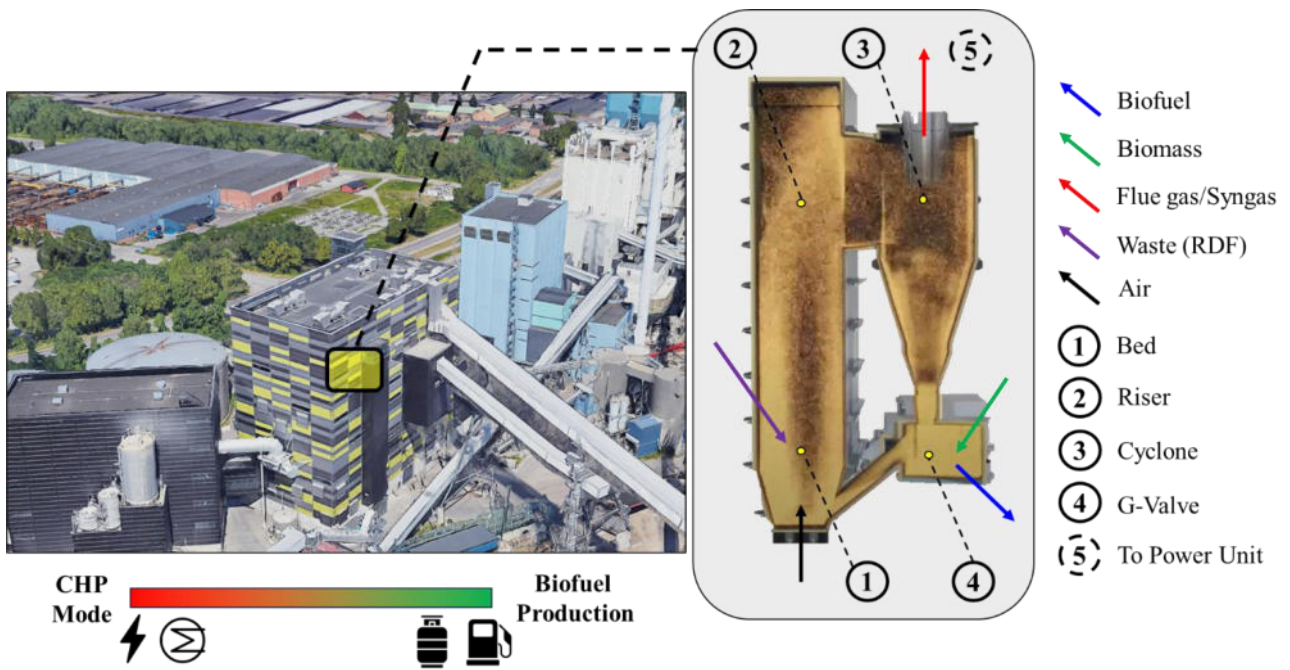


Fig. 5-1. Circulating fluidized bed boiler (CFB). Image taken from Google Earth of one the Milarenergi boilers [227], [228].

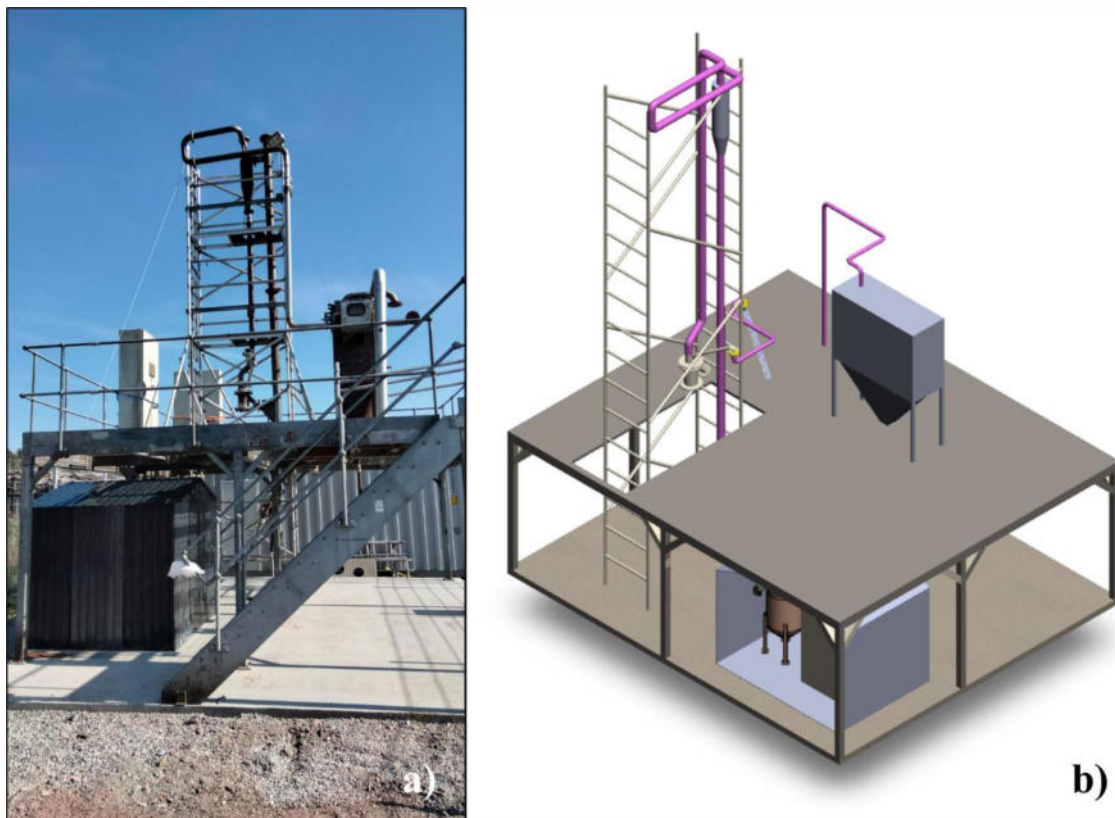


Fig. 5-2. Picture of the Pilot Plant (a) and its axonometric view (b).

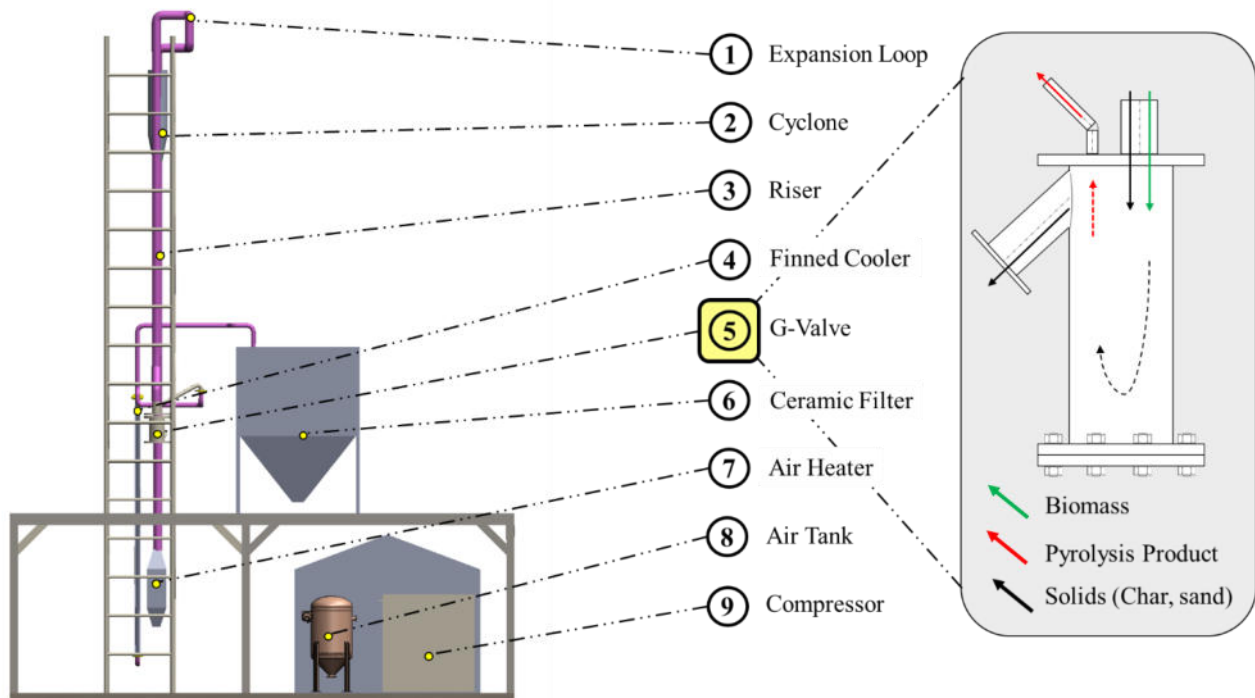


Fig. 5-3. Side view of the Pilot Plant and list of the various components.

As shown in Fig. 5-3, the residual char and sand particles separated in the cyclone return to the G-valve, where biomass retrofitting takes place. The pyrolysis product exits on the top of the pyrolyser while the solids return to the riser. The gases are condensed with a finned heat exchanger, and the liquid fraction is then collected and analysed with a thermal conductivity detector (TCD) of a Gas-Chromatograph (GC) nearby. Finally, the uncondensable pyrolysis gas is sent to a ceramic filter for particle removal and then to a safety flare. The air compressor, tank, and heater group are required for feeding air at 600 °C with slight overpressure (1 barg). The riser, i.e. the reactor itself, can be run in combustion or gasification mode. In this last case, the syngas is ulteriorly analysed in the GC.

The role of the plant is to investigate experimentally if the pyrolysis integration is possible and to assess the yields and composition of the resulting products. Moreover, the implementation of additional renewable energy sources is expected in the future, especially related to sustainable hydrogen production that could be used for the bio-crude upgrading into biofuel in situ.

5.3 Problem Statement

The scope of this configuration is to decide whether or not to allocate thermal power to other heat sinks when DH demand is changing dynamically. Therefore, instantaneous variations of the biomass flow rates are expected. The prediction of the system response under these fluctuations is crucial for the best outcome of the integration. Decision-based algorithms could support and provide information

about the most optimal way to run the process and derive a simplified “digital twin” of the plant, but preliminary dynamic models of the most crucial components should initially support the digitalisation. A steady-state thermodynamic model of the CFB and pyrolizer can be done relatively easily with commercial software [164], [229], but a dynamic model requires more flexibility and adaptability.

Having clear the importance of the product, initial work is presented in this Chapter about a 0D Matlab model of the pyrolizer with tuning parameters used for validation. A similar approach used for the fluidized bed gasifier model of Chapter 3 is adopted as a consequence of the size of the equipment used for experiments reported in the literature. The packed geometries of the reactors allow the formulation of simplified assumptions in the domain of calculus. The model presented after does not consider any discretisation of the volume, which is instead done in 1D-2D models. The latter can better describe the dynamics of full-scaled pyrolysis components, like the one in Fig. 5-1.

Next, in the section 5.5.4, the model of the pyrolyser has been readapted for characterise a full-scaled version of the pyrolysis reactor to be integrated into the layout of gasification system described in the Fig. 4-2. The reactor is designed to extract a certain amount of the thermal power from the flue gas before their passage in the evaporator of the downstream power unit. The ORC configuration is maintained since the analyses reported in Chapter 4 highlighted major flexibility compared to the other systems. Toluene is chosen as the working fluid, and the same boundary conditions of the CS1 scenario involving a temperature level of 75 °C for the DHN are assumed.

5.4 Methodology

5.4.1 Pyrolysis kinetics

Wooden biomass is generally composed of three pseudocomponents: cellulose, hemicellulose, and lignin polymers, in addition to moisture and ash. The complex chemistry of fast pyrolysis encompasses the devolatilization of these molecules into light and heavy molecules, and subsequently, the tar-cracking reactions to form additional light compounds [89], [230]. Two main stages can be defined: the first biomass decomposition to solid biochar, gas compounds, and tars, and the second decomposition of some tars to further gas and char. These steps of decomposition can be described by several chemical reactions occurring in parallel according to their rates and the initial concentrations of the reagents. The most detailed and completed descriptions of the pyrolysis mechanism may count up to 29 reactions [47] in the form [231]:

$$\frac{d\Gamma}{dt} = K(T)f(\Gamma) \quad (5.1)$$

where Γ [-] is the conversion rate of a chemical element, t [s] the time, $K(T)$ [s^{-1}] the reaction constant depending on the temperature of the surroundings and $f(\Gamma)$ [-] the reaction order function. For instances, a reaction rate of the k order has the following formulation:

$$f(\Gamma) = (1 - \Gamma)^k \quad (5.2)$$

with Γ defined as:

$$\Gamma(t) = \frac{m_i - m(t)}{m_i - m_f} \quad (5.3)$$

where m [kg] is the initial mass sample, and the subscripts i and f mean initial and final. The time evolution of equation 5.1, can be related to the heating rate δ [$^{\circ}C s^{-1}$] as:

$$\delta = \frac{dT}{dt} \quad (5.4)$$

If the Arrhenius equation is recalled for the constant $K(T)$, then the following equation is obtained:

$$\frac{d\Gamma}{dT} = \frac{A}{\delta} e^{-\frac{E}{RT}} f(\Gamma) \quad (5.5)$$

where E is the activation energy [$J mol^{-1}$], R the universal gas constant ($8.314 J mol^{-1}$), and A the pre-exponential factor [$1 s^{-1}$]. Equation 5.5 is useful for estimating the characterizing parameters of the reactions by coupling thermogravimetric analyses [90], [232]. However, the evolution of the single component in terms of formation and consumption, as well as evolutions of the gas phase in the volume should be derived with other approaches. The most complex, yet accurate approach is using the computational fluid-dynamic (CFD) methodology [233], [234] so that the mass, momentum, and energy equations are solved in a discretized grid for each element involved in the pyrolysis reactions. However, a transient simulation may require up to several months to run as reported by Mellin et al. [233]. For this reason, a trade-off between computational time and fidelity should be done. A simplified way to proceed is the definition of mass and energy inventories in a generic control volume [235]:

$$\frac{dX}{dt} = X_{in} - X_{out} + X_{gen} - X_{con} \quad (5.6)$$

where X is the inventory of the quantity that is considered (inside the system's boundary), $\frac{dX}{dt}$ is the change in the inventory per unit of time, $X_{in} - X_{out}$ is net supplied through the system's boundary (with mass flows or through the wall) and $X_{gen} - X_{con}$ is net supplied internally in the system. For conserved quantities (mass and energy), $X_{gen} = X_{loss} = 0$. However, the molar quantity is not conserved, so an additional term is defined for accounting the generation and consumption in chemical reactions. The mass inventory formulation is then:

$$\frac{dm}{dt} = \dot{m}_{in} - \dot{m}_{out} \quad (5.7)$$

The dynamic component balance is instead:

$$\frac{dn_l}{dt} = F_{in,l} - F_{out,l} + G_l \quad (5.8)$$

where n_l [mol] is the inventory (amount) of component l inside the system's boundary, $F_{in,l}$ [mol s⁻¹] is the molar flow rates of l in the streams at the inlet and $F_{out,l}$ [mol s⁻¹] at the outlet of the control volume. G_l [mol s⁻¹] is the net quantity generated in the chemical reactions. This can be calculated as:

$$G_i = \int_0^V \sum_{j=1}^n \nu_{lj} r_j dV \quad (5.9)$$

where V [m³] is the volume of the system, ν_{lj} [-] the stoichiometric coefficient of the component l in the reaction j , and r_j [mol m⁻³ s⁻¹] the reaction rate of the j -th reaction, written in the simplest form as:

$$r_j = K(T)_j c(t)_l \quad (5.10)$$

where $c(t)_l$ [mol m⁻³] is the molar concentration of the component l if l is the unique reagent of the reaction j . The reaction rate is a function of concentration and composition, and generally varies with the position in the reactor. For a continuous stirred tank reactor (CSTR) of volume V , where the reaction $A \rightarrow B$ occurs with the reaction rate r_V , and with a simple plug flow regime and perfect mixing, the dynamic component balance for A and B becomes:

$$V \frac{dc_A}{dt} = c_{in,A} q_{in} - c_A q_{out} - r_V V \quad (5.11)$$

$$V \frac{dc_B}{dt} = -c_B q_{out} + r_V V \quad (5.12)$$

given c_A [mol m⁻³] the molar concentration of the component A and q [m³ s⁻¹] the volumetric flow rate. Not only is the mass balance important, but also energy balance must also be accounted to quantify the variation of the temperature inside the reactor. The final temperature form of the energy equation is:

$$mCp_m \frac{dT}{dt} = F_{in} \int_T^{T_{in}} Cp_{m,in}(T) dT + \sum_j [-\Delta H_j(T)] r_j V + \dot{Q} \quad (5.13)$$

Equation 5.12 is the total moles in the system, Cp_m [J kg⁻¹ K⁻¹] the mass heat capacity of the mixture inside the reactor, ΔH_j [J K⁻¹ mol⁻¹] the enthalpy of the reaction j , and \dot{Q} [W] the additional heat transfer mechanisms between the control volume and the surroundings.

By using equations 5.10 and 5.12 it is possible to derive the dynamic behavior of the biomass pyrolysis. The reactions assumed for the model described in the next section are the same used by Mellin et al. [233], which are 16 reactions (R1-R16) for devolatilization and 10 reactions (R17-R26) for tar cracking, involving a total of 33 components. The reactions are listed in Table 5-1. An explanation of the abbreviations can be found at the end of the Chapter.

Table 5-1. List of the reactions used in the pyrolysis model [47], [233].

ID	Reaction	Type
R1	Cell → CellA	Endothermic
R2	Cell → 5H ₂ O + 6Char	Exothermic
R3	CellA → LVG	Endothermic
R4	CellA → 0.95HAA + 0.25Glyoxal + 0.2Acetaldehyd + 0.25HMFU + 0.2Acetone + 0.16CO ₂ + 0.23CO + 0.9H ₂ O + 0.1CH ₄ + 0.61 Char	Endothermic
R5	HCell → 0.4HCell ₁ + 0.6HCell ₂	Endothermic
R6	HCell ₁ → 0.75H ₂ + 0.8CO ₂ + 1.4CO + 0.5Formaldehyde + 0.25Methanol + 0.125Ethanol + 0.125H ₂ O + 0.625CH ₄ + 0.25C ₂ H ₄ + 0.675Char	Endothermic
R7	HCell ₁ → Xylan	Endothermic
R8	HCell ₂ → CO ₂ + 0.5CH ₄ + 0.25C ₂ H ₄ + 0.8CO + 0.8H ₂ + 0.7Formaldehyde + 0.25Methanol + 0.125Ethanol + 0.125H ₂ O + Char	Endothermic
R9	LignC → 0.35LignCC + 0.1p-Coumaryl + 0.08Phenol + 0.41C ₂ H ₄ + H ₂ O + 0.495CH ₄ + 1.32CO + H ₂ + 5.735Char	Endothermic
R10	LignH → LignOH + Acetone	Endothermic
R11	LignO → LignOH + CO ₂	Endothermic
R12	LignCC → 0.3p-Coumaryl + 0.2Phenol + 0.35Acrylic-acid + 0.7H ₂ O + 0.65CH ₄ + 0.6C ₂ H ₄ + 1.8CO + H ₂ + 6.4Char	Endothermic
R13	LignOH → Lign + H ₂ O + Methanol + 0.45CH ₄ + 0.2C ₂ H ₄ + 2CO + 0.7H ₂ + 4.15Char	Endothermic
R14	Lign → Lumped-phenol	Endothermic
R15	Lign → H ₂ O + 2CO + 0.2Formaldehyde + 0.4Methanol + 0.2Acetaldehyd + 0.2Acetone + 0.6CH ₄ + 0.65C ₂ H ₄ + 0.5H ₂ + 5.5Char	Exothermic

R16	$\text{H}_2\text{O}(\text{l}) \rightarrow \text{H}_2\text{O}(\text{g})$	Endothermic
R17	$\text{HMFU} \rightarrow 3\text{CO} + 1.5\text{C}_2\text{H}_4$	Endothermic
R18	$\text{Acetone} \rightarrow 0.5\text{CO}_2 + 0.5\text{H}_2 + 1.25\text{C}_2\text{H}_4$	Endothermic
R19	$\text{pCoumaryl} \rightarrow \text{CO}_2 + 2.5\text{C}_2\text{H}_4 + 3\text{Char}$	Exothermic
R20	$\text{Phenol} \rightarrow 0.5\text{CO}_2 + 1.5\text{C}_2\text{H}_4 + 2.5\text{Char}$	Exothermic
R21	$\text{Xylan} \rightarrow 2\text{CO}_2 + \text{H}_2 + 1.5\text{C}_2\text{H}_4$	Exothermic
R22	$\text{LVG} \rightarrow 2.5\text{CO}_2 + 1.5\text{H}_2 + 1.75\text{C}_2\text{H}_4$	Endothermic
R23	$\text{HAA} \rightarrow 2\text{CO} + 2\text{H}_2$	Endothermic
R24	$\text{Glyoxal} \rightarrow 2\text{CO} + \text{H}_2$	Exothermic
R25	$\text{Lumped phenol} \rightarrow 2\text{CO}_2 + 3\text{C}_2\text{H}_4 + 3\text{Char}$	Exothermic
R26	$\text{Acrylic-acid} \rightarrow \text{CO}_2 + \text{C}_2\text{H}_4$	Exothermic

The pre-exponential factor, activation energy, and enthalpy of the various reactions can be seen in the code reported in Appendix III. Other data is taken from the reference [233].

5.4.2 Matlab Model

The sketch of the model is reported in the Fig. 5-4. The main input required to describe the dynamics are wood composition, i.e. cellulose, hemicellulose, and lignin content, the geometry of the reactor, the mass rate \dot{m} [kg s^{-1}] of the feedstock as a function of time, the time step Δt , the kinetic parameters of the 26 reactions, the initial temperature T_0 (500 °C) and pressure P_0 (1.013 bar) of the system, the temperature of the feed T_{feed} (25 °C) and its specific heat Cp_{feed} (1,500 $\text{J kg}^{-1} \text{K}^{-1}$), and the additional heat transfers that contribute to the energy balance. The control volume of the model is initially filled with nitrogen as an inert gas, having a constant mass flow rate of 0.45 g s^{-1} . This initialization must be done to have an initial volumetric flow rate q . The Cp of the pyrolysis gas, used in equation 5.12, is calculated with the correlation of [233]:

$$C_p = 979.043 + 0.418 \times T - 0.001 \times T^2 + (1.674\text{e} - 6) \times T^3 - (7.256\text{e} - 10) \times T^4 \quad (5.14)$$

A better description of the C_p would be given if external fluid packages like Refprop [236], [237] and Coolprop, but the computational time for simulating the process would increase significantly.

The term \dot{Q} [W] is defined as following:

$$\dot{Q} = \dot{Q}_{wood} + \dot{Q}_{N_2} + \dot{Q}_{W1} + \dot{Q}_{W2} + \dot{Q}_{wall} + \dot{Q}_{loss} + \dot{Q}_{CHP} \quad (5.15)$$

where \dot{Q}_{wood} [W] is the thermal power required to warm the wood from T_{feed} to the reactor temperature $T(t)$, while \dot{Q}_{N_2} [W] for the nitrogen, \dot{Q}_{W1} [W] and \dot{Q}_{W2} [W] for the sensible heat of the water, \dot{Q}_{wall} [W] and \dot{Q}_{loss} [W] accounts for the thermal power provided by the electrical heaters in

the wall and the eventual heat dispersions, and \dot{Q}_{CHP} [W] is the heat that is taken from the boiler as a direct mixed stream of sand and char. In this work, it is assumed a $\dot{Q}_{CHP} = 0$ since the thermal power is provided by isothermal wall heaters. The formulation of each term, which depends on the geometry of the reactor, its instantaneous temperature, the overall heat exchange coefficients, can be found in the Appendix III under the section “Derivative Code”.

Additionally, the boundary conditions assume a fixed wall temperature equal to T_0 , and no positive pressure gradients at the gas outlet. Moreover, heat dispersions and heat for sensible heating of the feedstock and the water are implemented. Water and nitrogen properties are taken from the Refprop fluid package [236], addressed outside the model.

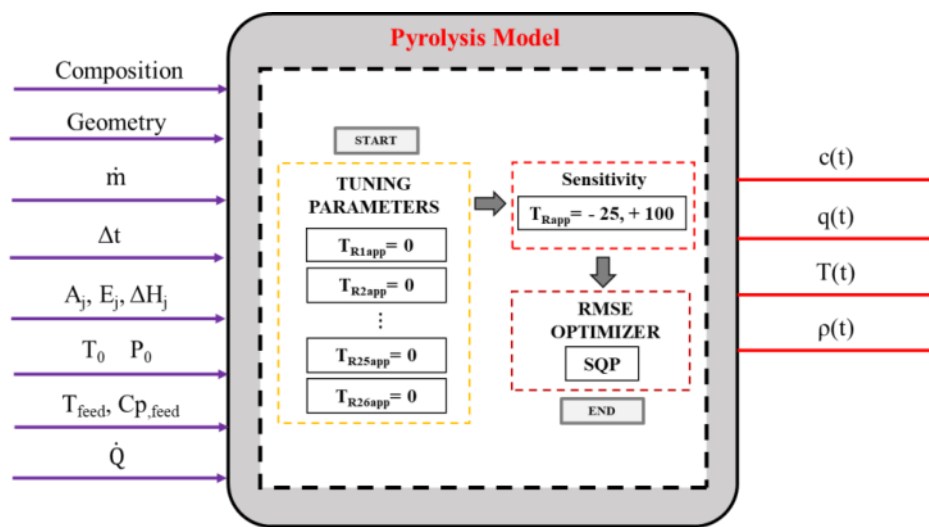


Fig. 5-4. Sketch of the pyrolysis model coded in Matlab.

The final form of the reaction constant can be defined according to equation 5.14:

$$K_j = A_j e^{-\frac{E_j}{R(T-T_{Rapp,j})}} \quad (5.16)$$

The definition of the temperature approach term $T_{Rapp,j}$ [°C] introduces the possibility of using additional tuning parameters in the model that may optimize the validation progress. A preliminary sensitivity analysis is carried out by assuming the values of -100 °C and +25 °C, to detect the governing ones that improve the model. Then, starting from the results of the sensitivity, the Matlab optimization toolbox [238] has been used to reduce the deviation concerning the model of Mellin et al., by using the sequential quadratic programming (SQP) algorithm implemented in the “FMINCON” function for multi-constrained problems. In particular, the root mean squared error (RMSE) of the mass flow rates is defined by equation 5.15 (similar to equation 3.7):

$$RMSE = \sqrt{\frac{1}{n} \sum_{l=1}^n \left(\frac{\Delta \dot{m}_{ref,l}}{\dot{m}_{ref,l}} \right)^2} \quad (5.17)$$

where $\dot{m}_{ref,l}$ [kg s^{-1}] is the mass-rate of the l -th element in the pyrolysis gas, taken from [233] and reported in Table 5-2, $\Delta \dot{m}_{ref,l}$ [kg s^{-1}] is the difference between the simulated results, and n the number of elements in the formula. It is important to note that the compounds acrylic acid and lumped phenol were not used in the 5.15 since the reference mass flow rates are significantly lower, around 1,000 times lower than the one of the other chemical elements. Their inclusion would give a higher relative deviation even if their flow rates are negligible compared to the total in absolute terms (less than 0.02%).

Table 5-2. Mass flow rates obtained in [233] and used in the RMSE formula.

Element	Phase	\dot{m}_{ref} [kg s^{-1}]	Used
CH ₄	Gas	1.1200E-05	Yes
CO	Gas	4.4200E-05	Yes
CO ₂	Gas	4.5300E-05	Yes
H ₂	Gas	2.5700E-06	Yes
H ₂ O	Gas	7.4000E-05	Yes
Formaldehyde	Liquid	1.4600E-05	Yes
Acetaldehyde	Liquid	9.3700E-07	Yes
Methanol	Liquid	7.0700E-06	Yes
Glyoxal	Liquid	1.3900E-06	Yes
Ethylene	Liquid	1.7300E-05	Yes
HAA	Liquid	5.4600E-06	Yes
Ethanol	Liquid	4.5700E-06	Yes
Acrylic-acid	Liquid	1.8700E-09	No
Acetone	Liquid	6.4100E-06	Yes
Xylan	Liquid	4.7500E-05	Yes
LVG	Liquid	1.0300E-04	Yes
Phenol	Liquid	3.2700E-06	Yes
HMFA	Liquid	3.0100E-06	Yes
pCoumaryl	Liquid	6.5200E-06	Yes
Lumped phenol	Liquid	6.4100E-08	No
Char	Solid	6.7600E-05	Yes

Equations from 5.10 to 5.12 form a system of ordinary differential equations (ODE) that can be solved with the ODE packages of Matlab. Seldom, reaction rates have high values which characterise the problem as “stiff” [239], therefore high values for the derivative terms are expected in the system of equations. The “ODE15s” solver has been used for its trade-off between accuracy, velocity and

reliability for stiff problems [240]. The logic of the solver has been conceptualized in a way that the initial conditions $c(t)$, $T(t)$, $q(t)$, $\rho(t)$ and $Cp(t)$ are taken by solving the system at the time $c(t - \Delta t)$, $T(t - \Delta t)$, $q(t - \Delta t)$, $\rho(t - \Delta t)$ and $Cp(t - \Delta t)$. Furtherly, each time step is discretized in 5000 points. In this way, the system can be updated if instant variations of $\dot{m}(t)$ are given as input.

5.5 Result and Discussions

5.5.1 Model Validation

The validation of the model has been carried out by comparing the deviation from the mass rates reported in Table 5-2 at a total time of 1.4 s (nitrogen initialization) + 10.75 s (duration of the transient CFD simulation), and a time step of 0.02025 seconds. Table 5-3 reports the RMSE values referred to the baseline model, after the sensitivity on the temperature approaches and after their optimization.

Table 5-3. Validation of the model with sensitivity and optimization.

Element	\dot{m}_{ref} [kg s ⁻¹]	$\dot{m}_{baseline}$ [kg s ⁻¹]	Error [%]	$\dot{m}_{sensitivity}$ [kg s ⁻¹]	Error [%]	$\dot{m}_{baseline}$ [kg s ⁻¹]	Error [%]
CH ₄	1.1200E-05	1.4937E-05	33%	1.0243E-05	-9%	1.1036E-05	-1%
CO	4.4200E-05	5.6824E-05	29%	3.8523E-05	-13%	4.2334E-05	-4%
CO ₂	4.5300E-05	5.6629E-05	25%	4.1521E-05	-8%	4.3347E-05	-4%
H ₂	2.5700E-06	2.9675E-06	15%	2.2711E-06	-12%	2.3770E-06	-8%
H ₂ O	7.4000E-05	8.8995E-05	20%	8.5064E-05	15%	8.6969E-05	18%
Formaldehyde	1.4600E-05	2.2197E-05	52%	1.5197E-05	4%	1.5662E-05	7%
Acetaldehyde	9.3700E-07	7.2348E-07	-23%	7.0815E-07	-24%	9.7757E-07	4%
Methanol	7.0700E-06	1.1316E-05	60%	7.6010E-06	8%	8.0747E-06	14%
Glyoxal	1.3900E-06	1.0236E-06	-26%	1.0010E-06	-28%	1.4150E-06	2%
Ethylene	1.7300E-05	1.5664E-05	-9%	1.2918E-05	-25%	1.3522E-05	-22%
HAA	5.4600E-06	4.0247E-06	-26%	3.9359E-06	-28%	5.5630E-06	2%
Ethanol	4.5700E-06	6.9672E-06	52%	4.3273E-06	-5%	4.6379E-06	1%
Acrylic-acid	1.8700E-09	7.7296E-09	-	7.5601E-09	-	8.0610E-09	-
Acetone	6.4100E-06	2.3510E-06	-63%	2.2800E-06	-64%	2.6435E-06	-59%
Xylan	4.7500E-05	8.3317E-06	-82%	6.0189E-05	27%	4.6113E-05	-3%
LVG	1.0300E-04	1.1216E-04	9%	1.0916E-04	6%	1.0490E-04	2%
Phenol	3.2700E-06	3.2741E-06	0%	3.1588E-06	-3%	3.2222E-06	-1%
HMFA	3.0100E-06	2.2244E-06	-26%	2.1753E-06	-28%	3.0745E-06	2%
pCoumaryl	6.5200E-06	6.5327E-06	0%	6.3029E-06	-3%	6.4269E-06	-1%
Lumped phenol	6.4100E-08	6.6907E-06	-	6.5033E-06	-	6.4538E-06	-
Char	6.7600E-05	4.9468E-05	-27%	4.4469E-05	-34%	4.6005E-05	-32%
RMSE [%]	-	37.38		23.43		17.25	
Weighted RMSE [%]	-	8.23		4.65		3.79	

The model itself is not very accurate the average RMSE reaches almost 37.38%. Several components significantly deviate from the simulated results reported by [233]. Xylan has the highest deviation (-82%), followed by acetone (-63%), methanol (60%), ethanol and formaldehyde (52%). Noteworthy, phenol, pCoumaryl, LVG, and ethylene have acceptable deviations. In turn, if the weighted RMSE_w is defined as:

$$RMSE_W = \sqrt{\frac{1}{n} \sum_{l=1}^n w_l \left(\frac{\Delta \dot{m}_{ref,l}}{\dot{m}_{ref,l}} \right)^2} \quad (5.18)$$

$$w_l = \frac{m_l}{\sum_{l=1}^n m_l} \quad (5.19)$$

to account for the influence of the abundance of a chemical component with the weight w_k defined in 5.18, then the RMSE reduces to 8%. Due to its high yield, xylan is the liquid component with the highest weighted deviation of 6.9%, followed by char (1%) and formaldehyde (0.8%). The sensitivity analysis significantly improves the accuracy of the model, mostly governed by the single reaction R6 with a temperature approach of +100° C. The RMSE decreases from 37.38% to 23.43% while RMSE_w from 8.23% to 4.65%. The maximum deviation (-64%) is still above a reasonable threshold, and it is associated with acetone, followed again by char (-34%), glyoxal-HAA-HMFA (-28%), and xylan (-27%). Every other element has a difference of less than 25% to the CFD model. In weighted terms, only four elements impact the RMSE_w: char effects for 1.7%, xylan for 0.73%, and Acetone for 0.57%. The final optimization stage allows a further reduction of the RMSW down to 17.25% and for the RMSE_w to 3.79%. While the deviations of the acetone and char are not reduced (respectively -54% and -32%), the others stay under 25%. Ethylene is the highest one among them with -22%. Table 5-4 reports the Tapp of the model, while Fig. 5-5 reports the result of the optimization algorithm.

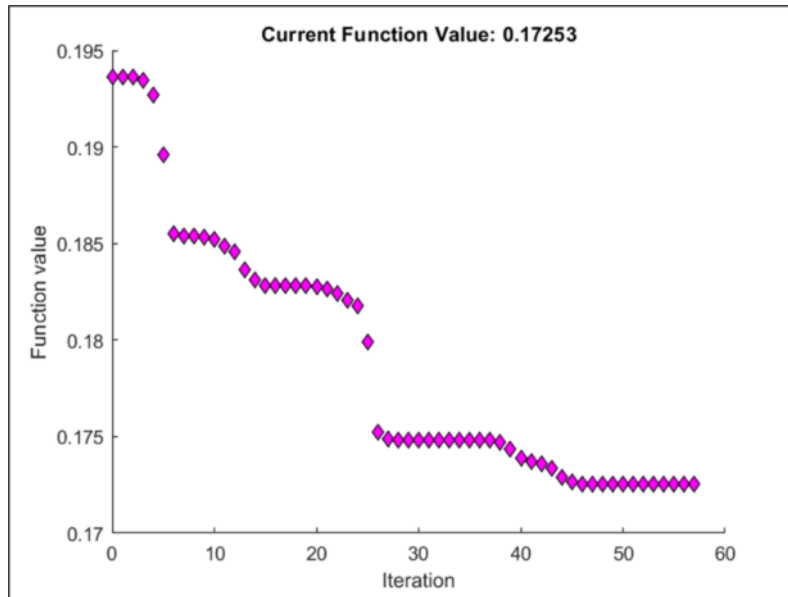


Fig. 5-5. RMSE minimization with SQP algorithm, down to 17.25%.

Table 5-4. Temperature approaches of the chemical reactions used in the model.

ID	Temperature approaches [°C]		
	Baseline	Sensitivity	Optimization
R1	0	0	-0.0867
R2	0	0	-4.2500
R3	0	0	3.2936
R4	0	0	-10.2256
R5	0	0	3.6406
R6	0	+100	78.4844
R7	0	0	7.3742
R8	0	0	4.6855
R9	0	0	-5.3780
R10	0	0	-0.1408
R11	0	0	-0.0603
R12	0	0	-0.1297
R13	0	0	-0.4784
R14	0	0	1.0442
R15	0	0	-3.1148
R16	0	0	-0.2553
R17	0	0	-0.3608
R18	0	0	2.5325
R19	0	0	-0.3368
R20	0	0	-0.02379
R21	0	0	-5.6837
R22	0	0	-0.3460
R23	0	0	-0.1890
R24	0	0	-0.4251
R25	0	0	-0.0025
R26	0	0	-6.4878

The stiff system of ODEs nature can be noted by comparing the RMSE to the temperature approaches provided in Table 5-4. Relatively small variations have the power to change the accuracy of the

model. Reaction R6 has shown to be the most impacting one, i.e. related to the decomposition of the hemicellulose in the other volatile products. The optimization algorithms did not strongly modify the temperature approaches of the reactions R1-R26. Every value is physically coherent with the temperatures in the reactor. The maximum operating temperature predicted in the CFD simulation is 500 °C, i.e. the temperature of the heated wall of the reactor but slightly higher temperatures could be locally expected due to the presence of exothermic reactions that can occur and release additional heat. The time evolution of the molar concentrations inside the pyrolysis reactor can be seen in Fig. 5-6 and Fig. 5-7 at 4.05 s, 8.10 s, and 12.15 s. In particular, Fig. 5-6 shows the trends for the five main solid pseudocomponents in the wood: cellulose, hemicellulose, and three types of lignin (types “H”, “O”, and “C”). The wood enters the reactor at 1.4 s. Then, the solid concentrations vary at different rates according to the initial amount and the rate of the reactions where the components are consumed as reagents. It is supposed that the pseudocomponents do not exit the reactor as particles entrained in the pyrolysis gas, therefore their molar concentration can be reduced with chemical reactions only. Such combinations define the lignin type “H” as the fastest solid compound that is almost completely consumed, in a time frame of around 0.5 s, followed by lignin type “O” that is converted in just 1 s after feedstock entry. A different trend is detected for cellulose, hemicellulose, and lignin “C”. The mole balance equation retrieves a chemical equilibrium for the last two, and a slight concentration increase after 8 s. Cellulose, having the highest initial concentration, overall (42.27% in total weight including ashes and moisture), cannot be consumed as fast as the amount that enters in the pyrolyzer, therefore there is a mole accumulation in the reactor, up to 3.7 mol/m³. Fig. 5-7 reports the concentration of two non-condensable gases, CO₂ and CH₄, two tars, LVG and xylan, and the temperature profile reported at the same time frames of Fig. 5-7. The concentrations of CO₂ and CH₄ slowly increase over time, with more CO₂ than CH₄ (1.18 mol m⁻³ vs. 0.52 mol m⁻³) but do not arrive at a steady state value. The same trend is noted for LVG, but with a less pronounced increasing rate. For xylan, instead, the concentration curve reaches the plateau at the end of the simulation (0.26 mol m⁻³) and then remains constant. Regarding the temperature, the initial negative peak is due to the complete evaporation of the water ($\Delta h = +2,260 \text{ kJ kg}^{-1}$, high endothermic) present as moisture in the wood feedstock. The same peak was detected in the CFD model as stated by the authors and could mislead the comprehension of the pyrolysis process. However, shortly after the temperature assesses to around 400 °C in the whole reactor.

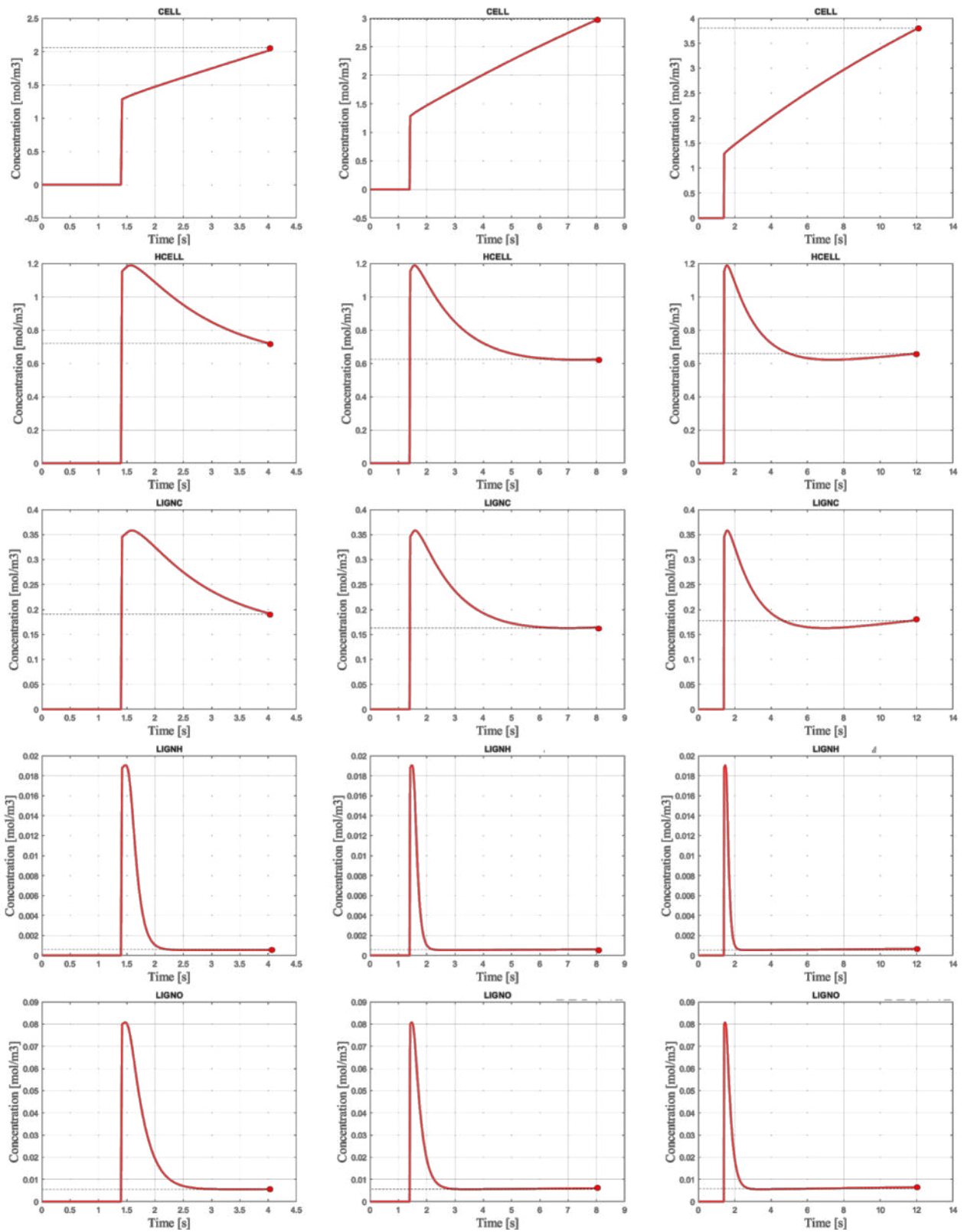


Fig. 5-6. The concentration of the various solid wood constituents at 4.05 s, 8.10 s, and 12.15 s.

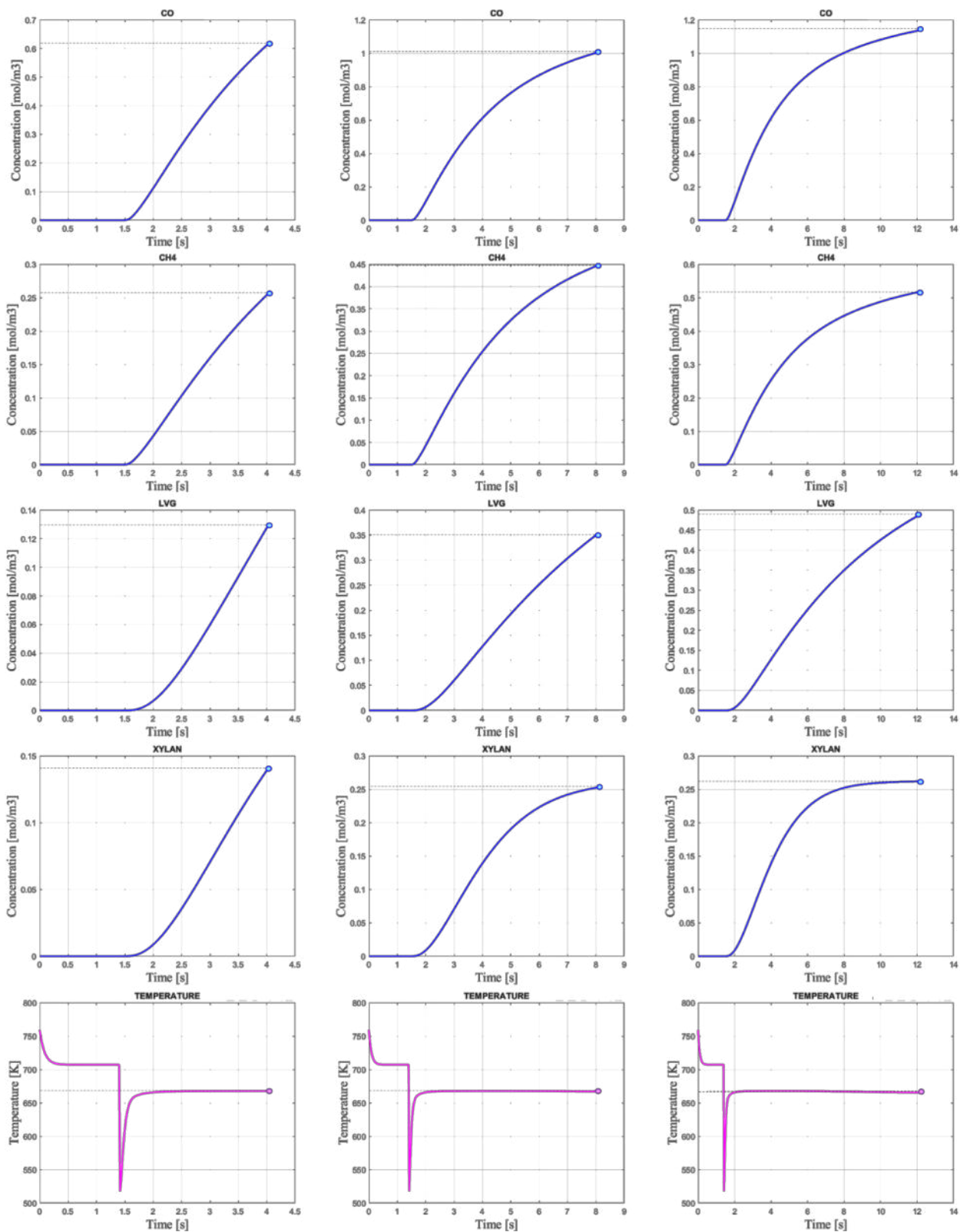


Fig. 5-7. Concentrations of the CO, CH₄, LVG, xylan, and temperature profile at 4.05 s, 8.10 s, and 12.15 s.

5.5.2 Time Extension

In Fig. 5-8 is reported the concentration and temperature profiles by extending the time of simulation up to 100 s, for the cellulose, CO, CH₄, and LVG. The same boundary conditions of 5.5.1 apply here, and a proper time step is defined to limit the number of global iterations to 2,000.

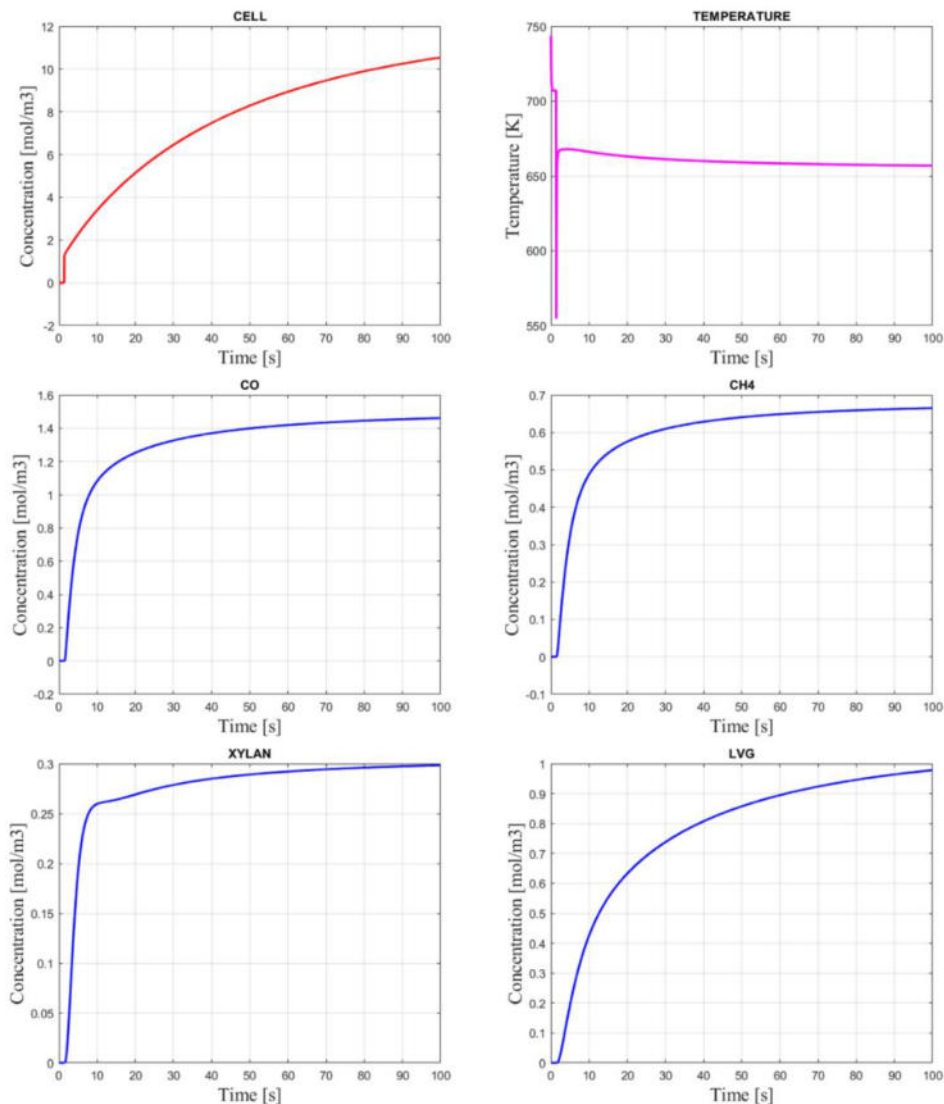


Fig. 5-8. Temperature (magenta) and concentration profile of cellulose (red), CO, CH₄, xylan, and LVG (blue) in the extended simulation.

This simulation expresses that the majority of the elements have an asymptotic trend towards a fixed molar concentration at the outlet of the pyrolizer, by the nature of the ODEs used to set the physical model. CO, CH₄, xylan, and moderately LVG are almost at the chemical equilibrium, while cellulose is still accumulating due to its lower pace of consumption in reaction R1. Table 5-5 reports the concentrations of the various elements every 10 seconds and the relative increment Δ_i .

Table 5-5. Molar concentration and relative increment for the various components during pyrolysis.

Element	MOLAR CONCENTRATION [mol m ⁻³]										INCREMENT [%]								
	10 s	20 s	30 s	40 s	50 s	60 s	70 s	80 s	90 s	100 s	Δ ₁	Δ ₂	Δ ₃	Δ ₄	Δ ₅	Δ ₆	Δ ₇	Δ ₈	Δ ₉
Cell	3.415	5.168	6.493	7.526	8.347	9.006	9.541	9.978	10.336	10.631	51.35%	25.64%	15.91%	10.90%	7.90%	5.94%	4.58%	3.59%	2.85%
CellA	0.137	0.188	0.222	0.246	0.265	0.279	0.290	0.299	0.306	0.312	37.54%	17.91%	10.94%	7.41%	5.33%	3.98%	3.06%	2.39%	1.89%
H ₂ O	3.589	3.714	3.782	3.827	3.859	3.884	3.902	3.917	3.928	3.938	3.47%	1.83%	1.19%	0.85%	0.63%	0.48%	0.37%	0.30%	0.24%
Char	2.783	3.115	3.295	3.411	3.491	3.550	3.595	3.630	3.658	3.680	11.92%	5.79%	3.51%	2.36%	1.69%	1.26%	0.97%	0.76%	0.60%
LVG	0.426	0.632	0.737	0.807	0.857	0.894	0.923	0.946	0.963	0.978	48.28%	16.61%	9.44%	6.19%	4.37%	3.22%	2.45%	1.90%	1.49%
HAA	0.062	0.086	0.096	0.103	0.107	0.110	0.112	0.114	0.115	0.116	39.42%	11.75%	6.38%	4.08%	2.83%	2.05%	1.54%	1.19%	0.92%
Glyoxal	0.016	0.023	0.025	0.027	0.028	0.029	0.029	0.030	0.030	0.031	39.42%	11.74%	6.38%	4.08%	2.83%	2.05%	1.54%	1.19%	0.92%
Acetaldehyde	0.015	0.021	0.024	0.025	0.026	0.027	0.028	0.028	0.029	0.029	42.72%	12.75%	6.93%	4.44%	3.08%	2.23%	1.68%	1.29%	1.00%
HMFCU	0.016	0.023	0.025	0.027	0.028	0.029	0.029	0.030	0.030	0.031	39.42%	11.75%	6.38%	4.08%	2.83%	2.06%	1.54%	1.19%	0.92%
Acetone	0.032	0.038	0.041	0.043	0.044	0.045	0.045	0.046	0.046	0.046	18.59%	6.98%	4.04%	2.67%	1.88%	1.38%	1.05%	0.81%	0.63%
CO ₂	0.676	0.863	0.923	0.955	0.973	0.985	0.993	0.999	1.004	1.007	27.65%	7.05%	3.36%	1.94%	1.24%	0.85%	0.61%	0.45%	0.34%
CO	1.081	1.252	1.326	1.369	1.398	1.418	1.433	1.445	1.454	1.461	15.73%	5.92%	3.29%	2.10%	1.45%	1.06%	0.79%	0.61%	0.48%
CH ₄	0.488	0.575	0.609	0.628	0.640	0.648	0.654	0.659	0.662	0.665	17.82%	5.94%	3.12%	1.91%	1.28%	0.91%	0.67%	0.51%	0.40%
HCELL	0.642	0.741	0.811	0.860	0.897	0.925	0.947	0.964	0.978	0.990	15.45%	9.38%	6.07%	4.25%	3.13%	2.38%	1.85%	1.46%	1.16%
HCELL ₁	0.210	0.232	0.249	0.261	0.269	0.275	0.280	0.284	0.287	0.290	10.26%	7.37%	4.66%	3.21%	2.34%	1.76%	1.36%	1.07%	0.85%
HCELL ₂	1.306	1.800	2.109	2.322	2.476	2.593	2.683	2.754	2.811	2.857	37.84%	17.17%	10.10%	6.66%	4.71%	3.48%	2.65%	2.06%	1.63%
H ₂	0.835	0.989	1.047	1.079	1.099	1.112	1.122	1.129	1.134	1.139	18.45%	5.88%	3.03%	1.85%	1.23%	0.87%	0.64%	0.49%	0.38%
Formaldehyde	0.355	0.463	0.499	0.518	0.529	0.536	0.541	0.545	0.548	0.550	30.25%	7.88%	3.77%	2.17%	1.38%	0.94%	0.67%	0.49%	0.37%
Xylan	0.260	0.269	0.279	0.285	0.289	0.292	0.295	0.296	0.298	0.299	3.67%	3.58%	2.24%	1.47%	1.04%	0.77%	0.58%	0.45%	0.36%
C ₂ H ₄	0.340	0.406	0.430	0.443	0.451	0.457	0.461	0.464	0.466	0.468	19.62%	5.85%	2.99%	1.83%	1.22%	0.87%	0.64%	0.49%	0.38%
Methanol	0.171	0.229	0.255	0.270	0.280	0.288	0.293	0.298	0.301	0.304	34.18%	11.04%	6.04%	3.85%	2.66%	1.92%	1.44%	1.10%	0.85%
Ethanol	0.069	0.088	0.094	0.097	0.099	0.101	0.101	0.102	0.102	0.103	27.17%	7.15%	3.41%	1.95%	1.23%	0.83%	0.59%	0.43%	0.33%
LignC	0.172	0.210	0.239	0.259	0.275	0.288	0.298	0.306	0.312	0.317	22.44%	13.42%	8.71%	6.12%	4.52%	3.44%	2.67%	2.12%	1.69%
LignCC	0.399	0.800	1.213	1.634	2.059	2.488	2.918	3.350	3.783	4.214	100.68%	51.69%	34.68%	26.03%	20.80%	17.30%	14.80%	12.92%	11.40%
pCoumaryl	0.032	0.032	0.033	0.033	0.033	0.033	0.033	0.034	0.034	0.034	-0.51%	1.34%	0.92%	0.66%	0.51%	0.41%	0.35%	0.30%	0.27%
Phenol	0.026	0.026	0.026	0.026	0.026	0.027	0.027	0.027	0.027	0.027	-0.55%	1.31%	0.89%	0.63%	0.48%	0.39%	0.32%	0.28%	0.24%
LignH	0.001	0.001	0.001	0.001	0.001	0.001	0.001	0.001	0.001	0.001	17.53%	10.11%	6.61%	4.67%	3.45%	2.63%	2.05%	1.63%	1.30%
LignOH	0.293	0.472	0.611	0.721	0.808	0.877	0.933	0.979	1.016	1.046	61.30%	29.47%	17.90%	12.06%	8.61%	6.39%	4.86%	3.77%	2.95%
LignO	0.006	0.007	0.008	0.008	0.008	0.008	0.009	0.009	0.009	0.009	12.80%	7.37%	4.81%	3.39%	2.51%	1.91%	1.49%	1.18%	0.94%
Acrylic acid	0.000	0.000	0.000	0.000	0.000	0.000	0.000	0.001	0.001	0.001	108.88%	46.17%	30.26%	22.75%	18.33%	15.41%	13.33%	11.76%	10.49%
Lign	0.015	0.024	0.030	0.036	0.039	0.043	0.045	0.047	0.049	0.050	61.61%	28.01%	16.68%	11.11%	7.87%	5.80%	4.39%	3.39%	2.64%
Lumped phenol	0.019	0.035	0.044	0.051	0.056	0.060	0.063	0.066	0.068	0.069	79.23%	27.81%	15.52%	10.01%	6.95%	5.05%	3.78%	2.89%	2.23%
Moisture	0.000	0.000	0.000	0.000	0.000	0.000	0.000	0.000	0.000	0.000	10.91%	6.27%	4.09%	2.89%	2.13%	1.63%	1.27%	1.00%	0.80%

According to the data reported in the table, at the end of the simulation, most of the components have reached a steady state value. LignCC, acrylic acid, lignOH, and cellulose are the four components having the highest positive increment in the last interval (between 90-100 seconds), highlighted in bold. In turn, the concentration of acrylic acid is very low (0.001) therefore in absolute terms its variation is still negligible.

5.5.3 Mass rate sensitivity

To test the response of the model to variations in the quantity of biomass pyrolyzed, a dummy mass flow rate profile has been defined as follows:

$$\dot{m}(t) = \begin{cases} 0, & 0 \leq x < 1.4 \\ 2, & 1.4 \leq x < 5 \\ 3, & 5 \leq x < 10 \\ 0, & 10 \leq x < 30 \\ 1, & 30 \leq x < 50 \end{cases} \quad (5.20)$$

The simulation, long 50 seconds, is discretized with 2,500 time steps, offering a detailed perspective on the dynamic evolution of the process. A visual representation of the simulation results is available in Fig. 5-9. Despite variations in molar concentrations unique to each compound, there are common features observed in their profiles. Initially, as biomass enters the reactor, concentrations rise until an asymptotical value; however, they rapidly plummet to zero when feedstock material is depleted (notably during the fourth interval in section 5.19). The rate of decrease is fairly consistent among CO, CH₄, and LVG, with xylan exhibiting a slightly higher decrease rate. Following this decline, concentrations surge again in the fifth interval, stabilizing at a value proportionate to the mass flow rate. This trend is noted also for the temperature profile, with a conspicuous drop in reactor temperature during the third interval (reaching approximately 390 °C) when more feedstock is provided. Subsequently, the temperature rises during the fourth interval and decreases again in the last one to 410 °C.

Despite its inherent limitations in accuracy, a 0D modeling approach proves moderate reliability for gaining insights into the dynamic aspects of the pyrolysis process. This model can anticipate the instantaneous yields of both gaseous and liquid compounds. However, the model should be upgraded by including the geometry of the reactor (1D or 2D) since industrial G-valves have voluminous dimensions and different residence times.

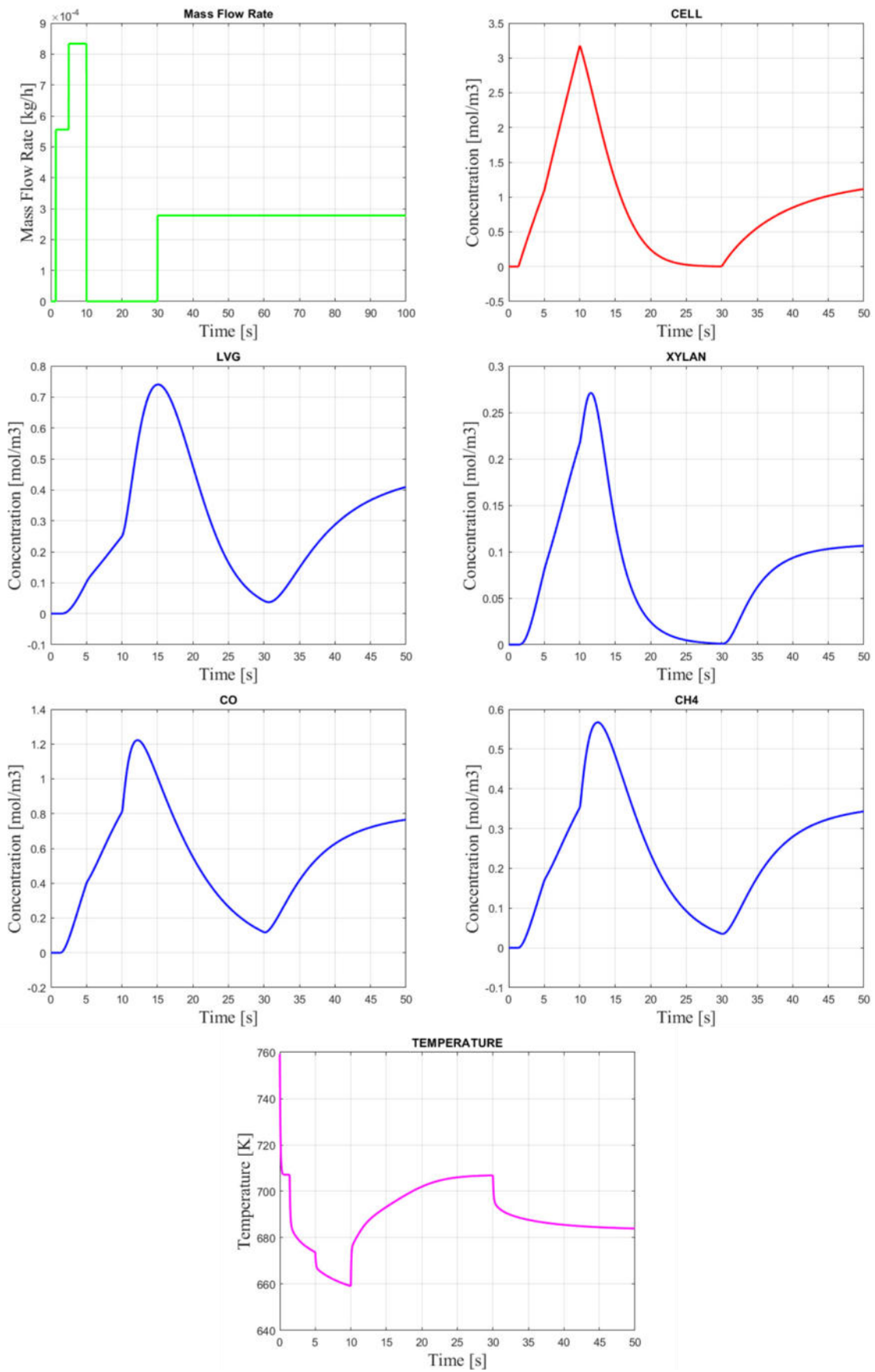


Fig. 5-9. Mass flow rate (green), concentrations (red and blue), and temperature (magenta) profiles were obtained with the model.

5.5.4 Upscaling and integration into the gasification system

In this section, the pyrolyser is upscaled and connected to the main treatment system according to the conceptual and process layout presented in Fig. 5-10 and Fig. 5-11. The external heat supply, previously referred as \dot{Q}_{CHP} , is transferred from the flue gases to the reactor volume by an indirect heat exchange [241].

With reference to the design case of CS1, the total flue gas flow rate is 9.96 kg/s (36,000 kg/h). The splitting into two sub-streams is necessary to limit the internal flue gas velocity to reasonable values (less than 30 m/s) while having still a compact design for the reactor. One stream is directed to the pyrolysis section while the other is to the ORC power system. The upscaled reactor is assumed to have a maximum height of 10 m and a diameter of 0.7 m, hence it is 1,100 bigger compared to its laboratory-scale version in Mellin et al. [233]. A configuration similar to a coaxial and co-current heat exchanger is assumed, in which the flue gases of the combustor section pass through the external annular area, having a diameter of 0.9 m. Internal tube passages are not feasible since higher pressure drops may occur inside the reactor and in the piping circuit. Next, the value of the heat flux is determined in a way that the average temperature of the inner wall is as close as possible to 500 °C. By using a dedicated model of the process in Aspen Plus, it is obtained a value of 1,500 MW (around 25% of the total thermal power available in Table 4-1) for the heat transfer, which results in an average temperature of 475 °C for the heat transfer. The minimum length of the exchange is 8.6 m, lower than the total height of the pyrolysis reactor. The flue gases exit at a temperature close to 150 °C, then mixed with the parallel stream after having passed to the ORC power unit section. The calculated velocity of the flue gases is equal to 24.5 m/s, below the maximum threshold.

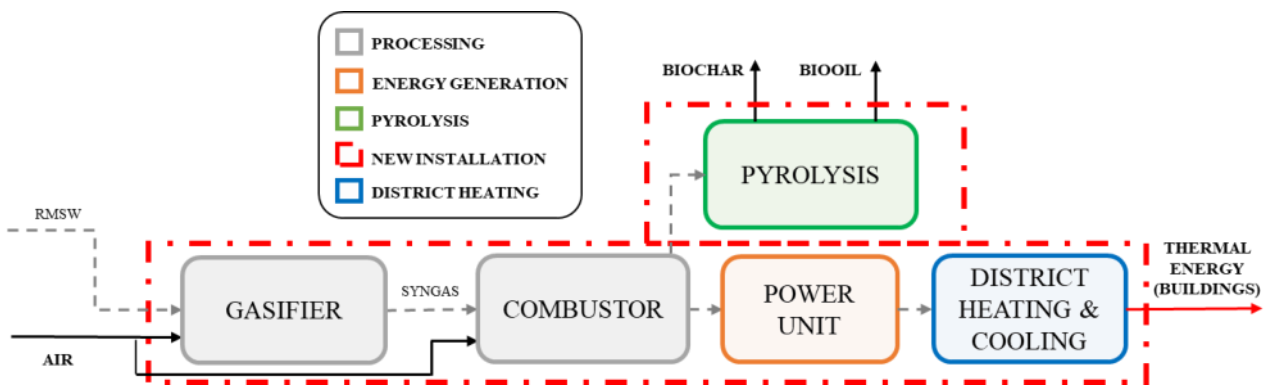


Fig. 5-10. Conceptual layout of the integrated gasification system including the pyrolysis section.

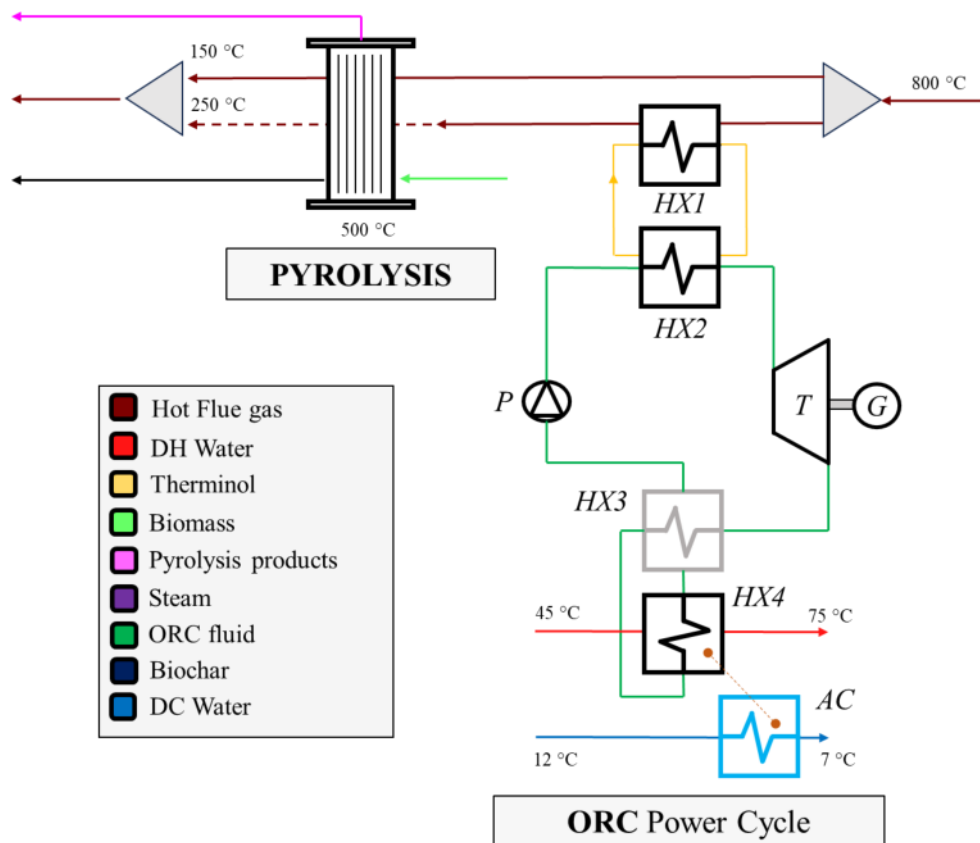


Fig. 5-11. Detailed process layout of the system including the pyrolysis section.

The 0D model presented in the previous sections works properly for small geometries but it must be readapted at larger scales because it assumes perfect mixing among the chemical elements in the whole domain, a reasonable assumption at smaller scales, but not in the other case. The momentum balance equation accounts for the pressure profile along the reactor and the momentum transfers between biomass particles, sand, and gas phase [242], which increases the complexity of the model. However, the cross-sectional gas velocity can be still derived from the gas residence time, fixed to 1.8 s and it is equal to 5.6 m/s. Then, new temperature approaches of Table 5-4 are calculated again, obtaining a RMSE value of 0.2065. The fluidizing gas (nitrogen) mass flow rate is iteratively changed until the pressure of 1 bar inside the reactor is obtained. The boundary condition for wall temperature is 500 °C for 60 s (empty reactor, nitrogen flushing only) and then 475 °C in operation. The mass flow rate of the wooden biomass is varied until the heat flux at 300 s (steady state) is equal to 1.5 MW. The final biomass flow rate is 2,760 kg/h, which is coherent with the increment of 1,100 of the total volume of the reactor.

The boundary conditions for the ORC power cycle are unvaried except for the thermal power introduced in the system, imposed as 75% of the designed one. No further analytical/empirical relationships have been used to describe the efficiencies of the components and heat exchangers

despite the mass flow rate varying from the design condition. The outcome of the joint simulation is given in the Fig. 5-12. The ORC performance is compared with the response at design condition.

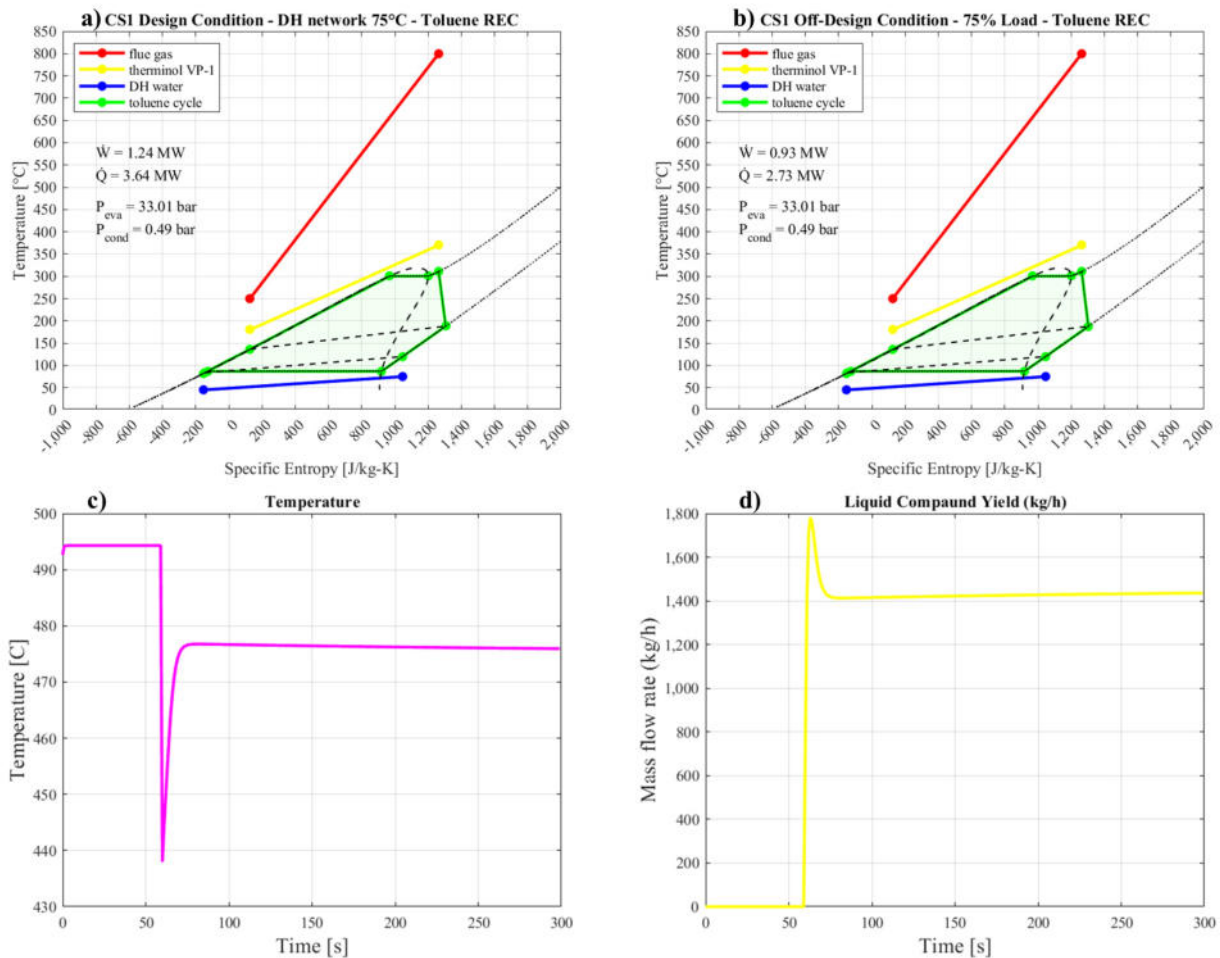


Fig. 5-12. The output of the simulation concerning the ORC cycle in a) design condition and at b) 75% load, and for the biomass pyrolysis. The c) temperature of the reactor and d) overall liquid yield are reported.

As expected, the thermal power delivered to the DHCN is 75% of the design condition (2.73 MW instead of 3.64 MW). The direct consequence is a reduction of the net electrical power, too. However, a gain of 1,463 kg/h of biocrude can be obtained in the process. After having cooled the pyrolysis products, the water can be removed with simple procedures, and a total biocrude amount of 1,054 kg/h is obtained. The final amount of solid biochar is 277 kg/h, which can be sold in the market or used for co-gasification, as a possible road to increase the already low conversion efficiency of the gasifier, which is around 0.5. It is worth mentioning that the specific heat required to convert the biomass is 2.169 MJ/kg (referred to as dry biomass). This value is comparable to the one reported in the study of Jerzak et al. [243] for a pyrolysed biomass with high cellulose content (40%), which is 2.02 MJ/kg.

Further studies should be focused on the economic feasibility of this integrated system. Moreover, only 25% of the maximum load can be reverted to the pyrolysis with the given geometry. Additional reactors, bigger dimensions, or other heat-consuming commodities should be included to extend the range of partialization.

5.6 Conclusions

In this Chapter, the dynamic 0D model of a ligneous biomass feedstock is presented and discussed. Pyrolysis can be integrated into circulating fluidized bed combustors or gasifiers and solve the problem related to partialization and off-design penalizing performances of waste treatment systems. When the district heating demand is low, the thermal power provided by this type of reactor can be used in crude production. A peculiar pilot plant system is currently under construction to investigate with experimental campaigns the feasibility of this integration. Before this, a tool for studying analytically the dynamics of the pyrolysis, which will typically occur during the operational lifespan of such systems, has been developed by including a detailed and comprehensive biomass kinetic model. The model does not include the geometry of the reactor but has however an overall good estimation of the pyrolysis products. The optimized overall root mean squared error is 17.25% compared to computational fluid dynamics models. Moreover, the dynamic response inducted by simple biomass flow rate variations is well described. However, modifications were required for its upscaling and integration with the gasification system described in Chapter 4. With the upscaled geometry, is it possible to convert 2,760 kg/h of wooden biomass into 1,054 kg/h of biocrude and 277 kg/h of biochar by using 1.5 MW of thermal power from the flue gases, i.e. 25% of the design condition. The response of the ORC system, fed with a parallel feed line, is reduced accordingly.

Nomenclature

A	Pre-exponential factor [s^{-1}]
c	Molar concentration [$mol\ m^{-3}$]
C _p	Mass heat capacity [$J\ kg^{-1}\ K^{-1}$]
ΔH	Enthalpy of reaction [$J\ mol^{-1}$]
E	Activation energy [$J\ mol^{-1}$]
F	Mol flow rate [$mol\ s^{-1}$]
G	Molar generation term [$mol\ s^{-1}$]
K	Reaction constant [s^{-1}]

m	Mass [kg]
\dot{m}	Mass flow rate [kg s ⁻¹]
P	Pressure [bar]
q	Volumetric flow rate [m ³ s ⁻¹]
\dot{Q}	Thermal power [W]
R	Universal gas constant [8.031 J mol ⁻¹ K ⁻¹]
r	Reaction rate [mol m ⁻³ s]
t	Time [s]
T	Temperature [°C]
V	Volume [m ³]
v	Stoichiometric coefficient [-]
w	Weight factor [-]
X	Inventory quantity [-]
n	Total number of reactions [-]

Abbreviations

Cell	Cellulose
CellA	Activated Cellulose
CFB	Circulating Fluidized Bed
CFD	Computational Fluid dynamics
CHP	Combined Heat and Power
CSTR	continuous stirred tank reactor
DH	District Heating
DHCN	District Heating and Cooling Network
DME	Dimethyl ether
GC	Gas Chromatography
HAA	Hydroxyacetaldehyde
Hcell	Hemicellulose
HMFU	5-hydroxymethyl-furfural
ICE	Internal Combustion Engine
LignC	Carbon-rich lignin
LignCC	Carbon-rich lignin 2
LignH	Hydrogen-rich lignin
LignOH	OH-rich lignin

LVG	Levoglygluxan
NREL	National Renewable Energy Laboratory
ODE	Ordinary differential equation
PBP	Payback Period
RDF	Refuse-Derived Fuels
RMSE	Root mean squared error
RMSW	Residual Municipal Solid Waste
SQP	Sequential Quadratic Programming
TCD	Thermal Conductivity Detector
W2E	Waste-to-Energy

Subscripts

con	consumed
f	final
gen	generated
i	initial
in	inlet
k	reaction order
l	reaction index
m	mixture
n	number of reactions
out	outlet
Rapp	(Temperature) approach
ref	reference

Greek letters

Δ	Difference
δ	heating rate [$^{\circ}\text{C s}^{-1}$]
Γ	Conversion rate [-]
ρ	Density [kg m^{-3}]

CHAPTER 6

MICROALGAE HARVESTING FOR BIOFUEL PRODUCTION

6.1 Introduction

In this Chapter, the focus on a possible environmental and energetic enhancement of the waste treatment system is moved to the investigation and implementation of novel solutions for enhancing the treatment of the liquid emissions produced in the waste treatment facility described in Chapter 2. The goal of this study is to evaluate the growth performance of the green microalga *S. obliquus* in a laboratory PBR where a fraction of synthetic leachate is diluted in the bulk of the reactor, using a similar approach described in [244], [100] and [245]. The leachate and wastewater synthetic compositions are based on the real ones of the samples collected in the anaerobic digestion plant and the landfill of the waste treatment facility. Two experimental campaigns were conducted in the laboratory between May 2022 and February 2023. The first one (RS1) was used to screen if the leachate concentration was high enough to not harm *S. obliquus*. Then, the second campaign was finalized for the characterization of the long-term growth in the medium. Three experiments (R1-R2-R3) were done consequentially. Then, Gas-chromatography (GC) was employed to ascertain the lipid profile after acid esterification of the lipids obtained with solvent extraction and rotoevaporator quantification. The study has not only been carried out from an experimental point of view but also using a modelling approach. A biodiesel production process from microalgae oil has been realised in Aspen Plus starting from a process flowsheet related to a real process based on sunflower oil. In addition, complicated molecular structures such as galactolipids (GLL), mono-di-triglycerides (MG, DG, TG) and free fatty acids (FFA) compositions [101], [246] have been accounted for. Finally, a comparison has been made to characterize the advantages and disadvantages of the two processes in terms of utilities and operating costs (OPEX). The materials and methods section outlines the laboratory equipment and procedures, along with the method employed for the preparation of the growth medium. The transformation of fatty acids, existing in triglyceride structure (TG), free (FFA), or within polar lipid molecules, into fatty acid methyl esters (FAME), is detailed in the Aspen Plus model. The biomass yield, the distinctive growth curves, lipid content, chromatograms, and results of the numerical simulations are expounded upon in the results and discussion section. Appendix III

reports the images taken under the microscope of the experiments R1 and R2. R3 is not reported since similar to R1.

6.2 Materials and Methods

6.2.1 Leachate and Wastewaters

An average value of 15,000 ton year⁻¹ of liquid waste are produced in the facility. In detail, 11,969 tons year⁻¹ come from landfill leachates, while the wastewater from composting is 4,052 ton y⁻¹ in 2019. The composition is periodically checked before collection and delivered to dedicated external treatment facilities. Data about the liquid characterization is given in Table 2-3 and Table 2-4.

The synthetic waste used in the experiment is characterized by the weighted average (annual production rate) of leachate and wastewater composition especially for nitrogen and chlorides. Metals have not been injected into the synthetic leachate, since in this case their concentrations are negligible compared to nitrogen and chlorine. The final concentration of NaNO₃ (used for nitrogen) is 37 g l⁻¹, while the one for NaCl (used for chlorine) is 12.1 g l⁻¹.

6.2.2 Medium Preparation

6.2.2.1 Medium Preparation for RSI

Different litres of sterilized 3N-BBM+V [247] solution has been prepared with the following stocks:

- Stock I (10 ml per litre of 3N-BBM+V), with NaNO₃ 75 g l⁻¹;
- Stock II (10 ml per litre of 3N-BBM+V), with CaCl₂·2H₂O 2.5 g l⁻¹;
- Stock III (10 ml per litre of 3N-BBM+V), with MgSO₄·7H₂O 7.5 g l⁻¹;
- Stock IV (10 ml per litre of 3N-BBM+V), with K₂HPO₄·3H₂O 7.5 g l⁻¹;
- Stock V (10 ml per litre of 3N-BBM+V), with KH₂PO₄ 10 g l⁻¹;
- Stock VI (10 ml per litre of 3N-BBM+V), with NaCl 2.5 g l⁻¹;
- Stock VII (6 ml per litre of 3N-BBM+V), trace elements in sequence of Na₂EDTA 0.75 g l⁻¹, FeCl₃·6H₂O 0.097 g l⁻¹, MnCl₂·4H₂O 0.041 g l⁻¹, ZnCl₂ 0.005 g l⁻¹, CoCl₂·6H₂O 0.002 g l⁻¹, Na₂MoO₄·2H₂O 0.004 g l⁻¹,
- Stock VIII (1 ml per litre of 3N-BBM+V) with vitamin B1 0.12 g/100 ml,
- Stock IX (1 ml per litre of 3N-BBM+V) with vitamin B12 0.1 g/100 ml.

First, a preliminary *S. obliquus* medium was prepared and put in a controlled incubator for two weeks. The solution is magnetically stirred with a stir bar. After, another solution was prepared in the following way: 100 ml of new nutrient 3N-BBM+V, 50 ml of the previous culture containing *S.*

obliquus, and 5 ml of synthetic leachate (3.3% v/v concentration) for a first microalga adaption in the synthetic leachate. Then, the solution was stirred for another week in the incubator until a bright green in the flask was reached, labelled as solution “A”. Every flask and stirrer were preliminarily autoclaved at 1.2 bar and 120 °C. Fig. 6-1 reports the microalgae strains and the solution obtained at the end of the incubation time. Afterward, the PBR was loaded with the following final solution: 250 ml of leachate, 89 ml of harvested *Scenedesmus obliquus*, and 3526.6 ml of 3N-BBM+V labelled as solution “B”. The total volume of “B” was 3865.6 ml, with a total leachate concentration of 7.1% v/v excluding solution “A”, 6.6% v/v including solution “A”.

6.2.2.2 Medium Preparation for R1-R2-R3

The same preparation method of RS1 has been used for R1, R2, and R3. For ease of preparation, 212 ml of synthetic leachate was diluted in 3 litres of 3N-BBM+V. Solutions “A” was prepared but different volumes were inoculated in the PBR: 180.8 ml for R1, 177.3 ml for R2, 280.6 ml for R3.



Fig. 6-1. On the left, *S. obliquus* strains. On the right: solution A flask status after 3% v/v dilution (Solution “A”).

6.2.3 Laboratory Equipment

In this section are reported the different devices and instruments used to monitor the microalga growth in the medium and its lipidic content.

6.2.3.1 Photobioreactor

The core of the experiment is the Biobench Biostream PBR [248], with 5L (349x230 mm) of nominal volume capacity. The reactor has several instruments and sensors suited for working as a chemostat

reactor. There are four peristaltic pumps (feed, anti-foam, acid, and base injection), a display set, a bacterial motor, and a water jacket that includes a stainless-steel head plate, a jacketed glass vessel, mechanical seals, a J-sparger and different needles. The internal stirring is given by a pitch blade impeller with a 60 mm diameter moved by a brushless magnetic motor. Moreover, sensors for pH, temperature, light, optical density (OD), and oxygen saturation (pO_2) are installed. One additional magnetic pump is used for carrying the liquid to the external OD sensor. Up to four LED panels (1 strip of 10 LEDs each) can be installed and envelop the water jacket and a day/night mode can be set in each experiment. The unit comes with software used for setting and controlling the process parameters, e.g. temperature, light intensity, stirring velocity, pH level, and for calibrating the sensors. The parameters used in the proportional-integrating-derivative control algorithms can be tuned as well in the software. The temperature of the reactor is regulated by an internal heat exchanger connected to aqueduct water. During operation, no control of the pH of the medium was done. In addition, filtered air was bubbled in the reactor with a content of CO_2 around 350 ppm.

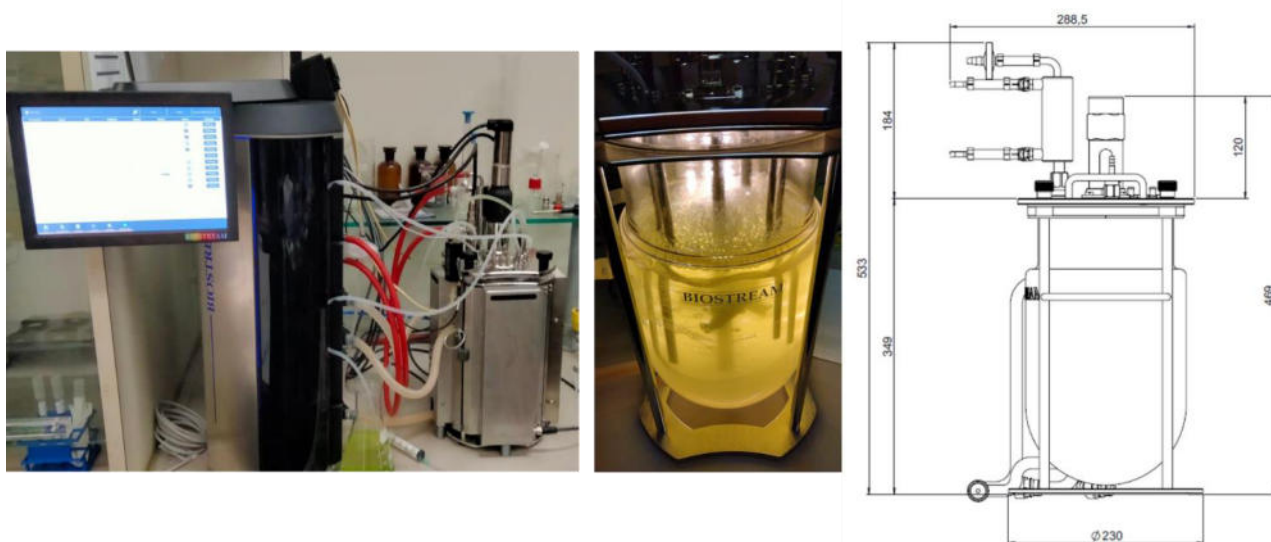


Fig. 6-2. Biobench PBR. Dimensions reported in mm.

In every experiment, the temperature and stirring velocity were fixed respectively to $25^{\circ}C$ and 200 rpm. The light intensity was 20% of the maximum, but a day/light mode (LED switched on/off every 12 hours automatically) was set in RS1 by using every LED panel. Instead, the experiments R1-R2-R3 were conducted in full-day mode with a single panel, to not overheat the reactor.

6.2.3.2 Microalgae incubation

The equipment (incubator and thermostatic fridge) used for growing *S. obliquus* at $20^{\circ}C$ and 50% relative humidity, in pure 3N-BBM+V or solution “A” is shown in Fig. 6-3.



Fig. 6-3. Incubator a) and laboratory refrigerator b).

The incubator was built in the laboratory of Marche Polytechnic University and has several magnetic stirrers inside a warming plate, a led panel, and a moisture control device. The laboratory-lighted refrigerator of VELP SCIENTIFICA [249] was used to stock the prepared media and the microalgae strains. The flasks were positioned in a way that the incoming light flux was $50 \mu\text{mol m}^{-2} \text{s}^{-1}$, measured with the Apogee full-spectrum quantum meter [250].

6.2.3.3 *Microalgae growth*

Different samples were taken from the PBR to address the daily microalgae growth in the medium. Fig. 6-4 reports the laboratory instruments used in the experimental campaigns.

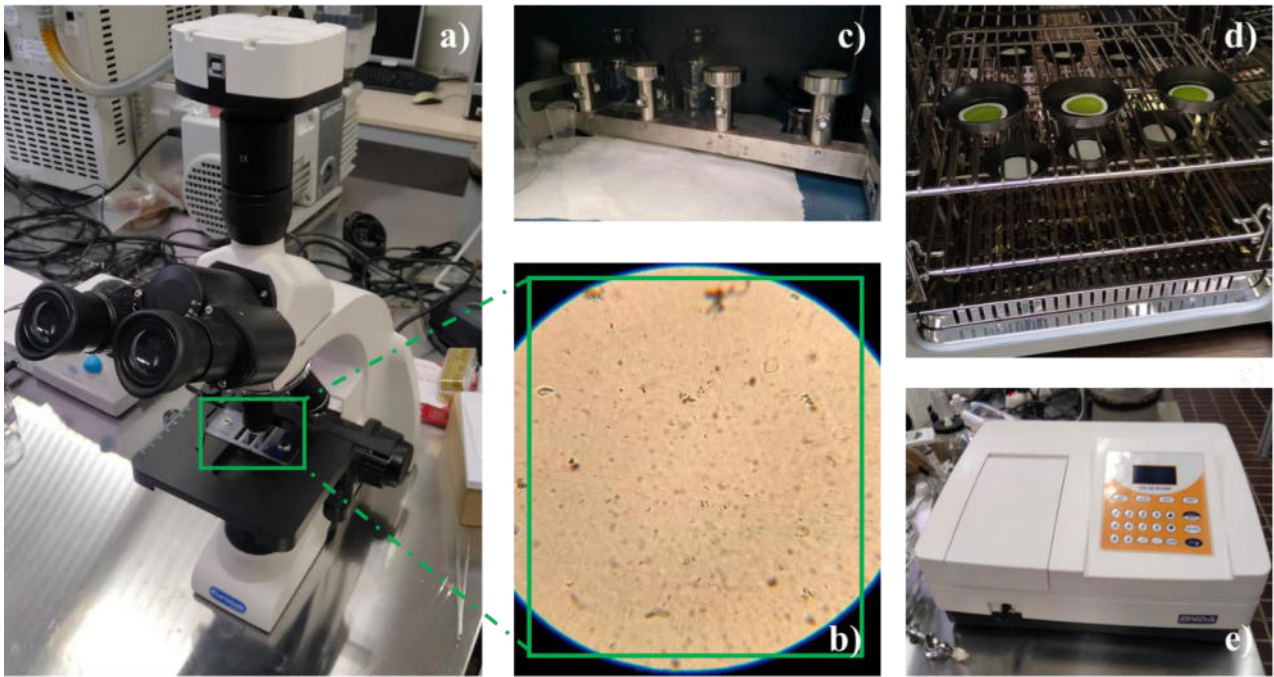


Fig. 6-4. Laboratory equipment used for measuring the microalga growth: a) optical microscope, b) Burkler cell counter chamber, c) filter ramp, d) ARGO TCN 50 oven, e) spectrophotometer UV-30.

An optical microscope was used for taking the images of the culture inside a Burkler cell counter chamber [251] hemacytometer with Neubauer reticular. The images were collected and saved with CamLabLite software and used later for manual population counting. For RS1, a total of 12 square cells + boundary (6 in the first chamber and 6 in the second, 2 by 2 adjacent) were selected randomly in the counting, whereas in R1-R2-R3 the domain was extended to 48 square cells (24 in the first chamber and 24 in the second, 2 by 2 adjacent). The following formula was used to get the cell concentration [cells μl^{-1}] of *S. Obliquus*:

$$C = \frac{N}{A \times b \times D} \quad (6.1)$$

where N [cells] is the number of corpuscles counted, A [mm^2] is the overall surface of counting, b [mm] is the depth of the chamber, and D [-] is the dilution of the sample. The area of the single Neubauer cell (0.025 x 0.025 mm) is 0.00625 mm^2 , and the depth is 0.1 mm. No dilution was applied to any sample. Furthermore, dry mass and OD measurements were done in parallel. The measurement of the biomass dry mass is performed with a triplicate sample filtered with a Munktell filter paper in a filter ramp. The paper disk is dried in an ARGO TCN 50 [252] oven overnight at 100° C. Excess salts are removed with the use of distilled water flushing in the filter ramp glass. The biomass concentration Y [g l^{-1}] is obtained as follows:

$$Y = \frac{w_S - w_D}{V_S} \quad (6.2)$$

where w_S [g] is the weight of the sample, w_D [g] is the dry weight of the same sample, and V_S [l] is the volume filtered in the filter ramp. The weight was addressed with a SHIMADZU AUW120D analytic balance. The measurements were conducted with slightly different variations in order to find the most efficient way to conduct the experiments, as reported in Table 6-1.

Table 6-1. Summary of the differences between the various experiments in terms of dry mass and cell counting.

Conditions	Experiment			
	RS1	R1	R2	R3
A [mm ²]	12x0.025 ²	48x0.025 ²	48x0.025 ²	48x0.025 ²
V _s [ml]	30	10	20	20
Light Intensity	20%, 4 panels	20%, 1 panel	20%, 4 panels	20%, 4 panels
Dry mass sampling frequency	Once per day	Twice per day	Once per day	Once per day
OD measurement frequency	-	Twice per day	Three times per day	Three times per day
Cell counting sampling frequency	Four in total	Twice per day	Three times per day	Three times per day
Lipid sampling (discussed later)	Four in total	One per run	One per run	One per run

Regarding the OD, the spectrophotometer ONDA UV-30 was used to evaluate the sample absorbance at different wavelengths (λ) [100]: 565 nm, 600 nm, 680 nm, and 750 nm.

6.2.3.4 Lipid Extraction and Conversion to FAME

The following procedure was used for lipid separation. The samples were centrifugated at 5000 rpm for supernatant removal. The centrifuge UNIVERSAL 320R, used in this case, is able to cool the samples down to 10 °C, which improves the separation efficiency. Then, the supernatant has been diluted in ethanol (RS1) and methanol (R1-R2-R3) for binding the polar molecules. After one hour of ultrasonic bath for cell rupture and overnight resting, the samples were centrifugated again to remove other microalgae corpuscles besides lipids. In conclusion, the solutions were evaporated with the BUCHI R-210 rotavapor at the proper pressure/temperature conditions required for solvent evaporation. The glass bulb was weighted after and before the extraction with the Shimadzu AUW1200 balance to assess the amount of lipids in the sample. One extraction per experiment was done. Then, the lipids were dissolved again in methanol and stored in the freezer inside 20 ml vials waiting to be used for the esterification reaction for conversion to biodiesel.



Fig. 6-5. Other equipment used for lipid extraction. Rotavapor BUCHI R-210 on the left, centrifuge UNIVERSAL 320R on the right.

The preparation of the biodiesel as fatty acid methyl esters (FAME) has been done according to the following procedure:

- In a 4 ml vial, 1 ml of the sample is diluted with 1 ml of $\text{CH}_3\text{OH} + 0.6\text{M HCl}$;
- Vortex shaking for 15 minutes of the previous solution;
- Solution left in the oven for 24 hours at $80\text{ }^\circ\text{C}$;
- When cooled, addition of 2 ml of Hexane in the vial;
- Waiting one hour for the complete phase separation, and then collected the upper phase containing FAME. The samples were labelled as “RX-MeOH”.

6.2.3.5 Wastewater analysis

After the supernatant removal, the kit Nanocolor Macherey-Nagel and compact photometer PF-12 [253] were used to quantify the total nitrogen and phosphorus [254], [255] concentrations reduction due to the nutrient consumption by *S. Obliquus*. However, there were some unspecified problems concerning the instrument and/or the compensation agent, which gave out-of-range values for the nitrogen content, even with pure water (i.e. without nitrogen). Therefore, the nutrient removal efficiency of the microalga could not be assessed during the analyses.

6.2.4 Gas Chromatography

The RX-MeOH samples were analysed with the gas-chromatograph (GC) SHIMADZU GC-2010 suited with AOC-20i autoinjector for batch analyses, external compact electrolyser for hydrogen generation used for the flame ionization detector (FID) together with high-quality pure air, helium as carrier gas, hexane as solvent (99.99 % purity, for HPLC, Sigma-Aldrich), Restek 30 m capillary

separation column, on-column direct injection mode. Prior to RX-MeOH sample analyses, a calibration process has been performed to obtain the calibration curves by using the Supelco FAME mix C14-C22 [256] 100 mg, which have the followings acids:

- Methyl myristate (C14:0), CAS# 124-10-7, 3.96 ± 0.21 WT%;
- Methyl palmitate (C16:0), CAS# 112-39-0, 9.91 ± 0.43 WT%;
- Methyl stearate (C18:0), CAS# 112-61-8, 5.98 ± 0.23 WT%;
- Methyl trans-9 eladiate (C18:1), CAS# 1937-62-8, 10.00 ± 0.44 WT%;
- Methyl cis-9 oleate (C18:1), CAS# 112-62-9, 24.9 ± 1.3 WT%;
- Methyl linolelaidate (C18:2), CAS# 2566-97-4, 2.00 ± 0.11 WT%;
- Methyl linoleate (C18:2), CAS# 112-63-0, 33.7 ± 1.6 WT%;
- Methyl arachidiate (C20:0), CAS# 1120-28-1, 1.98 ± 0.09 WT%;
- Methyl linolenate (C18:3), CAS# 301-00-8, 4.95 ± 0.28 WT%;
- Methyl behenate (C22:0), CAS# 929-77-1, 1.99 ± 0.13 WT%;

The FAME sample was firstly diluted in 0.5 ml of hexane (FAME concentration 200 mg ml^{-1}). Then, 50 ml of the of the solution are taken and diluted in 0.5 ml, and so forth, obtaining six calibrating samples with the following FAME concentrations: 200 mg ml^{-1} (C0), 18.18 mg ml^{-1} (C1), 1.65 mg ml^{-1} (C2), 0.15 mg ml^{-1} (C3), 0.014 mg ml^{-1} (C4), $0.0012 \text{ mg ml}^{-1}$ (C5), $0.00013 \text{ mg ml}^{-1}$ (C6). The correlation between the area of the peaks in the chromatograph chart and the sample concentration (C1 to C6) was done using the manual peak integration technique in OpenChrome software. It was immediately noted that the GC column had a penalising high limit of quantification (LOQ) which gave to no FAME detection in sample C6. Fig. 6-6 reports an example of calibration for two fatty acids based on the area of the peaks detected during the GC analysis. It is worth noting that the column was conditioned every week, and a run with only hexane was done prior to any sample analysis in order to clean the column from any elements that did not evaporate during the previous runs. The Table 6-2 reports the correlations for the various FAME present in the sample. C18:3 methyl linolenate was only detected once and hence no calibration curve is reported for it.

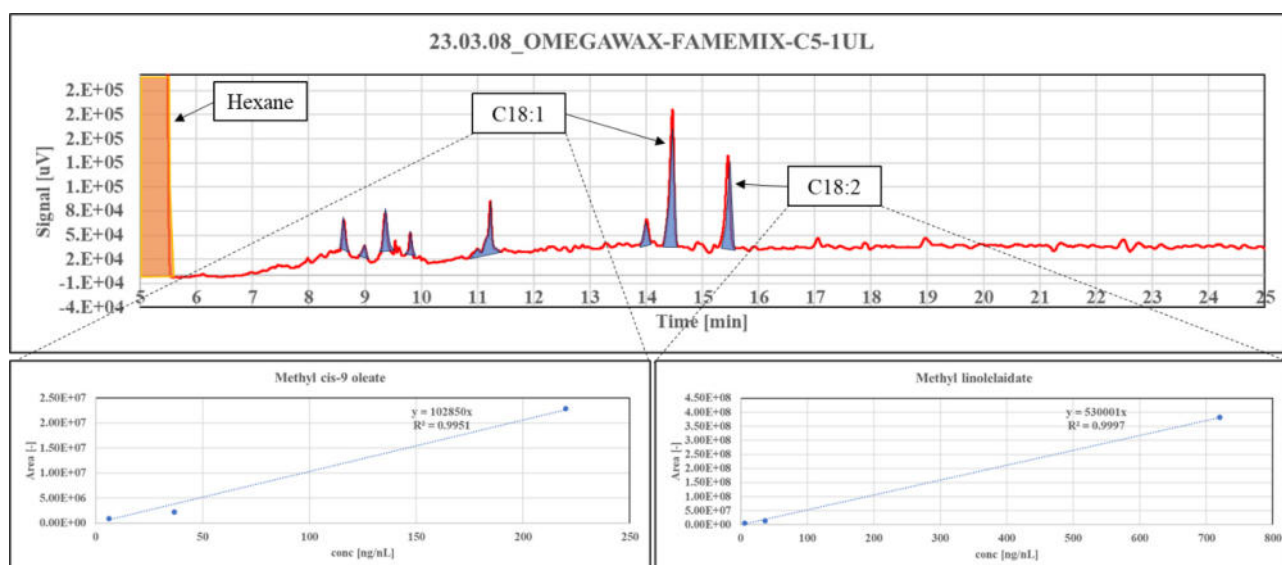


Fig. 6-6. Example of calibration for C18:1 and C18:2.

Table 6-2. Correlations obtained after the calibration with FAME mix.

FAME	REFERENCE PEAK [min]*	EXPERIMENTAL PEAK [min]	Correlation y (peak area) = Mx (concentration [ng nl ⁻¹])		
			M	points	R^2
Methyl myristate	13.63	9.30	54976	4	0.9662
Methyl palmitate	15.08	10.90	131413	4	0.9513
Methyl stearate	17.01	13.32	28353	2	0.9915
Methyl trans-9 eladiate	17.57	13.90	486961	4	0.9436
Methyl cis-9 oleate	17.84	14.63	102850	3	0.9951
Methyl linolelaidate	18.44	15.16	530001	3	0.9997
Methyl linoleate	19.07	16.03	68315	2	0.9373
Methyl arachidate	19.34	17.75	27085	2	0.9977
Methyl behenate	21.92	26.30	28601	3	0.9956

* Obtained with in-house assay GC method.

6.2.5 Numerical Model

Biodiesel is typically derived through the esterification/transesterification reaction of FFA with methanol, resulting in the production of FAME [103]. The appropriate selection of a catalyst, whether alkaline or acidic, is crucial for optimizing the augmentation of reactant products. Typically, the most convenient and productive approach at the industrial level is the utilization of alkaline transesterification for the conversion of vegetable oil [103]. The oil composition in question exhibits a reduced quantity of FFA, which can potentially lead to complications during saponification when an alkaline catalyst is employed. Typically, the microalga crude oil has a greater degree of heterogeneity, with several fatty acids being detectable. The review conducted by Hoekman [101] reported a complete characterization of the FA, from Capriotic acid (C6:0) to nervonic acid (C24:1) in SO. The prominent FA is Myristoleic acid C14:1 (21.7% of total lipids), followed by heptadecanoic acid C17:0 (20.4%), linoleic acid C18:2 (17.5%), palmitic acid C16:0 (11.6%) and stearic acid C18:0

(10%). Other studies report a well-characterized lipid profile [257]–[259], however there is currently a lack of consensus regarding the precise structural characteristics of these lipids. The technology of high-precision lipid chromatography is widely recognized as a highly efficient method for assessing the complex characteristics of lipids [260]. In addition to the identification of conventional lipids such as triglycerides (TG), diglycerides (DG), and monoglycerides (MG), the presence of glycolipids, specifically mono-galactosyls-glycerides (MGG) and di-galactosyl-glycerides (DGG), has also been observed. Such detailed composition has been founded elsewhere [246], [261]. The consideration of such compounds for the purpose of modeling is of utmost importance. The selection of Aspen Plus software has been made to facilitate the examination of biodiesel generation from *S. obliquus* oil. The composition reported by Hoekman has been preliminary assumed for the biodiesel production facility model, then, if possible, the lipidic profile obtained after GC analysis will be used. Next, a comparison is made between the most significant results and the identical biodiesel synthesis process using a traditional vegetable oil, i.e. from sunflower oil (SFO), based on an actual operational plant. This facility is designed to achieve a consistent production rate of 2000 kg h⁻¹ of premium-grade biodiesel. It uses a two-step transesterification reaction in methanol (3.03:1 molar ratio) and KOH as alkaline catalyst. The conversion is defined upon the following reactions at 60° C:



The glycerol (GLY) is recovered with decanters, whereas methanol with liquid-liquid extraction and distillation downstream the process. The catalyst is recovered with K₃PO₄. Then, the process has then been modified for accommodate *S. obliquus* oil as feedstock without changing the basic structure of the model, as shown in the process diagram of Fig. 6-7 and the Aspen Plus flowsheet reported in the Fig. 6-8.

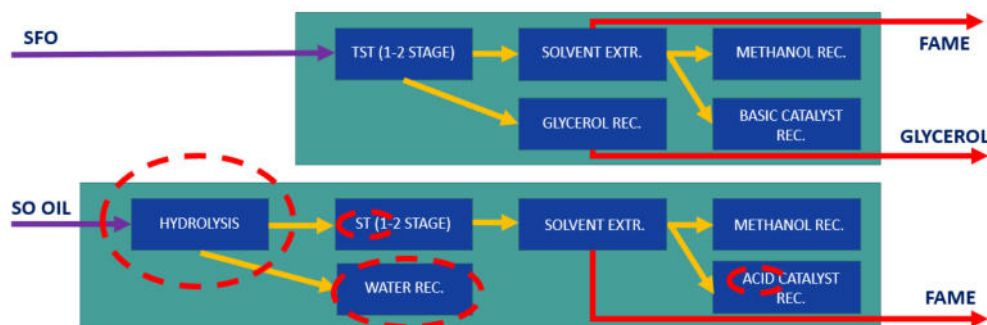


Fig. 6-7. Process comparison between *S. obliquus* oil and SFO.

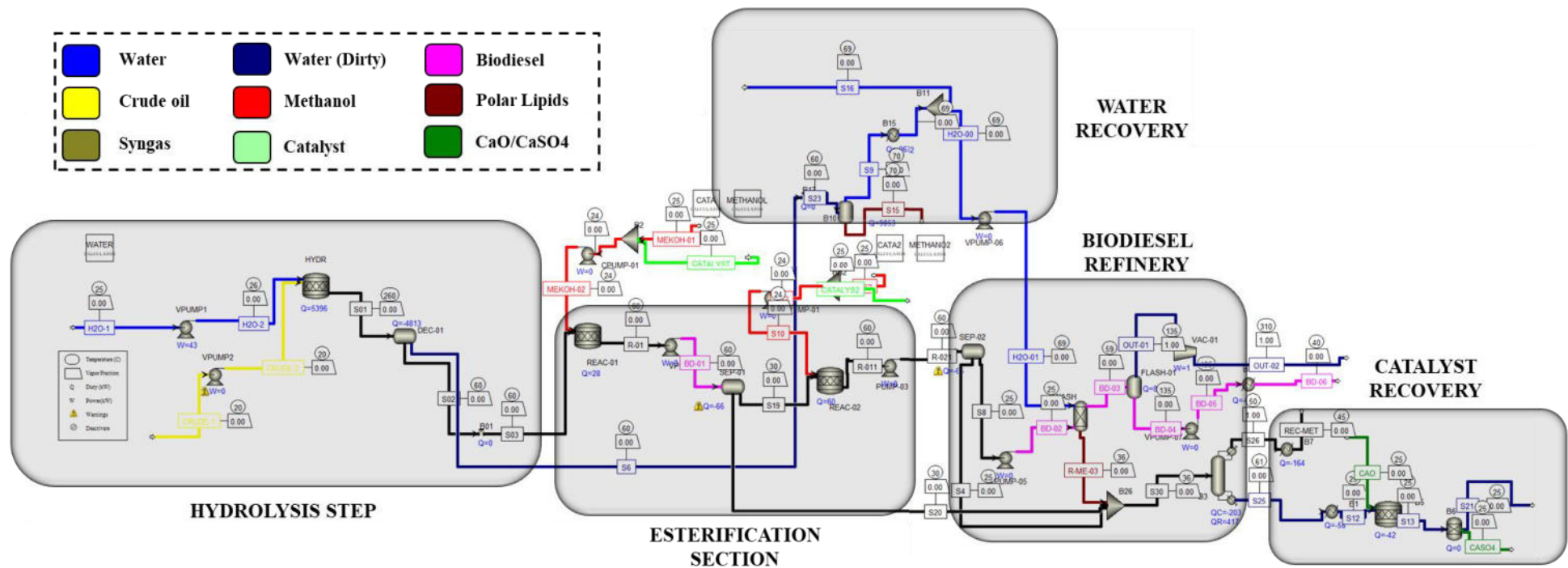


Fig. 6-8. Aspen Plus flowsheet of the biodiesel from microalgae production process.

The aforementioned procedure, characterized by elevated temperatures and pressures, has the capability to fragment intricate molecules, encompassing both polar and non-polar lipids, into smaller constituents. Consequently, this technique yields a substantial quantity of pure FFA, comparable to the Colgate-Emery method [262]–[264].

The model is based upon the following assumptions:

- The FFA variety utilized in this study is derived from Hoekman et al. [101]. A minimum criterion of 5% in mass is established as the cut-off point for each element. Consequently, the acids that have been selected are as follows: The fatty acid composition includes C14:1, C17:0, C18:2, C16:0, C18:0, C18:1, C15:1, and C16:1.
- The lipid structure is defined according to [261] for non-polar lipid (FFA and TG), while the [260] was used for the definition of polar lipids. They found presence of MGG, DGG and DGTS (Diacylglycerol-O-(N,N,N-trimethyl) homoserine). Due to the potential for solver instabilities, the model employs solely DGG for the characterization of these molecules, with a quantity equivalent to the combined amount of polar lipids.
- The overall amount of FFA, TG and DGG has been normalized to have a coherent sum.
- Data about hydrolysis performance (temperature, pressure and fractional conversion) are taken from [262], [265]. The ratio between water to oil is 4 v/v.
- DGG hydrolysis is defined in a similar way as [266], as per the following reaction:



- Methanol quantity is defined as [265] (5 g / 2 ml of oil, i.e. 2.43:1). The same has been done for the acid catalyst H₂SO₄ (3.3% g/100 ml).
- The catalyst is recovered downstream the process with CaO [267].
- The binary interaction of each molecule has been evaluated with the modified UNIFAC (Dortmund) method [141], [268]. Each molecular structure has been downloaded from Pubchem and then analysed for the quantification of UNIFAC functional groups. Fig. 6-9 illustrates two examples of lipid molecules used in the model, in particular TG C17:0, DGG C14:1, and the various functional group used to characterize the molecules.
- The esterification reaction, implemented for the eight FFA, is:



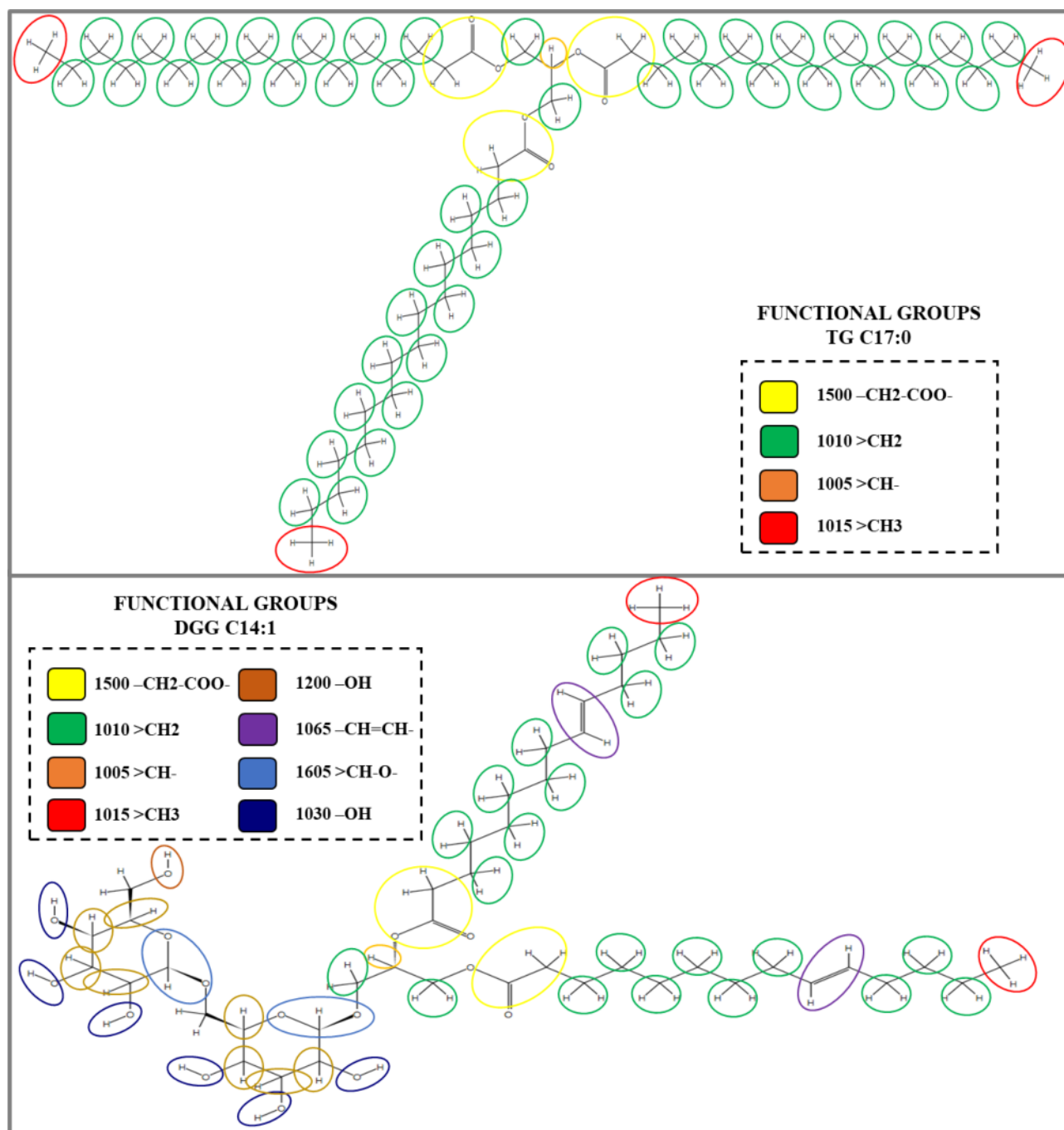


Fig. 6-9. Examples of lipids, TG form of C17:1 on top, and di-galactosyl-diacylglyceride C14:1 glycolipid, on the bottom.

The esterification process has been characterized by the utilization of various apparatus, including reactors, decanters, pumps, and calculators. The reactors REAC-01/02 are designed as stoichiometric reactors in which reaction R5 is carried out. The determination of methanol and catalyst (METHANOL/METHANO₂ and CATA/CATA₂, respectively) has been conducted using calculator blocks, as indicated in the references. The resultant product of the esterification process is subsequently directed to decanter separators, specifically SEP-01 and SEP-02.

6.3 Results and Discussion

6.3.1 Experimental campaign April-May 2022

At the beginning of experiment RS1 (14/04/22), cells were counted in solution “B”. Right after the inoculation, 74,300 cells/ μl were enumerated and the dry mass was 0.023 g l^{-1} . No significant variations of the experiment condition were noted for two weeks, i.e. until the end of April, then the growing activity of *Scenedesmus* became evident during the month of May as reported in the Fig. 6-10. Seven samples were taken during the whole month of May. The cells counted in the first sample (06/05/22) collected from the PBR are 117,700 cells μl^{-1} . Therefore, the microalgae adapted in the medium and continued to grow. Then, two additional cells counting were done in data 17/05/2022 and 25/05/2022, giving respectively 111,300 and 47,700 cells μl^{-1} . As shown in the Fig. 6-10, there was an upward trend for both pO_2 and pH, which can be attributed to the reproduction of the microalga after inoculation. The peaks of O_2 are due to the influence of day/night mode that promoted photosynthesis reactions with oxygen formation especially right after the LED were turned on.

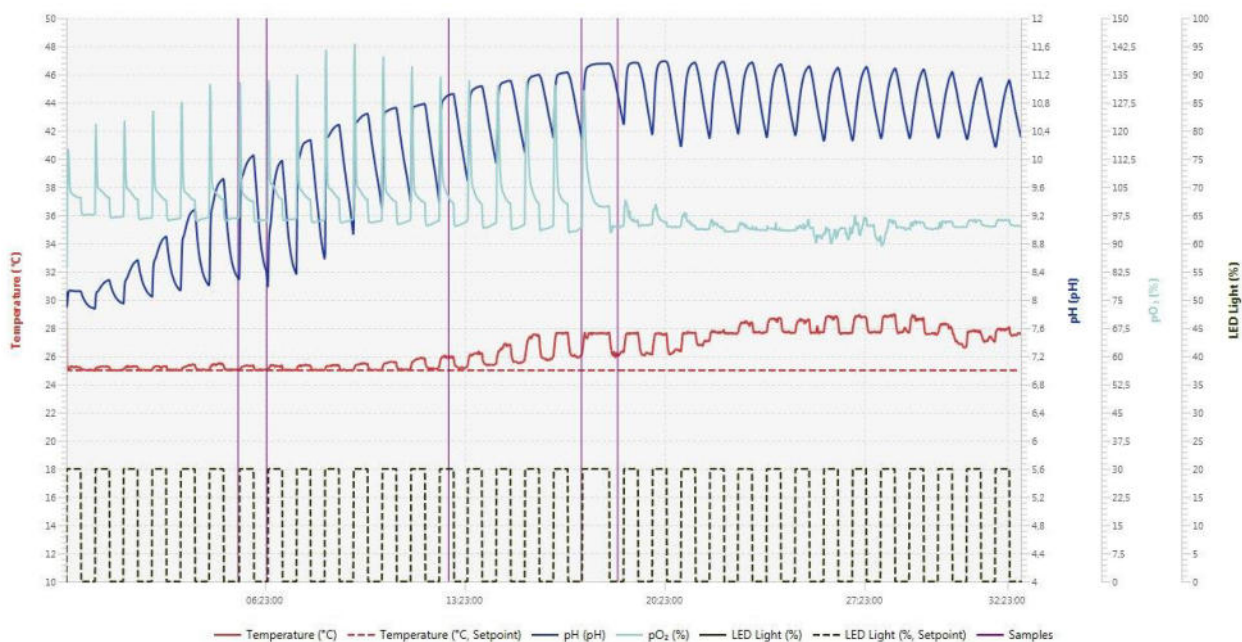


Fig. 6-10. Trends of temperature, O_2 , pH and pressure inside the PBR after one week from solution A injection.

The observed biomass concentration exhibited a significant increase, rising from an initial value of 0.023 g l^{-1} to the following values: 0.0743 ± 0.0094 g l^{-1} (05/05/22), 0.0924 ± 0.0108 g l^{-1} (10/05/22), 0.1499 ± 0.0121 g l^{-1} (12/05/22), 0.1912 ± 0.011 g l^{-1} (17/05/22), 0.1718 ± 0.007 g l^{-1} (18/05/22), 0.07 ± 0.006 g l^{-1} (23/05/22) and 0.08 ± 0.008 g l^{-1} (25/05/22). A reduction of the biomass was noted in the latest two samples, coherently to the cells counted in 25/05/22, as well as the reduction of the saturated oxygen pO_2 . The maximum concentration (0.1912 g l^{-1}) is very low when considered in

absolute terms. The observed phenomenon is likely attributable to the presence of a day/night mode, which acts as a limiting factor on the development rate of microalgae. Same methodology has been applied to the determination of lipid contents. In the first sample, the rotavapor bulb was measured before and after ethanol evaporation. The ratio between lipid and biomass amount is 11.56% (0.0024 g), coherent with literature. For the second and third sample, the lipid content was overestimated, respectively to 83% (0.0155 g) and 70% (0.0105 g). Slightly lower values were registered in the fourth and fifth samples (43% and 55%), while for the sixth the lipids were reasonably around 33% of the total biomass sample. No lipid quantification was done in the seventh sample. The issue of lipid overestimation is due probably to an uncompleted breakdown of *S. obliquus* during the ultrasonic bath, which affects the biomass removal after the centrifugation and the low amount of biomass and lipids to be measured which introduces random errors and extreme sensibility when weighting the bulb. The samples were not used for the characterization of the lipid profile due to a rupture of the FID detector, replaced in 2023. No OD measurements were conducted as well during the experiments conducted under the RS1 campaign.

6.3.2 Experimental campaign November 2022- February 2023

Fig. 6-11 to Fig. 6-13 report the temperature pH, pO₂, and LED intensity for registered in the PBR during the second experimental campaign. The first run R1 lasted from 17/11/2022 to 06/12/2022, the second run R2 from 14/12/2022 to 23/12/2022, while R3 from 25/01/2023 to 14/02/2023.

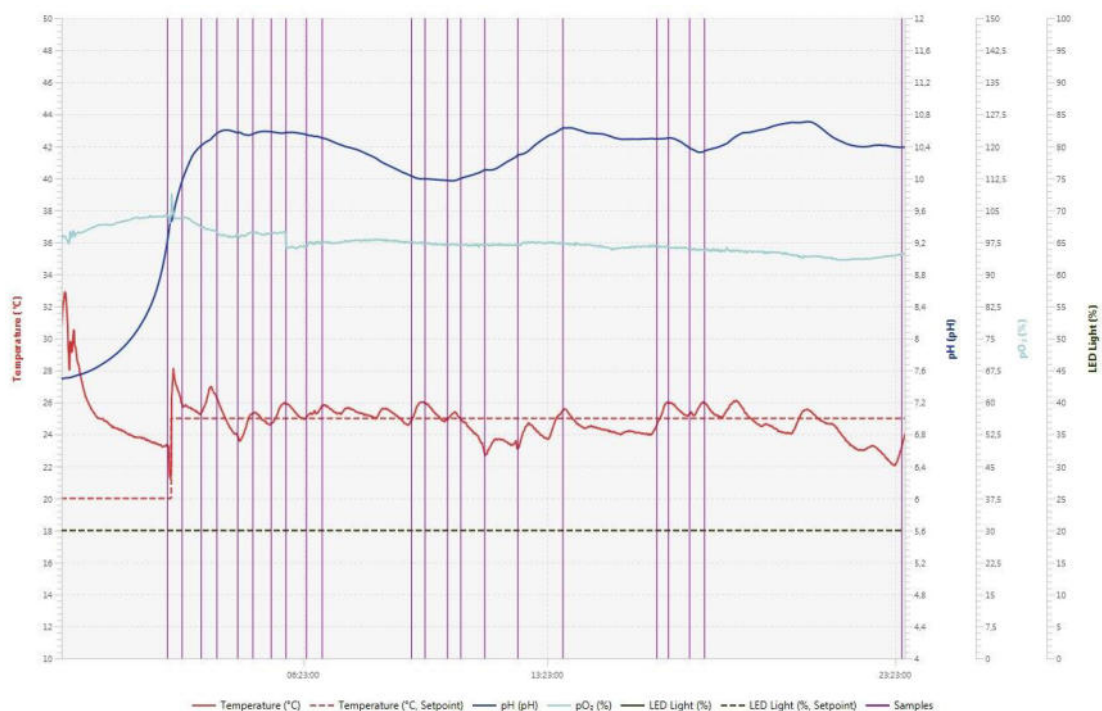


Fig. 6-11. Experiment conditions registered in the PBR during R1. The vertical purple lines represent some of the dry mass samplings.

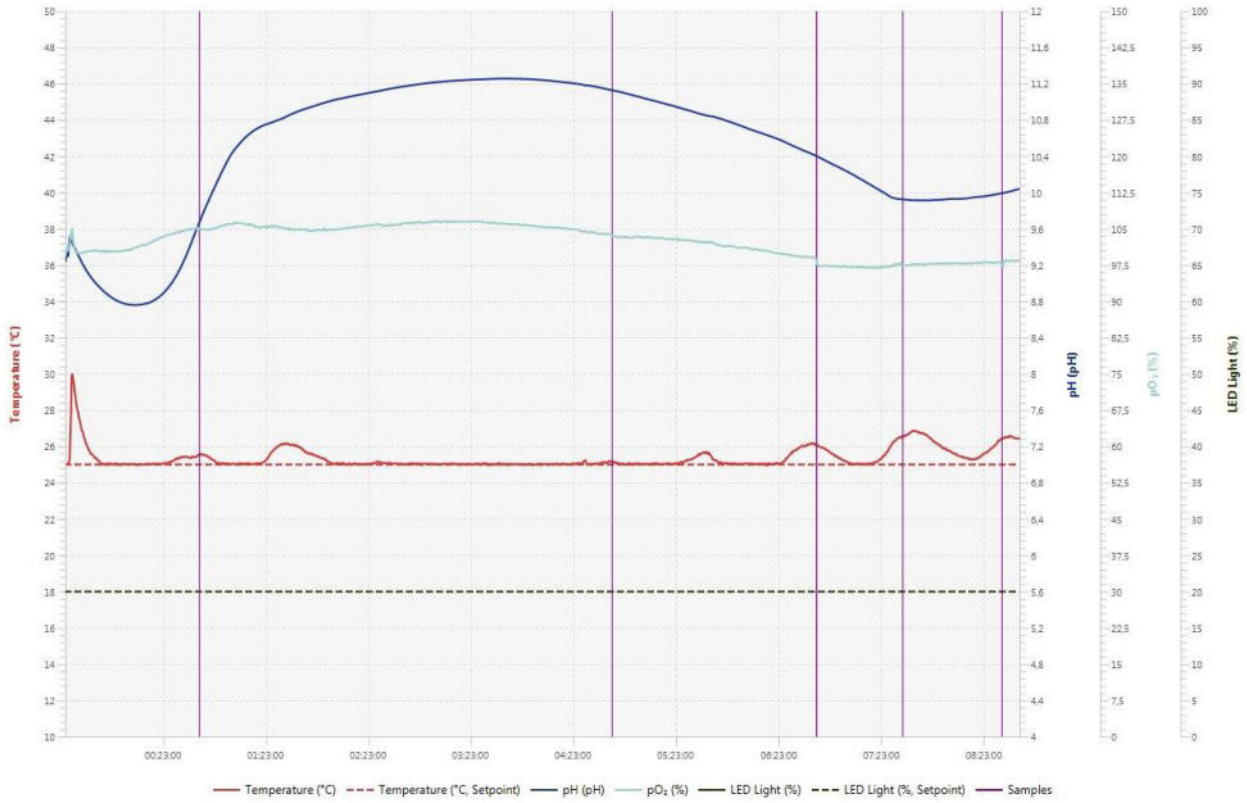


Fig. 6-12. Experiment conditions registered in the PBR during R2. The vertical purple lines represent some of the dry mass samplings.

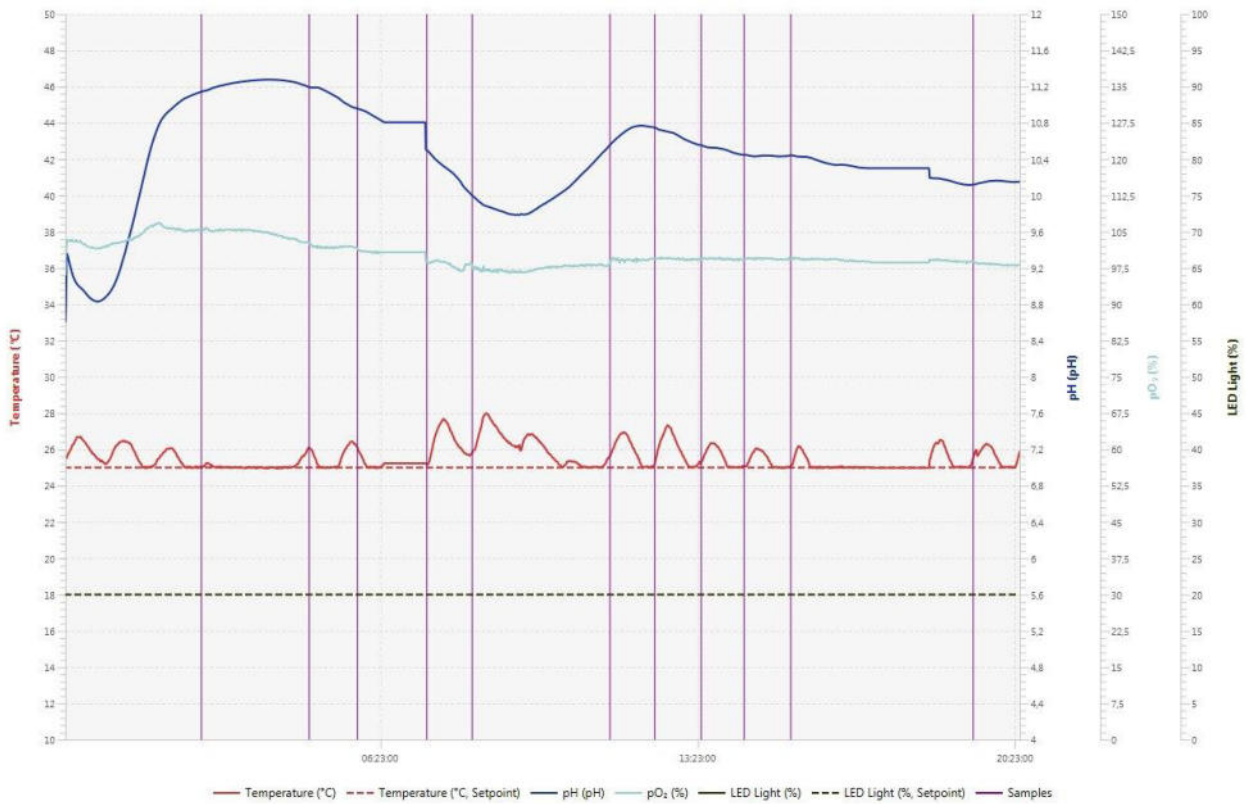


Fig. 6-13. Experiment conditions registered in the PBR during R3. The vertical purple lines represent some of the dry mass samplings.

In general, the condition inside the PBR were almost constant beside little fluctuations of temperature and more pronounced pH variations. The pH rises through photosynthesis process due to CO₂ absorption of microalgae [269]. In fact, it rises fast at the beginning of every run due to the accelerated metabolism of *Scenedesmus*, then arrives to a plateau and stay constant around 10. As suggested by Qiu et al. [270], higher pH limits the availability of CO₂ thus inhibits cell growth.

While R1 and R3 cover a long-time span, R2 is shorter but gave an equal interest since it was useful to better understand the growth behaviour of *Scenedesmus* since similar to R1 and R3 curves in their first section. The Fig. 6-14, positioned at the end of the section, summarises the data collected in R1 (blue color), R2 (orange color) and R3 (grey color). The graphs provide the natural logarithm of the number of cells C [cells ml⁻¹], the dry mass concentration Y [g l⁻¹] and the OD [-] obtained at different wavelengths.

The growth of *S. Obliquus* is characterized by the growth rate μ [day⁻¹] and division time T_d [day] defined as following [271]:

$$\mu = \frac{\ln(C_1) - \ln(C_0)}{T_1 - T_0} \quad (6.3)$$

$$T_d = \frac{\ln(2)}{\mu} \quad (6.4)$$

where C_1 , C_0 are the number of cells countered between the time range $T_1 - T_0$ from the first inoculation in the PBR during the exponential growing phase, converted in [cells ml⁻¹]. μ is the slope of the linear regression used to interpolate the values of the cells countered every time, excluding the outliers.

R1		R2		R3	
T [day]	C [cells μ l-1]	T [day]	C [cells μ l-1]	T [day]	C [cells μ l-1]
4.21	2,167	1.19	2,444	1.25	4,000
5.00	2,250	2.21	2,528	2.25	2,917
6.21	4,000	5.24	4,194	3.06	5,000
7.21	3,458	6.19	4,083	5.22	5,972
8.21	1,250	7.21	4,444	6.24	6,806
11.21	5,208	8.22	2,806	7.26	5,250
12.21	7,792	9.19	6,000	8.21	10,139
13.13	6,333			9.22	4,389
14.04	12,500			12.22	12,917
15.38	15,167			13.24	13,806
18.23	34,292			14.26	22,583
19.23	31,375			15.24	22,639
20.13	42,083			16.19	35,361
				17.04	13,833

19.47 53,917
20.22 59,972

reports the daily averaged concentration C of microalgae counted each time.

Table 6-3. Elements counted in each experimental run, based on a daily average.

R1		R2		R3	
T [day]	C [cells μl^{-1}]	T [day]	C [cells μl^{-1}]	T [day]	C [cells μl^{-1}]
4.21	2,167	1.19	2,444	1.25	4,000
5.00	2,250	2.21	2,528	2.25	2,917
6.21	4,000	5.24	4,194	3.06	5,000
7.21	3,458	6.19	4,083	5.22	5,972
8.21	1,250	7.21	4,444	6.24	6,806
11.21	5,208	8.22	2,806	7.26	5,250
12.21	7,792	9.19	6,000	8.21	10,139
13.13	6,333			9.22	4,389
14.04	12,500			12.22	12,917
15.38	15,167			13.24	13,806
18.23	34,292			14.26	22,583
19.23	31,375			15.24	22,639
20.13	42,083			16.19	35,361
				17.04	13,833
				19.47	53,917
				20.22	59,972

The statistical comparison between the regression lines has been done in GraphPad Prism 8 [272], to check the replicability of the experiment. Due to the different time ranges of the experiments (the time extension of R2 is half of the one of R1-R3), the p-value associated to the slope comparison is 0.03, hence pointing out an undeniable difference not driven by systemic errors. However, if the ranges are restricted to T_1 equal to 9 days, then the p-value is 0.6254 and the pooled slope is equal to 0.1229 day^{-1} . R1 and R3 are similar to each other if the first two days of data are excluded. In this case, the p-value obtained is 0.0923, and the growth rate is 0.1680 day^{-1} . Moreover, the values of R^2 close to one suggest that the microalgae are in the exponential part of the growing curve, even after 15-20 days, which is coherent to the high value of the division time (3.773 to 6.129 days) obtained from the linear regressions. With reference to R1 and R3, after 12-14 days it is noted a consistent increase of the number of corpuscles counted with the Burkert chamber, up to 40,000-60,000 cells μl^{-1} at the end of the experiments. The images taken with the microscope of the microalgae are reported in Appendix III for R1 and R2. The images of R3 are not reported since the similarities to R1.

The maximum dry mass concentrations were noted in R1 with 0.327 g l^{-1} and in R3 with 0.286 g l^{-1} . Even if higher compared to RS1, such concentrations are achieved after a long permanency time in the

PBR, around 18-20 days. With reference to graph of R1, the biomass concentration tends to slightly decrease from its maximum value. Instead, for R3, this plateau seems to have not been reached yet. the data collected for R2 do not provide any useful information, except that the yield in biomass is in line with R1 and R3 up to ten days from inoculation and with the last samples of RS1 (0.07-0.08 g l⁻¹). The volumetric productivity Z [g l⁻¹ day⁻¹] can be defined as:

$$Z = \frac{Y_1 - Y_0}{T_1 - T_0} \quad (6.5)$$

The value is shown in the Table 6-4 together with the data of the linear regressions.

Table 6-4. Summary table for growth rate and division time of the three runs.

RUN	Linear regression $\ln(C) = \mu T + \ln(C_0)$, C in [cells ml ⁻¹]							
	Equation	Points	T ₀ [day]	T ₁ [day]	μ [day ⁻¹]	T _d [day]	Z [mg l ⁻¹ day ⁻¹]	R ²
R1	$\ln(C) = 0.1837 T + 13.722$	12	4.21	20.13	0.1837	3.773	17.1	0.9540
R2	$\ln(C) = 0.1131 T + 14.551$	6	1.19	9.19	0.1131	6.129	11.0	0.9675
R3	$\ln(C) = 0.15 T + 14.756$	14	1.25	20.21	0.15	4.621	10.0	0.9564

The OD trends have the similar characteristics of C and Y. For future studies, such data may be used to correlate C and Y to the OD in order to have a faster quantification of the dry mass content. Moreover, the influence of the wavelength does not exert consistent graph variations. The use of the wavelength of 750 nm tends to underestimate the OD measurement compared to the other ones, especially after a long period of time. It is not clear why there is a peak at T = 5.4 in R2, not in line with the general raising trend of the experiment, maybe due to a wrong calibration of the spectrophotometer or dirty samples. In conclusion, the use of 24h light helps in the growing of *S. obliquus* compared to day/night mode.

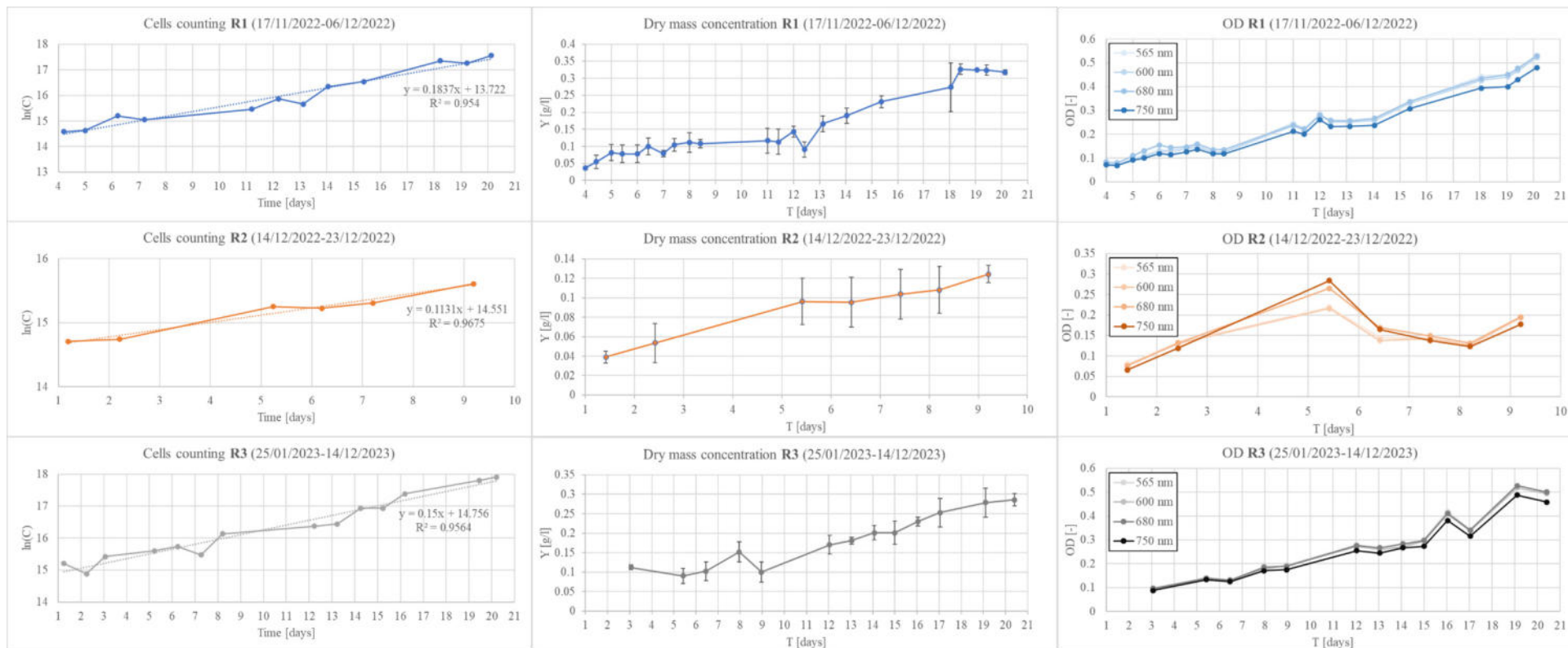


Fig. 6-14. Outcome of the experimental analyses for R1, R2 and R3 in terms of Cells counted, Dry mass concentration and OD.

6.3.3 Lipid Analysis R1-R2-R3

The lipids were extracted with the rotavapor by evaporating the methanol contained in the glass bulb. The amount of lipids detected after evaporation, in R1-MeOH (7/12/2022), R2-MeOH (22/12/2022) and R3-MeOH (3/2/2023) are respectively 1.35 mg (8% total dry mass), 2.93 mg (54%) and 1.17 mg (20%). While the lipid quantification is coherent for R1 and R3, the same problem noted for RS1 was noted in R2 for the overestimation of the lipid content. Noteworthy, the microalgae dimensions are higher than in the other experiments (Fig. X3-37 to Fig. X3-73 of Appendix III), so more lipids were expected to be noted. However, these amounts are low in absolute terms, and difficult to analyse in the following GC analyses. The samples were converted to FAME according to the procedure described in the previous section, left in the freezer and then analysed in the GC (April-May 2023) by injecting 2 μ l of the liquid volume in the column (signal S1). Each analysis is coupled with a run having hexane solvent only (signal CS2), in order to subtract S2 from S1 and to reduce the background noise that affect the FID signal. Fig. 6-15 reports an example of the GC chart for R3-MeOH. The signal S1 is represented in black, while S2 in magenta, while in grey the difference S1-S2. As the image suggests, the intensity of the peak signals is not enough to characterize properly every FAME species inside the sample. In fact, after 11 minutes, the ratio signal/noise do not provide any useful information for the characterization of the lipidic profile. Nonetheless, four peaks were detected between 8 and 11 minutes, even though the first two cannot be associated to the calibration curves since the peak detection time are outside from the one obtained in the calibration process. The small but clear peaks may represent some lipids having an equivalent chain length (ECL) [273], [274] lower than 14, i.e. the one associated to myristic acid. Vice versa, the two bigger peaks at 9.289 min and 10.178 min represent the FAMEs C14 and C16. Their detection was obtained also by Qiu et al. A sharp peak shape would mean a clear FAME molecular structure, and ease of element separation during the movement in the column. The irregular shape, which comprehends the phenomenon of “tailing” enveloped in other secondary lower peaks, suggests two aspects: other FAME are separated slightly after C14 and C16 (comprehending unsaturated forms of those lipids), and the upstream lipid structure before FAME conversion is more complicated than the basic FFA molecule in a profile that cannot be addressed with the type and configuration of the GC used in laboratory. The concentration has been calculated by simply associate the whole peak area to the two FAMEs, obtaining 0.246 mg/ml for C14:0 and 0.048 mg/ml for C16:0. Referred to the amount of lipids obtained in R3, these FA correspond respectively to 42.17% and 8.17% (50.34% in total). The other half is represented by the two unknown peaks before C14:0 and other FAME with ECL > 16, scattered after the peak signal of C16:0.

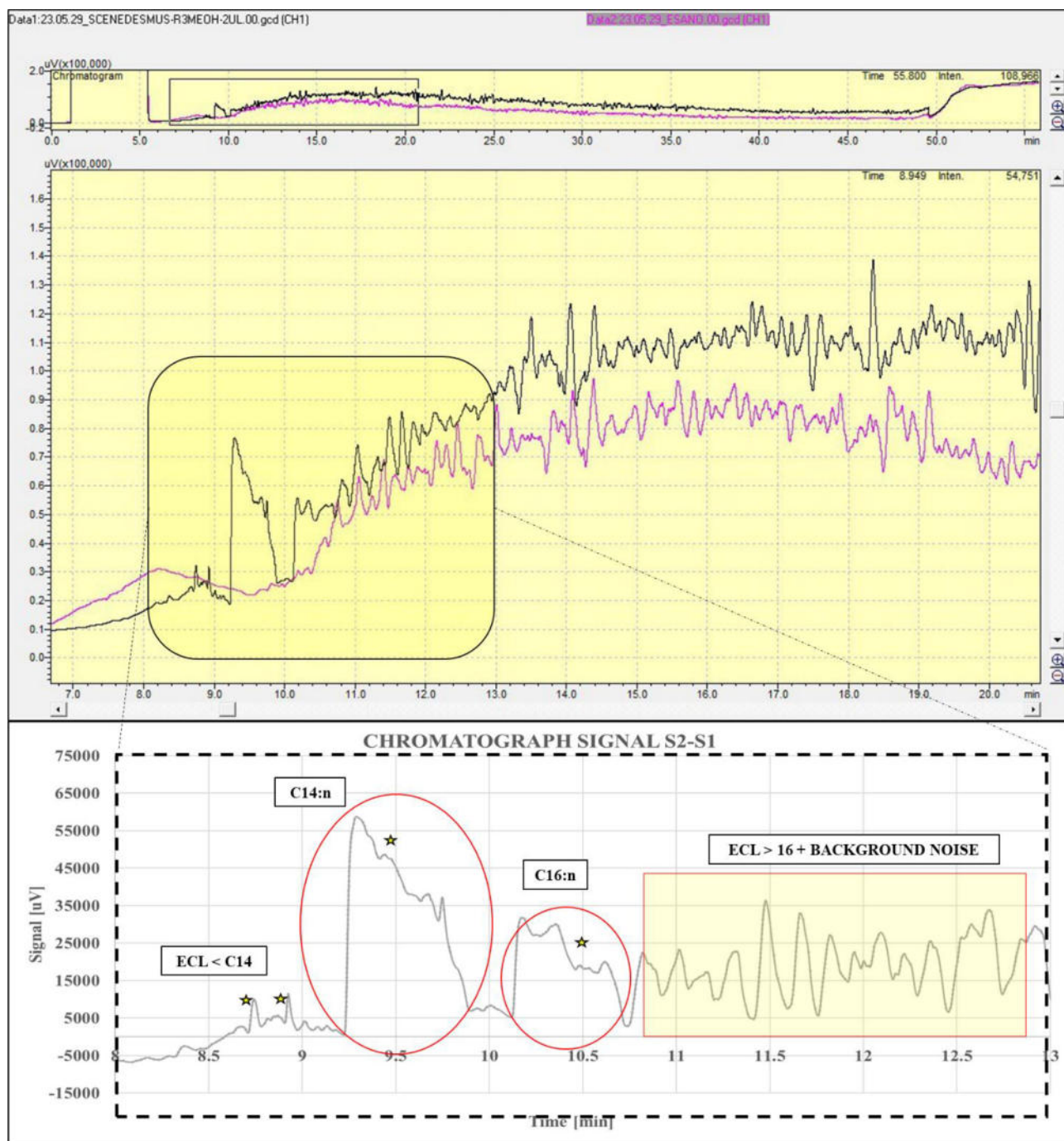


Fig. 6-15. R3 chromatograph chart obtained with GC solutions, with details of the peaks detected in the analysis.

The GC graphs obtained for R2-MeOH present similar characteristics of the one of Fig. 6-15 for R3-MeOH. The FAMES ascribable to C14:0 and C16:0 or their unsaturated form is 17.34% of the total lipidic amount detected in R2. C14:0 has a concentration of 0.222 mg ml^{-1} (15.16%) whereas C16:0 is present in 0.032 mg ml^{-1} (2.18%). The C16:0 FAME peak was not detected in R1-MeOH due to the already low percentage of lipid in the sample, and the one of C14:0 gives a concentration of 0.048 mg l^{-1} (7.08% of R1 total lipids). The average value between 7.08%, 15.16% and 42.17% for the myristic acid gives 21.47%, a value similar to the one reported in the review of Hoekman [101] of

21.7% for myristoleic acid C14:1. Therefore, this peak contain C14:0 and C14:1 but the column cannot separate the two elements properly.

6.3.4 Estimation of biofuel production

The estimation of the biofuel production BD [kg/year] from an indoor PBR is addressed as following:

$$BD = 365 \times Z \times V_R \times L \times \eta^2 \quad (6.6)$$

Where V_R [m³] is the volume of the PBR, L [%] the lipid content in the biomass, η the conversion efficiency of the reaction R5 (0.98, two esterification step). Recalling that the value of L is 7.08%, 15.16% and 42.17%, and referring to a dummy PBR volume of 1 m³, then the following value of BD are obtained: Upper bound (UB) 1.48 kg m⁻³ year⁻¹ (R3), and lower bound (LB) the average between 0.48 kg m⁻³ year⁻¹ for R1 0.58 kg m⁻³ year⁻¹ for R2, i.e. 0.53 kg m⁻³ year⁻¹. In the best-case biodiesel scenario (BSBD), an indoor PBR having a volume of 67.5 m³ should be used to produce 100 kg of biodiesel from microalgae, while in the worst-case biodiesel scenario (WSBD) a reactor with 235.6 m³ of total volume is required to achieve that production. A mere indication of the number of medium replacements in closed PBR can be estimated on the nutrient consumption and pollutant removal efficiency. Since the determination of the microalga attitude of the wastewater phytoremediation was not possible in laboratory, the relevant data are taken in literature. Chaudhary et al. [275] reported an ammonia and phosphate reduction of 91.4% for *Scenedesmus* after 10 days in a indoor PBR. If the exponential growth phase of *S. obliquus* is the average value of the growing time between R1 and R3 (17.44 days), then it will be possible to treat all of the wastewater diluted in the medium. The number of replacements will be 21 (365/17.44) in a year. The amount of wastewater/leachate is 7% v/v of the total medium. Thus, in the BSBD, 92.7 m³ of leachate and wastewaters can be treated annually, whereas in WSBD the amount treated increases to 323.7 m³. Therefore, WCBD corresponds the to the best-case wastewater treatment scenario (BSWW), and BCBD to the worst-case wastewater treatment scenario (WSWW). In WSWW the amount of waste that can potentially be treated is the 2% of the total liquid waste produced in the facility.

6.3.5 Numerical analysis

Since a clear composition of the oil from *S. obliquus* cannot be characterized at experimental level, data from Hoekman was used as the input of the numeric model related to the biodiesel production process. The dominant critical point is the hydrolysis step (Fig. 6-8). The calculator block provided an oil mass flow rate of 2,600 kg h⁻¹ for produce 2,000 kg h⁻¹ of biodiesel. The difference is driven by glycerol and galactolipids content. The water required in the hydrolysis is 15,108 kg h⁻¹ (because

of the volumetric ratio 4:1 used in literature), leading to a considerable amount of thermal utility needed (5,400 kW). The majority of this water stream can be recovered after appropriate cleaning treatment required for removing glycerol and glycolipids.

Regarding the purity of Biodiesel, standard UNI EN 14214 [276] has been taken as reference. Based on the provided oil composition and process circumstances, the biodiesel adheres to several standards, as documented in Table 6-5. The ester content, viscosity, and density of biodiesel meet the required specifications. The levels of methanol, water, MG, DG, and GLY are within the acceptable range, with the exception of TG, which slightly exceeds the permissible limit by 0.02% (0.22% instead of 0.2%).

Table 6-5. Biodiesel specifications as per UNI EN 14214.

UNI EN 14214	U.M.	Min	Max	Model
Esters Content	% (m/m)	96.5	-	99.05
Density	kg/m ³	860	900	857
Viscosity (at 40°C)	cS	3.5	5	3.81
Water	% (m/m)	-	0.05	0.049
Methanol	% (m/m)	-	0.2	0
MG	% (m/m)	-	0.8	0
DG	% (m/m)	-	0.2	0
TG	% (m/m)	-	0.2	0.22
Glycerol	% (m/m)	-	0.25	0

The assessment of operational costs necessary for the conversion of microalgae oil involves the definition of thermal and electric utilities. The latter is also employed for refrigeration reasons, specifically as a condenser in distillation units. The thermal energy demand in the hydrolysis treatment surpasses the thermal energy use in the process of producing biodiesel from SFO. Table 6-6 shows the differences in terms of utility costs between standard vegetable oil and microalgae oil. Electric cost is taken from “Gestore Servizi Elettrici” (GME) in 2019, equal to 52.32 €/MWh on average [277], while natural gas cost is taken from ARERA [278]. The overall price for 1 kg of biodiesel is € 0.297 from *S. obliquus* and € 0.024 for SFO. This discrepancy is to be attributed to the hydrolysis treatment step, required for breaking the molecular structure of the microalgae biomass.

Table 6-6. Utilities usage in biodiesel production from SO and SFO.

Utility	U.M.	SO	SFO
Electricity for refrigeration	kWh kg ⁻¹	0.24	0.22
Electricity	kWh kg ⁻¹	0.05	≈0
Thermal (steam)	kWh kg ⁻¹	8.15	0.33

6.4 Discussion

In this Chapter, a feasibility analysis of the integration of microalgae harvesting and integration in waste treatment facilities is presented. In particular, the indoor PBR configuration is chosen to both treat the wastewater and leachates produced in the facility and estimate the biofuel production. Experimental analyses are conducted in a laboratory-scale controlled chemostat, where the resistant microalga *Scenedesmus obliquus* is harvested in a medium containing 3N-BBM+V and around 7% v/v of synthetic wastewater. The PBR is controlled in temperature (25°C) and light only (10% of the maximum intensity). No pH control is set. Filtered air is supplied only. Two experimental campaigns with a total of four runs (RS1, R1, R2 and R3) are presented. RS1 was used to check if *S. obliquus* could grow in the medium in a 12h-day mode. Once this had been verified, the second campaign started with 24h-day mode. Besides R2, each run lasts more than 20 days. The biomass is characterized in terms of cell concentration, dry mass weight, OD, lipid quantification, and lipid profile. The maximum dry mass concentrations obtained in each run are 0.17 g l⁻¹ (RS1), 0.328 g l⁻¹ (R1), 0.124 g l⁻¹ (R2) and 0.286 g l⁻¹ (R3). The growth rates and division times are addressed in the second campaign, and in the time frame common to each run μ is equal to 0.1229 day⁻¹. The full exponential phase is however detected in R1-R3, characterized by a growth rate of 0.1680 day⁻¹. The volumetric productivity is low as well, from 10 g l⁻¹ day⁻¹ to 17 g l⁻¹ day⁻¹ Table 6-4. This low yield in biomass production reflects practical difficulties related to lipid detection. The average lipid content is 27%, and the peaks of C14:0 and C16:0 FAMES could be detected by gas chromatography, but there are uncertainties related to the possible presence of unsaturated molecules with similar ECL of these acids. Concerning this laboratory data, it is required a PBR of 67.5 m³ (BSBD) to produce 100 kg of fuels per year. Some benefits can still be achieved in the BSWW involving a PBR of 235.6 m³ that can treat 323.7 m³ of wastewater per year, equal to 2% of the total. No measurements for the phytoremediation were taken in the laboratory, but different studies in the literature report a successful removal efficiency of microalgae applied to leachates [275], [279], which has been assumed to happen also in this study. A composition from literature is used to model in Aspen Plus the esterification of the fatty acids produced with microalgae. No remarkable differences from the traditional vegetable oil transesterification process are present besides the needed implementation of a preliminary hydrolysis step to break lipid bounds and separate simple FFA molecules. This treatment is energy intensive since performed with water at 250 °C and 50 bar.

Compared to other studies, this work underlines the importance of controlling the conditions of the reactor when the microalga is growing. For instance, the review of Umamaheswari and Shanthakumar

[280] highlighted the importance of the pH, which should be limited to the range 7-9. In this condition, the microalgae growth is not inhibited, and the productivity can be much higher than the values obtained in the experiments. In cheese whey permeate, *Scenedesmus* may arrive at concentrations up to 4.9 g l⁻¹ and a lipid volumetric content of 37.8 mg l⁻¹ day⁻¹. Converted to our case, the BSBD reactor would produce around 900 kg of biodiesel instead, nine times higher than the amount estimated in this work. When this microalga is grown in brewery wastewater (maximum pH 8.85) at different permanence times [281], the dry mass (ash-free basis) can vary in the range 0.26 - 0.95 g l⁻¹, while the volumetric productivity between 84-217 mg l⁻¹ day⁻¹. Indeed, the lower bound of this range is comparable to the experiments conducted in this work. Moreover, these results are similar to the ones reported by Abhilash et al. [282] for the cultivation of *C. pyrenoidosa* in pre-treated landfill leachate (0.07-0.12 g l⁻¹ day⁻¹). Therefore, this work should be used as a conservative estimation of the microalgae harvesting potential in closed PBR, with no pH control, for valorise wastewaters with high COD content. It is clear that such systems do not provide a justifiable amount of biomass/biofuel, and other solutions should be pursued like cultivation in open ponds [283] associated with waste treatment.

6.5 Conclusions

The integration of microalgae harvesting in the waste treatment sector represents a potential solution that fully embraces and fosters the paradigms of the circular economy. Microalgae can reduce the impact associated with liquid wastewater and in the meantime offer biomass that can be valorised for energy production. This framework suggests the definition of a holistic design methodology that pursues a careful investigation of the technology feasibility supported by the insights of numerical analyses. In this work, the microalga *S. obliquus* is grown in a medium diluted with synthetic leachate emulated according to the data provided by the company. Several experiments were conducted in the laboratory, confirming that this microalga can adapt in the medium diluted with wastewater but with a relatively low yield in biomass production, not suited for biodiesel generation. The PBR used for the experiments registered high pH values that penalized the productivity. Similar experiments will be carried out in the future with the addition of pH control to determine any variations in the volumetric productivity.

Nomenclature

A	area [mm ²]
b	hemacytometer depth [mm]

BD	biodiesel production [kg year ⁻¹]
C	cell concentration [cells ml ⁻¹]
D	sample dilution [-]
L	lipid content [%]
N	number of cells in the hemacytometer [cells]
Td	division time [day]
V	volume [l]
w	weight [g]
Y	biomass concentration [g l ⁻¹]
Z	volumetric productivity [g l ⁻¹ day ⁻¹]

Abbreviations

BBM	Bold Basal Medium
BSBD	Best Scenario Biodiesel Production
BSWW	Best Scenario Wastewater Treatment
CF	Composting Facility
COD	Chemical Oxygen Demand
DG	Diglyceride
DGG	Di-Galactosyl-Glycerides
ECL	Equivalent Chain Length
EWC	European Waste Codes
FAME	Fatty Acids Methyl Esters
FFA	Free Fatty Acids
FID	Flame Ionization Detector
GAL	Galactose
GC	Gas Chromatography
GLY	Glycerol
GME	Gestore Servizi Elettrici
LF	Landfill
LOQ	Limit of Quantification
MG	Monoglyceride
MGG	Mono-Galactosyls-Glycerides
MSW	Municipal Solid Waste

OD	Optical Density
OFMSW	Organic Fraction of Municipal Solid Waste
OPEX	Operating Costs
PBR	Photobioreactor
RDF	Refuse-Derived Fuel
RMSW	Residual Municipal Solid Waste
SFO	Sunflower Oil
TG	Triglyceride
WSBD	Worst Scenario Biodiesel Production
WSWW	Worst Scenario Wastewater Treatment
WWTP	Wastewater Treatment Plant
W2E	Waste-To-Energy

Subscripts

S	Sample
D	Dry
R	Reactor

Greek letters

η	Wavelength [nm]
μ	Growth rate [day ⁻¹]
η	esterification efficiency [-]

CHAPTER 7

LIFE CYCLE ASSESSMENT OF THE MUNICIPAL SOLID WASTE TREATMENT FACILITY

7.1 Introduction

The LCA has 4 major steps [284]: goal and scope, Life Cycle Inventory (LCI), Life Cycle Impact Assessment (LCIA), and an interpretation phase on the results obtained. These steps present an iterative framework, where many assumptions are revised, especially for background data in the LCI.

LCA employs a functional unit, which is a standardized measure representing the intended function of the product or process. This enables meaningful comparisons between different options and a proper formulation of the goal and scope of the studio.

In the LCI phase, data about input (materials, energy, water) and output (emissions, waste) are collected and associated with each stage of the product's life cycle. This data helps to establish a quantitative understanding of the system assessment. Data quality significantly affects the accuracy and reliability of LCA results. Data can be sourced from various places, including databases, literature, and industry standards.

During the LCIA phase, the gathered inventory data are scrutinized to establish potential environmental effects across categories such as climate change, resource depletion, human health, and ecosystem quality. This stage involves attributing indicators to inventory data to gauge their probable implications. LCIA findings can manifest as singular measures, such as a carbon footprint, or as exhaustive analyses encompassing multiple impact categories, presenting a more comprehensive perspective on environmental performance. LCIA serves to pinpoint significant pressures on the system, like sources of intensive material and energy consumption or operational inefficiencies. Subsequently, once the objective is defined, viable measures can be appraised as alternative scenarios to the baseline. The interpretation phase involves dissecting the outcomes of the impact assessment within the study's framework, accounting for its objectives, scope, constraints, and uncertainties inherent to the evaluation.

In this chapter, the LCA approach is applied to the composting facility under investigation. In particular, the following aspects are considered: (i) the comparative scenarios analysis for the environmental impact reduction of an MSW site; (ii) the photovoltaic integration in the site; (iii) the environmental impact analysis of plastic and paper residues use in the gasification process described in chapter 3-4, by considering the CS1 scenario.

7.2 Materials and Methods

7.2.1 System Description

The system under investigation is in Chapter 2. The system has been specifically engineered to handle a yearly treatment capacity of 100,000 metric tonnes of MSW, comprehending both organic fraction OFMSW and RMSW. The building of the composting portion was finalised in the year 2018. Following a preliminary evaluation phase to facilitate its initiation, the composting section became fully operational in the subsequent year, 2019. During the initial phase of the pandemic, the facility experienced a saturation of its capacity as a result of the heightened volume of waste that needed to be treated. This rise may be attributed mostly to the temporary closure of neighboring treatment facilities, which subsequently impacted the quality of the produced biogas, as will be further elaborated upon.

7.2.2 Goal and scope

The objective of the current environmental analysis is two-fold: firstly, to provide an unbiased quantification of the actual performance of the entire site during its ongoing operation, and secondly, to assess the environmental impact if additional renewable energy and circular economy solutions are implemented. As per the ISO standard, the aforementioned objectives are classified under the "A" category, which entails the assessment of the main energy consumption and carbon footprint associated with the product or process. The emissions and advantages inside the system have been carefully balanced. The emissions, encompassing liquid (wastewaters and leachates), gaseous (flue gases emitted by generator units), and solid (pollutants found in the compost), were derived from primary data sources. Contrarily, the advantages derived from the composting facility, such as the reduction in fertiliser production and the recovery of metals, are derived from existing background information. The assumed functional unit for the life cycle assessment (LCA) is defined as one metric tonne of waste processed by the system, a widely employed metric in various environmental evaluations. [111], [285], [286]. Hence, different LCA analyses were carried out for a complete comprehension of the impacts as follows:

- The evaluation of the environmental performance of the initial configuration and the exploration of the impact of various operational factors through the application of the Monte-Carlo approach (MC);
- The present analysis aims to compare the impacts of the aforementioned system with those of a general sanitary landfill included in the Ecoinvent database, serving as a benchmark;
- a sensitivity analysis for the determination of the benefits introduced by the CHP unit coupled with the anaerobic digesters;
- the installation of a PV plant on the roof of the anaerobic digesters section. In this particular scenario, a Monte Carlo analysis is conducted to assess the impact of the variation in the data;
- the environmental impact resulting from the gasification of residual solid waste. Specifically, we will compare these impacts with secondary data obtained from the Ecoinvent database, which pertains to incineration and landfill treatment operations;
- the inclusion of microalgae implementation has not been considered due to the low amount of biomass produced in a laboratory. The results of Chapter 6 explained that the biomass yield from microalgae harvested in the synthetic medium was not enough to produce biofuels due to the high pH and high salt content. Therefore, the implementation of that technology could at maximum treat the wastewater, but with high costs and low revenue. Moreover, there is a limited use of the leachate in the medium, being only 7% v/v, with the leftover 93% attributed to the creation of the 3N-BBM medium. This will increase the overall amount of resources used in the process and hence may reflect a worse environmental footprint of the system.

7.2.3 *System Boundaries*

In this work, the LCA study was conducted according to the methodology described in the ISO standard 14044 [123]. A gate-to-grave approach [13] has been used in the description of the system as also shown in Fig. 7-1. In literature, different studies included also the contribution of waste collection and transport [285], [287], [288], here has not been included. The primary objective of this study is to quantify the direct emissions generated by the treatment facility. Specifically, the focus is on measuring the fuel consumption occurring within the facility's limits.

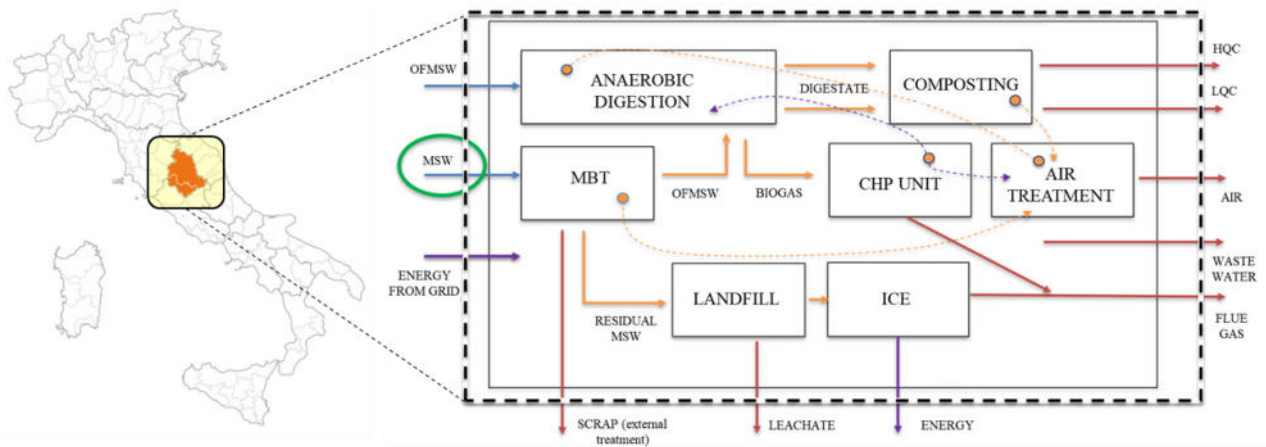


Fig. 7-1. Detailed diagram of the material and energy flows in the analysed domain (blue lines for energy and waste inputs, red for material outputs, violet for energy output, and orange for internal flows).

The system exhibits distinct sub-processes that are interconnected. As mentioned earlier, the system receives an annual input exceeding 100 kilotons per year of solid waste, which is divided into two primary input streams. The composting area receives an average annual quantity of 48 kilotons of waste, while the landfill immediately receives a second stream of 56 kilotons per year. As an initial measure, the MBT unit undertakes the process of refining the municipal solid waste MSW to further segregate the OFMSW. Subsequently, this segregated fraction is directed towards anaerobic digestion and compost generation. The quantity of residual waste generated by the MBT facility and subsequently disposed of in landfills is approximately 19,000 metric tonnes per year. The composting department generates a yearly production of 2,000 metric tonnes of HQC, along with 12,000 metric tonnes of low-quality compost LQC specifically intended for use as landfill cover. Additionally, the section produces 9,400 metric tonnes of digester sludge, 750 metric tonnes of biogas, 233 metric tonnes of recovered scrap metals, and 4,600 metric tonnes of liquid wastewater. Consequently, a total of 87 kilotons each year (comprising 56 kilotons of one type, 19 kilotons of another type, and 12 kilotons of still another type) of waste material is transported to the sanitary landfill in a diverse combination of residual municipal solid waste.

7.2.4 Inventory analysis

The system has been constructed based on primary data obtained from the company as well as supplementary data sourced from the Ecoinvent database. More accurately, the data has been annually-averaged, whenever feasible, based on the recorded energy, material, and emissions data over the period from 2019 to 2021. Secondary data are taken from the EcoInvent version 3.6 database [289], [290]. The simulations have been run with Simapro v. 9.1.1.8. The CML-IA baseline impact method [291] of the Institute of Environmental Sciences (CML) is chosen in the LCIA since it has

been commonly used in several studies [116], [285], [292], [293]. The material and energy flows have been modelled according to Fig. 7-1. Various emissions points were taken into account at the site, encompassing a range of both liquid and gaseous pollutants. Liquid emissions have a significant role in the context of wastewater, mostly originating from the composting process and landfill leachates. Gaseous emissions, on the other hand, mostly pertain to the air treatment unit. To prevent overpressure and the release of odorous emissions into the surrounding environment, a total of six scrubbers are employed to collect air from the MBT, digesters, and compost stabilisation section. Additional sources of gaseous emissions can be found in the CHP and ICE sub-sections. In these areas, the flue gas is continuously monitored to ensure compliance with legal restrictions. It is postulated that the soil emissions consist of contaminants, such as metals, that are found in high-quality compost.

7.2.4.1 Residual solid waste characterization

The MBT unit is considered the most crucial aspect of the composting facility. The process involves shredding and sorting the municipal solid waste. The organic component is also segregated and subsequently directed towards stabilisation and composting in conjunction with the OFMSW. The residual matter consists of a heterogeneous mixture of various components, including plastics, paper, and textiles, with a minimal presence of metals and glass. Based on a comprehensive set of examinations conducted from 2019 to 2021, it was determined that the processed waste exhibited an average composition consisting of 45% unrecovered plastics, 27% paper, and cardboard, 13% textiles, 5% diapers, 4% leather, and the remaining percentage attributed to miscellaneous elements.

7.2.4.2 Energy production and biogas profile

Biogas is produced from the anaerobic digestion plant and the actual sanitary landfill. The amount of biogas produced, and consequential energy production are reported in chapter 2.

7.2.4.3 Electricity and fuel consumption

The equipment utilised in the operation necessitates a uniform quantity of energy. The range of the ratio between electric generation from CHP and the input of energy in the system varies from 3.5% in the worst-case scenario to 52% in the best case scenario. Every month, the average ratio is 21%. The aforementioned number has been utilised in the assessment of the energy demand of the system, specifically amounting to 4.5 GWh. **Errore. L'autoriferimento non è valido per un segnalibro.** reports the distribution of the energy consumption in the relevant sub-systems of the site.

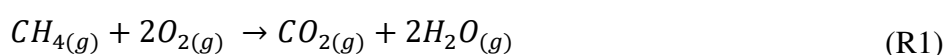
Table 7-1. Energy distribution in the system boundary.

Activity	Amount [mg/Nm ³]		
	Nominal Power [kW]	Annual Consumption [kWh]	% of the total
Anaerobic Digesters	50	247,800	5.5
Volumetric Dome	82	467,400	10.4
Biofilter	585	2,160,200	48.1
Aerobic stabilization	114	441,300	9.8
Biotunnel	105	483,300	10.8
Landfill	75	197,900	4.4
Waste pre-treatment	203	496,500	11

Diesel and Liquid Petrol Gas (LPG) are used in the process as well. LPG, however, is destined to office heating only, and the quantity is negligible (1.76 tons) compared to the annual diesel consumption: 200 m³/year for machinery operations (internal movement, shredding, digestate mixing, company vehicles) and 35 m³/year for anaerobic digestion in a back-up boiler. The thermal power generated by the CHP unit involved a 37% reduction of the diesel consumption required by the anaerobic digestion. Despite the positive outcome in terms of fuel savings, the CHP operates at partial load. Primary data on instantaneous operability, e.g. on CHP and biogas storage, is not given, and only a qualitative assumption of continuous operation has been formulated. In this context, it has been estimated that the electrical efficiency ranges from a minimum value of 0.22 to a maximum of 0.34, lower than the efficiency of 50% load. The characterization of the energy commodity has been done according to the data of the municipality [27] where the facility is built.

7.2.4.4 Gas Emissions

The data on the gaseous emissions are reported in Chapter 2. The company did not provide either the biogas or flue gas composition. The quantification of CO₂ resulting from the combustion of the methane part of biogas has been achieved using a simple chemical methodology. Because these emissions originate from a renewable source, these substances have been designated as biogenic sources. [294]. The following reaction (R1) implies the determination of CO₂ and water after methane combustion in the CHP and ICE once the biogas composition is known.



The data given by the company does not specify a clear composition of the biogas from the landfill and the anaerobic digestion. According to previous studies [118], [121], [295]–[297], a typical composition of biogas may have 50-60% of methane content, and the residual fraction as carbon

dioxide. In this study, the composition has been reconstructed based on the values of the biogas net volume and mass, i.e. V [Nm^3] and M [kg], its density ρ [kg/m^3], and the monthly averaged energy production from the CHP and ICE, E . The mass balance is easily obtained according to equation 7.1, where the subscript i either stands for Anaerobic Digestion (AD) and Landfilling (LF), ρ is expressed at the normal conditions ($0.72 \text{ kg}/\text{m}^3$ for methane and $1.87 \text{ kg}/\text{m}^3$ for carbon dioxide), while other minor elements like nitrogen and oxygen are neglected:

$$M_i = \rho_{CO_2,i}V_{CO_2,i} + \rho_{CH_4,i}V_{CH_4,i} \quad (7.1)$$

The average biogas yield, α_i [kWh/m^3] can be defined as the ratio of the total energy produced, E [kWh], and the total volume of biogas V produced reduced by the biogas sent to flares. Equation 7.2 can be derived by certain manipulations and thereafter employed for the estimation of methane and carbon dioxide concentration.

$$V_{CH_4,i} = \frac{\rho_{CO_2,i}E_i - \alpha_i M_i}{\alpha_i(\rho_{CO_2,i} - \rho_{CH_4,i})} \quad (7.2)$$

7.2.4.5 Liquid Emissions

Similarly to the airborne pollutants, the leachate and wastewater compositions have been considered as the main liquid emissions of the system. On average, $11,000 \text{ m}^3$ of leachate and $4,600 \text{ m}^3$ of wastewater are sent to external treatment plants. The compositions are reported in Table 2-3 and Table 2-4.

7.2.4.6 Soil Emissions

Soil emissions are assessed according to the composition of the HQC multiplied by the annual production (2,082 tons). The nitrogen content of the compost is around 95% on a dry basis. Further details about compost composition are reported in Table 2-6.

7.2.5 Impact categories and Life Cycle Impact Assessment

The primary objective of a LCA study is to evaluate the environmental impacts using a designated characterisation approach. As per the methods outlined in the CML-IA baseline V3.06, a total of eleven impact categories have been established as intermediate indicators. The indicators used in this study include Abiotic Depletion (AB) [kg Sb_{eq}], Abiotic Depletion from fossil fuels (ABFF) [MJ], Global Warming Potential (GWP) [$\text{kg CO}_{2\text{eq}}$], Ozone layer Depletion (ODP) [$\text{kg CFC-11}_{\text{eq}}$], Human Toxicity (HT) [$\text{kg 1,4-dB}_{\text{eq}}$], Fresh-Marine water Ecotox (FW-MWEX) [$\text{kg 1,4-dB}_{\text{eq}}$], Terrestrial Ecotox (TRES) [$\text{kg 1,4-dB}_{\text{eq}}$], Photochemical Oxidation (PHOX) [$\text{kg C}_2\text{H}_{4\text{eq}}$], Acidification (AC)

[kg SO_{2eq}], and Eutrophication (EU) [kg PO_{4eq3-}]. Some of these midpoint indicators are present in other studies [122], [125], [126], [293] where the interpretation of the analyses is based upon GWP, ODP, AC, EU, PHOX, and HT. The Environmental Footprint (EF) 3.0 method is adopted for the impact assessment of the gasification system in terms of endpoint indicators. Each impact category is considered without a detailed subgroup influence (biogenic, fossil, organic, etc). Hence the environmental load of the system is described by fifteen midpoint indicators, some of which are already present in the CML baseline. These are Acidification, Climate Change (CC) [kg CO_{2eq}], Freshwater Ecotoxicity, Eutrophication (terrestrial and marine, fresh waters), Human Toxicity, Ionizing Radiation (IR) [kBq U-235_{eq}], Land Use (LU) [-], Ozone Layer Depletion, Particulate Matter [-], Photochemical Ozone Formation, Fossil Resource Use (RE-FU) [MJ], Mineral-Metal Resource Use (RE-MM) [kg Sb_{eq}] and Water Use (WU) [m³]. No modification of the weights associated with the method is applied.

7.3 Results and discussions

The findings of the LCA assessments have been documented in this particular area. The investigation of the fundamental case scenario is derived from the available inventory data. The simulation results are corroborated by three additional investigations. These investigations include an assessment of sensitivity scenarios, a comparison with a sanitary landfill using secondary data from Ecoinvent, and a quantification of data uncertainty using the Monte-Carlo method, which is implemented in Simapro as a default feature. Additionally, a sensitivity analysis has been conducted to evaluate the potential impacts of installing a solar plant on the rooftop of the digesters. The objective of the analysis is to examine the potential decrease in electrical energy consumption in waste treatment, which has significant practical value. The Monte-Carlo approach is employed as a supplementary tool to the primary findings derived from the environmental evaluation of integrating the photovoltaic plant, similar to its application in the base case scenario. The final portion addressed in this chapter presents an analysis of the advantages that can be obtained through the gasification of RDF and the subsequent utilisation of the resulting syngas for energy generation in a steam power plant. The findings are presented based on the mass and energy equilibrium of the system, and a comparative analysis of the various treatment methods is provided to facilitate a comprehensive understanding of the environmental impact associated with each treatment system. In addition to the environmental assessment of the photovoltaic plant, the construction materials considered in the Ecoinvent database include concrete and steel structures, piping, and machinery. It is important to note that the scenarios analysed in this study do not take into account the impact of the construction process itself. However,

it should be noted that these materials have a design life exceeding twenty years, indicating that the environmental loads associated with their construction would be relatively insignificant compared to the operational phase of the plant. In addition, the consideration of long-term emissions has not been accounted for.

7.3.1 Base case Scenario

The environmental analysis of the base case is presented in Fig. 7-2. The system utilises various hues to emphasise and distinguish each subprocess that has been simulated. The initial outcome arises from the system expansion methodology, which results in a favourable environmental impact by substituting the manufacture of nitrogen fertiliser (shown by the dark red colour) with the sale of HQC in the market. Additional positive contributions to the environmental burden include the utilisation of energy derived from the burning of biogas in the internal combustion engine (cyan) and combined heat and power unit (yellow) situated within the landfill. Furthermore, a small quantity of scrap steel is recovered in the mechanical-biological treatment unit (bright red). The maxima reductions obtained are ODP -42%, ABFF -38%, AC -25%, and -15% for AB. The nature of the material deposited in the landfill is heterogeneous, consisting of organic matter, paper, and non-recyclable plastic. The non-recyclable plastic constitutes around 45% of the total mass. The disposal of waste plastic mixtures in landfills is a significant source of environmental burden across various categories. The indication of terrestrial ecotoxicity is primarily contingent upon the contaminants present inside the Hazard Quotient Calculation (HQC). The observed pattern aligns with the findings presented in [125] wherein the implementation of compost and steel recovery methods resulted in a notable reduction in the overall environmental impact of the composting system. GWP, ODP, and PHOX are lower, as follows: 137.35 vs 1081 kg CO_{2eq}, 2.18E-06 vs 4.8E-05 kg CFC-11_{eq} and 0.026 vs 0.185 kg C₂H_{4eq}. Since the impact of transportation and plastic bags is not included within the system boundary, it is difficult to perform a clear comparison. The GWP in Cadena [126] is, instead, lower (63 kg CO_{2eq}) whereas EU is far higher (7.13/3.7 vs 0.138 kg PO_{4eq3-}). The studies [125], [126] report a similar amount of HT (15.86/14.54 vs 13.95 kg 1,4-DB_{eq}).

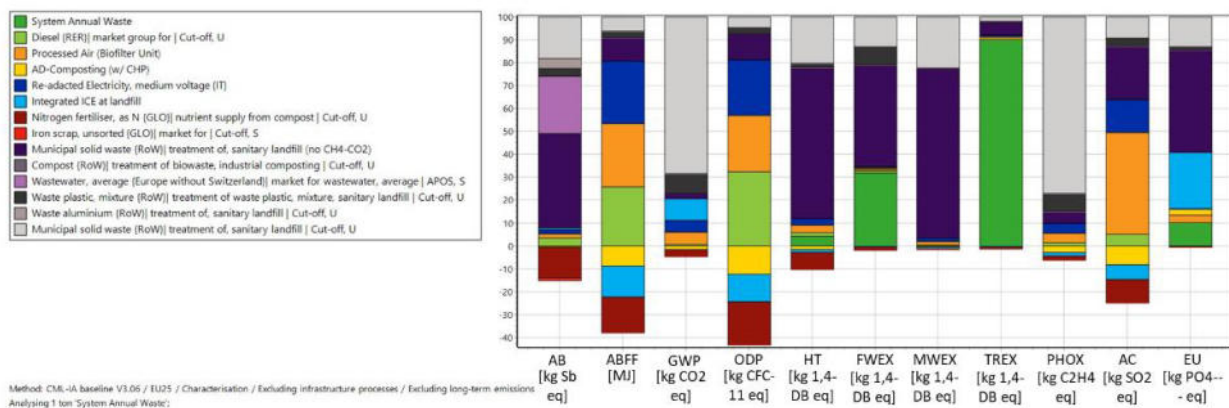


Fig. 7-2. Results of the LCA for the facility under investigation (colors represent the different subprocesses).

The values of the impact categories reported in Fig. 7-2 MWEX (172603 kg 1,4-DB_{eq}) represent the main impact and it is associated with the waste disposed at the landfill. The index provides an estimation of the enduring contamination of the aquatic ecosystem, encompassing rivers, oceans, and groundwater sources. Hence, the breach of the safety-containment layers of the LF landfill has the potential to result in enduring environmental harm. Following the first impact category, the subsequent category is Eutrophication and Global Warming. If the MWEX index is excluded from consideration, the resulting allocation percentages for the other effect categories are as follows: EU 47.92%, GWP 25.8%, TREX 6.89%, ABFF 6.7%, FWEX 4.84%, AC 4.45%, PHOX 2.75%, HU 1.63%, AD 0.1%, ODP 0.02%.

7.3.1.1 Monte Carlo Analysis

In a LCA study, it is imperative that the data utilised is both consistent and numerous, with several measurements being linked to each individual process. Nevertheless, it is not always feasible to achieve this objective. In such cases, a Monte-Carlo Analysis can be employed to assess the effects of input values on the various impact categories. The Monte-Carlo methodology utilises a computational technique to determine the aggregate probability of an intricate system that is affected by a collection of variables, each possessing its own probability distribution. The proposed approach offers a simplified mathematical formulation, as the inclusion of random variables in algebraic calculations would necessitate increased computational resources for systems with several parameters. The evaluation of the simulation error is conducted based on equation 7.3, where σ_M is the standard deviation of the mean, σ the deviation of the system generated data, and N is the number of samples.

$$\sigma_M = \frac{\sigma}{\sqrt{N}} \quad (7.3)$$

It is advisable to consider suitable probability density functions to provide the most accurate representation of the data. The normal distribution is considered in this model, taking into consideration the historical temporal data series, if feasible. The data exhibiting a notable deviation has been represented by a uniform distribution centered around the mean value of the provided data. Through the execution of 30,000 iterations, it was determined that the overall standard error reached a level below 10E-6, ensuring a high degree of precision. Furthermore, a 95% confidence interval was established to provide a reliable estimate of the true population parameter. Table 7-2 reports the results of the MC analysis while Fig. 7-3 depicts the characterization and normalisation of the impact categories. The facility performances can be characterised by best- and worst-case scenarios when attention is directed on the maximum extent of variation in each impact category. The terrestrial ecotoxicity is the most significantly impacted aspect, which is associated with the presence of trace pollutants in the HQC system. Fantin et al. [122] reported lower variations for ODP, EU, and resources depletion, the latter with the highest coefficient of variation (111%). The increased volatility of the index could also be attributed to the impact of the pandemic, as the implementation of limitations has resulted in the closure of neighboring treatment systems and subsequently led to a greater volume of waste being deposited at the landfill site. Consequently, the production of biogas and compost has also been impacted in terms of their quality and content. The normalisation process demonstrates a greater degree of variation for MWEX, FWEX, and EU, as anticipated.

Table 7-2. Outcome of the Monte-Carlo simulation.

Impact Factor	Monte Carlo Analysis – Variation in percentage terms	
	Best Case	Worst Case
Abiotic depletion	-33%	64%
Abiotic depletion (fossil fuels)	-25%	24%
Acidification	-23%	44%
Eutrophication	-44%	97%
Freshwater aquatic ecotox.	-58%	140%
Global warming (GWP100a)	-41%	71%
Human toxicity	-54%	108%
Marine aquatic ecotoxicity	-52%	100%
Ozone layer depletion (ODP)	-43%	76%
Photochemical oxidation	-47%	81%
Terrestrial ecotoxicity	-66%	246%

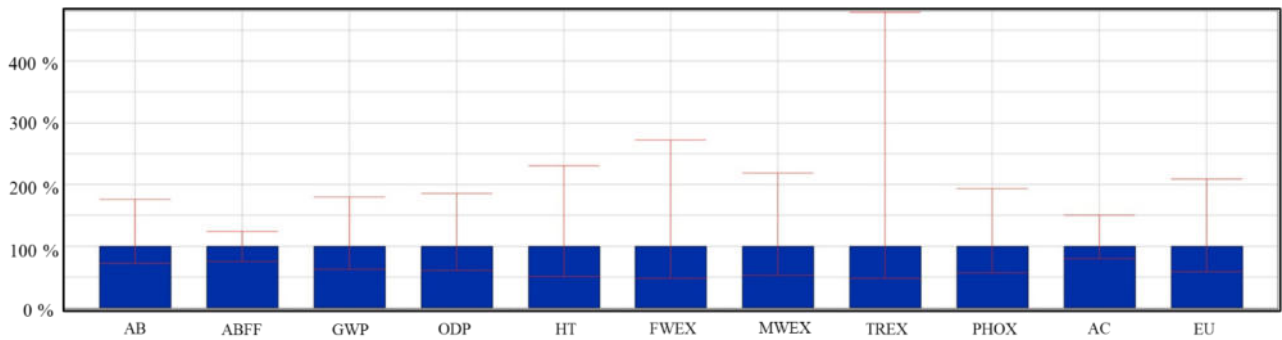


Fig. 7-3. Impact factors vary according to the results of the uncertainty analysis. There is a non-negligible deviation of the data.

7.3.1.2 System Comparison with Ecoinvent database

The significant quantity of waste being disposed of in landfills, amounting to 87 kilotons per year, results in a substantial proportion of environmental consequences associated with this particular waste management method. To address this matter, a comprehensive analysis has been conducted to compare the system under consideration with a sanitary landfill that is documented in the Ecoinvent database. The primary findings of this comparison are depicted in Fig. 7-4

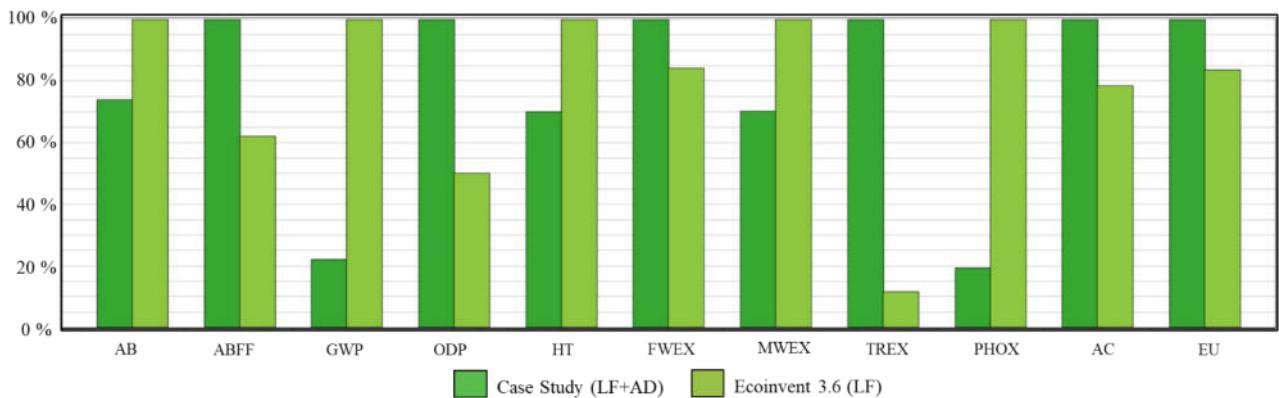


Fig. 7-4. Comparison of the impact categories in the facility under investigation with those of a standard sanitary landfilling treatment process.

Various factors can contribute to the superiority of a certain effect category in one scenario over another. Regarding the matter of abiotic depletion, it is observed that the composting process combined with MBT yields a positive benefit of 25% in terms of both material and energy recovery. However, this positive outcome does not extend to ABFF. In the context of a conventional sanitary landfill, the utilisation of fossil fuels for waste compaction and movement is evident, but there is no corresponding thermal demand. In contrast, anaerobic digestion necessitates the application of heat to sustain an optimal internal temperature conducive to the activity of degrading bacteria, as indicated by a notable increase of approximately 54% in the index. The histogram fails to adequately represent

the primary factors influencing fuel consumption and the utilisation of fossil fuels in the energy composition of the municipality in which the facility is situated. The ODP index may be similarly attributed to fossil fuel burning due to a minor correlation. The process of energy recovery and biogas combustion has a favourable impact on global warming, resulting in a reduction of around 75%. Regardless of whether the biogas is biogenic or not, this compound contributes to the warming of the atmosphere. In the context of HT, there is a desire to achieve a 30% decrease in many parameters, including gaseous emissions, power usage, and liquid emissions. The observed disparity between the FWEX (+18%) and MWEX (-30%) trends is a subject of controversy. The decrease in MWEX can likely be attributed to the reduced waste associated with each unit of functional output. Conversely, the increase in FWEX may be linked to the wastewater generated during the composting process, which is subsequently treated externally alongside landfill leachates. About the TREX, it exhibits a notable surge of 733% attributed to the presence of contaminants in the compost and their association with soil emissions. Conversely, the PHOX experiences a substantial decrease of approximately 80%. Lastly, eutrophication demonstrates a modest increase of 16%. The effect categories MWEX, GWP, and EU are the most influential. The uncertainty analysis performed concerning this comparison is reported in Fig. 7-5. The utilisation of the Ecoinvent database results in a reduction of environmental effects across various categories.: AB 15.17%, ABFF 98.43%, AC 84.83%, EU 58.33%, FWEX 37.9%, GWP 0%, HT 56.77%, MWEX 41.16%, ODP 99.2%, PHOX 0%, TREX 62.5%.

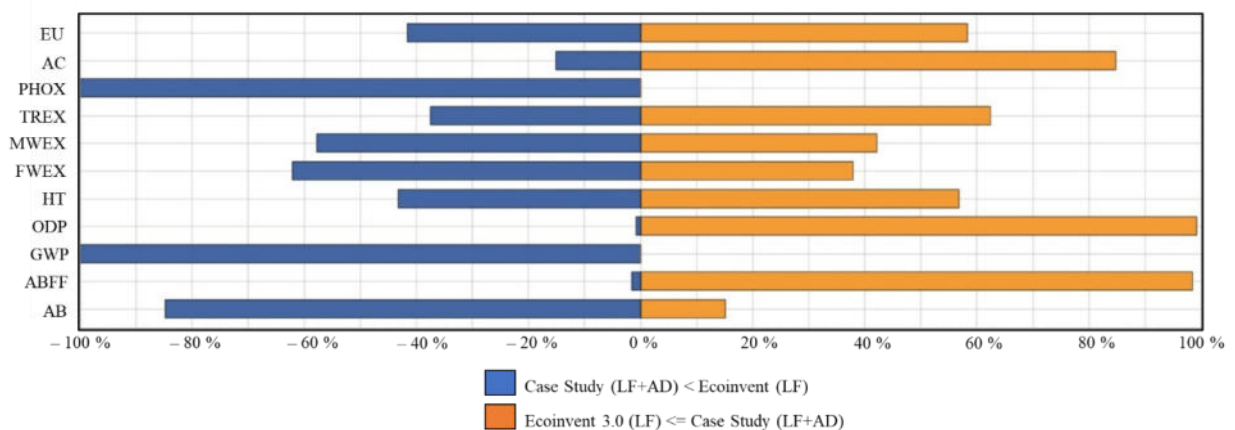


Fig. 7-5. Sensitivity analysis between the base case system (blue color) and that with Ecoinvent data (orange).

7.3.2 Sensitivity Analysis

The final sensitivity analysis pertains to the operability of the CHP unit in the base case scenario. To date, the CHP unit has predominantly operated under part-load conditions, with its highest power production in 2020 reaching 235 kW_e. Consequently, it is vital to evaluate the actual environmental advantages associated with its operation. A comparative analysis is conducted between the base case

and the scenario without the CHP unit. It is observed that the construction of the CHP unit resulted in a significant reduction in diesel consumption for heating the anaerobic digesters. Specifically, the consumption decreased by approximately 40%, from 27,000 l to 17,000 l per year. Concerning the scenario without the CHP unit, the following assumptions are considered: i) no electricity is produced; ii) no thermal energy is available to substitute the fuel used in the anaerobic digestion; and iii) direct atmospheric emissions due to methane combustion in the safety flare, according to equation 7.1. As can be noticed in Fig. 7-6, four impact indexes (ABFF, ODP, AC, and GWP) benefit significantly from the use of the CHP unit. In details, the GWP impact reduces of about 9% (151 to 137 kg of CO_{2eq}), AC of 25% (0.185 to 0.138 of kg C₂H_{4eq}), ODP of 31% (3.17E-6 kg CFC-11 to 2.18E-6) and ABFF of 46% (426 MJ to 231 MJ). Minor reductions (0-5%) are obtained for the other impact categories (PHOX, AB, HU, FWEX, MWEX, TREX, EU) as expected. The Monte-Carlo analysis confirms the benefits stated above. Indeed, four out of eleven indicators perform better in 100% of the total cases (ABFF, AC, ODP, and GWP), followed by PHOX (86%), AB (80%), and TREX (76%). The sensitivity analysis does not consider the impacts of eutrophication, human toxicity, and the effects on fresh and marine water. These impact categories are solely influenced by liquid emissions and waste disposal practices at the landfill. The changes in terrestrial toxicity are minimal, as it is mostly associated with the HQC.

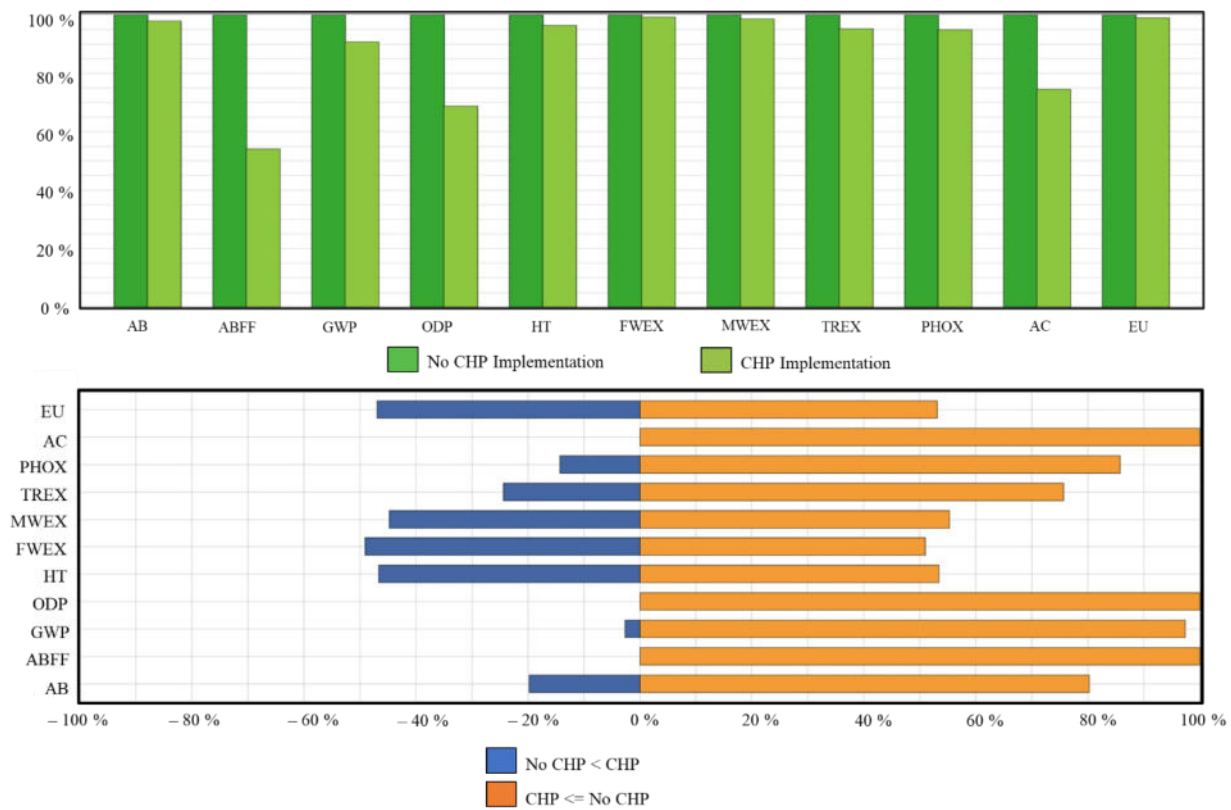


Fig. 7-6. Comparison analysis of the system with and without the CHP functioning.

7.3.3 Photovoltaic implementation

The second type of renewable energy investigated in this paper is the integration of a photovoltaic (PV) plant on the digesters' rooftops. As depicted in Fig. 7-7 the PV plant is partitioned into two distinct sections, denoted as blocks A and B, as a result of the existence of certain obstructions. Block A consists of 185 modules (5x37). On the other hand, block B comprises 373 (11x33), along with an additional string containing 10 modules. Considering a power nominal capacity of 330 W per panel [298], the total power of the PV plant is about 184 kW. Therefore, it can be anticipated that the considered location will generate an annual electricity production of around 232,000 kWh, constituting approximately 5% of the total electricity demand of the entire system. This is equivalent to a savings of 43.4 tonnes of oil equivalent (TOE). The findings of the LCA investigations are presented in Fig. 7-8. The PV plant has a modest impact on three specific impact categories, namely the AP, ODP, and AC. It results in a decrease of 6% in AP, 5% in ODP, and 2% in AC. The electricity generated from photovoltaic (PV) systems has been found to have a favourable impact on categories associated with the usage of fossil fuels, such as the ABFF and ODP but not much to the GWP which has a positive variation of 1% only. The higher variations of the indexes above are also in the tornado chart of Fig. 7-7. AC (85.77%), ODP (77.33%), and AC (75.07%) are the most affected indexes in the photovoltaic implementation, followed by GWP (55.93%), PHOX (54.17%), AB (53.57%) and TREX (51.77%). No other impact categories will be affected as there are no anticipated variations in the waste process treatment or negative effects on land usage, given that the solar panels are situated on the facility rooftop.

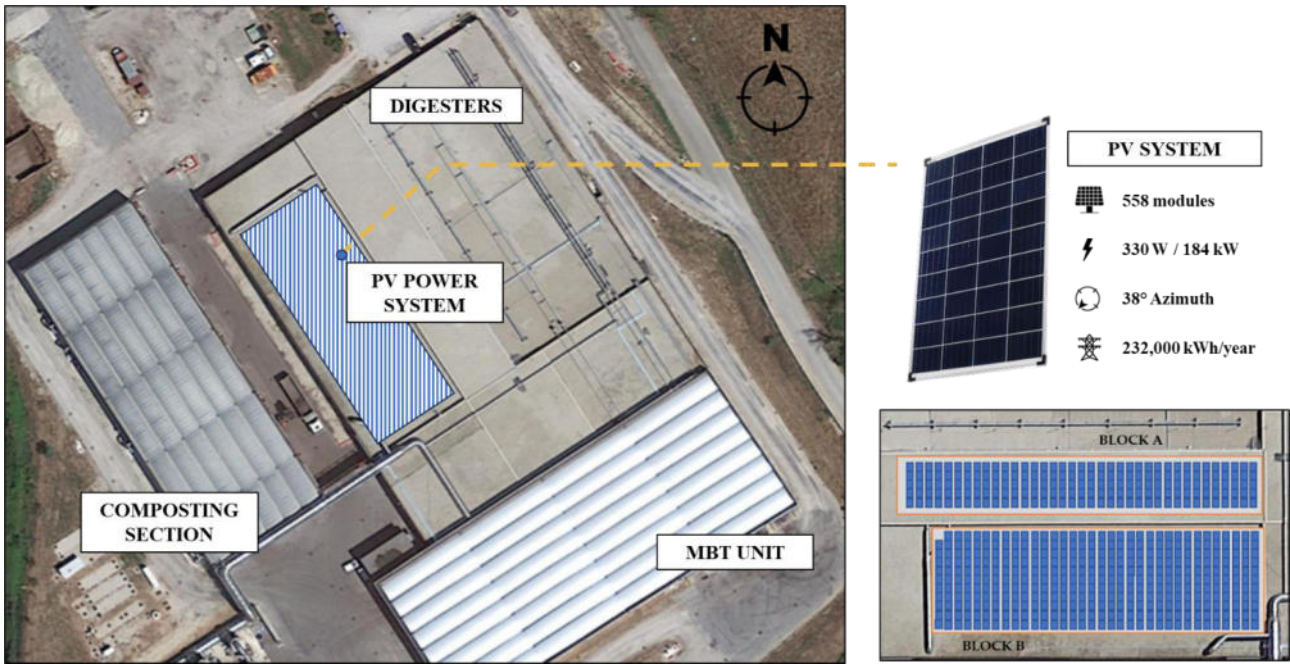


Fig. 7-7. Top view of the proposed PV plant above the facility rooftop.

Based on the available literature, it appears that there is a lack of LCA studies that specifically examine the incorporation of PV technology within waste treatment plants. Conversely, several inquiries have been conducted within residential structures. For example, the work of Herrando et al. [299] compared different LCA scenarios related to PV implementation in residential areas finding a CO₂ emissions reduction of 29% with a PV plant able to cover 35% of the total energy consumption of the building in the Mediterranean climate. Nevertheless, as emphasised by Roux et al. [300], PV systems have the potential to result in minimal fluctuations in carbon emissions if the production-side energy market is predominantly composed of renewable sources.

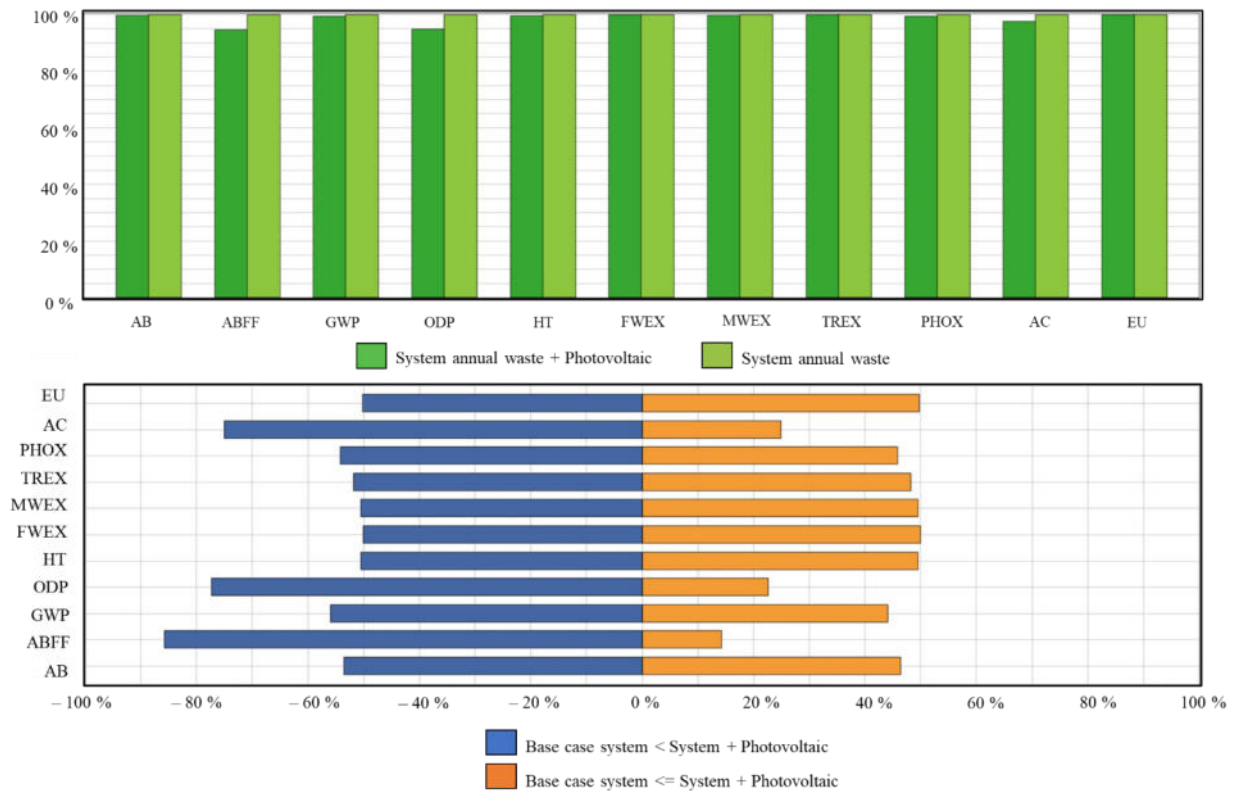
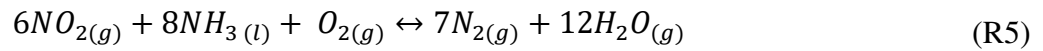
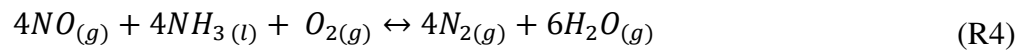
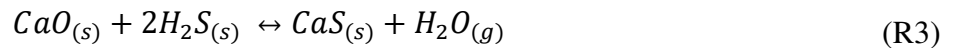
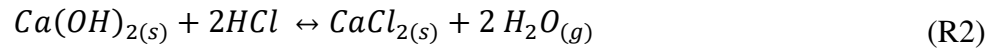


Fig. 7-8. Uncertainty analysis related to PV implementation.

7.3.4 Gasification process implementation

While combustion is the prevailing approach in waste-to-energy practices, pyrolysis and gasification methods provide more ecologically sustainable alternatives. Conventional incineration systems are known to emit substantial quantities of carbon dioxide and nitrogen oxides into the surrounding environment. Moreover, the diverse composition of MSW can lead to a substantial range of variance in the heating value of the fuel. In contrast, gasification is a process that transforms a feedstock material primarily composed of solids into syngas, resulting in reduced emissions as a consequence of the limited air utilisation during the conversion. The most common chemical reactions that take place during the gasification process both heterogeneous reactions (Boudouard, Water-Gas, Hydrogasification) and homogeneous ones (Water-Gas shift, Methanation, Reforming) evolve parallelly inside the gasifier in a complicated interaction. The thermodynamical model is utilised to forecast the quantity of syngas generated from 20,000 metric tonnes per year of RDF. The characteristics of the RDF material are determined by analysing the chemical composition of the RMSW generated in the MBT facility being studied. More precisely, 2,281 kg/h of RDF enters the gasifier following the energy conversion process shown in Fig. 7-9 in which the most significant process parameters are reported. Specifically, the syngas is directed towards an external combustion

chamber (combustion efficiency $\eta = 0.95$, recirculation factor $x = 0.2$) and the flue gas enters the shell-and-tube evaporator of the steam power plant, which works according to a single pressure level Hirn cycle (turbine inlet temperature of 500 °C, medium pressure 70 bar). Activated Carbons, Ca(OH)_2 and CaO , and ammonia (NH_3) are used in the gas cleaning section for the acid compounds removal (H_2S and HCl) at 250°C [301]. The following reactions have been used to estimate the amount of solids used in flue gas cleaning [201], [302], [303]:



The steam power plant has a nominal electrical power output of 1,500 MW and a thermal power output of 3,700 MW and a capacity factor of 0.8 is assumed for the subsequent calculation. The inventory analysis is based on the system boundary defined in Fig. 7-9, where the green and grey colours are used for material-based inputs and outputs and violet colour for energy streams (straight line for electrical type and dashed for thermal one). The total amount of air required in the gasification (primary air) and the combustion (secondary air) is about 33,500 kg/h. The flue gas is composed by carbon dioxide (3,098 kg/h), vapor (1,858 kg/h), oxygen (4,984 kg/h), and nitrogen (25,740 kg/h); 14 kg/h of activated carbon (lime) and ammonia are used for the removal of acid compounds, and the overall quantity of ashes and unreacted char produced is equal to 136 kg/h.

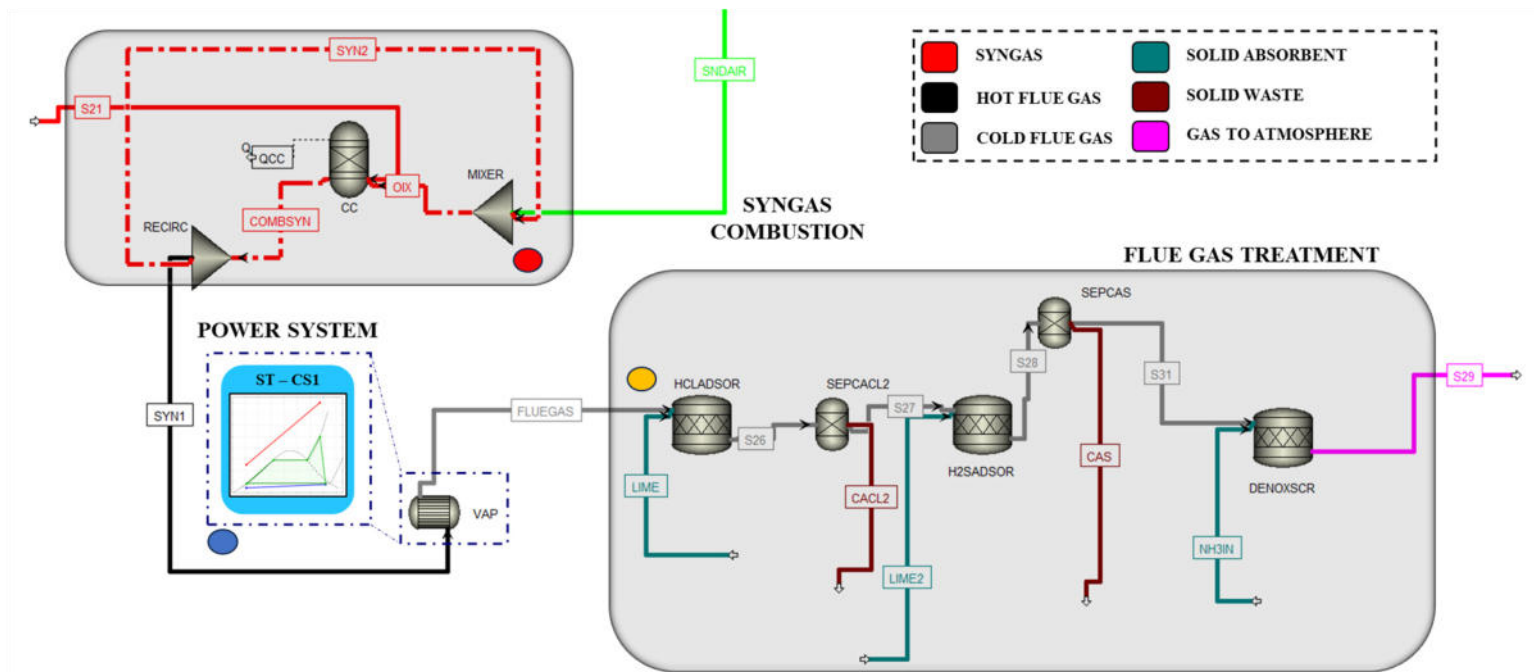
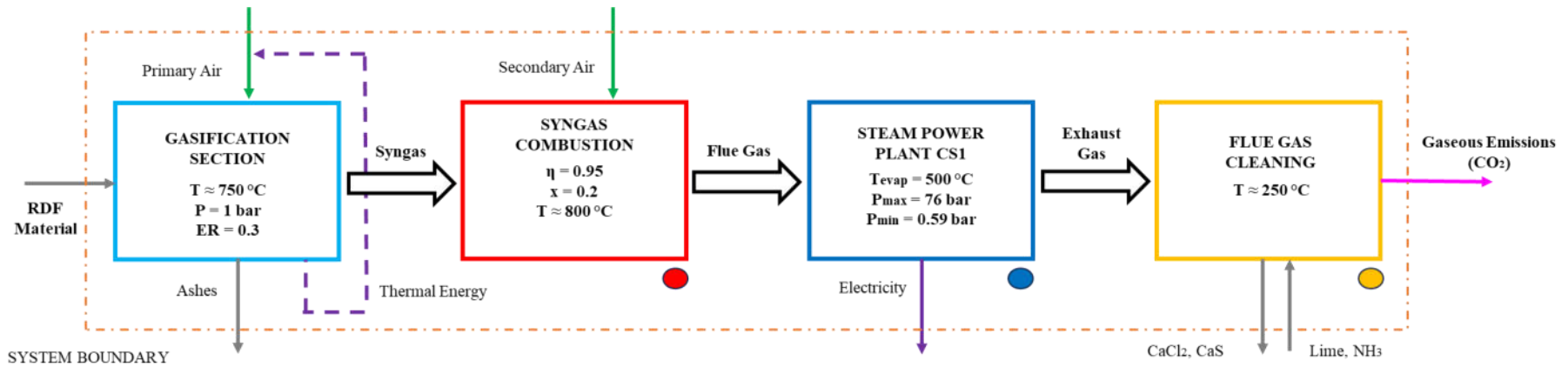


Fig. 7-9. Process diagram of the gasifier combined with the steam power plant unit.

The results of the corresponding LCIA are reported in Fig. 7-10. The RDF gasifier system is compared with the base case scenario, with an incineration system (Italy background data) and a standard sanitary landfilling in Europe. In general, incineration is the worst solution for most of the impact categories (AB, ODP, HT, FWEX, MWEX, TREX, AC), landfilling for GWP and PHOX while the basic system for the ABFF. The gasification implementation does not dominate any impact category, but it is worse than the nominal scenario in terms of GWP emissions (+148%). The reason lies in the increased amount of CO₂ production due to the syngas combustion. However, this negative effect is counterbalanced by the lower amount of waste that is sent to the facility landfill. Indeed, the variations of the other indicators are: AB -11.7%, ABFF -5.1%, ODP -4.3%, HT -11.5%, FWEX -10.4%, MWEX -11.3%, PHOX -41.1%, AC -7.4%, EU -7.1%, calculated according to the data of Table 7-3.

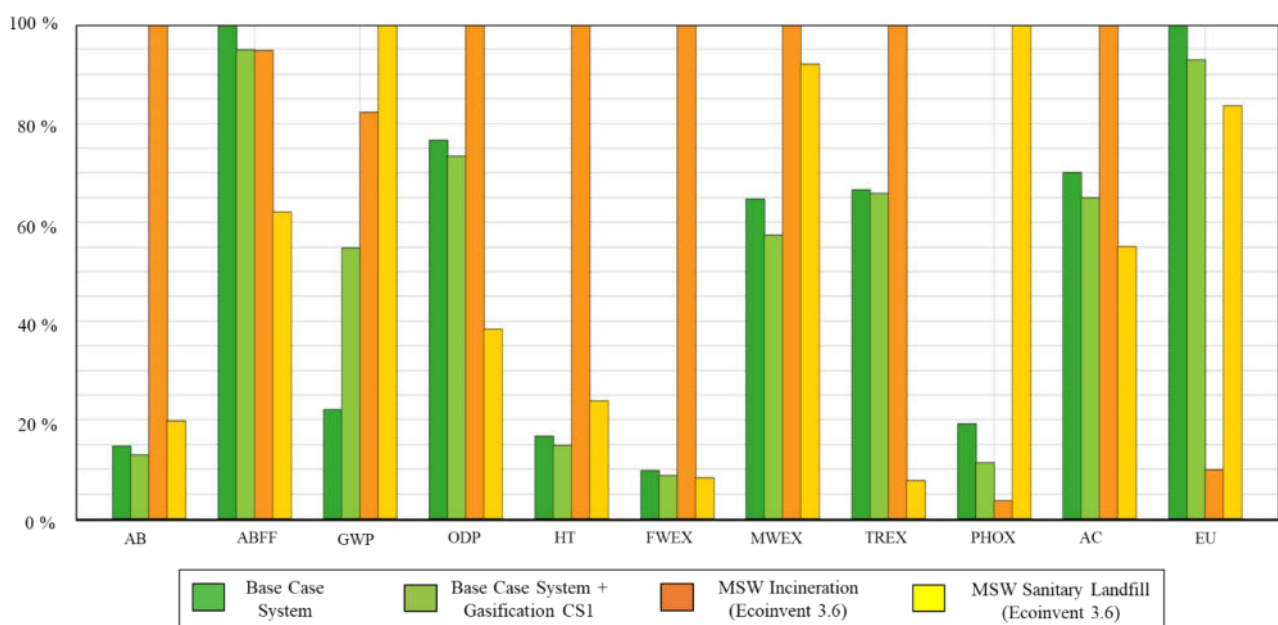


Fig. 7-10. LCIA of the facility integrated with the gasifier compared to incineration (orange) and landfilling (yellow).

Table 7-3. Characterization of the impact factors related to the scenarios compared to RDF gasification implementation.

Impact Factor	Characterization	Analysed Case			
		Base Case	CS1 Gasification	MSW Incineration	Sanitary Landfill
AB	[kg Sb _{eq}]	9.36864E-06	8.27272E-06	6.40124E-05	1.26672E-05
ABFF	[MJ]	230.9462169	219.2082479	218.839066	143.3276608
GWP	[kg CO ₂ _{eq}]	137.3503973	341.6060266	512.6599606	623.1065875
ODP	[kg CFC-11 _{eq}]	2.18394E-06	2.09094E-06	2.85011E-06	1.09273E-06
HT	[kg 1,4-DB _{eq}]	13.94518915	12.33623454	83.38466568	19.89651147

Impact Factor Characterization		Analysed Case			
		Base Case	CS1 Gasification	MSW Incineration	Sanitary Landfill
FWEX	[kg 1,4-DB _{eq}]	2.76645732	2.478190522	28.29727625	2.329612823
MWEX	[kg 1,4-DB _{eq}]	172,603.0985	153,098.0429	266,897.9012	245,536.5574
TREX	[kg 1,4-DB _{eq}]	0.365422428	0.361764419	0.549152347	0.042360738
PHOX	[kg C ₂ H ₄ _{eq}]	0.025667117	0.015116793	0.00487331	0.133445373
AC	[kg SO ₂ _{eq}]	0.138055157	0.127896305	0.196995917	0.108478345
EU	[kg PO ₄ ⁻⁻⁻ _{eq}]	0.696789395	0.647377113	0.069082204	0.582796912

In conclusion, Fig. 7-11 reports the endpoint indicator provided by the EF method for the various treatment systems.

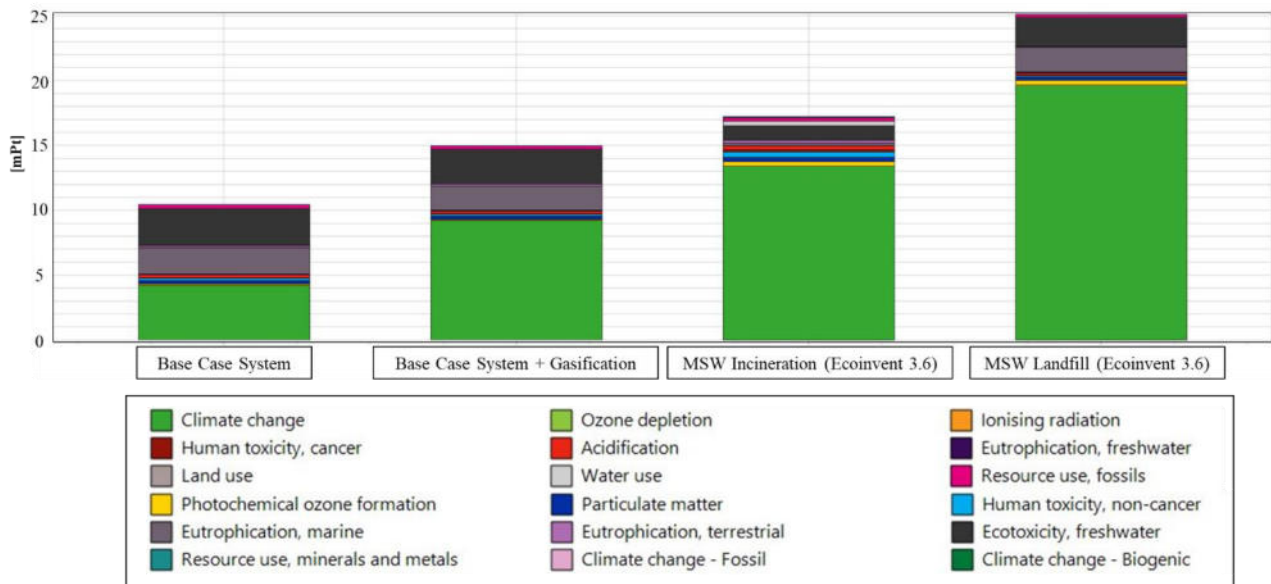


Fig. 7-11. Endpoint indicator (EF 3.0 method) for the different treatment systems.

The total score [mPt] for the systems is 10.45 mPt for the base case system, 14.99 mPt for the base case with gasification, 17.23 mPt for incineration, and 25.12 mPt for landfill. Compared to the CML method, which provided a significative difference between gasification and incineration related to different impact categories (AB, HT, FWEX, MWEX, AC), the EF method smooths the differences when the various impact categories are grouped. In numbers, the difference from the baseline is: +43.8%, +64.8%, and +140.3%. It is clearly shown that the governing impact category is climate change, which groups all the CO₂ emissions produced by the system. Concerning the base case, which has a climate change score of 4.20 mPt, the others present higher scores due to the thermal waste treatment or disposal (worst scenario), respectively + 119.2%, +218.5% and +367.7%. The difference between gasification and incineration is 45.3%.

7.4 Conclusions

The present study showcases an analysis that illustrates the potential reduction in environmental effects associated with the use of renewable energy technology and energy efficiency measures in a MSW composting facility. More precisely, the following main conclusions can be formulated:

- The utilisation of biogas derived from anaerobic digestion and sanitary waste in power units has the potential to mitigate the environmental impact of composting facilities across many categories. Specifically, in the examined case study, both the CHP and the ICE units contribute to a reduction of the ODP to up to -42%, of the ABFF to about -38%, of the AC to -25%, and of the AB of -15%;
- Even though the organic portion of MSW's quality might exhibit significant fluctuations, encompassing several impact categories as TREX LB and UB +246%, its conversion into valuable material by anaerobic digestion yields evident advantages from an ecological perspective;
- The PV incorporation at the examined location has a modest effect on diminishing the ecological footprint, with a reduction of 6% for ABFF and 5% for ODP. This outcome is mostly attributed to the constrained surface area offered by the existing roofs;
- the RDF gasification and the use of the produced syngas in a conventional steam power plant have a significant influence on many impact categories. In particular, for the case study under investigation, characterized by 20 ktons/year of RMSW, corresponding syngas production can add 1.5/3.7 MW of power capacity determining consistent variations of AB -11.7%, ABFF -5.1%, ODP -4.3%, HT -11.5%, FWEX -10.4%, MWEX -11.3%, PHOX -41.1%, AC -7.4%, EU -7.1%.

In summary, this study has demonstrated that the incorporation of energy efficiency measures and the integration of renewable energy technologies in composting facilities can significantly enhance environmental performance within the sector and promote global sustainable development.

Nomenclature

AB	Abiotic Depletion, kg Sb _{eq}
ABFF	Abiotic Depletion Fossil Fuel, MJ

AC	Acidification, kg SO _{2eq}
AD	Anaerobic digestion
CHP	Heat and Power cogeneration
CML-IA	Institute of Environmental Sciences (CML) Baseline Method
COD	Chemical Oxygen Demand, mg/l
e	Air excess
E	Energy production, kWh
EU	Eutrophication, kg PO _{4eq} ⁻⁻⁻
FWEX	Fresh Water Ecotoxicity, kg 1,4-DB _{eq}
GHG	Greenhouse gas (emissions)
GWP	Global Warming Potential, kg CO _{2eq}
HT	Human Toxicity, kg 1,4-DB _{eq}
ICE	Internal Combustion Energy
LB	Lower Bound
LCA	Life Cycle Assessment
LCI	Life Cycle Inventory
LCIA	Life Cycle Impact Assessment
LF	Landfill
LPG	Liquid Petrol Gas
LQC	Low quality compost
LQC	High Quality Compost
M	Mass, kg
MBT	Mechanical biological treatment unit
MC	Monte-Carlo
MSW	Municipal Solid Waste
MWEX	Marine Water Ecotoxicity, kg 1,4-DB _{eq}
N	Number of samples (Monte-Carlo)
ODP	Ozone Layer Depletion, kg CFC-11 _{eq}
OFMSW	Organic Fraction of Municipal solid waste
P	Pressure, bar
PHOX	Photochemical Oxidation, kg C ₂ H _{4eq}
RMSW	Residual Municipal solid waste
T	Temperature, °C

TOC	Total Organic Carbon, g/kg
TOE	Ton of Oil Equivalent
TON	Total Organic Nitrogen
TREX	Terrestrial Ecotoxicity, kg 1,4-DB _{eq}
UB	Upper Bound
V	Volume, Nm ³
VOS	Volatile organic Substances, g/kg
W2E	Waste to Energy
x	Flue gas recirculation

Greek Letters

α	Average biogas yield, kWh/m ³
ρ	Density, kg/m ³
η	Combustion efficiency
σ	Standard deviation
σ_M	Standard error of the mean (Monte-Carlo)

CONCLUSIONS AND FUTURE WORKS

Waste management has emerged as a critical topic within contemporary decades due to the substantial increase in waste generation resulting from human activities. To safeguard the environment and promote sustainable development, the implementation of efficient waste management strategies is of crucial significance. One of the primary objectives is to mitigate the environmental burden resulting from not optimal disposal of waste materials. There exist various approaches to effectively mitigate the impact of the end-of-life of most waste categories, including the adoption of specific treatment methods such as recycling, composting, and innovative technologies that enhance the valorisation of wastes into energy production.

Recycling is the best treatment scenario possible. It has the dual purpose of safeguarding valuable natural resources and reducing energy consumption and greenhouse gas emissions. However, it is not possible to recover any material and inevitable waste streams are still present. This is particularly evident in Mechanical-biological treatment systems, special facilities that sort and recover materials from municipal solid waste. Moreover, they can treat the organic fraction of municipal solid wastes and convert them into compost, a valuable resource that promotes sustainable agricultural practices and enhances soil productivity. In addition, the combination of composting with anaerobic digestion provides a sustainable biogas production that can be used for internal uses or converted into biomethane and sold to the grid. This “cold” waste treatment offers undeniably less airborne emissions compared to traditional “hot” waste treatments, which are typically represented by incineration. Thermal treatments provide a lower rank of valorisation compared to recycling, but there are noteworthy intrinsic advantages obtained by using them instead of direct landfilling.

The residual municipal solid waste produced by mechanical and biological units cannot be always sent to centralized incinerations. Reasons space between high cost of treatment, difficulty of transportation, and lack of specific and nearby infrastructures that can valorise the potential of this waste. Indeed, this material contains a considerable amount of plastic content and hence be considered as a particular waste-derived fuel. Therefore, the main goal of this research was to investigate other thermal treatment configurations that can be implemented in waste treatment systems similar to the one described in Chapter 2 and used as a case study. Fluidized bed municipal solid waste gasification with air is the solution assumed to answer the research question RQ1. A thermodynamic model was developed and calibrated in Aspen Plus according to literature data, then scaled to a 14 MW gasifier which is finally coupled with different power systems, i.e. traditional Hirn cycle, organic Rankine

cycles, and supercritical carbon dioxide Brayton cycle. Despite having a similar power production, the systems perform slightly differently according to the final energy use desired. When electricity is prioritized, steam cycles are to be chosen. If adaptability is the key aspect, ORC is the best choice while sCO₂ is the best system when priority is given to thermal usage. Moreover, the use of the latest generation of district heating networks increments the power production but penalises the thermal energy that can be delivered to the users linked to the network. In the best case, the provision of 1,000 dwellings can be satisfied. Due to the low cold gas efficiency, around 50% of the initial chemical energy of the waste is lost. The efficiency is lower than incineration because of the partial combustion reactions, but the environmental analyses conducted with the life cycle assessment methodology showed less emissions compared to the other thermal treatment. This result can partially answer the research question RQ4. The complete answer is addressed by additional sensitivity analyses set in the software Simapro. Despite the data used to describe the system being affected by a non-negligible dispersion, which is due to the relatively low timeframe of operation and influence of the Covid pandemic, some important results can be stated. Coherently to the literature, the implementation of renewable resources such as anaerobic digestion and photovoltaic can improve the footprint of these systems, in addition to the ones brought by compost production and material recovery. The air treatment section represents a hot spot of the system due to the high usage of electrical energy required to run the scrubbers. Therefore, the implementation of PV systems may provide only marginal improvements to the various impact categories.

Another residue produced during the treatment process is represented by liquid wastewater and leachates from landfills. These liquids are collected during the year and sent to external treatment. A way to treat in situ the wastewater in a sustainable way is of interest, in analogy to the residual municipal solid waste stream valorised with gasification. Microalgae represent a valid solution to the problem. Many studies in the literature reported a successful phytoremediation treatment of wastewater by using a variety of microalgae strains and growing conditions. While reducing the chemical oxygen demand and nitrate/phosphate concentrations, the resulting biomass can be used for biofuel production, either gaseous (stimulant of anaerobic digestion) or liquid (biocrude and biodiesel). The scope of the question RQ3 was exactly this. Different experimental campaigns were done in the laboratory to assess the growth behaviour of the microalga *Scenedesmus obliquus* in a controlled indoor photobioreactor, inside a medium composed of 7% synthetic liquid waste. Its composition was derived as a weighted average of wastewater and leachate compositions provided by the company of the case studio. The outcome of the analyses pointed out that the combination of a salty medium, without pH control, results in slow growth with little biomass expected to be

produced. The low amounts obtained in the laboratory posed a challenging assessment of the lipid profile (with gas-chromatography) and lipid content. Moreover, a numeric model was used to assess the utilities required for biodiesel production, showing that the complex lipid structure in the microalga oil can be a disadvantage factor in the process. Additional experimental analyses will be performed to optimise the biomass yield and numerically model other microalgae compositions to give consistency to the study.

Despite the limited benefits quantified with microalgae integration in the waste treatment process, this research pointed out the importance of adopting a circular economy approach centered upon biofuel generation. The last research question RQ2 expands the investigation of this topic by focusing on biomass pyrolysis. The pyrolysis can be used to generate biofuels from wood biomasses and can sustain with the heat that is not used to satisfy the demand of the district heating (cooling) network. The best pyrolysis integration is with the Hirn cycle since steam can be partitioned between the pyrolysis reactor and the steam turbine, but another possible configuration is by using the thermal power of the flue gases when the district heating demand is low. Every process involving biofuels must be numerically described properly. For this reason, a 0D fast pyrolysis model was developed in Matlab and validated concerning more advanced numerical models of small-scale pyrolysis reactors. The model describes the concentration evolution for different chemical elements produced in the various steps of pyrolysis and can follow instantaneous variations of the boundary conditions, like heat supplied or wood mass flow rate. The non-dimensional approach can be used for packed pyrolyzers but modifications of the model are required to deal with upscaled reactors. With the upscaled geometry, is it possible to convert 2,760 kg/h of wooden biomass into 1,054 kg/h of biocrude and 277 kg/h of biochar by using 1.5 MW of thermal power from the flue gases, i.e. 25% of the design condition. The response of the ORC system, chosen as the main power cycle due to its flexibility, is reduced accordingly.

The research activities on waste treatment will be concluded with a dedicated study of the scheduling and economic assessment of the system. The optimal point of operation of integrated waste facilities will be addressed by considering different sections (gasification, digestion, cogeneration, and so forth) interoperating under a variety of market scenarios. The inclusion of sewage sludge drying, a process that was not considered in this thesis, will be finalised in the future as a possible candidate for exploiting the waste heat and avoiding the partialisation of the gasification system. The problem will be constrained in terms of profitability and environmental impact.

ACKNOWLEDGEMENTS

After these three years, I still do not know what research is. I am not referring to the various methods and technical skills that a researcher will constantly learn and teach during his/her career, but to the intrinsic meaning of the word. If I have to make a comparison between what I was three years ago, and what I am now, then I can affirm that research provided something very valuable to me.

Several silent nights passed by, trying to figure out how to solve the complex problems reported in this thesis, in company of unpleasant and noisy thoughts. We face uncertainties almost every day. However, in this journey, I've found something that is definitely sure. The importance of listening. I was very lucky to have met people able to listen.

Dear Luca, Barbara, and Matteo, you had shown this quality. You have truly listened my voice when I was expressing my desires, my ambitions, my happiness, and sadness. You gave me opportunities and freedom, but at the same time continued to guide my path in academia with the tools of philosophical thinking. You have demonstrated what a Professor is. It was a fantastic journey, which I am very happy to have gone through together, from the beginning to the end.

Dear Evelyn, you once have said that it is not a coincidence that I came up to have a job which is constant research. It had always meant for me, because in parallel I was looking for something which I still do not know what is between justice, truth, or love. In analogy to the outcome of some studies in literature, I have just obtained more and more questions than the answers. However, you have thought to me the essential, yet difficult, importance of research our deeper needs inside us.

Dear Dad, thank you for being a hard worker. Life is not gentle with hard workers. I've understood the price of your sacrifices for providing us everything we needed. I hope that you are proud of me, everywhere you are.

APPENDIX I: MATLAB CODES FOR POWER CYCLES

This appendix presents some of the codes developed in Matlab for coupling the different power units to the RMSW gasifier. In particular, here it is reported the steam turbine configuration in design and off-design operation, ORC with recuperator and toluene as working fluid, sCO₂ Brayton cycle with recuperator. The summer variant has been reported, too, for the former. The other power unit configurations discussed in the Chapter 4 are slightly variants of the codes. The calculations of the NTU and ORC adimensional parameters are provided in an external Excel spreadsheet, not reported here.

STEAM TURBINE POWER CYCLE

```
close all
clc
clear
Fluid = 'water';
```

flue gas conditions - DESIGN

```
T_in_HF = 800; %C;           %input
T_out_HF = 250; %C;         %input
T_in_HF = T_in_HF + 273.15; %K;
T_out_HF = T_out_HF + 273.15; %K;
```

water critical properties

```
T_crit = CoolProp.PropsSI(Fluid,'Tcrit'); %K
P_crit = CoolProp.PropsSI(Fluid,'Pcrit'); %Pa
```

steam cycle conditions

```
Q_flue = 6375000; %W           %from Aspen
eta_turb_design = 0.85        %input
TIT = 500;                    %input
TIT = TIT + 273.15;
epsilon_HX_EVA = linspace(0.5,0.60,500); %input
eta_HX_eva = 0.9;             %input
T_out_pump = (TIT - epsilon_HX_EVA*T_in_HF)./(1-epsilon_HX_EVA);
P_max_guess = 100; %bar       %input
P_max_guess = P_max_guess*10^5;
```

steam turbine mass flow rate kg/s

```
for i=1:length(T_out_pump);
    H_TIT = CoolProp.PropsSI('H','T',TIT,'P',P_max_guess,Fluid);
    H_out_pump(i) = CoolProp.PropsSI('H','T',T_out_pump(i),'P',P_max_guess,Fluid);
    S_out_pump(i) = CoolProp.PropsSI('S','T',T_out_pump(i),'P',P_max_guess,Fluid);
    DELTA_H(i) = H_TIT-H_out_pump(i);
end
m_ST = Q_flue*eta_HX_eva./DELTA_H;
```

TOT

```
P_min_guess = 0.8; %bar %input
P_min_guess = P_min_guess*10^5;
S_TIT = CoolProp.PropsSI('S','T',TIT,'P',P_max_guess,Fluid);
H_TOT_ID = CoolProp.PropsSI('H','S',S_TIT,'P',P_min_guess,Fluid);
T_TOT_ID = CoolProp.PropsSI('T','H',H_TOT_ID,'P',P_min_guess,Fluid);
H_TOT = H_TIT-eta_turb_design*(H_TIT-H_TOT_ID);
T_TOT = CoolProp.PropsSI('T','H',H_TOT,'P',P_min_guess,Fluid);
%title check
H_L = CoolProp.PropsSI('H','Q',0,'P',P_min_guess,Fluid);
H_V = CoolProp.PropsSI('H','Q',1,'P',P_min_guess,Fluid);
title_design = (H_TOT-H_L)/(H_V-H_L);
T_SAT_COND = CoolProp.PropsSI('T','H',H_V,'P',P_min_guess,Fluid);
%pinch
T_pinch = T_SAT_COND - 10; %assumption
if title_design < 1
    T_out_CF = T_pinch;
    p_DH = 1; %bar %input
    p_DH = p_DH * 10^5;
    H_out_CF = CoolProp.PropsSI('H','T',T_out_CF,'P',p_DH,Fluid);
    DELTA_T_DH = 30; %input
    T_in_CF = T_pinch - DELTA_T_DH;
    H_in_CF = CoolProp.PropsSI('H','T',T_in_CF,'P',p_DH,Fluid);
    subcooling = 5; %input
    T_in_pump = T_SAT_COND - subcooling;
    H_in_pump = CoolProp.PropsSI('H','T',T_in_pump,'P',P_min_guess,Fluid);
    S_in_pump = CoolProp.PropsSI('S','T',T_in_pump,'P',P_min_guess,Fluid);
    Q_cond_id = m_ST*(H_TOT-H_in_pump);
    eta_HX_cond = 0.9; %input
    m_DH = Q_cond_id*eta_HX_cond/(H_out_CF-H_in_CF);
else
    print("TOT outside water saturation bell")
end
```

setting the temperature output for CF DH

```
T_out_CF_target = 75; %cold fluid district heating target
T_out_CF_target = T_out_CF_target +273.15;

if abs(T_out_CF-T_out_CF_target) > 0.5;
    for i =1:5000
        P_min(i) = P_min_guess-0.001*i*P_min_guess;
        H_TOT_ID = CoolProp.PropsSI('H','S',S_TIT,'P',P_min(i),Fluid);
        T_TOT_ID = CoolProp.PropsSI('T','H',H_TOT_ID,'P',P_min(i),Fluid);
```

```

H_TOT = H_TIT-eta_turb_design*(H_TIT-H_TOT_ID);
T_TOT = CoolProp.PropsSI('T','H',H_TOT,'P',P_min(i),Fluid);
S_TOT = CoolProp.PropsSI('S','H',H_TOT,'P',P_min(i),Fluid);
%title check
H_L = CoolProp.PropsSI('H','Q',0,'P',P_min(i),Fluid);
H_V = CoolProp.PropsSI('H','Q',1,'P',P_min(i),Fluid);
title_design = (H_TOT-H_L)/(H_V-H_L);
T_SAT_COND = CoolProp.PropsSI('T','H',H_V,'P',P_min(i),Fluid);
T_pinch = T_SAT_COND - 10;
if title_design < 1
    T_out_CF = T_pinch;
    if abs(T_out_CF-T_out_CF_target) < 0.5;
        H_out_CF = CoolProp.PropsSI('H','T',T_out_CF,'P',p_DH,Fluid);
        T_in_CF = T_pinch - DELTA_T_DH;
        H_in_CF = CoolProp.PropsSI('H','T',T_in_CF,'P',p_DH,Fluid);
        T_in_pump = T_SAT_COND - subcooling;
        H_in_pump = CoolProp.PropsSI('H','T',T_in_pump,'P',P_min(i),Fluid);
        S_in_pump = CoolProp.PropsSI('S','T',T_in_pump,'P',P_min(i),Fluid);
        Q_cond_id = m_ST*(H_TOT-H_in_pump);
        m_DH = Q_cond_id*eta_HX_cond/(H_out_CF-H_in_CF);
        P_min_final = P_min(i);
        break
    end
end
end
end
end

```

selection of the best cycle in terms of isentropic efficiency and HX effectiveness

```

S_out_pump_id = CoolProp.PropsSI('S','T',T_in_pump,'P',P_max_guess,Fluid);
H_out_pump_id = CoolProp.PropsSI('H','S',S_out_pump_id,'P',P_max_guess,Fluid);
T_out_pump_id = CoolProp.PropsSI('T','H',H_out_pump_id,'P',P_max_guess,Fluid);
eta_pump_design = (H_out_pump_id-H_in_pump)./(H_out_pump-H_in_pump);
idx = eta_pump_design > 0.7 & eta_pump_design < 0.8;
eta_pump_design_max = max(eta_pump_design(idx));
EVA_effectiveness = epsilon_HX_EVA(idx);

```

title check

```

turbine_title_design = 0.95; %input
if abs(title_design-turbine_title_design)>0.01;
    if title_design > turbine_title_design; %pressure decrease check
        print("maximum pressure too low. increase")
    else
        for i=1:500;
            P_max = P_max_guess-0.01*i*P_max_guess;
            for i=1:length(T_out_pump);
                H_TIT = CoolProp.PropsSI('H','T',TIT,'P',P_max,Fluid);
                H_out_pump(i) = CoolProp.PropsSI('H','T',T_out_pump(i),'P',P_max,Fluid);
                S_out_pump(i) = CoolProp.PropsSI('S','T',T_out_pump(i),'P',P_max,Fluid);
                DELTA_H(i) = H_TIT-H_out_pump(i);
            end
            m_ST = Q_flue*eta_HX_eva./DELTA_H;
            P_min_guess = 0.8; %bar
            P_min_guess = P_min_guess*10^5;
        end
    end
end

```



```

S_TIT = CoolProp.PropsSI('S','T',TIT,'P',P_max,Fluid);
H_TOT_ID = CoolProp.PropsSI('H','S',S_TIT,'P',P_min_guess,Fluid);
T_TOT_ID = CoolProp.PropsSI('T','H',H_TOT_ID,'P',P_min_guess,Fluid);
H_TOT = H_TIT-eta_turb_design*(H_TIT-H_TOT_ID);
T_TOT = CoolProp.PropsSI('T','H',H_TOT,'P',P_min_guess,Fluid);
%title check
H_L = CoolProp.PropsSI('H','Q',0,'P',P_min_guess,Fluid);
H_V = CoolProp.PropsSI('H','Q',1,'P',P_min_guess,Fluid);
title_design = (H_TOT-H_L)/(H_V-H_L);
T_SAT_COND = CoolProp.PropsSI('T','H',H_V,'P',P_min_guess,Fluid);
%pinch
T_pinch = T_SAT_COND - 10;
if title_design < 1
    T_out_CF = T_pinch;
    H_out_CF = CoolProp.PropsSI('H','T',T_out_CF,'P',p_DH,Fluid);
    T_in_CF = T_pinch - DELTA_T_DH;
    H_in_CF = CoolProp.PropsSI('H','T',T_in_CF,'P',p_DH,Fluid);
    T_in_pump = T_SAT_COND - subcooling;
    H_in_pump = CoolProp.PropsSI('H','T',T_in_pump,'P',P_min_guess,Fluid);
    S_in_pump = CoolProp.PropsSI('S','T',T_in_pump,'P',P_min_guess,Fluid);
    Q_cond_id = m_ST*(H_TOT-H_in_pump);
    m_DH = Q_cond_id*eta_HX_cond/(H_out_CF-H_in_CF);
else
    print("TOT outside water saturation bell")
end
if abs(T_out_CF-T_out_CF_target) > 0.5;
    for i =1:5000
        P_min(i) = P_min_guess-0.001*i*P_min_guess;
        H_TOT_ID = CoolProp.PropsSI('H','S',S_TIT,'P',P_min(i),Fluid);
        T_TOT_ID = CoolProp.PropsSI('T','H',H_TOT_ID,'P',P_min(i),Fluid);
        H_TOT = H_TIT-eta_turb_design*(H_TIT-H_TOT_ID);
        T_TOT = CoolProp.PropsSI('T','H',H_TOT,'P',P_min(i),Fluid);
        S_TOT = CoolProp.PropsSI('S','H',H_TOT,'P',P_min(i),Fluid);
        %title check
        H_L = CoolProp.PropsSI('H','Q',0,'P',P_min(i),Fluid);
        H_V = CoolProp.PropsSI('H','Q',1,'P',P_min(i),Fluid);
        title_design = (H_TOT-H_L)/(H_V-H_L);
        T_SAT_COND = CoolProp.PropsSI('T','H',H_V,'P',P_min(i),Fluid);
        T_pinch = T_SAT_COND - 10;
        if title_design < 1
            T_out_CF = T_pinch;
            if abs(T_out_CF-T_out_CF_target) < 0.5;
                H_out_CF = CoolProp.PropsSI('H','T',T_out_CF,'P',p_DH,Fluid);
                T_in_CF = T_pinch - DELTA_T_DH;
                H_in_CF = CoolProp.PropsSI('H','T',T_in_CF,'P',p_DH,Fluid);
                T_in_pump = T_SAT_COND - subcooling;
                H_in_pump = CoolProp.PropsSI('H','T',T_in_pump,'P',P_min(i),Fluid);
                S_in_pump = CoolProp.PropsSI('S','T',T_in_pump,'P',P_min(i),Fluid);
                Q_cond_id = m_ST*(H_TOT-H_in_pump);
                m_DH = Q_cond_id*eta_HX_cond/(H_out_CF-H_in_CF);
                P_min_final = P_min(i);
                break
            end
        end
    end
end
end
S_out_pump_id = CoolProp.PropsSI('S','T',T_in_pump,'P',P_max,Fluid);
H_out_pump_id = CoolProp.PropsSI('H','S',S_out_pump_id,'P',P_max,Fluid);

```

```

T_out_pump_id = CoolProp.PropsSI('T','H',H_out_pump_id,'P',P_max,Fluid);
eta_pump_design = (H_out_pump_id-H_in_pump)./(H_out_pump-H_in_pump);
idx = eta_pump_design > 0.7 & eta_pump_design < 0.8;
eta_pump_design_max = eta_pump_design(idx);
EVA_effectiveness = epsilon_HX_EVA(idx);
m_ST_final = m_ST(idx);
m_DH_final = m_DH(idx);
H_out_pump_final = H_out_pump(idx);
Q_cond_id_final = Q_cond_id(idx);
if abs(title_design-turbine_title_design)<0.005
    break
end
end
end
end
end

```

points and graph for the design configuration

```

%hot fluid
T_HF = [T_in_HF T_out_HF];
S_HF = [S_TIT S_out_pump(idx)];
%cold fluid
T_CF = [T_in_CF T_out_CF];
S_CF = [S_in_pump S_TOT];
%cycle
T_sat_l_p_max = CoolProp.PropsSI('T','Q',0,'P',P_max,Fluid);
S_sat_l_p_max = CoolProp.PropsSI('S','Q',0,'P',P_max,Fluid);
S_sat_v_p_max = CoolProp.PropsSI('S','Q',1,'P',P_max,Fluid);
S_sat_l_p_min = CoolProp.PropsSI('S','Q',0,'P',P_min_final,Fluid);
T_cycle = [T_in_pump T_out_pump(idx) T_sat_l_p_max T_sat_l_p_max TIT T_TOT T_SAT_COND]
S_cycle = [S_in_pump S_out_pump(idx) S_sat_l_p_max S_sat_v_p_max S_TIT S_TOT S_sat_l_p_min]

```

global efficiency

```

Q_EVA = Q_flue
Q_COND = Q_cond_id_final*eta_HX_cond
eta_e1 = 0.97
eta_mecc = 0.95
W_turb = m_ST_final*(H_TIT-H_TOT)*eta_mecc*eta_e1
W_pump = m_ST_final*(H_out_pump_final-H_in_pump)/eta_mecc/eta_e1

eta_e1_cycle = (W_turb-W_pump)/Q_EVA
eta_t_cycle = Q_COND/Q_EVA
eta_tot = eta_e1_cycle+eta_t_cycle

```

curves

```

P = logspace(log10(0.01e6), log10(P_crit), 1000);
T_sat = zeros(size(P));
sL_sat = zeros(size(P));
sV_sat = zeros(size(P));
for i = 1:length(P)
    T_sat(i) = CoolProp.PropsSI('T','P', P(i), 'Q', 0, 'Water');
    sL_sat(i) = CoolProp.PropsSI('S','P', P(i), 'Q', 0, 'Water');

```

```

    sv_sat(i) = CoolProp.PropsSI('S', 'P', P(i), 'Q', 1, 'Water');
end

%isobaric curve p min
T_min = 280
T_max = 1000
T = linspace(T_min, T_max, 500);
s = zeros(size(T));
for i = 1:length(T)
    s1(i) = CoolProp.PropsSI('S', 'P', P_min_final, 'T', T(i), Fluid);
end
for i = 1:length(T)
    s2(i) = CoolProp.PropsSI('S', 'P', P_max, 'T', T(i), Fluid);
end
set(groot, 'DefaultAxesFontName','Times New Roman')
xlabel('X-Axis Label', 'FontName', 'Times New Roman')
ylabel('Y-Axis Label', 'FontName', 'Times New Roman')
set(gca, 'FontName', 'Times New Roman','FontSize', 14)
plot(S_HF, T_HF-273.15, 'red', 'Linewidth', 2, 'Marker','*')
hold on
plot(S_CF, T_CF-273.15, 'blue', 'Linewidth', 2, 'Marker','*')
hold on
plot(S_cycle, T_cycle-273.15, 'green', 'Linewidth', 2, 'Marker','*')
fill(S_cycle, T_cycle-273.15, 'g', 'FaceAlpha', 0.05);
text(4500, 500-273.15, "El. Power = " + string(round((W_turb-W_pump)/10^6,2)) + " MW", 'FontSize',
10, 'HorizontalAlignment','center');
text(4500, 450-273.15, "Th. Power = " + string(round(Q_COND/10^6,2)) + " MW", 'FontSize', 10,
'HorizontalAlignment','center');
text(4500, 400-273.15, "Title = " + string(round(title_design,3)), 'FontSize', 10,
'HorizontalAlignment','center');
hold on
plot(sv_sat, T_sat-273.15, 'black', 'Linewidth', 1, 'LineStyle','--')
hold on
plot(sL_sat, T_sat-273.15, 'black', 'Linewidth', 1, 'LineStyle','--')
hold on
plot(s1, T-273.15, 'black', 'Linewidth', 1, 'LineStyle',':')
hold on
plot(s2, T-273.15, 'black', 'Linewidth', 1, 'LineStyle',':')
text(7000, 800-273.15, "P_{max} = " + string(round(P_max/10^5,2)) + " bar", 'FontSize', 10,
'HorizontalAlignment','left');
text(7000, 750-273.15, "P_{min} = " + string(round(P_min_final/10^5,2)) + " bar", 'FontSize', 10,
'HorizontalAlignment','left')
hold on
legend('Hot fluid','Cold fluid','Steam cycle', Location='northwest')
title('RDF Design Condition - DH network 75°C');
xlabel('Specific Entropy [J/kg-K]')
ylabel('Temperature [°C]')
grid on
ylim([0 T_HF(1,1)+50-273.15])
yticks(0:50:T_HF(1,1)+50-273.15)
xlim([0 8500])
set(gcf, 'Name', 'Design')
hold off

```

```

%EVA - HX type = boiler, HYP: C_MIN = water
M_flue = 35771/3600; %from aspen
CP_flue_in = 1233.66; %from aspen
CP_water_in = CoolProp.PropsSI('C', 'T', T_out_pump(idx), 'P', P_max , 'water');
filename = 'HX-ST.xlsx'; % specify the file name
sheet = 2; % Second spreadsheet
xlswrite(filename, T_in_HF, sheet, 'D4');
xlswrite(filename, T_out_HF, sheet, 'D5');
xlswrite(filename, T_out_pump(idx), sheet, 'D6');
xlswrite(filename, TIT, sheet, 'D7');
xlswrite(filename, M_flue*3600, sheet, 'H3');
xlswrite(filename, CP_flue_in, sheet, 'H6');
xlswrite(filename, m_ST_final*3600, sheet, 'L3');
xlswrite(filename, CP_water_in, sheet, 'L6');
range = 'H7'
C_flue = xlsread(filename, sheet, range)
range = 'L7'
C_water = xlsread(filename, sheet, range)
C_min = min(C_flue, C_water)
range = 'H16'
msg = "Wrong Cmin statement -> Cmin = water, Cmax = unmixed"
NTU_EVA = xlsread(filename, sheet, range)
UA_EVA = NTU_EVA*C_min

%COND- HX type = SH, HYP: C_MIN = water cycle
CP_water_in_DH = CoolProp.PropsSI('C', 'T', T_in_CF, 'P', p_DH , 'water');
CP_water_in_turb = CoolProp.PropsSI('C', 'S', S_TOT, 'P', P_min_final , 'water');
sheet = 3; % Second spreadsheet epsilon = 0.8
xlswrite(filename, T_TOT, sheet, 'D4');
xlswrite(filename, T_in_pump, sheet, 'D5');
xlswrite(filename, T_in_CF, sheet, 'D6');
xlswrite(filename, T_out_CF, sheet, 'D7');
xlswrite(filename, m_ST_final*3600, sheet, 'H3');
xlswrite(filename, CP_water_in_turb, sheet, 'H6');
xlswrite(filename, m_DH(idx)*3600, sheet, 'L3');
xlswrite(filename, CP_water_in_DH, sheet, 'L6');
range = 'H7'
C_hot = xlsread(filename, sheet, range)
range = 'L7'
C_cold = xlsread(filename, sheet, range)
C_min = min(C_hot, C_cold)
range = 'H17'
NTU_COND = xlsread(filename, sheet, range)
UA_COND = NTU_COND*C_min

```

off-design condition DH network at 55°C cold side

```

%step 1) evaluation of the new surge pressure that achieves the target
%temperature
T_out_CF_target_off1 = 55; %cold fluid district heating target
T_out_CF_target_off1 = T_out_CF_target_off1 + 273.15;
T_out_CF_off1 = T_out_CF;
if abs(T_out_CF_off1-T_out_CF_target_off1) > 0.5;
    for i =1:5000
        P_min_off1(i) = P_min_guess-0.001*i*P_min_guess;
        H_TOT_ID_off1 = CoolProp.PropsSI('H', 'S', S_TIT, 'P', P_min_off1(i), Fluid);
    end
end

```

```

T_TOT_ID_off1 = CoolProp.PropsSI('T','H',H_TOT_ID_off1,'P',P_min_off1(i),Fluid);
H_TOT_off1 = H_TIT-eta_turb_design*(H_TIT-H_TOT_ID_off1);
T_TOT_off1 = CoolProp.PropsSI('T','H',H_TOT_off1,'P',P_min_off1(i),Fluid);
S_TOT_off1 = CoolProp.PropsSI('S','H',H_TOT_off1,'P',P_min_off1(i),Fluid);
%title check
H_L_off1 = CoolProp.PropsSI('H','Q',0,'P',P_min_off1(i),Fluid);
H_V_off1 = CoolProp.PropsSI('H','Q',1,'P',P_min_off1(i),Fluid);
title_off1 = (H_TOT_off1-H_L_off1)/(H_V_off1-H_L_off1);
T_SAT_COND_off1 = CoolProp.PropsSI('T','H',H_V_off1,'P',P_min_off1(i),Fluid);
T_pinch_off1 = T_SAT_COND_off1 - 10;
if title_off1 < 1
    T_out_CF_off1 = T_pinch_off1;
    if abs(T_out_CF_off1-T_out_CF_target_off1) < 0.5;
        H_out_CF_off1 = CoolProp.PropsSI('H','T',T_out_CF_off1,'P',p_DH,Fluid);
        T_in_CF_off1 = T_pinch_off1 - DELTA_T_DH;
        H_in_CF_off1 = CoolProp.PropsSI('H','T',T_in_CF_off1,'P',p_DH,Fluid);
        T_in_pump_off1 = T_SAT_COND_off1 - subcooling;
        H_in_pump_off1 = CoolProp.PropsSI('H','T',T_in_pump_off1,'P',P_min_off1(i),Fluid);
        S_in_pump_off1 = CoolProp.PropsSI('S','T',T_in_pump_off1,'P',P_min_off1(i),Fluid);
        P_min_final_off1 = P_min_off1(i);
        break
    end
end
end
end
end
% step 2) evaluation of the new mass flow rate of the system
%assumption: the same design efficiency of design conditions are used,
%since the pump work is negligible, and P max is now fixed if the title and
%the end is >0.9. since the fluegas flow rate is always constant, it is
%supposed that UA does not change much but change Cmin.

eta_pump_off1 = eta_pump_design_max;
H_out_pump_ID_off1 = CoolProp.PropsSI('H','S',S_in_pump_off1,'P',P_max,Fluid);
H_out_pump_off1 = H_in_pump_off1 + (H_out_pump_ID_off1-H_in_pump_off1)/eta_pump_off1;
S_out_pump_off1 = CoolProp.PropsSI('S','H',H_out_pump_off1,'P',P_max,Fluid);
T_out_pump_off1 = CoolProp.PropsSI('T','H',H_out_pump_off1,'P',P_max,Fluid);
DELTA_H_off1 = H_TIT-H_out_pump_off1;
m_ST_off1 = Q_flue*eta_HX_eva/DELTA_H_off1;
Q_cond_id_off1 = m_ST_off1*(H_TOT_off1-H_in_pump_off1);
m_DH_off1 = Q_cond_id_off1*eta_HX_cond/(H_out_CF_off1-H_in_CF_off1);

%step 3) evaluate the new turbine efficiency
%since pressure and TIT are fixed, no variation in terms of density are
%foreseen

eta_turb_off1 = eta_turb_design*sin(pi/2*(m_ST_off1/m_ST_final)^0.1)
if eta_turb_off1/eta_turb_design >0.99
    msg = "no variation from design conditions"
end

% step 4) global efficiency
Q_EVA = Q_flue
Q_COND_off1 = Q_cond_id_off1*eta_HX_cond
W_turb_off1 = m_ST_off1*(H_TIT-H_TOT_off1)*eta_mecc*eta_e1
W_pump_off1 = m_ST_off1*(H_out_pump_off1-H_in_pump_off1)/eta_mecc/eta_e1

eta_e1_cycle_off1 = (W_turb_off1-W_pump_off1)/Q_EVA
eta_t_cycle_off1 = Q_COND_off1/Q_EVA

```

```

eta_tot_off1 = eta_el_cycle_off1+eta_t_cycle_off1

% step 5) curves

% step 6) get the new HX effectiveness
CP_water_in_off1 = CoolProp.PropsSI('C', 'T', T_out_pump_off1, 'P', P_max , 'water');
filename = 'HX-ST.xlsx'; % specify the file name
sheet = 4; % Second spreadsheet
xlswrite(filename, T_in_HF, sheet, 'D4');
xlswrite(filename, T_out_HF, sheet, 'D5');
xlswrite(filename, T_out_pump_off1, sheet, 'D6');
xlswrite(filename, TIT, sheet, 'D7');
xlswrite(filename, M_flue*3600, sheet, 'H3');
xlswrite(filename, CP_flue_in, sheet, 'H6');
xlswrite(filename, m_ST_off1*3600, sheet, 'L3');
xlswrite(filename, CP_water_in_off1, sheet, 'L6');
range = 'L7'
C_water_off1 = xlsread(filename, sheet, range)
C_min_off1 = min(C_flue, C_water_off1)
range = 'H16'
NTU_EVA_off1 = xlsread(filename, sheet, range)
UA_EVA_off1 = NTU_EVA*C_min_off1

%COND- HX type = SH, HYP: C_MIN = water cycle
CP_water_in_DH_off1 = CoolProp.PropsSI('C', 'T', T_in_CF_off1, 'P', p_DH , 'water');
CP_water_in_turb_off1 = CoolProp.PropsSI('C', 'S', S_TOT_off1, 'P', P_min_final_off1 , 'water');
sheet = 5; % Second spreadsheet
xlswrite(filename, T_TOT_off1, sheet, 'D4');
xlswrite(filename, T_in_pump_off1, sheet, 'D5');
xlswrite(filename, T_in_CF_off1, sheet, 'D6');
xlswrite(filename, T_out_CF_off1, sheet, 'D7');
xlswrite(filename, m_ST_off1*3600, sheet, 'H3');
xlswrite(filename, CP_water_in_turb_off1, sheet, 'H6');
xlswrite(filename, m_DH_off1*3600, sheet, 'L3');
xlswrite(filename, CP_water_in_DH_off1, sheet, 'L6');
range = 'H7'
C_hot = xlsread(filename, sheet, range)
range = 'L7'
C_cold = xlsread(filename, sheet, range)
C_min = min(C_hot, C_cold)
range = 'H17'
NTU_COND_off1 = xlsread(filename, sheet, range)
UA_COND_off1 = NTU_COND*C_min

```

ORC POWER UNIT (TOLUENE WITH RECUPERATOR)

```

close
clc
clear

Fluid = 'Toluene';

```

Fluid conditions - DESIGN

```

T_in_term = 370 %C;
T_out_term = 180 %C;
T_in_term = T_in_term + 273.15 %K;
T_out_term = T_out_term + 273.15 %K;
T_in_term = 370 %C;
T_out_term = 180 %C;
T_in_term = T_in_term + 273.15 %K;
T_out_term = T_out_term + 273.15 %K;

```

Water critical properties

```

T_crit = CoolProp.PropsSI(Fluid,'Tcrit');      %K
P_crit = CoolProp.PropsSI(Fluid,'Pcrit');     %Pa
P_max = 0.8*P_crit;

```

Superheating & Subcooling

```

SH = 10;
subcooling = 5

```

Efficiencies

```

eta_is_t = 1 %first stage
eta_e1 = 0.97
eta_mec = 0.95
eta_HX1 = 0.9
eta_HX2 = 0.95
eta_HX3 = 0.95
eta_HX4 = 0.9

```

Flue gas load

```

Q_flue = 6375000 %W

```

Therminol VP-1 properties

```

CP_term_in = cp_term(T_in_term) %J/kgK
CP_term_out = cp_term(T_out_term) %J/kgK
H_term = H_int_term(T_out_term,T_in_term) %J/kg
M_term = double(Q_flue*eta_HX1/H_term) %kg/s

```

HX1 effectiveness check

```

%the first HX is always Cmin = C fluegas
M_flue = 35771/3600;
T_in_flue = 800;
T_out_flue = 250;
T_in_flue = T_in_flue+273.15;
T_out_flue = T_out_flue+273.15;
CP_flue_in = 1233.66;

```

```

filename = 'HX-REC.xlsx'; % specify the file name
sheet = 2; % Second spreadsheet
xlswrite(filename, T_in_flue, sheet, 'D4');
xlswrite(filename, T_out_flue, sheet, 'D5');
xlswrite(filename, T_out_term, sheet, 'D6');
xlswrite(filename, T_in_term, sheet, 'D7');
xlswrite(filename, M_flue*3600, sheet, 'H3');
xlswrite(filename, CP_flue_in, sheet, 'H6');
xlswrite(filename, M_term*3600, sheet, 'L3');
xlswrite(filename, CP_term_in, sheet, 'L6');
range = 'D9'
eps_HX1 = xlsread(filename, sheet, range)
range = 'H15'
NTU_HX1 = xlsread(filename, sheet, range);
% Define the variable value

```

ORC initial mass flow rate with no recuperator

```

Q_eva = Q_flue*eta_HX1; %W %from Aspen
T_EVA_ORC = CoolProp.PropsSI('T','Q',1,'P',P_max,Fluid);
TIT = T_EVA_ORC + SH;
TIT_TARGET = TIT;
epsilon_HX2 = linspace(0.60,0.75,550); %input
T_out_pump_unrec = T_in_term - (T_in_term-T_out_term)./epsilon_HX2;
for i=1:length(T_out_pump_unrec);
    H_TIT = CoolProp.PropsSI('H','T',TIT,'P',P_max,Fluid);
    H_out_pump_unrec_is(i) = CoolProp.PropsSI('H','T',T_out_pump_unrec(i),'P',P_max,Fluid);
    S_out_pump_unrec_is(i) = CoolProp.PropsSI('S','T',T_out_pump_unrec(i),'P',P_max,Fluid);
    DELTA_H(i) = H_TIT-H_out_pump_unrec_is(i);
end
m_ORC_unrec_is = Q_eva*eta_HX2./DELTA_H;

```

TOT and other outlet turbine conditions

```

P_min_guess = 0.50; %bar %input
P_min_guess = P_min_guess*10^5;
S_TIT = CoolProp.PropsSI('S','T',TIT,'P',P_max,Fluid);
H_TOT_unrec_ID = CoolProp.PropsSI('H','S',S_TIT,'P',P_min_guess,Fluid);
T_TOT_unrec_ID = CoolProp.PropsSI('T','H',H_TOT_unrec_ID,'P',P_min_guess,Fluid);
H_TOT_unrec_is = H_TIT-eta_is_t*(H_TIT-H_TOT_unrec_ID);
T_TOT_unrec_is = CoolProp.PropsSI('T','H',H_TOT_unrec_is,'P',P_min_guess,Fluid);
%title check
H_L = CoolProp.PropsSI('H','Q',0,'P',P_min_guess,Fluid);
H_V = CoolProp.PropsSI('H','Q',1,'P',P_min_guess,Fluid);
T_SAT_COND = CoolProp.PropsSI('T','H',H_V,'P',P_min_guess,Fluid);
T_in_pump_unrec_is = T_SAT_COND - subcooling;
H_in_pump_unrec_is = CoolProp.PropsSI('H','T',T_in_pump_unrec_is,'P',P_min_guess,Fluid);
S_in_pump_unrec_is = CoolProp.PropsSI('S','T',T_in_pump_unrec_is,'P',P_min_guess,Fluid);
Q_cond_unrec_id_is = m_ORC_unrec_is*(H_TOT_unrec_is-H_in_pump_unrec_is);

% pinch evaluation with no regeneration
p_DH = 1; %bar
p_DH = p_DH*10^5
DT_DH = 30;
T_in_CF = 45; %input
T_in_CF = T_in_CF + 273.15;

```



```

DELTA_H_star = H_TOT_unrec_is-H_V;
Q_star = m_ORC_unrec_is*DELTA_H_star;
Q_knee = Q_cond_unrec_id_is - Q_star;
T_pinch_unrec_is = T_in_CF + DT_DH./Q_cond_unrec_id_is.*Q_knee;
DT_check = T_SAT_COND-T_pinch_unrec_is(1);
DT_LIM = 15
DT_LIM;
    if DT_check >
for i =1:5000
    P_min(i) = P_min_guess-0.001*i*P_min_guess;
    H_TOT_unrec_ID = CoolProp.PropsSI('H','S',S_TIT,'P',P_min(i),Fluid);
    T_TOT_unrec_ID = CoolProp.PropsSI('T','H',H_TOT_unrec_ID,'P',P_min(i),Fluid);
    H_TOT_unrec_is = H_TIT-eta_is_t*(H_TIT-H_TOT_unrec_ID);
    T_TOT_unrec_is = CoolProp.PropsSI('T','H',H_TOT_unrec_is,'P',P_min(i),Fluid);
    S_TOT_unrec = CoolProp.PropsSI('S','H',H_TOT_unrec_is,'P',P_min(i),Fluid);
    %title check
    H_L = CoolProp.PropsSI('H','Q',0,'P',P_min(i),Fluid);
    H_V = CoolProp.PropsSI('H','Q',1,'P',P_min(i),Fluid);
    title_design = (H_TOT_unrec_is-H_L)/(H_V-H_L);
    T_SAT_COND = CoolProp.PropsSI('T','H',H_V,'P',P_min(i),Fluid);
    T_in_pump_unrec_is = T_SAT_COND - subcooling;
    H_in_pump_unrec_is = CoolProp.PropsSI('H','T',T_in_pump_unrec_is,'P',P_min(i),Fluid);
    S_in_pump_unrec_is = CoolProp.PropsSI('S','T',T_in_pump_unrec_is,'P',P_min(i),Fluid);
    Q_cond_unrec_id_is = m_ORC_unrec_is*(H_TOT_unrec_is-H_in_pump_unrec_is);
    if title_design > 1
        DELTA_H_star = H_TOT_unrec_is-H_V;
        Q_star = m_ORC_unrec_is*DELTA_H_star;
        Q_knee = Q_cond_unrec_id_is - Q_star;
        T_pinch = T_in_CF + DT_DH./Q_cond_unrec_id_is.*Q_knee;
        DT_check = T_SAT_COND-T_pinch(1);
        if DT_check < DT_LIM;
            T_out_CF = T_in_CF + DT_DH;
            H_out_CF = CoolProp.PropsSI('H','T',T_out_CF,'P',p_DH,'water');
            H_in_CF = CoolProp.PropsSI('H','T',T_in_CF,'P',p_DH,'water');
            T_in_pump_unrec_is = T_SAT_COND - subcooling;
            H_in_pump_unrec_is =
CoolProp.PropsSI('H','T',T_in_pump_unrec_is,'P',P_min(i),Fluid);
            S_in_pump_unrec_is =
CoolProp.PropsSI('S','T',T_in_pump_unrec_is,'P',P_min(i),Fluid);
            Q_cond_unrec_id_is = m_ORC_unrec_is*(H_TOT_unrec_is-H_in_pump_unrec_is);
            m_DH = Q_cond_unrec_id_is*eta_HX4/(H_out_CF-H_in_CF);
            P_min_final_unrec_is = P_min(i);
            break
        end
    end
end
end
end
end

```

Selection of the best cycle in terms of isentropic efficiency and HX effectiveness

```

S_out_pump_unrec_id_is = CoolProp.PropsSI('S','T', T_in_pump_unrec_is,'P',P_max,Fluid);
H_out_pump_unrec_id_is = CoolProp.PropsSI('H','S',S_in_pump_unrec_is,'P',P_max,Fluid);
T_out_pump_unrec_id_is = CoolProp.PropsSI('T','S',S_in_pump_unrec_is,'P',P_max,Fluid);
eta_pump_design_unrec_is = (H_out_pump_unrec_is-H_in_pump_unrec_is)/(H_out_pump_unrec_id_is-
H_in_pump_unrec_is);
logicalIndex = eta_pump_design_unrec_is > 0.7 & eta_pump_design_unrec_is < 0.8;
eta_pump_design_max_unrec_is = eta_pump_design_unrec_is(logicalIndex);

```

```

idx = find(logicalIndex);
if length(idx)>1
    idx = max(idx)
end
EVA_effectiveness = epsilon_HX2(idx);
m_ORC_final_unrec_is = m_ORC_unrec_is(idx)

```

Check Macchi Parameters

```

rho_in_turb = CoolProp.PropsSI('D','S',S_TIT,'P',P_max,Fluid)
rho_out_turb = CoolProp.PropsSI('D','S',S_TIT,'P',P_min_final_unrec_is,Fluid)
v_in = m_ORC_final_unrec_is/rho_in_turb;
v_out = m_ORC_final_unrec_is/rho_out_turb
h_in_turb = CoolProp.PropsSI('H','S',S_TIT,'P',P_max,Fluid)/1000
h_out_turb = CoolProp.PropsSI('H','S',S_TIT,'P',P_min_final_unrec_is,Fluid)/1000
filename = 'MACCHI_new.xlsx'; % specify the file name
sheet = 1;
xlswrite(filename, v_in, sheet, 'A2');
xlswrite(filename, v_out, sheet, 'A3');
xlswrite(filename, h_in_turb, sheet, 'B2');
xlswrite(filename, h_out_turb, sheet, 'B3');
range = 'C2';
SP_is_unrec = xlsread(filename, sheet, range);
range = 'D2';
VR = xlsread(filename, sheet, range);
if SP_is_unrec<1
    range = 'F2';
    eta_is_t_final = xlsread(filename, sheet, range);
end

```

Initial hot out temperature for recuperation

```

T_ex_HF_rec = 120 %%%% input
T_ex_HF_rec = T_ex_HF_rec+273.15
h_ex_HF_rec = CoolProp.PropsSI('H','T',T_ex_HF_rec,'P',P_min_final_unrec_is,Fluid);

```

Starting recuperation

```

control = "off";
for j=1:500;
    H_TOT_rec_is = [];
    TIT_rec_is = [];
    for i=1:50;
        if i==1;
            H_TOT_rec_is(i,1) = H_TOT_unrec_is;
            TIT_rec_is(i,1) = TIT;
            Q_rec_is(i,1) = m_ORC_final_unrec_is*(H_TOT_rec_is(i,1)-h_ex_HF_rec)*eta_HX3;
            h_ex_CF_rec_is(i,1) = H_out_pump_unrec_is(idx)+Q_rec_is(i,1)/m_ORC_final_unrec_is
            T_ex_CF_rec_is(i,1) = CoolProp.PropsSI('T','H',h_ex_CF_rec_is(i,1),'P',P_max,Fluid);
            H_TIT_rec_is(i,1) = h_ex_CF_rec_is(i,1) + Q_flue*eta_HX2*eta_HX1/m_ORC_final_unrec_is;
            %kg/s
            TIT_rec_is(i,1) = CoolProp.PropsSI('T','H',H_TIT_rec_is(i,1),'P',P_max,Fluid);
            S_TIT_rec_is(i,1) = CoolProp.PropsSI('S','T',TIT_rec_is(i,1),'P',P_max,Fluid);
            TOT_rec_is(i,1)=

```

```

CoolProp.ProppSI('T','S',S_TIT_rec_is(i,1),'P',P_min_final_unrec_is,Fluid);
    H_TOT_rec_is(i,1) =
CoolProp.ProppSI('H','S',S_TIT_rec_is(i,1),'P',P_min_final_unrec_is,Fluid);
    else
        H_TOT_rec_is(i,1) = H_TOT_rec_is(i-1,1);
        Q_rec_is(i,1) = m_ORC_final_unrec_is*(H_TOT_rec_is(i,1)-h_ex_HF_rec)*eta_HX3;
        h_ex_CF_rec_is(i,1) = H_out_pump_unrec_is(idx)+Q_rec_is(i,1)/m_ORC_final_unrec_is;
        T_ex_CF_rec_is(i,1) = CoolProp.ProppSI('T','H',h_ex_CF_rec_is(i,1),'P',P_max,Fluid);
        H_TIT_rec_is(i,1) = h_ex_CF_rec_is(i,1) + Q_flue*eta_HX2*eta_HX1/m_ORC_final_unrec_is;
%kg/s
        TIT_rec_is(i,1) = CoolProp.ProppSI('T','H',H_TIT_rec_is(i,1),'P',P_max,Fluid);
        S_TIT_rec_is(i,1) = CoolProp.ProppSI('S','T',TIT_rec_is(i,1),'P',P_max,Fluid);
        TOT_rec_is(i,1)=
CoolProp.ProppSI('T','S',S_TIT_rec_is(i,1),'P',P_min_final_unrec_is,Fluid);
        H_TOT_rec_is(i,1) =
CoolProp.ProppSI('H','S',S_TIT_rec_is(i,1),'P',P_min_final_unrec_is,Fluid);
    end
    if i>1;
        if TIT_rec_is(i,1)-TIT_rec_is(i-1,1) <0.01;
            TIT_rec_final_is = TIT_rec_is(i);
            H_TIT_rec_final_is = H_TIT_rec_is(i,1);
            h_ex_CF_rec_final_is = h_ex_CF_rec_is(i,1);
            H_TOT_rec_final_is = H_TOT_rec_is(i,1);
            break
        end
    end
end
% increasing mass flow rate to achieve fixed TIT
i = 1
for i = 1:5000
    if i ==1
        M_orc_new(i,1) = m_ORC_final_unrec_is;
        h_ex_CF_rec_is_new(i,1) = h_ex_CF_rec_final_is;
        TIT_rec_is_new(i,1) = TIT_rec_final_is;
        h_in_t_rec_is_new(i,1) = H_TIT_rec_final_is;
        M_orc_new(i,1) = M_orc_new(i,1) + 0.0001;
    elseif i ~=1
        h_in_t_rec_is_new(i,1) = h_ex_CF_rec_is_new(i-1,1) +
Q_flue*eta_HX2*eta_HX1/M_orc_new(i-1); %kg/s
        TIT_rec_is_new(i,1) = CoolProp.ProppSI('T','H',h_in_t_rec_is_new(i,1),'P',P_max,Fluid);
        s_in_t_rec_is_new(i,1) = CoolProp.ProppSI('S','T',TIT_rec_is_new(i,1),'P',P_max,Fluid);
        T_ex_t_rec_is_new(i,1)=
CoolProp.ProppSI('T','S',s_in_t_rec_is_new(i,1),'P',P_min_final_unrec_is,Fluid);
        h_ex_t_rec_is_new(i,1) =
CoolProp.ProppSI('H','S',s_in_t_rec_is_new(i,1),'P',P_min_final_unrec_is,Fluid);
        Q_rec_is_new(i,1) = M_orc_new(i-1)*(h_ex_t_rec_is_new(i,1)-h_ex_HF_rec)*eta_HX3;
        h_ex_CF_rec_is_new(i,1) = H_out_pump_unrec_is(idx)+Q_rec_is_new(i,1)/M_orc_new(i-1,1);
        M_orc_new(i,1) = M_orc_new(i-1,1) + 0.001;
    end
    if abs(TIT_rec_is_new(i,1)-TIT_TARGET)<=0.1;
        TIT_rec_final_is=TIT_rec_is_new(i,1);
        S_TIT_rec_final_is = CoolProp.ProppSI('S','T',TIT_rec_final_is,'P',P_max,Fluid);
        M_final_rec_is = M_orc_new(i-1,1);
        Q_rec_end_is=Q_rec_is_new(i,1);
        break
    end
end
end
q_cond_rec_is = M_final_rec_is*(h_ex_HF_rec-H_in_pump_unrec_is);

```

```

DELTA_H_star = h_ex_HF_rec-H_V;
Q_star = M_final_rec_is*DELTA_H_star;
Q_knee = q_cond_rec_is - Q_star;
T_pinch_rec_is = T_in_CF + DT_DH/q_cond_rec_is.*Q_knee;
DT_check = T_SAT_COND-T_pinch_rec_is(1);
if DT_check<DT_LIM;
    if control == "off";
        P_min_final_unrec_is = P_min_final_unrec_is+0.002*j*P_min_final_unrec_is;
        H_V = CoolProp.PropsSI('H','Q',1,'P',P_min_final_unrec_is,Fluid);
        T_SAT_COND = CoolProp.PropsSI('T','H',H_V,'P',P_min_final_unrec_is,Fluid);
        T_in_pump_unrec_is = T_SAT_COND - subcooling;
        H_in_pump_unrec_is =
CoolProp.PropsSI('H','T',T_in_pump_unrec_is,'P',P_min_final_unrec_is,Fluid);
        S_in_pump_unrec_is =
CoolProp.PropsSI('S','T',T_in_pump_unrec_is,'P',P_min_final_unrec_is,Fluid);
        % selection of the best cycle in terms of isentropic efficiency and HX effectiveness
        % S_out_pump_unrec_id_is =
CoolProp.PropsSI('S','T',T_in_pump_unrec_is,'P',P_max,Fluid);
        H_out_pump_unrec_id_is = CoolProp.PropsSI('H','S',S_in_pump_unrec_is,'P',P_max,Fluid);
        T_out_pump_unrec_id_is = CoolProp.PropsSI('T','S',S_in_pump_unrec_is,'P',P_max,Fluid);
        eta_pump_design_unrec_is = (H_out_pump_unrec_id_is-
H_in_pump_unrec_is)/(H_out_pump_unrec_id_is-H_in_pump_unrec_is);
        logicalIndex = eta_pump_design_unrec_is > 0.7 & eta_pump_design_unrec_is < 0.8;
        eta_pump_design_max_unrec_is = eta_pump_design_unrec_is(logicalIndex);
        idx = find(logicalIndex);
        if length(idx)>1
            idx = max(idx)
        end
    else
        break
    end
else
    if control == "on";
        break
    end
    P_min_final_rec_is = P_min_final_unrec_is;
    T_SAT_COND = CoolProp.PropsSI('T','H',H_V,'P',P_min_final_rec_is,Fluid);
    T_in_pump_unrec_is = T_SAT_COND - subcooling;
    H_in_pump_unrec_is =
CoolProp.PropsSI('H','T',T_in_pump_unrec_is,'P',P_min_final_rec_is,Fluid);
    S_in_pump_unrec_is =
CoolProp.PropsSI('S','T',T_in_pump_unrec_is,'P',P_min_final_rec_is,Fluid);
    % selection of the best cycle in terms of isentropic efficiency and HX effectiveness
    % S_out_pump_unrec_id_is = CoolProp.PropsSI('S','T',T_in_pump_unrec_is,'P',P_max,Fluid);
    H_out_pump_unrec_id_is = CoolProp.PropsSI('H','S',S_in_pump_unrec_is,'P',P_max,Fluid);
    T_out_pump_unrec_id_is = CoolProp.PropsSI('T','S',S_in_pump_unrec_is,'P',P_max,Fluid);
    eta_pump_design_unrec_is = (H_out_pump_unrec_id_is-
H_in_pump_unrec_is)/(H_out_pump_unrec_is-H_in_pump_unrec_is);
    logicalIndex = eta_pump_design_unrec_is > 0.7 & eta_pump_design_unrec_is < 0.8;
    eta_pump_design_max_unrec_is = eta_pump_design_unrec_is(logicalIndex);
    idx = find(logicalIndex);
    if length(idx)>1
        idx = max(idx)
    end
    P_min_final_rec_is = P_min_final_unrec_is
    control = "on";

```

```

end
end

```

Final mass flow rate in the isentropic case and calculation of machi parameters

```

m_ORC_final_rec_is = M_final_rec_is
rho_in_turb = CoolProp.PropsSI('D','S',S_TIT_rec_final_is,'P',P_max,Fluid)
rho_out_turb = CoolProp.PropsSI('D','S',S_TIT_rec_final_is,'P',P_min_final_rec_is,Fluid)
v_in = m_ORC_final_rec_is/rho_in_turb
v_out = m_ORC_final_rec_is/rho_out_turb
h_in_turb = CoolProp.PropsSI('H','S',S_TIT_rec_final_is,'P',P_max,Fluid)/1000
h_out_turb = CoolProp.PropsSI('H','S',S_TIT_rec_final_is,'P',P_min_final_rec_is,Fluid)/1000
filename = 'MACCHI_new.xlsx'; % specify the file name
sheet = 1;
xlswrite(filename, v_in, sheet, 'A2');
xlswrite(filename, v_out, sheet, 'A3');
xlswrite(filename, h_in_turb, sheet, 'B2');
xlswrite(filename, h_out_turb, sheet, 'B3');
range = 'C2';
SP_is_rec = xlsread(filename, sheet, range);
range = 'D2';
VR = xlsread(filename, sheet, range);
if SP_is_rec<1
    range = 'F2';
    eta_is_t_final = xlsread(filename, sheet, range);
end

```

Reiterating the system with the new efficiency

```

Q_eva = Q_flue*eta_HX1; %W %from Aspen
T_EVA_ORC = CoolProp.PropsSI('T','Q',1,'P',P_max,Fluid);
TIT = T_EVA_ORC + SH;
TIT_TARGET = TIT;
epsilon_HX2 = linspace(0.60,0.75,550); %input
T_out_pump_unrec = T_in_term - (T_in_term-T_out_term)./epsilon_HX2;
for i=1:length(T_out_pump_unrec);
    H_TIT = CoolProp.PropsSI('H','T',TIT,'P',P_max,Fluid);
    H_out_pump_unrec(i) = CoolProp.PropsSI('H','T',T_out_pump_unrec(i),'P',P_max,Fluid);
    S_out_pump_unrec(i) = CoolProp.PropsSI('S','T',T_out_pump_unrec(i),'P',P_max,Fluid);
    DELTA_H(i) = H_TIT-H_out_pump_unrec(i);
end
m_ORC_unrec = Q_eva*eta_HX2./DELTA_H;
P_min_guess = 0.50; %bar %input
P_min_guess = P_min_guess*10^5;
S_TIT = CoolProp.PropsSI('S','T',TIT,'P',P_max,Fluid);
H_TOT_unrec_ID = CoolProp.PropsSI('H','S',S_TIT,'P',P_min_guess,Fluid);
T_TOT_unrec_ID = CoolProp.PropsSI('T','H',H_TOT_unrec_ID,'P',P_min_guess,Fluid);
H_TOT_unrec = H_TIT-eta_is_t_final*(H_TIT-H_TOT_unrec_ID);
T_TOT_unrec = CoolProp.PropsSI('T','H',H_TOT_unrec,'P',P_min_guess,Fluid);
%title check
H_L = CoolProp.PropsSI('H','Q',0,'P',P_min_guess,Fluid);
H_V = CoolProp.PropsSI('H','Q',1,'P',P_min_guess,Fluid);
T_SAT_COND = CoolProp.PropsSI('T','H',H_V,'P',P_min_guess,Fluid);
T_in_pump_unrec = T_SAT_COND - subcooling;
H_in_pump_unrec = CoolProp.PropsSI('H','T',T_in_pump_unrec,'P',P_min_guess,Fluid);

```

```

S_in_pump_unrec = CoolProp.PropsSI('S','T',T_in_pump_unrec,'P',P_min_guess,Fluid);
Q_cond_unrec_id = m_ORC_unrec*(H_TOT_unrec-H_in_pump_unrec);
p_DH = 1; %bar
p_DH = p_DH*10^5
DT_DH = 30;
DELTA_H_star = H_TOT_unrec-H_V;
Q_star = m_ORC_unrec*DELTA_H_star;
Q_knee = Q_cond_unrec_id - Q_star;
T_pinch_unrec = T_in_CF + DT_DH./Q_cond_unrec_id.*Q_knee;
DT_check = T_SAT_COND-T_pinch_unrec(1);
if DT_check > DT_LIM;
    for i =1:5000
        P_min(i) = P_min_guess-0.001*i*P_min_guess;
        H_TOT_unrec_ID = CoolProp.PropsSI('H','S',S_TIT,'P',P_min(i),Fluid);
        T_TOT_unrec_ID = CoolProp.PropsSI('T','H',H_TOT_unrec_ID,'P',P_min(i),Fluid);
        H_TOT_unrec = H_TIT-eta_is_t_final*(H_TIT-H_TOT_unrec_ID);
        T_TOT_unrec = CoolProp.PropsSI('T','H',H_TOT_unrec,'P',P_min(i),Fluid);
        S_TOT_unrec = CoolProp.PropsSI('S','H',H_TOT_unrec,'P',P_min(i),Fluid);
        %title check
        H_L = CoolProp.PropsSI('H','Q',0,'P',P_min(i),Fluid);
        H_V = CoolProp.PropsSI('H','Q',1,'P',P_min(i),Fluid);
        title_design = (H_TOT_unrec-H_L)/(H_V-H_L);
        T_SAT_COND = CoolProp.PropsSI('T','H',H_V,'P',P_min(i),Fluid);
        T_in_pump_unrec = T_SAT_COND - subcooling;
        H_in_pump_unrec = CoolProp.PropsSI('H','T',T_in_pump_unrec,'P',P_min(i),Fluid);
        S_in_pump_unrec = CoolProp.PropsSI('S','T',T_in_pump_unrec,'P',P_min(i),Fluid);
        Q_cond_unrec_id = m_ORC_unrec*(H_TOT_unrec-H_in_pump_unrec);
        if title_design > 1
            DELTA_H_star = H_TOT_unrec-H_V;
            Q_star = m_ORC_unrec*DELTA_H_star;
            Q_knee = Q_cond_unrec_id - Q_star;
            T_pinch = T_in_CF + DT_DH./Q_cond_unrec_id.*Q_knee;
            DT_check = T_SAT_COND-T_pinch(1);
            if DT_check < DT_LIM & DT_check > 1;
                T_out_CF = T_in_CF + DT_DH;
                H_out_CF = CoolProp.PropsSI('H','T',T_out_CF,'P',p_DH,'water');
                H_in_CF = CoolProp.PropsSI('H','T',T_in_CF,'P',p_DH,'water');
                T_in_pump_unrec = T_SAT_COND - subcooling;
                H_in_pump_unrec = CoolProp.PropsSI('H','T',T_in_pump_unrec,'P',P_min(i),Fluid);
                S_in_pump_unrec = CoolProp.PropsSI('S','T',T_in_pump_unrec,'P',P_min(i),Fluid);
                Q_cond_unrec_id = m_ORC_unrec*(H_TOT_unrec-H_in_pump_unrec);
                m_DH = Q_cond_unrec_id*eta_HX4/(H_out_CF-H_in_CF);
                P_min_final_unrec = P_min(i);
                break
            end
        end
    end
end
end
% S_out_pump_unrec_id = CoolProp.PropsSI('S','T',T_in_pump_unrec,'P',P_max,Fluid);
H_out_pump_unrec_id = CoolProp.PropsSI('H','S',S_in_pump_unrec,'P',P_max,Fluid);
T_out_pump_unrec_id = CoolProp.PropsSI('T','S',S_in_pump_unrec,'P',P_max,Fluid);
eta_pump_design_unrec = (H_out_pump_unrec-H_in_pump_unrec)/(H_out_pump_unrec_id-H_in_pump_unrec);
logicalIndex = eta_pump_design_unrec > 0.7 & eta_pump_design_unrec < 0.8;
eta_pump_design_max_unrec = eta_pump_design_unrec(logicalIndex);
idx = find(logicalIndex);
if length(idx)>1
    idx = max(idx)
end

```

```

EVA_effectiveness = epsilon_HX2(idx);
m_ORC_final_unrec = m_ORC_unrec(idx);
rho_in_turb = CoolProp.PropsSI('D','S',S_TIT,'P',P_max,Fluid)
rho_out_turb = CoolProp.PropsSI('D','S',S_TIT,'P',P_min_final_unrec,Fluid)
v_in = m_ORC_final_unrec/rho_in_turb
v_out = m_ORC_final_unrec/rho_out_turb
h_in_turb = CoolProp.PropsSI('H','S',S_TIT,'P',P_max,Fluid)/1000
h_out_turb = CoolProp.PropsSI('H','S',S_TIT,'P',P_min_final_unrec,Fluid)/1000
filename = 'MACCHI_new.xlsx'; % specify the file name
sheet = 1;
xlswrite(filename, v_in, sheet, 'A2');
xlswrite(filename, v_out, sheet, 'A3');
xlswrite(filename, h_in_turb, sheet, 'B2');
xlswrite(filename, h_out_turb, sheet, 'B3');
range = 'C2';
SP_unrec = xlsread(filename, sheet, range);
range = 'D2';
VR = xlsread(filename, sheet, range);
control = "off";
for l = 1:100
    H_TOT_rec = [];
    TIT_rec = [];
    for i=1:50;
        if i==1;
            H_TOT_rec(i,1) = H_TOT_unrec;
            TIT_rec(i,1) = TIT;
            Q_rec(i,1) = m_ORC_final_unrec*(H_TOT_rec(i,1)-h_ex_HF_rec)*eta_HX3;
            h_ex_CF_rec(i,1) = H_out_pump_unrec(idx)+Q_rec(i,1)/m_ORC_final_unrec;
            T_ex_CF_rec(i,1) = CoolProp.PropsSI('T','H',h_ex_CF_rec(i,1),'P',P_max,Fluid);
            H_TIT_rec(i,1) = h_ex_CF_rec(i,1) + Q_flue*eta_HX2*eta_HX1/m_ORC_final_unrec; %kg/s
            TIT_rec(i,1) = CoolProp.PropsSI('T','H',H_TIT_rec(i,1),'P',P_max,Fluid);
            S_TIT_rec(i,1) = CoolProp.PropsSI('S','T',TIT_rec(i,1),'P',P_max,Fluid);
            TOT_rec_ID(i,1)= CoolProp.PropsSI('T','S',S_TIT_rec(i,1),'P',P_min_final_unrec,Fluid);
            H_TOT_rec_ID(i,1) =
CoolProp.PropsSI('H','S',S_TIT_rec(i,1),'P',P_min_final_unrec,Fluid);
            H_TOT_rec(i,1) = H_TIT_rec(i,1)-eta_is_t_final*(H_TIT_rec(i,1)-H_TOT_rec_ID(i,1));
        else
            H_TOT_rec(i,1) = H_TOT_rec(i-1,1);
            Q_rec(i,1) = m_ORC_final_unrec*(H_TOT_rec(i,1)-h_ex_HF_rec)*eta_HX3;
            h_ex_CF_rec(i,1) = H_out_pump_unrec(idx)+Q_rec(i,1)/m_ORC_final_unrec;
            T_ex_CF_rec(i,1) = CoolProp.PropsSI('T','H',h_ex_CF_rec(i,1),'P',P_max,Fluid);
            H_TIT_rec(i,1) = h_ex_CF_rec(i,1) + Q_flue*eta_HX2*eta_HX1/m_ORC_final_unrec; %kg/s
            TIT_rec(i,1) = CoolProp.PropsSI('T','H',H_TIT_rec(i,1),'P',P_max,Fluid);
            S_TIT_rec(i,1) = CoolProp.PropsSI('S','T',TIT_rec(i,1),'P',P_max,Fluid);
            TOT_rec_ID(i,1)= CoolProp.PropsSI('T','S',S_TIT_rec(i,1),'P',P_min_final_unrec,Fluid);
            H_TOT_rec_ID(i,1) =
CoolProp.PropsSI('H','S',S_TIT_rec(i,1),'P',P_min_final_unrec,Fluid);
            H_TOT_rec(i,1) = H_TIT_rec(i,1)-eta_is_t_final*(H_TIT_rec(i,1)-H_TOT_rec_ID(i,1));
        end
    end
    if i>1;
        if TIT_rec(i,1)-TIT_rec(i-1,1) <0.01;
            TIT_rec_final = TIT_rec(i);
            H_TIT_rec_final = H_TIT_rec(i,1);
            h_ex_CF_rec_final = h_ex_CF_rec(i,1);
            j = i;
            break
        end
    end
end
end

```

```

end
i = 1;
for i = 1:5000;
    if i ==1;
        M_orc_new(i,1) = m_ORC_final_unrec;
        h_ex_CF_rec_new(i,1) = h_ex_CF_rec_final;
        TIT_rec_new(i,1) = TIT_rec_final;
        h_in_t_rec_new(i,1) = H_TIT_rec_final;
        M_orc_new(i,1) = M_orc_new(i,1) + 0.0001;
    elseif i ~=1
        h_in_t_rec_new(i,1) = h_ex_CF_rec_new(i-1,1) + Q_flue*eta_HX2*eta_HX1/M_orc_new(i-1);
%kg/s
        TIT_rec_new(i,1) = CoolProp.PropsSI('T','H',h_in_t_rec_new(i,1),'P',P_max,Fluid);
        s_in_t_rec_new(i,1) = CoolProp.PropsSI('S','T',TIT_rec_new(i,1),'P',P_max,Fluid);
        h_ex_t_rec_new_ID(i,1)=
CoolProp.PropsSI('H','S',s_in_t_rec_new(i,1),'P',P_min_final_unrec,Fluid);
        h_ex_t_rec_new(i,1) = h_in_t_rec_new(i,1)-eta_is_t_final*(h_in_t_rec_new(i,1)-
h_ex_t_rec_new_ID(i,1));
        Q_rec_new(i,1) = M_orc_new(i-1)*(h_ex_t_rec_new(i,1)-h_ex_HF_rec)*eta_HX3;
        h_ex_CF_rec_new(i,1) = H_out_pump_unrec(idx)+Q_rec_new(i,1)/M_orc_new(i-1,1);
        M_orc_new(i,1) = M_orc_new(i-1,1) + 0.001;
    end
    if abs(TIT_rec_new(i,1)-TIT_TARGET)<=0.1;
        TIT_rec_final=TIT_rec_new(i,1);
        H_TIT_rec_final = h_in_t_rec_new(i,1);
        S_TIT_rec_final = CoolProp.PropsSI('S','T',TIT_rec_final,'P',P_max,Fluid);
        M_final_rec = M_orc_new(i-1,1);
        Q_rec_end = Q_rec_new(i,1);
        T_ex_CF_rec_final = CoolProp.PropsSI('T','H', h_ex_CF_rec_new(i,1), 'P',P_max,Fluid);
        H_TOT_rec_final = h_ex_t_rec_new(i,1);
        T_TOT_rec_final = CoolProp.PropsSI('T','H',
H_TOT_rec_final, 'P',P_min_final_unrec,Fluid);
        S_TOT_rec_final = CoolProp.PropsSI('S','H',
H_TOT_rec_final, 'P',P_min_final_unrec,Fluid);
        break
    end
end
q_cond_rec = M_final_rec*(h_ex_HF_rec-H_in_pump_unrec);
DELTA_H_star = h_ex_HF_rec-H_V;
Q_star = M_final_rec*DELTA_H_star;
Q_knee = q_cond_rec - Q_star;
T_pinch_rec = T_in_CF + DT_DH/q_cond_rec.*Q_knee;
DT_check = T_SAT_COND-T_pinch_rec(1);
if DT_check<DT_LIM;
    if control == "off";
        P_min_final_unrec = P_min_final_unrec+0.001*1*P_min_final_unrec;
        H_V = CoolProp.PropsSI('H','Q',1,'P',P_min_final_unrec,Fluid);
        H_L = CoolProp.PropsSI('H','Q',0,'P',P_min_final_unrec,Fluid);
        T_SAT_COND = CoolProp.PropsSI('T','H',H_V,'P',P_min_final_unrec,Fluid);
        T_SAT_COND_L = CoolProp.PropsSI('T','H',H_L,'P',P_min_final_unrec,Fluid);
        T_in_pump_unrec = T_SAT_COND_L - subcooling;
        H_in_pump_unrec =
CoolProp.PropsSI('H','T',T_in_pump_unrec,'P',P_min_final_unrec,Fluid);
        S_in_pump_unrec =
CoolProp.PropsSI('S','T',T_in_pump_unrec,'P',P_min_final_unrec,Fluid);
        H_out_pump_unrec_id = CoolProp.PropsSI('H','S',S_in_pump_unrec,'P',P_max,Fluid);
        T_out_pump_unrec_id = CoolProp.PropsSI('T','S',S_in_pump_unrec,'P',P_max,Fluid);
        eta_pump_design_unrec = (H_out_pump_unrec-H_in_pump_unrec)./(H_out_pump_unrec_id-

```



```

H_in_pump_unrec);
    logicalIndex = eta_pump_design_unrec > 0.7 & eta_pump_design_unrec < 0.8;
    eta_pump_design_max_unrec = eta_pump_design_unrec(logicalIndex);
    idx = find(logicalIndex);
    if length(idx)>1
        idx = max(idx)
    end
    else
        break
    end
else
    if control == "on";
        break
    end
    control = "on";
    H_V = CoolProp.PropsSI('H','Q',1,'P',P_min_final_unrec,Fluid);
    H_L = CoolProp.PropsSI('H','Q',0,'P',P_min_final_unrec,Fluid);
    T_SAT_COND = CoolProp.PropsSI('T','H',H_V,'P',P_min_final_unrec,Fluid);
    T_SAT_COND_L = CoolProp.PropsSI('T','H',H_L,'P',P_min_final_unrec,Fluid);
    T_in_pump_unrec = T_SAT_COND - subcooling;
    H_in_pump_unrec = CoolProp.PropsSI('H','T',T_in_pump_unrec,'P',P_min_final_unrec,Fluid);
    S_in_pump_unrec = CoolProp.PropsSI('S','T',T_in_pump_unrec,'P',P_min_final_unrec,Fluid);
    H_out_pump_unrec_id = CoolProp.PropsSI('H','S',S_in_pump_unrec,'P',P_max,Fluid);
    T_out_pump_unrec_id = CoolProp.PropsSI('T','S',S_in_pump_unrec,'P',P_max,Fluid);
    eta_pump_design_unrec = (H_out_pump_unrec_id-H_in_pump_unrec)./(H_out_pump_unrec-
H_in_pump_unrec);
    logicalIndex = eta_pump_design_unrec > 0.7 & eta_pump_design_unrec < 0.8;
    eta_pump_design_max_unrec = eta_pump_design_unrec(logicalIndex);
    idx = find(logicalIndex);
    if length(idx)>1
        idx = max(idx)
    end
    P_min_final_rec = P_min_final_unrec
end
end

m_ORC_final_rec = M_final_rec
rho_in_turb = CoolProp.PropsSI('D','S',S_TIT_rec_final,'P',P_max,Fluid)
rho_out_turb = CoolProp.PropsSI('D','S',S_TIT_rec_final,'P',P_min_final_rec,Fluid)
v_in = m_ORC_final_rec/rho_in_turb
v_out = m_ORC_final_rec/rho_out_turb
h_in_turb = CoolProp.PropsSI('H','S',S_TIT_rec_final,'P',P_max,Fluid)/1000
h_out_turb = CoolProp.PropsSI('H','S',S_TIT_rec_final,'P',P_min_final_rec,Fluid)/1000
filename = 'MACCHI_new.xlsx'; % specify the file name
sheet = 1;
xlswrite(filename, v_in, sheet, 'A2');
xlswrite(filename, v_out, sheet, 'A3');
xlswrite(filename, h_in_turb, sheet, 'B2');
xlswrite(filename, h_out_turb, sheet, 'B3');
range = 'C2';
SP_rec = xlsread(filename, sheet, range);
range = 'D2';
VR = xlsread(filename, sheet, range);

```

HX2 effectiveness check

%the second HX is always Cmin = C ORC

```
filename = 'HX-REC.xlsx'; % specify the file name
sheet = 3;
xlswrite(filename, T_in_term, sheet, 'D4');
xlswrite(filename, T_out_term, sheet, 'D5');
xlswrite(filename, T_ex_CF_rec_final, sheet, 'D6');
CP_orc = CoolProp.PropsSI('C','T',T_ex_CF_rec_final,'P',P_max,Fluid)
xlswrite(filename, TIT_rec_final, sheet, 'D7');
xlswrite(filename, M_term*3600, sheet, 'H3');
xlswrite(filename, CP_term_in, sheet, 'H6');
xlswrite(filename, m_ORC_final_rec*3600, sheet, 'L3');
xlswrite(filename, CP_orc, sheet, 'L6');
range = 'D9'
eps_HX2 = xlsread(filename, sheet, range)
range = 'H23'
NTU_HX2 = xlsread(filename, sheet, range);
```

HX3 effectiveness check

```
filename = 'HX-REC.xlsx'; % specify the file name
sheet = 4;
xlswrite(filename, T_TOT_rec_final, sheet, 'D4');
xlswrite(filename, T_ex_HF_rec, sheet, 'D5');
xlswrite(filename, T_out_pump_unrec(idx), sheet, 'D6');
CP_rec_CF = CoolProp.PropsSI('C','T',T_out_pump_unrec(idx),'P',P_max,Fluid)
CP_rec_HF = CoolProp.PropsSI('C','T',T_TOT_rec_final,'P',P_min_final_rec,Fluid)
xlswrite(filename, T_ex_CF_rec_final, sheet, 'D7');
xlswrite(filename, m_ORC_final_rec*3600, sheet, 'H3');
xlswrite(filename, CP_rec_HF, sheet, 'H6');
xlswrite(filename, m_ORC_final_rec*3600, sheet, 'L3');
xlswrite(filename, CP_rec_CF, sheet, 'L6');
range = 'D9'
eps_HX3 = xlsread(filename, sheet, range)
range = 'H15'
NTU_HX3 = xlsread(filename, sheet, range);
```

HX4 effectiveness check

%the second HX is always Cmin = C ORC

```
filename = 'HX-REC.xlsx'; % specify the file name
sheet = 5;
xlswrite(filename, T_ex_HF_rec, sheet, 'D4');
CP_orc = CoolProp.PropsSI('C','T',T_ex_HF_rec,'P',P_min_final_rec,Fluid)
xlswrite(filename, T_in_pump_unrec, sheet, 'D5');
xlswrite(filename, T_in_CF, sheet, 'D6');
CP_CF = CoolProp.PropsSI('C','T',T_in_CF,'P',p_DH,'water')
xlswrite(filename, T_out_CF, sheet, 'D7');
xlswrite(filename, m_ORC_final_rec*3600, sheet, 'H3');
xlswrite(filename, CP_orc, sheet, 'H6');
xlswrite(filename, m_DH(idx)*3600, sheet, 'L3');
xlswrite(filename, CP_CF, sheet, 'L6');
range = 'D9'
eps_HX4 = xlsread(filename, sheet, range)
```

```
range = 'H23'
NTU_HX4 = xlsread(filename, sheet, range);
```

global efficiency

```
eta_e1 = 0.97
eta_mecc = 0.95
Q_COND = m_ORC_final_rec*(h_ex_HF_rec-H_in_pump_unrec)*eta_HX4
W_turb = m_ORC_final_rec*(H_TIT_rec_final-H_TOT_rec_final)*eta_mecc*eta_e1
W_pump = m_ORC_final_rec*(H_out_pump_unrec(idx)-H_in_pump_unrec)/eta_mecc/eta_e1
eta_e1_cycle = (W_turb-W_pump)/Q_flue
eta_t_cycle = Q_COND/Q_flue
eta_tot = eta_e1_cycle+eta_t_cycle
```

sCO₂ POWER UNIT (+ SUMMER VARIANT)

```
close
clc
clear

Fluid = 'CO2';
```

CO2 critical properties

```
T_crit = CoolProp.Props1SI(Fluid, 'Tcrit'); %K
P_crit = CoolProp.Props1SI(Fluid, 'Pcrit'); %Pa
```

CO2 Design Condition

```
P_max = 250; %bar
P_max = P_max*1e5;
P_min = 75; %bar
P_min = P_min*1e5;
% efficiencies
eta_is_t = 0.85
eta_is_c = 0.8
eta_e1 = 0.97
eta_mec = 0.95
eta_HX1 = 0.9
eta_HX2 = 0.95
eta_HX3 = 0.9
eta_HX4 = 0.9
eta_HX5 = 0.9
%TIT
TIT = 550; %input
TIT = TIT + 273.15;
TIT_TARGET = TIT;
```

Pinch

```
pinch = 10;
D_DH = 30;
```

Flue gas load

```
Q_flue = 6375000 %W
M_flue = 35771/3600;
T_in_flue = 800;
T_in_flue = T_in_flue + 273.15;
T_out_flue = 250 + 273.15;
Q_eva = Q_flue
```

```
epsilon_HX1 = linspace(0.7, 0.90, 300); %input

T_out_compr = T_in_flue - (T_in_flue - T_out_flue) ./ epsilon_HX1;
H_TIT = CoolProp.PropsSI('H', 'T', TIT, 'P', P_max, Fluid);
S_TIT = CoolProp.PropsSI('S', 'T', TIT, 'P', P_max, Fluid);
for i = 1:length(T_out_compr);
    H_out_compr(i) = CoolProp.PropsSI('H', 'T', T_out_compr(i), 'P', P_max, Fluid);
    S_out_compr(i) = CoolProp.PropsSI('S', 'T', T_out_compr(i), 'P', P_max, Fluid);
    DELTA_H(i) = H_TIT - H_out_compr(i);
end
m_CO2_unrec = Q_eva ./ DELTA_H;
```

HX1 effectiveness (trial) check

```
%the first HX is always Cmin = C fluegas

M_CO2_trial = 73000/3600
CP_co2_trial = 1448

CP_flue_in = 1233.66;
filename = 'HX-REC - CO2.xlsx'; % specify the file name
sheet = 2; % Second spreadsheet
xlswrite(filename, T_in_flue, sheet, 'D4');
xlswrite(filename, T_out_flue, sheet, 'D5');
xlswrite(filename, T_out_compr(55), sheet, 'D6');
xlswrite(filename, TIT, sheet, 'D7');
xlswrite(filename, M_flue*3600, sheet, 'H3');
xlswrite(filename, CP_flue_in, sheet, 'H6');
xlswrite(filename, M_CO2_trial*3600, sheet, 'L3');
xlswrite(filename, CP_co2_trial, sheet, 'L6');
range = 'D9'
eps_HX1 = xlsread(filename, sheet, range)
range = 'H15'
NTU_HX1 = xlsread(filename, sheet, range);
% Define the variable value
```

Turbine discharge conditions

```
S_TOT_is = S_TIT
H_TOT_is = CoolProp.PropsSI('H', 'S', S_TOT_is, 'P', P_min, Fluid);
H_TOT = H_TIT - (H_TIT - H_TOT_is) * eta_is_t
```

```
S_TOT = CoolProp.PropsSI('S','H',H_TOT,'P',P_min,Fluid);
T_TOT = CoolProp.PropsSI('T','H',H_TOT,'P',P_min,Fluid);
```

DH specification

```
T_in_water = 45;
T_in_water = T_in_water+273.15;
p_DH = 1;
p_DH = p_DH *1e5;
T_out_water = T_in_water + D_DH;
H_in_water = CoolProp.PropsSI('H','T',T_in_water,'P',p_DH,'water');
H_out_water = CoolProp.PropsSI('H','T',T_out_water,'P',p_DH,'water');
T_out_cond = T_in_water + pinch
H_out_cond = CoolProp.PropsSI('H','T',T_out_cond,'P',P_min,Fluid);
S_out_cond = CoolProp.PropsSI('S','T',T_out_cond,'P',P_min,Fluid);
Q_cond = m_CO2_unrec*(H_TOT-H_out_cond);
m_DH = -Q_cond*eta_HX3/(H_in_water-H_out_water);
```

%check on NTU

```
filename = 'HX-REC - CO2.xlsx'; % specify the file name
sheet = 5; % Second spreadsheet

xlswrite(filename, T_TOT, sheet, 'D4');
CP_CO2 = CoolProp.PropsSI('C','T',T_TOT,'P',P_min,Fluid);
xlswrite(filename, T_out_cond, sheet, 'D5');
xlswrite(filename, T_in_water, sheet, 'D6');
CP_CF = CoolProp.PropsSI('C','T',T_in_water,'P',p_DH,'water')
xlswrite(filename, T_out_water, sheet, 'D7');
xlswrite(filename, m_CO2_unrec(55)*3600, sheet, 'H3');
xlswrite(filename, CP_CO2, sheet, 'H6');
xlswrite(filename, m_DH(55)*3600, sheet, 'L3');
xlswrite(filename, CP_CF, sheet, 'L6');
range = 'D9';
eps_HX3 = xlsread(filename, sheet, range);
range = 'H22' %no condensing
NTU_HX3 = xlsread(filename, sheet, range);
```

Second cooling (T air + 10)

```
T_air = 14.1 % in line with EPI SPREADSHEET (october), conservative scenario
T_air = T_air +273.15; % in line with UNI 10349
T_air_out = 30; % guess outlet temperature
T_air_out = T_air_out+273.15; % guess outlet temperature
p_air = 1; %bar
p_air = p_air*1e5;
H_in_air = CoolProp.PropsSI('H','T',T_air,'P',p_air,'air');
H_out_air = CoolProp.PropsSI('H','T',T_air_out,'P',p_air,'air');
S_in_air = CoolProp.PropsSI('S','T',T_air,'P',p_air,'air');
S_out_air = CoolProp.PropsSI('S','T',T_air_out,'P',p_air,'air');
T_in_cond2 = T_out_cond;
T_out_cond2 = 35;
T_out_cond2 = T_out_cond2 + 273.15;
H_out_cond2 = CoolProp.PropsSI('H','T',T_out_cond2,'P',P_min,Fluid);
S_out_cond2 = CoolProp.PropsSI('S','T',T_out_cond2,'P',P_min,Fluid);
```

```

Q_cond2 = m_CO2_unrec*(H_out_cond-H_out_cond2);
M_air = Q_cond2/eta_HX4/(H_out_air-H_in_air);

%check on NTU

filename = 'HX-REC - CO2.xlsx'; % specify the file name
sheet = 6; % Second spreadsheet

xlswrite(filename, T_in_cond2, sheet, 'D4');
CP_CO2 = CoolProp.PropsSI('C','T',T_in_cond2,'P',P_min,Fluid);
xlswrite(filename, T_out_cond2, sheet, 'D5');
xlswrite(filename, T_air, sheet, 'D6');
CP_CF = CoolProp.PropsSI('C','T',T_air,'P',p_DH,'air')
xlswrite(filename, T_air_out, sheet, 'D7');
xlswrite(filename, m_CO2_unrec(55)*3600, sheet, 'H3');
xlswrite(filename, CP_CO2, sheet, 'H6');
xlswrite(filename, M_air(55)*3600, sheet, 'L3');
xlswrite(filename, CP_CF, sheet, 'L6');
range = 'D9';
eps_HX4 = xlsread(filename, sheet, range);
range = 'H22' %no condensing
NTU_HX4 = xlsread(filename, sheet, range);

```

Chiller cooling (T air + 10)

```

T_chill_out = T_out_cond2
H_chill_out = CoolProp.PropsSI('H','T',T_chill_out,'P',P_min,Fluid);
S_chill_out = CoolProp.PropsSI('S','T',T_chill_out,'P',P_min,Fluid);
Q_cond3 = m_CO2_unrec*(H_out_cond2-H_chill_out);
COP = 3.5; %assumption
chiller_work = Q_cond3/COP/eta_HX5;
% T_in_ref_chil = 5;
% T_out_ref_chil = 10;
% T_in_ref_chil = T_in_ref_chil+273.15
% T_out_ref_chil = T_out_ref_chil+273.15

```

Index evaluation for the correct mass flow rate

```

S_in_compr = S_chill_out
H_in_compr = H_chill_out
H_out_compr_id = CoolProp.PropsSI('H','S',S_in_compr,'P',P_max,Fluid);
T_out_compr_id = CoolProp.PropsSI('T','S',S_in_compr,'P',P_max,Fluid);
eta_compr_is = (H_out_compr_id-H_in_compr)/(H_out_compr-H_in_compr);
epsilon = 0.01
logicalIndex = eta_compr_is > (eta_is_c-epsilon) & eta_compr_is < (eta_is_c+epsilon);
idx = find(logicalIndex);
if length(idx)>1
    idx = max(idx)
end
EVA_effectiveness = epsilon_HX1(idx);
T_out_compr_final = T_out_compr(idx)
S_out_compr_final = S_out_compr(idx)
H_out_compr_final = H_out_compr(idx)
m_CO2_unrec_final = m_CO2_unrec(idx)

```

%%heat exchanger specification

```
CP_CO2 = CoolProp.PropsSI('C','S',s_out_compr_final,'P',P_max,Fluid);  
filename = 'HX-REC - CO2.xlsx'; % specify the file name
```

```
sheet = 2; % Second spreadsheet  
xlswrite(filename, T_in_flue, sheet, 'D4');  
xlswrite(filename, T_out_flue, sheet, 'D5');  
xlswrite(filename, T_out_compr_final, sheet, 'D6');  
xlswrite(filename, TIT, sheet, 'D7');  
xlswrite(filename, M_flue*3600, sheet, 'H3');  
xlswrite(filename, CP_flue_in, sheet, 'H6');  
xlswrite(filename, m_CO2_unrec_final*3600, sheet, 'L3');  
xlswrite(filename, CP_CO2, sheet, 'L6');  
range = 'D9'  
eps_HX1 = xlsread(filename, sheet, range)  
range = 'H22'  
NTU_HX1 = xlsread(filename, sheet, range);
```

```
sheet = 5; % Second spreadsheet  
xlswrite(filename, T_TOT, sheet, 'D4');  
CP_CO2 = CoolProp.PropsSI('C','T',T_TOT,'P',P_min,Fluid);  
xlswrite(filename, T_out_cond, sheet, 'D5');  
xlswrite(filename, T_in_water, sheet, 'D6');  
CP_CF = CoolProp.PropsSI('C','T',T_in_water,'P',p_DH,'Water')  
xlswrite(filename, T_out_water, sheet, 'D7');  
xlswrite(filename, m_CO2_unrec_final*3600, sheet, 'H3');  
xlswrite(filename, CP_CO2, sheet, 'H6');  
xlswrite(filename, m_DH(idx)*3600, sheet, 'L3');  
xlswrite(filename, CP_CF, sheet, 'L6');  
range = 'D9';  
eps_HX3 = xlsread(filename, sheet, range);  
range = 'H22' %no condensing  
NTU_HX3 = xlsread(filename, sheet, range);
```

```
sheet = 6; % Second spreadsheet  
xlswrite(filename, T_in_cond2, sheet, 'D4');  
CP_CO2 = CoolProp.PropsSI('C','T',T_in_cond2,'P',P_min,Fluid);  
xlswrite(filename, T_out_cond2, sheet, 'D5');  
xlswrite(filename, T_air, sheet, 'D6');  
CP_CF = CoolProp.PropsSI('C','T',T_air,'P',p_DH,'air')  
xlswrite(filename, T_air_out, sheet, 'D7');  
xlswrite(filename, m_CO2_unrec_final*3600, sheet, 'H3');  
xlswrite(filename, CP_CO2, sheet, 'H6');  
xlswrite(filename, M_air(idx)*3600, sheet, 'L3');  
xlswrite(filename, CP_CF, sheet, 'L6');  
range = 'D9';  
eps_HX4 = xlsread(filename, sheet, range);  
range = 'H22' %no condensing  
NTU_HX4 = xlsread(filename, sheet, range);
```

Recuperator

```
H_TOT_rec = [];  
TIT_rec = [];
```

```

T_ex_HF_rec = 280 %%% input, 160 unfeasible, 170 minimo
T_ex_HF_rec = T_ex_HF_rec+273.15
h_ex_HF_rec = CoolProp.PropsSI('H','T',T_ex_HF_rec,'P',P_min,Fluid);
for i=1:500;
    if i==1;
        H_TOT_rec(i,1) = H_TOT;
        TIT_rec(i,1) = TIT;
        Q_rec(i,1) = m_CO2_unrec_final*(H_TOT_rec(i,1)-h_ex_HF_rec)*eta_HX2;
        h_ex_CF_rec(i,1) = H_out_compr_final+Q_rec(i,1)/m_CO2_unrec_final;
        T_ex_CF_rec(i,1) = CoolProp.PropsSI('T','H',h_ex_CF_rec(i,1),'P',P_max,Fluid);
        H_TIT_rec(i,1) = h_ex_CF_rec(i,1) + Q_flue*eta_HX1/m_CO2_unrec_final; %kg/s
        TIT_rec(i,1) = CoolProp.PropsSI('T','H',H_TIT_rec(i,1),'P',P_max,Fluid);
        S_TIT_rec(i,1) = CoolProp.PropsSI('S','T',TIT_rec(i,1),'P',P_max,Fluid);
        TOT_rec_ID(i,1)= CoolProp.PropsSI('T','S',S_TIT_rec(i,1),'P',P_min,Fluid);
        H_TOT_rec_ID(i,1) = CoolProp.PropsSI('H','S',S_TIT_rec(i,1),'P',P_min,Fluid);
        H_TOT_rec(i,1) = H_TIT_rec(i,1)-eta_is_t*(H_TIT_rec(i,1)-H_TOT_rec_ID(i,1));
    else
        H_TOT_rec(i,1) = H_TOT_rec(i-1,1);
        Q_rec(i,1) = m_CO2_unrec_final*(H_TOT_rec(i,1)-h_ex_HF_rec)*eta_HX2;
        h_ex_CF_rec(i,1) = H_out_compr_final+Q_rec(i,1)/m_CO2_unrec_final;
        T_ex_CF_rec(i,1) = CoolProp.PropsSI('T','H',h_ex_CF_rec(i,1),'P',P_max,Fluid);
        H_TIT_rec(i,1) = h_ex_CF_rec(i,1) + Q_flue*eta_HX1/m_CO2_unrec_final; %kg/s
        TIT_rec(i,1) = CoolProp.PropsSI('T','H',H_TIT_rec(i,1),'P',P_max,Fluid);
        S_TIT_rec(i,1) = CoolProp.PropsSI('S','T',TIT_rec(i,1),'P',P_max,Fluid);
        TOT_rec_ID(i,1)= CoolProp.PropsSI('T','S',S_TIT_rec(i,1),'P',P_min,Fluid);
        H_TOT_rec_ID(i,1) = CoolProp.PropsSI('H','S',S_TIT_rec(i,1),'P',P_min,Fluid);
        H_TOT_rec(i,1) = H_TIT_rec(i,1)-eta_is_t*(H_TIT_rec(i,1)-H_TOT_rec_ID(i,1));
        TOT_rec(i,1)= CoolProp.PropsSI('T','H',H_TOT_rec(i,1),'P',P_min,Fluid);
    end
    if i>1;
        if TIT_rec(i,1)-TIT_rec(i-1,1) <0.01;
            TIT_rec_final = TIT_rec(i);
            H_TIT_rec_final = H_TIT_rec(i,1);
            h_ex_CF_rec_final = h_ex_CF_rec(i,1);
            H_TOT_rec_final = H_TOT_rec(i,1)
            TOT_rec_final = TOT_rec(i,1)
            j = i;
            break
        end
    end
end
i = 1;
lambda = 1; %accelerator parameter
for i = 1:5000;
    if i ==1;
        M_orc_new(i,1) = m_CO2_unrec_final;
        h_ex_CF_rec_new(i,1) = h_ex_CF_rec_final;
        TIT_rec_new(i,1) = TIT_rec_final;
        h_in_t_rec_new(i,1) = H_TIT_rec_final;
        M_orc_new(i,1) = M_orc_new(i,1) + 0.01;
        d = abs(TIT_rec_new(i,1)-TIT_TARGET);
    elseif i ~1
        h_in_t_rec_new(i,1) = h_ex_CF_rec_new(i-1,1) + Q_flue*eta_HX1/M_orc_new(i-1); %kg/s
        TIT_rec_new(i,1) = CoolProp.PropsSI('T','H',h_in_t_rec_new(i,1),'P',P_max,Fluid);
        s_in_t_rec_new(i,1) = CoolProp.PropsSI('S','T',TIT_rec_new(i,1),'P',P_max,Fluid);
        h_ex_t_rec_new_ID(i,1)= CoolProp.PropsSI('H','S',s_in_t_rec_new(i,1),'P',P_min,Fluid);
        h_ex_t_rec_new(i,1) = h_in_t_rec_new(i,1)-eta_is_t*(h_in_t_rec_new(i,1)-
h_ex_t_rec_new_ID(i,1));

```



```

Q_rec_new(i,1) = M_orc_new(i-1)*(h_ex_t_rec_new(i,1)-h_ex_HF_rec)*eta_HX2;
h_ex_CF_rec_new(i,1) = H_out_compr_final+Q_rec_new(i,1)/M_orc_new(i-1,1);
d = abs(TIT_rec_new(i,1)-TIT_TARGET)
if d >=500 ;
    lambda = 100;
elseif d >= 100 & d < 500;
    lambda = 50;
elseif d >= 20 & d < 100;
    lambda = 10;
else
    lambda = 1;
end
M_orc_new(i,1) = M_orc_new(i-1,1) + 0.001*lambda;
end
if d <= 1
    TIT_rec_final=TIT_rec_new(i,1);
    H_TIT_rec_final = h_in_t_rec_new(i,1);
    S_TIT_rec_final = CoolProp.PropsSI('S','T',TIT_rec_final,'P',P_max,Fluid);
    M_final_rec = M_orc_new(i-1,1);
    Q_rec_end = Q_rec_new(i,1);
    T_ex_CF_rec_final = CoolProp.PropsSI('T','H', h_ex_CF_rec_new(i,1),'P',P_max,Fluid);
    H_TOT_rec_final = h_ex_t_rec_new(i,1);
    T_TOT_rec_final = CoolProp.PropsSI('T','H', H_TOT_rec_final,'P',P_min,Fluid);
    S_TOT_rec_final = CoolProp.PropsSI('S','H', H_TOT_rec_final,'P',P_min,Fluid);
    break
end
end
%final exchangers
Q_cond_rec = M_final_rec*(h_ex_HF_rec-H_out_cond);
m_DH_rec = -Q_cond_rec*eta_HX3/(H_in_water-H_out_water);
Q_cond2_rec = M_final_rec*(H_out_cond-H_out_cond2);
M_air_rec = Q_cond2_rec/eta_HX4/(H_out_air-H_in_air);
Q_cond3_rec = M_final_rec*(H_out_cond2-H_chill_out);
COP = 3.5; %assumption
chiller_work = Q_cond3_rec/COP/eta_HX5;

```

final NTU check

```

%eva
sheet = 2; % Second spreadsheet
CP_CO2 = CoolProp.PropsSI('C','T',T_ex_CF_rec_final,'P',P_max,Fluid);
xlswrite(filename, T_in_flue, sheet, 'D4');
xlswrite(filename, T_out_flue, sheet, 'D5');
xlswrite(filename, T_ex_CF_rec_final, sheet, 'D6');
xlswrite(filename, TIT, sheet, 'D7');
xlswrite(filename, M_flue*3600, sheet, 'H3');
xlswrite(filename, CP_flue_in, sheet, 'H6');
xlswrite(filename, M_final_rec*3600, sheet, 'L3');
xlswrite(filename, CP_CO2, sheet, 'L6');
range = 'D9'
eps_HX1 = xlsread(filename, sheet, range)
range = 'H22'
NTU_HX1 = xlsread(filename, sheet, range);

%rec
sheet = 4; % Second spreadsheet

```

```

xlswrite(filename, T_TOT_rec_final, sheet, 'D4');
CP_CO2 = CoolProp.PropsSI('C','T',T_TOT_rec_final,'P',P_min,Fluid);
xlswrite(filename, T_ex_HF_rec, sheet, 'D5');
xlswrite(filename, T_out_compr_final, sheet, 'D6');
CP_CF = CoolProp.PropsSI('C','T',T_out_compr_final,'P',P_max,Fluid)
xlswrite(filename, T_ex_CF_rec_final, sheet, 'D7');
xlswrite(filename, M_final_rec*3600, sheet, 'H3');
xlswrite(filename, CP_CO2, sheet, 'H6');
xlswrite(filename, M_final_rec*3600, sheet, 'L3');
xlswrite(filename, CP_CF, sheet, 'L6');
range = 'D9';
eps_HX2 = xlsread(filename, sheet, range);
range = 'H15' %no condensing
NTU_HX2 = xlsread(filename, sheet, range);

%DH
sheet = 5; % Second spreadsheet
xlswrite(filename, T_ex_HF_rec, sheet, 'D4');
CP_CO2 = CoolProp.PropsSI('C','T',T_ex_HF_rec,'P',P_min,Fluid);
xlswrite(filename, T_out_cond, sheet, 'D5');
xlswrite(filename, T_in_water, sheet, 'D6');
CP_CF = CoolProp.PropsSI('C','T',T_in_water,'P',p_DH,'Water')
xlswrite(filename, T_out_water, sheet, 'D7');
xlswrite(filename, M_final_rec*3600, sheet, 'H3');
xlswrite(filename, CP_CO2, sheet, 'H6');
xlswrite(filename, m_DH_rec*3600, sheet, 'L3');
xlswrite(filename, CP_CF, sheet, 'L6');
range = 'D9';
eps_HX3 = xlsread(filename, sheet, range);
range = 'H22' %no condensing
NTU_HX3 = xlsread(filename, sheet, range);

%air
sheet = 6; % Second spreadsheet
xlswrite(filename, T_in_cond2, sheet, 'D4');
CP_CO2 = CoolProp.PropsSI('C','T',T_in_cond2,'P',P_min,Fluid);
xlswrite(filename, T_out_cond2, sheet, 'D5');
xlswrite(filename, T_air, sheet, 'D6');
CP_CF = CoolProp.PropsSI('C','T',T_air,'P',p_DH,'air')
xlswrite(filename, T_air_out, sheet, 'D7');
xlswrite(filename, M_final_rec*3600, sheet, 'H3');
xlswrite(filename, CP_CO2, sheet, 'H6');
xlswrite(filename, M_air_rec*3600, sheet, 'L3');
xlswrite(filename, CP_CF, sheet, 'L6');
range = 'D9';
eps_HX4 = xlsread(filename, sheet, range);
range = 'H22' %no condensing
NTU_HX4 = xlsread(filename, sheet, range);

```

Second cooling (T air + 10) ACTIVE ONLY IN SUMMER (DEDICATED SCRIPT)

```

T_air = 30 % in line with summer temperature
T_air = T_air +273.15; % in line with UNI 10349
T_air_out = 45; % guess outlet temperature

```

```

T_air_out = T_air_out+273.15; % guess outlet temperature
p_air = 1; %bar
p_air = p_air*1e5;
H_in_air = CoolProp.PropsSI('H','T',T_air,'P',p_air,'air');
H_out_air = CoolProp.PropsSI('H','T',T_air_out,'P',p_air,'air');
S_in_air = CoolProp.PropsSI('S','T',T_air,'P',p_air,'air');
S_out_air = CoolProp.PropsSI('S','T',T_air_out,'P',p_air,'air');
T_in_cond2 = T_out_cond;
T_out_cond2 = T_air+pinch;
H_out_cond2 = CoolProp.PropsSI('H','T',T_out_cond2,'P',P_min,Fluid);
S_out_cond2 = CoolProp.PropsSI('S','T',T_out_cond2,'P',P_min,Fluid);
Q_cond2 = m_CO2_unreg*(H_out_cond-H_out_cond2);
M_air = Q_cond2/eta_HX4/(H_out_air-H_in_air);

%check on NTU

filename = 'HX-REG - CO2.xlsx'; % specify the file name
sheet = 16; % Second spreadsheet

xlswrite(filename, T_in_cond2, sheet, 'D4');
CP_CO2 = CoolProp.PropsSI('C','T',T_in_cond2,'P',P_min,Fluid);
xlswrite(filename, T_out_cond2, sheet, 'D5');
xlswrite(filename, T_air, sheet, 'D6');
CP_CF = CoolProp.PropsSI('C','T',T_air,'P',p_DH,'air')
xlswrite(filename, T_air_out, sheet, 'D7');
xlswrite(filename, m_CO2_unreg(55)*3600, sheet, 'H3');
xlswrite(filename, CP_CO2, sheet, 'H6');
xlswrite(filename, M_air(55)*3600, sheet, 'L3');
xlswrite(filename, CP_CF, sheet, 'L6');
range = 'D9';
eps_HX4 = xlsread(filename, sheet, range);
range = 'H22' %no condensing
NTU_HX4 = xlsread(filename, sheet, range);

```

chiller cooling (T air + 10) ACTIVE ONLY IN SUMMER (DEDICATED SCRIPT)

```

T_chill_out = 35
T_chill_out = T_chill_out +273.15
H_chill_out = CoolProp.PropsSI('H','T',T_chill_out,'P',P_min,Fluid);
S_chill_out = CoolProp.PropsSI('S','T',T_chill_out,'P',P_min,Fluid);
Q_cond3 = m_CO2_unreg*(H_out_cond2-H_chill_out);
COP = 2; %assumption
chiller_work = Q_cond3/COP/eta_HX5;
T_in_ref_chil = 5;
T_out_ref_chil = 10;
T_in_ref_chil = T_in_ref_chil+273.15
T_out_ref_chil = T_out_ref_chil+273.15

```

global efficiency

```

eta_e1 = 0.97
eta_mecc = 0.95
Q_COND = M_final_rec*(h_ex_HF_rec-H_out_cond)*eta_HX3
W_turb = M_final_rec*(H_TIT_rec_final-H_TOT_rec_final)*eta_mecc*eta_e1
W_compr = M_final_rec*(H_out_compr_final-H_in_compr)/eta_mecc/eta_e1

```

```
eta_el_cycle = (w_turb-w_compr)/Q_flue  
eta_t_cycle = Q_COND/Q_flue  
eta_tot = eta_el_cycle+eta_t_cycle
```

APPENDIX II: MATLAB CODES FOR WOOD PYROLYSIS

This appendix presents the code developed in Matlab that describes the transient behaviour of a wood pyrolyzer, validated according to the experimental data reported in literature. Due to the limited scale of the experiment, a 0D modelling approach has been used. The model consists of three main parts. The first one, “Main Solver”, need to define the experimental data and the boundary conditions, whereas the second one “Derivative Solver” is used to set the system of ODE for obtaining the concentration of the chemical species during time. The last one, “RMSE optimiser” is used for optimising the temperature approaches of the 26 reactions present in the model required for describing the formation/reduction of the 32 chemical species inside the reactor, either with SQP and Levenberg-Marquardt algorithms.

MAIN SOLVER

```
D = 0.0721
A = 3.1415*0.25*D^2
Z = 0.95
V = Z*A; % reactor volume [m3];
R = 8.314;
MM_H = 1.008;
MM_C = 12.01;
MM_O = 15.99;
MM_N2 = 14.01*2;

weight_cell = 0.3801;
weight_hcell = 0.2781;
weight_lignC = 0.1628;
weight_lignH = 0.0145;
weight_lignO = 0.0637;
weight_water_liq = 0.098;
weight_ash = 0.0028;

MM_cell = 6*MM_C+10*MM_H+5*MM_O; %kg/kmol;
MM_hcell = 5*MM_C+8*MM_H+4*MM_O;
MM_lignC = 15*MM_C+14*MM_H+4*MM_O;
MM_lignH = 16*MM_C+10*MM_H+6*MM_O+4*MM_C+12*MM_H+4*MM_O;
MM_lignO = 17*MM_C+13*MM_H+4*MM_O+5*MM_C+15*MM_H+5*MM_O;
MM_water_liq = 2*MM_H+1*MM_O;
MM_ash = 1;

MM_lignOH = 19*MM_C+22*MM_H+8*MM_O;
MM_lign = 11*MM_C+12*MM_H+4*MM_O;
```

```

MM_CH4 = 1*MM_C+4*MM_H+0*MM_O;
MM_C2H4 = 2*MM_C+4*MM_H+0*MM_O;
MM_CO = 1*MM_C+0*MM_H+1*MM_O;
MM_CO2 = 1*MM_C+0*MM_H+2*MM_O;
MM_H2 = 0*MM_C+2*MM_H+0*MM_O;
MM_water = MM_water_liq;
MM_Formaldehyde = 1*MM_C+2*MM_H+1*MM_O;
MM_Acetaldehyde = 2*MM_C+4*MM_H+1*MM_O;
MM_Methanol = 1*MM_C+4*MM_H+1*MM_O;
MM_Glyoxal = 2*MM_C+2*MM_H+2*MM_O;
MM_Ethylene = 2*MM_C+4*MM_H+0*MM_O;
MM_HAA = 2*MM_C+4*MM_H+2*MM_O;
MM_Ethanol = 2*MM_C+6*MM_H+1*MM_O;
MM_Acrylic_acid = 3*MM_C+4*MM_H+2*MM_O;
MM_Acetone = 3*MM_C+6*MM_H+1*MM_O;
MM_Xylan = 5*MM_C+8*MM_H+4*MM_O;
MM_LVG = 6*MM_C+10*MM_H+5*MM_O;
MM_Phenol = 6*MM_C+6*MM_H+1*MM_O;
MM_HMFU = 6*MM_C+6*MM_H+3*MM_O;
MM_pCoumaryl = 9*MM_C+10*MM_H+2*MM_O;
MM_Lumped_phenol = 11*MM_C+12*MM_H+4*MM_O;

time = 50;
n = (2500) +1;
dt = time/(n-1);
t = linspace(0,time,n);

for i = 1:(n-1)
if t(i) < 1.4
    mass_rate(i) = 0/3600; %kg/s;
else
    if t(i) <= 5
        mass_rate(i) = 2/3600;
    else
        if t(i) > 5 & t(i) <= 10
            mass_rate(i) = 3/3600;
        else
            if t(i) > 10 & t(i) <= 30
                mass_rate(i) = 0/3600;
            else
                mass_rate(i) = 1/3600;
            end
        end
    end
end

if i == 1

T_pyro =500+273.15;
% start with N2;
pressure = 101325
dens =refpropm('D', 'T', T_pyro, 'P', pressure/1000, 'nitrogen'); %kg/m3 pressure kPa;
cp = refpropm('C', 'T', T_pyro, 'P', pressure/1000, 'nitrogen'); %kg/m3 pressure kPa;

residence_time = 1.8;
mass_rate_nitrogen = 0.00045;

```

```

% vol_tot = V/residence_time;
vol_tot = mass_rate_nitrogen/dens;
vol_tot_0 = vol_tot

c_cell_F=mass_rate(i)*weight_cell/MM_cell*1000/vol_tot;
c_Hcell_F=mass_rate(i)*weight_Hcell/MM_Hcell*1000/vol_tot;
c_lignC_F=mass_rate(i)*weight_lignC/MM_lignC*1000/vol_tot;
c_lignH_F=mass_rate(i)*weight_lignH/MM_lignH*1000/vol_tot;
c_lignO_F = mass_rate(i)*weight_lignO/MM_lignO*1000/vol_tot;
c_H2O_L_F=mass_rate(i)*weight_water_liq/MM_water_liq*1000/vol_tot;
c_cellA_F=0;
c_H2O_F=0;
c_char_F=0;
c_LVG_F=0;
c_HAA_F=0;
c_glyoxal_F=0;
c_acetaldehyd_F=0;
c_HMFU_F=0;
c_acetone_F=0;
c_CO2_F=0;
c_CO_F=0;
c_CH4_F=0;
c_Hcell1_F=0;
c_Hcell2_F=0;
c_H2_F=0;
c_formaldehyde_F=0;
c_xylaF_F=0;
c_C2H4_F=0;
c_methanol_F=0;
c_ethanol_F=0;
c_lignCC_F = 0;
c_pCoumaryl_F = 0;
c_phenol_F = 0;
c_lignOH_F = 0;
c_acry_F = 0;
c_lign = 0;
c_lumPhe = 0;
rho_F = dens;
c_N2_F = dens/MM_N2*1000;
y = [c_cell_F c_cellA_F c_H2O_F c_char_F c_LVG_F c_HAA_F c_glyoxal_F c_acetaldehyd_F c_HMFU_F
c_acetone_F ...;
c_CO2_F c_CO_F c_CH4_F c_Hcell_F c_Hcell1_F c_Hcell2_F c_H2_F c_formaldehyde_F c_xylaF_F c_C2H4_F
c_methanol_F c_ethanol_F ...;
c_lignC_F c_lignCC_F c_pCoumaryl_F c_phenol_F c_lignH_F c_lignOH_F c_lignO_F c_acry_F c_lign
c_lumPhe c_H2O_L_F T_pyro rho_F];
y_0 = y;
save('init.mat', 'y_0','MM_cell','MM_Hcell','MM_lignC','MM_lignH','MM_lignO','MM_lignOH', ...;
'MM_lign','MM_water_liq','MM_HMFU','MM_Acetone','MM_pCoumaryl','MM_Phenol','MM_Xylan','MM_LVG','MM_
HAA', ...;
'MM_Glyoxal','MM_Lumped_phenol','MM_Acrylic_acid', 'dens','vol_tot', ...;
'mass_rate','weight_cell','weight_Hcell','weight_lignC', 'weight_lignH', ...
'weight_lignO','weight_water_liq','i','cp', 'V', 'mass_rate_nitrogen', 'residence_time', 't');

else
    if mass_rate(i) == mass_rate(i-1)
        y = [Y(nn,1) Y(nn,2) Y(nn,3) Y(nn,4) Y(nn,5) Y(nn,6) Y(nn,7) Y(nn,8) Y(nn,9) Y(nn,10) ...;
Y(nn,11) Y(nn,12) Y(nn,13) Y(nn,14) Y(nn,15) Y(nn,16) Y(nn,17) Y(nn,18) Y(nn,19) Y(nn,20)

```

```

Y(nn,21) Y(nn,22) ...;
    Y(nn,23) Y(nn,24) Y(nn,25) Y(nn,26) Y(nn,27) Y(nn,28) Y(nn,29) Y(nn,30) Y(nn,31) Y(nn,32)
Y(nn,33) Y(nn,34) Y(nn,35)];
    save('init.mat', 'y_0', 'MM_cell', 'MM_Hcell', 'MM_lignC', 'MM_lignH', 'MM_ligno', 'MM_lignOH',
...;

'MM_lign', 'MM_water_liq', 'MM_HMFU', 'MM_Acetone', 'MM_pCoumaryl', 'MM_Phenol', 'MM_Xylan', 'MM_LVG', 'MM_
HAA', ...;
    'MM_Glyoxal', 'MM_Lumped_phenol', 'MM_Acrylic_acid', 'dens', 'vol_tot', ...;
    'mass_rate', 'weight_cell', 'weight_Hcell', 'weight_lignC', 'weight_lignH', ...
    'weight_ligno', 'weight_water_liq', 'i', 'cp', 'V', 'mass_rate_nitrogen', 'residence_time',
't');
else
    c_cell_F=mass_rate(i)*weight_cell/MM_cell*1000/vol_tot;
    c_Hcell_F=mass_rate(i)*weight_Hcell/MM_Hcell*1000/vol_tot;
c_lignC_F=mass_rate(i)*weight_lignC/MM_lignC*1000/vol_tot;
c_lignH_F=mass_rate(i)*weight_lignH/MM_lignH*1000/vol_tot;
    c_ligno_F = mass_rate(i)*weight_ligno/MM_ligno*1000/vol_tot;
    c_H2O_L_F=mass_rate(i)*weight_water_liq/MM_water_liq*1000/vol_tot;
    c_cellA_F=0;
    c_H2O_F=0;
    c_char_F=0;
    c_LVG_F=0;
    c_HAA_F=0;
    c_glyoxal_F=0;
    c_acetaldehyd_F=0;
    c_HMFU_F=0;
    c_acetone_F=0;
    c_CO2_F=0;
    c_CO_F=0;
    c_CH4_F=0;
    c_Hcell1_F=0;
    c_Hcell2_F=0;
    c_H2_F=0;
    c_formaldehyde_F=0;
    c_xyla_F=0;
    c_C2H4_F=0;
    c_methanol_F=0;
    c_ethanol_F=0;
    c_lignCC_F = 0;
    c_pCoumaryl_F = 0;
    c_phenol_F = 0;
    c_lignOH_F = 0;
    c_acry_F = 0;
    c_lign = 0;
    c_lumpHe = 0;
    T_pyro = Y(nn,34);
    rho_F = Y(nn,35);
    y = [c_cell_F c_cellA_F c_H2O_F c_char_F c_LVG_F c_HAA_F c_glyoxal_F c_acetaldehyd_F
c_HMFU_F c_acetone_F ...;
    c_CO2_F c_CO_F c_CH4_F c_Hcell_F c_Hcell1_F c_Hcell2_F c_H2_F c_formaldehyde_F c_xyla_F_F
c_C2H4_F c_methanol_F c_ethanol_F ...;
    c_lignC_F c_lignCC_F c_pCoumaryl_F c_phenol_F c_lignH_F c_lignOH_F c_ligno_F c_acry_F
c_lign c_lumpHe c_H2O_L_F T_pyro rho_F];
    y_0 = y;

y = [Y(nn,1) Y(nn,2) Y(nn,3) Y(nn,4) Y(nn,5) Y(nn,6) Y(nn,7) Y(nn,8) Y(nn,9) Y(nn,10) ...;
Y(nn,11) Y(nn,12) Y(nn,13) Y(nn,14) Y(nn,15) Y(nn,16) Y(nn,17) Y(nn,18) Y(nn,19) Y(nn,20)

```



```

Y(nn,21) Y(nn,22) ...;
    Y(nn,23) Y(nn,24) Y(nn,25) Y(nn,26) Y(nn,27) Y(nn,28) Y(nn,29) Y(nn,30) Y(nn,31) Y(nn,32)
Y(nn,33) Y(nn,34) Y(nn,35)];
    save('init.mat', 'y_0', 'MM_cell', 'MM_Hcell', 'MM_lignC', 'MM_lignH', 'MM_ligno', 'MM_lignOH',
...;

'MM_lign', 'MM_water_liq', 'MM_HMFU', 'MM_Acetone', 'MM_pCoumaryl', 'MM_Phenol', 'MM_Xylan', 'MM_LVG', 'MM_
HAA', ...;
    'MM_Glyoxal', 'MM_Lumped_phenol', 'MM_Acrylic_acid', 'dens', 'vol_tot', ...;
    'mass_rate', 'weight_cell', 'weight_Hcell', 'weight_lignC', 'weight_lignH', ...
    'weight_ligno', 'weight_water_liq', 'i', 'cp', 'V', 'mass_rate_nitrogen', 'residence_time',
't');
    end
end

if i ==1
timestep = linspace(0, i*dt,5000);
else
timestep = linspace((i-1)*dt, i*dt,5000);
end

[T, Y] = ode15s(@DYDT, timestep, y);
nn = size(Y,1);

M1 = Y(nn,13)*MM_CH4/1000;
M2 = Y(nn,12)*MM_CO/1000;
M3 = Y(nn,11)*MM_CO2/1000;
M4 = Y(nn,17)*MM_H2/1000;
M5 = Y(nn,3)*MM_water/1000;
M6 = Y(nn,18)*MM_Formaldehyde/1000;
M7 = Y(nn,8)*MM_Acetaldehyde/1000;
M8 = Y(nn,21)*MM_Methanol/1000;
M9 = Y(nn,7)*MM_Glyoxal/1000;
M10 = Y(nn,20)*MM_Ethylene/1000;
M11 = Y(nn,6)*MM_HAA/1000;
M12 = Y(nn,22)*MM_Ethanol/1000;
M13 = Y(nn,30)*MM_Acrylic_acid/1000;
M14 = Y(nn,10)*MM_Acetone/1000;
M15 = Y(nn,19)*MM_Xylan/1000;
M16 = Y(nn,5)*MM_LVG/1000;
M17 = Y(nn,26)*MM_Phenol/1000;
M18 = Y(nn,9)*MM_HMFU/1000;
M19 = Y(nn,25)*MM_pCoumaryl/1000;
M20 = Y(nn,32)*MM_Lumped_phenol/1000;
M21 = Y(nn,35);

dens = M1+M2+M3+M4+M5+M6+M7+M8+M9+M10+M11+M12+M13+M14+M15+M16+M17+M18+M19+M20+M21

M22 = Y(nn,4)*MM_C/1000;

n1(i) = Y(nn,13)*V;
n2(i) = Y(nn,12)*V;
n3(i) = Y(nn,11)*V;
n4(i) = Y(nn,17)*V;
n5(i) = Y(nn,3)*V;
n6(i) = Y(nn,18)*V;
n7(i) = Y(nn,8)*V;
n8(i) = Y(nn,21)*V;

```

```

n9(i) = Y(nn,7)*V;
n10(i) = Y(nn,20)*V;
n11(i) = Y(nn,6)*V;
n12(i) = Y(nn,22)*V;
n13(i) = Y(nn,30)*V;
n14(i) = Y(nn,10)*V;
n15(i) = Y(nn,19)*V;
n16(i) = Y(nn,5)*V;
n17(i) = Y(nn,26)*V;
n18(i) = Y(nn,9)*V;
n19(i) = Y(nn,25)*V;
n20(i) = Y(nn,32)*V;
n21(i) = Y(nn,35)/MM_N2*1000*V;

n_tot(i) =
n1(i)+n2(i)+n3(i)+n4(i)+n5(i)+n6(i)+n7(i)+n8(i)+n9(i)+n10(i)+n11(i)+n12(i)+n13(i)+n14(i)+n15(i)+n16
(i)+n17(i)+n18(i)+n19(i)+n20(i)+n21(i);
% new_pressure(i) = R*Y(nn,34)/V*n_tot(i)
if i ==1
    DF_TOT(i) = 0;
    vol(i) = vol_tot_0;
else
    DF_TOT(i) = (n_tot(i)-n_tot(i-1))/V*vol(i-1);
    vol(i) = vol(i-1) + DF_TOT(i)*R*Y(nn,34)/pressure;
end

vol_tot = vol(i);

```

DERIVATIVE SOLVER (ODE15S)

```

function DYDT=f(t,y)
A = load('init.mat');
y_0 = A.y_0;
MM_cell = A.MM_cell;
MM_Hcell = A.MM_Hcell;
MM_lignC = A.MM_lignC;
MM_lignH = A.MM_lignH;
MM_lignO = A.MM_lignO;
MM_lignOH = A.MM_lignOH;
MM_lign = A.MM_lign;
MM_water_liq = A.MM_water_liq;
MM_HMFU =A.MM_HMFU;
MM_Acetone=A.MM_Acetone;
MM_pCoumaryl=A.MM_pCoumaryl;
MM_Phenol=A.MM_Phenol;
MM_Xylan=A.MM_Xylan;
MM_LVG=A.MM_LVG;
MM_HAA=A.MM_HAA;
MM_Glyoxal=A.MM_Glyoxal;
MM_Lumped_phenol=A.MM_Lumped_phenol;
MM_Acrylic_acid=A.MM_Acrylic_acid;

mass_rate = A.mass_rate;
rho = A.dens;

```

```

mass_rate_nitrogen = A.mass_rate_nitrogen;
tau = A.residence_time;

V = A.V;

c_cell_F=y_0(1); % feed concentration of A [mol/m3]
c_cellA_F=y_0(2); % feed concentration of B [mol/m3]
c_H2O_F=y_0(3); % feed concentration of C [mol/m3]
c_char_F=y_0(4); % feed concentration of D [mol/m3]
c_LVG_F=y_0(5); % feed concentration of E [mol/m3]
c_HAA_F=y_0(6); % feed concentration of F [mol/m3]
c_glyoxal_F=y_0(7); % feed concentration of G [mol/m3]
c_acetaldehyd_F=y_0(8); % feed concentration of H [mol/m3]
c_HMFU_F=y_0(9); % feed concentration of I [mol/m3]
c_acetone_F=y_0(10); % feed concentration of J [mol/m3]
c_CO2_F=y_0(11); % feed concentration of K [mol/m3]
c_CO_F=y_0(12); % feed concentration of L [mol/m3]
c_CH4_F=y_0(13); % feed concentration of M [mol/m3]
c_Hcell_F=y_0(14); % feed concentration of N [mol/m3]
c_Hcell1_F=y_0(15); % feed concentration of O [mol/m3]
c_Hcell2_F=y_0(16); % feed concentration of P [mol/m3]
c_H2_F=y_0(17); % feed concentration of Q [mol/m3]
c_formaldehyde_F=y_0(18); % feed concentration of R [mol/m3]
c_xylan_F=y_0(19); % feed concentration of S [mol/m3]
c_C2H4_F=y_0(20); % feed concentration of T [mol/m3]
c_methanol_F=y_0(21); % feed concentration of U [mol/m3]
c_ethanol_F=y_0(22); % feed concentration of V [mol/m3]
c_lignC_F=y_0(23); % feed concentration of W [mol/m3]
c_lignCC_F=y_0(24); % feed concentration of X [mol/m3]
c_pCoumaryl_F=y_0(25); % feed concentration of Y [mol/m3]
c_phenol_F=y_0(26); % feed concentration of Z [mol/m3]
c_lignH_F=y_0(27); % feed concentration of AA [mol/m3]
c_lignOH_F=y_0(28); % feed concentration of AB [mol/m3]
c_lignO_F=y_0(29); % feed concentration of AC [mol/m3]
c_acry_F=y_0(30); % feed concentration of AD [mol/m3]
c_lign_F=y_0(31); % feed concentration of AE [mol/m3]
c_lumpPhe_F=y_0(32); % feed concentration of AF [mol/m3]
c_H2OL_F=y_0(33); % feed concentration of AG [mol/m3]

TF=25+273; % feed temperature [K]

dhr1= 447700*MM_cell/1000; % Heat of reaction [J/mol]
dhr2= -1087800*MM_cell/1000; % Heat of reaction [J/mol]
dhr3= 732200*MM_cell/1000; % Heat of reaction [J/mol]
dhr4= 899600*MM_cell/1000; % Heat of reaction [J/mol]
dhr5= 548100*MM_Hcell/1000; % Heat of reaction [J/mol]
dhr6= 447700*MM_Hcell/1000; % Heat of reaction [J/mol]
dhr7= 707100*MM_Hcell/1000; % Heat of reaction [J/mol]
dhr8= 259400*MM_Hcell/1000; % Heat of reaction [J/mol]
dhr9= 602500*MM_lignC/1000; % Heat of reaction [J/mol]
dhr10= 523000*MM_lignH/1000; % Heat of reaction [J/mol]
dhr11= 510400*MM_lignO/1000; % Heat of reaction [J/mol]
dhr12= 288700*MM_lignC/1000; % Heat of reaction [J/mol]
dhr13= 100400*MM_lignOH/1000; % Heat of reaction [J/mol]
dhr14= 577400*MM_lign/1000; % Heat of reaction [J/mol]
dhr15= -209200*MM_lign/1000; % Heat of reaction [J/mol]
dhr16= 2260000*MM_water_liq/1000; % Heat of reaction [J/mol]
dhr17= 642700*MM_HMFU/1000; % Heat of reaction [J/mol]

```

```

dhr18= 1878200*MM_Acetone/1000; % Heat of reaction [J/mol]
dhr19= -359600*MM_pCoumaryl/1000; % Heat of reaction [J/mol]
dhr20= -143100*MM_Phenol/1000; % Heat of reaction [J/mol]
dhr21= 1701600*MM_LVG/1000; % Heat of reaction [J/mol]
dhr22= 3562700*MM_HAA/1000; % Heat of reaction [J/mol]
dhr23= -156600*MM_Glyoxal/1000; % Heat of reaction [J/mol]
dhr24= -693800*MM_Lumped_phenol/1000; % Heat of reaction [J/mol]
dhr25= -912900*MM_Acrylic_acid/1000; % Heat of reaction [J/mol]
dhr26= -563000*MM_Xylan/1000; % Heat of reaction [J/mol]
i = A.i;

T =y(34);
qq = A.vol_tot;
q(i) = qq;
if i == 1
    cp= A.cp;
else
    cp= 979.043+0.4179639*T-0.001176279*T^2+1.674394e-6*T^3-7.256297e-10*T^4; % specific heat
    capacity [J/kg K]
end

E1 = 192500; % rx1: activation energy [J/mol]
A1 = 8*10^13;
E2 = 133900;
A2 = 8*10^7;
E3 = 41800;
A3 = 4*T;
E4 = 125500;
A4 = 1*10^9;
E5 = 129700;
A5 = 1*10^10;
E6 = 113000;
A6 = 3*10^9;
E7 = 46000;
A7 = 3*T;
E8 = 138100;
A8 = 1*10^10;
E9 = 202900;
A9 = 4*10^15;
E10 = 156900;
A10 = 2*10^13;
E11 = 106700;
A11 = 1*10^9;
E12 = 131800;
A12 = 5*10^6;
E13 = 125500;
A13 = 3*10^8;
E14 = 50200;
A14 = 8*T;
E15 = 125500;
A15 = 1.2*10^9;
E16 = 88000;
A16 = 5.3*10^10;
E_cracking = 108000;
A_cracking = 4.28*10^6;

R = 8.314; % gas constant [J/K mol]

```

```

c_cell=y(1); % [mol/m3]
c_cellA=y(2); % [mol/m3]
c_H2O=y(3); % [mol/m3]
c_char=y(4); % [mol/m3]
c_LVG=y(5); % [mol/m3]
c_HAA=y(6); % [mol/m3]
c_glyoxal=y(7); % [mol/m3]
c_acetaldehyd=y(8); % [mol/m3]
c_HMFU=y(9); % [mol/m3]
c_acetone=y(10); % [mol/m3]
c_CO2 = y(11); % [mol/m3]
c_CO = y(12); % [mol/m3]
c_CH4 = y(13); % [mol/m3]
c_Hcell=y(14); % [mol/m3]
c_Hcell1=y(15); % [mol/m3]
c_Hcell2=y(16); % [mol/m3]
c_H2=y(17); % [mol/m3]
c_formaldehyde=y(18); % [mol/m3]
c_xylan=y(19); % [mol/m3]
c_C2H4=y(20); % [mol/m3]
c_methanol=y(21); % [mol/m3]
c_ethanol=y(22); % [mol/m3]
c_lignC=y(23); % [mol/m3]
c_lignCC=y(24); % [mol/m3]
c_pCoumaryl=y(25); % [mol/m3]
c_phenol =y(26); % [mol/m3]
c_lignH=y(27); % [mol/m3]
c_lignOH=y(28); % [mol/m3]
c_lignO=y(29); % [mol/m3]
c_acry=y(30); % [mol/m3]
c_lign=y(31); % [mol/m3]
c_lumPhe=y(32); % [mol/m3]
c_H2OL=y(33); % [mol/m3]
rho_N2=y(35); % [mol/m3]

load('shared_value.mat', 'TR');
Tr1 = TR(1);
Tr2 = TR(2);
Tr3 = TR(3);
Tr4 = TR(4);
Tr5 = TR(5);
Tr6 = TR(6);
Tr7 = TR(7);
Tr8 = TR(8);
Tr9 = TR(9);
Tr10 = TR(10);
Tr11 = TR(11);
Tr12 = TR(12);
Tr13 = TR(13);
Tr14 = TR(14);
Tr15 = TR(15);
Tr16 = TR(16);
Tr17 = TR(17);
Tr18 = TR(18);
Tr19 = TR(19);
Tr20 = TR(20);
Tr21 = TR(21);
Tr22 = TR(22);

```

```

Tr23 = TR(23);
Tr24 = TR(24);
Tr25 = TR(25);
Tr26 = TR(26);

k1 = A1 * exp(-(E1/R) * (1/(T-Tr1)));
k2 = A2 * exp(-(E2/R) * (1/(T-Tr2)));
k3 = A3 * exp(-(E3/R) * (1/(T-Tr3)));
k4 = A4 * exp(-(E4/R) * (1/(T-Tr4)));
k5 = A5 * exp(-(E5/R) * (1/(T-Tr5)));
k6 = A6 * exp(-(E6/R) * (1/(T-Tr6)));
k7 = A7 * exp(-(E7/R) * (1/(T-Tr7)));
k8 = A8 * exp(-(E8/R) * (1/(T-Tr8)));
k9 = A9 * exp(-(E9/R) * (1/(T-Tr9)));
k10 = A10 * exp(-(E10/R) * (1/(T-Tr10)));
k11 = A11 * exp(-(E11/R) * (1/(T-Tr11)));
k12 = A12 * exp(-(E12/R) * (1/(T-Tr12)));
k13 = A13 * exp(-(E13/R) * (1/(T-Tr13)));
k14 = A14 * exp(-(E14/R) * (1/(T-Tr14)));
k15 = A15 * exp(-(E15/R) * (1/(T-Tr15)));
k16 = A16 * exp(-(E16/R) * (1/(T-Tr16)));
k_cracking(1) = A_cracking * exp(-(E_cracking/R) * (1/(T-Tr17)));
k_cracking(2) = A_cracking * exp(-(E_cracking/R) * (1/(T-Tr18)));
k_cracking(3) = A_cracking * exp(-(E_cracking/R) * (1/(T-Tr19)));
k_cracking(4) = A_cracking * exp(-(E_cracking/R) * (1/(T-Tr20)));
k_cracking(5) = A_cracking * exp(-(E_cracking/R) * (1/(T-Tr21)));
k_cracking(6) = A_cracking * exp(-(E_cracking/R) * (1/(T-Tr22)));
k_cracking(7) = A_cracking * exp(-(E_cracking/R) * (1/(T-Tr23)));
k_cracking(8) = A_cracking * exp(-(E_cracking/R) * (1/(T-Tr24)));
k_cracking(9) = A_cracking * exp(-(E_cracking/R) * (1/(T-Tr25)));
k_cracking(10) = A_cracking * exp(-(E_cracking/R) * (1/(T-Tr26)));
r1 = k1*c_cell;
r2 = k2*c_cell;
r3 = k3*c_cellA;
r4 = k4*c_cellA;
r5 = k5*c_Hcell;
r6 = k6*c_Hcell1;
r7 = k7*c_Hcell1;
r8 = k8*c_Hcell2;
r9 = k9*c_lignC;
r10 = k10*c_lignH;
r11 = k11*c_lignO;
r12 = k12*c_lignCC;
r13 = k13*c_lignOH;
r14 = k14*c_lign;
r15 = k15*c_lign;
r16 = k16*c_H2OL;
r17 = k_cracking(1)*c_HMFU;
r18 = k_cracking(2)*c_acetone;
r19 = k_cracking(3)*c_pCoumaryl;
r20 = k_cracking(4)*c_phenol;
r21 = k_cracking(5)*c_LVG;
r22 = k_cracking(6)*c_HAA;
r23 = k_cracking(7)*c_glyoxal;
r24 = k_cracking(8)*c_lumPhe;
r25 = k_cracking(9)*c_acry;
r26 = k_cracking(10)*c_xylan;

```

m_N2_in = A.mass_rate_nitrogen;

```
vdc_cell_dt = q(i)*c_cell_F - 0*q(i)*c_cell - r1*v - r2*v; % [mol A/s]
vdc_cellA_dt = 0*q(i)*c_cellA_F - 0*q(i)*c_cellA + r1*v-r3*v-r4*v; % [mol B/s]
vdc_H2O_dt = 0*q(i)*c_H2O_F - q(i)*c_H2O + 5*r2*v+0.9*r4*v+0.125*r8*v+
r9*v+0.7*r12*v+r13*v+r15*v+r16*v+0.125*r6*v; % [mol C/s]
vdc_char_dt = 0*q(i)*c_char_F - q(i)*c_char + 6*r2*v+0.61*r4*v+r8*v+
5.735*r9*v+6.4*r12*v+4.15*r13*v+5.5*r15*v+3*r19*v+2.5*r20*v+3*r24*v+0.675*r6*v; % [mol C/s]
vdc_LVG_dt = 0*q(i)*c_LVG_F - q(i)*c_LVG + r3*v-r21*v; % [mol C/s]
vdc_HAA_dt = 0*q(i)*c_HAA_F - q(i)*c_HAA + 0.95*r4*v-r22*v; % [mol C/s]
vdc_glyoxal_dt = 0*q(i)*c_glyoxal_F - q(i)*c_glyoxal + 0.25*r4*v-r23*v; % [mol C/s]
vdc_acetaldehyd_dt = 0*q(i)*c_acetaldehyd_F - q(i)*c_acetaldehyd + 0.2*r4*v+0.2*r15*v; % [mol
C/s]
vdc_HMFU_dt = 0*q(i)*c_HMFU_F - q(i)*c_HMFU + 0.25*r4*v-r17*v; % [mol C/s]
vdc_acetone_dt = 0*q(i)*c_acetone_F - q(i)*c_acetone + 0.2*r4*v +r10*v+0.2*r15*v-
r18*v; % [mol C/s]
vdc_CO2_dt = 0*q(i)*c_CO2_F - q(i)*c_CO2 +
0.16*r4*v+0.8*r6*v+r8*v+r11*v+0.5*r18*v+r19*v+0.5*r20*v+2.5*r21*v+2*r24*v+r25*v+2*r26*v; % [mol
C/s]
vdc_CO_dt = 0*q(i)*c_CO_F - q(i)*c_CO + 0.23*r4*v+1.4*r6*v+0.8*r8*v+
1.32*r9*v+1.8*r12*v+2*r13*v+2*r15*v+3*r17*v+2*r22*v+2*r23*v; % [mol C/s]
vdc_CH4_dt = 0*q(i)*c_CH4_F - q(i)*c_CH4 + 0.1*r4*v+0.5*r8*v+
0.495*r9*v+0.65*r12*v+0.45*r13*v+0.6*r15*v+0.625*r6*v; % [mol C/s]
vdc_Hcell_dt = q(i)*c_Hcell_F - 0*q(i)*c_Hcell - r5*v; % [mol A/s]
vdc_Hcell1_dt = 0*q(i)*c_Hcell1_F - 0*q(i)*c_Hcell1 + 0.4*r5*v-r6*v-r7*v; % [mol
C/s]
vdc_Hcell2_dt = 0*q(i)*c_Hcell2_F - 0*q(i)*c_Hcell2 + 0.6*r5*v-r8*v; % [mol C/s]
vdc_H2_dt = 0*q(i)*c_H2_F - q(i)*c_H2 + 0.75*r6*v+0.8*r8*v +
r9*v+r12*v+0.7*r13*v+0.5*r15*v+0.5*r18*v+1.5*r21*v+2*r22*v+r23*v+r26*v; % [mol C/s]
vdc_formaldehyde_dt = 0*q(i)*c_formaldehyde_F -q(i)*c_formaldehyde +
0.5*r6*v+0.7*r8*v+0.2*r15*v; % [mol C/s]
vdc_xylan_dt = 0*q(i)*c_xylan_F - q(i)*c_xylan + r7*v-r26*v; % [mol C/s]
vdc_C2H4_dt = 0*q(i)*c_C2H4_F - q(i)*c_C2H4 + 0.25*r8*v+
0.41*r9*v+0.6*r12*v+0.2*r13*v+0.65*r15*v+1.5*r17*v+1.25*r18*v+2.5*r19*v+1.5*r20*v+1.75*r21*v+3*r24*
v+r25*v+1.5*r26*v+0.25*r6*v; % [mol C/s]
vdc_methanol_dt = 0*q(i)*c_methanol_F - q(i)*c_methanol +
0.25*r8*v+r13*v+0.4*r15*v+0.25*r6*v; % [mol C/s]
vdc_ethanol_dt = 0*q(i)*c_ethanol_F - q(i)*c_ethanol + 0.125*r8*v+0.125*r6*v; % [mol
C/s]
vdc_lignC_dt = q(i)*c_lignC_F - 0*q(i)*c_lignC + -r9*v; % [mol C/s]
vdc_lignCC_dt = 0*q(i)*c_lignCC_F - 0*q(i)*c_lignCC + 0.35*r9*v-r12*v; % [mol C/s]
vdc_pCoumaryl_dt = 0*q(i)*c_pCoumaryl_F - q(i)*c_pCoumaryl + 0.1*r9*v +0.3*r12*v-r19*v; %
[mol C/s]
vdc_phenol_dt = 0*q(i)*c_phenol_F - q(i)*c_phenol + 0.08*r9*v+0.2*r12*v-r20*v; %
[mol C/s]
vdc_lignH_dt = q(i)*c_lignH_F - 0*q(i)*c_lignH + -r10*v; % [mol C/s]
vdc_lignOH_dt = 0*q(i)*c_lignOH_F - 0*q(i)*c_lignOH +r10*v+r11*v-r13*v; % [mol C/s]
vdc_lignO_dt = q(i)*c_lignO_F - 0*q(i)*c_lignO -r11*v; % [mol C/s]
vdc_acry_dt = 0*q(i)*c_acry_F - q(i)*c_acry +0.35*r12*v-r25*v; % [mol C/s]
vdc_lign_dt = 0*q(i)*c_lign_F - 0*q(i)*c_lign +r13*v-r14*v-r15*v; % [mol C/s]
vdc_lumPhe_dt = 0*q(i)*c_lumPhe_F - q(i)*c_lumPhe +r14*v-r24*v; % [mol C/s]
vdc_H2OL_dt = q(i)*c_H2OL_F - q(i)*c_H2OL -r16*v; % [mol C/s]
vdrho_N2_dt = m_N2_in -rho_N2*q(i); % [mol C/s]
```

cp_wood = 1500;

```

weight_water_liq = A.weight_water_liq;

T_sens = 100 +273.15;
Q_wood = (TF-T)*mass_rate(i)*cp_wood*(1-weight_water_liq);
T_wall = 500 +273.15;

cp_N2_ini = 1106;
cp_N2_fine = -4.20523E-07*T^3+0.000963577*T^2-0.491330025*T+1113.961169;    %kg/m3 pressure kPa;
cp_water_ini_1 = 4181;
cp_water_fine_1 = 4215;
cp_water_ini_2 = 2075;
cp_water_fine_2 = -1.04248E-05*T^3+0.019868216*T^2-11.90843959*T+4268.511;

cp_N2_avg = (cp_N2_ini+cp_N2_fine)*0.5;
cp_water_avg_1 = (cp_water_ini_1+cp_water_fine_1)*0.5;
cp_water_avg_2 = (cp_water_ini_2+cp_water_fine_2)*0.5;

Q_N2 = mass_rate_nitrogen*cp_N2_avg*(463+273.15-T);

Q_water_1 = weight_water_liq*mass_rate(i)*cp_water_avg_1*(TF-T_sens);
Q_water_2 = weight_water_liq*mass_rate(i)*cp_water_avg_2*(T_sens-T);

Q = 0;
t = A.t;

area_heated = 0.0721*3.1415*(0.65-0.15);
area_loss = 0.0721*3.1415*(0.95-0.65-0.05);
U = 130; %Watt/mq/K from reference
U_loss = 130; %Watt/mq/K from reference, trial

Q_wall = U*area_heated*(T_wall-T);
Q_loss = -U_loss*area_loss*(T-300-273.15);

mcpdTdt = ...
+r1*v*(-dhr1) + r2*v*(-dhr2)+ r3*v*(-dhr3) + r4*v*(-dhr4)+ r5*v*(-dhr5)+r6*v*(-dhr6) ...
+r7*v*(-dhr7) +r8*v*(-dhr8) +r9*v*(-dhr9)+r10*v*(-dhr10)+r11*v*(-dhr11)+r12*v*(-dhr12)+r13*v*(-
dhr13)+r14*v*(-dhr14)+r15*v*(-dhr15)+r16*v*(-dhr16) ...
+r17*v*(-dhr17)+r18*v*(-dhr18)+r19*v*(-dhr19)+r20*v*(-dhr20)+r21*v*(-dhr21)+r22*v*(-dhr22)+r23*v*(-
dhr23)+r24*v*(-dhr24)+r25*v*(-dhr25)+r26*v*(-dhr26)+...
Q+Q_wood+Q_N2+Q_water_1+Q_water_2+Q_wall+Q_loss; % [J/s]
% end

f1 = vdc_cell_dt./V;
f2 = vdc_cellA_dt./V;
f3 = vdc_H2O_dt./V;
f4 = vdc_char_dt./V;
f5 = vdc_LVG_dt./V;
f6 = vdc_HAA_dt./V;
f7 = vdc_glyoxal_dt./V;
f8 = vdc_acetaldehyd_dt./V;
f9 = vdc_HMFU_dt./V;
f10 = vdc_acetone_dt./V;
f11 = vdc_CO2_dt./V;
f12 = vdc_CO_dt./V;
f13 = vdc_CH4_dt./V;
f14 = vdc_Hcell_dt./V;

```



```

f15 = vdc_Hcell11_dt./V;
f16 = vdc_Hcell12_dt./V;
f17 = vdc_H2_dt./V;
f18 = vdc_formaldehyde_dt./V;
f19 = vdc_xyln_dt./V;
f20 = vdc_C2H4_dt./V;
f21 = vdc_methanol_dt./V;
f22 = vdc_ethanol_dt./V;
f23 = vdc_lignC_dt./V;
f24 = vdc_lignCC_dt./V;
f25 = vdc_pCoumaryl_dt./V;
f26 = vdc_phenol_dt./V;
f27 = vdc_lignH_dt./V;
f28 = vdc_lignOH_dt./V;
f29 = vdc_lignO_dt./V;
f30 = vdc_acry_dt./V;
f31 = vdc_lign_dt./V;
f32 = vdc_lumPhe_dt./V;
f33 = vdc_H2O_dt./V;
f35 = vdrho_N2_dt/V;

if t(i)<1.4
    cp = cp_N2_avg;
end
f34 = mcpdTdt/(rho*cp*v);

DYDT=[f1(1); f2(1); f3(1); f4(1); f5(1);
f6(1); f7(1); f8(1); f9(1); f10(1); f11(1); f12(1); f13(1); f14(1); f15(1); f16(1); f17(1); f18(1); f19(1); f20(1
); f21(1); f22(1); f23(1); f24(1); f25(1); f26(1); f27(1); f28(1); f29(1); f30(1); f31(1); f32(1); f33(1); f34(1
); f35(1)];

end

```

RMSE OPTIMIZER

```

exp_M1 = 1.1200E-05;
exp_M2 =4.4200E-05;
exp_M3 =4.5300E-05;
exp_M4 =2.5700E-06;
exp_M5 =7.4000E-05;
exp_M6 =1.4600E-05;
exp_M7 =9.3700E-07;
exp_M8 =7.0700E-06;
exp_M9 =1.3900E-06;
exp_M10 =1.7300E-05;
exp_M11 =5.4600E-06;
exp_M12 =4.5700E-06;
exp_M14 =6.4100E-06;
exp_M15 =4.7500E-05;
exp_M16 =1.0300E-04;
exp_M17 =3.2700E-06;
exp_M18 =3.0100E-06;
exp_M19 =6.5200E-06;
exp_M21 =6.7600E-05;

```

```

exp_masses_rmse = [exp_M1 exp_M2 exp_M3 exp_M4 exp_M5 exp_M6 exp_M7 exp_M8 exp_M9 exp_M10 exp_M11
exp_M12 exp_M14 exp_M15 exp_M16 exp_M17 exp_M18 exp_M19 exp_M21];
% x0 = [0; 0; 0; 0; 0 ;100; 0; 0 ;0; 0; 0 ;0; 0; 0; 0;
0; 0; 0 ;0 ;0 ;0 ;0 ;0 ;0 ;0; 0; 0];
load('shared_value.mat', "TR")
x0 = TR
ub = 101*ones(26,1);
lb = -26*ones(26,1);
A = [];
b = [];
Aeq = [];
beq = [];
% nonlcon = @(x) parameterBounds(x, lb, ub);

options = optimset('TolCon',1e-18,'TolX',1e-
19,'PlotFcns',@optimplotfval,'Algorithm','sqp','Display','off');
% options = optimoptions('fmincon', 'Display', 'iter','Algorithm','sqp');
% options = optimset('Display','iter','PlotFcns',@optimplotfval,'Algorithm','sqp');
[x,fval] = fmincon(@(x)rmse(x,exp_masses_rmse),x0,A,b,Aeq, beq,lb,ub,@parameterBounds, options);
%[x,fval] = fminsearch(@(x)rmse(x,exp_masses_rmse),x0,options);

function [c, ceq] = parameterBounds(x)
    c = [];
    ceq = [];
end

function r = rmse (x,exp_masses_rmse);
TR = x
save('shared_value.mat', "TR")

run('FINAL_SAVED.m');
load('masses_rmse.mat', "masses_rmse")
B = masses_rmse;
r = sqrt(sum(((exp_masses_rmse(:)-B(:))./exp_masses_rmse(:)).^2/numel(exp_masses_rmse)))

end

```

APPENDIX III: MICROALGAE GROWTH IN LABORATORY

This appendix presents a collection of the images obtained through microscopic examination, aimed at evaluating the growth dynamics of *Scenedesmus obliquus* within a synthetic medium composed of 7% wastewater and 3N-BBM. The second campaign includes three distinct runs conducted between November 2022 and February 2023, each characterized by disparate temporal spans: denoted as R1 (from November 22, 2017, to December 7, 2022), R2 (from December 14, 2022, to December 23, 2022), and R3 (from January 25, 2023, to February 14, 2023). For each day within these periods, measurements of dry biomass and cell counting were acquired, although it is worth noting that R3 comprises a greater frequency of daily measurements relative to R1 and R2.

At the conclusion of the observation period, the highest and lowest cell concentrations [cells μl^{-1}] were documented as 42,083 cells μl^{-1} for R1 and 12,333 cells μl^{-1} for R2. It is important to note only R1 and R2 pictures are reported, being R3 comparable to R1 in terms of growth. While R1 demonstrates a trajectory similar to that of R3, it is worth mentioning that R1 had a smaller number of microcells captured. The image acquisition program utilized in this study was CamLabLite. Various contrasts were systematically modified in order to enhance the quality of the results. The process of cell quantification in the Bürker chamber haemocytometer did not involve the use of separate software or algorithms. Instead, imaging was carried out exclusively upon the identification of cellular entities. Figures X3-1 through X3-36 document the temporal evolution of the microalgal population throughout the R1 phase. There is a noticeable increase in the size of the population, particularly after a period of 14 days. Based on the positive growth trends observed in laboratory settings and supported by the ongoing increase in cellular dimensions in R2, it is hypothesized that *Scenedesmus obliquus* was in the exponential growth phase and more microcells would have been expected in the samples after the limited timeline of R2

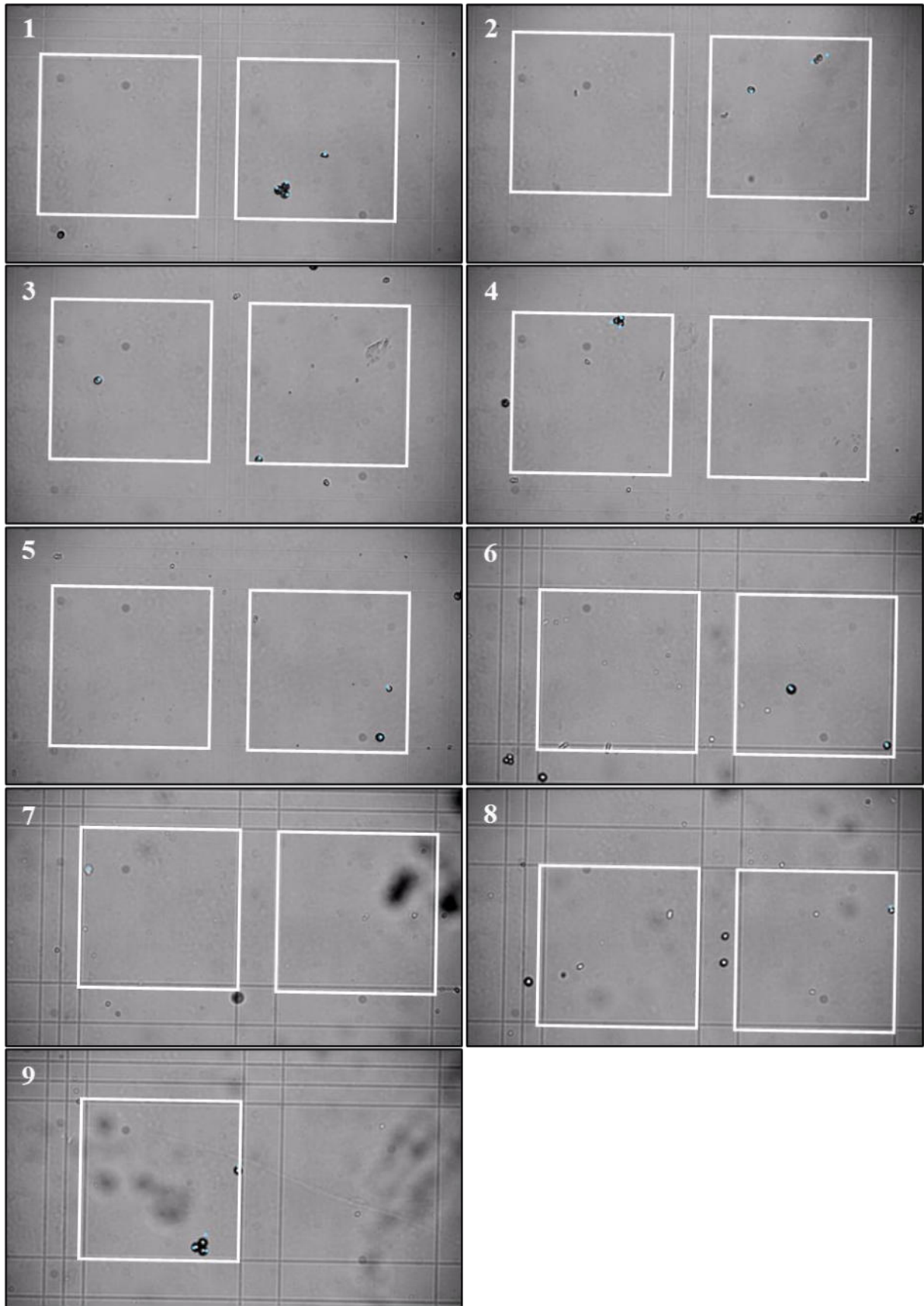


Fig. X3-1. Bürker haemocytometer RI, 22-11-21 (DAY 4) 9:00, 1,833 cells μl^{-1} .

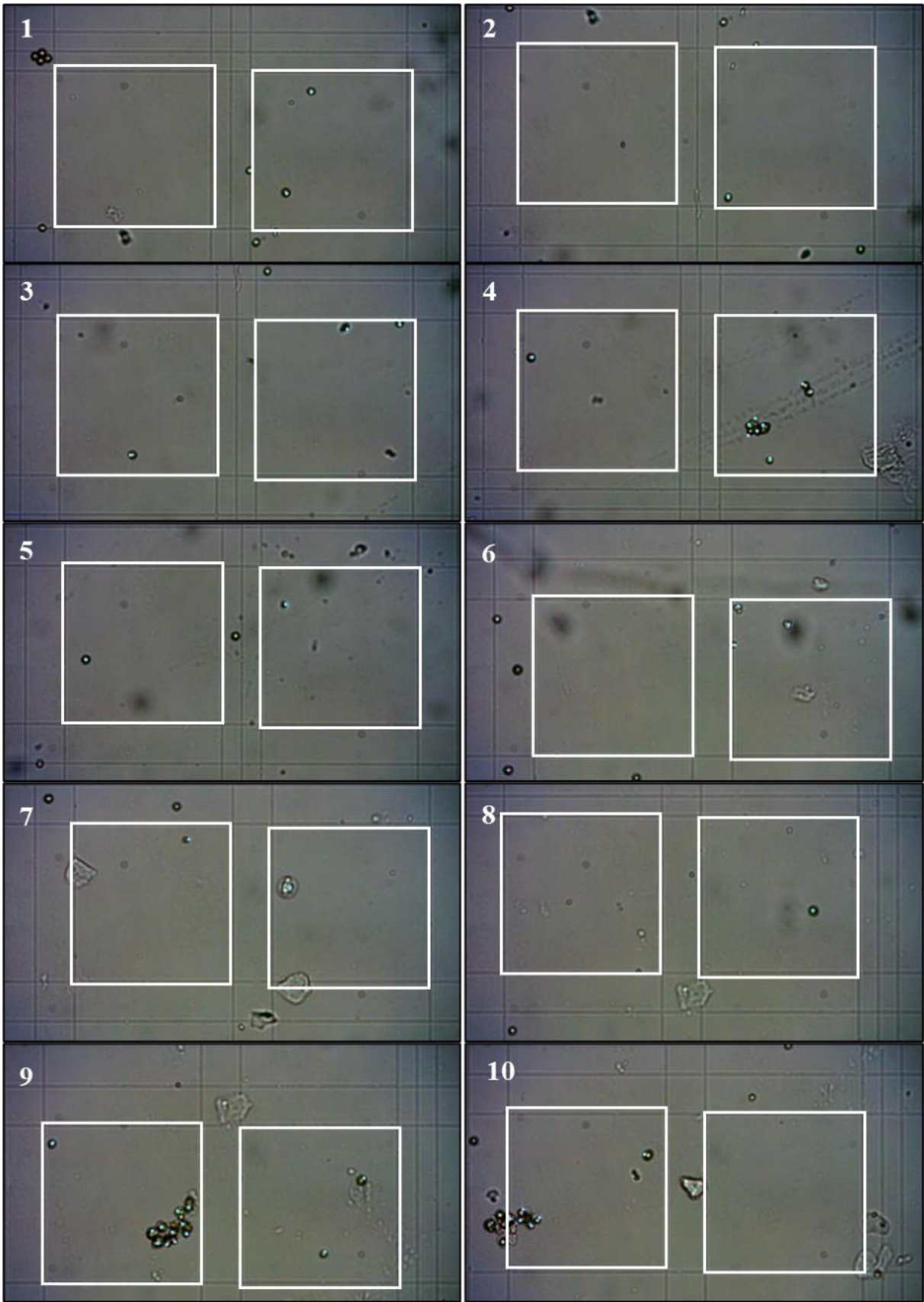


Fig. X3-2. Bürker haemocytometer R1, 22-11-21 (PR DAY 4.4) 19:00, 2,500 cells μl^{-1} .

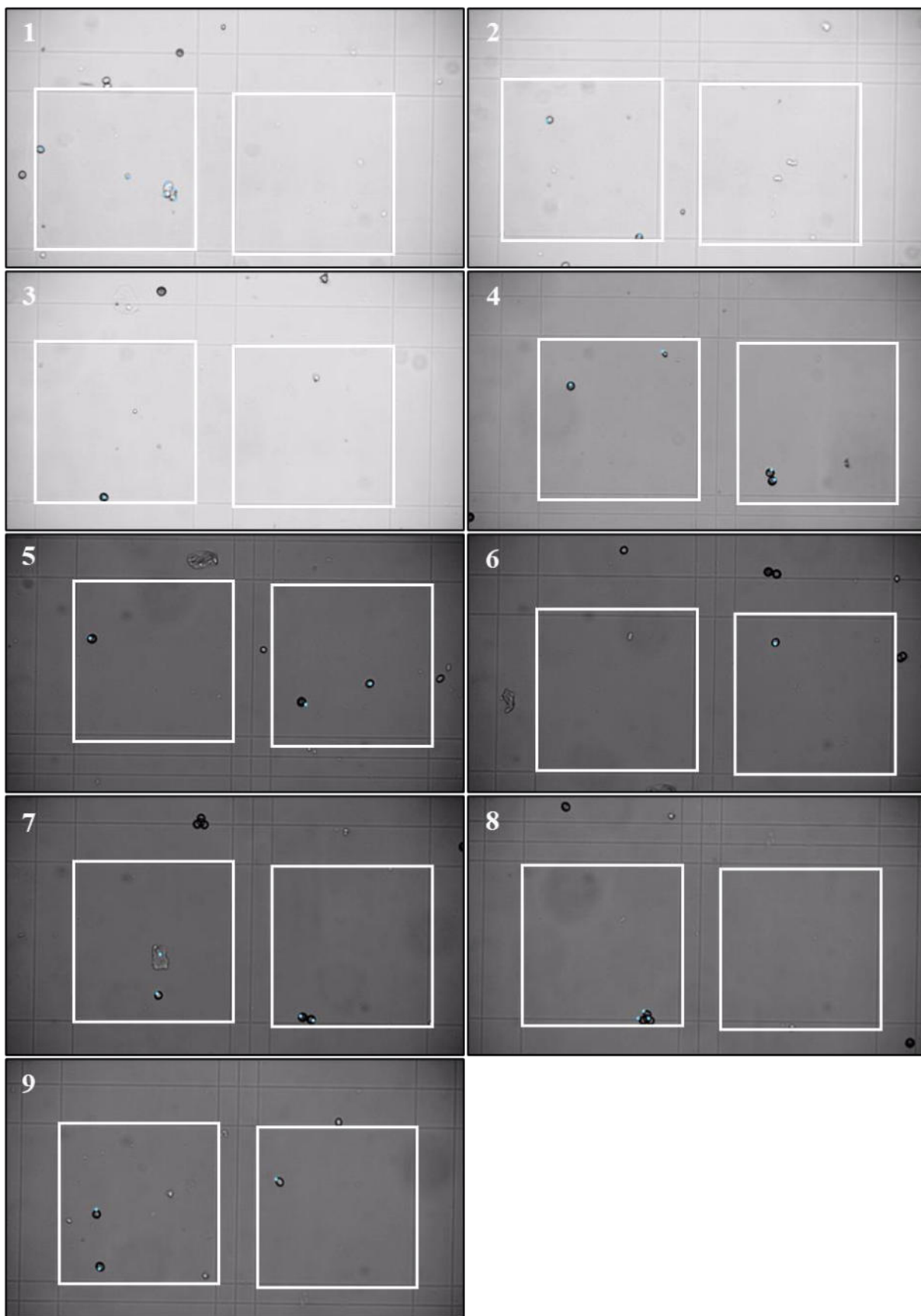


Fig. X3-3. Bürker haemocytometer **RI**, 22-11-21 (PR DAY 6) 9:00, 2,250 cells μl^{-1} .

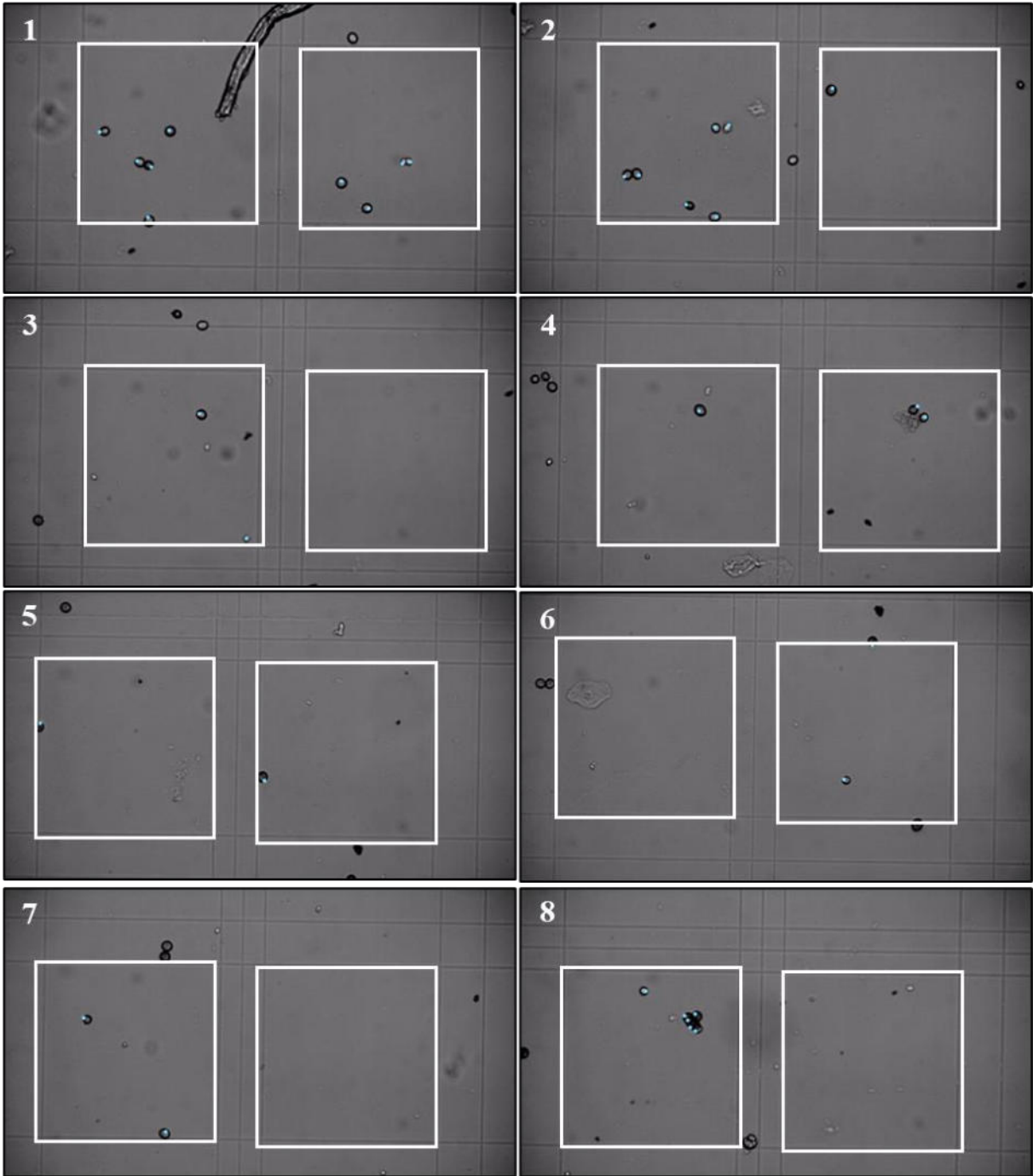


Fig. X3-4. Bürker haemocytometer R1, 22-11-21 (PR DAY 6) 9:00, 2,750 cells μl^{-1} .

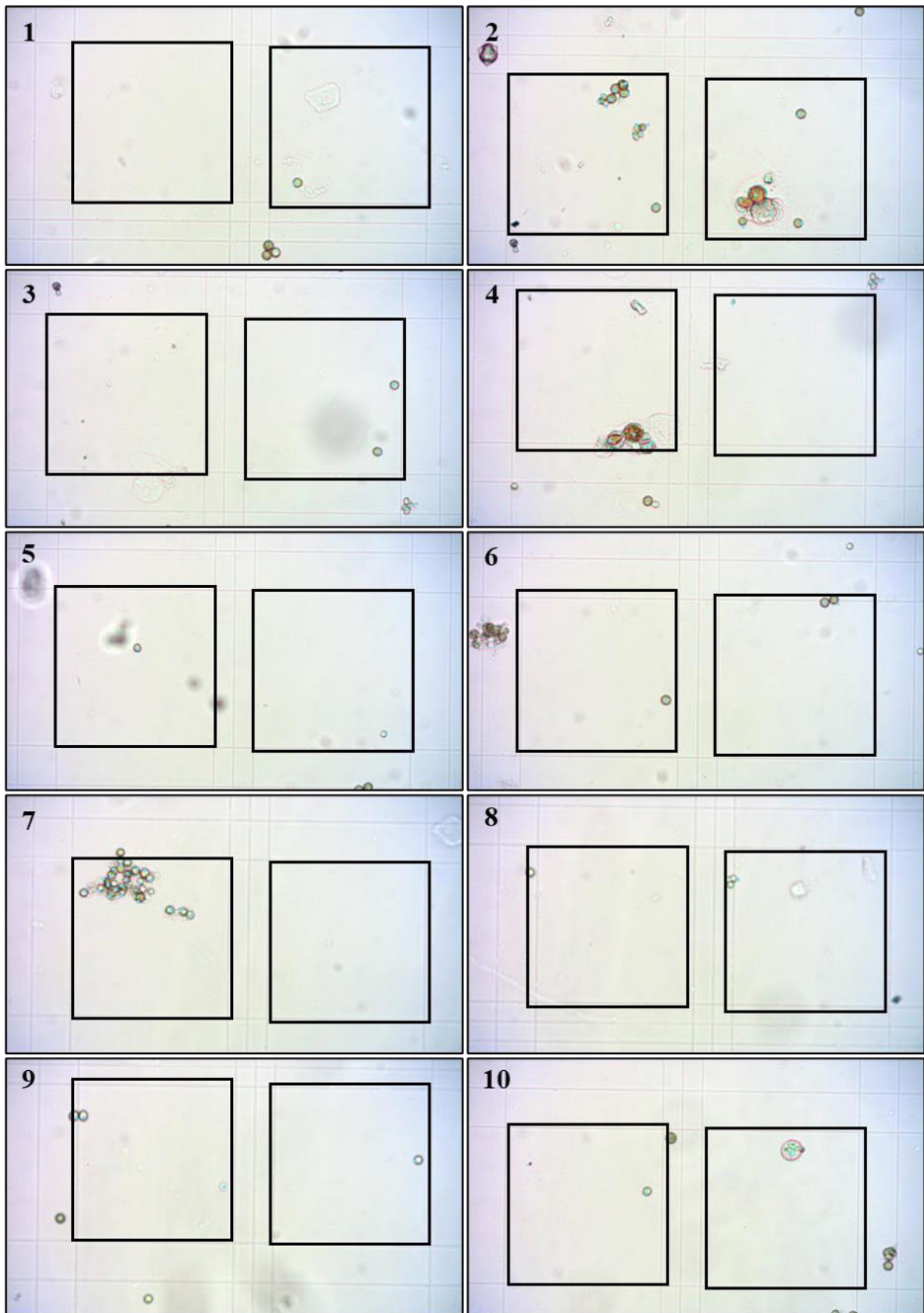


Fig. X3-5. Bürker haemocytometer **RI**, 22-11-23 (PR DAY 6.4) 19:00, 5,250 cells μl^{-1} (1).

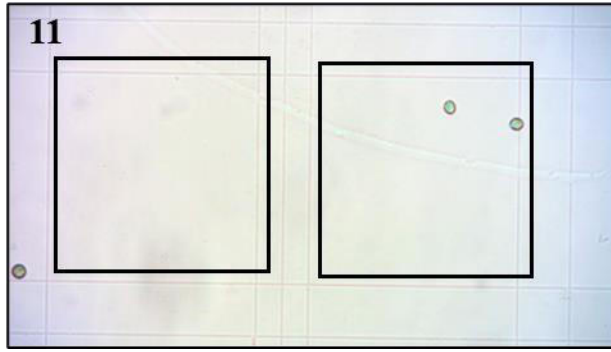


Fig. X3-6. Bürker haemocytometer **RI**, 22-11-23 (PR DAY 6.4) 19:00, 5,250 cells μl^{-1} (2).

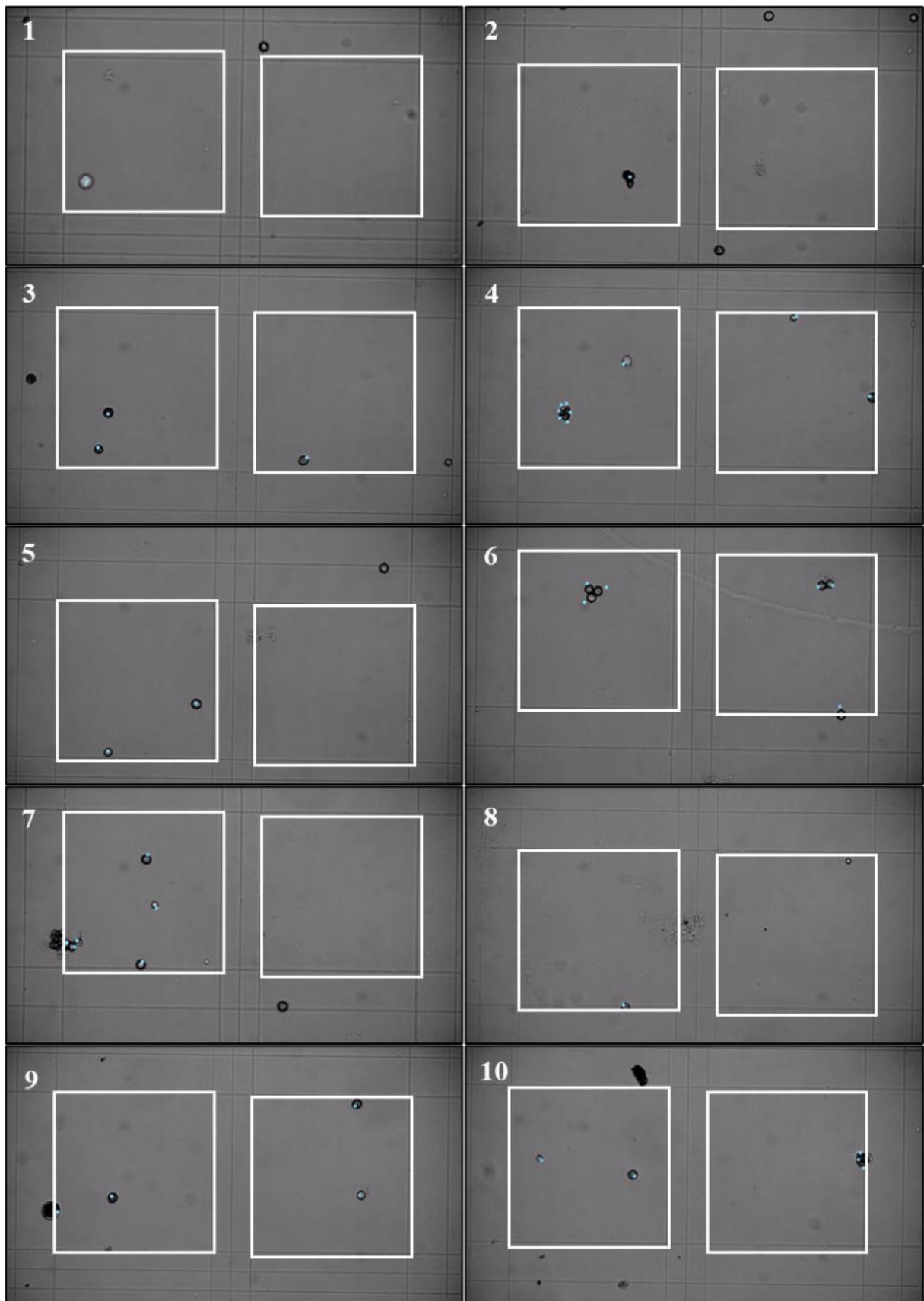


Fig. X3-7. Bürker haemocytometer **RI**, 22-11-24 (PR DAY 7) 9:00, 3,667 cells μl^{-1} (1).

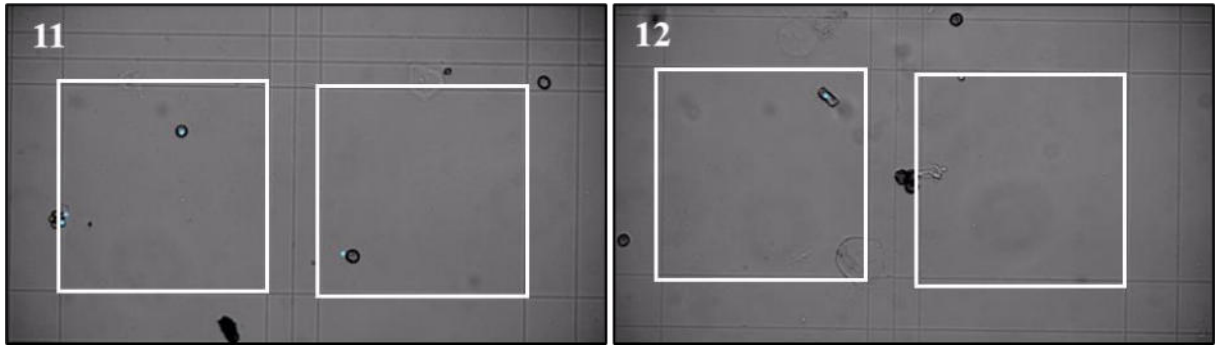


Fig. X3-8. Bürker haemocytometer **RI**, 22-11-24 (PR DAY 7) 9:00, 3,667 cells μl^{-1} (2).

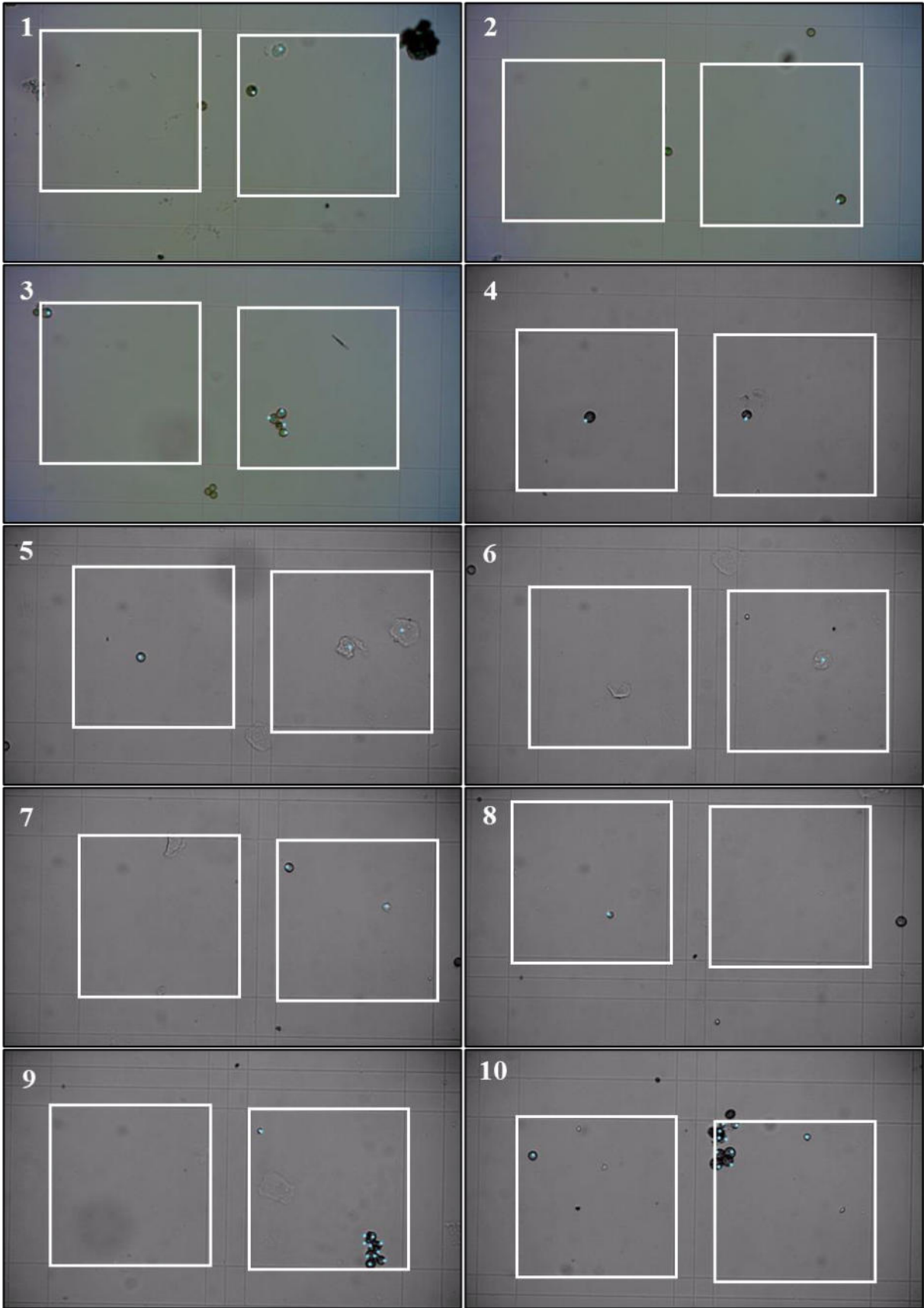


Fig. X3-9. Bürker haemocytometer **RI**, 22-11-24 (PR DAY 7.4) 19:00, 3250 cells μl^{-1} .

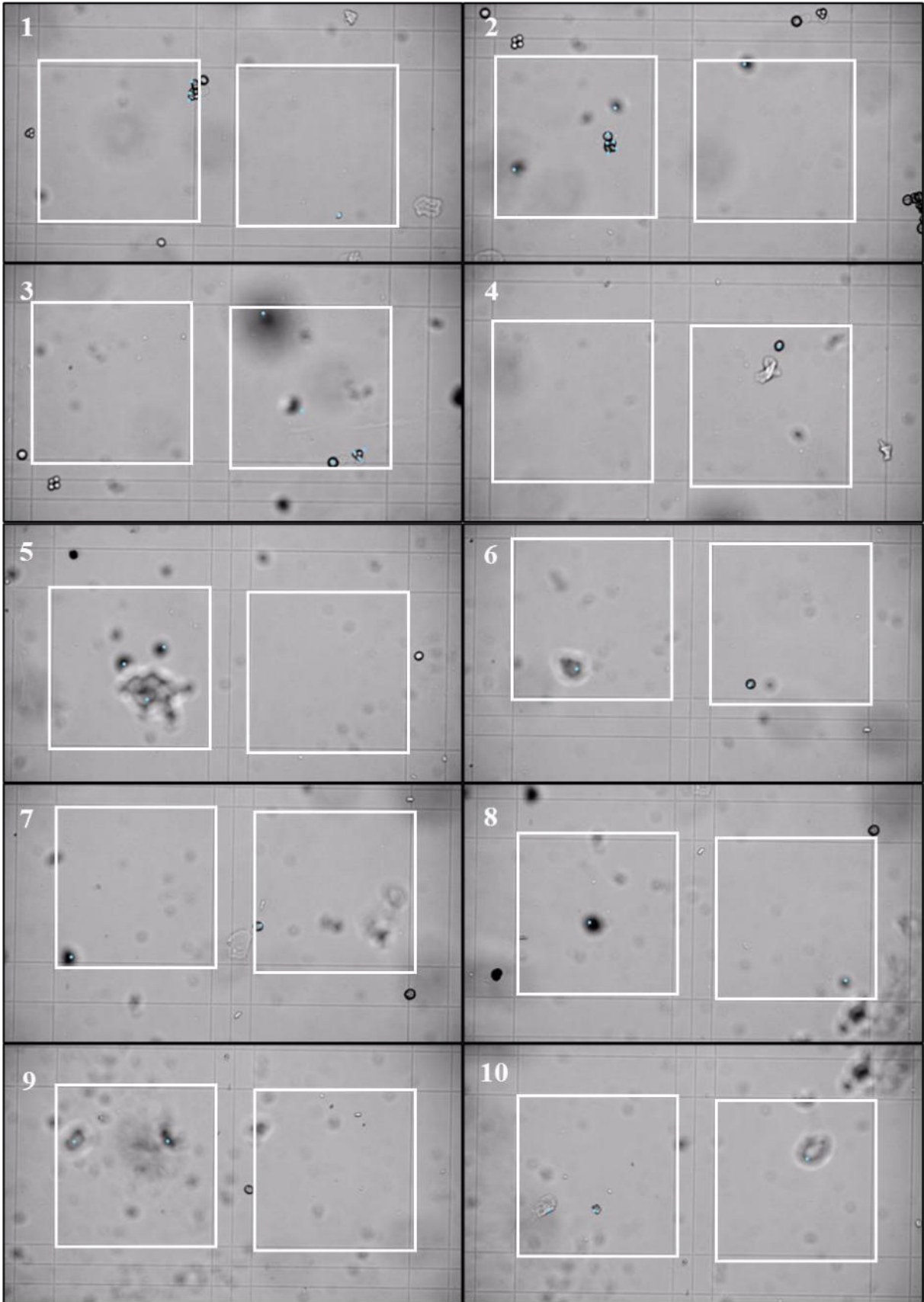


Fig. X3-10. Bürker haemocytometer **RI**, 22-11-25 (PR DAY 8) 9:00, 2,167 cells μl^{-1} .

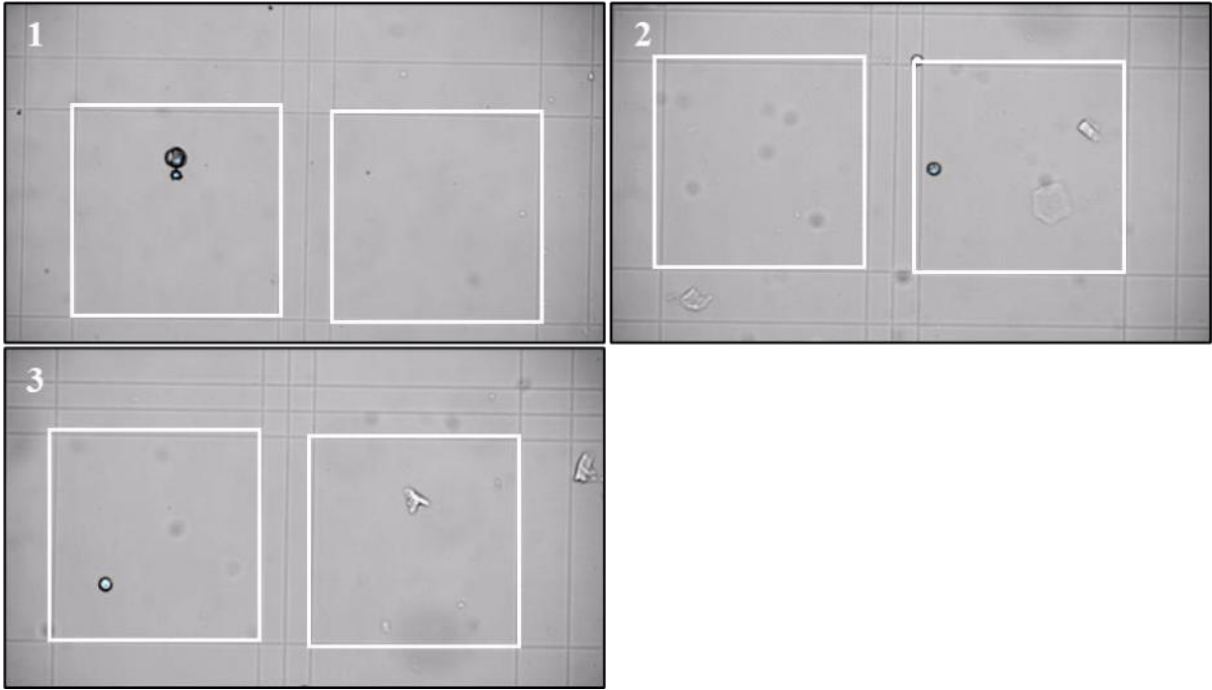


Fig. X3-11. Bürker haemocytometer **R1**, 22-11-25 (PR DAY 8.4) 19:00, 333 cells μl^{-1} .

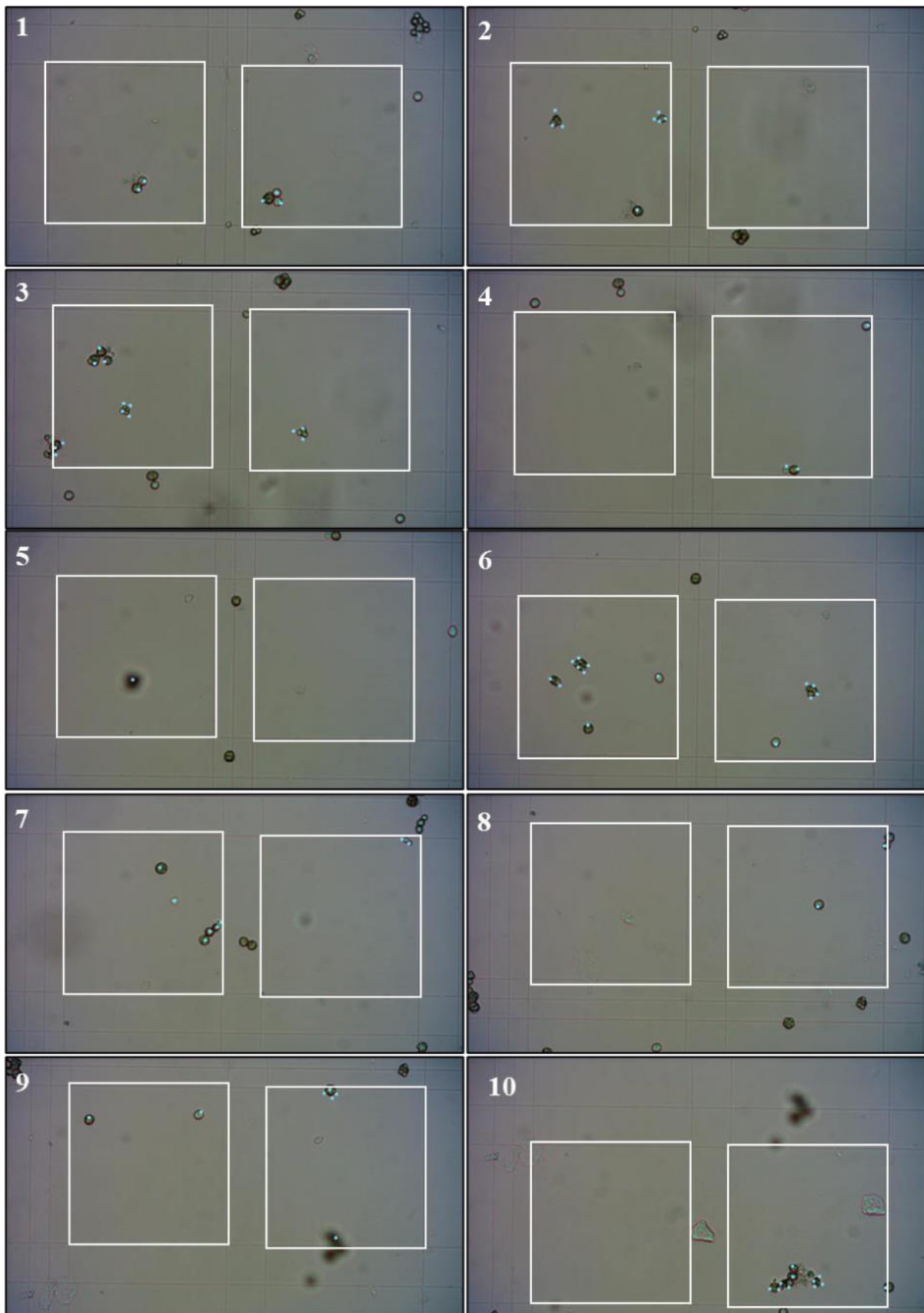


Fig. X3-12. Bürker haemocytometer **RI**, 22-11-28 (PR DAY 11) 9:00, 6,750 cells μl^{-1} (1).

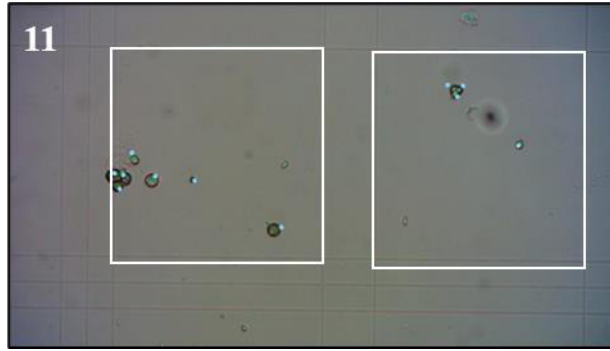


Fig. X3-13. Bürker haemocytometer **RI**, 22-11-28 (PR DAY 11) 9:00, 6,750 cells μl^{-1} (2).

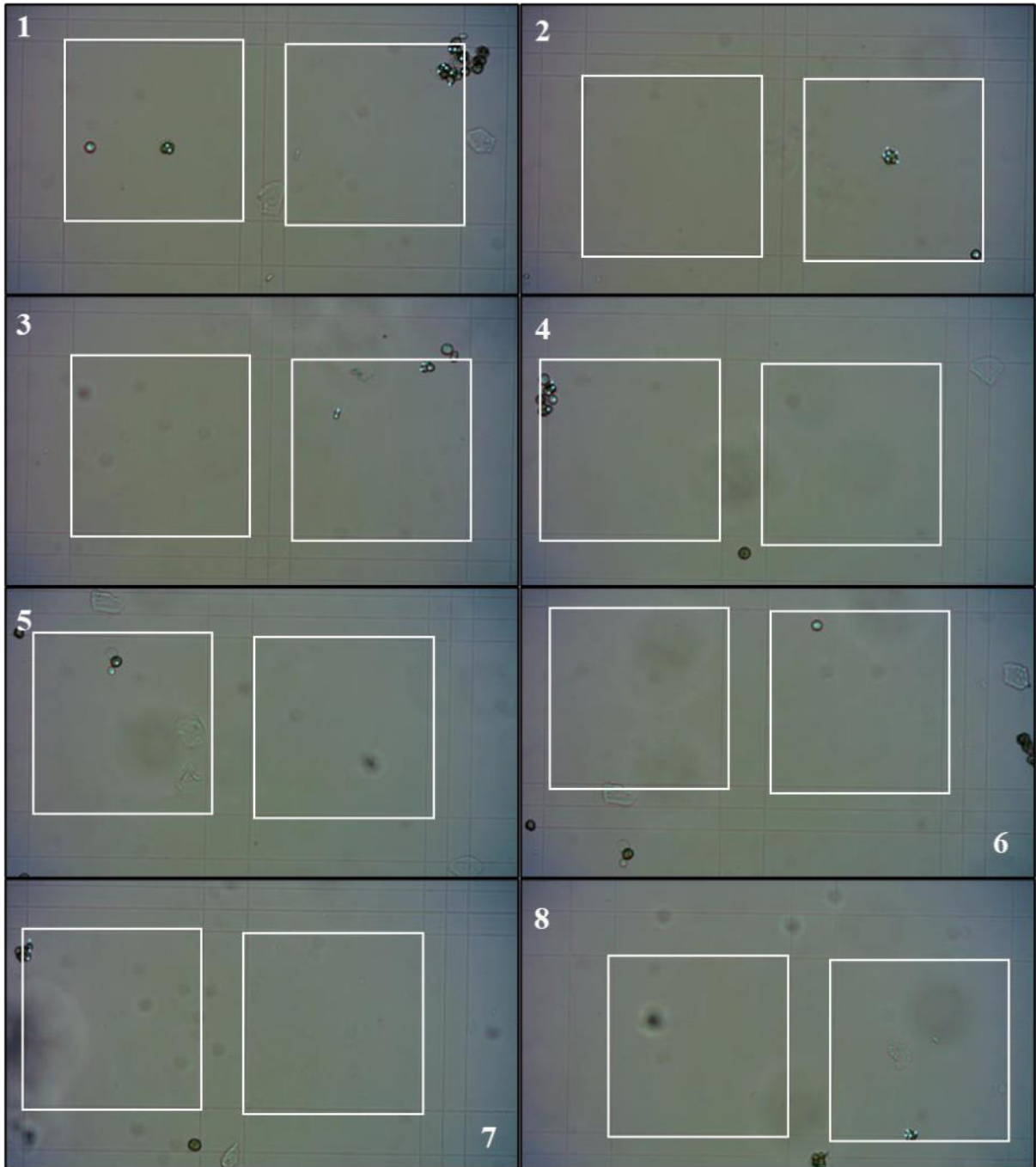


Fig. X3-14. Bürker haemocytometer **R1**, 22-11-28 (PR DAY 11.4) 19:00, 3,667 cells μl^{-1} .

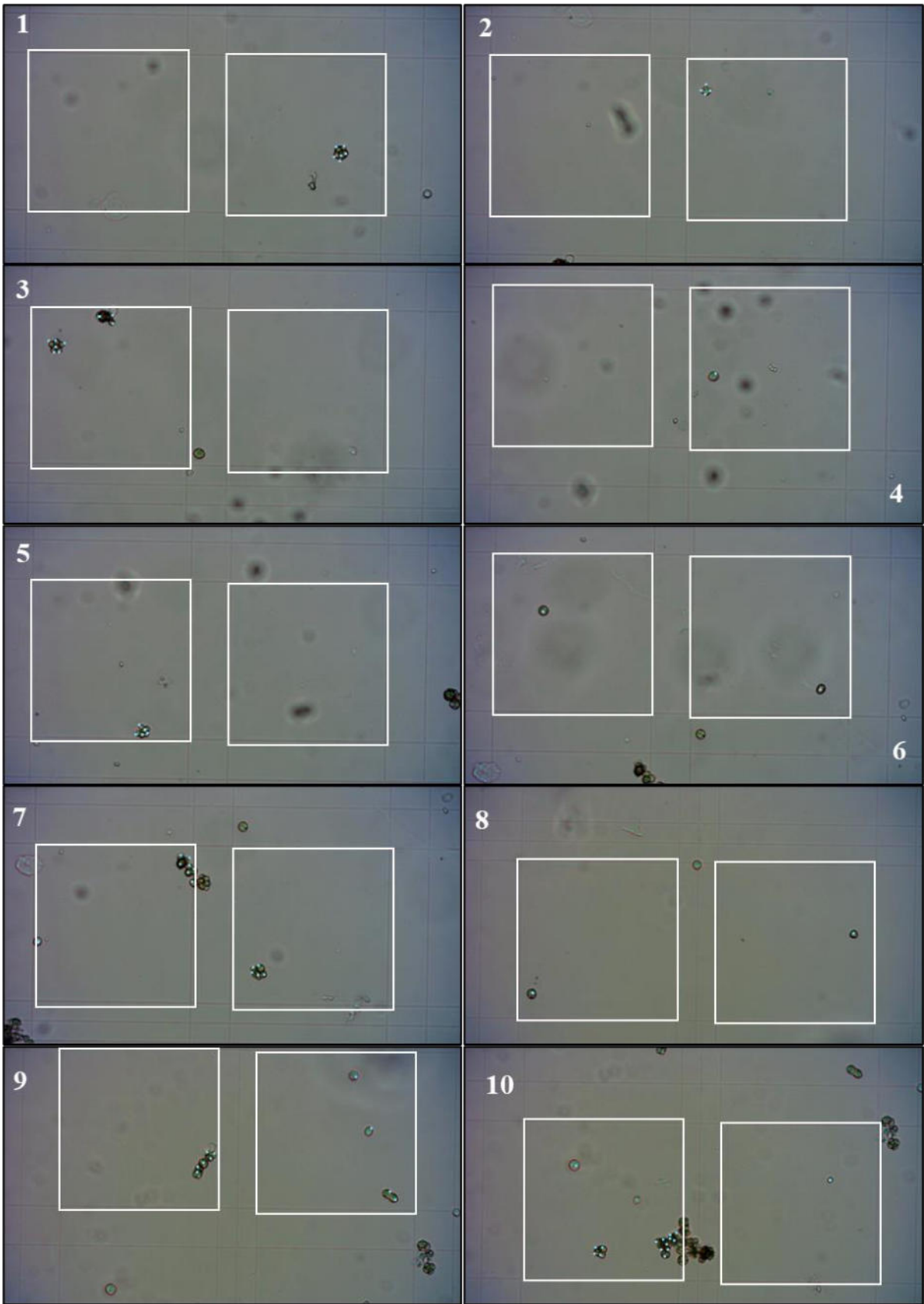


Fig. X3-15. Bürker haemocytometer **RI**, 22-11-29 (PR DAY 12) 9:00, 9,833 cells μl^{-1} (1).

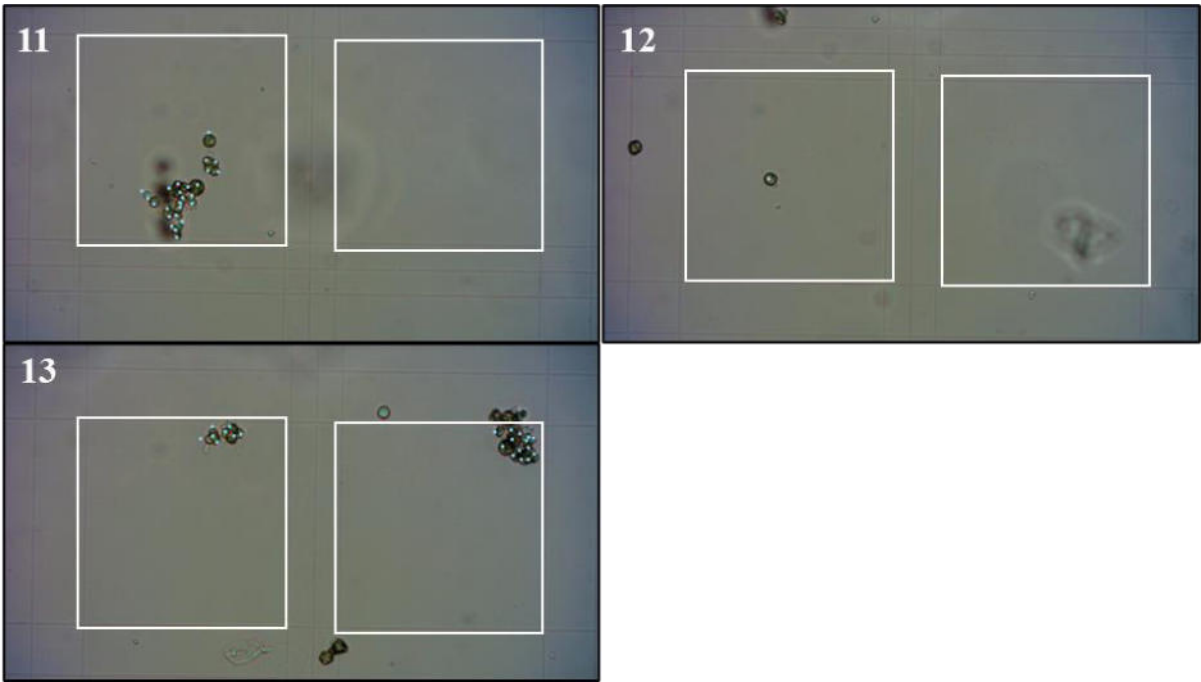


Fig. X3-16. Bürker haemocytometer **RI**, 22-11-29 (PR DAY 12) 9:00, 9,833 cells μl^{-1} (2).

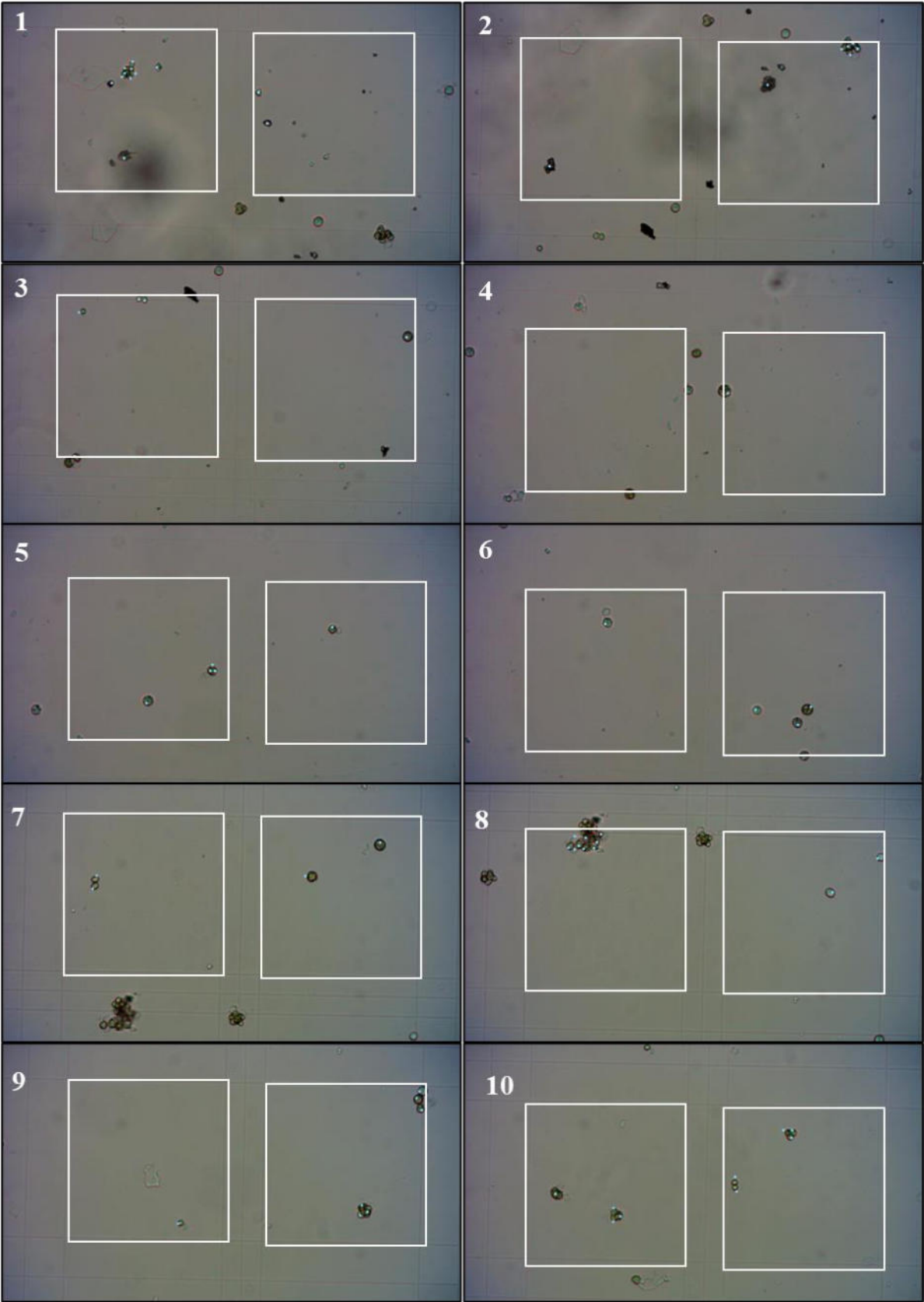


Fig. X3-17. Bürker haemocytometer RI, 22-11-29 (PR DAY 12.4) 19:00, 5,750 cells μl^{-1} (1).

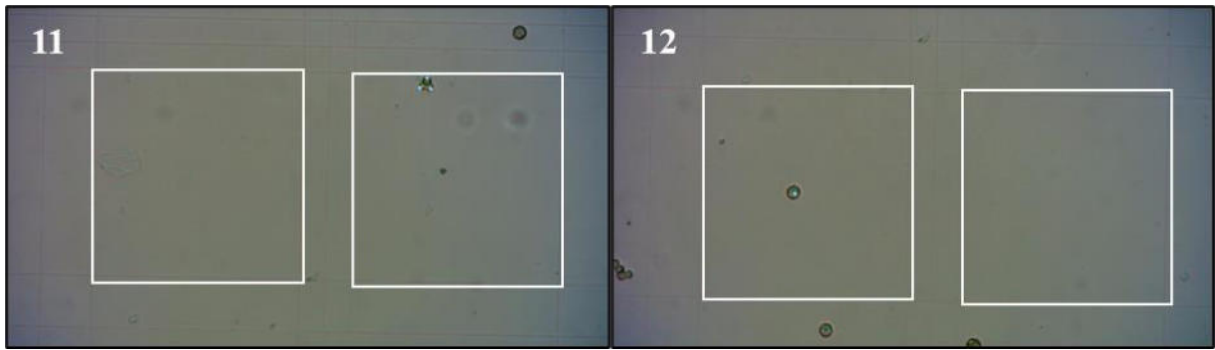


Fig. X3-18. Bürker haemocytometer **R1**, 22-11-29 (PR DAY 12.4) 19:00, 5,750 cells μl^{-1} (2).

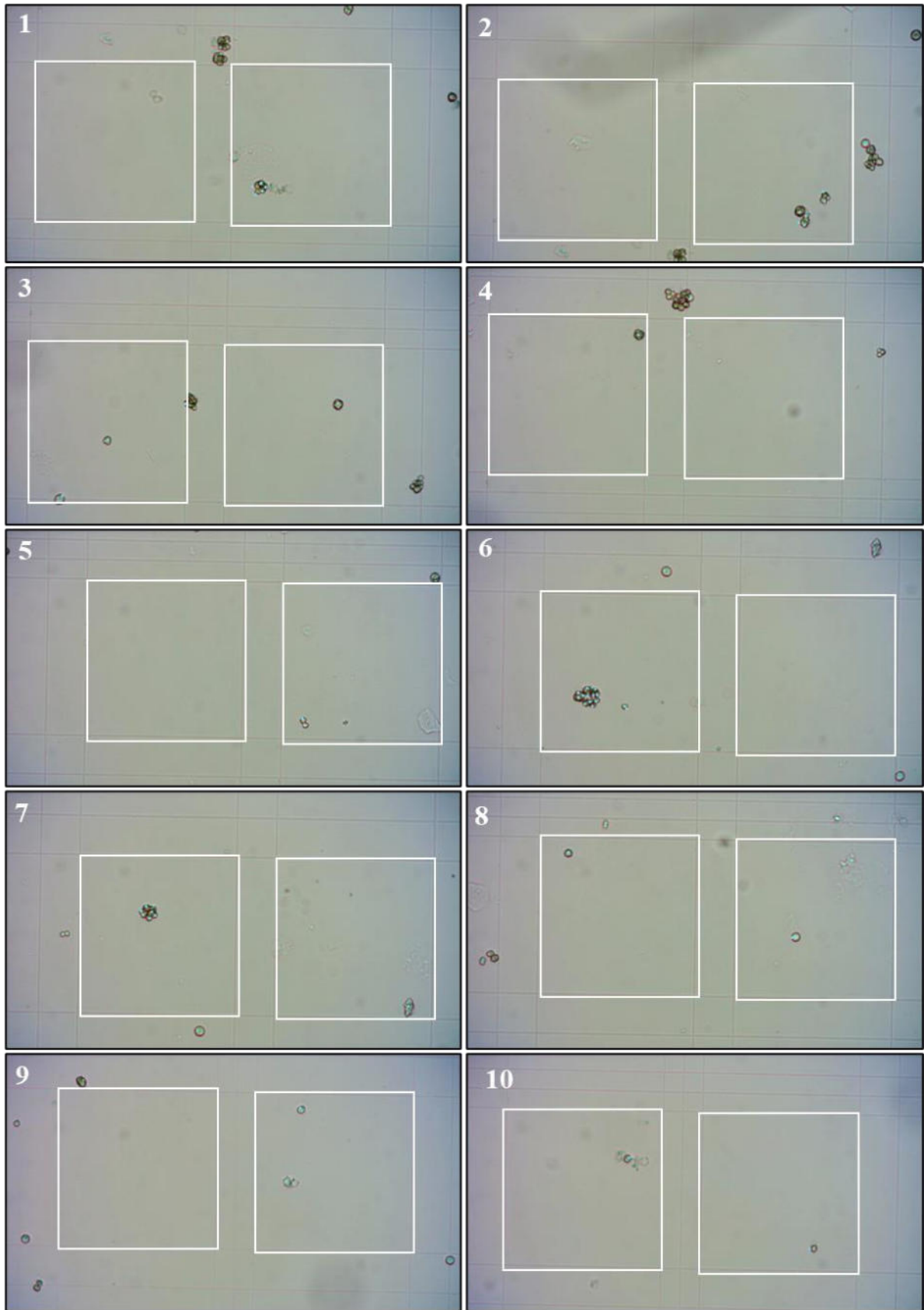


Fig. X3-19. Bürker haemocytometer **RI**, 22-11-30 (PR DAY 13.1) 13:00, 6,333 cells μl^{-1} (1).

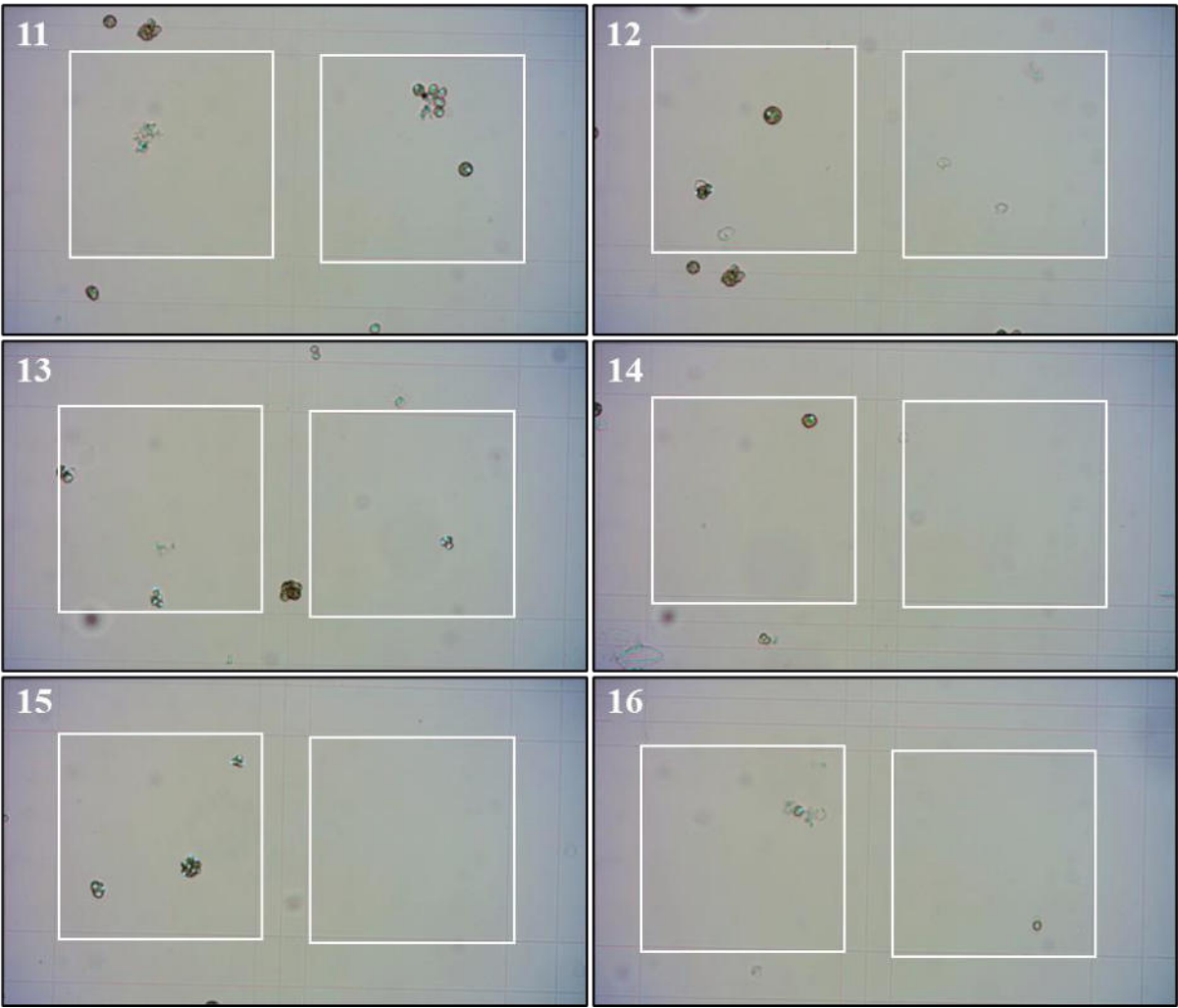


Fig. X3-20. Bürker haemocytometer **RI**, 22-11-30 (PR DAY 13.1) 13:00, 6,333 cells μl^{-1} (2).

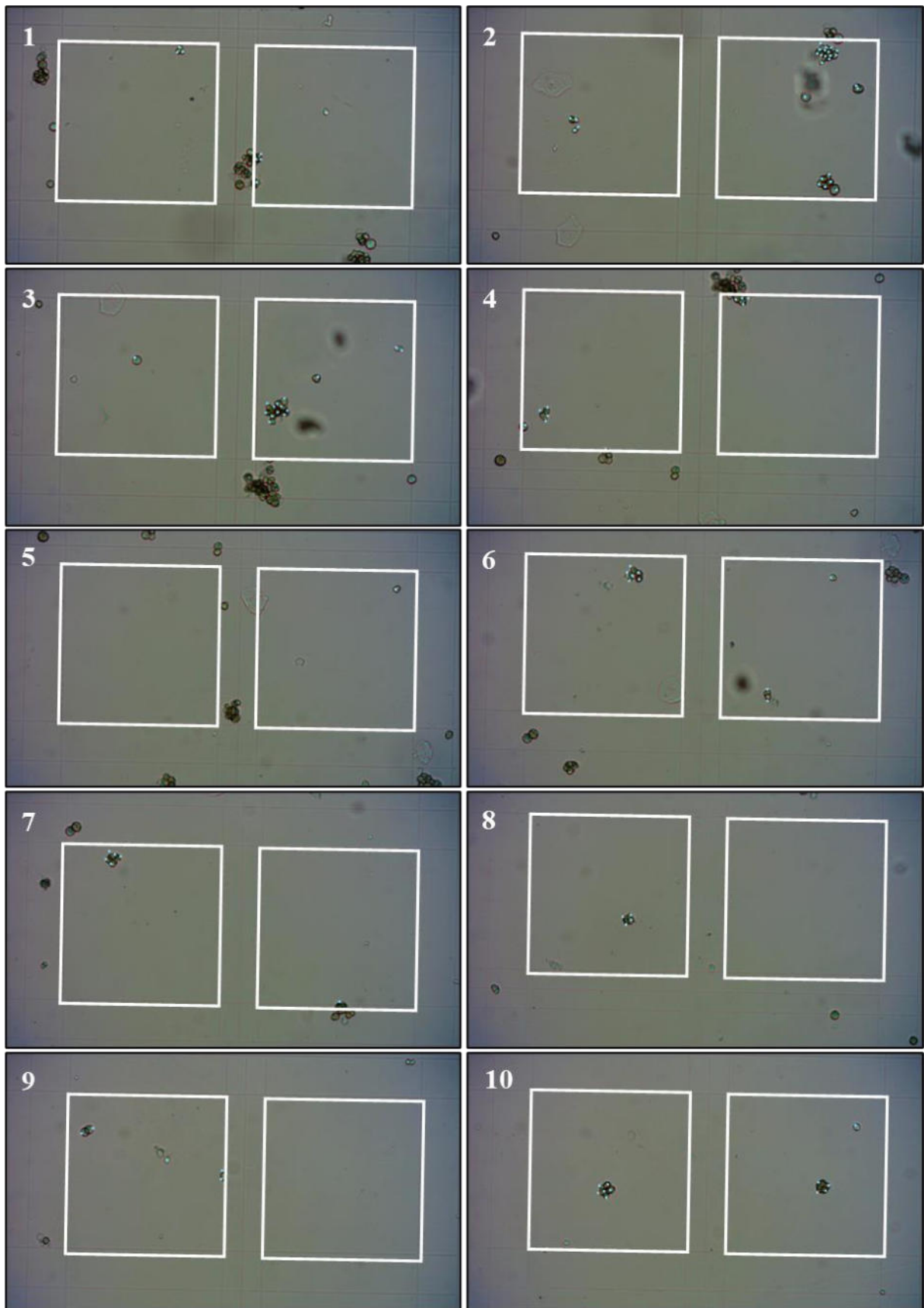


Fig. X3-21. Bürker haemocytometer RI, 22-12-01 (PR DAY 14) 9:00, 12,500 cells μL^{-1} (1).

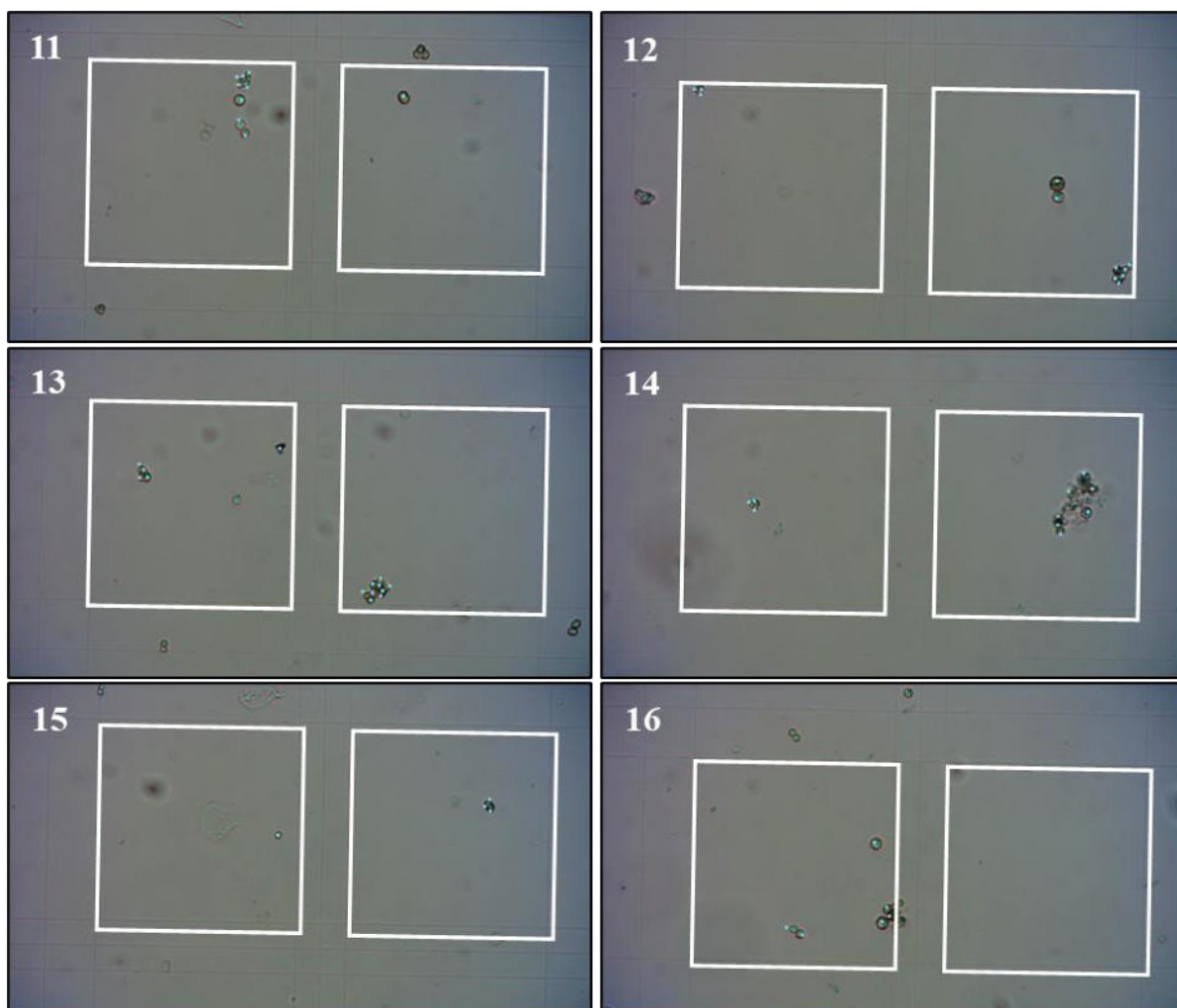


Fig. X3-22. Bürker haemocytometer **RI**, 22-12-01 (PR DAY 14) 9:00, 12,500 cells μl^{-1} (2).

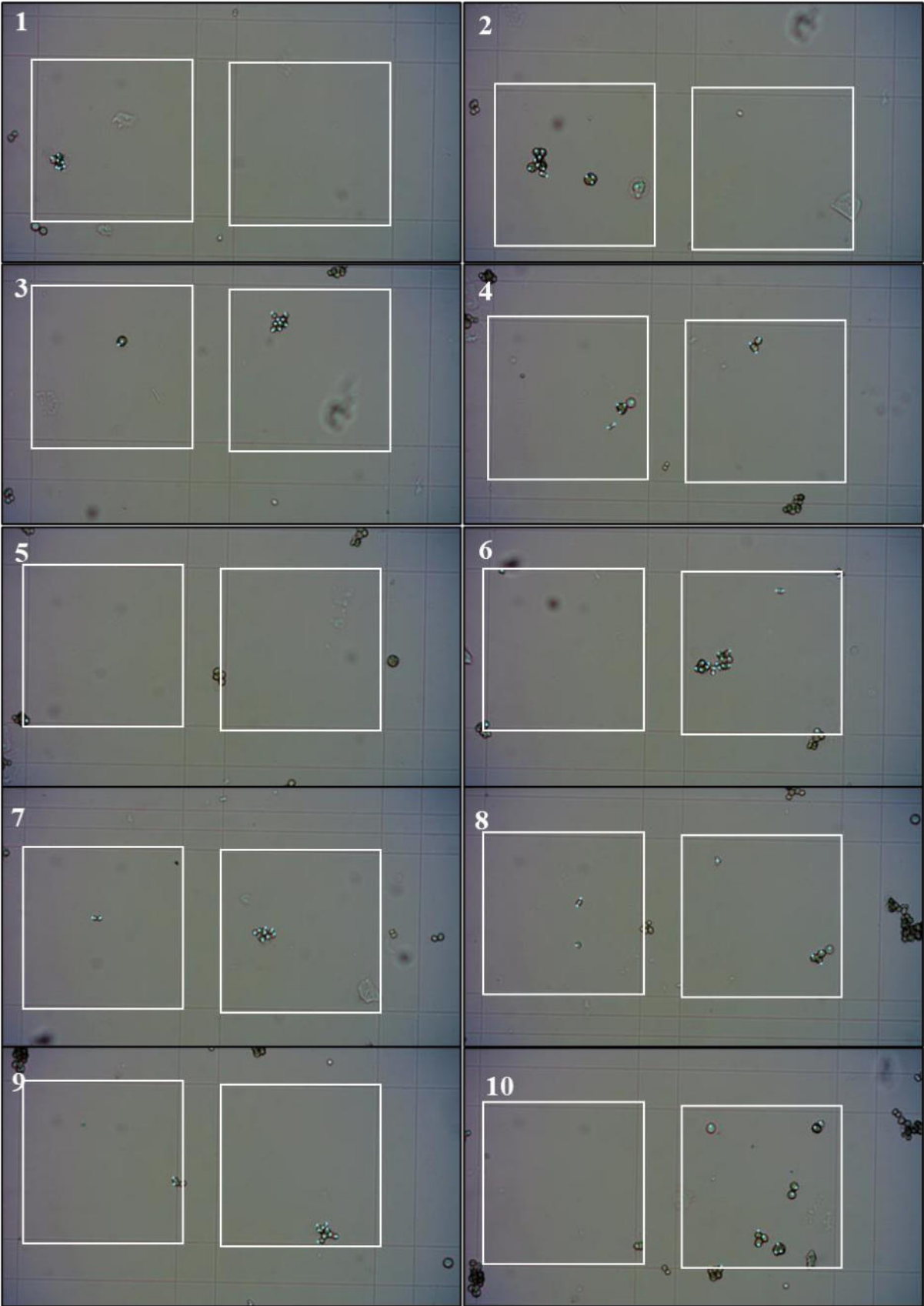


Fig. X3-23. Bürker haemocytometer **RI**, 22-12-02 (PR DAY 15.4) 19:00, 15,167 cells μl^{-1} (1).

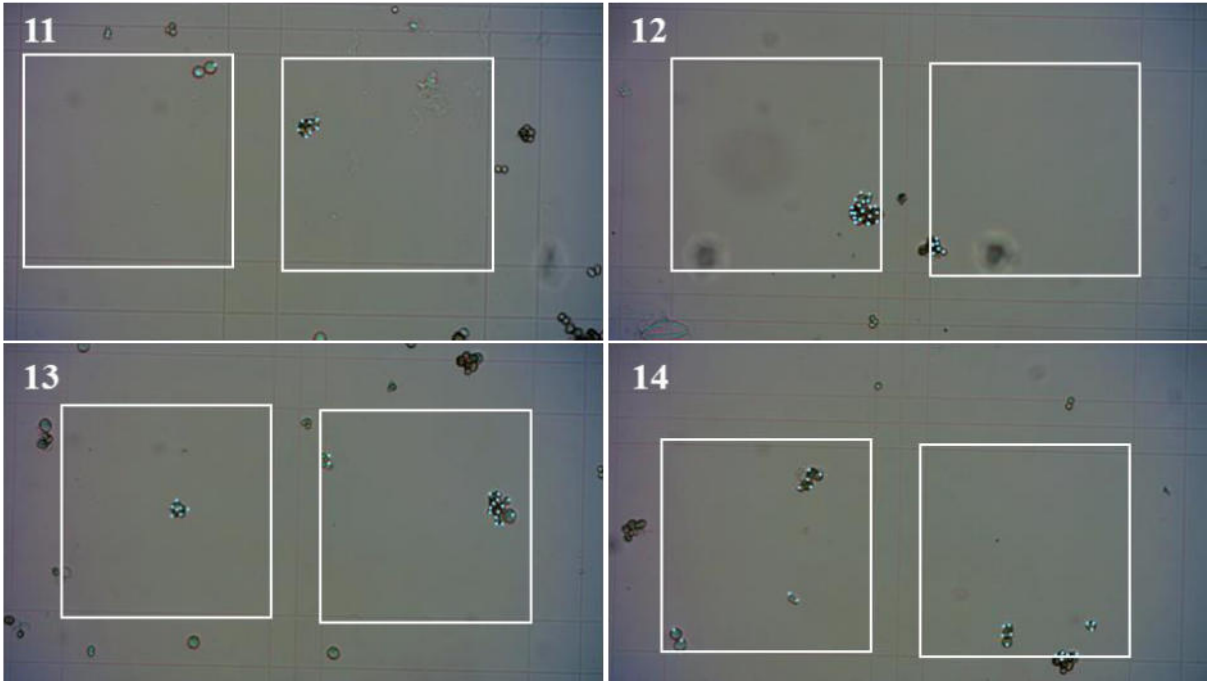


Fig. X3-24. Bürker haemocytometer RI, 22-12-02 (PR DAY 15.4) 19:00, 15,167 cells μl^{-1} (2).

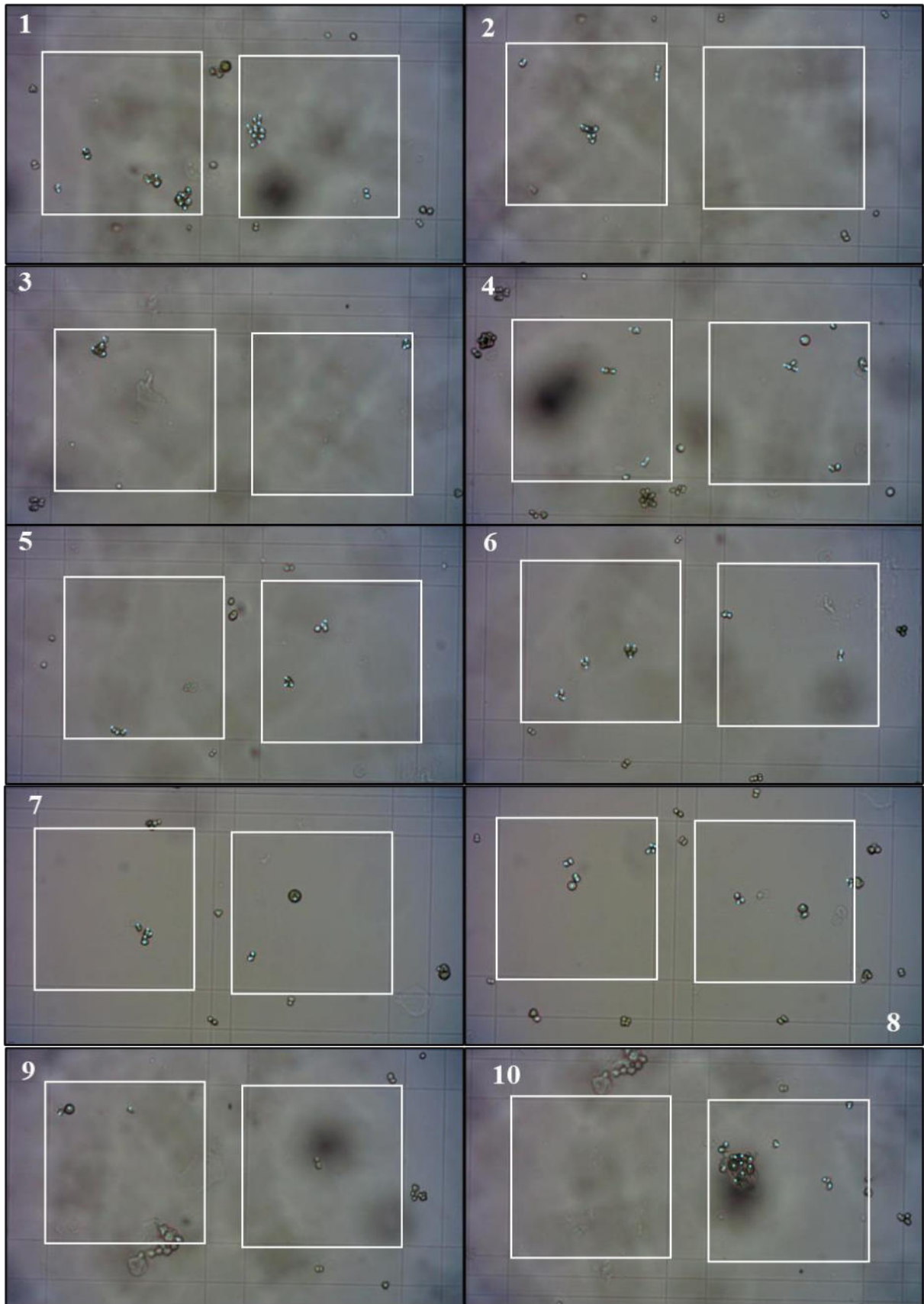


Fig. X3-25. Bürker haemocytometer RI, 22-12-05 (PR DAY 18) 9:00, 31,750 cells μL^{-1} (1).

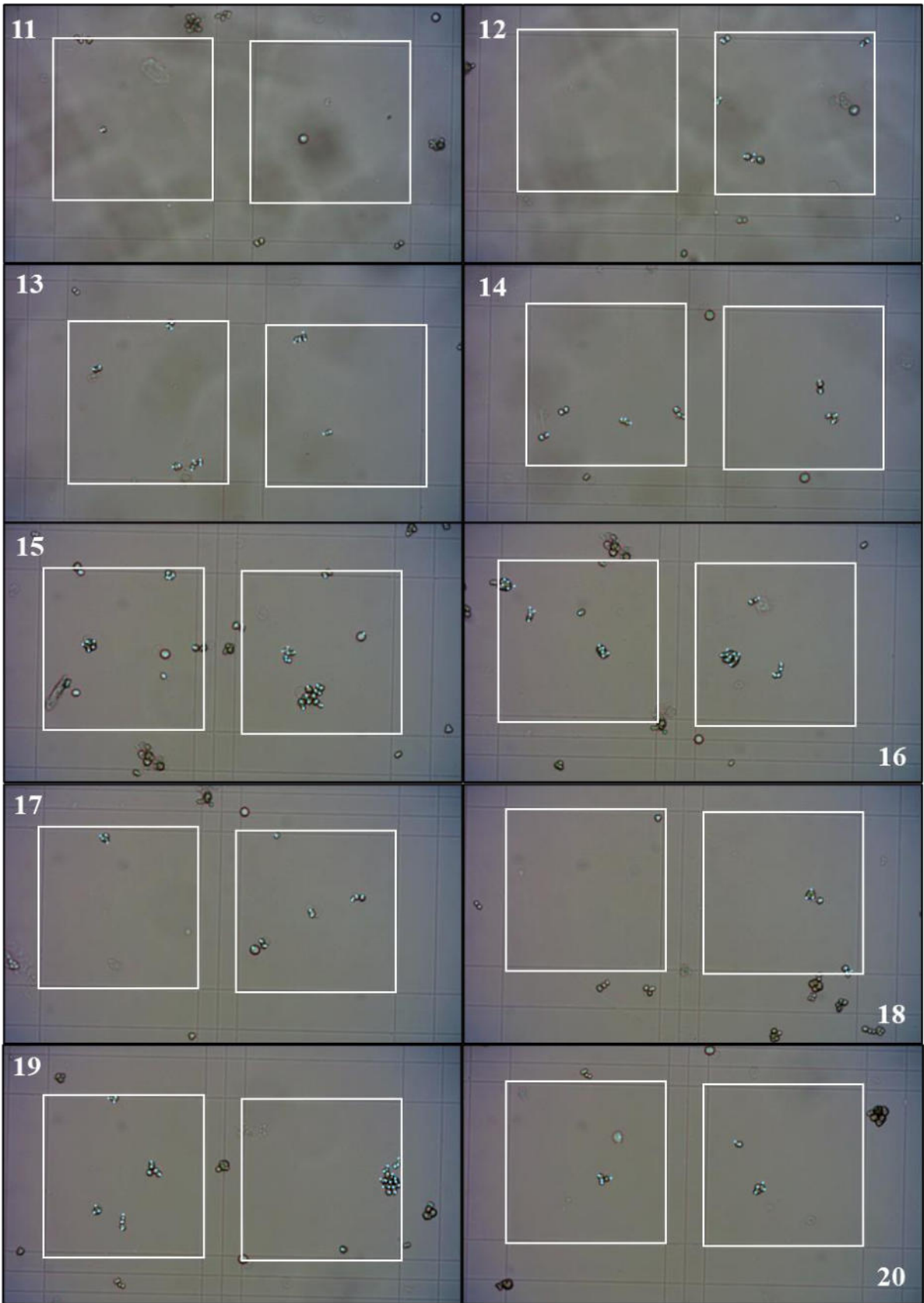


Fig. X3-26. Bürker haemocytometer RI, 22-12-05 (PR DAY 18) 9:00, 31,750 cells μl^{-1} (2).

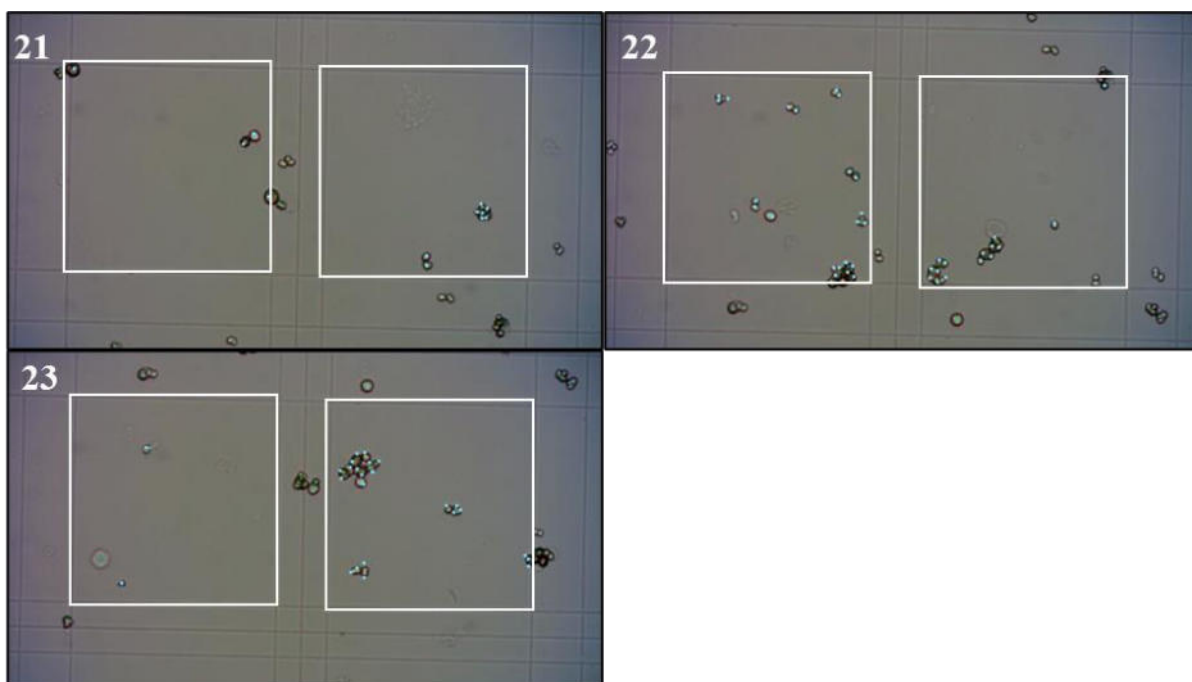


Fig. X3-27. Bürker haemocytometer **RI**, 22-12-05 (PR DAY 18) 9:00, 31,750 cells μl^{-1} (3).

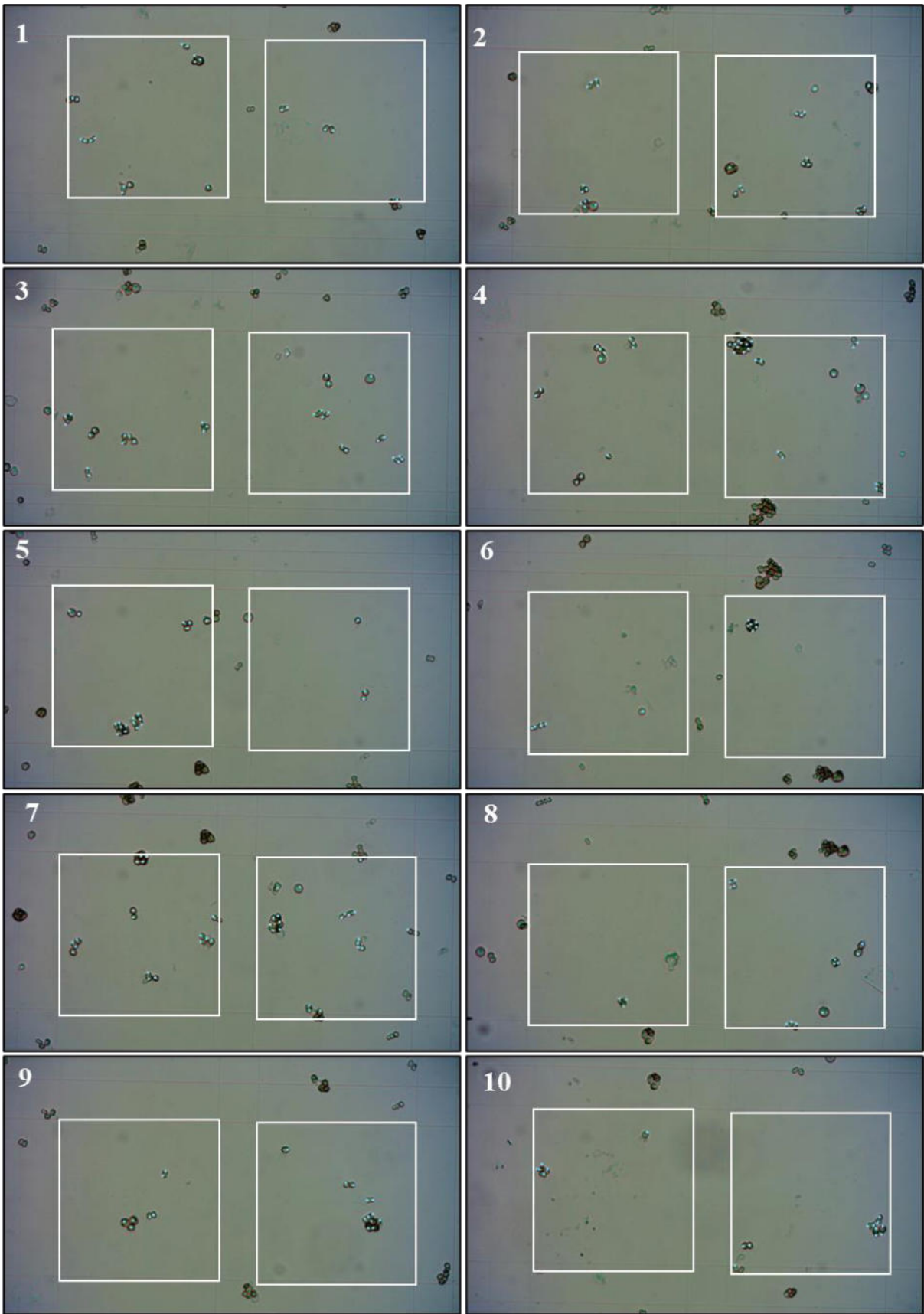


Fig. X3-28. Bürker haemocytometer **RI**, 22-12-05 (PR DAY 18.4) 19:00, 36,833 cells μl^{-1} (1).

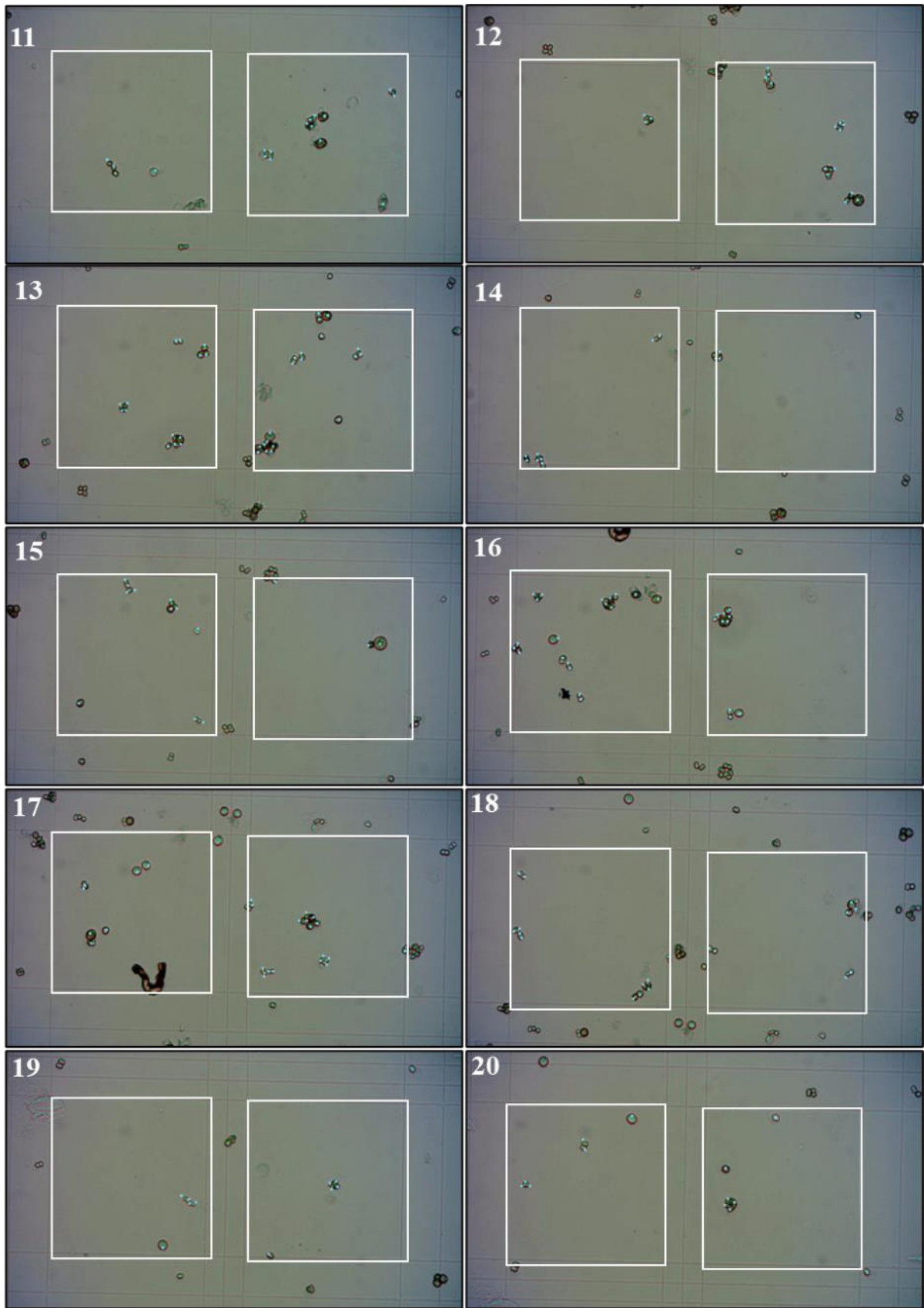


Fig. X3-29. Bürker haemocytometer RI, 22-12-05 (PR DAY 18.4) 19:00, 36,833 cells μl^{-1} (2).

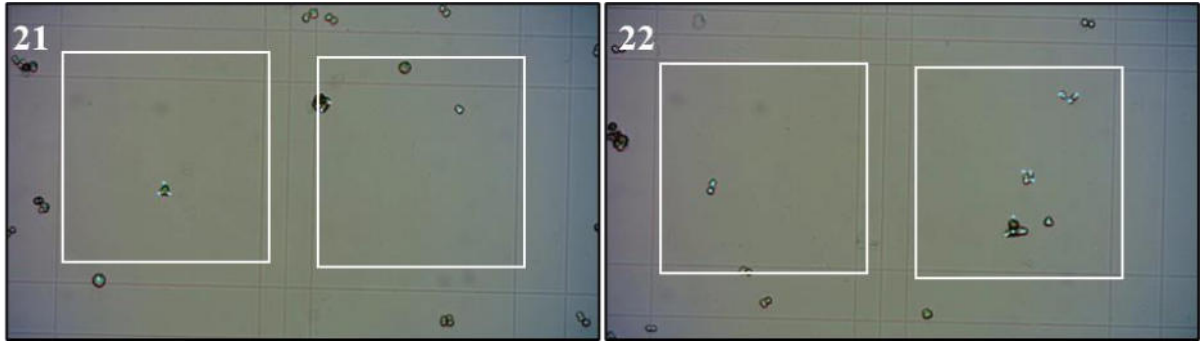


Fig. X3-30. Bürker haemocytometer RI, 22-12-05 (PR DAY 18.4) 19:00, 36,833 cells μL^{-1} (3).

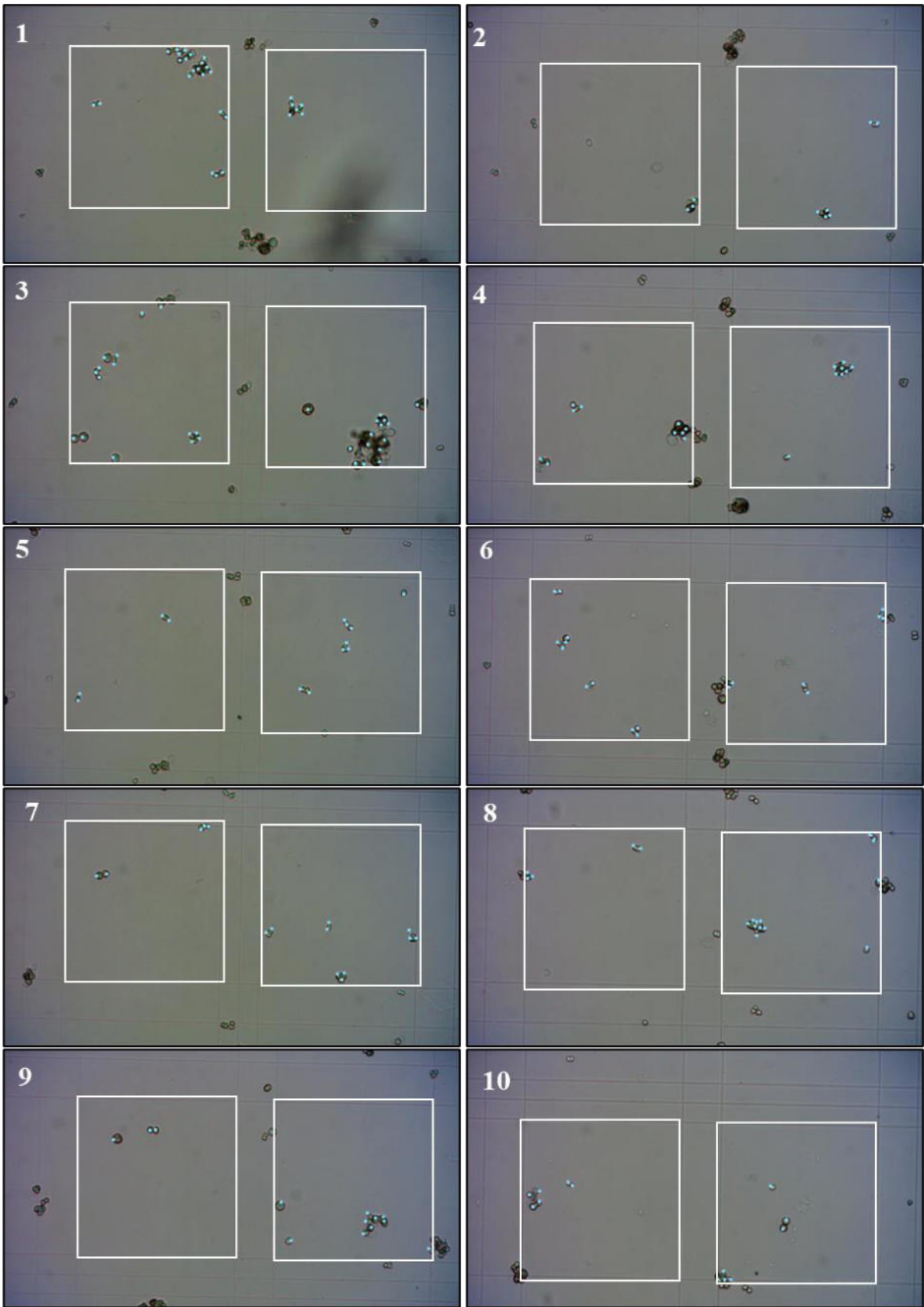


Fig. X3-31. Bürker haemocytometer **RI**, 22-12-06 (PR DAY 19) 9:00, 26,333 cells μl^{-1} (1).

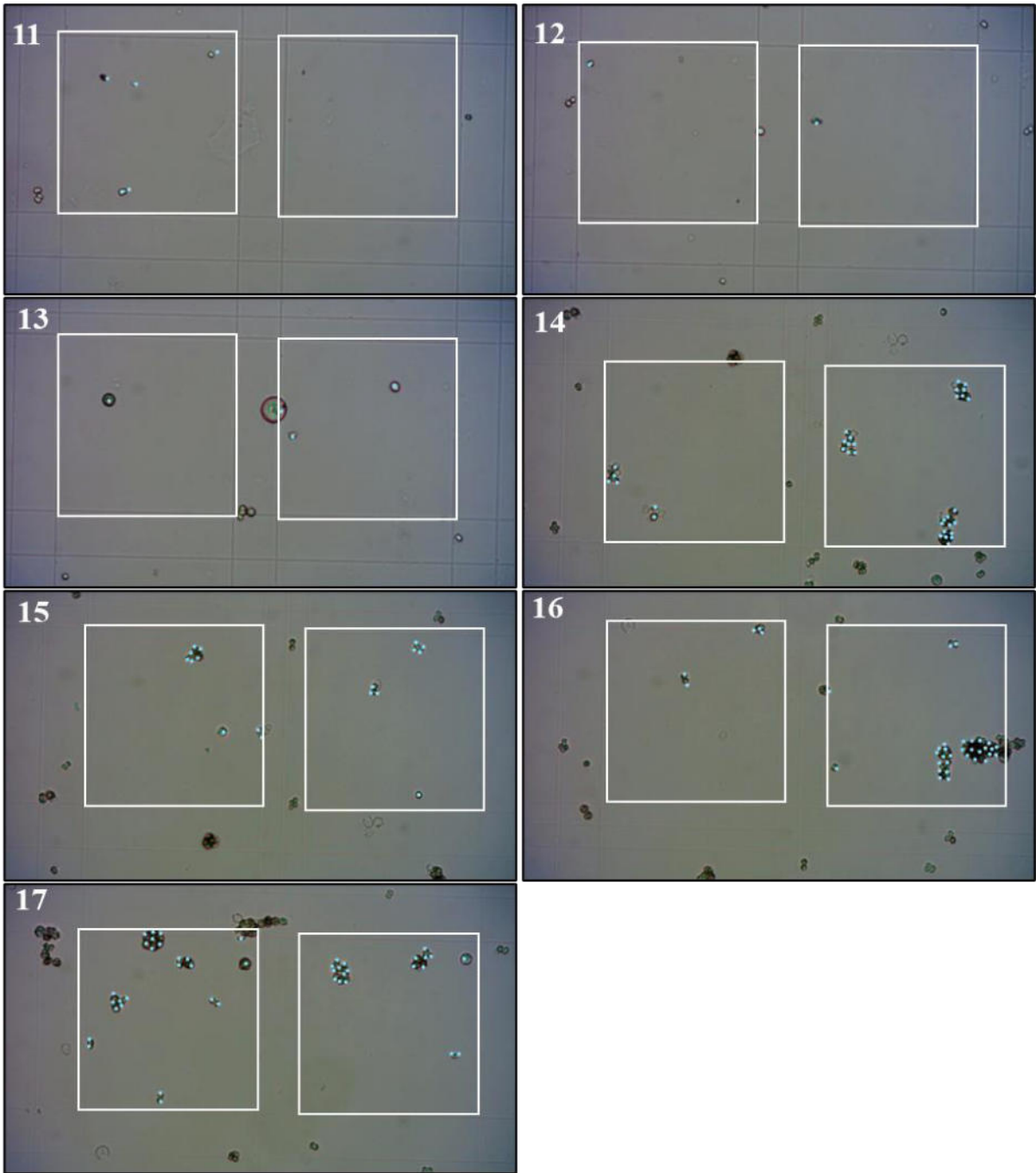


Fig. X3-32. Bürker haemocytometer R1, 22-12-06 (PR DAY 19) 9:00, 26,333 cells μl^{-1} (2).

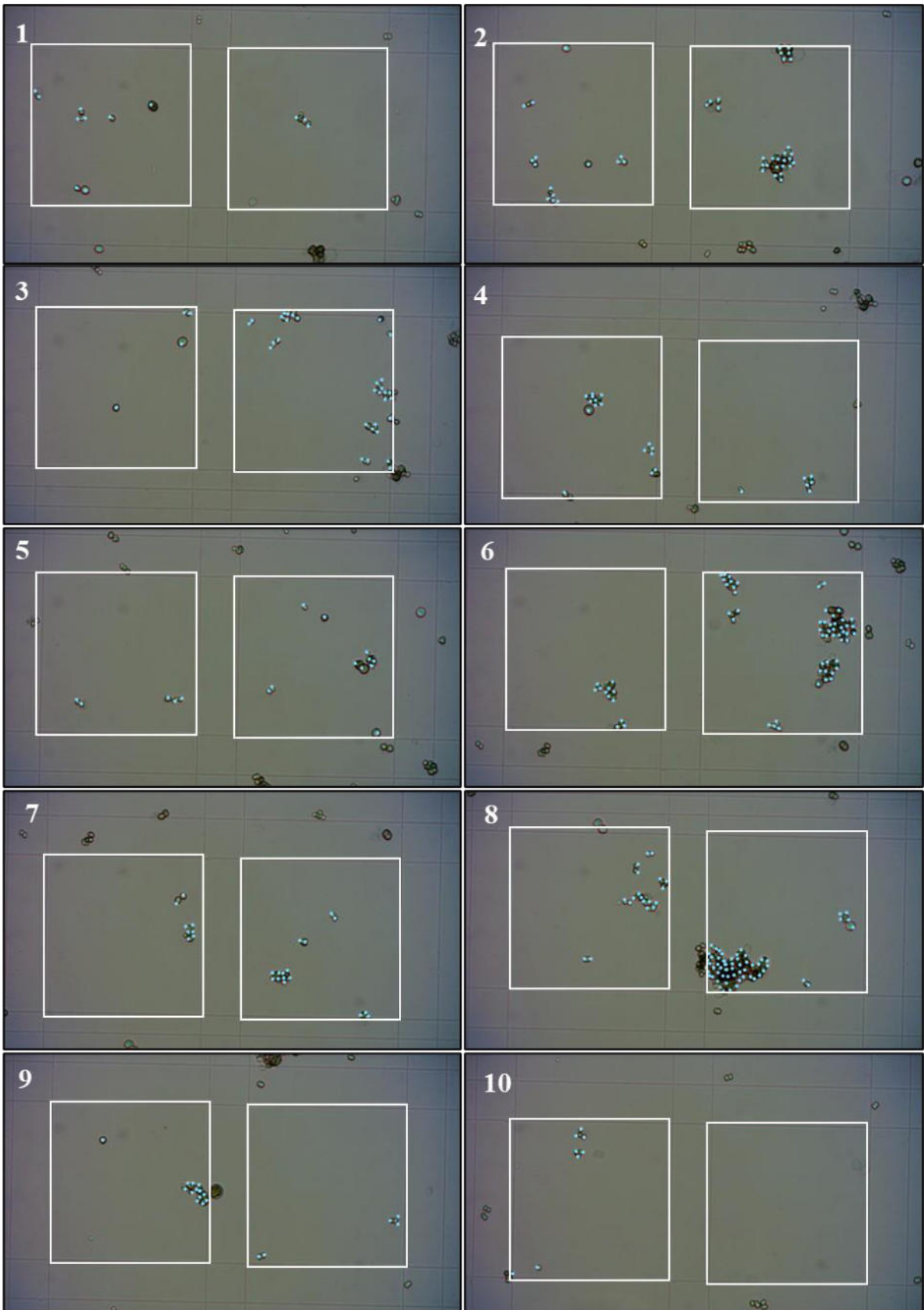


Fig. X3-33. Bürker haemocytometer R1, 22-12-06 (PR DAY 19.4) 19:00, 36,413 cells μL^{-1} (1).

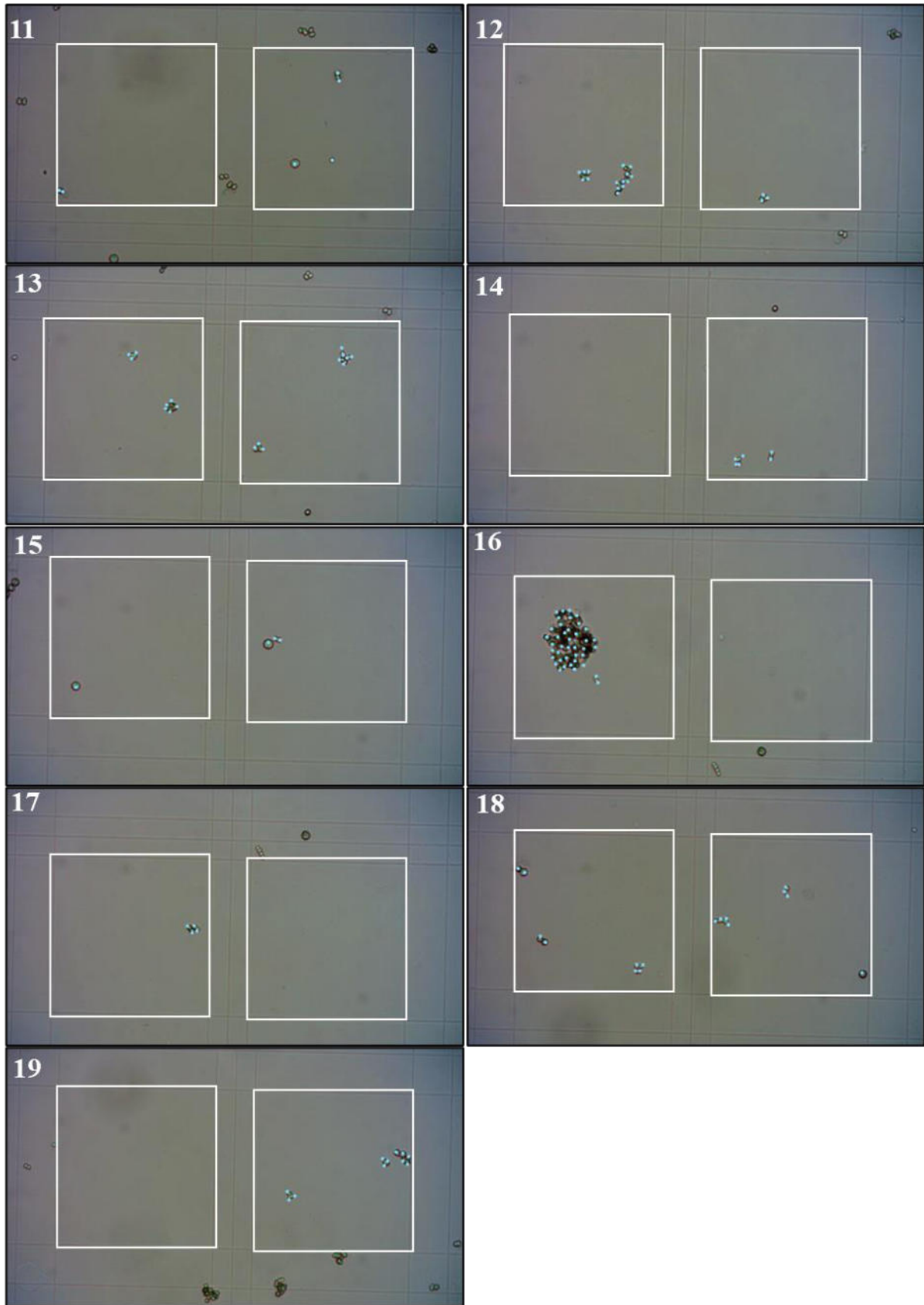


Fig. X3-34. Bürker haemocytometer **RI**, 22-12-06 (PR DAY 19.4) 19:00, 36,413 cells μl^{-1} (2).

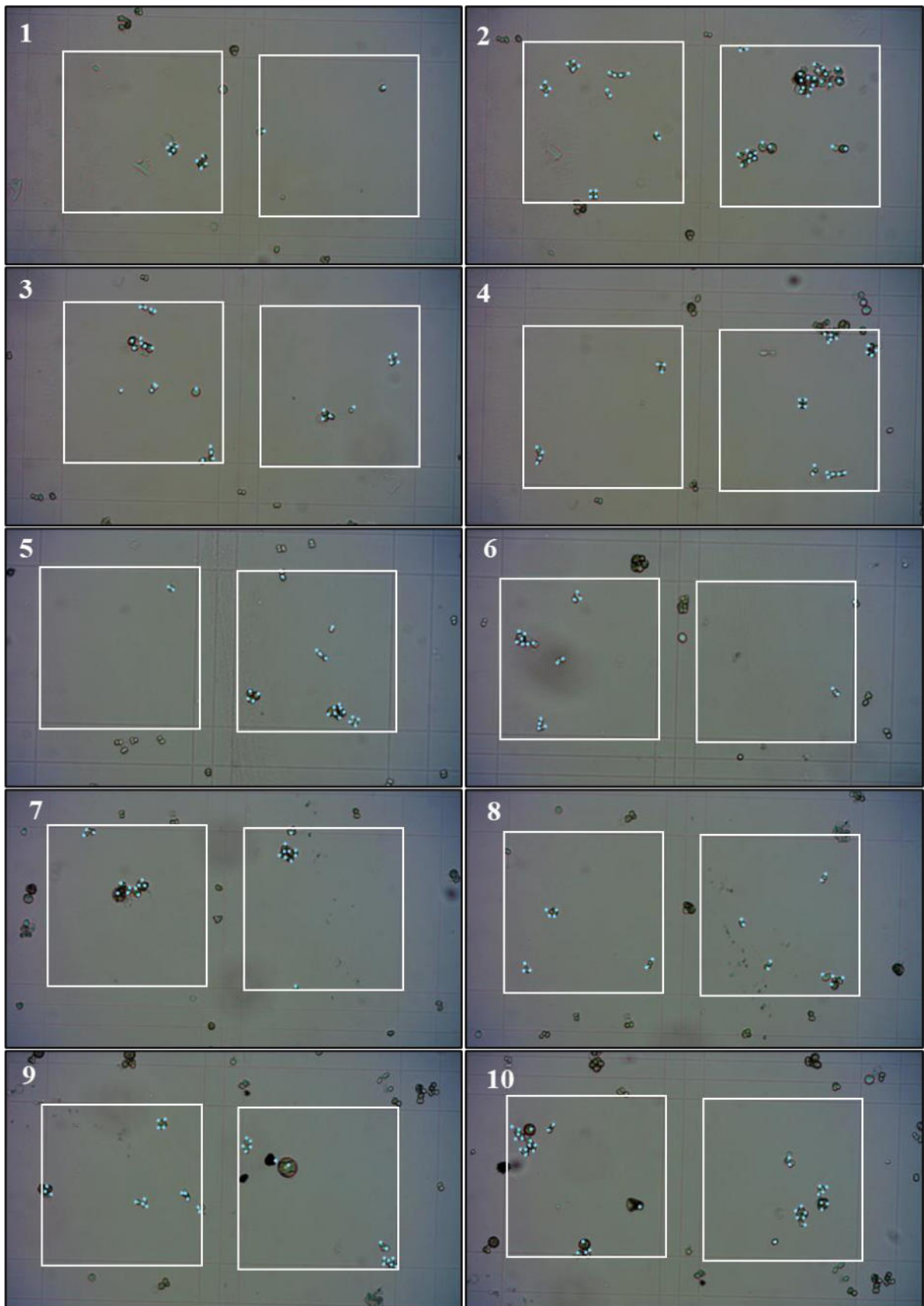


Fig. X3-35. Bürker haemocytometer RI, 22-12-07 (PR DAY 20.1) 13:00, 42,083 cells μl^{-1} (1).

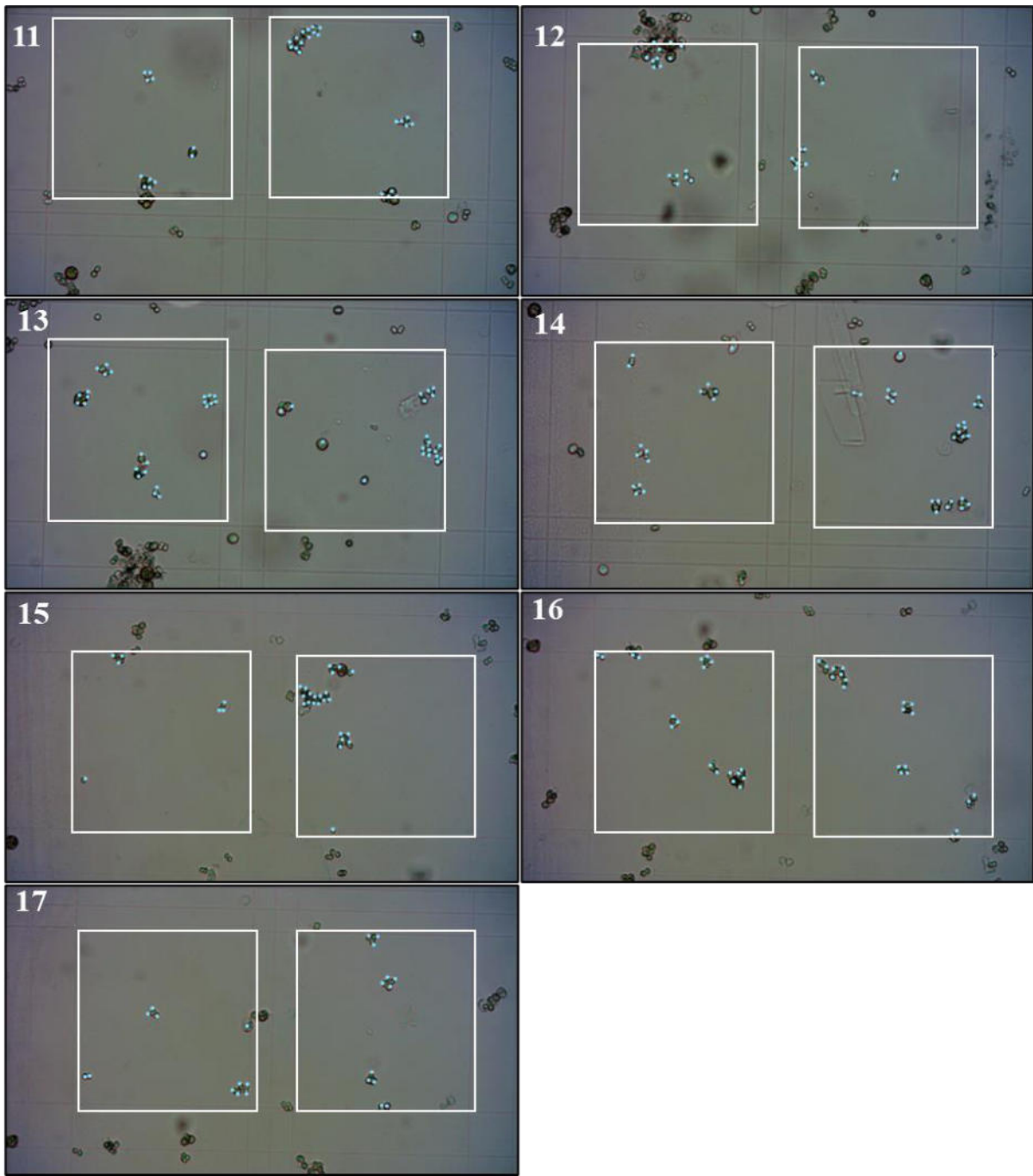


Fig. X3-36. Bürker haemocytometer RI, 22-12-07 (PR DAY 20.1) 13:00, 42,083 cells $\mu\text{l}^{-1}(2)$.

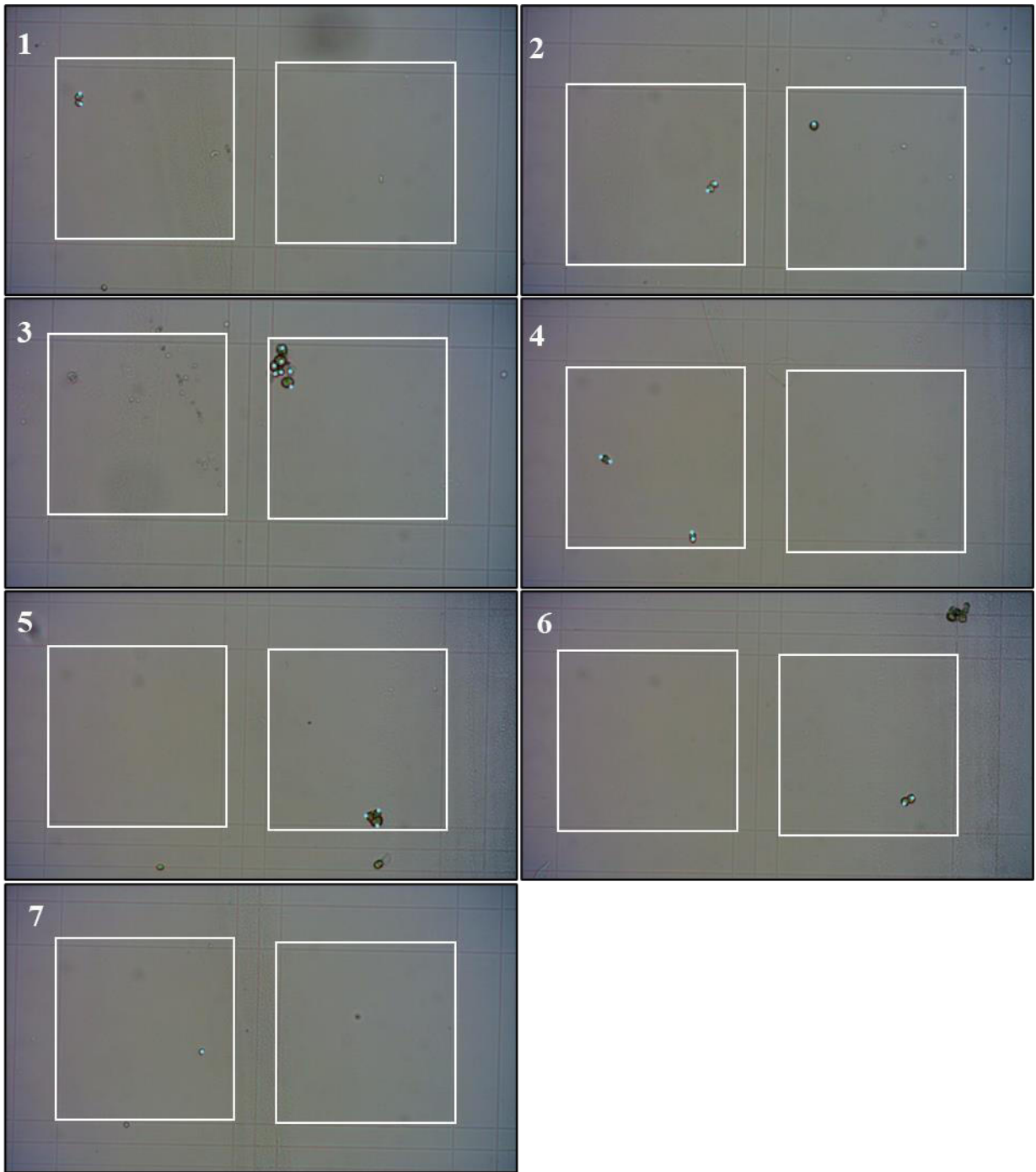


Fig. X3-37. Bürker haemocytometer **R2**, 22-12-15 (PR DAY 1) 9:00, 1,833 cells μl^{-1} .

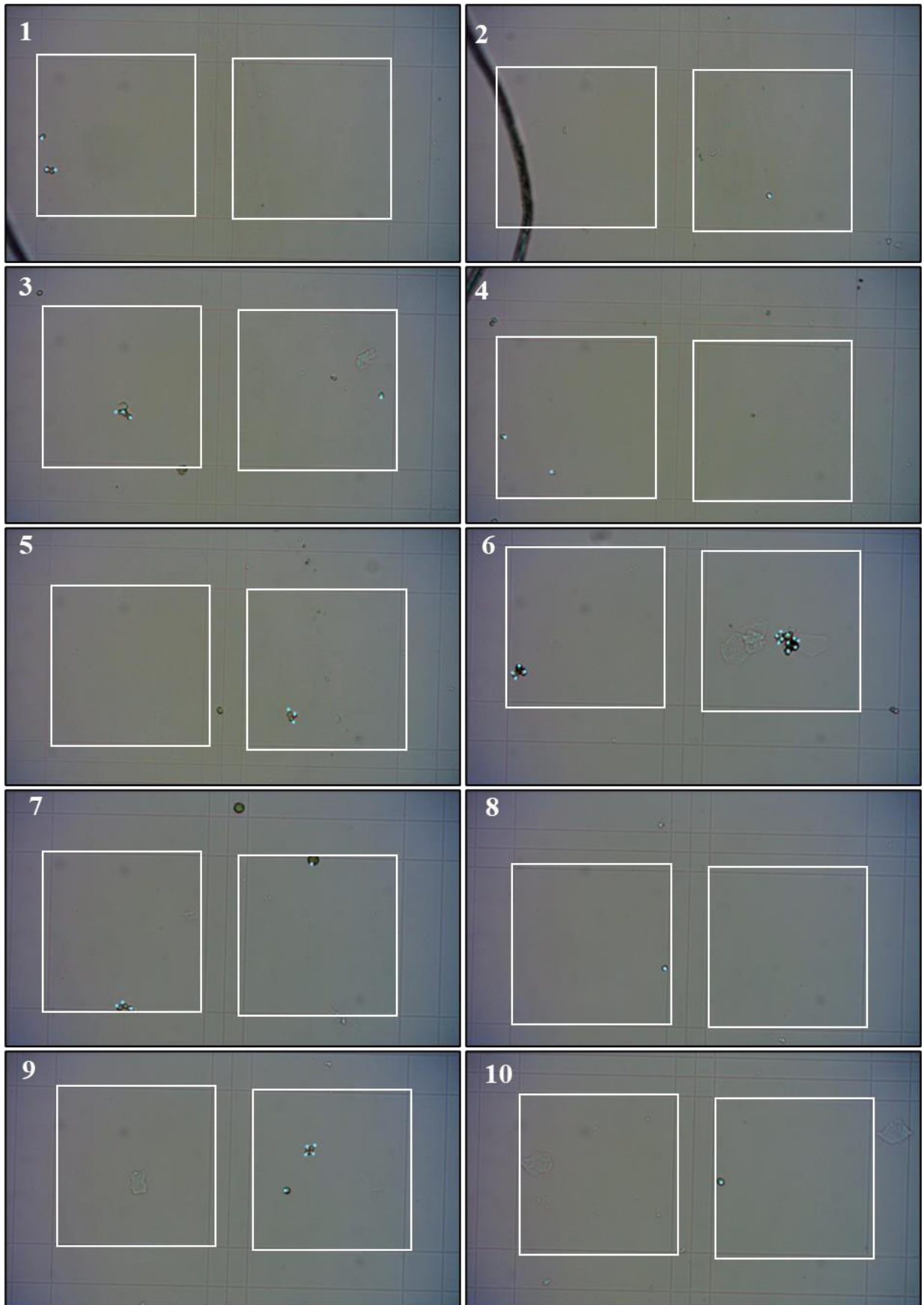


Fig. X3-38. Bürker haemocytometer R2, 22-12-15 (PR DAY 1.2) 13:00, 3,167 cells μl^{-1} .

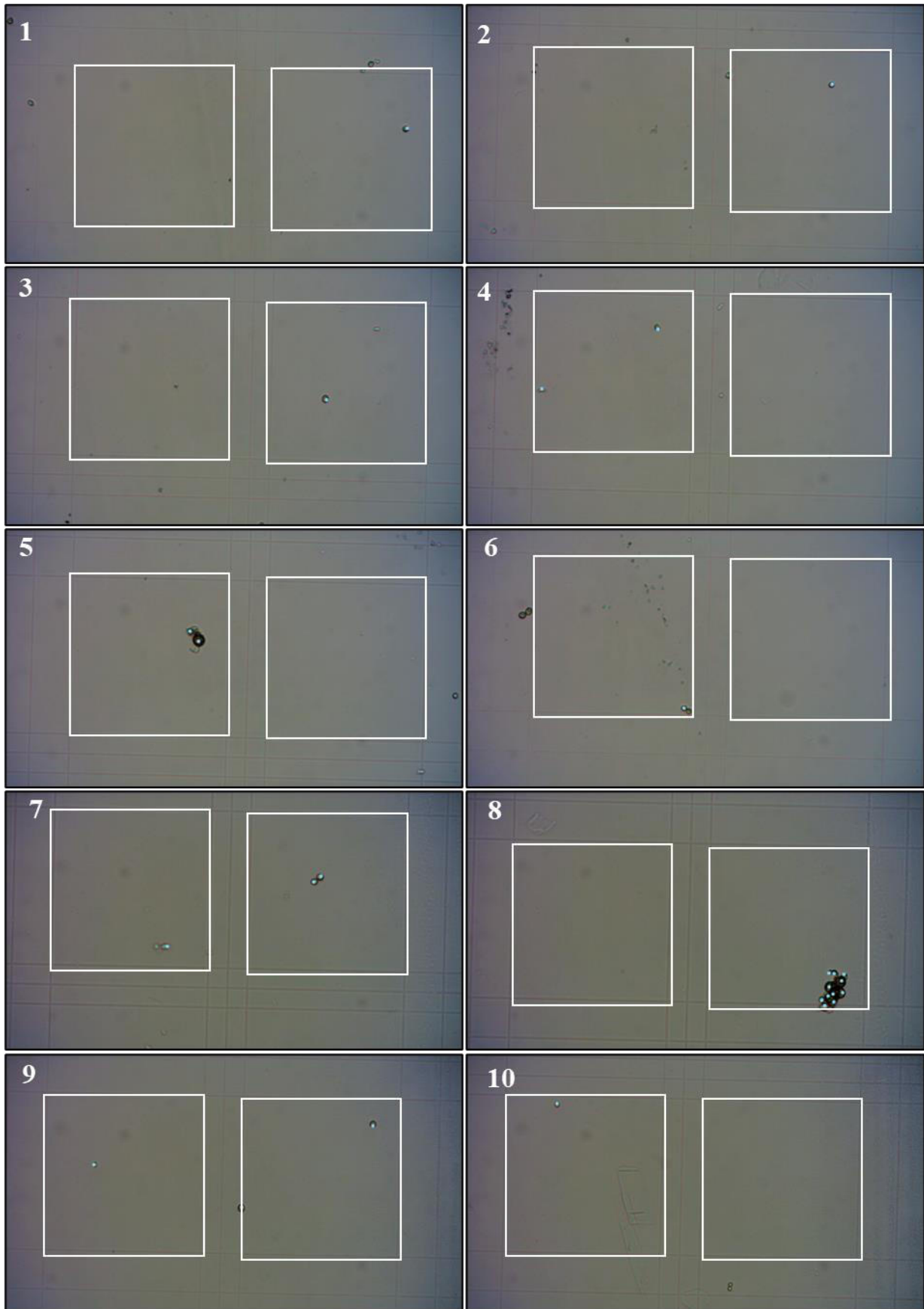


Fig. X3-39. Bürker haemocytometer R2, 22-12-15 (PR DAY 1.4) 19:00, 2,333 cells μl^{-1} (1).

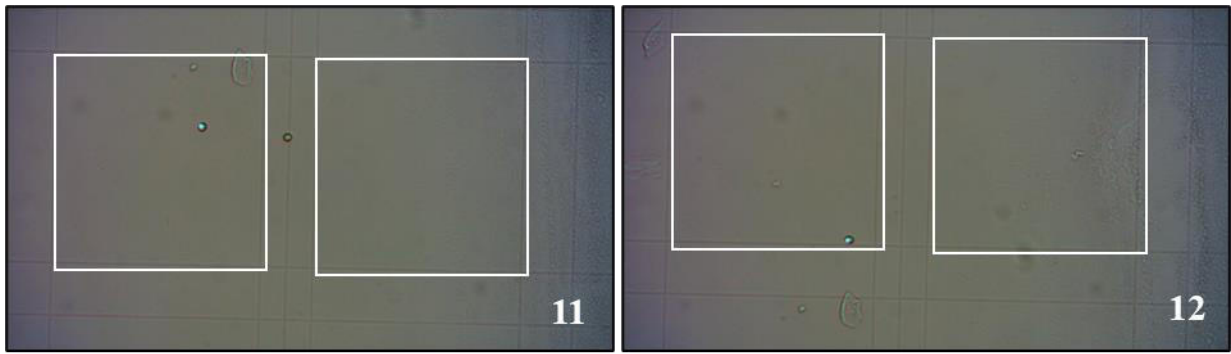


Fig. X3-40. Bürker haemocytometer R2, 22-12-15 (PR DAY 1.4) 19:00, 2,333 cells μl^{-1} (2).

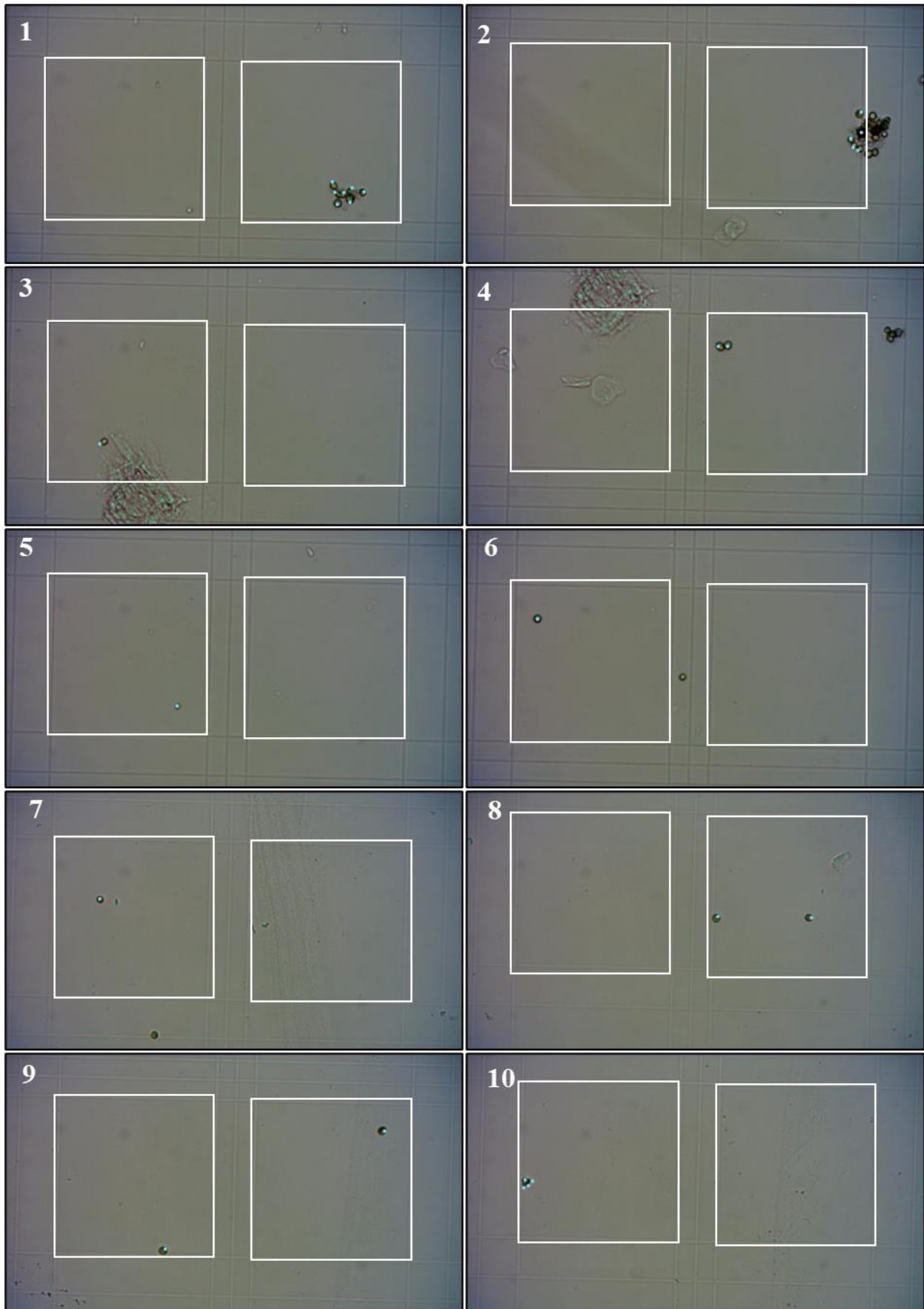


Fig. X3-41. Bürker haemocytometer R2, 22-12-16 (PR DAY 2) 9:00, 2,667 cells μl^{-1} (1).

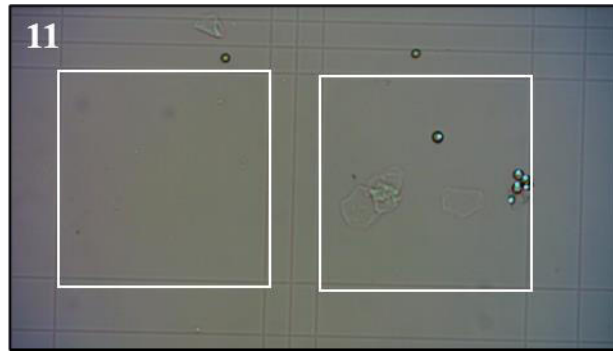


Fig. X3-42. Bürker haemocytometer **R2**, 22-12-16 (PR DAY 2) 9:00, 2,667 cells μl^{-1} (2).

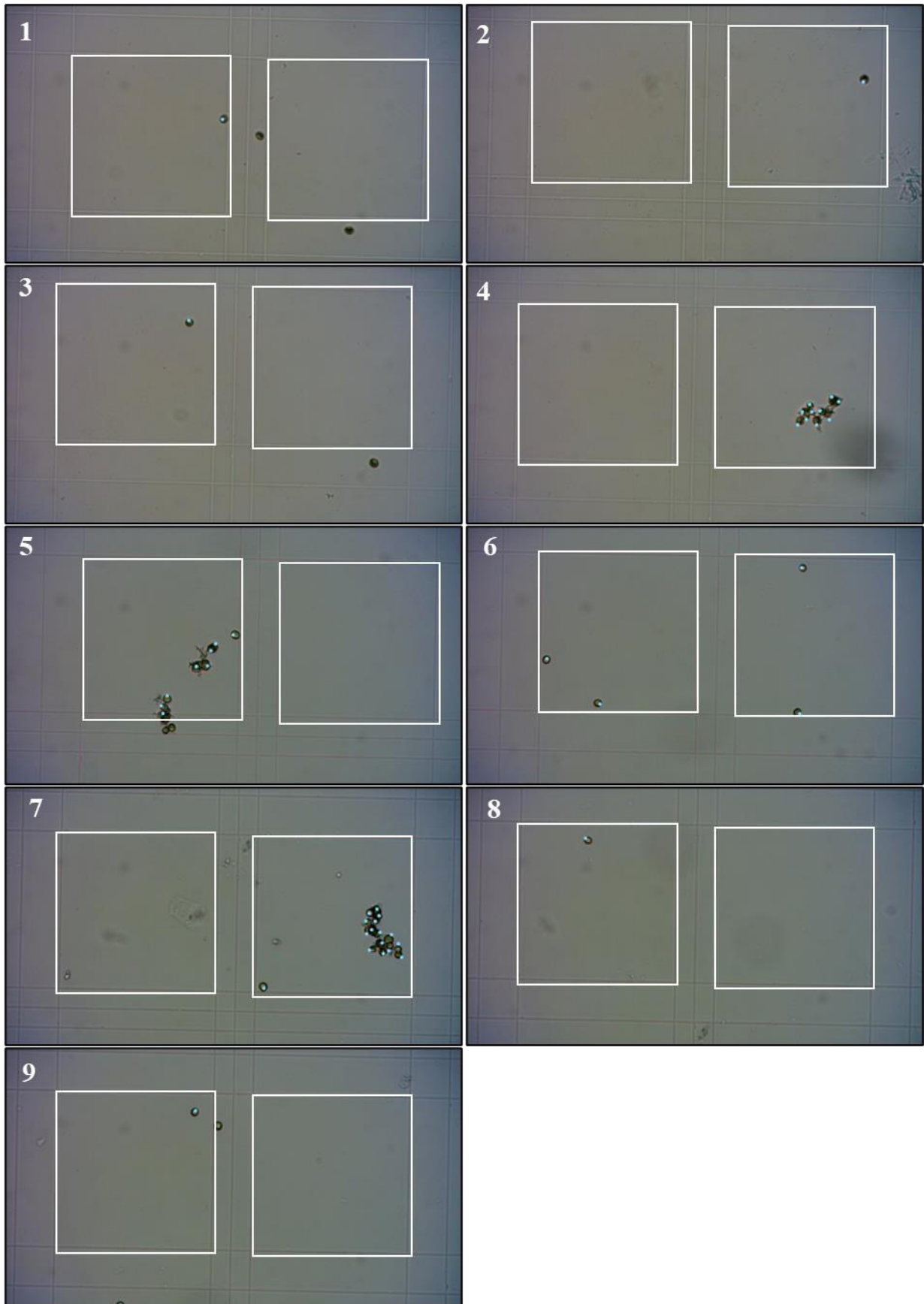


Fig. X3-43. Bürker haemocytometer **R2**, 22-12-16 (PR DAY 2.2) 13:00, 3,583 cells μl^{-1} .

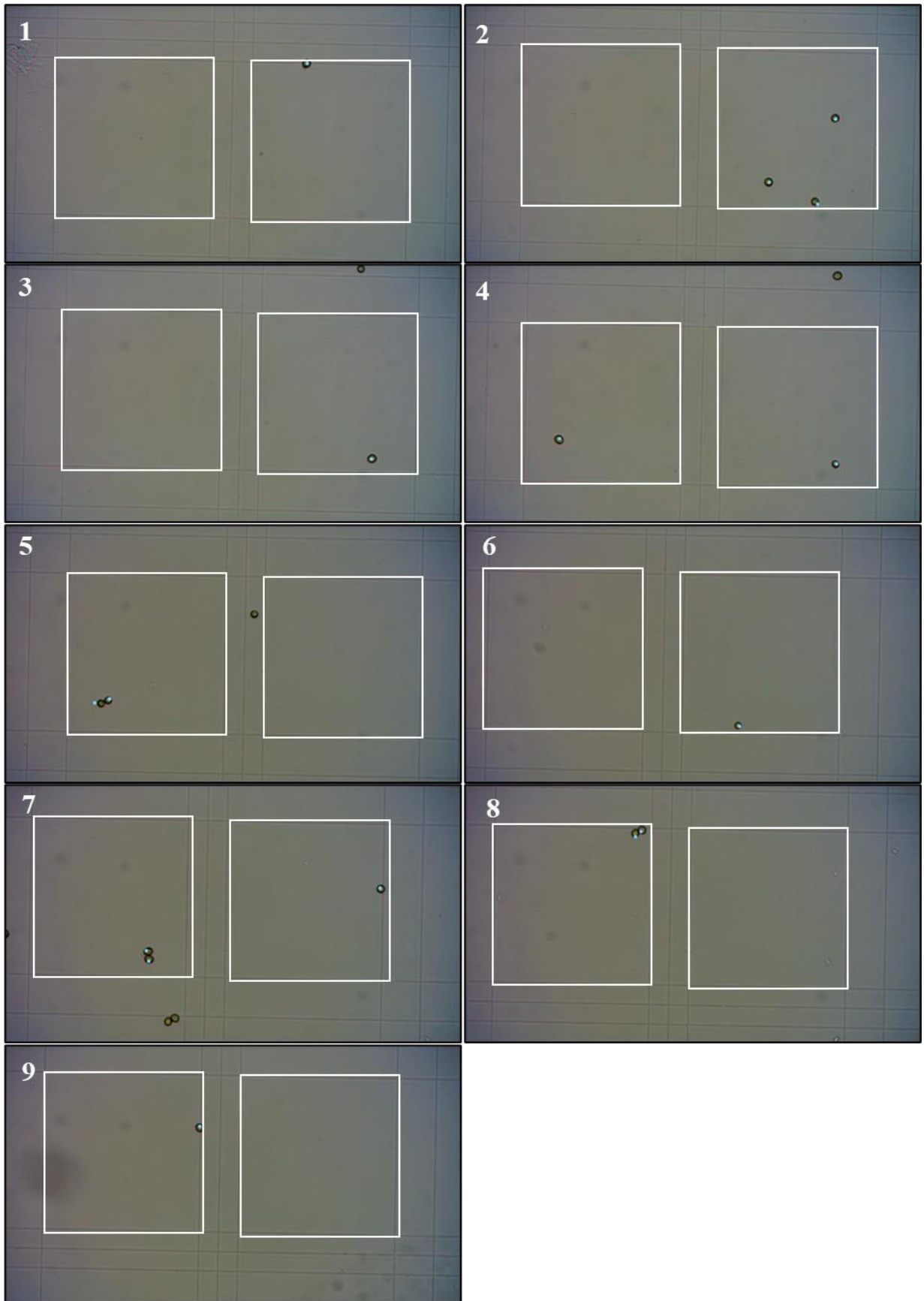


Fig. X3-44. Bürker haemocytometer **R2**, 22-12-16 (PR DAY 2.4) 19:00, 1,333 cells μl^{-1} .

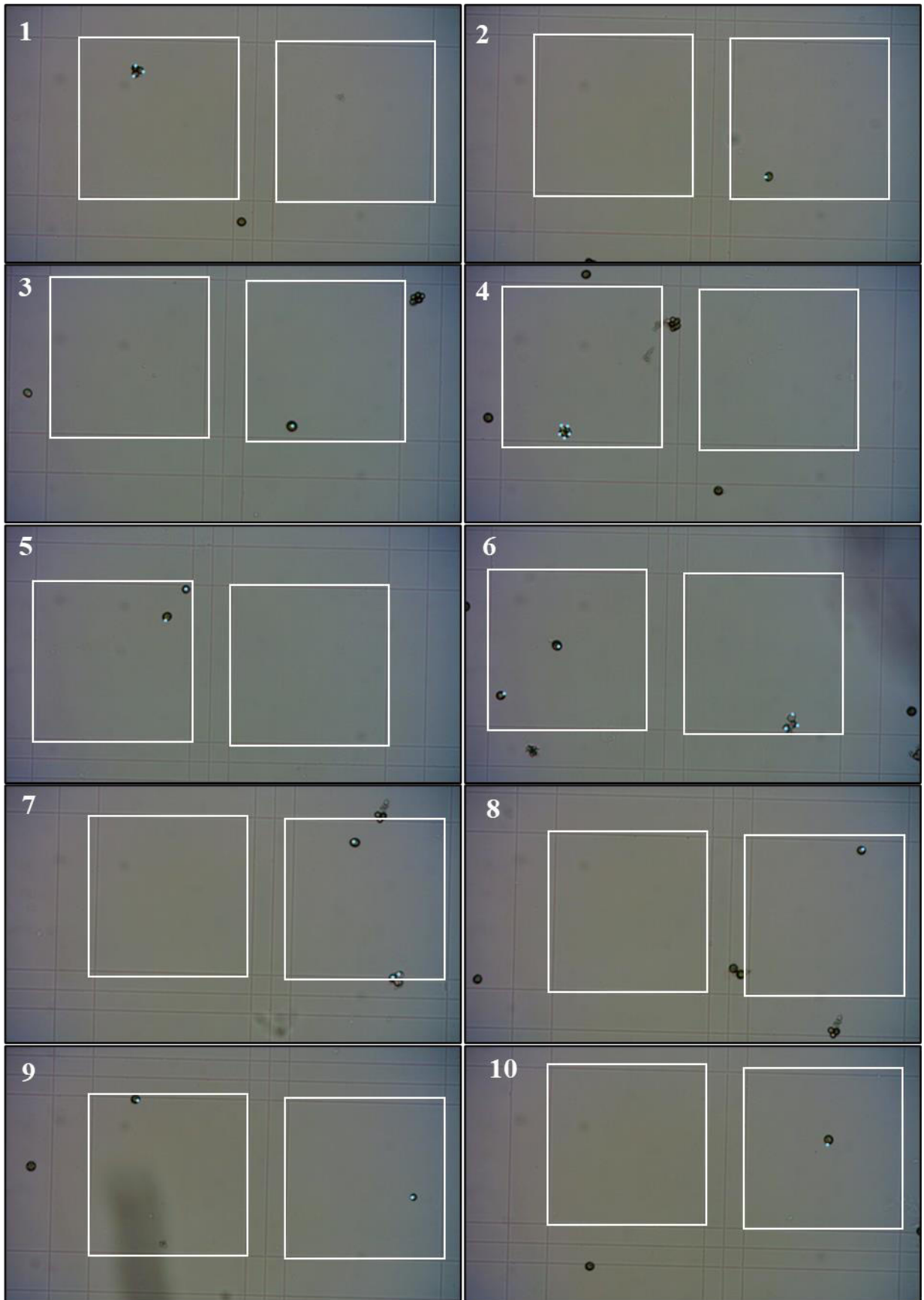


Fig. X3-45. Bürker haemocytometer R2, 22-12-19 (PR DAY 5) 9:00, 2,083 cells μl^{-1} (1).

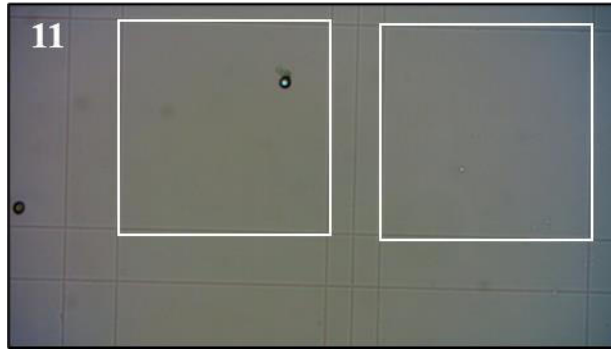


Fig. X3-46. Bürker haemocytometer **R2**, 22-12-19 (PR DAY 5) 9:00, 2,083 cells μl^{-1} (2).

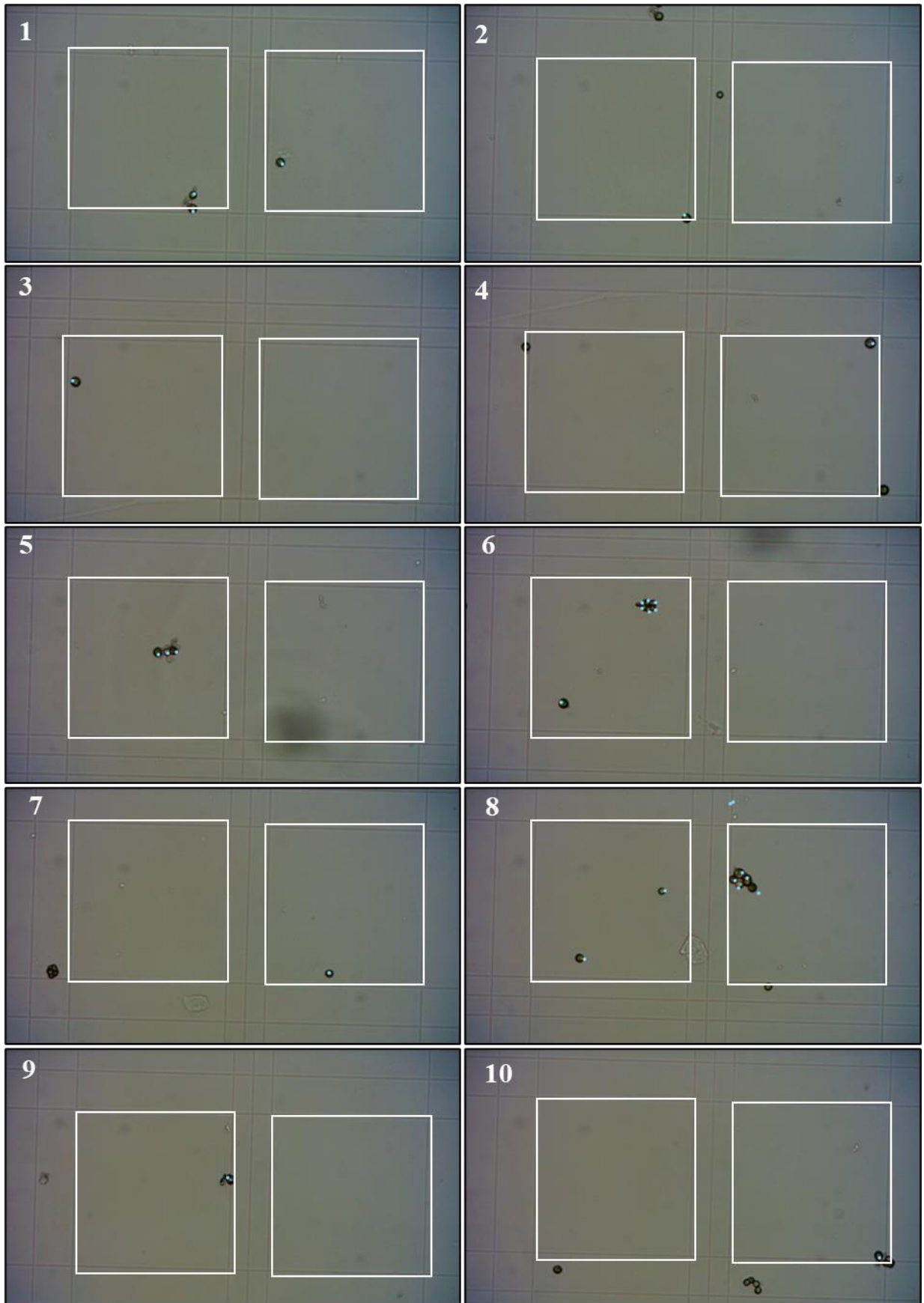


Fig. X3-47. Bürker haemocytometer R2, 22-12-19 (PR DAY 5.2) 13:00, 2,833 cells μl^{-1} (1).

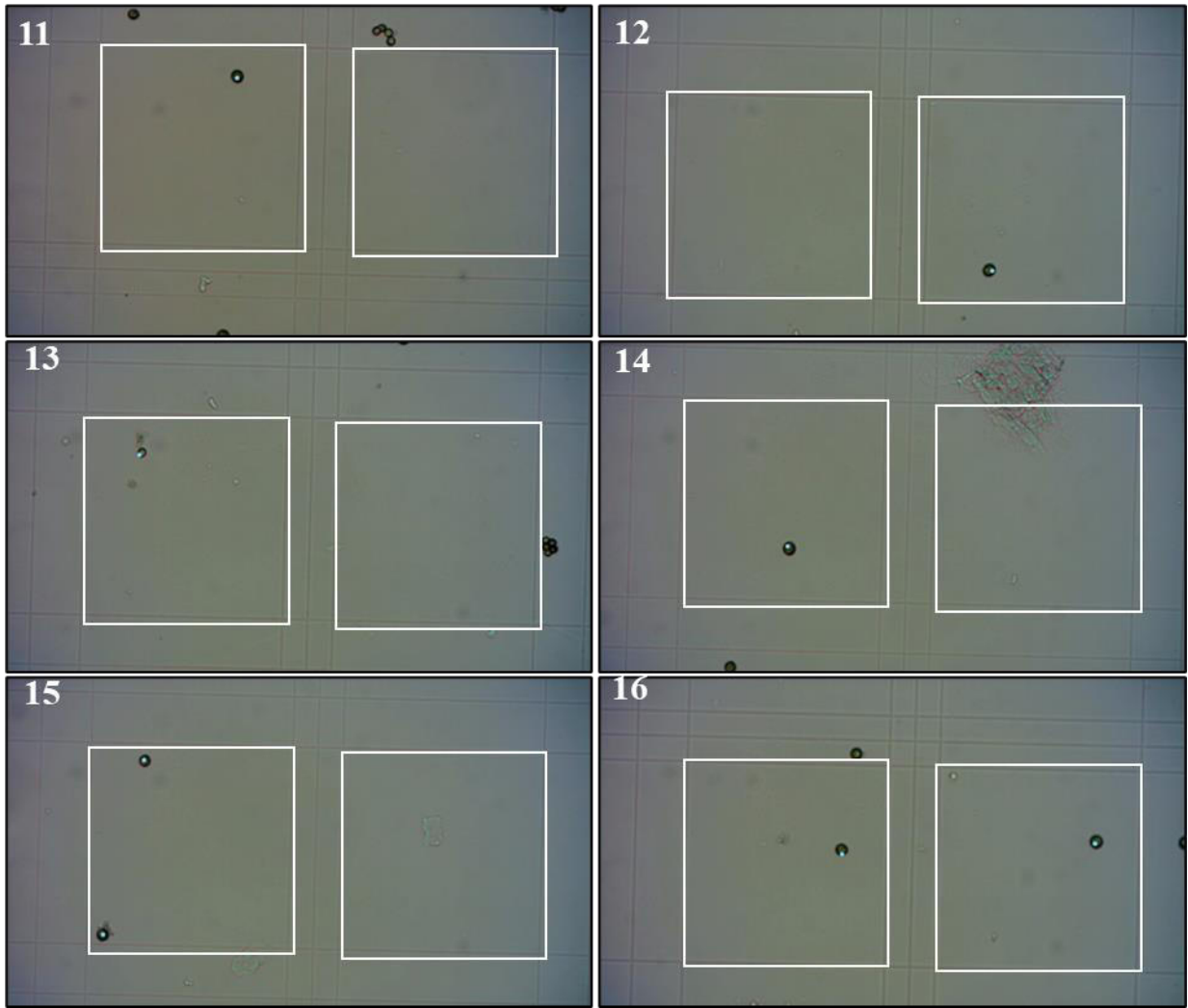


Fig. X3-48. Bürker haemocytometer **R2**, 22-12-19 (PR DAY 5.2) 13:00, 2,833 cells μL^{-1} (2).

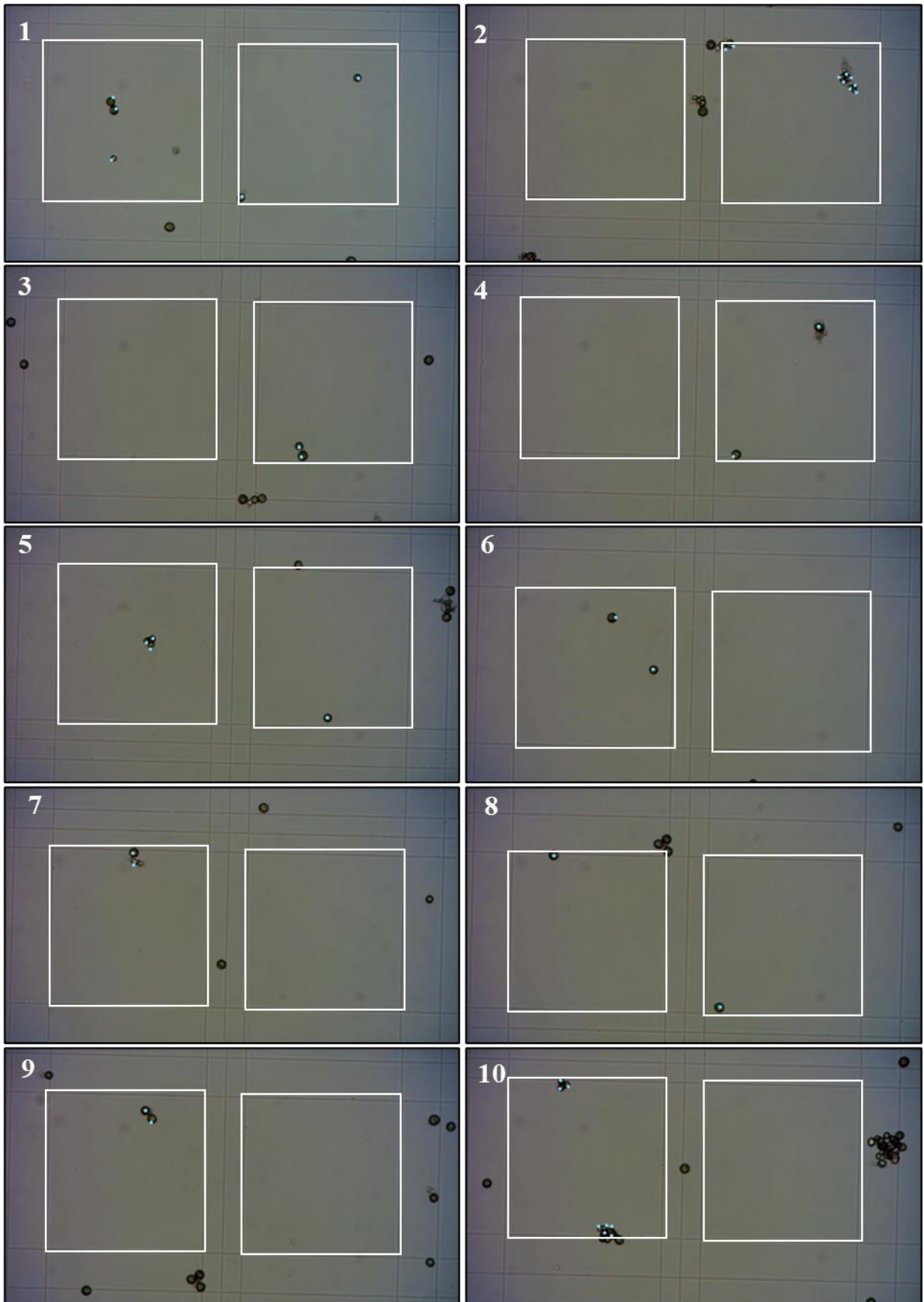


Fig. X3-49. Bürker haemocytometer R2, 22-12-19 (PR DAY 5.4) 19:00, 7,667 cells μL^{-1} (1).

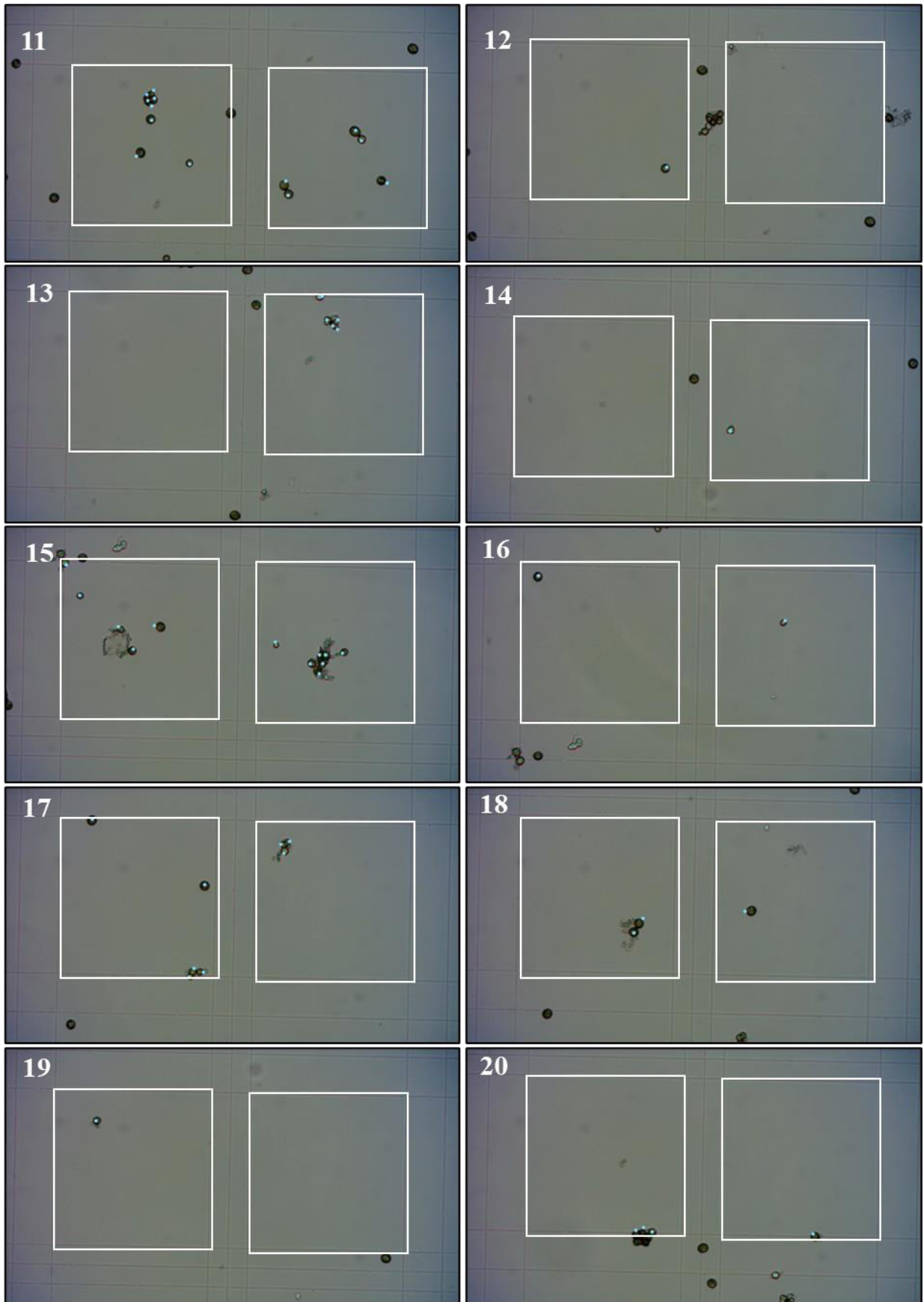


Fig. X3-50. Bürker haemocytometer R2, 22-12-19 (PR DAY 5.4) 19:00, 7,667 cells μL^{-1} (2).

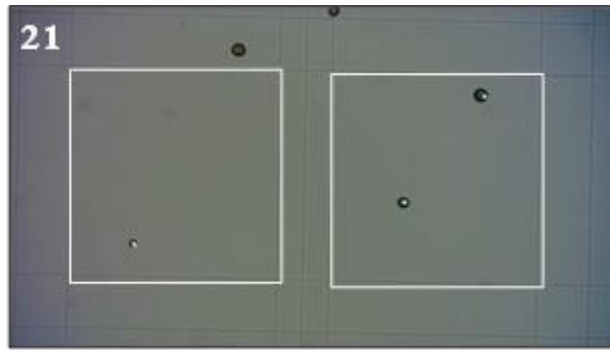


Fig. X3-51. Bürker haemocytometer **R2**, 22-12-19 (PR DAY 5.4) 19:00, 7,667 cells μl^{-1} (3).

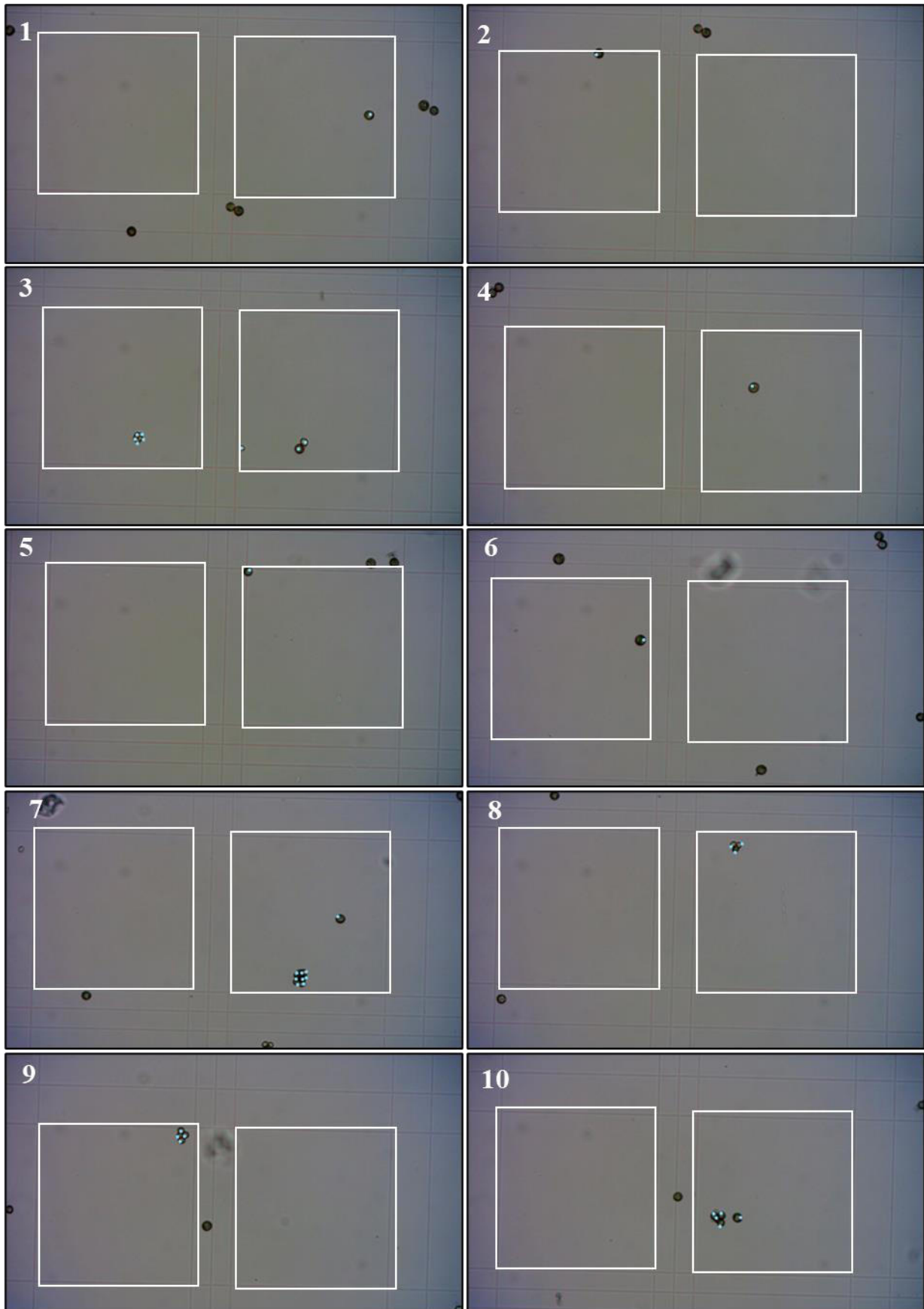


Fig. X3-52. Bürker haemocytometer R2, 22-12-20 (PR DAY 6) 9:00, 4,083 cells μl^{-1} (1).

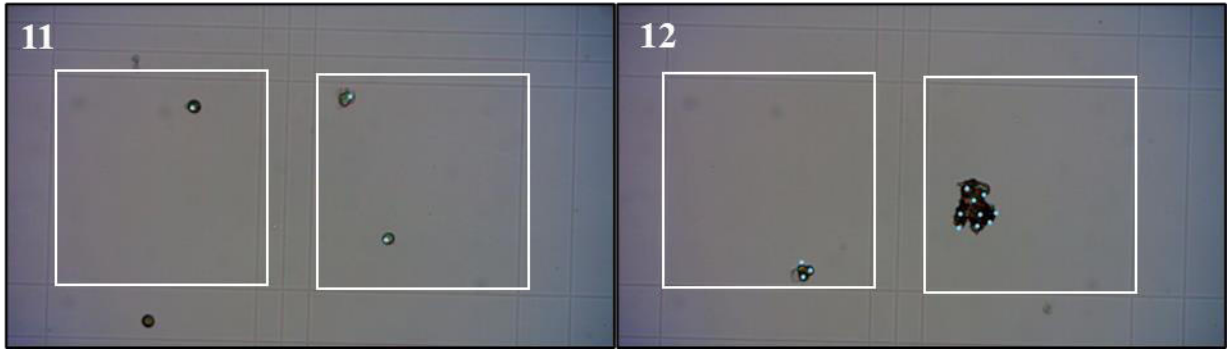


Fig. X3-53. Bürker haemocytometer **R2**, 22-12-20 (PR DAY 6) 9:00, 4,083 cells μl^{-1} (2).

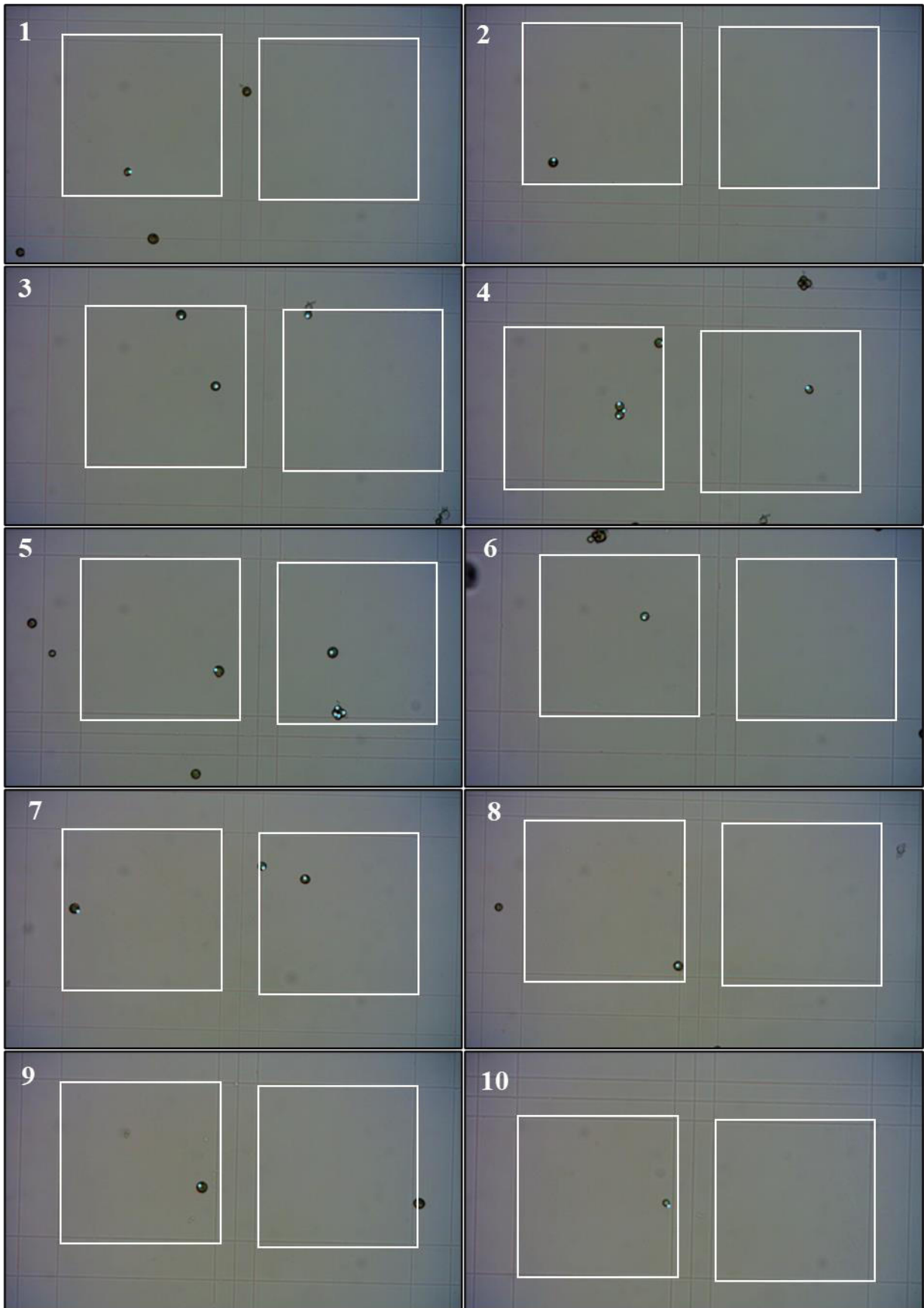


Fig. X3-54. Bürker haemocytometer **R2**, 22-12-20 (PR DAY 6.2) 13:00, 2,083 cells μl^{-1} (1).

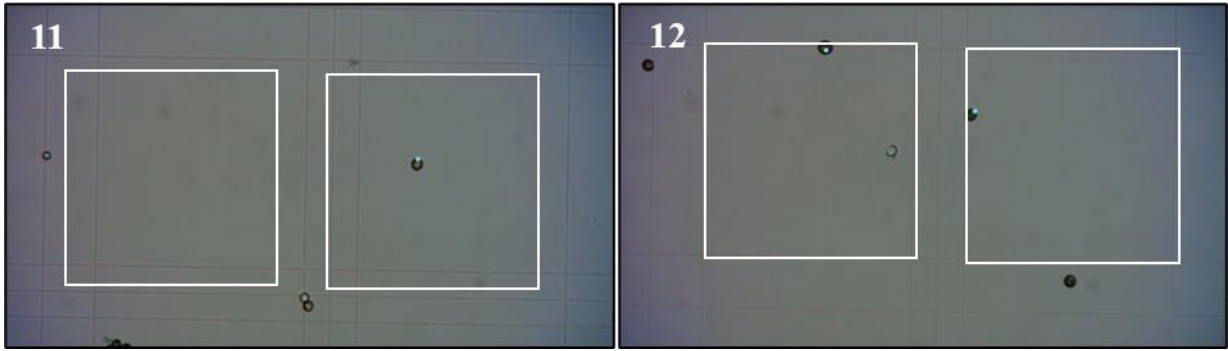


Fig. X3-55. Bürker haemocytometer **R2**, 22-12-20 (PR DAY 6.2) 13:00, 2,083 cells μl^{-1} (2).

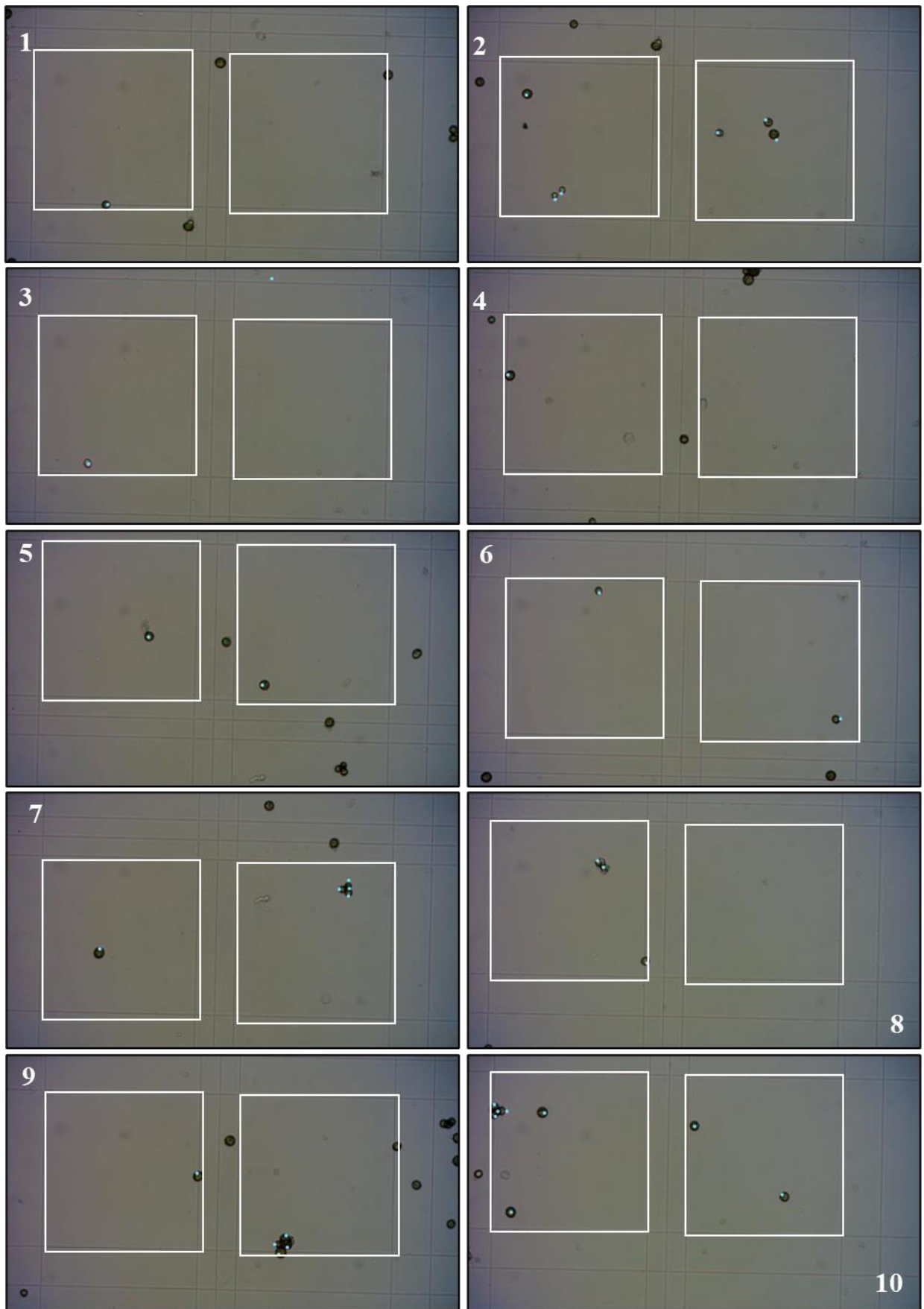


Fig. X3-56. Bürker haemocytometer R2, 22-12-20 (PR DAY 6.4) 19:00, 6,083 cells μl^{-1} (1).

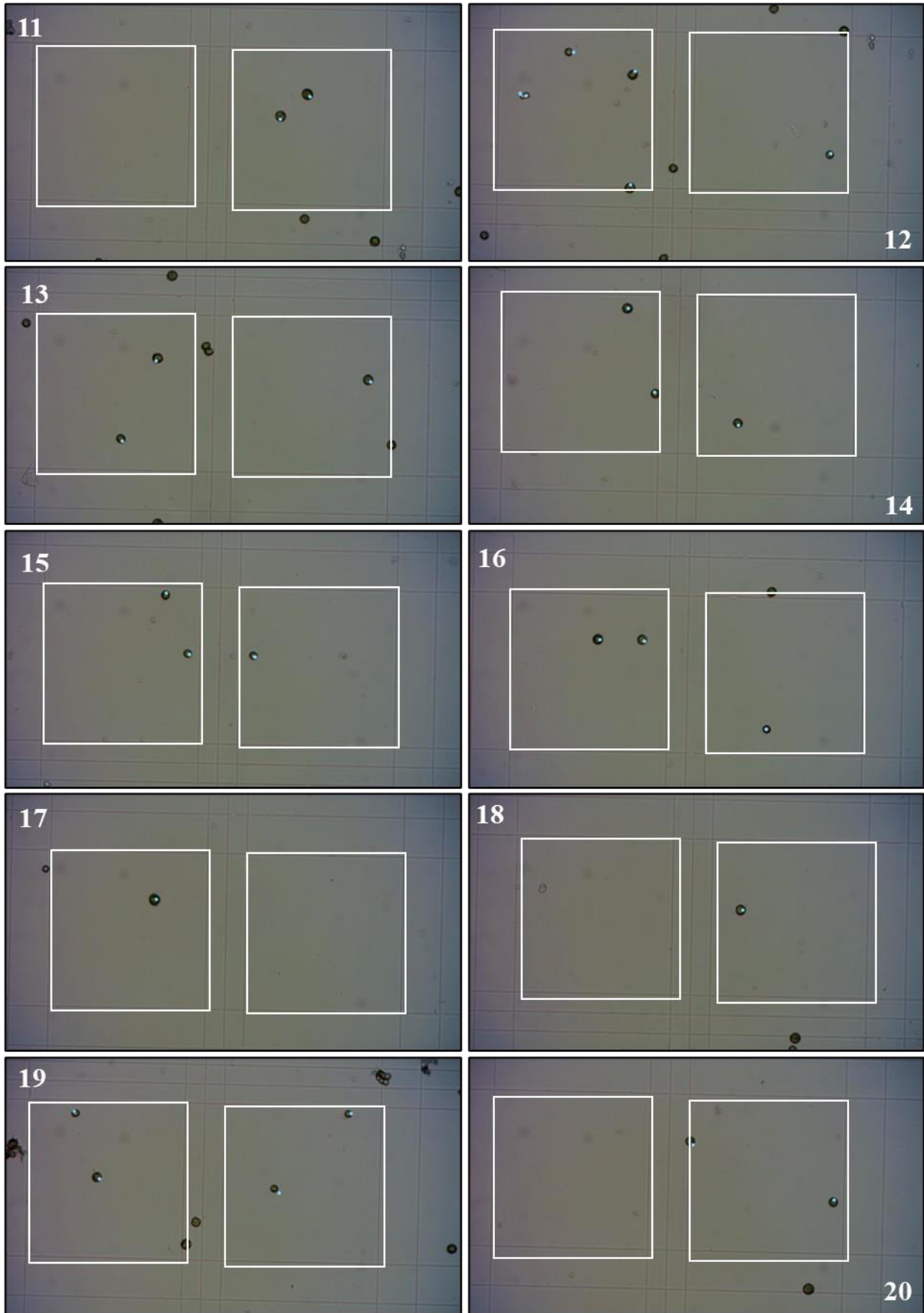


Fig. X3-57. Bürker haemocytometer R2, 22-12-20 (PR DAY 6.4) 19:00, 6,083 cells μL^{-1} (2).

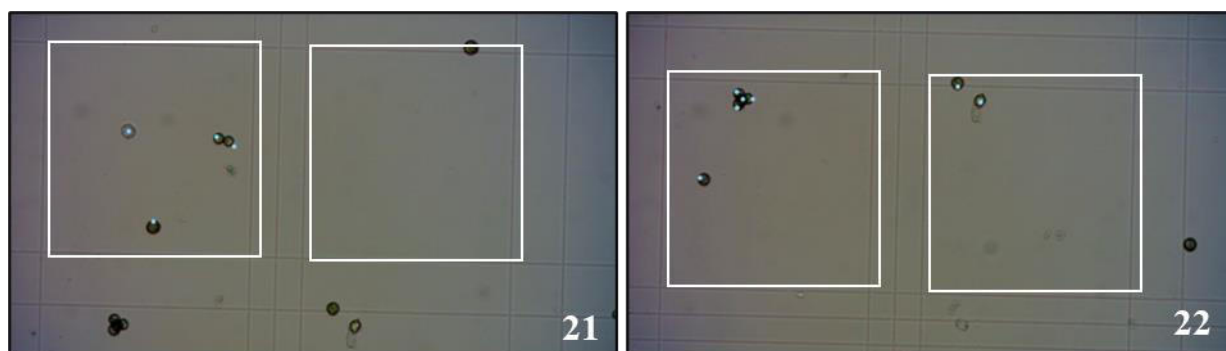


Fig. X3-58. Bürker haemocytometer **R2**, 22-12-20 (PR DAY 6.4) 19:00, 6,083 cells μl^{-1} (3).

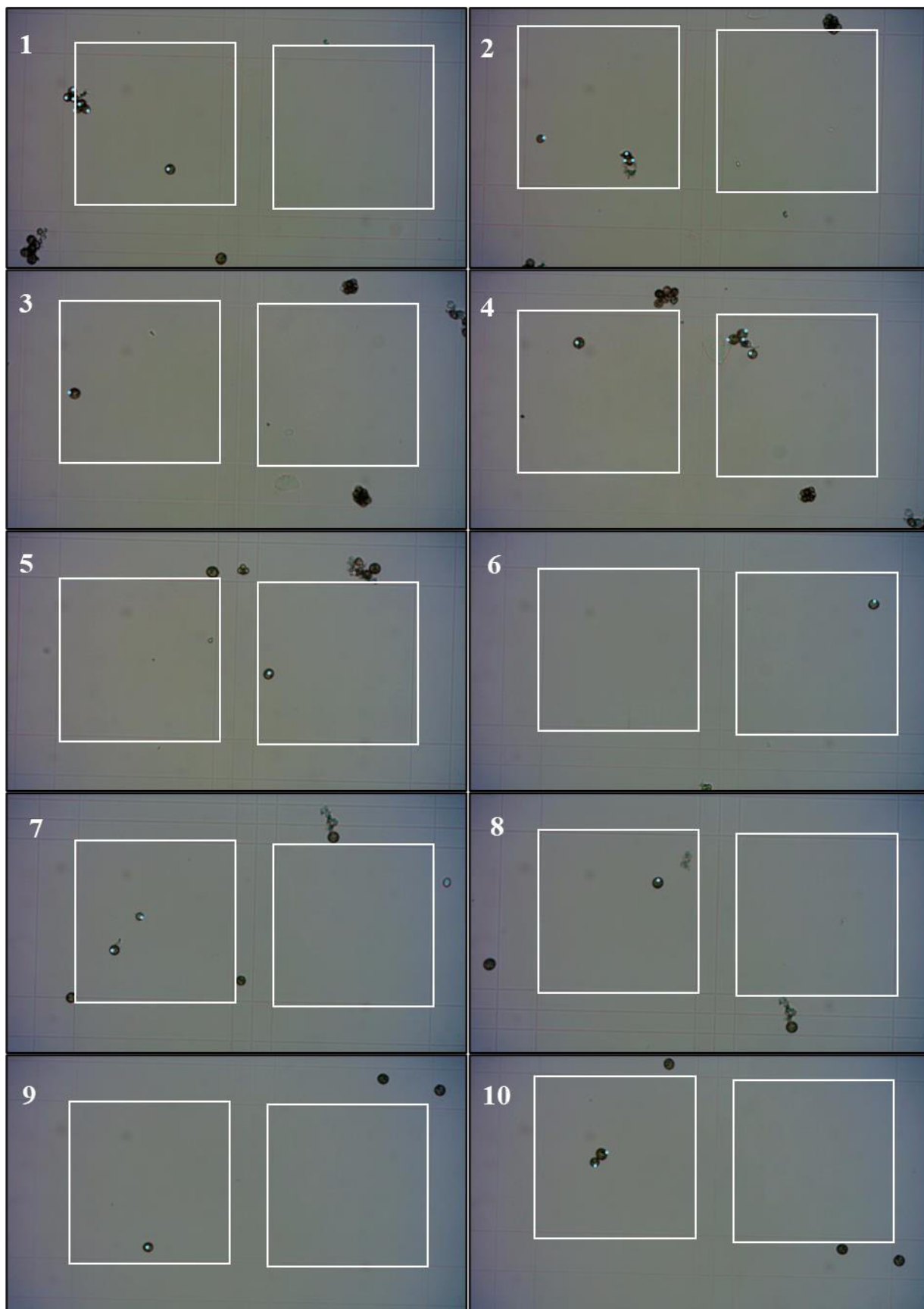


Fig. X3-59. Bürker haemocytometer R2, 22-12-21 (PR DAY 7) 9:00, 4,417 cells μl^{-1} (1).

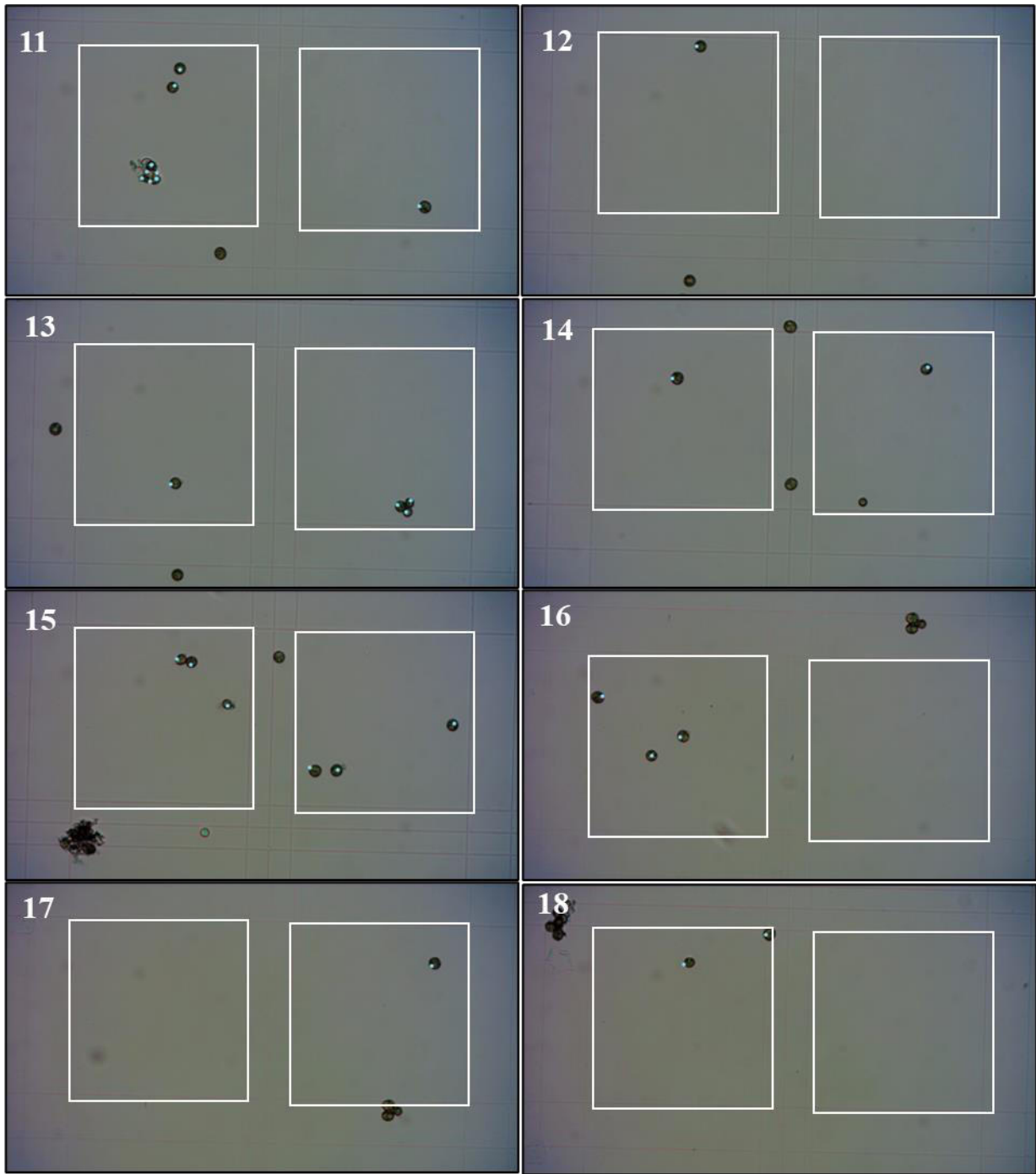


Fig. X3-60. Bürker haemocytometer R2, 22-12-21 (PR DAY 7) 9:00, 4,417 cells μl^{-1} (2).

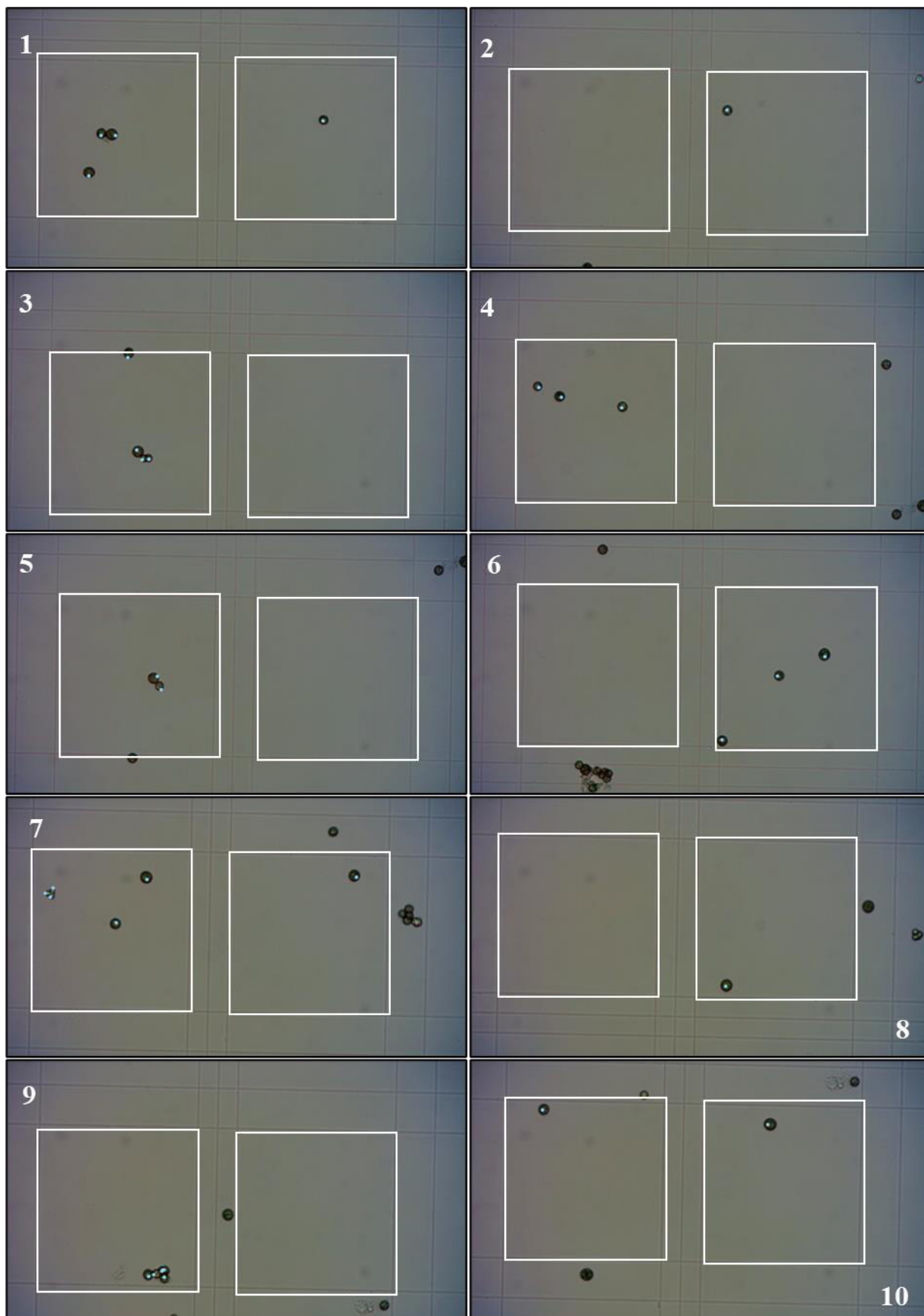


Fig. X3-61. Bürker haemocytometer R2, 22-12-21 (PR DAY 7.2) 13:00, 4,583 cells μl^{-1} (1).

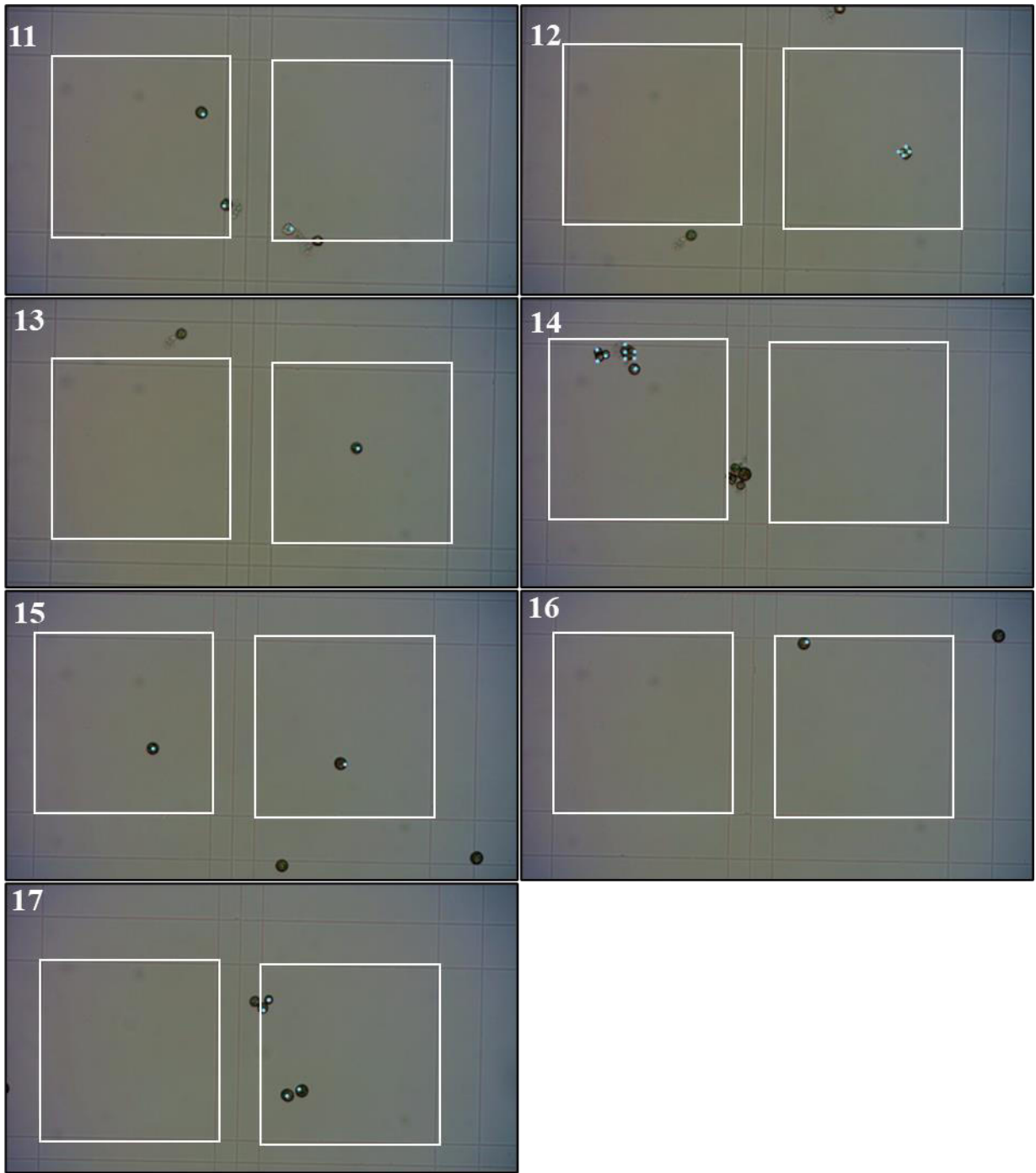


Fig. X3-62. Bürker haemocytometer **R2**, 22-12-21 (PR DAY 7.2) 13:00, 4,583 cells μl^{-1} (2).

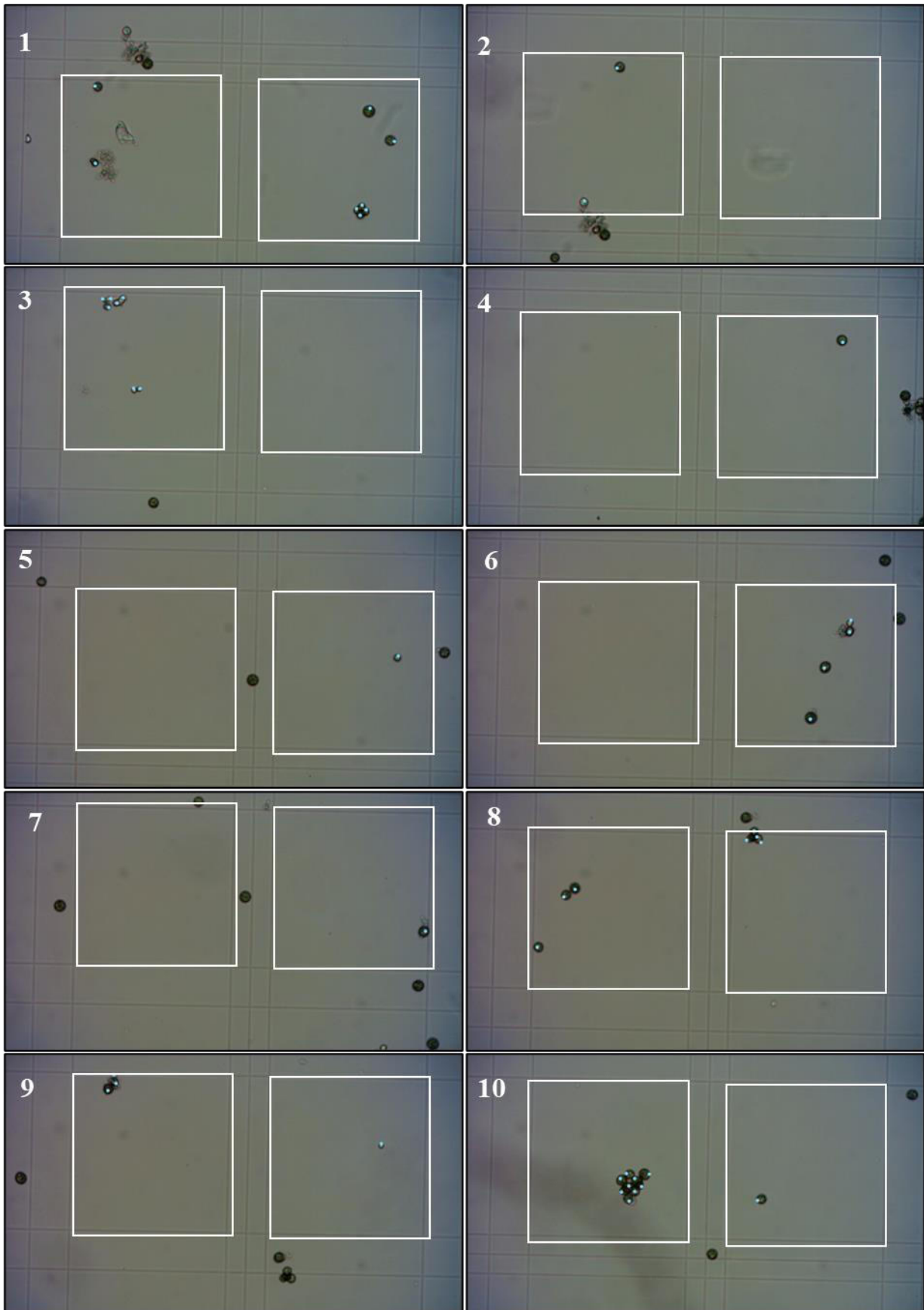


Fig. X3-63. Bürker haemocytometer R2, 22-12-21 (PR DAY 7.4) 19:00, 4,333 cells μL^{-1} (1).

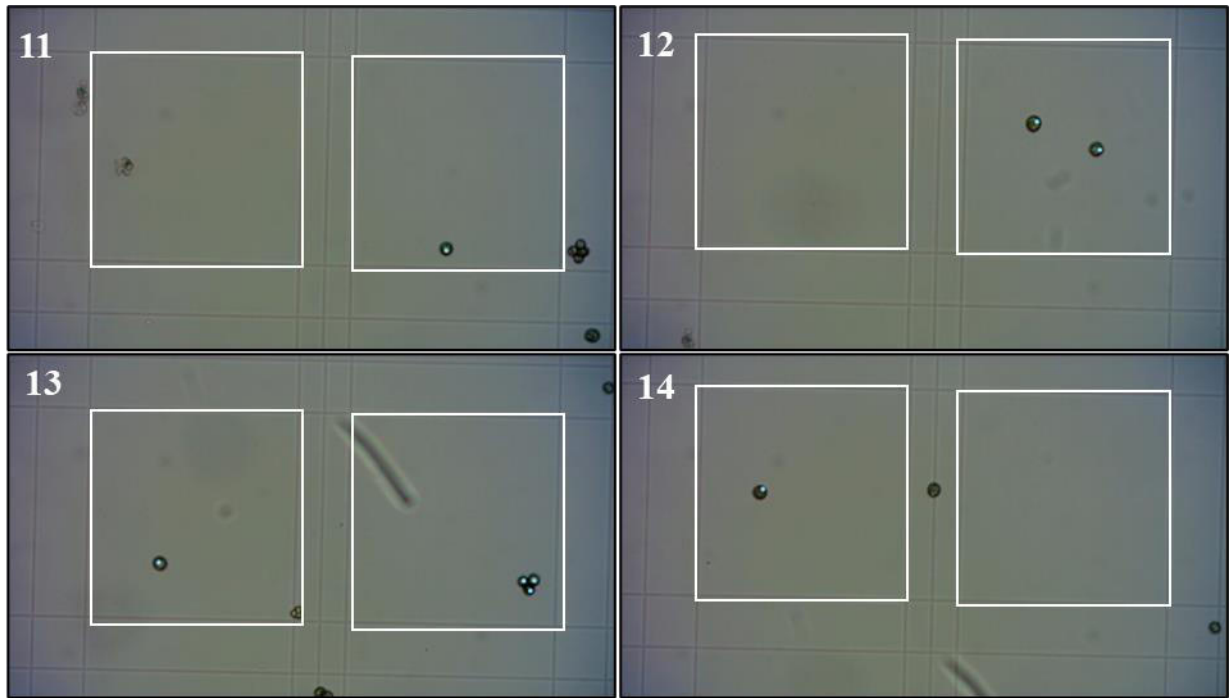


Fig. X3-64. Bürker haemocytometer R2, 22-12-21 (PR DAY 7.4) 19:00, 4,333 cells μl^{-1} (2).

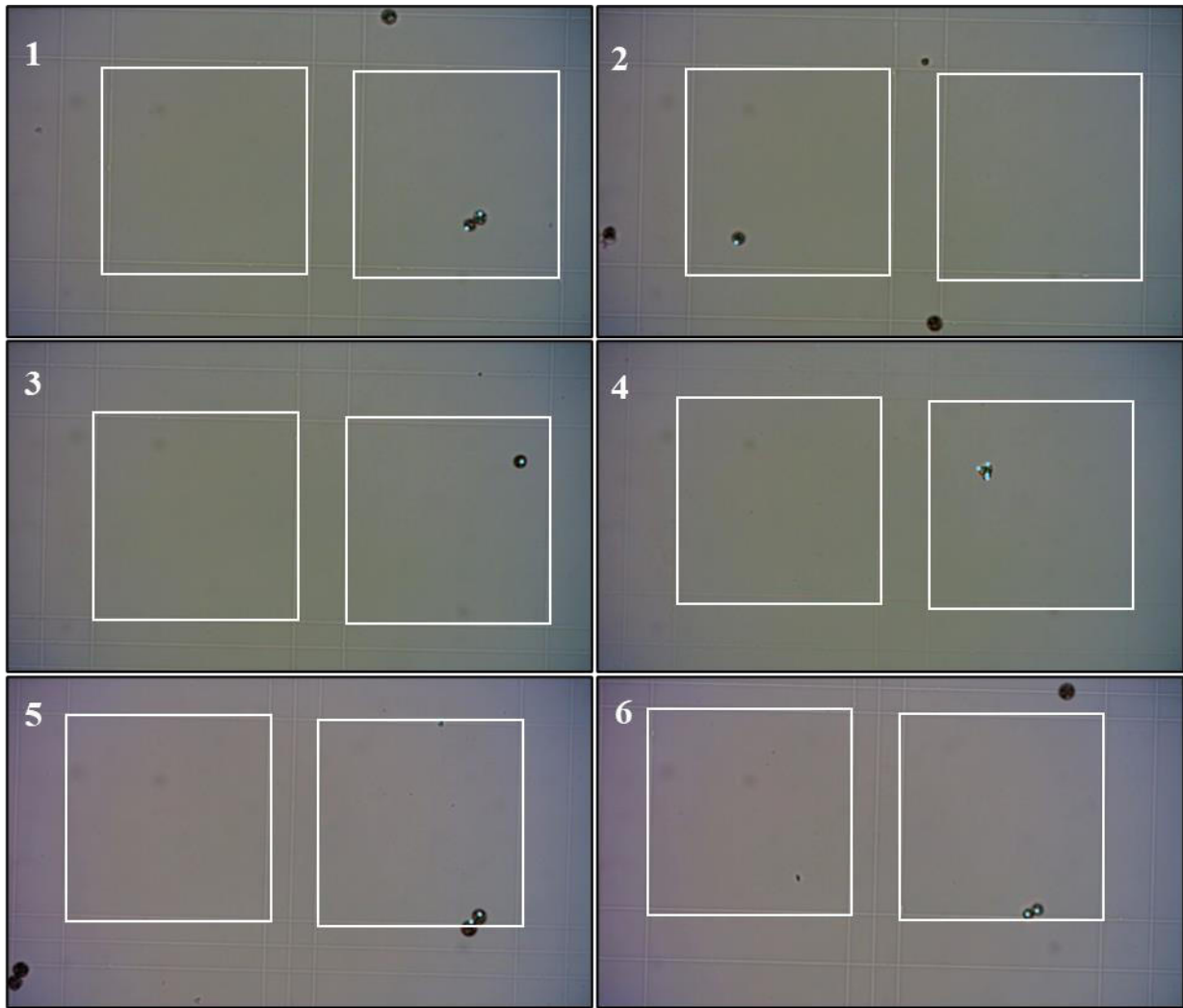


Fig. X3-65. Bürker haemocytometer R2, 22-12-22 (PR DAY 8) 9:00, 1,000 cells μl^{-1} .

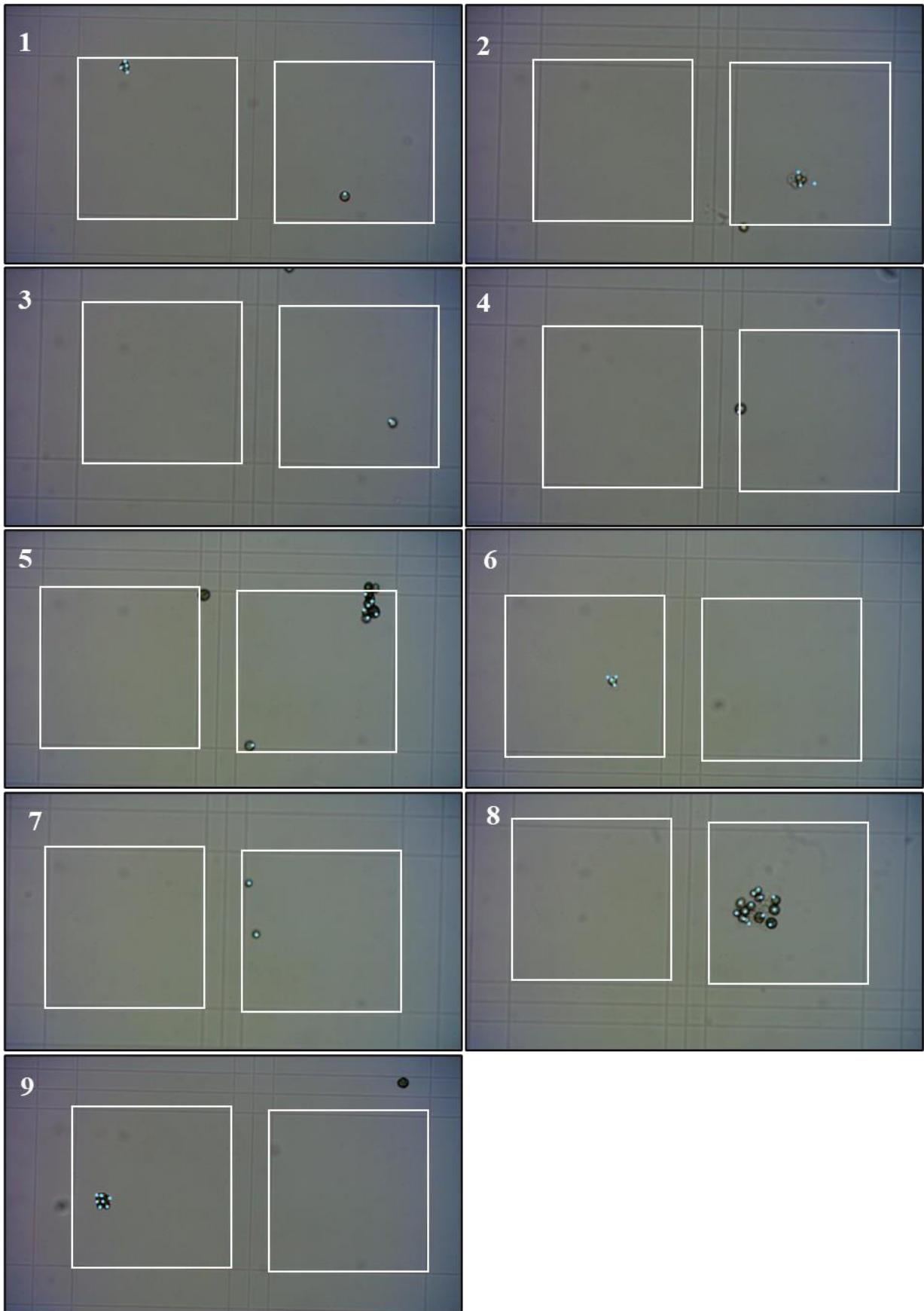


Fig. X3-66. Bürker haemocytometer **R2**, 22-12-22 (PR DAY 8.2) 13:00, 3,583 cells μl^{-1} .

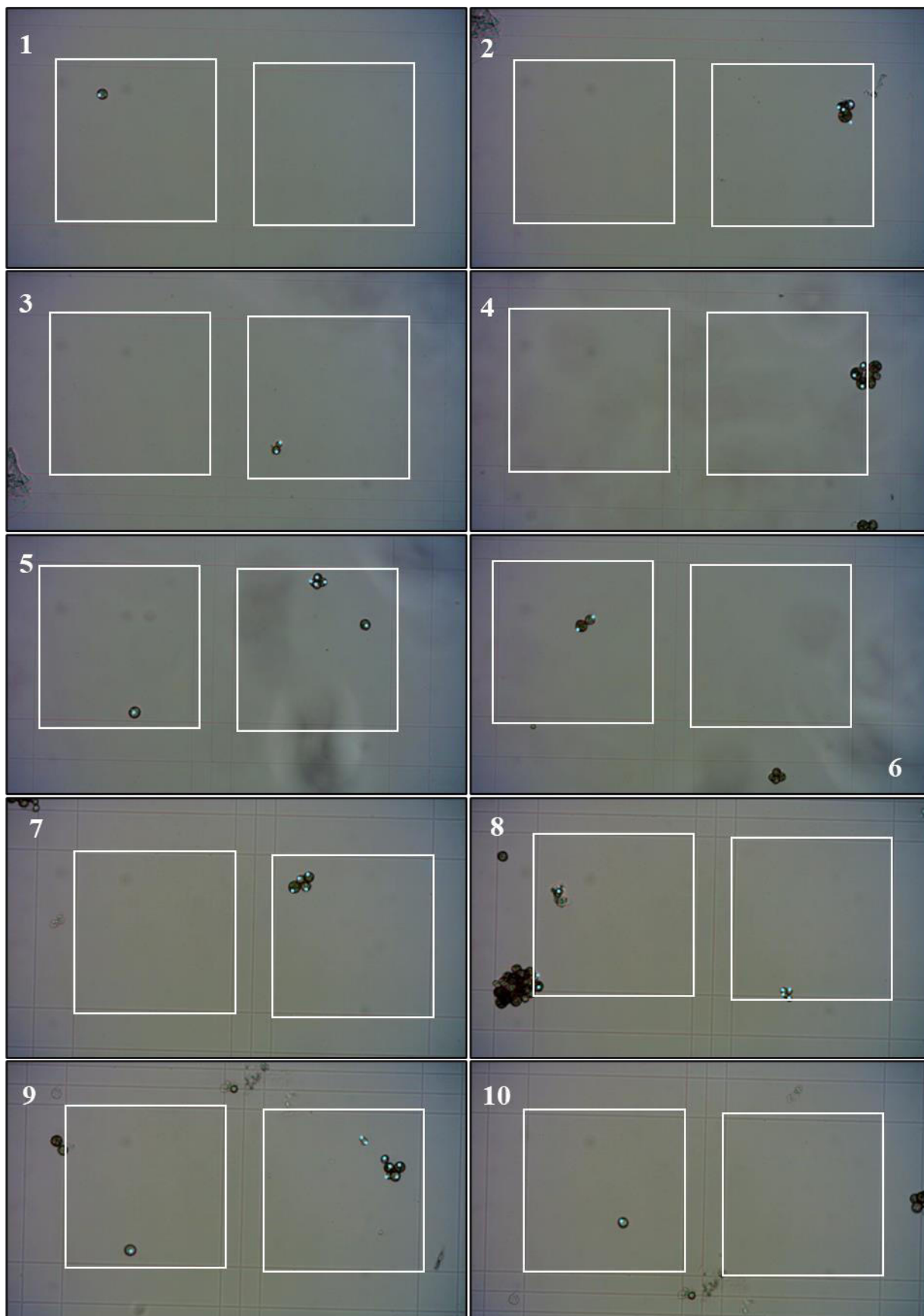


Fig. X3-67. Bürker haemocytometer R2, 22-12-22 (PR DAY 8.4) 19:00, 3,883 cells μL^{-1} (1).

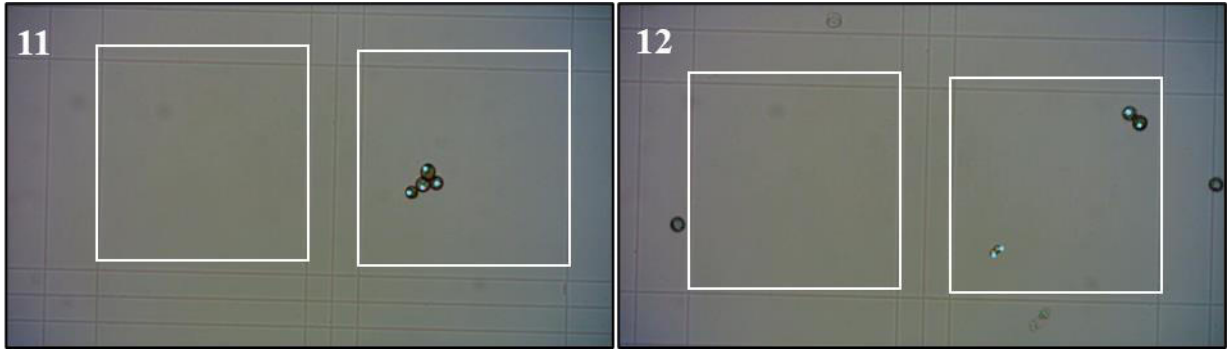


Fig. X3-68. Bürker haemocytometer **R2**, 22-12-22 (PR DAY 8.4) 19:00, 3,883 cells μl^{-1} (2).

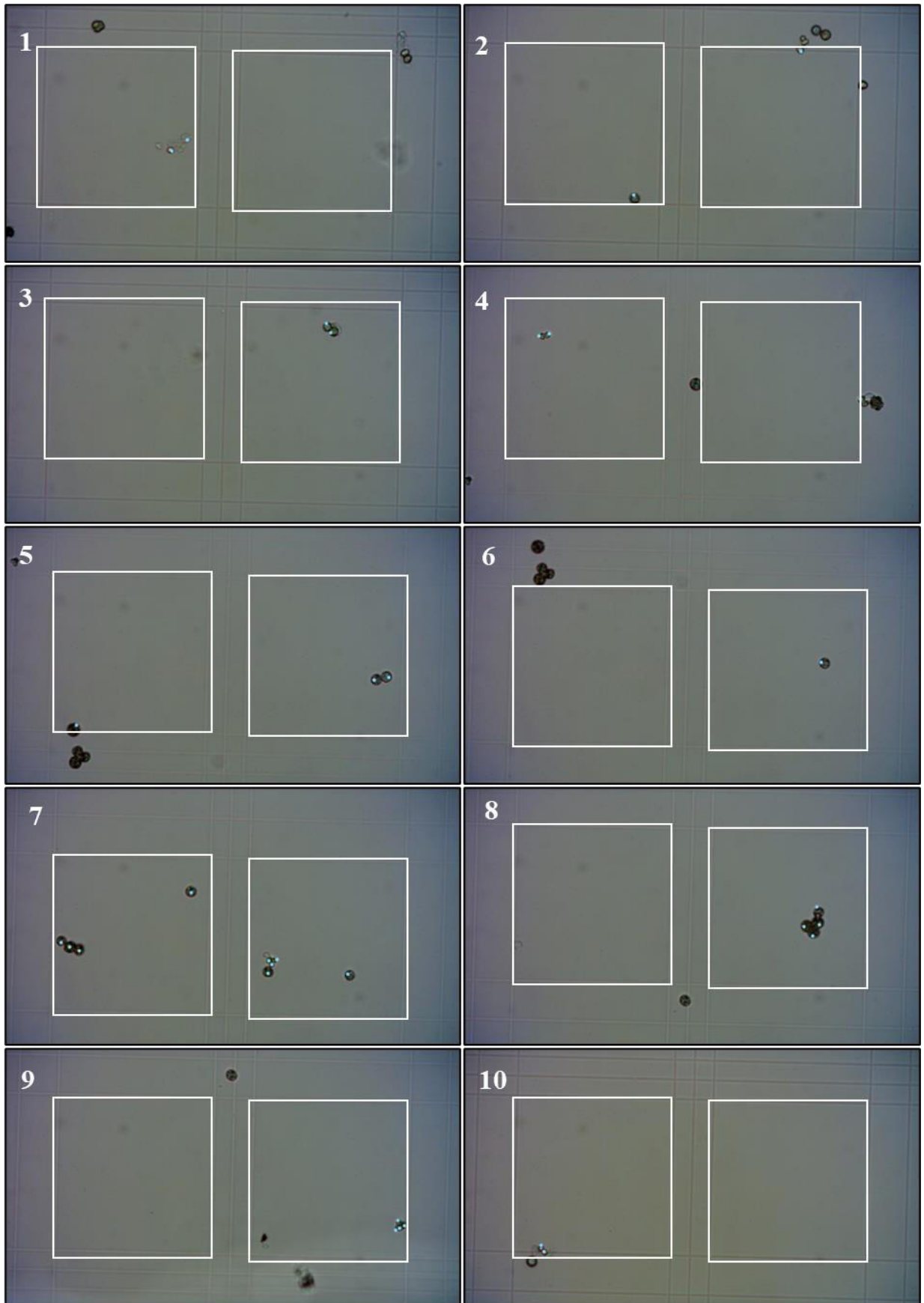


Fig. X3-69. Bürker haemocytometer **R2**, 22-12-23 (PR DAY 9) 9:00, 3,167 cells μl^{-1} (1).

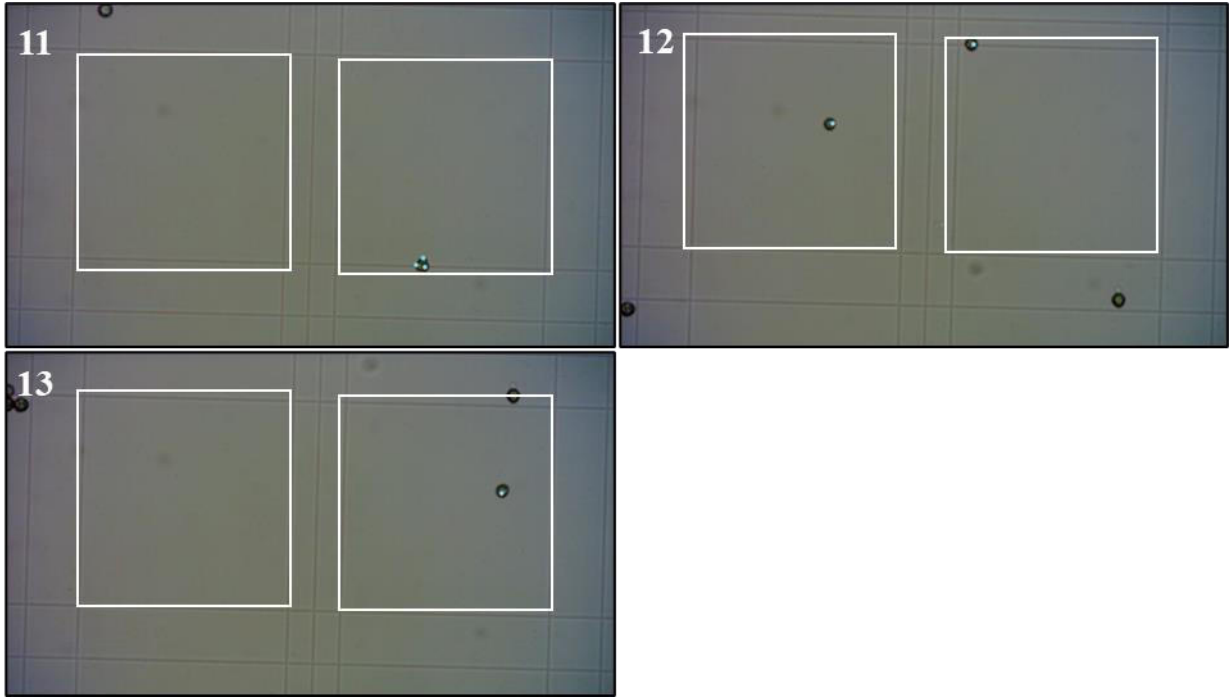


Fig. X3-70. Bürker haemocytometer R2, 22-12-23 (PR DAY 9) 9:00, 3,167 cells μl^{-1} (2).

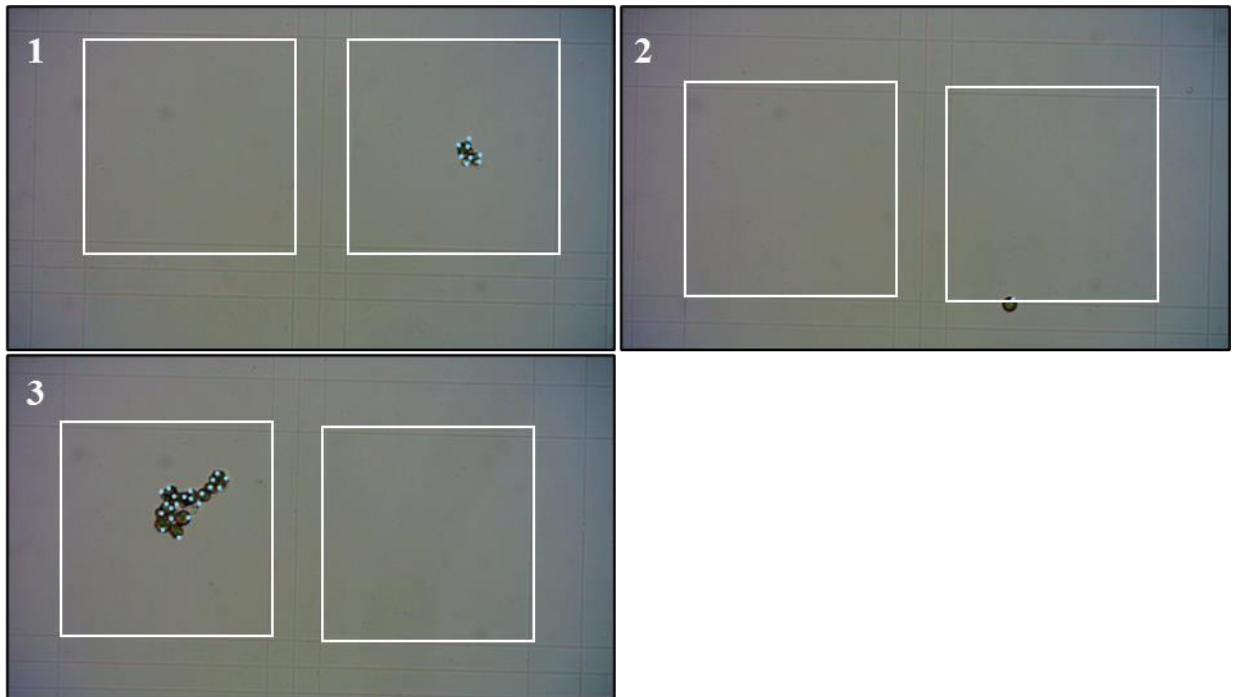


Fig. X3-71. Bürker haemocytometer R2, 22-12-23 (PR DAY 9.2) 13:00, 2500 cells μl^{-1} .

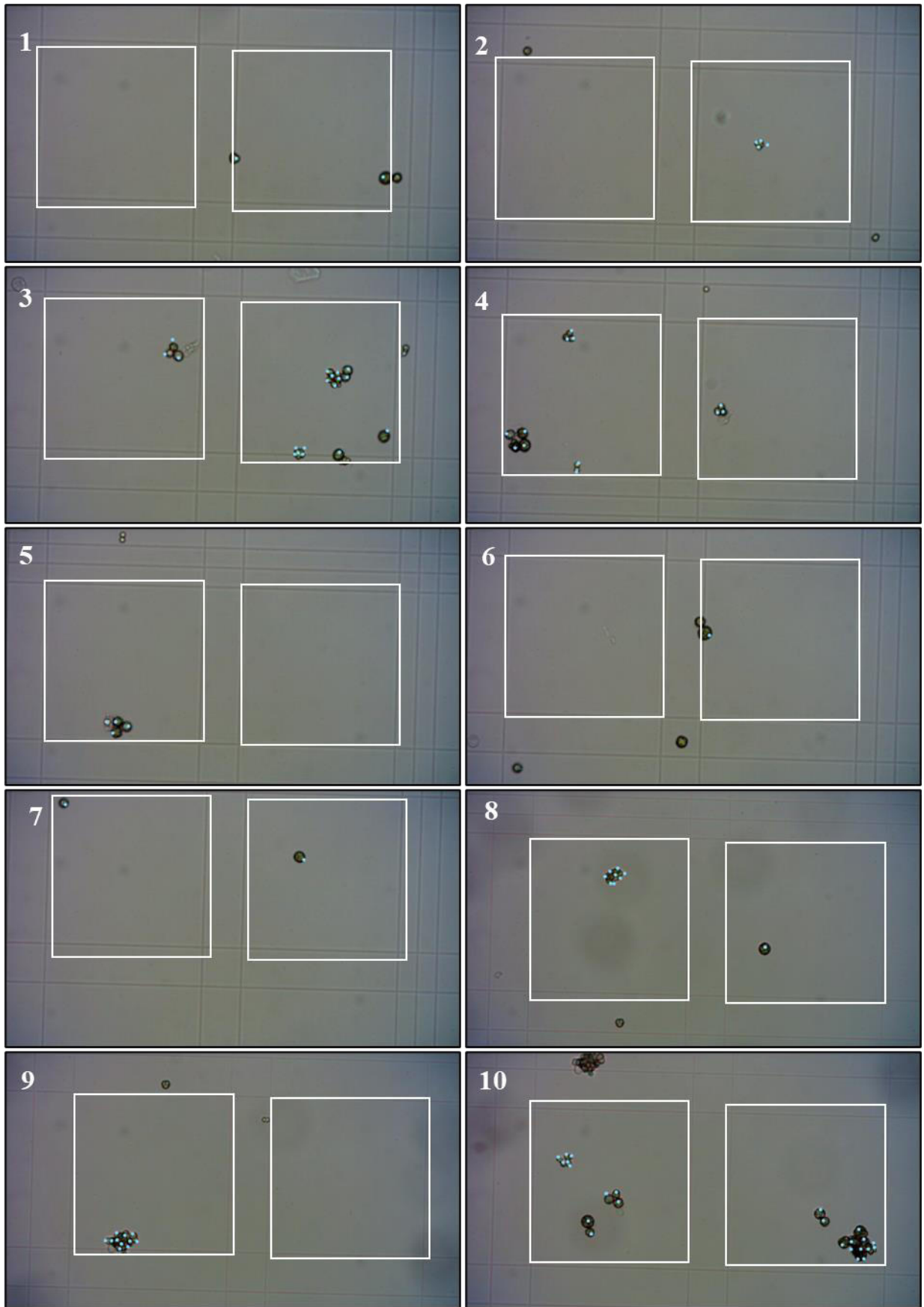


Fig. X3-72. Bürker haemocytometer R2, 22-12-23 (PR DAY 9.4) 19:00, 12,333 cells μl^{-1} (1).

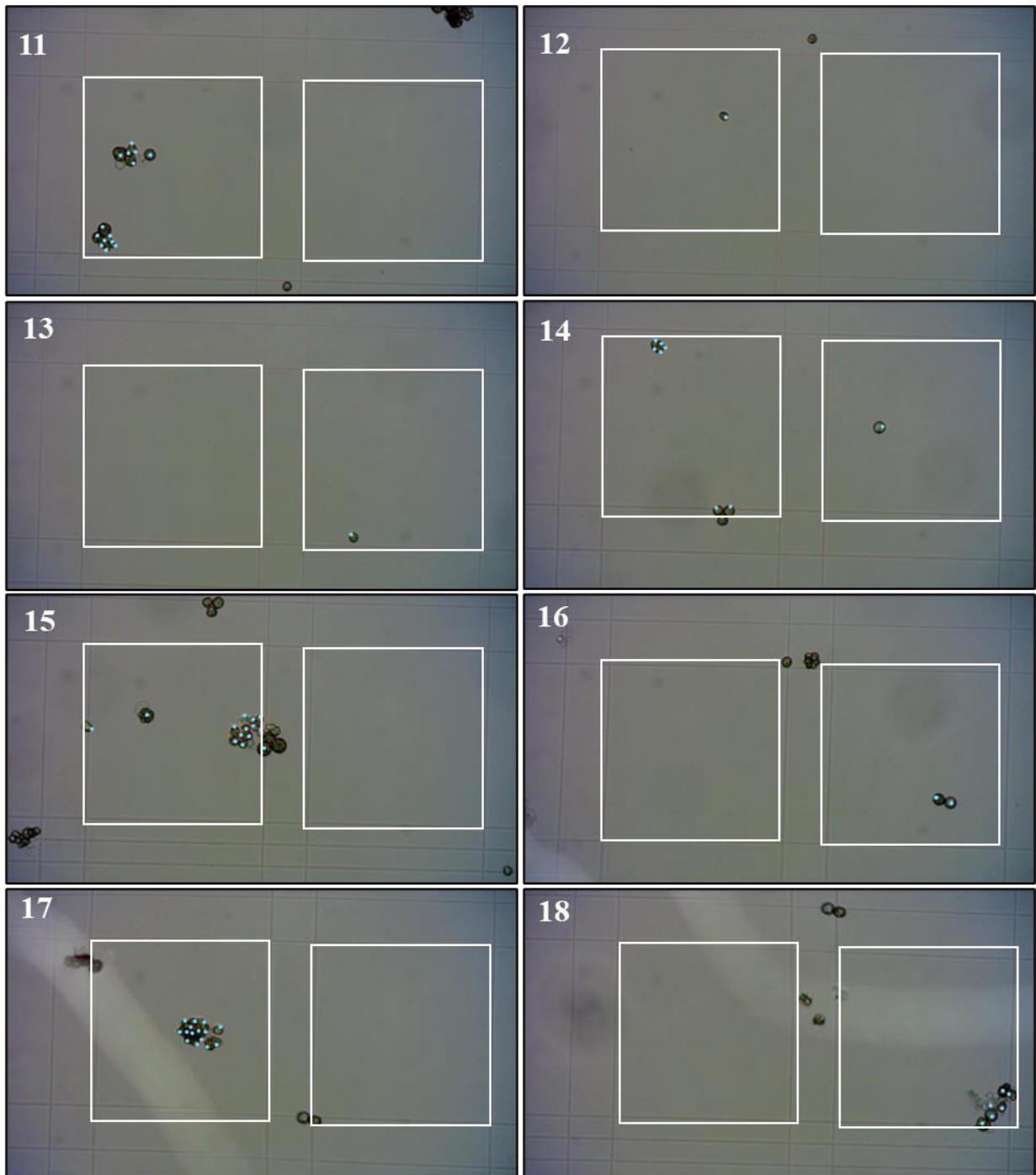


Fig. X3-73. Bürker haemocytometer R2, 22-12-23 (PR DAY 9.4) 19:00, 12,333 cells μl^{-1} (2).

APPENDIX IV: LIST OF PAPERS

I) Biancini G, Cioccolanti L, Marchetti B, Moglie M. **EVALUATION OF MUNICIPAL LANDFILL LEACHATE TREATMENT BY MICROALGAE** [39].

Paper presented at the European Biomass Conference and Exhibition Proceedings, 2022, 79-85.
<http://dx.doi.org/10.5071/30thEUBCE2022-1BO.13.2>.

II) Biancini G, Moglie M, Marchetti B, Cioccolanti L. (2022). **Life cycle impact assessment of municipal solid waste management systems: Improved design for environmental footprint minimization** [304].

IC-REST 2022 Conference, 2022. <https://doi.org/10.1109/REST54687.2022.10022921>.

III) Biancini G, Marchetti B, Cioccolanti L, Moglie M. **Comprehensive life cycle assessment analysis of an Italian composting facility concerning environmental footprint minimization and renewable energy integration** [138].

Sustainability, 2022;14(22). <https://doi.org/10.3390/su142214961>.

IV) Biancini G, Moradi R, Cioccolanti L, Marchetti B, Moglie M, Del Zotto L. **A general model for air gasification of heterogenous municipal solid waste** [176]. Energy Conversion & Management, 2023; <https://doi.org/10.1016/j.enconman.2023.116749>

V) Cioccolanti L, Biancini G, Moradi R, Del Zotto L, Moglie M. **PERFORMANCE OF ORGANIC RANKINE CYCLE SYSTEM IN COMBINATION WITH RESIDUAL MUNICIPAL SOLID WASTE GASIFICATION: A SIMULATION ANALYSIS**. Paper presented at the 7th international Seminar on Organic Rankine Cycle Power Systems Proceedings, not yet published (20/12/2023).

VI) Moglie M, Biancini G, Norici A, Mugnini A, Cioccolanti L. **Valorisation of Olive Mill Wastewater for Arthrospira platensis Production**. Cell Reports Sustainability. Accepted on 10/12/2023.

Under Peer Review:

VII) Moglie M, Biancini G, Cioccolanti L. **Environmental and Economic Analysis of an Olive Mill Wastewater Integrated Treatment System with Microalgae Production**. The International Journal of Life Cycle Assessment, Springer.

VIII) Biancini G, Moradi M, Cioccolanti L, Moglie M. **Comparative study of steam, organic Rankine cycle and supercritical CO₂ power plants integrated with residual municipal solid waste gasification for district heating and cooling**. Applied Thermal Engineering, Elsevier.

APPENDIX V: LIST OF SOFTWARE

- Aspen Plus V10-11. Gasification, Syngas Combustion, ORC, Biodiesel model.
- Matlab R2021: Steam Rankine Cycle, ORC cycle, sCO₂ cycle, 0D Pyrolysis model.
- Simapro V9.1: Life cycle assessment of the MSW and OMW integrated treatment systems.
- Python: Figure and images.
- CamLabLite: microscope images acquisition.
- Solidworks: Pilot plant drawings.
- Openchrom / GC solutions: Gas Chromatography and chromatograph chart analysis.
- GraphPad Prism 8: Statistical analysis.

REFERENCES

- [1] L. Mercalli, *Il clima che cambia. Perché il riscaldamento globale è un problema vero, e come fare per fermarlo*. Milano: BUR Biblioteca Univ. Rizzoli, 2019.
- [2] B. Bednar-Friedl *et al.*, ‘Europe’, in *Climate Change 2022: Impacts, Adaptation and Vulnerability. Contribution of Working Group II to the Sixth Assessment Report of the Intergovernmental Panel on Climate Change*, H. O. Pörtner, D. C. Roberts, M. Tignor, E. S. Poloczanska, K. Mintenbeck, A. Alegría, M. Craig, S. Langsdorf, S. Löschke, V. Möller, A. Okem, B. Rama, H. O. Pörtner, D. C. Roberts, M. Tignor, E. S. Poloczanska, K. Mintenbeck, A. Alegría, M. Craig, S. Langsdorf, S. Löschke, V. Möller, A. Okem, and B. Rama, Eds., Cambridge, UK and New York, USA, 2022, pp. 1817–1927.
- [3] M. Farooque, A. Zhang, M. Thürer, T. Qu, and D. Huisingh, ‘Circular supply chain management: A definition and structured literature review’, *Journal of Cleaner Production*, vol. 228, pp. 882–900, Aug. 2019, doi: 10.1016/j.jclepro.2019.04.303.
- [4] E. Loiseau *et al.*, ‘Green economy and related concepts: An overview’, *Journal of Cleaner Production*, vol. 139, pp. 361–371, Dec. 2016, doi: 10.1016/j.jclepro.2016.08.024.
- [5] F. Gu, J. Guo, W. Zhang, P. A. Summers, and P. Hall, ‘From waste plastics to industrial raw materials: A life cycle assessment of mechanical plastic recycling practice based on a real-world case study’, *Science of The Total Environment*, vol. 601–602, pp. 1192–1207, Dec. 2017, doi: 10.1016/j.scitotenv.2017.05.278.
- [6] R. Puertas and L. Martí, ‘Renewable energy production capacity and consumption in Europe’, *Science of The Total Environment*, vol. 853, p. 158592, Dec. 2022, doi: 10.1016/j.scitotenv.2022.158592.
- [7] ‘Home - Italia Domani - Portale PNRR’. Accessed: Oct. 13, 2023. [Online]. Available: <https://www.italiadomani.gov.it:443/content/sogei-ng/it/it/home.html>
- [8] E. Iacovidou *et al.*, ‘A pathway to circular economy: Developing a conceptual framework for complex value assessment of resources recovered from waste’, *Journal of Cleaner Production*, vol. 168, pp. 1279–1288, Dec. 2017, doi: 10.1016/j.jclepro.2017.09.002.
- [9] ‘Municipal waste statistics’. Accessed: Jul. 14, 2022. [Online]. Available: https://ec.europa.eu/eurostat/statistics-explained/index.php?title=Municipal_waste_statistics
- [10] ‘Waste statistics’. Accessed: Sep. 12, 2023. [Online]. Available: https://ec.europa.eu/eurostat/statistics-explained/index.php?title=Waste_statistics
- [11] ‘Rapporto Rifiuti Urbani - Edizione 2020’, ISPRA Istituto Superiore per la Protezione e la Ricerca Ambientale. Accessed: Aug. 24, 2023. [Online]. Available: <https://www.isprambiente.gov.it/it/pubblicazioni/rapporti/rapporto-rifiuti-urbani-edizione-2020>
- [12] ‘Rapporto Rifiuti Urbani - Edizione 2021’, ISPRA Istituto Superiore per la Protezione e la Ricerca Ambientale. Accessed: Aug. 24, 2023. [Online]. Available: <https://www.isprambiente.gov.it/it/pubblicazioni/rapporti/rapporto-rifiuti-urbani-edizione-2021>
- [13] ‘Rapporto Rifiuti Urbani Edizione 2022’, ISPRA Istituto Superiore per la Protezione e la Ricerca Ambientale. Accessed: Aug. 24, 2023. [Online]. Available: <https://www.isprambiente.gov.it/it/pubblicazioni/rapporti/rapporto-rifiuti-urbani-edizione-2022>

- [14] B. Assamoi and Y. Lawryshyn, ‘The environmental comparison of landfilling vs. incineration of MSW accounting for waste diversion’, *Waste Management*, vol. 32, no. 5, pp. 1019–1030, May 2012, doi: 10.1016/j.wasman.2011.10.023.
- [15] T. Fruergaard, T. H. Christensen, and T. Astrup, ‘Energy recovery from waste incineration: Assessing the importance of district heating networks’, *Waste Management*, vol. 30, no. 7, pp. 1264–1272, Jul. 2010, doi: 10.1016/j.wasman.2010.03.026.
- [16] ‘Termovalorizzatore Bolzano’. Accessed: Aug. 24, 2023. [Online]. Available: <https://www.eco-center.it/it/attivita-servizi/ambiente/impianti/impianto-di-termovalorizzazione-897.html>
- [17] T. Astrup, C. Riber, and A. J. Pedersen, ‘Incinerator performance: effects of changes in waste input and furnace operation on air emissions and residues’, *Waste Manag Res*, vol. 29, no. 10_suppl, pp. S57–S68, Oct. 2011, doi: 10.1177/0734242X11419893.
- [18] J. Van Caneghem, J. De Greef, C. Block, and C. Vandecasteele, ‘NO_x reduction in waste incinerators by selective catalytic reduction (SCR) instead of selective non catalytic reduction (SNCR) compared from a life cycle perspective: a case study’, *Journal of Cleaner Production*, vol. 112, pp. 4452–4460, Jan. 2016, doi: 10.1016/j.jclepro.2015.08.068.
- [19] ‘Termovalorizzatore Ferrara | Herambiente’. Accessed: Aug. 24, 2023. [Online]. Available: <https://ha.gruppohera.it/lista-impianti/termovalorizzatore-di-ferrara>
- [20] ‘Il termovalorizzatore di San Vittore - Gruppo Acea’. Accessed: Aug. 24, 2023. [Online]. Available: <https://www.gruppo.acea.it/al-servizio-delle-persone/ambiente/termovalorizzazione/termovalorizzatore-san-vittore-del-lazio>
- [21] S. M. Al-Salem, A. Antelava, A. Constantinou, G. Manos, and A. Dutta, ‘A review on thermal and catalytic pyrolysis of plastic solid waste (PSW)’, *Journal of Environmental Management*, vol. 197, pp. 177–198, Jul. 2017, doi: 10.1016/j.jenvman.2017.03.084.
- [22] U. Arena, ‘Fluidized bed gasification’, in *Fluidized Bed Technologies for Near-Zero Emission Combustion and Gasification*, Elsevier, 2013, pp. 765–812. doi: 10.1533/9780857098801.3.765.
- [23] J. Alvarez *et al.*, ‘Hydrogen production from biomass and plastic mixtures by pyrolysis-gasification’, *International Journal of Hydrogen Energy*, vol. 39, no. 21, pp. 10883–10891, Jul. 2014, doi: 10.1016/j.ijhydene.2014.04.189.
- [24] U. Arena, ‘Gasification: An alternative solution for waste treatment with energy recovery’, *Waste Management*, vol. 31, no. 3, pp. 405–406, Mar. 2011, doi: 10.1016/j.wasman.2010.12.006.
- [25] U. Arena, ‘Process and technological aspects of municipal solid waste gasification. A review’, *Waste Management*, vol. 32, no. 4, pp. 625–639, Apr. 2012, doi: 10.1016/j.wasman.2011.09.025.
- [26] J. Dong, Y. Tang, A. Nzihou, Y. Chi, E. Weiss-Hortala, and M. Ni, ‘Life cycle assessment of pyrolysis, gasification and incineration waste-to-energy technologies: Theoretical analysis and case study of commercial plants’, *Science of The Total Environment*, vol. 626, pp. 744–753, Jun. 2018, doi: 10.1016/j.scitotenv.2018.01.151.
- [27] ‘Pubblicazioni Statistiche - Terna spa’. Accessed: Jul. 14, 2022. [Online]. Available: <https://www.terna.it/it/sistema-elettrico/statistiche/pubblicazioni-statistiche>
- [28] S. Nanda and F. Berruti, ‘A technical review of bioenergy and resource recovery from municipal solid waste’, *Journal of Hazardous Materials*, vol. 403, p. 123970, Feb. 2021, doi: 10.1016/j.jhazmat.2020.123970.
- [29] L. Zhang, A. Kuroki, and Y. W. Tong, ‘A Mini-Review on In situ Biogas Upgrading Technologies via Enhanced Hydrogenotrophic Methanogenesis to Improve the Quality of Biogas From Anaerobic Digesters’, *Front. Energy Res.*, vol. 8, p. 69, Apr. 2020, doi: 10.3389/fenrg.2020.00069.

- [30] M. Kim, Y.-H. Ahn, and R. E. Speece, 'Comparative process stability and efficiency of anaerobic digestion; mesophilic vs. thermophilic', *Water Research*, vol. 36, no. 17, pp. 4369–4385, Oct. 2002, doi: 10.1016/S0043-1354(02)00147-1.
- [31] C. Montejo, D. Tonini, M. D. C. Márquez, and T. Fruergaard Astrup, 'Mechanical–biological treatment: Performance and potentials. An LCA of 8 MBT plants including waste characterization', *Journal of Environmental Management*, vol. 128, pp. 661–673, Oct. 2013, doi: 10.1016/j.jenvman.2013.05.063.
- [32] A. C. (Thanos) Bourtsalas and N. J. Themelis, 'Materials and energy recovery at six European MBT plants', *Waste Management*, vol. 141, pp. 79–91, Mar. 2022, doi: 10.1016/j.wasman.2022.01.024.
- [33] 'DECRETO LEGISLATIVO 11 maggio 2005, n. 133 - Normattiva'. Accessed: Sep. 27, 2023. [Online]. Available: <https://www.normattiva.it/uri-res/N2Ls?urn:nir:stato:decreto.legislativo:2005;133>
- [34] 'DECRETO LEGISLATIVO 3 aprile 2006, n. 152 - Normattiva'. Accessed: Sep. 27, 2023. [Online]. Available: <https://www.normattiva.it/uri-res/N2Ls?urn:nir:stato:decreto.legislativo:2006-04-03;152>
- [35] 'UNI 9903-1:2004 - UNI Ente Italiano di Normazione'. Accessed: Sep. 27, 2023. [Online]. Available: <https://store.uni.com/uni-9903-1-2004>
- [36] 'Gazzetta Ufficiale'. Accessed: Sep. 27, 2023. [Online]. Available: <https://www.gazzettaufficiale.it/eli/id/2010/12/10/010G0235/sg>
- [37] 'Rapporto Rifiuti Urbani - Edizione 2021', Istituto Superiore per la Protezione e la Ricerca Ambientale. Accessed: Jul. 23, 2022. [Online]. Available: <https://www.isprambiente.gov.it/it/pubblicazioni/rapporti/rapporto-rifiuti-urbani-edizione-2021>
- [38] 'List Of Waste', Pure Planet Recycling. Accessed: Oct. 13, 2023. [Online]. Available: <https://www.pureplanetrecycling.co.uk/list-of-waste/>
- [39] G. Biancini, L. Cioccolanti, B. Marchetti, and M. Moglie, 'EVALUATION OF MUNICIPAL LANDFILL LEACHATE TREATMENT BY MICROALGAE', 2022.
- [40] M. Pradel, L. Aissani, J. Villot, J.-C. Baudez, and V. Laforest, 'From waste to added value product: towards a paradigm shift in life cycle assessment applied to wastewater sludge – a review', *Journal of Cleaner Production*, vol. 131, pp. 60–75, Sep. 2016, doi: 10.1016/j.jclepro.2016.05.076.
- [41] J. M. De Andrés, M. Vedrenne, M. Brambilla, and E. Rodríguez, 'Modeling and model performance evaluation of sewage sludge gasification in fluidized-bed gasifiers using Aspen Plus', *Journal of the Air & Waste Management Association*, vol. 69, no. 1, pp. 23–33, Jan. 2019, doi: 10.1080/10962247.2018.1500404.
- [42] L. Lombardi, C. Nocita, E. Bettazzi, D. Fibbi, and E. Carnevale, 'Environmental comparison of alternative treatments for sewage sludge: An Italian case study', *Waste Management*, vol. 69, pp. 365–376, Nov. 2017, doi: 10.1016/j.wasman.2017.08.040.
- [43] L. M. Cafiero, 'Gestione RSU e tecniche innovative di trattamento'.
- [44] M. Grosso, A. Motta, and L. Rigamonti, 'Efficiency of energy recovery from waste incineration, in the light of the new Waste Framework Directive', *Waste Management*, vol. 30, no. 7, pp. 1238–1243, Jul. 2010, doi: 10.1016/j.wasman.2010.02.036.
- [45] P. Basu, *Biomass gasification and pyrolysis: practical design and theory*. Burlington, MA: Academic Press, 2010.
- [46] J. A. Ruiz, M. C. Juárez, M. P. Morales, P. Muñoz, and M. A. Mendivil, 'Biomass gasification for electricity generation: Review of current technology barriers', *Renewable and Sustainable Energy Reviews*, vol. 18, pp. 174–183, Feb. 2013, doi: 10.1016/j.rser.2012.10.021.

- [47] J. Blondeau and H. Jeanmart, 'Biomass pyrolysis at high temperatures: Prediction of gaseous species yields from an anisotropic particle', *Biomass and Bioenergy*, vol. 41, pp. 107–121, Jun. 2012, doi: 10.1016/j.biombioe.2012.02.016.
- [48] S. D. Anuar Sharuddin, F. Abnisa, W. M. A. Wan Daud, and M. K. Aroua, 'A review on pyrolysis of plastic wastes', *Energy Conversion and Management*, vol. 115, pp. 308–326, May 2016, doi: 10.1016/j.enconman.2016.02.037.
- [49] D. Kong, S. Wang, K. Luo, Q. Xu, and J. Fan, 'Insights of biomass gasification combined with CO₂ absorption enhanced reforming in an 8 MWth dual fluidized bed', *Chemical Engineering Journal*, vol. 466, p. 142981, Jun. 2023, doi: 10.1016/j.cej.2023.142981.
- [50] D. Saebea, P. Ruengrit, A. Arpornwichanop, and Y. Patcharavorachot, 'Gasification of plastic waste for synthesis gas production', *Energy Reports*, vol. 6, pp. 202–207, Feb. 2020, doi: 10.1016/j.egyr.2019.08.043.
- [51] I. P. Lazzarotto *et al.*, 'The role of CaO in the steam gasification of plastic wastes recovered from the municipal solid waste in a fluidized bed reactor', *Process Safety and Environmental Protection*, vol. 140, pp. 60–67, Aug. 2020, doi: 10.1016/j.psep.2020.04.009.
- [52] U. Leone, U. Arena, and M. L. Mastellone, *Recupero di energia e materia da rifiuti solidi: i processi, le tecnologie, le esperienze, le norme*. Napoli: Regione Campania, Ricerca e innovazione, 2007.
- [53] European Commission. Joint Research Centre. Institute for Energy and Transport., *Study on the state of play of energy efficiency of heat and electricity production technologies*. LU: Publications Office, 2012. Accessed: Aug. 23, 2023. [Online]. Available: <https://data.europa.eu/doi/10.2790/57624>
- [54] S. Ge, M. Hussain Tahir, D. Chen, L. Hong, Y. Feng, and Z. Huang, 'MSW pyro-gasification using high-temperature CO₂ as gasifying agent: Influence of contact mode between CO₂, char and volatiles on final products', *Waste Management*, vol. 170, pp. 112–121, Oct. 2023, doi: 10.1016/j.wasman.2023.07.033.
- [55] M. Materazzi, P. Lettieri, L. Mazzei, R. Taylor, and C. Chapman, 'Thermodynamic modelling and evaluation of a two-stage thermal process for waste gasification', *Fuel*, vol. 108, pp. 356–369, Jun. 2013, doi: 10.1016/j.fuel.2013.02.037.
- [56] L. Mazzoni and I. Janajreh, 'Plasma gasification of municipal solid waste with variable content of plastic solid waste for enhanced energy recovery', *International Journal of Hydrogen Energy*, vol. 42, no. 30, pp. 19446–19457, Jul. 2017, doi: 10.1016/j.ijhydene.2017.06.069.
- [57] Z. Hameed *et al.*, 'Gasification of municipal solid waste blends with biomass for energy production and resources recovery: Current status, hybrid technologies and innovative prospects', *Renewable and Sustainable Energy Reviews*, vol. 136, p. 110375, Feb. 2021, doi: 10.1016/j.rser.2020.110375.
- [58] S. Fremaux, S.-M. Beheshti, H. Ghassemi, and R. Shahsavan-Markadeh, 'An experimental study on hydrogen-rich gas production via steam gasification of biomass in a research-scale fluidized bed', *Energy Conversion and Management*, vol. 91, pp. 427–432, Feb. 2015, doi: 10.1016/j.enconman.2014.12.048.
- [59] K. Ståhl, K. D. Ab, L. Waldheim, M. Morris, U. Johnsson, and L. Gårdmark, 'Biomass IGCC at Värnamo, Sweden – Past and Future', *Stanford University*, 2004.
- [60] S. Farzad, M. A. Mandegari, and J. F. Görgens, 'A critical review on biomass gasification, co-gasification, and their environmental assessments', *Biofuel Res. J.*, vol. 3, no. 4, pp. 483–495, Dec. 2016, doi: 10.18331/BRJ2016.3.4.3.
- [61] F. Parrillo, F. Ardolino, G. Cali, D. Marotto, A. Pettinau, and U. Arena, 'Fluidized bed gasification of eucalyptus chips: Axial profiles of syngas composition in a pilot scale reactor', *Energy*, vol. 219, p. 119604, Mar. 2021, doi: 10.1016/j.energy.2020.119604.

- [62] D. Vera, F. Jurado, J. Carpio, and S. Kamel, 'Biomass gasification coupled to an EFGT-ORC combined system to maximize the electrical energy generation: A case applied to the olive oil industry', *Energy*, vol. 144, pp. 41–53, Feb. 2018, doi: 10.1016/j.energy.2017.11.152.
- [63] F. Pinto, C. Franco, R. N. André, M. Miranda, I. Gulyurtlu, and I. Cabrita, 'Co-gasification study of biomass mixed with plastic wastes', 2002.
- [64] M. M. Win, M. Asari, R. Hayakawa, H. Hosoda, J. Yano, and S. Sakai, 'Characteristics of gas from the fluidized bed gasification of refuse paper and plastic fuel (RPF) and wood biomass', *Waste Management*, vol. 87, pp. 173–182, Mar. 2019, doi: 10.1016/j.wasman.2019.02.002.
- [65] J.-W. Kim, T.-Y. Mun, J.-O. Kim, and J.-S. Kim, 'Air gasification of mixed plastic wastes using a two-stage gasifier for the production of producer gas with low tar and a high caloric value', *Fuel*, vol. 90, no. 6, pp. 2266–2272, Jun. 2011, doi: 10.1016/j.fuel.2011.02.021.
- [66] M.-H. Cho, T.-Y. Mun, and J.-S. Kim, 'Air gasification of mixed plastic wastes using calcined dolomite and activated carbon in a two-stage gasifier to reduce tar', *Energy*, vol. 53, pp. 299–305, May 2013, doi: 10.1016/j.energy.2013.02.041.
- [67] Y.-S. Jeong, K.-B. Park, and J.-S. Kim, 'Hydrogen production from steam gasification of polyethylene using a two-stage gasifier and active carbon', *Applied Energy*, vol. 262, p. 114495, Mar. 2020, doi: 10.1016/j.apenergy.2020.114495.
- [68] Y. Yang *et al.*, 'Gasification of refuse-derived fuel from municipal solid waste for energy production: a review', *Environ Chem Lett*, vol. 19, no. 3, pp. 2127–2140, Jun. 2021, doi: 10.1007/s10311-020-01177-5.
- [69] 'Statista - The Statistics Portal for Market Data, Market Research and Market Studies'. Accessed: Sep. 11, 2023. [Online]. Available: https://www.statista.com/?kw=statista&crmtag=adwords&gclid=Cj0KCQjw9fqBhDSARIsAHlcQYTqhZL7ANDtAqK_hcqFC4iP1nBRc6rARo3wNAC4MHihUcvZxJLFbMsaAsC6EALw_wcB
- [70] F. Pinto, C. Franco, R. N. André, M. Miranda, I. Gulyurtlu, and I. Cabrita, 'Co-gasification study of biomass mixed with plastic wastes', *Fuel*, vol. 81, no. 3, pp. 291–297, Feb. 2002, doi: 10.1016/s0016-2361(01)00164-8.
- [71] M. L. Mastellone, L. Zaccariello, and U. Arena, 'Co-gasification of coal, plastic waste and wood in a bubbling fluidized bed reactor', *Fuel*, vol. 89, no. 10, pp. 2991–3000, Oct. 2010, doi: 10.1016/j.fuel.2010.05.019.
- [72] F. Parrillo *et al.*, 'Co-gasification of plastics waste and biomass in a pilot scale fluidized bed reactor', *Energy*, vol. 273, p. 127220, Jun. 2023, doi: 10.1016/j.energy.2023.127220.
- [73] M. S. Masnadi *et al.*, 'From coal towards renewables: Catalytic/synergistic effects during steam co-gasification of switchgrass and coal in a pilot-scale bubbling fluidized bed', *Renewable Energy*, vol. 83, pp. 918–930, Nov. 2015, doi: 10.1016/j.renene.2015.05.044.
- [74] J. Cai *et al.*, 'Synergistic effects of co-gasification of municipal solid waste and biomass in fixed-bed gasifier', *Process Safety and Environmental Protection*, vol. 148, pp. 1–12, Apr. 2021, doi: 10.1016/j.psep.2020.09.063.
- [75] K. G. Burra and A. K. Gupta, 'Synergistic effects in steam gasification of combined biomass and plastic waste mixtures', *Applied Energy*, vol. 211, pp. 230–236, Feb. 2018, doi: 10.1016/j.apenergy.2017.10.130.
- [76] M. Naqvi, E. Dahlquist, and J. Yan, 'Complementing existing CHP plants using biomass for production of hydrogen and burning the residual gas in a CHP boiler', *Biofuels*, vol. 8, no. 6, pp. 675–683, Nov. 2017, doi: 10.1080/17597269.2016.1153362.
- [77] J. Kurzke and I. Halliwell, 'Understanding Off-Design Behavior', in *Propulsion and Power*, Cham: Springer International Publishing, 2018, pp. 577–610. doi: 10.1007/978-3-319-75979-1_13.

- [78] Z. Liu and I. A. Karimi, ‘Simulating combined cycle gas turbine power plants in Aspen HYSYS’, *Energy Conversion and Management*, vol. 171, pp. 1213–1225, Sep. 2018, doi: 10.1016/j.enconman.2018.06.049.
- [79] M. Jakubcionis and J. Carlsson, ‘Estimation of European Union residential sector space cooling potential’, *Energy Policy*, vol. 101, pp. 225–235, Feb. 2017, doi: 10.1016/j.enpol.2016.11.047.
- [80] K. Jylhä *et al.*, ‘Energy demand for the heating and cooling of residential houses in Finland in a changing climate’, *Energy and Buildings*, vol. 99, pp. 104–116, Jul. 2015, doi: 10.1016/j.enbuild.2015.04.001.
- [81] C. A. Salman, M. Naqvi, E. Thorin, and J. Yan, ‘Gasification process integration with existing combined heat and power plants for polygeneration of dimethyl ether or methanol: A detailed profitability analysis’, *Applied Energy*, vol. 226, pp. 116–128, Sep. 2018, doi: 10.1016/j.apenergy.2018.05.069.
- [82] T. Kohl, T. P. Laukkanen, and M. P. Järvinen, ‘Integration of biomass fast pyrolysis and precedent feedstock steam drying with a municipal combined heat and power plant’, *Biomass and Bioenergy*, vol. 71, pp. 413–430, Dec. 2014, doi: 10.1016/j.biombioe.2014.09.014.
- [83] H. Li, E. Larsson, E. Thorin, E. Dahlquist, and X. Yu, ‘Feasibility study on combining anaerobic digestion and biomass gasification to increase the production of biomethane’, *Energy Conversion and Management*, vol. 100, pp. 212–219, Aug. 2015, doi: 10.1016/j.enconman.2015.05.007.
- [84] J. A. Conesa, JoséA. Caballero, A. Marcilla, and R. Font, ‘Analysis of different kinetic models in the dynamic pyrolysis of cellulose’, *Thermochimica Acta*, vol. 254, pp. 175–192, Apr. 1995, doi: 10.1016/0040-6031(94)02102-T.
- [85] M. M. Wright, J. A. Satrio, R. C. Brown, and I. S. University, ‘Techno-Economic Analysis of Biomass Fast Pyrolysis to Transportation Fuels’, *Renewable Energy*, 2010.
- [86] D. Mohan, A. Sarswat, Y. S. Ok, and C. U. Pittman, ‘Organic and inorganic contaminants removal from water with biochar, a renewable, low cost and sustainable adsorbent – A critical review’, *Bioresource Technology*, vol. 160, pp. 191–202, May 2014, doi: 10.1016/j.biortech.2014.01.120.
- [87] Y. Sorunmu, P. Billen, and S. Spatari, ‘A review of thermochemical upgrading of pyrolysis bio-oil: Techno-economic analysis, life cycle assessment, and technology readiness’, *GCB Bioenergy*, vol. 12, no. 1, pp. 4–18, Jan. 2020, doi: 10.1111/gcbb.12658.
- [88] Y. Zhang *et al.*, ‘A review of biomass pyrolysis gas: Forming mechanisms, influencing parameters, and product application upgrades’, *Fuel*, vol. 347, p. 128461, Sep. 2023, doi: 10.1016/j.fuel.2023.128461.
- [89] M. Calonaci, R. Grana, E. Barker Hemings, G. Bozzano, M. Dente, and E. Ranzi, ‘Comprehensive Kinetic Modeling Study of Bio-oil Formation from Fast Pyrolysis of Biomass’, *Energy Fuels*, vol. 24, no. 10, pp. 5727–5734, Oct. 2010, doi: 10.1021/ef1008902.
- [90] K.-L. Lam, A. O. Oyedun, K.-Y. Cheung, K.-L. Lee, and C.-W. Hui, ‘Modelling pyrolysis with dynamic heating’, *Chemical Engineering Science*, vol. 66, no. 24, pp. 6505–6514, Dec. 2011, doi: 10.1016/j.ces.2011.09.013.
- [91] ‘Empyro Hengelo, NL’, BTG Bioliquids. Accessed: Oct. 03, 2023. [Online]. Available: <https://www.btg-bioliquids.com/plant/empyro-hengelo/>
- [92] L. Björnsson, M. Pettersson, P. Börjesson, P. Ottosson, and C. Gustavsson, ‘Integrating bio-oil production from wood fuels to an existing heat and power plant - evaluation of energy and greenhouse gas performance in a Swedish case study’, *Sustainable Energy Technologies and Assessments*, vol. 48, p. 101648, Dec. 2021, doi: 10.1016/j.seta.2021.101648.
- [93] A. Dutta, A. Sahir, and E. Tan, ‘Process Design and Economics for the Conversion of Lignocellulosic Biomass to Hydrocarbon Fuels: Thermochemical Research Pathways with In Situ and Ex Situ Upgrading of Fast Pyrolysis Vapors’.

- [94] V. Ananthi, R. Raja, I. S. Carvalho, K. Brindhadevi, A. Pugazhendhi, and A. Arun, 'A realistic scenario on microalgae based biodiesel production: Third generation biofuel', *Fuel*, vol. 284, p. 118965, Jan. 2021, doi: 10.1016/j.fuel.2020.118965.
- [95] 'CATALOGUE OF VALUABLE PRODUCTS FROM LARGE-SCALE MICROALGAL BIOREFINERIES'. Accessed: Oct. 13, 2023. [Online]. Available: <https://ec.europa.eu/research/participants/documents/downloadPublic?documentIds=080166e5ccb18f6&appId=PPGMS>
- [96] M. I. Khan, J. H. Shin, and J. D. Kim, 'The promising future of microalgae: current status, challenges, and optimization of a sustainable and renewable industry for biofuels, feed, and other products', *Microb Cell Fact*, vol. 17, no. 1, p. 36, Dec. 2018, doi: 10.1186/s12934-018-0879-x.
- [97] M. A. Borowitzka, 'High-value products from microalgae—their development and commercialisation', *J Appl Phycol*, vol. 25, no. 3, pp. 743–756, Jun. 2013, doi: 10.1007/s10811-013-9983-9.
- [98] F. G. Acién, C. Gómez-Serrano, M. M. Morales-Amaral, J. M. Fernández-Sevilla, and E. Molina-Grima, 'Wastewater treatment using microalgae: how realistic a contribution might it be to significant urban wastewater treatment?', *Appl Microbiol Biotechnol*, vol. 100, no. 21, pp. 9013–9022, Nov. 2016, doi: 10.1007/s00253-016-7835-7.
- [99] G. Hodaifa, M. E. Martínez, and S. Sánchez, 'Use of industrial wastewater from olive-oil extraction for biomass production of *Scenedesmus obliquus*', *Bioresource Technology*, vol. 99, no. 5, pp. 1111–1117, Mar. 2008, doi: 10.1016/j.biortech.2007.02.020.
- [100] M. Massa *et al.*, 'Evaluation of anaerobic digestates from different feedstocks as growth media for *Tetradesmus obliquus*, *Botryococcus braunii*, *Phaeodactylum tricornutum* and *Arthrospira maxima*', *New Biotechnology*, vol. 36, pp. 8–16, May 2017, doi: 10.1016/j.nbt.2016.12.007.
- [101] S. K. Hoekman, A. Broch, C. Robbins, E. Cenicerros, and M. Natarajan, 'Review of biodiesel composition, properties, and specifications', *Renewable and Sustainable Energy Reviews*, vol. 16, no. 1, pp. 143–169, Jan. 2012, doi: 10.1016/j.rser.2011.07.143.
- [102] E. Thorin, J. Olsson, S. Schwede, and E. Nehrenheim, 'Co-digestion of sewage sludge and microalgae – Biogas production investigations', *Applied Energy*, vol. 227, pp. 64–72, Oct. 2018, doi: 10.1016/j.apenergy.2017.08.085.
- [103] G. Santori, A. Arteconi, G. Di Nicola, M. Moglie, and R. Stryjek, 'Quantitation of Compounds in Biodiesel Mixtures with Reversed-Phase Liquid Chromatography', *Energy Fuels*, vol. 23, no. 7, pp. 3783–3789, Jul. 2009, doi: 10.1021/ef900140r.
- [104] D. D. Bala, M. Misra, and D. Chidambaram, 'Single step esterification of algae oil using mesoporous solid acid catalyst', *Fuel*, vol. 117, pp. 1093–1095, Jan. 2014, doi: 10.1016/j.fuel.2013.10.031.
- [105] Y. H. Seo, M. Sung, Y.-K. Oh, and J.-I. Han, 'Lipid extraction and esterification for microalgae-based biodiesel production using pyrite (FeS₂)', *Bioresource Technology*, vol. 191, pp. 420–425, Sep. 2015, doi: 10.1016/j.biortech.2015.02.083.
- [106] M. Salisch, 'Mixing tank at the microalgae photobioreactor plant, Anhalt University of Applied Sciences, Köthen (Germany)'.
- [107] N. Eckelberry and T. R. Eckelberry, 'Algae growth system for oil production', US20090029445A1, Jan. 29, 2009 Accessed: Oct. 14, 2023. [Online]. Available: <https://patents.google.com/patent/US20090029445A1/en>
- [108] S.-H. Ho, W.-M. Chen, and J.-S. Chang, 'Scenedesmus obliquus CNW-N as a potential candidate for CO₂ mitigation and biodiesel production', *Bioresource Technology*, vol. 101, no. 22, pp. 8725–8730, Nov. 2010, doi: 10.1016/j.biortech.2010.06.112.
- [109] J. Trivedi, D. Agrawal, N. Atray, and A. Ray, 'Enhanced lipid production in *Scenedesmus obliquus* via nitrogen starvation in a two-stage cultivation process and evaluation for biodiesel production', *Fuel*, vol. 316, p. 123418, May 2022, doi: 10.1016/j.fuel.2022.123418.

- [110] European Commission. Joint Research Centre. Institute for Environment and Sustainability., *International Reference Life Cycle Data System (ILCD) Handbook :general guide for life cycle assessment : detailed guidance*. LU: Publications Office, 2010. Accessed: Jul. 24, 2022. [Online]. Available: <https://data.europa.eu/doi/10.2788/38479>
- [111] H. Khandelwal, H. Dhar, A. K. Thalla, and S. Kumar, ‘Application of life cycle assessment in municipal solid waste management: A worldwide critical review’, *Journal of Cleaner Production*, vol. 209, pp. 630–654, Feb. 2019, doi: 10.1016/j.jclepro.2018.10.233.
- [112] T. F. Astrup, D. Tonini, R. Turconi, and A. Boldrin, ‘Life cycle assessment of thermal Waste-to-Energy technologies: Review and recommendations’, *Waste Management*, vol. 37, pp. 104–115, Mar. 2015, doi: 10.1016/j.wasman.2014.06.011.
- [113] T. Fruergaard and T. Astrup, ‘Optimal utilization of waste-to-energy in an LCA perspective’, *Waste Management*, vol. 31, no. 3, pp. 572–582, Mar. 2011, doi: 10.1016/j.wasman.2010.09.009.
- [114] L. Morselli, C. De Robertis, J. Luzi, F. Passarini, and I. Vassura, ‘Environmental impacts of waste incineration in a regional system (Emilia Romagna, Italy) evaluated from a life cycle perspective’, *Journal of Hazardous Materials*, vol. 159, no. 2–3, pp. 505–511, Nov. 2008, doi: 10.1016/j.jhazmat.2008.02.047.
- [115] P. Buttol, P. Masoni, A. Bonoli, S. Goldoni, V. Belladonna, and C. Cavazzuti, ‘LCA of integrated MSW management systems: Case study of the Bologna District’, *Waste Management*, vol. 27, no. 8, pp. 1059–1070, Jan. 2007, doi: 10.1016/j.wasman.2007.02.010.
- [116] M. Grosso, C. Nava, R. Testori, L. Rigamonti, and F. Viganò, ‘The implementation of anaerobic digestion of food waste in a highly populated urban area: an LCA evaluation’, *Waste Manag Res*, vol. 30, no. 9_suppl, pp. 78–87, Sep. 2012, doi: 10.1177/0734242X12453611.
- [117] G. Sauve and K. Van Acker, ‘The environmental impacts of municipal solid waste landfills in Europe: A life cycle assessment of proper reference cases to support decision making’, *Journal of Environmental Management*, vol. 261, p. 110216, May 2020, doi: 10.1016/j.jenvman.2020.110216.
- [118] U. Lee, J. Han, and M. Wang, ‘Evaluation of landfill gas emissions from municipal solid waste landfills for the life-cycle analysis of waste-to-energy pathways’, *Journal of Cleaner Production*, vol. 166, pp. 335–342, Nov. 2017, doi: 10.1016/j.jclepro.2017.08.016.
- [119] A. Damgaard, S. Manfredi, H. Merrild, S. Stensøe, and T. H. Christensen, ‘LCA and economic evaluation of landfill leachate and gas technologies’, *Waste Management*, vol. 31, no. 7, pp. 1532–1541, Jul. 2011, doi: 10.1016/j.wasman.2011.02.027.
- [120] M. D. Caprile and M. Ripa, ‘A Life Cycle Assessment of Landfilled Municipal Solid Waste in Argentina: The Influence of Waste Composition on Greenhouse Gases Emissions and Other Impacts’, *JEAM*, vol. 2, no. 2, pp. 145–162, Jun. 2014, doi: 10.5890/JEAM.2014.06.005.
- [121] M. A. Cusenza, M. Cellura, F. Guarino, and S. Longo, ‘Life Cycle Environmental Assessment of Energy Valorization of the Residual Agro-Food Industry’, *Energies*, vol. 14, no. 17, p. 5491, Sep. 2021, doi: 10.3390/en14175491.
- [122] V. Fantin, A. Giuliano, M. Manfredi, G. Ottaviano, M. Stefanova, and P. Masoni, ‘Environmental assessment of electricity generation from an Italian anaerobic digestion plant’, *Biomass and Bioenergy*, vol. 83, pp. 422–435, Dec. 2015, doi: 10.1016/j.biombioe.2015.10.015.
- [123] I. O. for Standardization, *Environmental management: life cycle assessment; Principles and Framework*. ISO, 2006.
- [124] K. Starr, X. Gabarrell, G. Villalba, L. Talens, and L. Lombardi, ‘Life cycle assessment of biogas upgrading technologies’, *Waste Management*, vol. 32, no. 5, pp. 991–999, May 2012, doi: 10.1016/j.wasman.2011.12.016.

- [125] G. A. Blengini, 'Using LCA to evaluate impacts and resources conservation potential of composting: A case study of the Asti District in Italy', *Resources, Conservation and Recycling*, vol. 52, no. 12, pp. 1373–1381, Oct. 2008, doi: 10.1016/j.resconrec.2008.08.002.
- [126] E. Cadena, J. Colón, A. Artola, A. Sánchez, and X. Font, 'Environmental impact of two aerobic composting technologies using life cycle assessment', *Int J Life Cycle Assess*, vol. 14, no. 5, pp. 401–410, Jul. 2009, doi: 10.1007/s11367-009-0107-3.
- [127] S. F. Mohsenpour, S. Hennige, N. Willoughby, A. Adeloje, and T. Gutierrez, 'Integrating micro-algae into wastewater treatment: A review', *Science of The Total Environment*, vol. 752, p. 142168, Jan. 2021, doi: 10.1016/j.scitotenv.2020.142168.
- [128] L. T. Arashiro, N. Montero, I. Ferrer, F. G. Acien, C. Gómez, and M. Garfi, 'Life cycle assessment of high rate algal ponds for wastewater treatment and resource recovery', *Science of The Total Environment*, vol. 622–623, pp. 1118–1130, May 2018, doi: 10.1016/j.scitotenv.2017.12.051.
- [129] R. de C. de S. Schneider, M. de Moura Lima, M. Hoeltz, F. de Farias Neves, D. K. John, and A. de Azevedo, 'Life cycle assessment of microalgae production in a raceway pond with alternative culture media', *Algal Research*, vol. 32, pp. 280–292, Jun. 2018, doi: 10.1016/j.algal.2018.04.012.
- [130] P. Pérez-López *et al.*, 'Comparative life cycle assessment of real pilot reactors for microalgae cultivation in different seasons', *Applied Energy*, vol. 205, pp. 1151–1164, Nov. 2017, doi: 10.1016/j.apenergy.2017.08.102.
- [131] J. Sun *et al.*, 'A promising microalgal wastewater cyclic cultivation technology: Dynamic simulations, economic viability, and environmental suitability', *Water Research*, vol. 217, p. 118411, Jun. 2022, doi: 10.1016/j.watres.2022.118411.
- [132] J. Ferreira, L. R. de Assis, A. P. de S. Oliveira, J. de S. Castro, and M. L. Calijuri, 'Innovative microalgae biomass harvesting methods: Technical feasibility and life cycle analysis', *Science of The Total Environment*, vol. 746, p. 140939, Dec. 2020, doi: 10.1016/j.scitotenv.2020.140939.
- [133] C. Tua, E. Ficara, V. Mezzanotte, and L. Rigamonti, 'Integration of a side-stream microalgae process into a municipal wastewater treatment plant: A life cycle analysis', *Journal of Environmental Management*, vol. 279, p. 111605, Feb. 2021, doi: 10.1016/j.jenvman.2020.111605.
- [134] S. Lo, H. Ma, and S. Lo, 'Quantifying and reducing uncertainty in life cycle assessment using the Bayesian Monte Carlo method', *Science of The Total Environment*, vol. 340, no. 1–3, pp. 23–33, Mar. 2005, doi: 10.1016/j.scitotenv.2004.08.020.
- [135] G. Doka and R. Hischer, 'Waste Treatment and Assessment of Long-Term Emissions (8pp)', *Int J Life Cycle Assessment*, vol. 10, no. 1, pp. 77–84, Jan. 2005, doi: 10.1065/lca2004.12.181.9.
- [136] T. Ekvall, G. Assefa, A. Björklund, O. Eriksson, and G. Finnveden, 'What life-cycle assessment does and does not do in assessments of waste management', *Waste Management*, vol. 27, no. 8, pp. 989–996, Jan. 2007, doi: 10.1016/j.wasman.2007.02.015.
- [137] R. Clift, A. Doig, and G. Finnveden, 'The Application of Life Cycle Assessment to Integrated Solid Waste Management', *Process Safety and Environmental Protection*, vol. 78, no. 4, pp. 279–287, Jul. 2000, doi: 10.1205/095758200530790.
- [138] G. Biancini, B. Marchetti, L. Cioccolanti, and M. Moglie, 'Comprehensive Life Cycle Assessment Analysis of an Italian Composting Facility concerning Environmental Footprint Minimization and Renewable Energy Integration', *Sustainability*, vol. 14, no. 22, p. 14961, Nov. 2022, doi: 10.3390/su142214961.
- [139] R. Dvořák, T. Pařízek, L. Bébar, and P. Stehlík, 'Incineration and gasification technologies completed with up-to-date off-gas cleaning system for meeting environmental limits', *Clean*

Techn Environ Policy, vol. 11, no. 1, pp. 95–105, Feb. 2009, doi: 10.1007/s10098-008-0170-7.

- [140] G. Ruoppolo, P. Ammendola, R. Chirone, and F. Miccio, ‘H₂-rich syngas production by fluidized bed gasification of biomass and plastic fuel’, *Waste Management*, vol. 32, no. 4, pp. 724–732, Apr. 2012, doi: 10.1016/j.wasman.2011.12.004.
- [141] R. H. Perry and D. W. Green, Eds., *Perry’s chemical engineers’ handbook*, 8th ed. New York: McGraw-Hill, 2008.
- [142] J. E. Lee, H. S. Choi, and Y. C. Seo, ‘Study of hydrodynamic characteristics in a circulating fluidized bed gasifier for plastic waste by computational fluid dynamics modeling and simulation’, *J Mater Cycles Waste Manag*, vol. 16, no. 4, pp. 665–676, Oct. 2014, doi: 10.1007/s10163-014-0275-5.
- [143] M.-H. Cho, Y.-K. Choi, and J.-S. Kim, ‘Air gasification of PVC (polyvinyl chloride)-containing plastic waste in a two-stage gasifier using Ca-based additives and Ni-loaded activated carbon for the production of clean and hydrogen-rich producer gas’, *Energy*, vol. 87, pp. 586–593, Jul. 2015, doi: 10.1016/j.energy.2015.05.026.
- [144] R. Xiao, B. Jin, H. Zhou, Z. Zhong, and M. Zhang, ‘Air gasification of polypropylene plastic waste in fluidized bed gasifier’, *Energy Conversion and Management*, vol. 48, no. 3, pp. 778–786, Mar. 2007, doi: 10.1016/j.enconman.2006.09.004.
- [145] U. Arena, L. Zaccariello, and M. L. Mastellone, ‘Fluidized bed gasification of waste-derived fuels’, *Waste Management*, vol. 30, no. 7, pp. 1212–1219, Jul. 2010, doi: 10.1016/j.wasman.2010.01.038.
- [146] V. Wilk and H. Hofbauer, ‘Co-gasification of Plastics and Biomass in a Dual Fluidized-Bed Steam Gasifier: Possible Interactions of Fuels’, *Energy Fuels*, vol. 27, no. 6, pp. 3261–3273, Jun. 2013, doi: 10.1021/ef400349k.
- [147] U. Arena, F. Di Gregorio, C. Amorese, and M. L. Mastellone, ‘A techno-economic comparison of fluidized bed gasification of two mixed plastic wastes’, *Waste Management*, vol. 31, no. 7, pp. 1494–1504, Jul. 2011, doi: 10.1016/j.wasman.2011.02.004.
- [148] V. Wilk and H. Hofbauer, ‘Conversion of mixed plastic wastes in a dual fluidized bed steam gasifier’, *Fuel*, vol. 107, pp. 787–799, May 2013, doi: 10.1016/j.fuel.2013.01.068.
- [149] A. M. L. Násner *et al.*, ‘Refuse Derived Fuel (RDF) production and gasification in a pilot plant integrated with an Otto cycle ICE through Aspen plus™ modelling: Thermodynamic and economic viability’, *Waste Management*, vol. 69, pp. 187–201, Nov. 2017, doi: 10.1016/j.wasman.2017.08.006.
- [150] U. Arena, L. Zaccariello, and M. L. Mastellone, ‘Tar removal during the fluidized bed gasification of plastic waste’, *Waste Management*, vol. 29, no. 2, pp. 783–791, Feb. 2009, doi: 10.1016/j.wasman.2008.05.010.
- [151] U. Arena, E. Romeo, and M. L. Mastellone, ‘Recursive Operability Analysis of a pilot plant gasifier’, *Journal of Loss Prevention in the Process Industries*, vol. 21, no. 1, pp. 50–65, Jan. 2008, doi: 10.1016/j.jlp.2007.05.013.
- [152] L. Waldheim, *Gasification of waste forenergy carriers: a review*. Netherlands: IEA Bioenergy, 2018.
- [153] M. Fernandez-Lopez, J. Pedroche, J. L. Valverde, and L. Sanchez-Silva, ‘Simulation of the gasification of animal wastes in a dual gasifier using Aspen Plus®’, *Energy Conversion and Management*, vol. 140, pp. 211–217, May 2017, doi: 10.1016/j.enconman.2017.03.008.
- [154] A. Gagliano, F. Nocera, M. Bruno, and G. Cardillo, ‘Development of an Equilibrium-based Model of Gasification of Biomass by Aspen Plus’, *Energy Procedia*, vol. 111, pp. 1010–1019, Mar. 2017, doi: 10.1016/j.egypro.2017.03.264.
- [155] W. Lan, G. Chen, X. Zhu, X. Wang, C. Liu, and B. Xu, ‘Biomass gasification-gas turbine combustion for power generation system model based on ASPEN PLUS’, *Science of The Total Environment*, vol. 628–629, pp. 1278–1286, Jul. 2018, doi: 10.1016/j.scitotenv.2018.02.159.

- [156] F. Paviet, F. Chazarenc, and M. Tazerout, ‘Thermo Chemical Equilibrium Modelling of a Biomass Gasifying Process Using ASPEN PLUS’, *International Journal of Chemical Reactor Engineering*, vol. 7, no. 1, Oct. 2009, doi: 10.2202/1542-6580.2089.
- [157] N. V. Raibhole and S. N. Sapali, ‘Simulation of Biomass Gasification with Oxygen/Air as Gasifying Agent by ASPEN Plus’, *AMR*, vol. 622–623, pp. 633–638, Dec. 2012, doi: 10.4028/www.scientific.net/AMR.622-623.633.
- [158] R. Timsina, R. K. Thapa, and M. S. Eikeland, ‘Aspen Plus simulation of biomass gasification for different types of biomass’, presented at the The 60th SIMS Conference on Simulation and Modelling SIMS 2019, August 12-16, Västerås, Sweden, Jan. 2020, pp. 151–157. doi: 10.3384/ecp20170151.
- [159] J. Han *et al.*, ‘Modeling downdraft biomass gasification process by restricting chemical reaction equilibrium with Aspen Plus’, *Energy Conversion and Management*, vol. 153, pp. 641–648, Dec. 2017, doi: 10.1016/j.enconman.2017.10.030.
- [160] M. B. Nikoo and N. Mahinpey, ‘Simulation of biomass gasification in fluidized bed reactor using ASPEN PLUS’, *Biomass and Bioenergy*, vol. 32, no. 12, pp. 1245–1254, Dec. 2008, doi: 10.1016/j.biombioe.2008.02.020.
- [161] P. Kaushal and R. Tyagi, ‘Advanced simulation of biomass gasification in a fluidized bed reactor using ASPEN PLUS’, *Renewable Energy*, vol. 101, pp. 629–636, Feb. 2017, doi: 10.1016/j.renene.2016.09.011.
- [162] M. Puig-Gamero, D. T. Pio, L. A. C. Tarelho, P. Sánchez, and L. Sanchez-Silva, ‘Simulation of biomass gasification in bubbling fluidized bed reactor using aspen plus®’, *Energy Conversion and Management*, vol. 235, p. 113981, May 2021, doi: 10.1016/j.enconman.2021.113981.
- [163] F. N. Rahma, C. Tamzysi, A. Hidayat, and M. A. Adnan, ‘Investigation of Process Parameters Influence on Municipal Solid Waste Gasification with CO₂ Capture via Process Simulation Approach’, *IJRED*, vol. 10, no. 1, pp. 1–10, Feb. 2021, doi: 10.14710/ijred.2021.31982.
- [164] K. I. M. Al-Malah, *Aspen plus: chemical engineering applications*. Hoboken, New Jersey: Wiley, 2017.
- [165] R. Moradi, V. Marcantonio, L. Cioccolanti, and E. Bocci, ‘Integrating biomass gasification with a steam-injected micro gas turbine and an Organic Rankine Cycle unit for combined heat and power production’, *Energy Conversion and Management*, vol. 205, p. 112464, Feb. 2020, doi: 10.1016/j.enconman.2019.112464.
- [166] E. Neau, O. Hernández-Garduza, J. Escandell, C. Nicolas, and I. Raspo, ‘The Soave, Twu and Boston–Mathias alpha functions in cubic equations of state Part I. Theoretical analysis of their variations according to temperature’, *Fluid Phase Equilibria*, 2009.
- [167] Ö. Ç. Mutlu and T. Zeng, ‘Challenges and Opportunities of Modeling Biomass Gasification in Aspen Plus: A Review’, *Chemical Engineering & Technology*, vol. 43, no. 9, pp. 1674–1689, 2020, doi: 10.1002/ceat.202000068.
- [168] ‘Fuels - Higher and Lower Calorific Values’. Accessed: Sep. 29, 2023. [Online]. Available: https://www.engineeringtoolbox.com/fuels-higher-calorific-values-d_169.html
- [169] V. Marcantonio, E. Bocci, J. P. Ouweltjes, L. Del Zotto, and D. Monarca, ‘Evaluation of sorbents for high temperature removal of tars, hydrogen sulphide, hydrogen chloride and ammonia from biomass-derived syngas by using Aspen Plus’, *International Journal of Hydrogen Energy*, vol. 45, no. 11, pp. 6651–6662, Feb. 2020, doi: 10.1016/j.ijhydene.2019.12.142.
- [170] Y. Zhang and Y. Liu, ‘Numerical Simulation of Hydrogen Combustion: Global Reaction Model and Validation’, *Front. Energy Res.*, vol. 5, p. 31, Nov. 2017, doi: 10.3389/fenrg.2017.00031.
- [171] S. A. Channiwala and P. P. Parikh, ‘A uni®ed correlation for estimating HHV of solid, liquid and gaseous fuelsq’, p. 13, 2002.

- [172] T. B. Reed, 'Principles and Technology of Biomass Gasification', in *Advances in Solar Energy: An Annual Review of Research and Development Volume 2*, K. W. Böer and J. A. Duffie, Eds., Boston, MA: Springer US, 1985, pp. 125–174. doi: 10.1007/978-1-4613-9951-3_3.
- [173] S. W. Han *et al.*, 'Gasification characteristics of waste plastics (SRF) in a bubbling fluidized bed: Use of activated carbon and olivine for tar removal and the effect of steam/carbon ratio', *Fuel*, vol. 314, p. 123102, Apr. 2022, doi: 10.1016/j.fuel.2021.123102.
- [174] P. García-Bacaicoa, J. F. Mastral, J. Ceamanos, C. Berrueco, and S. Serrano, 'Gasification of biomass/high density polyethylene mixtures in a downdraft gasifier', *Bioresource Technology*, vol. 99, no. 13, pp. 5485–5491, Sep. 2008, doi: 10.1016/j.biortech.2007.11.003.
- [175] A. C. (Thanos) Bourtsalas and N. J. Themelis, 'Materials and energy recovery at six European MBT plants', *Waste Management*, vol. 141, pp. 79–91, Mar. 2022, doi: 10.1016/j.wasman.2022.01.024.
- [176] G. Biancini, R. Moradi, L. Cioccolanti, B. Marchetti, M. Moglie, and L. Del Zotto, 'A general model for air gasification of heterogenous municipal solid waste', *Energy Conversion and Management*, vol. 278, p. 116749, Feb. 2023, doi: 10.1016/j.enconman.2023.116749.
- [177] J. Malinauskaite *et al.*, 'Municipal solid waste management and waste-to-energy in the context of a circular economy and energy recycling in Europe', *Energy*, vol. 141, pp. 2013–2044, Dec. 2017, doi: 10.1016/j.energy.2017.11.128.
- [178] R. Moradi, L. Cioccolanti, L. Del Zotto, and M. Renzi, 'Comparative sensitivity analysis of micro-scale gas turbine and supercritical CO₂ systems with bottoming organic Rankine cycles fed by the biomass gasification for decentralized trigeneration', *Energy*, vol. 266, p. 126491, Mar. 2023, doi: 10.1016/j.energy.2022.126491.
- [179] J. Ahrenfeldt, T. P. Thomsen, U. Henriksen, and L. R. Clausen, 'Biomass gasification cogeneration – A review of state of the art technology and near future perspectives', *Applied Thermal Engineering*, vol. 50, no. 2, pp. 1407–1417, Feb. 2013, doi: 10.1016/j.applthermaleng.2011.12.040.
- [180] D. Perrone, T. Castiglione, P. Morrone, F. Pantano, and S. Bova, 'Numerical and experimental assessment of a micro-combined cooling, heating, and power (CCHP) system based on biomass gasification', *Applied Thermal Engineering*, vol. 219, p. 119600, Jan. 2023, doi: 10.1016/j.applthermaleng.2022.119600.
- [181] M. Husmann, C. Hochenauer, X. Meng, W. D. Jong, and T. Kienberger, 'Evaluation of Sorbents for High Temperature In Situ Desulfurization of Biomass-Derived Syngas', *Energy Fuels*, vol. 28, no. 4, pp. 2523–2534, Apr. 2014, doi: 10.1021/ef402254x.
- [182] S. Cheah, D. L. Carpenter, and K. A. Magrini-Bair, 'Review of Mid- to High-Temperature Sulfur Sorbents for Desulfurization of Biomass- and Coal-derived Syngas', *Energy Fuels*, vol. 23, no. 11, pp. 5291–5307, Nov. 2009, doi: 10.1021/ef900714q.
- [183] A. V. Shah, V. K. Srivastava, S. S. Mohanty, and S. Varjani, 'Municipal solid waste as a sustainable resource for energy production: State-of-the-art review', *Journal of Environmental Chemical Engineering*, vol. 9, no. 4, p. 105717, Aug. 2021, doi: 10.1016/j.jece.2021.105717.
- [184] A. B. Trindade *et al.*, 'Advanced exergy analysis and environmental assesment of the steam cycle of an incineration system of municipal solid waste with energy recovery', *Energy Conversion and Management*, vol. 157, pp. 195–214, Feb. 2018, doi: 10.1016/j.enconman.2017.11.083.
- [185] Y. Liu, C. Liao, Y. Tang, J. Tang, Y. Sun, and X. Ma, 'Techno-environmental-economic evaluation of the small-scale municipal solid waste (MSW) gasification-based and incineration-based power generation plants', *Journal of the Taiwan Institute of Chemical Engineers*, vol. 141, p. 104594, Dec. 2022, doi: 10.1016/j.jtice.2022.104594.

- [186] C. Wieland *et al.*, ‘Innovations for organic Rankine cycle power systems: Current trends and future perspectives’, *Applied Thermal Engineering*, vol. 225, p. 120201, May 2023, doi: 10.1016/j.applthermaleng.2023.120201.
- [187] T. Yatsunthea and N. Chaiyat, ‘A very small power plant – Municipal waste of the organic Rankine cycle and incinerator from medical and municipal wastes’, *Thermal Science and Engineering Progress*, vol. 18, p. 100555, Aug. 2020, doi: 10.1016/j.tsep.2020.100555.
- [188] E. Özahi, A. Tozlu, and A. Abuşoğlu, ‘Thermoeconomic multi-objective optimization of an organic Rankine cycle (ORC) adapted to an existing solid waste power plant’, *Energy Conversion and Management*, vol. 168, pp. 308–319, Jul. 2018, doi: 10.1016/j.enconman.2018.04.103.
- [189] A. Ustaoglu, H. Torlaklı, A. Ergün, E. Erdoğan, and M. Emin Akay, ‘Advanced exergy analysis of an integrated solid waste fueled cogeneration system based on organic Rankine Cycle for different working fluids’, *Energy Conversion and Management*, vol. 270, p. 116294, Oct. 2022, doi: 10.1016/j.enconman.2022.116294.
- [190] H. Li, Y. Zhang, M. Yao, Y. Yang, W. Han, and W. Bai, ‘Design assessment of a 5 MW fossil-fired supercritical CO₂ power cycle pilot loop’, *Energy*, vol. 174, pp. 792–804, May 2019, doi: 10.1016/j.energy.2019.02.178.
- [191] M. T. White, G. Bianchi, L. Chai, S. A. Tassou, and A. I. Sayma, ‘Review of supercritical CO₂ technologies and systems for power generation’, *Applied Thermal Engineering*, vol. 185, p. 116447, Feb. 2021, doi: 10.1016/j.applthermaleng.2020.116447.
- [192] R. González-Almenara, P. Rodríguez De Arriba, F. Crespi, D. Sánchez, A. Muñoz, and T. Sánchez-Lencero, ‘Supercritical Carbon Dioxide Cycles for Concentrated Solar Power Plants: A Possible Alternative for Solar Desalination’, *Processes*, vol. 10, no. 1, p. 72, Dec. 2021, doi: 10.3390/pr10010072.
- [193] A. Yu, W. Su, X. Lin, and N. Zhou, ‘Recent trends of supercritical CO₂ Brayton cycle: Bibliometric analysis and research review’, *Nuclear Engineering and Technology*, vol. 53, no. 3, pp. 699–714, Mar. 2021, doi: 10.1016/j.net.2020.08.005.
- [194] J. Stepanek, J. Syblik, and S. Entler, ‘Axial sCO₂ high-performance turbines parametric design’, *Energy Conversion and Management*, vol. 274, p. 116418, Dec. 2022, doi: 10.1016/j.enconman.2022.116418.
- [195] Y. Cao *et al.*, ‘Multi-objective bat optimization for a biomass gasifier integrated energy system based on 4E analyses’, *Applied Thermal Engineering*, vol. 196, p. 117339, Sep. 2021, doi: 10.1016/j.applthermaleng.2021.117339.
- [196] H. Lund *et al.*, ‘The status of 4th generation district heating: Research and results’, *Energy*, vol. 164, pp. 147–159, Dec. 2018, doi: 10.1016/j.energy.2018.08.206.
- [197] A. Tozlu, A. Abusoglu, E. Ozahi, and A. Anvari-Moghaddam, ‘Municipal solid waste-based district heating and electricity production: A case study’, *Journal of Cleaner Production*, vol. 297, p. 126495, May 2021, doi: 10.1016/j.jclepro.2021.126495.
- [198] S. Buffa, M. Cozzini, M. D’Antoni, M. Baratieri, and R. Fedrizzi, ‘5th generation district heating and cooling systems: A review of existing cases in Europe’, *Renewable and Sustainable Energy Reviews*, vol. 104, pp. 504–522, Apr. 2019, doi: 10.1016/j.rser.2018.12.059.
- [199] L. Cioccolanti, M. Renzi, G. Comodi, and M. Rossi, ‘District heating potential in the case of low-grade waste heat recovery from energy intensive industries’, *Applied Thermal Engineering*, vol. 191, p. 116851, Jun. 2021, doi: 10.1016/j.applthermaleng.2021.116851.
- [200] ‘Termovalorizzatore Bologna | Herambiente’, 2022, [Online]. Available: <https://ha.gruppohera.it/lista-impianti/termovalorizzatore-di-bologna>
- [201] M. Catterin, ‘Abbattimento degli ossidi di azoto in un impianto di termovalorizzazione per rifiuti speciali: il caso del forno F3 (Centro Ecologico Baiona - Ravenna).’, 2017, [Online]. Available: <http://amslaurea.unibo.it/12658/>

- [202] Y. A. Çengel, *Heat and mass transfer : Fundamentals & applications*, Sixth edition. in *Heat and mass transfer : Fundamentals & applications*. New York: McGraw-Hill Education, 2020.
- [203] A. Cavallini, ‘Heat transfer and heat exchangers’, in *Organic Rankine Cycle (ORC) Power Systems*, Elsevier, 2017, pp. 397–470. doi: 10.1016/B978-0-08-100510-1.00013-2.
- [204] E. Macchi and M. Astolfi, ‘Axial flow turbines for Organic Rankine Cycle applications’, in *Organic Rankine Cycle (ORC) Power Systems*, Elsevier, 2017, pp. 299–319. doi: 10.1016/B978-0-08-100510-1.00009-0.
- [205] ‘Absorption chiller catalogue LG’, 2015. [Online]. Available: https://www.lg.com/global/business/download/resources/sac/Catalogue_Absorption%20Chillers_ENG_F.pdf
- [206] I. Vankeirsbilck, B. Vanslambrouck, S. Gusev, and M. D. Paepe, ‘Organic Rankine Cycle as Efficient Alternative to Steam Cycle for Small Scale Power Generation’.
- [207] ‘OLIO DIATERMICO’, 2021, [Online]. Available: <https://www.therminol.com/sites/therminol/files/documents/TF8691.pdf>
- [208] T. Tartière and M. Astolfi, ‘A World Overview of the Organic Rankine Cycle Market’, *Energy Procedia*, vol. 129, pp. 2–9, Sep. 2017, doi: 10.1016/j.egypro.2017.09.159.
- [209] ‘ORC units for Waste to Energy process | TURBODEN’, [Online]. Available: <https://www.turboden.com/solutions/1055/waste-to-energy>
- [210] X. Zhang and Y. Li, ‘An examination of super dry working fluids used in regenerative organic Rankine cycles’, *Energy*, vol. 263, p. 125931, Jan. 2023, doi: 10.1016/j.energy.2022.125931.
- [211] R. Vescovo and E. Spagnoli, ‘High Temperature ORC Systems’, *Energy Procedia*, vol. 129, pp. 82–89, Sep. 2017, doi: 10.1016/j.egypro.2017.09.160.
- [212] N. A. Lai, M. Wendland, and J. Fischer, ‘Working fluids for high-temperature organic Rankine cycles’, *Energy*, vol. 36, no. 1, pp. 199–211, Jan. 2011, doi: 10.1016/j.energy.2010.10.051.
- [213] ‘Fundamentals of Heat and Mass Transfer, 8th Edition | Wiley’, Wiley.com. Accessed: Oct. 01, 2023. [Online]. Available: <https://www.wiley.com/en-us/Fundamentals+of+Heat+and+Mass+Transfer%2C+8th+Edition-p-9781119537342>
- [214] Y. Ahn *et al.*, ‘Review of supercritical CO₂ power cycle technology and current status of research and development’, *Nuclear Engineering and Technology*, vol. 47, no. 6, pp. 647–661, Oct. 2015, doi: 10.1016/j.net.2015.06.009.
- [215] H. Lund *et al.*, ‘4th Generation District Heating (4GDH)’, *Energy*, vol. 68, pp. 1–11, Apr. 2014, doi: 10.1016/j.energy.2014.02.089.
- [216] M. Yuan, J. Z. Thellufsen, P. Sorknæs, H. Lund, and Y. Liang, ‘District heating in 100% renewable energy systems: Combining industrial excess heat and heat pumps’, *Energy Conversion and Management*, vol. 244, p. 114527, Sep. 2021, doi: 10.1016/j.enconman.2021.114527.
- [217] P. Sorknæs *et al.*, ‘The benefits of 4th generation district heating in a 100% renewable energy system’, *Energy*, vol. 213, p. 119030, Dec. 2020, doi: 10.1016/j.energy.2020.119030.
- [218] F. Pagliaro, ‘Rapporto Annuale sulla Certificazione Energetica degli Edifici 2022’.
- [219] ‘DECRETO DEL PRESIDENTE DELLA REPUBBLICA 26 agosto 1993 , n. 412’, 1993.
- [220] ‘ARERA - Elettricità: bonus sociale’, 2008, [Online]. Available: https://www.arera.it/it/com_stampa/08/080902.htm
- [221] G. Fan, Y. Du, H. Li, and Y. Dai, ‘Off-design behavior investigation of the combined supercritical CO₂ and organic Rankine cycle’, *Energy*, vol. 237, p. 121529, Dec. 2021, doi: 10.1016/j.energy.2021.121529.
- [222] R. D. O. Neto, C. A. R. Sotomonte, and C. J. R. Coronado, ‘Off-design model of an ORC system for waste heat recovery of an internal combustion engine’, *Applied Thermal Engineering*, vol. 195, p. 117188, Aug. 2021, doi: 10.1016/j.applthermaleng.2021.117188.

- [223] P. Ungar, Z. Özcan, G. Manfrida, Ö. Ekici, and L. Talluri, ‘Off-Design Modelling of ORC Turbines for Geothermal Application’, *E3S Web Conf.*, vol. 312, p. 11015, 2021, doi: 10.1051/e3sconf/202131211015.
- [224] D. R. McIlveen-Wright *et al.*, ‘A comparison of circulating fluidised bed combustion and gasification power plant technologies for processing mixtures of coal, biomass and plastic waste’, *Fuel Processing Technology*, vol. 87, no. 9, pp. 793–801, Sep. 2006, doi: 10.1016/j.fuproc.2006.04.002.
- [225] L. Chen, S. Z. Yong, and A. F. Ghoniem, ‘Oxy-fuel combustion of pulverized coal: Characterization, fundamentals, stabilization and CFD modeling’, *Progress in Energy and Combustion Science*, vol. 38, no. 2, pp. 156–214, Apr. 2012, doi: 10.1016/j.pecs.2011.09.003.
- [226] E. Dahlquist, M. Naqvi, E. Thorin, J. Yan, K. Kyprianidis, and P. Hartwell, ‘Experimental and numerical investigation of pellet and black liquor gasification for polygeneration plant’, *Applied Energy*, vol. 204, pp. 1055–1064, Oct. 2017, doi: 10.1016/j.apenergy.2017.05.008.
- [227] A. Haaker, “‘The world’s largest boiler for waste incineration’”, Bioenergy International. Accessed: Oct. 03, 2023. [Online]. Available: <https://bioenergyinternational.com/the-worlds-largest-boiler-for-waste-incineration/>
- [228] ‘The world’s biggest waste fired boiler at Mälarenergi’s power plant’. Accessed: Oct. 03, 2023. [Online]. Available: <https://www.valmet.com/about-us/references/energy-references/the-worlds-biggest-waste-fired-boiler-at-malarenergis-power-plant/>
- [229] ‘STEAG EBSILON’, Ebsilon. Accessed: Oct. 04, 2023. [Online]. Available: <https://www.ebsilon.com/en/>
- [230] A. Blanco and F. Chejne, ‘Modeling and simulation of biomass fast pyrolysis in a fluidized bed reactor’, *Journal of Analytical and Applied Pyrolysis*, vol. 118, pp. 105–114, Mar. 2016, doi: 10.1016/j.jaap.2016.01.003.
- [231] X. Tang *et al.*, ‘Dynamic pyrolysis behaviors, products, and mechanisms of waste rubber and polyurethane bicycle tires’, *Journal of Hazardous Materials*, vol. 402, p. 123516, Jan. 2021, doi: 10.1016/j.jhazmat.2020.123516.
- [232] S. Sobek and S. Werle, ‘Isoconversional determination of the apparent reaction models governing pyrolysis of wood, straw and sewage sludge, with an approach to rate modelling’, *Renewable Energy*, vol. 161, pp. 972–987, Dec. 2020, doi: 10.1016/j.renene.2020.07.112.
- [233] P. Mellin, E. Kantarelis, and W. Yang, ‘Computational fluid dynamics modeling of biomass fast pyrolysis in a fluidized bed reactor, using a comprehensive chemistry scheme’, *Fuel*, vol. 117, pp. 704–715, Jan. 2014, doi: 10.1016/j.fuel.2013.09.009.
- [234] Q. Xiong *et al.*, ‘Overview of Computational Fluid Dynamics Simulation of Reactor-Scale Biomass Pyrolysis’, *ACS Sustainable Chem. Eng.*, vol. 5, no. 4, pp. 2783–2798, Apr. 2017, doi: 10.1021/acssuschemeng.6b02634.
- [235] S. Skogestad, *Chemical and energy process engineering*. CRC press, 2008.
- [236] ‘REFPROP’, *NIST*, Apr. 2013, Accessed: Oct. 06, 2023. [Online]. Available: <https://www.nist.gov/srd/refprop>
- [237] ‘Welcome to CoolProp — CoolProp 6.5.0 documentation’. Accessed: Oct. 06, 2023. [Online]. Available: <http://www.coolprop.org/>
- [238] ‘Optimization Toolbox Documentation - MathWorks Italia’. Accessed: Oct. 06, 2023. [Online]. Available: https://it.mathworks.com/help/optim/index.html?searchHighlight=optimization%20toolbox&s_tid=srchtitle_support_results_1_optimization%20toolbox
- [239] R. Ferretti, ‘Appunti del corso di Analisi Numerica’.
- [240] ‘Choose an ODE Solver - MATLAB & Simulink - MathWorks Italia’. Accessed: Oct. 06, 2023. [Online]. Available: https://it.mathworks.com/help/matlab/math/choose-an-ode-solver.html?searchHighlight=ode%20example&s_tid=srchtitle_support_results_3_ode%20example

- [241] ‘Pyrolysis Reactors - Task 34’. Accessed: Dec. 20, 2023. [Online]. Available: <https://task34.ieabioenergy.com/pyrolysis-reactors/>
- [242] D. Humbird, A. Trendewicz, R. Braun, and A. Dutta, ‘One-Dimensional Biomass Fast Pyrolysis Model with Reaction Kinetics Integrated in an Aspen Plus Biorefinery Process Model’, *ACS Sustainable Chem. Eng.*, vol. 5, no. 3, pp. 2463–2470, Mar. 2017, doi: 10.1021/acssuschemeng.6b02809.
- [243] W. Jerzak, M. Reinmüller, and A. Magdziarz, ‘Estimation of the heat required for intermediate pyrolysis of biomass’, *Clean Techn Environ Policy*, vol. 24, no. 10, pp. 3061–3075, Dec. 2022, doi: 10.1007/s10098-022-02391-1.
- [244] H. V. de Mendonça, M. H. Otenio, L. Marchão, A. Lomeu, D. S. de Souza, and A. Reis, ‘Biofuel recovery from microalgae biomass grown in dairy wastewater treated with activated sludge: The next step in sustainable production’, *Science of The Total Environment*, vol. 824, p. 153838, Jun. 2022, doi: 10.1016/j.scitotenv.2022.153838.
- [245] S. Mandal and N. Mallick, ‘Waste Utilization and Biodiesel Production by the Green Microalga *Scenedesmus obliquus*’, *Appl Environ Microbiol*, vol. 77, no. 1, pp. 374–377, Jan. 2011, doi: 10.1128/AEM.01205-10.
- [246] K. J. Choi, Z. Nakhost, E. Barzana, and M. Karel, ‘Lipid content and fatty acid composition of green algae *scenedesmus obliquus* grown in a constant cell density apparatus’, *Food Biotechnology*, vol. 1, no. 1, pp. 117–128, Jan. 1987, doi: 10.1080/08905438709549660.
- [247] ‘CCAP’. Accessed: Oct. 16, 2023. [Online]. Available: <https://www.ccap.ac.uk/>
- [248] ‘BioBench - Biostream International’. Accessed: Oct. 16, 2023. [Online]. Available: <https://www.biostream-international.com/biobench/>
- [249] ‘FTC 120 Frigotermostato’. Accessed: Oct. 16, 2023. [Online]. Available: <https://www.velp.com/it-it/ftc-120-frigotermostato.aspx>
- [250] ‘MQ-500: Full-Spectrum Quantum Meter’, Apogee Instruments, Inc. Accessed: Oct. 16, 2023. [Online]. Available: <https://www.apogeeinstruments.com/mq-500-full-spectrum-quantum-meter/>
- [251] ‘Counting chambers, Bürker-Türk pattern, BLAUBRAND® | BRAND’. Accessed: Oct. 16, 2023. [Online]. Available: <https://shop.brand.de/en/p955>
- [252] ‘TCN 50 PLUS- Natural Oven, capacity 50LT, with 7 programs x 10 steps’. Accessed: Oct. 16, 2023. [Online]. Available: <https://www.giorgiobormac.com/catalogo/modelli/41100002/stufa-tcn-50-plus-a-convezione-naturale.htm>
- [253] ‘Compact photometer PF-12Plus’, MACHEREY-NAGEL. Accessed: Oct. 17, 2023. [Online]. Available: <https://www.mn-net.com/compact-photometer-pf-12plus-919250>
- [254] ‘Tube test NANOCOLOR total-Nitrogen TNb 60’, MACHEREY-NAGEL. Accessed: Oct. 17, 2023. [Online]. Available: <https://www.mn-net.com/tube-test-nanocolor-total-nitrogen-tnb-60-985092>
- [255] ‘Tube test NANOCOLOR ortho- and total Phosphate LR 1’, MACHEREY-NAGEL. Accessed: Oct. 17, 2023. [Online]. Available: <https://www.mn-net.com/tube-test-nanocolor-ortho-and-total-phosphate-lr-1-985095>
- [256] ‘F.A.M.E. Mix C14 - C22, certified reference material, wt. % (varied conc.), ampule of 100 mg’. Accessed: Oct. 17, 2023. [Online]. Available: <http://www.sigmaaldrich.com/>
- [257] M. M. Basova, ‘Fatty acid composition of lipids in microalgae’, *Inter J Algae*, vol. 7, no. 1, pp. 33–57, 2005, doi: 10.1615/InterJAlgae.v7.i1.30.
- [258] P. W. Behrens and D. J. Kyle, ‘MICROALGAE AS A SOURCE OF FATTY ACIDS’, *J Food Lipids*, vol. 3, no. 4, pp. 259–272, Dec. 1996, doi: 10.1111/j.1745-4522.1996.tb00073.x.
- [259] Z. Hussain and R. Kumar, ‘Esterification of free fatty acids: experiments, kinetic modeling, simulation & optimization’, *International Journal of Green Energy*, vol. 15, no. 11, pp. 629–640, Sep. 2018, doi: 10.1080/15435075.2018.1525736.

- [260] D. K. Sharma *et al.*, ‘UPLC-MS analysis of *Chlamydomonas reinhardtii* and *Scenedesmus obliquus* lipid extracts and their possible metabolic roles’, *J Appl Phycol*, vol. 27, no. 3, pp. 1149–1159, Jun. 2015, doi: 10.1007/s10811-014-0407-2.
- [261] L. Yao, J. A. Gerde, S.-L. Lee, T. Wang, and K. A. Harrata, ‘Microalgae Lipid Characterization’, *J. Agric. Food Chem.*, vol. 63, no. 6, pp. 1773–1787, Feb. 2015, doi: 10.1021/jf5050603.
- [262] W.-C. Wang, T. L. Turner, L. F. Stikeleather, and W. L. Roberts, ‘Exploration of process parameters for continuous hydrolysis of canola oil, camelina oil and algal oil’, *Chemical Engineering and Processing: Process Intensification*, vol. 57–58, pp. 51–58, Jul. 2012, doi: 10.1016/j.cep.2012.04.001.
- [263] E. d’Avila Cavalcanti-Oliveira, P. R. da Silva, A. P. Ramos, D. A. G. Aranda, and D. M. G. Freire, ‘Study of Soybean Oil Hydrolysis Catalyzed by *Thermomyces lanuginosus* Lipase and Its Application to Biodiesel Production via Hydroesterification’, *Enzyme Research*, vol. 2011, pp. 1–8, Oct. 2011, doi: 10.4061/2011/618692.
- [264] R. L. Holliday, J. W. King, and G. R. List, ‘Hydrolysis of Vegetable Oils in Sub- and Supercritical Water’, *Ind. Eng. Chem. Res.*, vol. 36, no. 3, pp. 932–935, Mar. 1997, doi: 10.1021/ie960668f.
- [265] L. Chen, T. Liu, W. Zhang, X. Chen, and J. Wang, ‘Biodiesel production from algae oil high in free fatty acids by two-step catalytic conversion’, *Bioresource Technology*, vol. 111, pp. 208–214, May 2012, doi: 10.1016/j.biortech.2012.02.033.
- [266] P. S. Sastry and M. Kates, ‘Hydrolysis of Monogalactosyl and Digalactosyl Diglycerides by Specific Enzymes in Runner-Bean Leaves *’, *Biochemistry*, vol. 3, no. 9, pp. 1280–1287, Sep. 1964, doi: 10.1021/bi00897a016.
- [267] S. N. Gebremariam and J. M. Marchetti, ‘Techno-economic feasibility of producing biodiesel from acidic oil using sulfuric acid and calcium oxide as catalysts’, *Energy Conversion and Management*, vol. 171, pp. 1712–1720, Sep. 2018, doi: 10.1016/j.enconman.2018.06.105.
- [268] D. Constantinescu and J. Gmehling, ‘Further Development of Modified UNIFAC (Dortmund): Revision and Extension 6’, *J. Chem. Eng. Data*, vol. 61, no. 8, pp. 2738–2748, Aug. 2016, doi: 10.1021/acs.jced.6b00136.
- [269] N. Bakuei, G. Amini, G. D. Najafpour, M. Jahanshahi, and M. Mohammadi, ‘Optimal cultivation of *Scenedesmus* sp. microalgae in a bubble column photobioreactor’.
- [270] R. Qiu, S. Gao, P. A. Lopez, and K. L. Ogden, ‘Effects of pH on cell growth, lipid production and CO₂ addition of microalgae *Chlorella sorokiniana*’, *Algal Research*, vol. 28, pp. 192–199, Dec. 2017, doi: 10.1016/j.algal.2017.11.004.
- [271] H. Miao, L. Sun, Q. Tian, S. Wang, and J. Wang, ‘Study on the Effect of Monochromatic Light on the Growth of the Red Tide Diatom *Skeletonema Costatum*’, *OPJ*, vol. 02, no. 03, pp. 152–156, 2012, doi: 10.4236/opj.2012.23022.
- [272] ‘Prism - GraphPad’. Accessed: Oct. 19, 2023. [Online]. Available: <https://www.graphpad.com/features>
- [273] K. Kittiratanapiboon, N. Jeyashoke, and K. Krisnangkura, ‘Forecasting Retention Times of Fatty Acid Methyl Esters in Temperature-Programmed Gas Chromatography’, *Journal of Chromatographic Science*, vol. 36, no. 11, pp. 541–546, Nov. 1998, doi: 10.1093/chromsci/36.11.541.
- [274] S. Nilratnisakorn, N. Jeyashoke, and K. Krisnangkura, ‘Effect of Column Length on Forecasted Retention Times and Carbon Numbers in an Isothermal and Temperature-programmed Gas Chromatography’, 1999.
- [275] R. Chaudhary, A. K. Dikshit, and Y. W. Tong, ‘Carbon-dioxide biofixation and phycoremediation of municipal wastewater using *Chlorella vulgaris* and *Scenedesmus obliquus*’, *Environ Sci Pollut Res*, vol. 25, no. 21, pp. 20399–20406, Jul. 2018, doi: 10.1007/s11356-017-9575-3.

- [276] ‘CTI Comitato Termotecnico Italiano’. Accessed: Oct. 21, 2023. [Online]. Available: <https://www.cti2000.it/biodiesel/index.php?contid=55>
- [277] ‘GME - Statistiche - dati di sintesi MPE-MGP’. Accessed: Oct. 21, 2023. [Online]. Available: <https://www.mercatoelettrico.org/it/Statistiche/ME/DatiSintesi.aspx>
- [278] ‘ARERA - Prezzi medi di vendita del gas sul mercato finale al netto delle imposte’. Accessed: Oct. 21, 2023. [Online]. Available: <https://www.arera.it/it/dati/gp35.htm>
- [279] J. H. Moreno Osorio, G. Pinto, A. Pollio, L. Frunzo, P. N. L. Lens, and G. Esposito, ‘Start-up of a nutrient removal system using *Scenedesmus vacuolatus* and *Chlorella vulgaris* biofilms’, *Bioresour. Bioprocess.*, vol. 6, no. 1, p. 27, Dec. 2019, doi: 10.1186/s40643-019-0259-3.
- [280] J. Umamaheswari and S. Shanthakumar, ‘Efficacy of microalgae for industrial wastewater treatment: a review on operating conditions, treatment efficiency and biomass productivity’, *Rev Environ Sci Biotechnol*, vol. 15, no. 2, pp. 265–284, Jun. 2016, doi: 10.1007/s11157-016-9397-7.
- [281] A. Ferreira *et al.*, ‘*Scenedesmus obliquus* mediated brewery wastewater remediation and CO₂ biofixation for green energy purposes’, *Journal of Cleaner Production*, vol. 165, pp. 1316–1327, Nov. 2017, doi: 10.1016/j.jclepro.2017.07.232.
- [282] A. T. Nair, J. Senthilnathan, and S. M. S. Nagendra, ‘Application of the phycoremediation process for tertiary treatment of landfill leachate and carbon dioxide mitigation’, *Journal of Water Process Engineering*, vol. 28, pp. 322–330, Apr. 2019, doi: 10.1016/j.jwpe.2019.02.017.
- [283] D. T. Zewdie and A. Y. Ali, ‘Cultivation of microalgae for biofuel production: coupling with sugarcane-processing factories’, *Energ Sustain Soc*, vol. 10, no. 1, p. 27, Dec. 2020, doi: 10.1186/s13705-020-00262-5.
- [284] ‘ISO 14040’. 2006.
- [285] L. Rigamonti, M. Grosso, and M. Giugliano, ‘Life cycle assessment of sub-units composing a MSW management system’, *Journal of Cleaner Production*, vol. 18, no. 16–17, pp. 1652–1662, Nov. 2010, doi: 10.1016/j.jclepro.2010.06.029.
- [286] I.-R. Istrate, D. Iribarren, J.-L. Gálvez-Martos, and J. Dufour, ‘Review of life-cycle environmental consequences of waste-to-energy solutions on the municipal solid waste management system’, *Resources, Conservation and Recycling*, vol. 157, p. 104778, Jun. 2020, doi: 10.1016/j.resconrec.2020.104778.
- [287] S. N. M. Menikpura, J. Sang-Arun, and M. Bengtsson, ‘Integrated Solid Waste Management: an approach for enhancing climate co-benefits through resource recovery’, *Journal of Cleaner Production*, vol. 58, pp. 34–42, Nov. 2013, doi: 10.1016/j.jclepro.2013.03.012.
- [288] E. C. Gentil *et al.*, ‘Models for waste life cycle assessment: Review of technical assumptions’, *Waste Management*, vol. 30, no. 12, pp. 2636–2648, Dec. 2010, doi: 10.1016/j.wasman.2010.06.004.
- [289] ‘ecoinvent Database’, ecoinvent. Accessed: Jul. 14, 2022. [Online]. Available: <https://ecoinvent.org/the-ecoinvent-database/>
- [290] G. Wernet, C. Bauer, B. Steubing, J. Reinhard, E. Moreno-Ruiz, and B. Weidema, ‘The ecoinvent database version 3 (part I): overview and methodology’, *Int J Life Cycle Assess*, vol. 21, no. 9, pp. 1218–1230, Sep. 2016, doi: 10.1007/s11367-016-1087-8.
- [291] ‘CML-IA Characterisation Factors’, Leiden University. Accessed: Jul. 14, 2022. [Online]. Available: <https://www.universiteitleiden.nl/en/research/research-output/science/cml-ia-characterisation-factors>
- [292] L. Rigamonti, A. Falbo, and M. Grosso, ‘Improving integrated waste management at the regional level: The case of Lombardia’, *Waste Manag Res*, vol. 31, no. 9, pp. 946–953, Sep. 2013, doi: 10.1177/0734242X13493957.
- [293] M. Giugliano, S. Cernuschi, M. Grosso, and L. Rigamonti, ‘Material and energy recovery in integrated waste management systems. An evaluation based on life cycle assessment’, *Waste*

- Management*, vol. 31, no. 9–10, pp. 2092–2101, Sep. 2011, doi: 10.1016/j.wasman.2011.02.029.
- [294] A. Rabl, A. Benoist, D. Dron, B. Peuportier, J. V. Spadaro, and A. Zoughaib, ‘How to account for CO₂ emissions from biomass in an LCA’, *Int J Life Cycle Assess*, vol. 12, no. 5, pp. 281–281, Jul. 2007, doi: 10.1065/lca2007.06.347.
- [295] B. Dastjerdi, V. Strezov, M. A. Rajaeifar, R. Kumar, and M. Behnia, ‘A systematic review on life cycle assessment of different waste to energy valorization technologies’, *Journal of Cleaner Production*, vol. 290, p. 125747, Mar. 2021, doi: 10.1016/j.jclepro.2020.125747.
- [296] S. You *et al.*, ‘A critical review on sustainable biochar system through gasification: Energy and environmental applications’, *Bioresource Technology*, vol. 246, pp. 242–253, Dec. 2017, doi: 10.1016/j.biortech.2017.06.177.
- [297] T. R. Ayodele, A. S. O. Ogunjuyigbe, and M. A. Alao, ‘Life cycle assessment of waste-to-energy (WtE) technologies for electricity generation using municipal solid waste in Nigeria’, *Applied Energy*, vol. 201, pp. 200–218, Sep. 2017, doi: 10.1016/j.apenergy.2017.05.097.
- [298] ‘MODULO FOTOVOLTAICO HF330KA MONOCRISTALLINO 330W 24V’. Accessed: Sep. 16, 2022. [Online]. Available: <http://www.solarenergypoint.it/shop/sun-earth-hf330ka-modulo-fotovoltaico-monocristallino-330w>
- [299] ‘Life Cycle Assessment of solar energy systems for the provision of heating, cooling and electricity in buildings: A comparative analysis | Elsevier Enhanced Reader’. Accessed: Sep. 17, 2022. [Online]. Available: <https://reader.elsevier.com/reader/sd/pii/S0196890422001984?token=F87483EE168BDA19D5E55C422931C19880FBAD2ADD16F90DC880933EC198A03D50C231DEDBDA4FCAE455CECAC4383515&originRegion=eu-west-1&originCreation=20220917085646>
- [300] ‘Integrating climate change and energy mix scenarios in LCA of buildings and districts | Elsevier Enhanced Reader’. Accessed: Sep. 17, 2022. [Online]. Available: <https://reader.elsevier.com/reader/sd/pii/S0306261916314830?token=DACD8C1FC2A4CB4281F9E0CC14D0F526AEB5B2F9D8FDDEF7F8D59437BD1984F213EF0051EE1166E66DA0A958AF1502A5&originRegion=eu-west-1&originCreation=20220917084708>
- [301] ‘Inceneritore F3 Rifiuti Urbani e Speciali di Ravenna - HERAmbiente’. Accessed: Sep. 19, 2022. [Online]. Available: https://ha.gruppohera.it/impianti/rifiuti_industriali/impianto_incenerimento_ravenna
- [302] K.-D. Kim *et al.*, ‘HCl removal characteristics of calcium hydroxide at the dry-type sorbent reaction accelerator using municipal waste incinerator flue gas at a real site’, *Korean J. Chem. Eng.*, vol. 34, no. 3, pp. 747–756, Mar. 2017, doi: 10.1007/s11814-016-0306-0.
- [303] M. Yumura and E. Furimsky, ‘Comparison of calcium oxide, zinc oxide, and iron(III) oxide hydrogen sulfide adsorbents at high temperatures’, *Ind. Eng. Chem. Proc. Des. Dev.*, vol. 24, no. 4, pp. 1165–1168, Oct. 1985, doi: 10.1021/i200031a045.
- [304] G. Biancini, M. Moglie, B. Marchetti, and L. Cioccolanti, ‘Life Cycle Impact Assessment of Municipal Solid Waste Management Systems: Improved design for environmental footprint minimization’, in *2022 International Conference on Renewable Energies and Smart Technologies (REST)*, Tirana, Albania: IEEE, Jul. 2022, pp. 1–5. doi: 10.1109/REST54687.2022.10022921.